CENTRAL RESEARCH LIBRARY

ORNL-5150

Cy. 1

Mechanical Properties Test Data for Structural Materials Quarterly Progress Report for Period Ending April 30, 1976

[redacted]

OAK RIDGE NATIONAL LABORATORY
CENTRAL RESEARCH LIBRARY
DOCUMENT COLLECTION
LIBRARY LOAN COPY
DO NOT TRANSFER TO ANOTHER PERSON
If you wish someone else to see this document, send in name with document and the library will arrange a loan.
UCN-7969
(3 3-67)

OAK RIDGE NATIONAL LABORATORY
OPERATED BY UNION CARBIDE CORPORATION FOR THE ENERGY RESEARCH AND DEVELOPMENT ADMINISTRATION

Printed in the United States of America. Available from
the Energy Research and Development Administration,
Technical Information Center
P.O. Box 62, Oak Ridge, Tennessee 37830
Price: Printed Copy $12.00 ; Microfiche $2.25

This report was prepared as an account of work sponsored by the United States Government. Neither the United States nor the Energy Research and Development Administration/United States Nuclear Regulatory Commission, nor any of their employees, nor any of their contractors, subcontractors, or their employees, makes any warranty, express or implied, or assumes any legal liability or responsibility for the accuracy, completeness or usefulness of any information, apparatus, product or process disclosed, or represents that its use would not infringe privately owned rights.

ORNL-5150
UC-79b, -h, -k
(Liquid Metal Fast
Breeder Reactors)

Contract No. W-7405-eng-26

METALS AND CERAMICS DIVISION

MECHANICAL PROPERTIES TEST DATA FOR STRUCTURAL MATERIALS QUARTERLY PROGRESS REPORT FOR PERIOD ENDING APRIL 30, 1976

Aerojet Nuclear Company
Argonne National Laboratory
Oak Ridge National Laboratory
Naval Research Laboratory
Hanford Engineering Development Laboratory
Westinghouse Advanced Reactors Division
University of Cincinnati
University of California at Los Angeles
General Electric Company

Compiled by M. R. Hill

JUNE 1976

OAK RIDGE NATIONAL LABORATORY
Oak Ridge, Tennessee 37830
operated by
UNION CARBIDE CORPORATION
for the
ENERGY RESEARCH AND DEVELOPMENT ADMINISTRATION

FOREWORD

This is the eleventh in a series of progress reports, the purpose of which is to record and distribute quarterly the collected results of all structural materials mechanical properties test programs sponsored by the Reactor Development and Demonstration Division of the Energy Research and Development Administration.

To be useful as resource documents, the reports in this series must be published and distributed in a timely manner to those in the reactor design and materials technology community who have a need of mechanical property test data for nuclear reactor and power plant applications. A test and material index is included to increase the effectiveness of the report.

Reports previously issued in this series are as follows: ORNL-4936, period ending October 31, 1973; ORNL-4948, period ending January 31, 1974; ORNL-4963, period ending April 30, 1974; ORNL-4998, period ending July 31, 1974; ORNL-5103, period ending October 31, 1974; ORNL-5104, period ending January 31, 1975; ORNL-5105, period ending April 30, 1975; ORNL-5106, period ending July 31, 1975; ORNL-5107, period ending October 31, 1975; and ORNL-5112 for period ending January 31, 1976. The next quarterly report will be for the period ending July 31, 1976, and contributions are due at ORNL by August 15, 1976.

W. R. Martin
Metals and Ceramics Division
Oak Ridge National Laboratory

CONTENTS

SUMMARY ix

1. AEROJET NUCLEAR COMPANY (No Report) 1

2. ARGONNE NATIONAL LABORATORY 3

2.1 INTRODUCTION 3

2.2 FRACTURE AND FATIGUE STUDIES ON STAINLESS STEELS 3

2.2.1 Statistical Analysis and Regression Fit of Elevated-Temperature Low-Cycle Fatigue Data on Type 304 Stainless Steel 3

2.2.2 A Unified and Mechanistic Approach to Creep-Fatigue Damage 34

2.2.2.1 Introduction 34

2.2.2.2 Basic Damage Equation 35

2.2.2.3 Application to Type 304 Stainless Steel 36

2.2.2.4 Conclusions 39

2.3 SODIUM EFFECTS ON LMFBR MATERIALS 40

2.3.1 Uniaxial Creep-Rupture Properties of Austenitic Stainless Steels 40

2.3.2 Influence of Sodium Environment on the Low-Cycle Fatigue Behavior of Austenitic Stainless Steels 48

2.4 REFERENCES 51

3. OAK RIDGE NATIONAL LABORATORY 55

3.1 INTRODUCTION 55

3.2 MECHANICAL PROPERTIES AND BEHAVIOR FOR STRUCTURAL MATERIALS 55

3.2.1 Mechanical Property Characterization of Type 316 Stainless Steel Reference Heat 55

3.2.1.1 Rational Polynomial Tensile Stress-Strain Equation for Low-Strain Behavior of Austenitic Type 316 Stainless Steel. 55

3.2.2 Heat-to-Heat Variations of Mechanical Properties of Austenitic Stainless Steels of Types 304 and 316 — Assessment of Tensile and Creep Data for Types 304 and 316 Stainless Steel 63

3.2.2.1 Data Selection and Characterization . . 64

3.2.2.2 Method of Analysis 66

3.2.2.3 Results 69

3.2.2.4 Discussion 86

3.2.2.5 Summary and Conclusion 90

3.2.3 Materials Behavior in Support of Development and Evaluation of Failure Criteria for Materials 91

3.2.3.1 Development of Creep Equation 91

3.2.3.2 Creep Evaluation for Type 316 Stainless Steel 108

3.2.4 Computerized Data Management System 121

3.2.5 Elastic Properties of Engineering Construction Materials 129

3.2.5.1 Elastic Properties Determined by Dynamic Tests 130

3.3 MECHANICAL AND METALLURGICAL BEHAVIOR OF WELDMENTS FOR LMFBR 135

3.3.1 Structure and Properties of a 16-8-2 Submerged-Arc Weld 135

3.4 MECHANICAL PROPERTIES OF STEAM GENERATOR MATERIALS . . . 147

3.4.1 High-Strain-Rate Properties of 2 1/4 Cr-1 Mo Steel 147

3.4.2 Creep-Rupture Properties of 2 1/4 Cr-1 Mo Steel 148

3.4.3 Observations of Curvature in Elevated-Temperature Stress-Rupture Isotherms 151

3.4.4 Fatigue Behavior of 2 1/4 Cr-1 Mo Steel 158

3.4.4.1 Time-Dependent Fatigue — Estimates of Worst Effects 158

3.4.4.2 Cyclic Stress-Strain Behavior 164

3.4.5 Mechanical Properties of Transition Weld Joint Materials 175

3.4.5.1 Tensile Properties of Inconel 82 Weld Metal 177

3.4.5.2 Tensile Properties of Transverse Weldment Specimens 180

3.4.5.3 Creep and Rupture Behavior of Inconel 82 Weld Metal 182

3.5 HIGH-TEMPERATURE DESIGN 187

3.6 MECHANICAL PROPERTIES OF HTGR STEAM GENERATOR AND PRIMARY CIRCUIT MATERIALS 187

3.6.1 Tensile Testing 187
3.6.2 Environmental Creep Testing 189
3.6.3 Fatigue-Life Testing 192
3.6.4 Subcritical Crack Growth Studies 205
3.6.4.1 Testing of 2 1/4 Cr-1 Mo Steel 205
3.6.4.2 Testing of Hastelloy X 209
3.7 REFERENCES 212
4. NAVAL RESEARCH LABORATORY 223
4.1 INTRODUCTION 223
4.2 RESPONSE OF AUSTENITIC STAINLESS STEEL WELDMENTS TO THERMAL CONDITIONING AS A FUNCTION OF DELTA FERRITE CONTENT 223
4.2.1 Background 223
4.2.2 Materials 224
4.2.3 Experimental Results 224
4.2.4 References 227
5. HANFORD ENGINEERING DEVELOPMENT LABORATORY 231
5.1 INTRODUCTION 231
5.2 LMFBR STRUCTURAL MATERIALS 231
5.2.1 Tensile Properties of A-286 231
5.2.1.1 Objective 231
5.2.1.2 Accomplishments and Status 231
5.2.1.3 Expected Accomplishments 241
5.2.2 Creep and Rupture Behavior of Weld-Deposited Type 16-8-2 Stainless Steel at 593°C 245
5.2.2.1 Objective 245
5.2.2.2 Accomplishments and Status 245
5.2.2.3 Expected Accomplishments 260
5.2.3 Tensile Properties of Wrought and Weld-Deposited Inconel-718 260
5.2.3.1 Objective 260
5.2.3.2 Accomplishments and Status 260
5.2.4 Effect of Temperature Upon Fatigue-Crack Growth in Nimonic PE16. J-Integral Toughness of Inconel Alloys 718 and X-750 268
5.2.4.1 Objective 268
5.2.4.2 Accomplishments and Status 268

5.2.4.3 Expected Accomplishments 280
5.3 MATERIALS INFORMATION DOCUMENTATION 280
5.3.1 Objective 280
5.3.2 Accomplishments and Status 280
5.4 REFERENCES 281
6. WESTINGHOUSE ADVANCED REACTORS DIVISION 285
6.1 INTRODUCTION 285
6.2 BASIC SPECIMEN TESTING 286
6.2.1 Type 304 Stainless Steel Tests in Progress . . . 286
6.2.1.1 BTW-2, Transverse Weld in B-Type Plate Model at 19 ksi (131 MPa) and 1100°F (593°C) 286
6.2.1.2 BAW-2, Axial Weld in B-Type Plate Model at 22 ksi (151.7 MPa) 286
6.2.1.3 C-4, Plate Model with Central Hole at a Net Section Stress of 18 ksi (124.1 MPa) at 1100°F (593°C) 287
6.2.2 Type 316 Stainless Steel Specimen Preparation . . 287
6.2.3 Type 316 Stainless Steel Tests in Progress . . . 288
6.2.4 Strain Distributions for GAW-1, Central Axial Weld in Type G Model of Type 304 Stainless Steel at 23 ksi (159 MPa) at 1100°F (593°C) . . . 288
6.2.4.1 Materials, Test Model and Instrumentation 288
6.2.4.2 Test Results 289
6.2.4.3 Discussion of Results 300
6.2.4.4 Conclusions 301
6.3 TUBULAR SPECIMEN TESTING 302
6.3.1 Type 304 Stainless Steel Testing 302
6.3.2 Type 304 Stainless Steel Data Correction 306
6.3.3 Type 304 SS Data Reduction 310
6.3.4 Type 304 SS Equation Comparison 331
6.3.5 Type 304 SS Loading Strain Comparison 334
6.3.6 Type 304 Stainless Steel Effect at Stress Ratio on Results 334
6.3.7 Type 316 Stainless Steel Heat Treatment 337
6.3.7.1 Heat Treatment 337

6.3.7.2 Tensile Properties and Hardness 337

6.3.7.3 Grain Size and Metallographic Examination. 346

6.3.7.4 Fabrication Sequence for Tubular Specimens. 346

6.4 SODIUM EFFECTS ON MECHANICAL PROPERTIES OF STRUCTURAL MATERIALS. 347

6.4.1 Type 316 Stainless Steel. 347

6.5 REFERENCES 361

7. UNIVERSITIES 363

7.1 UNIVERSITY OF CINCINNATI 363

7.1.1 Introduction 363

7.1.2 Experimental Program 363

7.1.2.1 Further Analysis of Fatigue Substructure Data for Incoloy 800 . . . 364

7.1.2.2 Creep-Microstructure Evaluation of AISI 330 Stainless Steel 375

7.1.2.3 Creep-Microstructure Evaluation of A286 379

7.1.2.4 Hot-Hardness Measurements on High Temperature Alloy Systems 381

7.1.3 References 381

7.2 UNIVERSITY OF CALIFORNIA, LOS ANGELES (No Report) . . . 384

8. GENERAL ELECTRIC COMPANY 385

8.1 INTRODUCTION 385

8.2 DECARBURIZATION KINETICS AND DESIGN METHODS VERIFICATION TESTING 386

8.2.1 Background 386

8.2.2 Decarburization Studies 388

8.2.3 Mechanical Properties of 2 1/4 Cr-1 Mo Steel in Decarburizing Sodium 389

8.3 MECHANICAL PROPERTIES OF STAINLESS STEEL IN CARBURIZING SODIUM 395

8.3.1 Fatigue Crack Growth Studies 395

8.3.1.1 Background 395

8.3.1.2 Current Progress 397

8.3.2 Creep/Fatigue Study 400

8.4 FRACTURE TOUGHNESS OF LMFBR STEAM GENERATOR MATERIALS . 402

8.4.1 Background 402

8.4.2 Current Progress 402

8.5 METALLURGICAL CHARACTERIZATION OF VAR AND ESR 2 1/4 Cr-1 Mo ALLOY STEEL 405

8.6 REFERENCES 407

APPENDIX 8.1 422

APPENDIX 8.2 426

INDEX 429

SUMMARY

1. AEROJET NUCLEAR COMPANY

(No Report)

2. ARGONNE NATIONAL LABORATORY

Elevated-temperature, low-cycle fatigue data from axially loaded, strain-controlled tests have been collected and analyzed. The results of 436 zero and tension hold-time tests and 38 compression and tension plus compression hold-time tests are summarized here. A regression analysis was performed on the zero and tension hold-time data, and an expression that relates cyclic life to total axial strain range, test temperature, total axial strain rate, and tension hold time was obtained. Statistical aspects of the regression analysis are discussed, and an estimate of a 95% confidence interval for life is presented.

A damage equation for analyzing creep-fatigue interaction is proposed and discussed. Instead of separating the plastic strain into time-independent and time-dependent components, the problem is cast in terms of the total plastic strain and strain rate as the fundamental damage rate-controlling variables. By integrating the damage equation along various deformation paths, one may treat such diverse processes as the effects of strain rate on time to monotonic or creep rupture and the effects of strain rate, hold time, and rising mean strain on fatigue life at elevated temperature in a quantitative and unified manner. The method is illustrated by means of available data for Type 304 austenitic stainless steel.

Uniaxial creep-rupture data have been obtained for Type 304 stainless steel in the solution-annealed and sodium-exposed conditions in the temperature range 600-700°C. The creep behavior of steel carburized in a sodium environment showed an increase in rupture life and a decrease in minimum creep rate when compared with material in the annealed condition. Creep correlations, isochronous stress-creep strain curves, and results on the calculations of the stress levels for 1% creep strain and long-term rupture life are also presented.

Additional low-cycle fatigue tests have been conducted in sodium on annealed and sodium-exposed Type 304 stainless steel at 600 and 700°C. At 600°C the fatigue life decreases with an increase in the sodium-exposure time of ∿1500 to 5000 h; however, the lifetimes are greater for the 5000-h preexposed steel than for the annealed material. The decrease in the fatigue life may be a result of the larger carbon penetration depth associated with the longer sodium-exposure time. The modest increase in the fatigue life of the sodium-exposed material at 700°C can be attributed to thermal aging since no significant carburization or decarburization of the material occurred during the 1500-h exposure period.

3. OAK RIDGE NATIONAL LABORATORY

A rational polynomial tensile stress-strain equation for low-strain behavior of type 316 austenitic stainless steel was developed. Excellent predictability was observed for data on both mill-annealed and reannealed materials.

Variations in tensile and creep properties of types 304 and 316 stainless steels were evaluated for United States data, including comparisons with the variations in data from two foreign countries: Japan (NRIM data) and Britain (BSCC data). Variations were evaluated for the data on different products separately and for the combined data on all products.

United States data contain the greatest variations in both tensile and creep properties, and Japanese data the least. For a given country no distinction could be made in variations in tensile properties of types 304 and 316 stainless steel. Standard error of estimate (SEE) in log t_r (where t_r is time to rupture), creep rupture stress exponent, 10^4-hr creep rupture strength, and creep total elongation are significantly less for the combined data on type 316 stainless steel than for type 304. The 10^4-hr creep rupture strength of type 316 stainless steel was indistinguishable for steels produced in the U.S. and the foreign countries investigated. Variations of creep rupture strengths of type 304 stainless steel were too large to permit a similar conclusion.

Results of this analysis suggested that U.S. and foreign data on types 304 and 316 stainless steel could possibly be combined for determination of design stress intensity limits.

A method has been developed by which the creep strain response of types 304 and 316 stainless steel can be predicted primarily from rupture life and minimum creep rate data. The method, based on a single rational polynomial creep equation, has been applied with good results to several heats of material. The method allows prediction of heat-to-heat variations in creep behavior.

Single-primary-term equations were fitted to data from 100 creep strain-time tests on type 316 stainless steel from various sources. Two-term equations were derived for only 34 tests. Comparisons indicate the acceptability of a single rational polynomial equation to define the creep response at constant load and temperature.

Equations for the three parameters in the single rational polynomial equation were fitted by least squares analysis over the entire domain of interest. Additional minimum creep rate data and strain-time data generally compared well with predictions from the new equation, particularly at 566°C (1050°F).

Some isochronous stress-strain curves are derived and compared with the present code case curves. Predicted relaxation response agrees very well with tests conducted at 593°C (1100°F).

Analytical computer programs were developed to process data from the ORNL Mechanical Properties Data Storage and Retrieval System (DSRS). The initial phase of the ASEND program was completed; it allows access of data in DSRS for generalized multiple regression analysis, including graphical display of results.

Dynamic elastic constants (E, G, and ν) were established for type 316 stainless steel (heat 8092297) and Incoloy 800H (heat HH6758A) in the solution annealed condition from room temperature to 871°C (1600°F) and to 899°C (1650°F), respectively. Cubic polynomials are presented for the individual constants, and estimates of the properties at 28°C (50°F) increments are tabulated.

A test program is in progress to characterize type 16-8-2 stainless steel submerged-arc welds. Test welds were made in 25-mm-thick (1-in.) type 316 stainless steel plate by Babcock and Wilcox Company. These welds and adjacent heat-affected zones are being evaluated by metallography, hardness traverses, chemical analysis, δ-ferrite measurement, tensile testing, and creep rupture testing.

The welds are austenitic with a small amount of δ-ferrite present, which varies from FN (Welding Research Council Ferrite Numbers) 0.8–1.6 at the root to FN 1.5–3.0 at the crown. Hardness clearly increases up the center of the weld from the root to the crown and decreases from the center of the weld toward the base metal. Samples taken both transverse and parallel to the welding direction were tensile tested at temperatures up to 650°C. Spot checks were performed to determine the effects of strain rate, location, and orientation on properties for selected test conditions. At room temperature the yield strength of the weld crown pass region was 70 MPa (10 ksi) less than that of the root pass region, and the yield strength of the base metal tends to decrease as the distance from the fusion line increases. Although the yield strength of the weld metal at elevated temperatures exceeds the values measured for base material and the minimum trend curve for the base metal, the tensile strength for the weld metal tends to be below corresponding measures of base metal tensile strength. The creep and creep-rupture properties of these welds are being investigated at 566 and 649°C (1050 and 1200°F). Nearly all the short-time rupture tests that we have completed to date show shorter rupture lives than the minimum expected life (−1.65 standard deviation) for type 316 base metal. Lower stress creep-rupture tests are in progress.

A report was issued on the studies of the tensile properties of a bainitic 2 1/4 Cr-1 Mo steel over the range 25 to 593°C (77–1100°F) and the strain rate range 2.67×10^{-6} to 144/sec. The results from that report are summarized.

The results of our studies on the effect of heat treatment on the creep-rupture properties of annealed 2 1/4 Cr-1 Mo steel at 454, 510, and 566°C (850, 950, and 1050°F) are discussed. The approach of rupture properties with increased rupture life is explained in terms of the evolution of microstructure during a test.

The rupture-life model submitted for the *Nuclear Systems Materials Handbook* for annealed 2 1/4 Cr-1 Mo steel for the temperature range 371 to 593°C (700–1100°F) is linear in log σ_R vs log t_R, where σ_R is the stress to cause rupture in time t_R. The data used for that correlation have been examined for curvature; some was detected at 600°C. However, for temperatures below about 566°C (1050°F) the curvature becomes important only at times greater than those of interest for CRBRP design ($>10^5$ hr). Even at the higher temperatures the proposed model adequately represents the sparse available data, and the lower limits, which reflect the uncertainty in the linear model, account for the error caused by the downward curvature.

Estimates of the cyclic stress-strain and relaxation behavior of 2 1/4 Cr-1 Mo steel were used in conjunction with the strain range partitioning approach to estimate the fatigue life of this alloy with long hold periods. In addition, "worst effects" curves showing the minimum expected fatigue life at a given strain range due to hold time effects were constructed.

Three heats of isothermally annealed 2 1/4 Cr-1 Mo steel have been fatigue tested to failure in strain control. Measurements of the stress range required to maintain the imposed strain range were used to indicate cyclic stress-strain behavior. Various techniques were then used to construct cyclic stress-strain curves.

Since the intermediate heat exchanger of the CRBRP is to be constructed of an austenitic material and the steam generator of a ferritic material, a transition joint is required. Studies are under way to determine the mechanical properties of transition joint materials. Tensile tests were made on Inconel 82 weld metal over the range 25 to 732°C (77–1350°F). Tensile tests were also made on transverse weldment specimens that contained 2 1/4 Cr-1 Mo steel, Inconel 82 weld metal, and type 316 stainless steel in the specimen gage section. Creep-rupture studies are under way on Inconel 82 weld metal at 454, 510, and 566°C (850, 950, and 1050°F). Results to date on these tests are reported.

Tensile tests on Inconel 617 show that the 0.2% yield strength is very little affected by temperature in the range from 288 to 816°C (550–1500°F). Three creep specimens that have been tested in simulated HTGR helium have been examined metallographically.

Results of fully reversed isothermal uniaxial strain-controlled fatigue tests conducted in air on Hastelloy X are presented. Total strain range is plotted against cycles to failure for room temperature, 538°C (1000°F), 649°C (1200°F), 760°C (1400°F), and 871°C (1600°F). Hastelloy X fatigue behavior is compared with that of other HTGR structural materials including Inconel 718, 2 1/4 Cr-1 Mo steel, and Incoloy 800. A few hold time tests were conducted to determine the influence of creep-fatigue interaction on the flow and failure behavior of Hastelloy X.

Fatigue crack propagation (FCP) studies on 2 1/4 Cr-1 Mo steel and Hastelloy X are updated. Effects of heat-to-heat variation, frequency, specimen geometry, steam and simulated HTGR coolant on the FCP of 2 1/4 Cr-1 Mo steel are discussed. Effects of temperature, specimen geometry, and simulated HTGR coolant on the FCP of Hastelloy X are discussed.

4. NAVAL RESEARCH LABORATORY

Further investigations were conducted on the special series of AISI Type 308 stainless steel weld deposits (shielded metal arc process) featuring a range of delta ferrite contents from ferrite number (FN) 5.2 to 19.0. The investigations included dynamic tear (DT) tests of the as-welded condition and the as-welded plus thermally-aged condition.

In the as-welded condition, a peak in DT energy absorption at 700°F (371°C) was revealed within the range 75°F to 900°F (24°C to 472°C). An explanation for the energy peak could not be found from yield strength behavior in the same temperature interval.

The thermal aging studies explored the effects of thermal conditioning at 500°F (260°C) and at 900°F (482°C) for 2500 hr. The results describe a detrimental effect of high delta ferrite contents on aging response. Specifically, welds with the delta ferrite contents of FN 5.2 and 10.4 exhibited no change in DT energy absorption while the welds with the higher delta ferrite contents of FN 15.7 and 19.0 experienced significant decreases in DT values. Tensile specimens representing 500°F (260°C), 700°F (371°C), and 900°F (482°C) aged conditions will be evaluated in the coming quarter.

5. HANFORD ENGINEERING DEVELOPMENT LABORATORY

The effects of test temperature, strain rate, thermal aging, and neutron irradiation on the tensile properties of A-286 have been experimentally determined. Irradiation conditions included fluences from 0.9 to 1.5 x 10^{21} n/cm^2 (E > 0.1 MeV) and an irradiation temperature of ∿405°C (760°F). Thermal aging was performed at 538°C (1000°F) for durations to 4,000 hours. Test parameters included strain rates from 3 x 10^{-5} to 1 sec^{-1} at temperatures from room temperatures to 649°C (1200°F). Results of the completed tests show that strength properties and ductility are not greatly influenced by strain rate, thermal exposure, or neutron irradiation for test temperatures to 538°C (1000°F). At 649°C (1200°F) the ultimate and 0.2% yield strengths and uniform elongation of unirradiated material increase with increasing strain rate while total elongation and reduction of area decrease. Neutron irradiation does not alter the strain rate sensitivity of strength properties at a temperature of 649°C, however ductility (total and uniform elongation and reduction of area) is significantly enhanced by increasing strain rate.

The time-dependent creep and rupture behavior of weld-deposited Type 16-8-2 stainless steel at 593°C has been studied experimentally and described analytically. Weld and wrought (Types 316 and 316H) materials, some of which are prototypic of those used in the FFTF primary piping system were examined in terms of the criteria which control the design of nuclear systems. The results of this investigation are summarized as follows.

The time to rupture, the time to the onset of tertiary creep, and the time to produce a given creep strain were described by the relations

$$\ln t_r = 81.3456 - 12.176 \ln \sigma$$

$$\ln t_t = 80.0786 - 12.176 \ln \sigma$$

$$\ln t_{\varepsilon_c} = A_{\varepsilon_c} - 13.0 \ln \sigma$$

$$A_{\varepsilon_c} = 87.3633 + 1.32066 \ln \varepsilon_c + 0.446428 (\ln \varepsilon_c)^2 + 1.08131 (\ln \varepsilon_c)^3 + 6.96513 \times 10^{-3} (\ln \varepsilon_c)^4$$

for a series of Type 16-8-2 weld deposited stainless steel materials. The description of creep deformation was combined with experimental flow curves for elastic/plastic deformation to construct isochronous stress strain curves for the weld materials.

Test results indicate that the control of welding process and parameters through realistic engineering weld procedure specifications can yield welds with consistent time-dependent mechanical properties. Limited data suggest that high temperature (1065°C) post-weld annealing significantly alters only the flow curve for plastic deformation, but long term thermal exposure at an intermediate temperature (565°C) produces only minor changes in either the plastic deformation or creep behavior of the weld materials.

Minimum values of stress to produce rupture, the stress to produce onset of tertiary creep, and the stress to produce a total strain of 0.01 in various times were determined from 95%/95% tolerance limits obtained from statistical analysis of the data. Comparison of these properties with time-dependent design allowable stress values for wrought Type 316 stainless steel shows that the base metal allowable stress values provide adequate protection against failure of the weld materials. Further work is needed to assess the relative mechanical performance of base metal and weld regions in engineering structures.

The effects of neutron irradiation and out-of-flux aging on the tensile properties of wrought and weld-deposited Inconel-718 have been investigated following fast-reactor (EBR-II) irradiation to total fluences ranging from 0.55×10^{22} n/cm^2 (∿400°C) to 6.6×10^{22} n/cm^2 (649°C) and thermal exposure at 538°C and 649°C for durations to 10,000 hours. Classical irradiation hardening is exhibited by this very strong material following irradiation at low temperature (400°C) to relatively low fluence (∿10^{22} n/cm^2) and also at high temperature when very high fluence (6.6×10^{22} n/cm^2) is accumulated. At test temperatures ≳538°C, ductility losses

arising from helium embrittlement are evident for all irradiation conditions and at high fluences are so severe as to restrict the strength to lower than expected values.

Low postirradiation strength, compared to that following out-of-flux aging for equivalent durations, suggests that irradiation accelerates the thermal overaging process at 538°C. At 649°C, the results are obscured by embrittlement and coincident limitations on strain hardenability.

The effect of temperature upon the fatigue-crack propagation behavior of precipitation heat-treated Nimonic PE16 was determined in an air environment over the range 75°-1200°F. In general, at a given value of ΔK, fatigue-crack growth rates increased with increasing test temperatures.

The fracture toughness of precipitation heat-treated alloys Inconel 718 and Inconel X-750 was determined at room temperature using the J-integral technique. The toughness (J_{Ic}) of Inconel 718 and Inconel X-750 was found to be 727 in-lb/(in)^2 and 544 in-lb/(in)^2, respectively, and this corresponds to K_{Ic} values of approximately 153,500 lb/(in)$^{1.5}$ and 136,100 lb/(in)$^{1.5}$, respectively.

6. WESTINGHOUSE ADVANCED REACTORS DIVISION

Testing of a flat plate of type 304 SS with a central axial type 308 weld has shown that cracking can initiate at a strain of about 4%. A damage mechanism based on the exhaustion of ductility was correlated with initiation of cracking in the heat affected zones of the weld and regions where the maximum strain exceeded about 4%. The cracks grow in a direction perpendicular to that of the maximum principal stress and initiate at regular axial spacing in the heat affected zones of the weld.

In preparing type 316 SS specimens for testing, it was found that the process of heat treating and then finish machining resulted in a surface hardness which was not uniform with penetration depth. When a re-heat treatment was employed after finish machining, the desired hardness uniformity with penetration depth was obtained. This method will now be used in future specimen preparations.

Data reduction of the corrected Type 304 SS tubular data continued using the CREEP-FIT data reduction computer program and has so far shown a marked variation from anticipated behavior based on previous uniaxial information. From graphical analysis it was found that a different creep mechanism was operating at high stresses (greater than the yield stress). This mechanism could not be accounted for by projection of the WARD equation or the ORNL equation.

Creep-rupture test results for solution-annealed Type 316 SS in 593°C sodium with test times to 2,319 hours are presented. Results of testing samples sodium pre-exposed at 718°C for 5,000 hours show a

significant decrease in rupture life and increase in ductility when compared to as-fabricated samples tested at the same conditions. This occurs in spite of the much larger strain-on-loading obtained for the as-fabricated samples. Consistent with in-air results reported in the literature for as-fabricated material, the minimum creep rate is lower and the rupture life is greater at 206.9 MPa (30 ksi) indicating a change in the creep mechanism below 224.1 MPa (32.5 ksi). This change is not apparent for the sodium pre-exposed samples.

Cyclic stress and strain response curves are presented for low-cycle fatigue tests of solution annealed Type 316 SS performed at 593°C in sodium. For the two strain ranges investigated (1.0% and 0.5%), the stress range for as-fabricated material is much higher than that obtained for samples pre-treated at 650°C and 718°C for 5,000 hours. At the lower strain range of 0.5%, the as-fabricated material demonstrated considerable secondary hardening. This was not the case for the pre-treated samples.

7. UNIVERSITIES

UNIVERSITY OF CINCINNATI

In the push-pull fatigued Incoloy 800 specimens, the subboundary intercept dependency on both stress and strain range was correlated into one parameter equation:

$$\tau_s = 2.4 \times 10^{-2}\ G\ (b\gamma_p/\lambda')^{0.20\pm0.014}$$

where τ_s is saturation shear stress, G is shear modulus, b is Burger's vector, γ_p is plastic shear strain and λ' is the diameter of subgrain. This is consistent with the "modified" Ashby's unidirectional work hardening theory for plastically nonhomogeneous materials. It was also found that precipitation does not affect the subgrain formation behavior in Incoloy 800. This was explained on the basis of the threshold microstructure concept.

A set of A-286 specimens was solid-solution annealed at 900°C for 2 hours and aged at 720°C for various times. It was found that rapid hardening occurs during the initial ageing period, the hardness increasing slowly thereafter.

A constant load creep rupture test was performed on AISI 330 stainless steel at 649°C with an applied stress of 30,000 psi. The minimum creep rate was 1.04×10^{-4} sec^{-1} and the rupture life and the rupture strain were 29.6 hours and 64.3%, respectively.

A comparison of the hot-hardness values of aged A-286 and solutioned AISI 330 stainless steel shows that A-286 is about three times harder than 330 SS in the temperature region of 200 to 900°C.

UNIVERSITY OF CALIFORNIA, LOS ANGELES

(No Report)

8. GENERAL ELECTRIC COMPANY

Test Matrices for Phase II testing of both uniaxial and biaxial stress states have been established for the mechanical properties study of decarburized 2 1/4 Cr-1 Mo steel. Previously reported anomalies in the 2 1/4 Cr-1 Mo steel biaxial creep data have been resolved. Pinhole porosity associated with weld metal specimens was a result of a high temperature, sodium purification cycle that preceeded testing. Decarburization studies to define the effects of meltint practices and heat treatment have been initiated in Decarb Pot #1. ESR, VAR and extra low carbon (Sumitomo) 2 1/4 Cr-1 Mo steel will be decarburized for 1500 hours (Run DP-9), 6000, and 10,000 hours.

Six additional control fatigue crack growth tests for Type 316 S.S. were completed. Testing in sodium, with a renewed carbon source, has been resumed. Test specimens from a GTA weld were fabricated. A cursory cyclic life analysis was performed, using current data, and illustrates the need for accurate definition of the fatigue crack growth equation.

The preparation of additional 2 1/4 Cr-1 Mo steel fracture toughness specimens has been completed, and higher temperature tests are being initiated. A SMAW weldment was prepared, and specimen preparation from this material is proceeding. Retesting of 2 1/4 Cr-1 Mo steel plate given a potential embrittling treatment [510°C (950°F) for 1000 hr], has verified a significant reduction in Charpy V-notch upper shelf energy, along with the expected increase in transition temperature. An analysis of crack opening displacement methods for determining critical values of J-Integral in fracture toughness tests was performed and demonstrates its applicability.

Isothermal transformation characteristics were studied for five heats of VAR, four heats of ESR and three heats of air metled 2 1/4 Cr-1 Mo steel. Microstructures and hardness were evaluated for hold times of from 30 to 300 minutes at isothermal transformation temperatures of 690°C (1275°F), 704°C (1300°F), 718°C (1325°F), and 732°C (1350°F). After a transformation time of 120 minutes there is more polygonal ferrite present for the 732°C (1350°F) temperature than for the lower temperatures.

1. AEROJET NUCLEAR COMPANY

(Contribution not received in time for inclusion in this issue.)

2. ARGONNE NATIONAL LABORATORY

R. W. Weeks

2.1 INTRODUCTION

Argonne National Laboratory (ANL) is conducting extensive programs to provide elevated-temperature, low-cycle fatigue data on Types 304 and 316 stainless steel and to study the effects of sodium environment on the elevated-temperature mechanical properties of these materials. Both programs are in support of LMFBR component design. In the present report, the results of a regression analysis on available low-cycle fatigue data on Type 304 stainless steel tested in air are summarized, a life-predictive method applicable to the creep-fatigue problem is presented, and the effects of sodium exposure on the creep and elevated-temperature, low-cycle fatigue behavior of Type 304 stainless steel are described.

2.2 FRACTURE AND FATIGUE STUDIES ON STAINLESS STEELS -- D. R. Diercks, P. S. Maiya, S. Majumdar, and D. T. Raske

2.2.1 Statistical Analysis and Regression Fit of Elevated-temperature Low-cycle Fatigue Data on Type 304 Stainless Steel -- D. R. Diercks and D. T. Raske

In the past 10 years, a considerable quantity of elevated-temperature [430°C (816°F) and above], low-cycle fatigue data on Type 304 stainless steel has been obtained under axial loading strain-controlled conditions. The results of an extensive effort to collect these data and analytically describe the observed variation of cyclic life with the principal test variables are reported here. A primary goal of the analysis is to produce cyclic-life relations for inclusion in the Nuclear Systems Materials Handbook. The results of the data-collection effort are summarized in Tables 2.1 and 2.2. Table 2.1 contains 436 data points from zero and tension hold-time (cyclic-relaxation) tests, and Table 2.2 contains 38 points from compression and tension plus compression hold-time tests. The sources of the data (Refs. 1-15) are listed, and footnote a in the two tables specifically points out the data included and not included in the analysis. Data generated for waveforms other than continuous cycling

Table 2.1. Summary of Elevated-temperature, Strain-controlled Zero and Tension Hold-time Low-cycle Fatigue Data for Type 304 Stainless Steel[a]

TOTAL STRAIN RANGE, %	PLASTIC STRAIN RANGE, %	TOTAL STRAIN RATE, 1/S	HOLD TIME, MIN[b]	STRESS RANGE, MPA[c]	HEAT NO.[d]	HEAT TREAT[e]	LAB	SPEC. NO.	OBSERVED CYCLES TO FAIL	COMPUTED CYCLES TO FAIL[f]	REF
TEST TEMPERATURE = 430 C (806 F)											
2.19	1.72	.004400	0.0	754	2	1	GE		1070	1148	8
2.07	1.65	.004100	0.0	326;345	2	5	ANL	12A-10	2361	1291	1
1.13	0.81	.004500	0.0	514	2	1	GE		4432	5702	8
1.07	0.81	.004300	0.0	188;232	2	5	ANL	13A-9	10192	6604	1
0.79	0.53	.004600	0.0	422	2	1	GE		10917	16736	8
0.60	0.36	.004800	0.0	387	2	1	GE		31450	45863	8
0.60	0.36	.005000	0.0	390	2	1	GE		34160	46011	8
0.52	0.28	.004200	0.0	183;165	2	5	ANL	15A-7	61818	83739	1
TEST TEMPERATURE = 482 C (900 F)											
2.02	1.53	.004000	0.0	385;415	6	10	ANC	BT-100	685	1137	11
2.01	1.55	.004000	0.0	353;357	1	3	ANL	T-26	1299	1149	1
2.00	1.33	.004000	0.0	386;420	6	10	ANC	BT-72	594	1161	11
2.00	1.53	.004000	0.0	749	2	5	ANL	60-11	1087	1161	1
1.96	1.48	.003900	0.0	758	2	5	ANL	7A-10	988	1209	1
1.00	0.69	.004000	0.0	248;234	1	3	ANL	T-34	6026	6023	1
0.99	0.59	.004000	0.0	281;274	6	10	ANC	BT-23	3809	6190	11
0.99	0.69	.004000	0.0	239;228	1	3	ANL	T-63	6601	6190	1
0.79	0.44	.004000	0.0	240;243	6	10	ANC	BT-24	7662	11906	11
0.73	0.48	.004000	0.0	206;206	1	3	ANL	T-364	16723	15287	7
0.60	0.36	.004000	0.0	194;185	1	3	ANL	T-137	27628	30189	1
0.50	0.21	.004000	0.0	208;208	6	10	ANC	BT-25	28176	62588	11
0.37	0.03	.004000	0.0	251;294	6	10	ANC	BT-28	692520	278723	11
0.33	0.01	.004000	0.0	165;194	6	10	ANC	BT-22	984324[g]	559665	11

Table 2.1 (Contd.)

TOTAL STRAIN RANGE, %	PLASTIC STRAIN RANGE, %	TOTAL STRAIN RATE, 1/S	HOLD TIME, MIN[b]	STRESS RANGE, MPA[c]	HEAT NO.[d]	HEAT TREAT[e]	LAB	SPEC. NO.	OBSERVED CYCLES TO FAIL	COMPUTED CYCLES TO FAIL[f]	REF
TEST TEMPERATURE = 482 C (900 F)											
1.98	1.51	.000400	0.0	362;377	1	3	ANL	T-328	880	919	7
0.99	0.65	.000400	0.0	256;262	1	3	ANL	T-325	6396	4652	7
0.60	0.33	.000400	0.0	216;208	1	3	ANL	T-130	26139	22831	1
1.98	1.51	.000039	0.0	372;370	1	3	ANL	T-27	955	720	1
0.99	0.61	.000040	0.0	611	1	3	ANL	T-292	4805	3544	7
0.98	0.62	.004000	0.6 T	274;280	6	10	ANC	BT-26	3818	4812	11
0.98	0.60	.004000	6.0 T	298;305	6	10	ANC	BT-27	3563	2128	11
0.59	0.29	.000390	10.0 T	490	1	3	ANL	T-166	5104	7090	2
2.02	1.52	.000040	45.0 T	823	1	3	ANL	T-95	388	336	1
0.99	0.61	.000040	45.0 T	635	1	3	ANL	T-87	1324	1303	2
1.98	1.54	.000040	600.0 T	796	1	3	ANL	T-178	123	126	2
TEST TEMPERATURE = 538 C (1000 F)											
3.96	3.41	.064000	0.0	855	2	1	GE	67-2	345	359	8
3.96	3.42	.032000	0.0	843	2	1	GE	67-1	347	331	8
2.94	2.50	.015000	0.0	800	2	1	BCL	SS-12	381	531	15
0.50	0.27	.008000	0.0	172;172	2	1	GE	67-3	43377	42365	8
3.96	3.42	.004000	0.0	421;421	2	1	GE	66-12	244	260	8
2.92	2.40	.004000	0.0	745	2	1	BCL	SS-1	390	454	15
2.04	1.63	.004000	0.0	717	2	1	BCL	SS-13	737	908	15
2.01	1.57	.004000	0.0	331;344	1	3	ANL	T-311	1100	936	7
2.01	1.57	.004000	0.0	342;345	2	5	ANL	60-10	1167	936	1
1.95	1.51	.004000	0.0	687	2	1	BCL	SS-3	812	995	15
1.01	0.53	.004100	0.0	217;212	2	1	ANL	3A-11	3931	4322	1
1.00	0.61	.004000	0.0	265;253	2	3	ANL	59-8	4232	4413	1
0.99	0.66	.004000	0.0	264;260	1	3	ANL	T-314	4951	4527	7

Table 2.1 (Contd.)

TOTAL STRAIN RANGE, %	PLASTIC STRAIN RANGE, %	TOTAL STRAIN RATE, 1/S	HOLD TIME, MIN[b]	STRESS RANGE, MPA[c]	HEAT NO.[d]	HEAT TREAT[e]	LAB	SPEC. NO.	OBSERVED CYCLES TO FAIL	COMPUTED CYCLES TO FAIL[f]	REF
TEST TEMPERATURE = 538 C (1000 F)											
0.96	0.63	.004000	0.0	524	2	1	BCL	SS-2	2876	4896	15
0.64	0.39	.004300	0.0	190;199	1	3	ANL	T-327	15416	15861	7
0.63	0.36	.004000	0.0	409	2	1	BCL	SS-21	10283	16490	15
0.39	0.20	.003100	0.0	153;144	2	1	ANL	3A-10	119358	106139	1
0.34	0.16	.004000	0.0	346	2	1	BCL	SS-4	31553	226122	15
0.27	0.04	.004000	0.0	332	2	1	BCL	SS-17	967734	978333	15
0.13	0.0	.004000	0.0	188	2	1	BCL	SS-6[h]	1520257[g]	1.09×10^{10}	15
2.00	1.55	.000800	0.0	331;345	1	3	ANL	T-332	871	758	7
2.00	1.56	.000400	0.0	336;346	1	3	ANL	T-363	975	691	7
1.99	1.54	.000440	0.0	692	1	3	ANL	T-310	1016	707	7
1.02	0.68	.000410	0.0	262;268	1	3	ANL	T-322	4411	2930	7
0.61	0.34	.000410	0.0	205;209	1	3	ANL	T-324	17702	12560	7
0.63	0.35	.000250	0.0	214;217	1	3	ANL	T-336	18707	10432	7
1.99	1.54	.000040	0.0	351;355	1	3	ANL	T-303	469	521	7
1.00	0.62	.000040	0.0	292;298	1	3	ANL	T-301	2336	2177	7
0.60	0.28	.000040	0.0	246;239	1	3	ANL	T-293	21102	9214	7
0.50	0.24	.004000	1.0 T	200;200	2	1	GE	67-4	17920	20428	8
3.96	3.46	.004000	10.0 T	427;427	2	1	GE	66-11	141	124	8
2.22	1.80	.004000	10.0 T	752	2	1	BCL	SS-7	366	294	15
1.04	0.65	.004000	10.0 T	547	2	1	BCL	SS-22	1431	1068	15
1.01	0.65	.000040	10.0 T	565	1	3	ANL	T-352	1137	1311	7
2.20	1.80	.004000	30.0 T	745	2	1	BCL	SS-9	223	213	15
2.21	1.82	.004000	60.0 T	731	2	1	BCL	SS-8	184	174	15
1.01	0.69	.000040	60.0 T	258;267	1	3	ANL	T-357	922	714	7
1.00	0.67	.000040	600.0 T	248;256	1	3	ANL	T-391	396	268	7

Table 2.1 (Contd.)

TOTAL STRAIN RANGE, %	PLASTIC STRAIN RANGE, %	TOTAL STRAIN RATE, 1/S	HOLD TIME, MIN[b]	STRESS RANGE, MPA[c]	HEAT NO.[d]	HEAT TREAT[e]	LAB	SPEC. NO.	OBSERVED CYCLES TO FAIL	COMPUTED CYCLES TO FAIL[f]	REF
TEST TEMPERATURE = 566 C (1050 F)											
2.06	1.58	.004100	0.0	664	2	5	ANL	12A-7	1139	805	1
2.01	1.58	.004000	0.0	651	2	2	ANL	5A-3	1070	841	1
2.01	1.59	.004000	0.0	652	2	1	ANL	8A-5	1127	841	1
2.00	1.58	.004000	0.0	645	2	1	ANL	8A-7	996	850	1
1.01	0.68	.004000	0.0	504	2	2	ANL	5A-1	4326	3675	1
0.99	0.63	.004000	0.0	559	2	1	ANL	8A-1	2811	3858	1
0.99	0.70	.003900	0.0	443	2	5	ANL	13A-7	6708	3840	1
0.57	0.36	.004500	0.0	325	2	5	ANL	13A-10	42034	18804	1
0.51	0.28	.004000	0.0	351	2	2	ANL	5A-6	29112	27090	1
0.50	0.27	.004000	0.0	363	2	1	ANL	8A-6	17273	29132	1
0.50	0.29	.004100	0.0	157;170	2	5	ANL	7A-5	28880	29273	1
0.50	0.28	.004200	0.0	338	2	8	ANL	14A-10	29568	29413	1
0.50	0.28	.004000	0.0	189;150	2	1	ANL	8A-3	33898	29132	1
0.45	0.23	.003600	0.0	334	2	8	ANL	14A-11	97807	42865	1
0.40	0.19	.004000	0.0	157;154	2	6	ANL	4A-4	57452	72214	1
0.40	0.19	.004000	0.0	154;163	2	5	ANL	1A-6	89513	72214	1
0.35	0.13	.004000	0.0	161;172	2	2	ANL	5A-8	212460	136740	1
0.33	0.12	.003800	0.0	171;161	2	5	ANL	7A-9	302467	184499	1
0.28	0.07	.003700	0.0	166;163	2	5	ANL	4A-1	506718	486826	1
1.02	0.67	.000041	0.0	267;273	2	5	ANL	15A-9	1176	1659	1
1.02	0.71	.004100	1.0 T	514	2	5	ANL	7A-7	3027	2308	1
1.01	0.69	.004000	1.0 T	513	2	2	ANL	5A-9	3574	2352	1
0.47	0.23	.003800	12.6 T	382	2	5	ANL	15A-10	3781	4751	1
1.00	0.71	.004000	15.0 T	482	2	5	ANL	15A-11	1509	828	1
0.87	0.45	.003500	15.0 T	679	2	5	ANL	15A-6	375	1063	1
1.03	0.73	.004100	28.8 T	502	2	5	ANL	15A-5	606	611	1
1.95	1.65	.003900	170.0 T	553	2	5	ANL	15A-8	190	145	1
1.35	1.05	.002700	180.0 T	498	2	5	ANL	14A-1	236	223	1

Table 2.1 (Contd.)

TOTAL STRAIN RANGE, %	PLASTIC STRAIN RANGE, %	TOTAL STRAIN RATE, 1/S	HOLD TIME, MIN[b]	STRESS RANGE, MPA[c]	HEAT NO.[d]	HEAT TREAT[e]	LAB	SPEC. NO.	OBSERVED CYCLES TO FAIL	COMPUTED CYCLES TO FAIL[f]	REF
TEST TEMPERATURE = 566 C (1050 F)											
2.13	1.84	.004300	600.0 T	582	2	5	ANL	12A-12	93	102	1
TEST TEMPERATURE = 593 C (1100 F)											
1.94	1.54	.039000	0.0	608	1	3	ANL	T-215	1041	1213	7
1.52	1.16	.040000	0.0	546	1	3	ANL	T-221	1849	2021	7
1.05	0.74	.042000	0.0	476	1	3	ANL	T-321	5467	4683	7
1.02	0.72	.041000	0.0	462	1	3	ANL	T-198	4662	4993	7
1.01	0.70	.040000	0.0	473	1	3	ANL	T-320	5096	5085	7
0.76	0.51	.040000	0.0	385	1	3	ANL	T-219	10512	10540	7
0.60	0.37	.039000	0.0	347	1	3	ANL	T-202	24062	20915	7
5.97	5.26	.004000	0.0	464;492	7	3	ANC	8-23	135	113	9
2.12	1.49	.004000	0.0	349;367	7	3	ANC	8-8	965	685	9
2.04	1.62	.004100	0.0	644	1	3	ANL	T-277	700	740	7
2.02	1.61	.004000	0.0	626	1	1	ANL	AA-2	737	751	1
2.02	1.59	.004000	0.0	656	1	1	ANL	T-17	753	751	1
2.02	1.60	.004100	0.0	628	1	3	ANL	AA-4	937	754	1
2.01	1.57	.004000	0.0	663	1	1	ANL	AA-1	766	758	1
2.01	1.40	.004000	0.0	373;395	6	10	ANC	BP-14	840	758	9
2.01	1.61	.004000	0.0	606	2	4	ANL	10A-3	941	758	1
2.01	1.67	.004200	0.0	631	1	1	ANL	T-14	1020	764	1
2.00	1.49	.004000	0.0	337;367	6	10	ANC	BT-92	590	765	9
2.00	1.60	.004000	0.0	612	2	5	ANL	60-6	841	765	1
2.00	1.48	.004000	0.0	322;349	2	3	ANC	A-233	1202	765	9
1.99	1.57	.004000	0.0	641	2	1	ANL	8A-8	806	772	1
1.99	1.56	.004000	0.0	656	3	3	ANL	845-10	1010	772	7
1.97	1.41	.004000	0.0	370;394	8	10	ANC	BT-73	594	787	9

Table 2.1 (Contd.)

TOTAL STRAIN RANGE, %	PLASTIC STRAIN RANGE, %	TOTAL STRAIN RATE, 1/S	HOLD TIME, MIN[b]	STRESS RANGE, MPA[c]	HEAT NO.[d]	HEAT TREAT[e]	LAB	SPEC. NO.	OBSERVED CYCLES TO FAIL	COMPUTED CYCLES TO FAIL[f]	REF
TEST TEMPERATURE = 593 C (1100 F)											
1.96	1.32	.004000	0.0	357;375	6	10	ANC	BT-14	915	795	9
1.96	1.47	.004000	0.0	313;325	2	11	ANC	A-225	940	795	9
1.95	1.48	.004000	0.0	307;325	2	3	ANC	A-232	663	803	9
1.94	1.41	.004000	0.0	382;379	8	10	ANC	BT-74	619	811	9
1.94	1.42	.004000	0.0	329;355	7	3	ANC	8-28	1176	811	9
1.58	1.21	.004200	0.0	560	1	3	ANL	T-29	1556	1220	1
1.52	1.12	.004000	0.0	596	1	3	ANL	AA-22	1768	1307	1
1.49	1.10	.004000	0.0	592	1	1	ANL	T-31	1625	1361	1
1.02	0.70	.004000	0.0	263;265	2	1	ANC	A-72	1950	3080	9
1.02	0.67	.004100	0.0	531	1	1	ANL	T-23	2853	3095	1
1.02	0.68	.004100	0.0	507	2	3	ANL	55-12	3740	3095	1
1.02	0.69	.004100	0.0	500	1	3	ANL	T-235	3826	3095	1
1.02	0.70	.004100	0.0	486	1	3	ANL	T-238	3938	3095	1
1.01	0.73	.004100	0.0	425	5	3	ANL	807-1	2091	3166	7
1.01	0.63	.004000	0.0	268;274	7	3	ANC	8-14	2143	3151	9
1.01	0.58	.004000	0.0	287;295	6	10	ANC	BP-67	2558	3151	14
1.01	0.71	.004000	0.0	459	2	4	ANL	10A-4	2674	3151	1
1.01	0.68	.004000	0.0	502	1	3	ANL	T-114	3431	3151	7
1.01	0.71	.004000	0.0	456	2	4	ANL	10A-11	3604	3151	1
1.01	0.69	.004000	0.0	494	1	3	ANL	T-145	3839	3151	7
1.01	0.69	.004000	0.0	494	1	3	ANL	T-120	3949	3151	7
1.01	0.69	.004000	0.0	481	1	3	ANL	AA-7	3980	3151	1
1.00	0.59	.004000	0.0	267;288	6	10	ANC	A1C6	2302	3225	9
1.00	0.65	.004000	0.0	529	1	1	ANL	AA-24	2651	3225	1
1.00	0.63	.004000	0.0	268;268	2	12	ANC	A-31	2737	3225	9
1.00	0.64	.004000	0.0	268;275	2	11	ANC	A-67	2904	3225	9
1.00	0.69	.004000	0.0	507	1	3	ANL	T-143	3006	3225	7
1.00	0.66	.004000	0.0	519	1	3	ANL	T-103	3019	3225	7

Table 2.1 (Contd.)

TOTAL STRAIN RANGE, %	PLASTIC STRAIN RANGE, %	TOTAL STRAIN RATE, 1/S	HOLD TIME, MIN[b]	STRESS RANGE, MPA[c]	HEAT NO.[d]	HEAT TREAT[e]	LAB	SPEC. NO.	OBSERVED CYCLES TO FAIL	COMPUTED CYCLES TO FAIL[f]	REF
TEST TEMPERATURE = 593 C (1100 F)											
1.00	0.65	.004000	0.0	535	1	9	ANL	AA-3	3098	3225	1
1.00	0.71	.004000	0.0	447	5	3	ANL	807-6	3328	3225	7
1.00	0.66	.004000	0.0	518	1	3	ANL	T-35	3395	3225	1
1.00	0.69	.004000	0.0	482	2	1	ANL	8A-10	3519	3225	1
1.00	0.66	.004000	0.0	512	4	3	ANL	544-1	3870	3225	7
1.00	0.67	.004000	0.0	248;264	7	3	ANL	813-1	3979	3225	7
1.00	0.66	.004000	0.0	521	1	3	ANL	T-305	4318	3225	7
1.00	0.71	.004000	0.0	435	5	3	ANL	807-2A	4328	3225	7
0.99	0.62	.004000	0.0	269;294	6	10	ANC	BT-97	2119	3301	12
0.99	0.60	.004000	0.0	270;291	6	10	ANC	BT-85	2292	3301	9
0.99	0.61	.004000	0.0	266;275	7	1	ANC	8-3	2914	3301	9
0.99	0.64	.004000	0.0	539	1	3	ANL	T-318	3522	3301	7
0.99	0.59	.004000	0.0	256;265	6	13	ANC	BP-2	3602	3301	14
0.99	0.69	.003900	0.0	461	5	3	ANL	807-5	4022	3284	7
0.99	0.65	.004000	0.0	517	3	3	ANL	845-2	4376	3301	7
0.97	0.65	.003900	0.0	488	1	3	ANL	T-232	3491	3445	7
0.95	0.62	.004000	0.0	504	1	3	ANL	T-100	3878	3638	7
0.94	0.62	.003600	0.0	489	3	3	ANL	845-1	5003	3653	7
0.80	0.44	.004000	0.0	257;265	6	10	ANC	BT-88	2347	5570	9
0.76	0.47	.004100	0.0	449	1	1	ANL	AA-11	4853	6406	1
0.76	0.49	.004000	0.0	407	2	1	ANL	8A-12	8133	6373	1
0.75	0.47	.004000	0.0	426	1	3	ANL	AA-21	7002	6602	1
0.59	0.34	.004000	0.0	392	3	3	ANL	845-9	18605	13188	7
0.53	0.30	.004200	0.0	179;175	1	3	ANL	T-381	21585	18856	7
0.53	0.30	.004200	0.0	346	1	3	ANL	T-329	27980	18856	4
0.53	0.31	.004200	0.0	334	1	3	ANL	T-335	73753	18856	4
0.52	0.22	.004000	0.0	217;211	6	10	ANC	BT-81	13122	19898	9
0.52	0.28	.004000	0.0	168;187	2	1	ANC	A-200	17419	19898	9

Table 2.1 (Contd.)

TOTAL STRAIN RANGE, %	PLASTIC STRAIN RANGE, %	TOTAL STRAIN RATE, 1/S	HOLD TIME, MIN[b]	STRESS RANGE, MPA[c]	HEAT NO.[d]	HEAT TREAT[e]	LAB	SPEC. NO.	OBSERVED CYCLES TO FAIL	COMPUTED CYCLES TO FAIL[f]	REF
TEST TEMPERATURE = 593 C (1100 F)											
0.52	0.28	.004100	0.0	359	1	3	ANL	T-302	37819	20006	4
0.51	0.27	.004000	0.0	183;178	1	1	ANL	T-16	16439	21270	1
0.51	0.22	.004000	0.0	204;218	6	10	ANC	BT-83	18333	21270	9
0.51	0.26	.004000	0.0	178;191	2	11	ANC	A-73	18618	21270	9
0.51	0.29	.004000	0.0	327	1	1	ANL	AA-9	25925	21270	1
0.51	0.31	.004100	0.0	312	1	3	ANL	AA-8	30498	21386	1
0.51	0.20	.004000	0.0	195;208	6	10	ANC	BP-23	38503	21270	9
0.50	0.21	.004000	0.0	190;205	7	1	ANC	8-4	16347	22791	9
0.50	0.29	.004000	0.0	323	1	1	ANL	AA-6	20834	22791	1
0.50	0.24	.004000	0.0	191;205	6	10	ANC	A1C8	24922	22791	9
0.50	0.23	.004000	0.0	188;194	7	3	ANC	8-19	26215	22791	9
0.50	0.31	.004000	0.0	297	2	4	ANL	10A-5	26832	22791	1
0.50	0.27	.004000	0.0	351	1	3	ANL	T-316	27552	22791	4
0.50	0.27	.004000	0.0	346	1	3	ANL	T-333	30507	22791	4
0.50	0.29	.004000	0.0	332	1	3	ANL	T-323	34052	22791	4
0.50	0.28	.004000	0.0	346	1	3	ANL	T-330	34626	22791	4
0.50	0.28	.004000	0.0	341	1	3	ANL	T-304	42040	22791	7
0.50	0.27	.004000	0.0	344	1	3	ANL	T-319	47003	22791	4
0.50	0.31	.004000	0.0	298	1	9	ANL	AA-5	84525	22791	7
0.50	0.28	.004000	0.0	324	1	1	ANL	T-15	98181	22791	1
0.49	0.26	.004000	0.0	352	1	3	ANL	T-334	29386	24482	4
0.48	0.25	.003900	0.0	340	2	1	ANL	8A-11	20853	26220	1
0.36	0.16	.004100	0.0	306	1	1	ANL	AA-12	52343	86664	1
0.35	0.15	.004000	0.0	148;175	2	1	ANC	A-207	37857	98520	9
0.35	0.15	.004000	0.0	201;181	6	10	ANC	BP-11	57666	98520	9
0.35	0.12	.004000	0.0	196;214	6	10	ANC	BT-12	81291	98520	9
0.35	0.17	.004100	0.0	278	1	3	ANL	AA-13	135937	99065	1
0.35	0.18	.004100	0.0	260	2	4	ANL	9A-11	546669	99065	1

Table 2.1 (Contd.)

TOTAL STRAIN RANGE, %	PLASTIC STRAIN RANGE, %	TOTAL STRAIN RATE, 1/S	HOLD TIME, MIN[b]	STRESS RANGE, MPA[c]	HEAT NO.[d]	HEAT TREAT[e]	LAB	SPEC. NO.	OBSERVED CYCLES TO FAIL	COMPUTED CYCLES TO FAIL[f]	REF
TEST TEMPERATURE = 593 C (1100 F)											
0.27	0.03	.004000	0.0	156;207	6	10	ANC	BT-16	577376[g]	413601	9
2.04	1.62	.000410	0.0	644	1	3	ANL	T-197	380	512	7
1.99	1.57	.000400	0.0	636	3	3	ANL	845-7	681	533	7
1.01	0.66	.000400	0.0	533	1	1	ANL	T-3	1516	2030	1
1.01	0.67	.000380	0.0	520	3	3	ANL	845-6	2935	2011	7
1.00	0.66	.000400	0.0	516	2	3	ANL	59-12	1740	2076	1
1.00	0.67	.000410	0.0	506	1	3	ANL	T-348	2595	2085	7
0.52	0.27	.000410	0.0	194;199	1	3	ANL	T-200	13016	12282	7
2.01	1.60	.000100	0.0	309;308	3	3	ANL	845-13	406	425	7
1.00	0.67	.000100	0.0	247;247	1	3	ANL	T-389	1697	1620	7
2.07	1.58	.000041	0.0	307;274	1	3	ANL	T-216	244	356	1
2.03	1.65	.000041	0.0	292;297	3	3	ANL	845-8	350	368	7
2.01	1.66	.000040	0.0	546	1	3	ANL	T-345	275	373	7
1.49	1.14	.000040	0.0	528	1	3	ANL	T-353	375	630	7
1.03	0.73	.000041	0.0	454	5	3	ANL	807-4A	1016	1305	7
1.02	0.69	.000041	0.0	252;247	5	3	ANL	807-3	1637	1332	7
1.01	0.71	.000040	0.0	212;230	5	3	ANL	807-3A	1163	1355	7
1.00	0.67	.000040	0.0	257;241	1	3	ANL	AA-25	851	1384	1
1.00	0.69	.000040	0.0	232;229	1	3	ANL	T-267	1105	1384	7
1.00	0.66	.000040	0.0	247;260	4	3	ANL	544-1A	1480	1384	7
1.00	0.68	.000040	0.0	444	5	3	ANL	807-1A	1630	1384	7
1.00	0.66	.000040	0.0	249;256	4	3	ANL	544-3	1658	1384	7
1.00	0.68	.000040	0.0	259;228	3	3	ANL	845-4	1707	1384	7
1.00	0.67	.000041	0.0	244;257	3	3	ANL	845-1A	1761	1390	7
0.99	0.69	.000039	0.0	452	1	1	ANL	T-7	1137	1408	1
0.97	0.64	.000039	0.0	258;253	7	3	ANL	813-2	1813	1472	7
0.74	0.45	.000041	0.0	452	1	3	ANL	T-340	2368	2810	7
0.59	0.32	.000041	0.0	411	1	3	ANL	T-355	5555	5251	7

Table 2.1 (Contd.)

TOTAL STRAIN RANGE, %	PLASTIC STRAIN RANGE, %	TOTAL STRAIN RATE, 1/S	HOLD TIME, MIN[b]	STRESS RANGE, MPA[c]	HEAT NO.[d]	HEAT TREAT[e]	LAB	SPEC. NO.	OBSERVED CYCLES TO FAIL	COMPUTED CYCLES TO FAIL[f]	REF
TEST TEMPERATURE = 593 C (1100 F)											
0.50	0.25	.000040	0.0	194;183	1	3	ANL	T-46	6487	8869	1
1.99	1.69	.000010	0.0	220;237	3	3	ANL	845-12	249	313	7
2.00	1.67	.000004	0.0	259;249	1	3	ANL	T-218	204	275	7
1.98	1.66	.000004	0.0	238;252	3	3	ANL	845-11	251	279	7
1.01	0.73	.000004	0.0	211;211	1	3	ANL	T-85	579	933	1
1.99	1.45	.004000	0.6 T	342;356	7	3	ANC	8-26	1068	608	9
1.98	1.54	.004000	0.6 T	319;330	6	13	ANC	BT-8	807	614	14
1.97	1.48	.004000	0.6 T	355;380	8	10	ANC	BT-76	545	620	9
1.01	0.64	.004000	0.6 T	278;300	6	10	ANC	BT-99	1256	2295	12
1.01	0.66	.004000	0.6 T	242;259	6	13	ANC	BT-10	3473	2295	14
1.00	0.64	.004000	0.6 T	269;271	2	12	ANC	A-32	1190	2345	9
1.00	0.64	.004000	0.6 T	284;291	6	10	ANC	A1T5	1484	2345	9
1.00	0.65	.004000	0.6 T	269;270	7	3	ANC	8-15	1650	2345	9
0.99	0.61	.004000	0.6 T	289;294	6	10	ANC	BT-80	1458	2398	12
0.52	0.24	.004000	0.6 T	200;203	7	3	ANC	8-17	13393	12939	9
0.51	0.20	.004000	0.6 T	221;252	6	10	ANC	BT-4	10756	13772	9
0.50	0.23	.004000	0.6 T	184;188	2	3	ANC	A-230	12083	14691	9
0.50	0.21	.004000	0.6 T	202;204	7	1	ANC	8-7	12860	14691	9
0.35	0.15	.004000	0.6 T	220;201	6	10	ANC	BP-10	18271	57562	9
2.05	1.68	.004100	1.0 T	613	1	3	ANL	T-209	378	521	2
1.05	0.75	.004200	1.0 T	477	1	3	ANL	T-331	1824	1850	4
1.01	0.70	.004000	1.0 T	491	2	4	ANL	10A-8	1046	1995	1
1.01	0.69	.004000	1.0 T	507	1	3	ANL	T-282	1171	1995	4
1.01	0.71	.004000	1.0 T	488	1	1	ANL	T-13	1328	1995	1
1.01	0.70	.004000	1.0 T	495	2	1	ANL	9A-1	1470	1995	1
1.01	0.69	.004000	1.0 T	518	1	1	ANL	T-91	1619	1995	1
1.01	0.70	.004000	1.0 T	499	1	3	ANL	T-315	1670	1995	4
1.01	0.72	.004000	1.0 T	457	1	3	ANL	T-309	2255	1995	4

Table 2.1 (Contd.)

TOTAL STRAIN RANGE, %	PLASTIC STRAIN RANGE, %	TOTAL STRAIN RATE, 1/S	HOLD TIME, MIN[b]	STRESS RANGE, MPA[c]	HEAT NO.[d]	HEAT TREAT[e]	LAB	SPEC. NO.	OBSERVED CYCLES TO FAIL	COMPUTED CYCLES TO FAIL[f]	REF
TEST TEMPERATURE = 593 C (1100 F)											
1.01	0.72	.004000	1.0 T	442	2	4	ANL	10A-7	2719	1995	1
1.01	0.74	.004000	1.0 T	442	2	4	ANL	10A-6	2961	1995	1
1.00	0.70	.004000	1.0 T	481	1	3	ANL	T-308	1528	2037	4
1.00	0.69	.004000	1.0 T	500	1	3	ANL	T-275	1560	2037	4
1.00	0.69	.004000	1.0 T	514	1	3	ANL	T-285	1593	2037	4
1.00	0.70	.004000	1.0 T	483	1	3	ANL	AA-10	1664	2037	1
1.00	0.70	.004000	1.0 T	486	1	3	ANL	T-307	1748	2037	4
1.00	0.70	.004000	1.0 T	477	1	3	ANL	T-326	2099	2037	4
1.00	0.70	.004000	1.0 T	496	4	3	ANL	544-2	2712	2037	7
1.00	0.69	.004000	1.0 T	499	3	3	ANL	845-3	3034	2037	7
0.99	0.68	.004000	1.0 T	515	1	1	ANL	T-72	1235	2082	1
0.99	0.72	.004000	1.0 T	437	5	3	ANL	807-2	2755	2082	7
0.50	0.28	.004000	1.0 T	360	2	3	ANL	62-6	10441	12111	1
0.49	0.29	.003900	1.0 T	316	2	4	ANL	10A-2	14970	12878	1
0.48	0.25	.003800	1.0 T	347	2	1	ANL	8A-9	9365	13725	1
1.04	0.74	.004000	5.0 T	457	3	3	ANL	845-23	2225	1031	7
1.03	0.69	.004000	5.0 T	486	3	3	ANL	845-25	2222	1050	7
2.00	1.55	.004000	6.0 T	332;344	6	13	ANC	BT-7	629	324	14
1.98	1.38	.004000	6.0 T	345;364	6	10	ANC	BT-15	382	329	9
1.97	1.52	.004000	6.0 T	306;328	2	11	ANC	A-223	369	331	9
1.95	1.41	.004000	6.0 T	328;357	8	10	ANC	BT-75	272	336	9
1.94	1.40	.004000	6.0 T	321;333	7	3	ANC	8-27	1008	339	9
1.02	0.73	.004000	6.0 T	266;260	6	10	ANC	BT-79	593	992	12
1.01	0.63	.004000	6.0 T	277;279	6	10	ANC	A1C2	631	1010	9
1.01	0.67	.004000	6.0 T	263;264	7	3	ANC	8-20	1708	1010	9
1.00	0.65	.004000	6.0 T	283;308	6	10	ANC	BT-31	790	1029	14
1.00	0.71	.004000	6.0 T	273;265	2	12	ANC	A-39	806	1029	9
1.00	0.63	.004000	6.0 T	262;255	7	1	ANC	8-6	1555	1029	9

Table 2.1 (Contd.)

TOTAL STRAIN RANGE, %	PLASTIC STRAIN RANGE, %	TOTAL STRAIN RATE, 1/S	HOLD TIME, MIN[b]	STRESS RANGE, MPA[c]	HEAT NO.[d]	HEAT TREAT[e]	LAB	SPEC. NO.	OBSERVED CYCLES TO FAIL	COMPUTED CYCLES TO FAIL[f]	REF
TEST TEMPERATURE = 593 C (1100 F)											
1.00	0.65	.004000	6.0 T	241;261	6	13	ANC	BT-1	2564	1029	14
0.52	0.24	.004000	6.0 T	178;181	2	3	ANC	A-231	5874	4306	9
0.51	0.28	.004000	6.0 T	187;192	2	3	ANC	A-234	3725	4535	9
0.50	0.19	.004000	6.0 T	214;248	6	10	ANC	BT-5	6245	4785	9
0.50	0.23	.004000	6.0 T	182;197	7	3	ANC	8-29	11680[g]	4785	9
1.01	0.73	.004000	10.0 T	459	1	1	ANL	T-56	553	821	1
1.01	0.71	.004000	10.0 T	453	1	3	ANL	AA-23	636	821	1
1.00	0.72	.004000	10.0 T	229;233	1	3	ANL	T-371	706	836	6
0.99	0.72	.004000	10.0 T	223;236	3	3	ANL	845-14	1826	851	7
0.50	0.28	.004000	10.0 T	345	1	3	ANL	AA-28	3803	3617	1
2.00	1.66	.004000	15.0 T	605	1	3	ANL	T-44	237	244	1
1.00	0.74	.004000	15.0 T	441	1	3	ANL	T-30	666	713	1
0.60	0.39	.004200	15.0 T	345	1	3	ANL	T-38	2765	1911	1
1.98	1.40	.004000	30.0 T	316;346	6	10	ANC	BT-6	271	204	9
1.96	1.56	.004000	30.0 T	299;318	2	1	ANC	A-224	190	207	9
1.00	0.62	.004000	30.0 T	259;293	6	10	ANC	A1B10	588	553	9
1.00	0.66	.004000	30.0 T	256;229	7	3	ANC	8-22	1574	553	9
1.98	1.66	.004000	60.0 T	562	1	3	ANL	T-217	112	171	1
1.00	0.71	.004000	60.0 T	230;247	2	12	ANC	A-33	593	440	9
0.99	0.72	.003900	60.0 T	410	1	3	ANL	AA-27	338	446	1
0.99	0.75	.004000	60.0 T	255;243	2	11	ANC	A-70	418	447	9
0.55	0.34	.004400	60.0 T	328	1	3	ANL	T-244	1253	1261	3
2.01	1.70	.000040	60.0 T	550	1	3	ANL	T-54	102	172	1
1.02	0.72	.000041	60.0 T	509	4	3	ANL	544-4	751	474	5
1.01	0.72	.000040	60.0 T	241;268	4	3	ANL	544-9	378	483	6
1.01	0.79	.000040	60.0 T	397	5	3	ANL	807-4	874	483	5
1.00	0.73	.000040	60.0 T	209;264	4	3	ANL	544-8	557	492	7
1.00	0.78	.000040	60.0 T	391	3	3	ANL	845-5	767	492	5

Table 2.1 (Contd.)

TOTAL STRAIN RANGE, %	PLASTIC STRAIN RANGE, %	TOTAL STRAIN RATE, 1/S	HOLD TIME, MIN[b]	STRESS RANGE, MPA[c]	HEAT NO.[d]	HEAT TREAT[e]	LAB	SPEC. NO.	OBSERVED CYCLES TO FAIL	COMPUTED CYCLES TO FAIL[f]	REF
TEST TEMPERATURE = 593 C (1100 F)											
0.99	0.72	.000040	60.0 T	471	1	3	ANL	T-70	305	500	1
0.60	0.38	.000043	60.0 T	376	1	3	ANL	T-62	1031	1327	1
2.02	1.74	.004000	180.0 T	526	1	3	ANL	T-163	63	131	2
0.62	0.42	.004100	180.0 T	339	1	3	ANL	T-168	1251	682	3
1.02	0.76	.004100	180.0 T	447	1	3	ANL	T-159	170	314	2
0.59	0.41	.004000	180.0 T	321	1	3	ANL	T-93	1284	743	2
1.00	0.75	.000040	300.0 T	224;233	1	3	ANL	T-368	233	287	7
1.03	0.82	.004100	600.0 T	390	1	3	ANL	T-190	212	237	3
1.00	0.77	.004000	600.0 T	218;216	1	3	ANL	T-390	252	245	7
2.01	1.74	.000040	600.0 T	242;274	1	3	ANL	T-358	87	94	7
TEST TEMPERATURE = 650 C (1202 F)											
3.95	3.49	.032000	0.0	694	2	1	GE	66-7	303	269	8
1.98	1.62	.032000	0.0	536	2	1	GE	63-12	765	952	8
1.89	1.50	.025000	0.0	710	2	1	BCL	SS-15	744	986	15
3.95	3.47	.016000	0.0	712	2	1	GE	66-5	223	240	8
3.95	3.49	.016000	0.0	686	2	1	GE	66-4	292	240	8
2.73	2.30	.015000	0.0	674	2	1	BCL	SS-18	385	452	15
1.98	1.61	.016000	0.0	549	2	1	GE	63-7	705	821	8
0.99	0.70	.016000	0.0	435	2	1	GE	66-2	2904	3316	8
1.98	1.61	.008000	0.0	539	2	1	GE	63-11	734	712	8
0.49	0.28	.008000	0.0	322	2	1	GE	66-3	11136	17561	8
3.95	3.49	.004000	0.0	342;342	2	1	GE	66-8	184	192	8
2.10	1.71	.004200	0.0	579	2	1	GE		566	565	8
2.01	1.62	.004000	0.0	288;292	2	5	ANL	4A-3	701	604	1
2.01	1.62	.004000	0.0	290;291	2	5	ANL	6A-4	724	604	1

Table 2.1 (Contd.)

TOTAL STRAIN RANGE, %	PLASTIC STRAIN RANGE, %	TOTAL STRAIN RATE, 1/S	HOLD TIME, MIN[b]	STRESS RANGE, MPA[c]	HEAT NO.[d]	HEAT TREAT[e]	LAB	SPEC. NO.	OBSERVED CYCLES TO FAIL	COMPUTED CYCLES TO FAIL[f]	REF
TEST TEMPERATURE = 650 C (1202 F)											
2.00	1.70	.004000	0.0	219;224	2	1	ANL	3A-3	714	610	1
1.99	1.64	.004000	0.0	259;263	2	7	ANL	4A-5	775	615	1
1.98	1.58	.004000	0.0	281;281	2	1	GE	54-5	546	621	8
1.98	1.58	.004000	0.0	274;274	2	1	GE	53-11	592	621	8
1.98	1.59	.004000	0.0	579	1	3	ANL	T-337	722	621	7
1.61	1.24	.004300	0.0	268;272	2	5	ANL	1A-9	1018	917	1
1.11	0.79	.004400	0.0	481	2	1	GE		1740	1903	8
1.10	0.78	.004400	0.0	239;237	2	7	ANL	4A-8	2214	1938	1
1.01	0.76	.004000	0.0	184;186	2	7	ANL	3A-7	2406	2268	1
1.01	0.70	.004000	0.0	228;217	2	3	ANL	59-10	2426	2268	1
1.00	0.69	.004000	0.0	243;230	2	5	ANL	4A-6	2217	2316	1
1.00	0.71	.004000	0.0	231;209	2	3	ANL	59-9	3082	2316	1
0.99	0.68	.004000	0.0	229;232	1	3	ANL	T-372	2604	2367	7
0.84	0.60	.004200	0.0	194;190	2	1	ANL	3A-2	3504	3449	1
0.80	0.52	.004200	0.0	210;204	2	5	ANL	1A-8	3489	3865	1
0.76	0.46	.004000	0.0	415	2	1	BCL	SS-14	3881	4316	15
0.75	0.47	.004000	0.0	411	2	5	ANL	6A-2	4507	4457	1
0.59	0.33	.004700	0.0	387	2	1	GE		7320	8697	8
0.59	0.33	.004700	0.0	393	2	1	GE		7944	8697	8
0.52	0.28	.004000	0.0	171;171	2	1	GE	54-11	14620	12064	8
0.50	0.31	.004000	0.0	143;146	2	7	ANL	3A-6	9504	13624	1
0.50	0.27	.004000	0.0	173;173	2	1	GE	54-12	13400	13624	8
0.49	0.28	.004200	0.0	120;102	2	1	ANL	3A-1	21121	14718	1
0.49	0.27	.003900	0.0	165;162	1	3	ANL	T-373	25771	14426	7
0.47	0.25	.004000	0.0	365	2	1	BCL	SS-5	6882	16627	15
0.44	0.22	.004000	0.0	334	2	1	BCL	SS-10	12253	20784	15
0.40	0.18	.004000	0.0	163;158	2	5	ANL	1A-7	21524	29331	1
0.33	0.16	.004100	0.0	132;130	2	5	ANL	4A-9	64929	65092	1

Table 2.1 (Contd.)

TOTAL STRAIN RANGE, %	PLASTIC STRAIN RANGE, %	TOTAL STRAIN RATE, 1/S	HOLD TIME, MIN[b]	STRESS RANGE, MPA[c]	HEAT NO.[d]	HEAT TREAT[e]	LAB	SPEC. NO.	OBSERVED CYCLES TO FAIL	COMPUTED CYCLES TO FAIL[f]	REF
TEST TEMPERATURE = 650 C (1202 F)											
0.31	0.15	.004000	0.0	227	2	1	BCL	SS-16	189891	86351	15
0.26	0.13	.004200	0.0	145;156	2	7	ANL	4A-11	226016	220504	1
0.25	0.11	.004000	0.0	105;105	2	1	GE	66-6	1000000[g]	273986	8
2.10	1.76	.000420	0.0	507	2	1	GE		310	370	8
1.10	0.80	.000440	0.0	449	2	1	GE		805	1170	8
0.58	0.34	.000470	0.0	355	2	1	GE		3549	5114	8
2.08	1.80	.000042	0.0	419	2	1	GE		261	257	8
1.98	1.68	.000040	0.0	219;219	2	1	GE	63-2	315	275	8
1.09	0.82	.000043	0.0	398	2	1	GE		660	750	8
0.57	0.35	.000045	0.0	314	2	1	GE		2134	3136	8
0.57	0.36	.000046	0.0	323	2	1	GE		3124	3151	8
1.98	1.76	.000004	0.0	326	2	1	GE	63-8	307	193	8
1.98	1.64	.004000	0.1 T	267;278	2	1	GE	57-2	570	588	8
1.98	1.64	.004000	0.1 T	272;284	2	1	GE	56-12	545	588	8
2.06	1.76	.004000	1.0 T	496	2	5	ANL	12A-6	311	405	1
1.98	1.66	.004000	1.0 T	264;281	2	1	GE	57-1	329	432	8
1.98	1.66	.004000	1.0 T	264;281	2	1	GE	56-11	331	432	8
1.00	0.80	.004000	1.0 T	342	2	5	ANL	6A-3	930	1439	1
0.50	0.33	.004000	1.0 T	271	2	5	ANL	4A-2	3198	7146	1
0.49	0.29	.004000	1.0 T	151;158	2	1	GE	57-11	3869	7570	8
0.49	0.28	.004000	1.0 T	162;167	2	1	GE	57-9	5351	7570	8
3.95	3.64	.004000	10.0 T	309;309	2	1	GE	66-9	59	89	8
2.02	1.77	.004000	10.0 T	469	2	1	ANL	4A-7	253	216	1
2.00	1.71	.004000	10.0 T	254;254	2	1	GE	56-5	193	219	8
2.00	1.71	.004000	10.0 T	254;254	2	1	GE	56-1	201	219	8
1.00	0.79	.004000	10.0 T	382	1	1	ANL	T-58	525	607	1
0.99	0.78	.004000	10.0 T	189;189	2	1	GE	66-10	547	617	8
0.98	0.77	.003900	10.0 T	390	2	5	ANL	6A-11	645	626	1

Table 2.1 (Contd.)

TOTAL STRAIN RANGE, %	PLASTIC STRAIN RANGE, %	TOTAL STRAIN RATE, 1/S	HOLD TIME, MIN[b]	STRESS RANGE, MPA[c]	HEAT NO.[d]	HEAT TREAT[e]	LAB	SPEC. NO.	OBSERVED CYCLES TO FAIL	COMPUTED CYCLES TO FAIL[f]	REF
TEST TEMPERATURE = 650 C (1202 F)											
0.49	0.32	.004000	10.0 T	139;151	2	1	GE	57-12	1703	2367	8
0.49	0.31	.004000	10.0 T	151;151	2	1	GE	65-1	1713	2367	8
0.25	0.10	.004000	10.0 T	113;113	2	1	GE	63-3	8640	19295	8
2.08	1.79	.004000	30.0 T	232;232	2	1	GE	53-10	146	158	8
2.02	1.76	.004000	30.0 T	232;232	2	1	GE	53-12	165	163	8
0.49	0.33	.004000	30.0 T	148;148	2	1	GE	56-3	1216	1461	8
0.48	0.34	.004000	30.0 T	144;144	2	1	GE	56-2	862	1527	8
1.98	1.74	.000040	30.0 T	218;232	2	1	GE	57-10	142	151	8
1.96	1.75	.000040	30.0 T	192;208	2	1	GE	57-4	182	153	8
1.98	1.77	.004000	60.0 T	245;245	2	1	GE	54-2	144	145	8
1.98	1.78	.004000	60.0 T	223;223	2	1	GE	54-1	158	145	8
0.49	0.34	.004000	60.0 T	137;137	2	1	GE	65-4	995	1142	8
2.00	1.80	.004000	180.0 T	209;219	2	1	GE	57-7	120	120	8
1.98	1.78	.004000	180.0 T	219;219	2	1	GE	57-6	150	121	8
1.05	0.87	.004200	180.0 T	360	1	3	ANL	T-242	313	263	2
2.02	1.80	.000040	180.0 T	425	1	3	ANL	T-76	146	105	7
1.01	0.84	.000040	180.0 T	351	1	3	ANL	T-115	213	254	7
1.98	1.80	.004000	600.0 T	193;207	2	1	GE	66-1	149	106	8
2.01	1.81	.000040	600.0 T	401	1	3	ANL	T-99	67	84	1
TEST TEMPERATURE = 700 C (1292 F)											
2.41	2.05	.000800	0.0	256;281	2	15	ANC	20-E	245	266	10
1.01	0.70	.000800	0.0	217;232	2	15	ANC	18-E	882	1127	10
0.55	0.31	.000800	0.0	168;206	2	15	ANC	19-E	3965	4210	10
0.35	0.14	.000800	0.0	153;152	2	15	ANC	30-E	18964	16843	10
1.00	0.78	.004000	6.0 T	208;203	2	14	ANC	A-44	1186	554	13

Table 2.1 (Contd.)

TOTAL STRAIN RANGE, %	PLASTIC STRAIN RANGE, %	TOTAL STRAIN RATE, 1/S	HOLD TIME, MIN[b]	STRESS RANGE, MPA[c]	HEAT NO.[d]	HEAT TREAT[e]	LAB	SPEC. NO.	OBSERVED CYCLES TO FAIL	COMPUTED CYCLES TO FAIL[f]	REF
TEST TEMPERATURE = 700 C (1292 F)											
0.56	0.43	.000800	60.0 T	143;133	2	14	ANC	A-41	601[g]	596	13
TEST TEMPERATURE = 816 C (1500 F)											
2.06	1.81	.004100	0.0	323	2	1	GE		260	296	8
2.02	1.78	.004000	0.0	305	2	5	ANL	7A-11	321	302	1
1.99	1.76	.004000	0.0	145;154	2	5	ANL	60-8	362	309	1
1.07	0.83	.004300	0.0	307	2	1	GE		784	806	8
0.57	0.36	.004500	0.0	271	2	1	GE		2477	2546	8
2.05	1.83	.000410	0.0	279	2	1	GE		145	168	8
1.06	0.86	.000420	0.0	256	2	1	GE		429	408	8
0.56	0.36	.000450	0.0	248	2	1	GE		1334	1182	8
0.56	0.36	.000450	0.0	259	2	1	GE		1351	1182	8
2.05	1.86	.000041	0.0	241	2	1	GE		130	103	8
1.05	0.87	.000042	0.0	233	2	1	GE		307	230	8
0.56	0.38	.000044	0.0	232	2	1	GE		788	591	8

Table 2.1 (Contd.)

Footnotes:

a. Included are essentially all of the axial strain-controlled data obtained at temperatures of 430°C and greater at Argonne National Laboratory (ANL), Aerojet Nuclear Company (ANC), General Electric Company - Nuclear Systems Program (GE), and Battelle Columbus Laboratories (BCL). Also included are GE diametral strain-controlled data (data for which no test numbers are given). Not included are block-loading, mean-strain, surface-finish-effects, or cyclic-creep tests, nor tests on weld metal, cold-worked, irradiated, or notched specimens.

b. T denotes hold time at constant peak tension strain.

c. For hold-time tests, stress values given are prior to relaxation. A single value corresponds to the total peak-to-peak stress range near $N_f/2$; when two numbers are given, the first is the tensile component of the stress range, and the second is the compressive component.

d. Material heat numbers are as follows:
   1. 9T2796
   2. 55697
   3. 346845
   4. 346544
   5. X22807 (Type 304L Stainless Steel)
   6. 600414
   7. 8043813
   8. 300380

3. Pretest heat treatments are as follows:
   1. Solution annealed
   2. Solution annealed and aged 1000 h at 566°C (1050°F)
   3. Solution annealed and aged 1000 h at 593°C (1100°F)
   4. Solution annealed and aged 1000 h at 650°C (1202°F)
   5. Stress relieved 15 min at 760°C (1400°F)
   6. Stress relieved and aged 47 h at 566°C (1050°F)
   7. Stress relieved and aged 160 h at 650°C (1202°F)

Table 2.1 (Contd.)

8. Stress relieved 30 min at 760°C (1400°F)
9. Hot rolled
10. As-fabricated or as-welded
11. Aged 3096 h at 410°C (770°F)
12. Aged 8760 h at 400°C (752°F)
13. Aged 8000 h at 593°C (1100°F)
14. Aged 8760 h at 750°C (1382°F)
15. Aged 9240 h at 750°C (1382°F)

f. Cycles to failure computed from regression-analysis equation.

g. Test terminated before failure.

h. Test not included in regression analysis, but tabulated here for completeness.

Table 2.2. Summary of Elevated-temperature, Strain-controlled, Compression and Tension Plus Compression Hold-time Low-cycle Fatigue Data for Type 304 Stainless Steel[a]

TOTAL STRAIN RANGE, %	PLASTIC STRAIN RANGE, %	TOTAL STRAIN RATE, 1/S	HOLD TIME, MIN[b]	STRESS RANGE, MPA[c]	HEAT NO.[d]	HEAT TREAT[e]	LAB	SPEC. NO.	OBSERVED CYCLES TO FAIL	REF
				TEST TEMPERATURE = 593 C (1100 F)						
1.03	0.70	.004000	1.0 C	255;242	3	3	ANL	845-24	2747	7
1.01	0.70	.004000	1.0 C	477	2	1	ANL	9A-2	2973	1
1.01	0.72	.004000	1.0 C	463	1	1	ANL	T-18	2995	1
1.01	0.70	.004000	1.0 C	475	1	3	ANL	AA-14	3344	1
0.99	0.71	.004000	1.0 C	461	2	4	ANL	10A-1	2353	1
0.99	0.69	.004000	1.0 C	487	2	4	ANL	10A-10	2272	1
0.99	0.67	.004000	1.0 C	480	3	3	ANL	845-21	2401	7
1.01	0.71	.004000	2.0 C	242;245	1	3	ANL	T-376	2993	7
0.99	0.69	.003900	2.0 C	244;243	3	3	ANL	845-17	2659	7
1.02	0.70	.004000	4.0 C	477	4	3	ANL	544-5	2366	7
1.02	0.71	.004100	4.0 C	258;254	1	3	ANL	T-378	2453	6
1.00	0.71	.004000	4.0 C	248;237	3	3	ANL	845-18	2997	7
1.01	0.74	.004000	10.0 C	441	2	3	ANL	51-9	2810	1
1.00	0.72	.004000	10.0 C	231;224	3	3	ANL	845-15	2624	7
1.02	0.72	.004000	1.0 S	487	1	3	ANL	AA-17	2207	1
1.01	0.72	.004000	1.0 S	446	2	4	ANL	9A-12	2065	1
1.01	0.70	.004000	1.0 S	492	1	1	ANL	T-20	2082	1
1.00	0.70	.004000	1.0 S	483	2	1	ANL	9A-5	2432	1
1.00	0.74	.004000	1.0 S	443	2	4	ANL	10A-12	3276	1
0.99	0.72	.004000	1.0 S	432	2	4	ANL	10A-9	3157	1
0.99	0.69	.004000	1.0 S	240;250	3	3	ANL	845-19	2880	7
1.03	0.74	.004000	2.0 S	243;247	1	3	ANL	T-377	2177	6
0.99	0.67	.004000	2.0 S	472	3	3	ANL	845-20	2348	7
1.02	0.77	.004000	10.0 S	421	2	3	ANL	55-10	1470	1

Table 2.2 (Contd.)

TOTAL STRAIN RANGE, %	PLASTIC STRAIN RANGE, %	TOTAL STRAIN RATE, 1/S	HOLD TIME, MIN[b]	STRESS RANGE, MPA[c]	HEAT NO.[d]	HEAT TREAT[e]	LAB	SPEC. NO.	OBSERVED CYCLES TO FAIL	REF
				TEST TEMPERATURE = 650 C (1202 F)						
0.98	0.71	.003900	1.0 C	432	2	5	ANL	7A-2	1944	1
1.98	1.71	.000040	5.5 C	226;226	2	1	GE	65-12	258	8
1.98	1.70	.004000	30.0 C	264;264	2	1	GE	54-3	480	8
1.97	1.70	.004000	30.0 C	234;234	2	1	GE	52-11	409	8
1.00	0.77	.004000	1.0 S	345	2	8	ANL	7A-8	1714	7
0.49	0.32	.004000	1.0 S	137;137	2	1	GE	57-8	6916	8
0.49	0.31	.004000	1.0 S	144;144	2	1	GE	65-3	10266	8
1.98	1.71	.004000	3.0 S	233;233	2	1	GE	53-8	526	8
0.49	0.37	.004000	10.0 S	130;130	2	1	GE	65-10	7001	8
1.98	1.80	.004000	30.0 S	214;214	2	1	GE	53-9	380	8
1.98	1.84	.004000	30.0 S	220;220	2	1	GE	54-9	416	8
0.49	0.34	.004000	10/3[f]	141;141	2	1	GE	63-1	4430	8
2.00	1.79	.004000	30/3[f]	232;233	2	1	GE	65-9	336	8
1.98	1.77	.004000	30/3[f]	230;230	2	1	GE	65-11	308	8

Table 2.2 (Contd.)

Footnotes:

a. Included are essentially all of the axial strain-controlled data obtained at temperatures of 430°C and greater at Argonne National Laboratory (ANL), Aerojet Nuclear Company (ANC), General Electric Company - Nuclear Systems Program (GE), and Battelle Columbus Laboratories (BCL). Not included are block loading, mean-strain, surface-finish-effects, or cyclic-creep tests, nor tests on weld metal, cold-worked, irradiated, or notched specimens.

b. C denotes hold time at constant peak compression strain; S denotes equal tension and compression (symmetrical) hold times.

c. For hold-time tests, stress values given are prior to relaxation. A single value corresponds to the total peak-to-peak stress range near $N_f/2$; when two numbers are given, the first is the tensile component of the stress range, and the second is the compressive component.

d. Material heat numbers are as follows:
   1. 9T2796
   2. 55697
   3. 346845
   4. 346544

e. Pretest heat treatments are as follows:
   1. Solution annealed
   3. Solution annealed and aged 1000 h at 593°C (1100°F)
   4. Solution annealed and aged 1000 h at 650°C (1202°F)
   5. Stress relieved 15 min at 760°C (1400°F)
   8. Stress relieved 30 min at 760°C (1400°F)

f. First number denotes hold time at peak tension strain per cycle; second number denotes hold time at peak compression strain per cycle.

at constant total axial strain rate and cyclic relaxation (hold time at constant total axial strain) are not included. The only exception is the inclusion of GE data generated at constant total diametral strain rate. In all cases, the tabulated strain-range and strain-rate values refer to axial strain.

The compression and tension plus compression hold-time data of Table 2.2 were considered insufficient to permit the development of a meaningful analytic description. However, the zero and tension hold-time data of Table 2.1 clearly form an adequate base for a regression analysis. The cyclic life N_f was selected as the dependent variable, and the independent variables chosen were total axial strain range $\Delta\varepsilon_t$, in percent; total axial strain rate $\dot{\varepsilon}$, in s^{-1}; test temperature T_c, in degrees celsius; and tensile hold time t_h, in minutes. The following transformations were employed to ensure that the numerical values of the independent variables were of the same order of magnitude:

$$S = \log_{10} (\Delta\varepsilon_t/100),$$

$$R = \log_{10} (\dot{\varepsilon}),$$

$$T = T_c/100,$$

and

$$H = \log_{10} (t_h + 1).$$

Note that the transformation on hold time is such that H drops out of the regression equation when $t_h = 0$.

The problem of choosing the appropriate transformation for the dependent variable N_f was somewhat more difficult. In performing a regression analysis, transformations on the dependent variable are generally made with three objectives in mind:[16] (a) to simplify the fitting equation obtained, (b) to obtain a distribution of residuals that does not vary systematically with any of the test variables (i.e., stabilize the variance), and (c) to obtain an approximately normal distribution of residuals. The transformation on N_f that most nearly satisfies these criteria is $(\log_{10} N_f)^{-1/2}$. This transformation was found to be superior

to the transformations $\log_{10} N_f$, $(\log_{10} N_f)^{-1}$, and $(\log_{10} N_f)^{1/2}$. Thus, in the regression analysis performed, $(\log_{10} N_f)^{-1/2}$ was assumed to be a polynomial function of S, R, T, and H as defined above. Cross-product terms of two independent variables were permitted in the equation, but cross-products of three or more variables were excluded to avoid inordinate mathematical complexities and excessive computation times. Terms of up to the fourth power in S and H and the second power in T and R were permitted.

"Cyclic-life" values from several tests terminated before failure were included in the regression analysis, since these data were considered to provide a useful lower bound on life. However, Battelle-Columbus Laboratories test SS-6 at 538°C was not included, since it was felt that this test had been terminated long before probable failure and its inclusion would unduly distort the model. C. E. Jaske, who conducted this test, concurred in this judgment.[17] Thus, 435 data points were used to perform the analysis.

The regression analysis was conducted on the IBM 370/195 digital computer using the Statistical Analysis System (SAS), a proprietary software package documented in Ref. 18. The Stepwise and Maximum R^2 Improvement procedures were used to select the appropriate variables to be included in the model, and final fitting and statistical analyses were accomplished with the Regression, Sort, Rank, Plot, and Means Procedures. The analytical model finally obtained to describe the data in Table 2.1 was:

$$
\begin{aligned}
(\log_{10} N_f)^{-1/2} = {} & 1.20551064 + 0.66002143 \cdot S \\
& + 0.18040042 \cdot S^2 - 0.00814329 \cdot S^4 \\
& + 0.00025308 \cdot R \cdot S^4 + 0.00021832 \cdot T \cdot S^4 \\
& - 0.00054660 \cdot R \cdot T^2 - 0.00555671 \cdot R \cdot H^2 \\
& - 0.00293919 \cdot H \cdot R^2 + 0.01197141 \cdot H \cdot T \\
& - 0.00051639 \cdot H^2 \cdot T^2 \ . \qquad (1)
\end{aligned}
$$

The correlation coefficient for this model is 0.9781. Table 2.3 lists the standard errors for the regression coefficients of Eq. (1) and the

Table 2.3. Standard Errors and Significance Levels for Coefficients of Eq. (1)

Independent Variable	Coefficient	Standard Error of Coefficient	Significance Level for Coefficient = 0
Intercept	1.20551064	0.12590008	<0.0001
S	0.66002143	0.17346963	0.0002
S^2	0.18040042	0.06626364	0.0067
S^4	-0.00814329	0.00277250	0.0035
$R \cdot S^4$	0.00025308	0.00010376	0.0151
$T \cdot S^4$	0.00021832	0.00008683	0.0123
$R \cdot T^2$	-0.00054660	0.00003993	<0.0001
$R \cdot H^2$	-0.00555671	0.00098693	<0.0001
$H \cdot R^2$	-0.00293919	0.00038466	<0.0001
$H \cdot T$	0.01197141	0.00067554	<0.0001
$H^2 \cdot T^2$	-0.00051639	0.00008020	<0.0001

significance level at which a given coefficient has a value of zero, i.e., the independent variable associated with this coefficient does not belong in the model. Thus, a significance level of 0.01 means that a 1% probability exists that the associated variable is included in the model erroneously. All of the variables included in the model are significant at the 0.02 level.

Since the above determination of significance levels assumes that the distribution of residuals is normal about zero, it is appropriate to verify this. Figure 2.1 is a plot of the percent of residuals on a normal probability scale versus residual value for the Eq. (1) model. The residual is here defined to be $(\log_{10} N_{obs})^{-1/2} - (\log_{10} N_{comp})^{-1/2}$, where N_{obs} is the experimentally observed cyclic life and N_{comp} is the life computed from Eq. (1). The residual plot corresponds closely to the standard normal line for a population that has a mean μ of zero and a standard deviation σ of 0.01348471. This σ value corresponds to the sample standard deviation s computed for the residuals. As an additional confirmation of normality, the distribution of residuals about zero was compared with a normal distribution using a χ^2 test. The distribution of residuals was found to be indistinguishable from a normal distribution at a 10% level of significance. This distribution may be considered to be close enough to a normal distribution that meaningful inferences concerning confidence limits and standard errors of the coefficients can be made.

The lack of dependence of the residuals on the other test parameters is indicated in Fig. 2.2, in which the residuals are plotted as a function of $(\log_{10} N_{obs})^{-1/2}$. No significant variation in the distribution of residuals with the transformed observed life is apparent. Similar plots of residuals versus $(\log_{10} N_{comp})^{-1/2}$, S, R, T, H, test laboratory, heat number, and heat treatment displayed no obvious systematic variation. The possible dependence of $(\log_{10} N_{comp})^{-1/2}$ on test laboratory, heat number, and heat treatment will be more thoroughly discussed in a subsequent report.

A plot of $\log N_{obs}$ versus $\log N_{comp}$ for the 435 data points used in the regression analysis is shown in Fig. 2.3. The dashed line corresponds

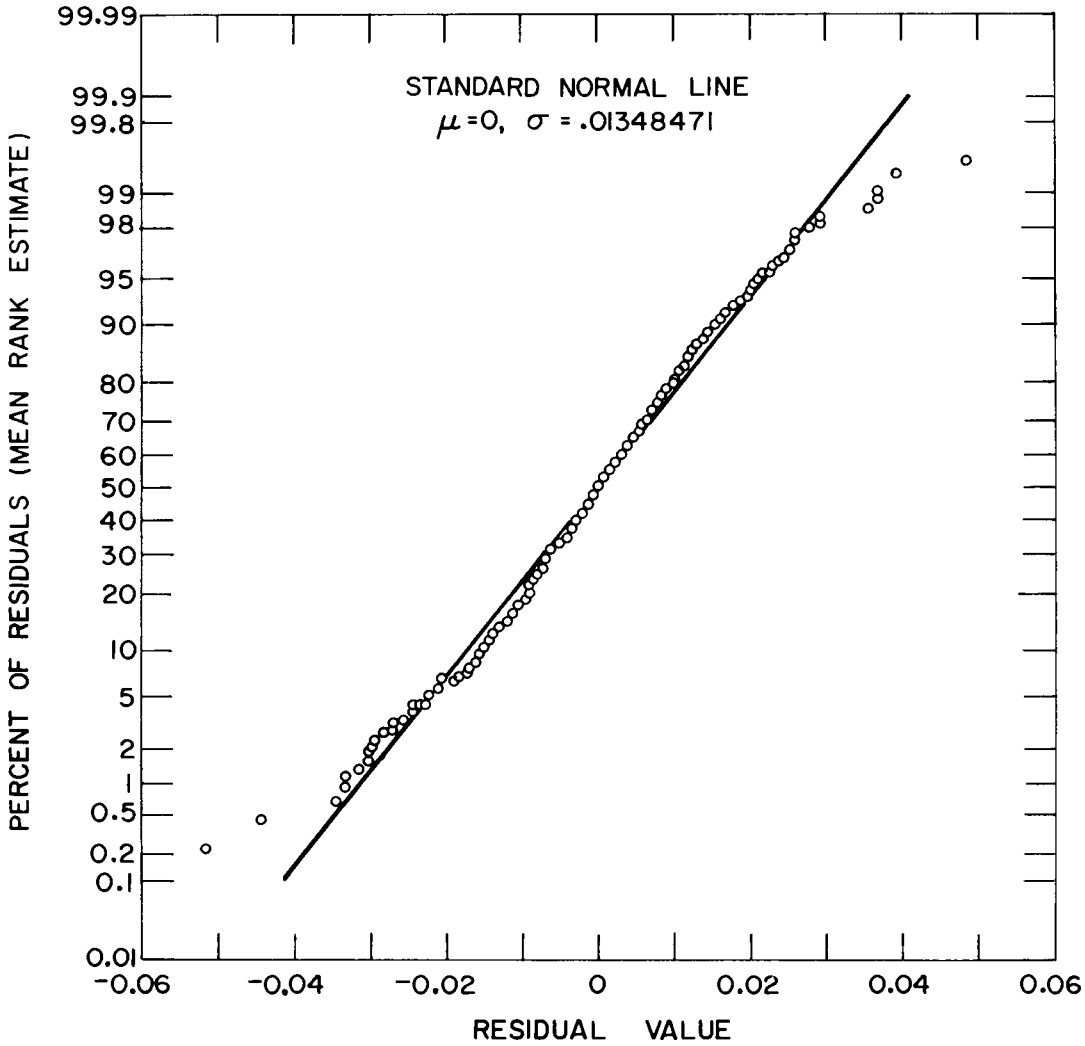

Fig. 2.1. Percent of Residuals That Have a Value Less Than or Equal to a Given Value versus That Value. The standard normal line for $\mu = 0$ and $\sigma = 0.01348471$ is also shown. Neg. No. MSD-62753.

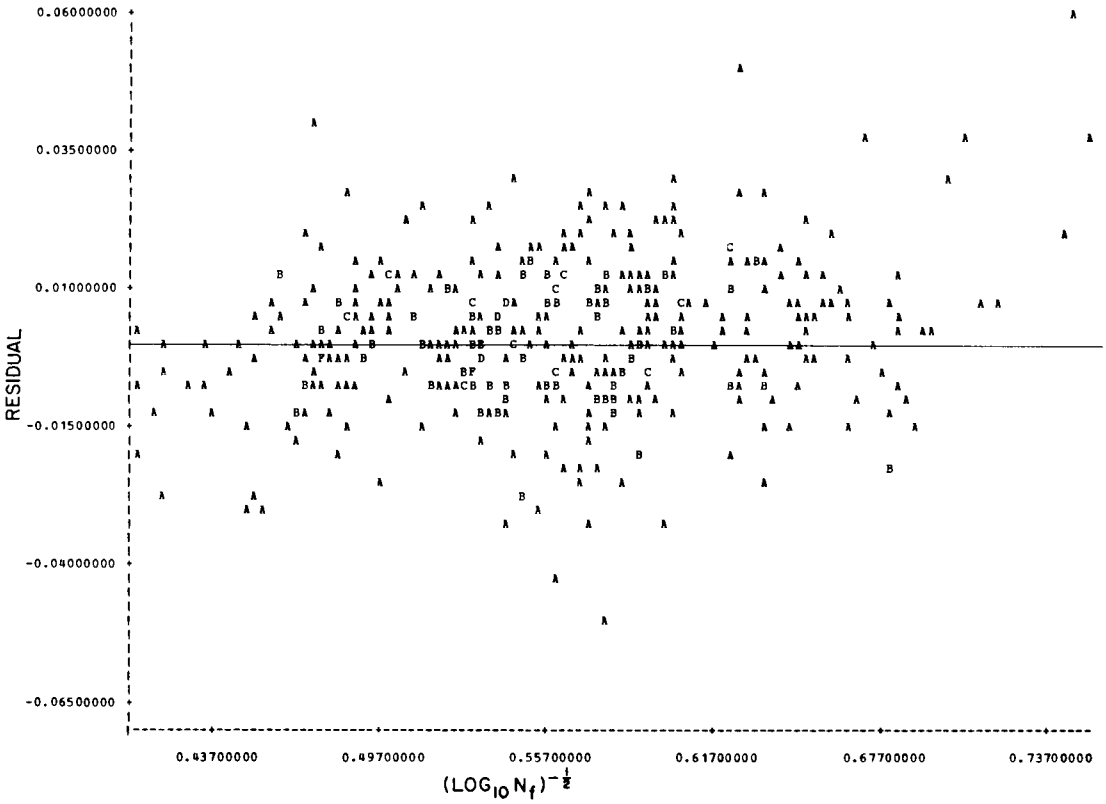

Fig. 2.2. Residual Value versus $(\log_{10} N_{obs})^{-1/2}$. Neg. No. MSD-62754.

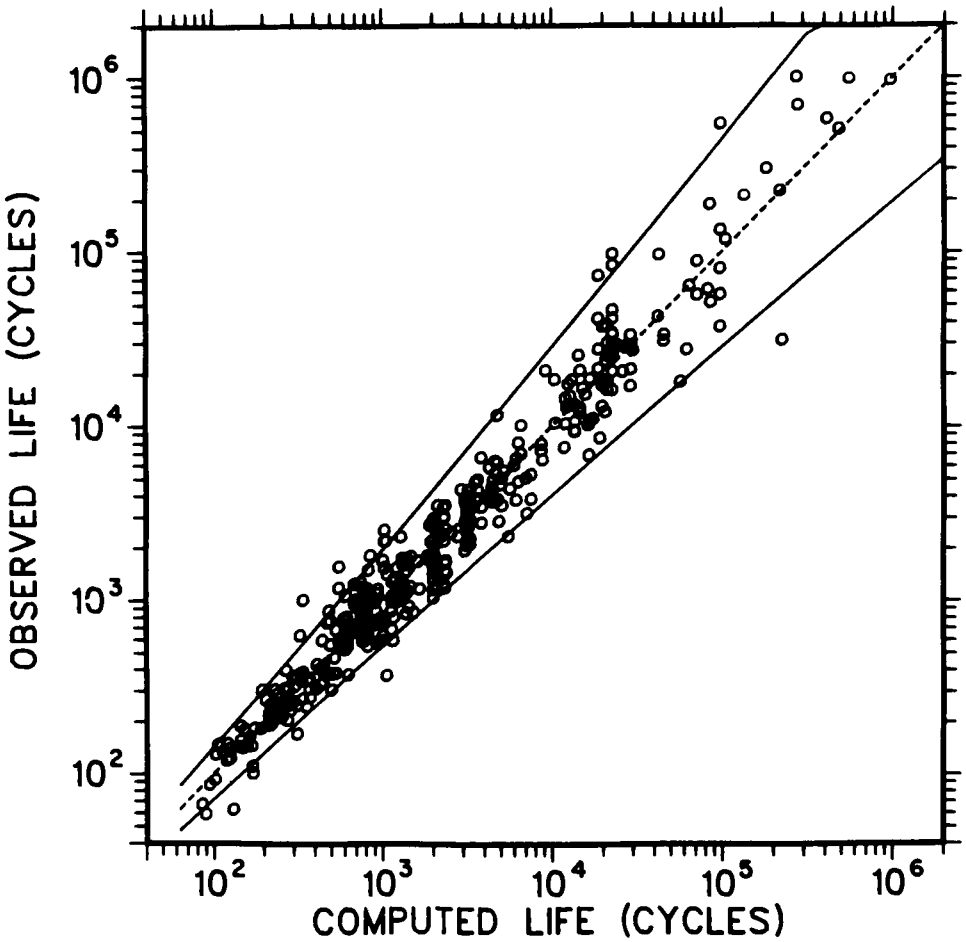

Fig. 2.3. Observed Cyclic Life versus Life Computed from the Regression Equation. The dashed line corresponds to equality of the two life values, and the solid lines define the 95% confidence interval for a given value of computed life. Neg. No. MSD-62657.

to $N_{obs} = N_{comp}$, and the solid lines above and below the dashed line define the 95% confidence interval for a new observation. Thus, if an additional test were run under a given set of conditions for which the computed value of cyclic life was N_{comp}, then one would expect the observed cyclic life N_{obs} for that test to fall within the indicated range about N_{comp} 95% of the time. In this case, the confidence interval is computed assuming (a) the mean expected value for N_{obs} is N_{comp} as given by Eq. (1), (b) the residuals are normally distributed about zero, and (c) the variance of the residuals with respect to

$(\log_{10} N_{comp})^{-1/2}$ is homogeneous. These conditions have already been shown to be approximately satisfied. For a normal distribution, 95% of the observations may be expected to fall in an interval 1.960 standard deviations to each side of the mean. Since the standard deviation for the residuals has already been found to be 0.01348471, the 95% confidence interval about any computed life (or mean value of expected life) N_{comp} is given by $(\log_{10} N_{comp})^{-1/2} \pm 0.02643003$. Because of the $(\log_{10})^{-1/2}$ transformation on N_{comp} employed, the confidence interval is much wider at long lives than at short lives and is slightly skewed in the direction of longer lives. This appears to be consistent with the actual distribution of data, as observed in Fig. 2.3. For a total of 435 data points, one would expect ∿22 points to fall outside the 95% confidence interval, with 11 to each side. In the present analysis, 14 points fell above the upper confidence limit and 9 below the lower confidence limit.

Figures 2.4 and 2.5 show comparisons of the data of Table 2.1 and the fit of Eq. (1) for the specific cases of zero hold-time, 4×10^{-3} s^{-1} strain-rate data at 593 and 650°C. In general the equation describes

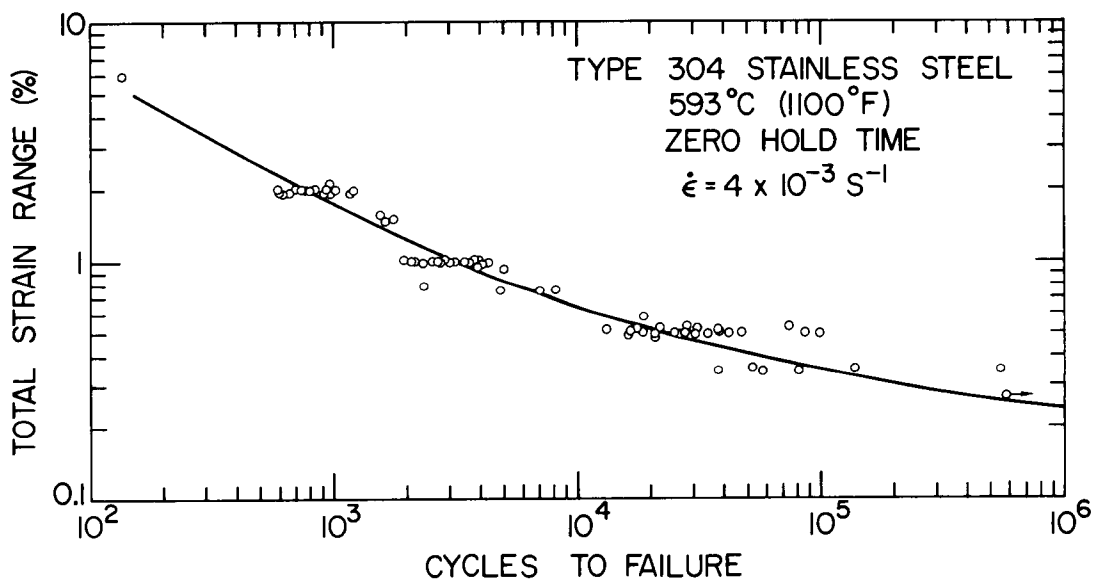

Fig. 2.4. Observed Low-cycle Fatigue Behavior of Type 304 Stainless Steel at 593°C (1100°F) Compared with Fit of Regression Equation. Neg. No. MSD-62751.

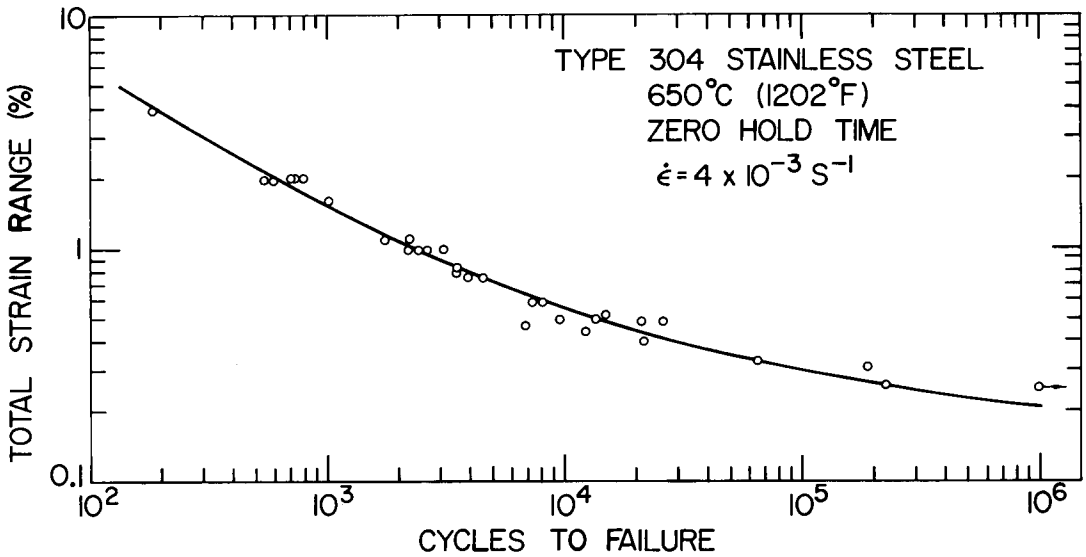

Fig. 2.5. Observed Low-cycle Fatigue Behavior of Type 304 Stainless Steel at 650°C (1202°F) Compared with Fit of Regression Equation. Neg. No. MSD-62752.

the observed behavior quite well. However, because of the interpolative character of Eq. (1), significant departures are sometimes observed in cases where data are sparse. It should be pointed out that Eq. (1) provides an estimate of mean life and confidence intervals under both conditions for which data exist and interpolative conditions. An attempt was also made to obtain a functional form that extrapolated in a reasonable manner, but no life-predictive capabilities outside the range of data are claimed for Eq. (1). In general, the results of any extrapolation of Eq. (1) must be viewed as questionable.

2.2.2 A Unified and Mechanistic Approach to Creep-Fatigue Damage -- S. Majumdar and P. S. Maiya

2.2.2.1 Introduction

The importance of plastic strain rate in elevated-temperature fatigue and creep is fairly well established.[19,20] For example, the cyclic life of most materials under continuous cycling decreases as the frequency (or strain rate) of loading decreases. This is not surprising in view of the fact that a lowering of the strain rate is

associated with more and more grain-boundary sliding, and, consequently, more damage to the material occurs with the resultant intergranular failure. However, in most of the currently available predictive methods for evaluation of the life of structural materials subjected to a general creep-fatigue loading, the effect of plastic strain rate is not explicitly taken into account.[19,21] The approach described in the present report does not separate the total inelastic strain into plastic (time independent) and creep (time dependent) components but explicitly considers the effect of plastic strain rate.

2.2.2.2 Basic Damage Equation

We assume that the current microcrack length a is a measure of damage and, during the majority of the life of a low-cycle fatigue specimen, preexistent microcracks of length a_o extend to a final length a_c. The current growth rate of the microcracks is assumed to be of the following form:

$$\frac{da}{dt} = \begin{cases} aT\,|\varepsilon_p|^m\,|\dot{\varepsilon}_p|^k & \text{(in the presence of tensile stress)} \\ aC\,|\varepsilon_p|^m\,|\dot{\varepsilon}_p|^k & \text{(in the presence of compressive stress)} \end{cases} \tag{2}$$

where ε_p and $\dot{\varepsilon}_p$ are the current plastic strain (including both time-dependent and time-independent components) and plastic strain rate, respectively. The terms T, C, m, and k are materials parameters that are functions of temperature, environment, and metallurgical state of the material. Although these parameters are constant over a limited range of plastic strain rate, they vary over a wide range of plastic strain rate in which different damage mechanisms may operate. Since plastic strain is not a state variable, a material structure state variable, rather than plastic strain, should be used in Eq. (2).[22] However, for all loading cases considered in the present report, the plastic strain reflects the material structure state variable, and, consequently, its use in Eq. (2) is acceptable for the present purposes.

For continuous cycling at a plastic strain range $\Delta\varepsilon_p$ and constant plastic strain rate $\dot{\varepsilon}_p$, Eq. (2) can be integrated to yield cycles to failure N_f as

$$N_f = \frac{m+1}{4A} \left(\frac{\Delta\varepsilon_p}{2} \right)^{-(m+1)} \dot{\varepsilon}_p^{\,1-k} , \tag{3}$$

where

$$A = \frac{C+T}{2} \Big/ \ln \frac{a_c}{a_o} \tag{3a}$$

For tests that involve specimens with indentical geometry and microstructure, A can be considered to be a materials parameter.

2.2.2.3 Application to Type 304 Stainless Steel

The parameters A, m, and k for Type 304 stainless steel at 593°C were determined by a least-squares fit of Eq. (3) to the extensive series of continuous-cycling, low-cycle fatigue data generated for this material at ANL.[1] Prior to fatigue testing, all specimens were solution annealed at 1092°C for 30 min and aged at 593°C for 1000 h to achieve a fairly stable microstructure. Figure 2.6 is a plot of parameters A, m, and k versus plastic strain rate. Although m and A show a transitional behavior, k does not exhibit such a variation within the experimental range of strain rates. However, k should saturate at a value of unity, beyond which an additional increase in strain rate does not affect fatigue life. It can also be shown that k cannot decrease indefinitely with a decrease in strain rate but should level off at a minimum value. Because of the lack of continuous-cycling fatigue data at low strain rates, this minimum value of k was determined by correlation with hold-time fatigue data. The transitional behavior of the parameters may be associated with the transition in the appearance of the fatigue fracture surface from a predominantly transgranular to a predominantly intergranular mode.

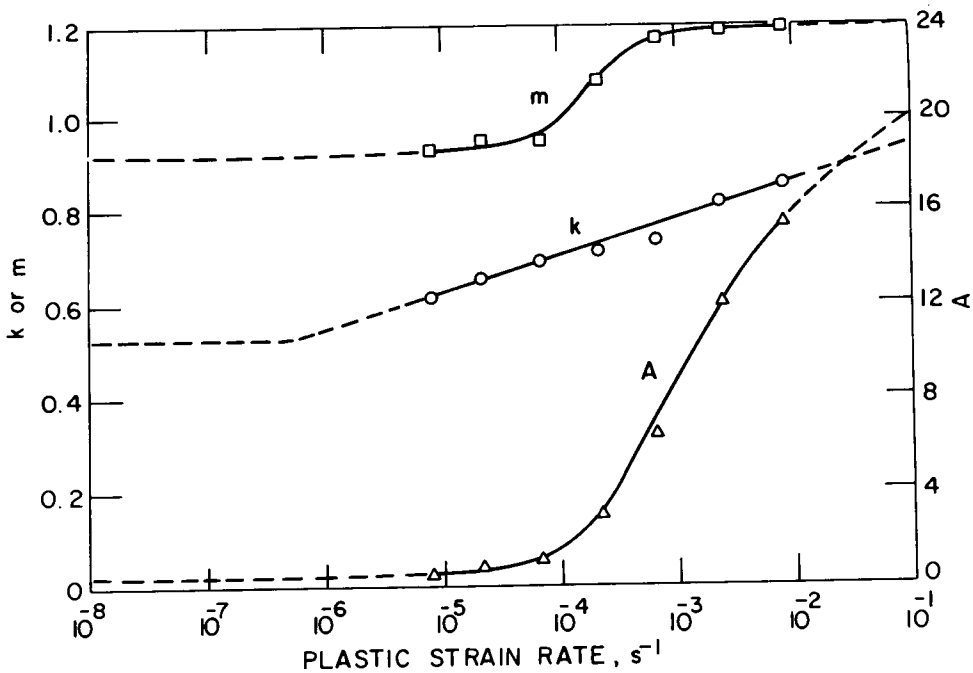

Fig. 2.6 Variation of Parameters A, m, and k with Plastic Strain Rate for Type 304 Stainless Steel at 593°C. Neg. No. MSD-61799.

2.2.2.3.1 Life Prediction for Various Loading Histories. For a given history of plastic strain and strain rate, the time (or cycles) to failure may be obtained by integrating Eq. (2) and using appropriate values of the parameters from Fig. 2.6. For this particular material, the coefficient T in Eq. (2) has been found to be approximately four times the value of C at 593°C.

Figure 2.7 shows a comparison of the calculated and experimentally observed lives for a representative sampling of hold-time fatigue data (both cyclic relaxation and cyclic creep tests) for Type 304 stainless steel at 593°C. The predicted life in all cases is within a factor of two (dashed lines) of the observed life.

Figure 2.8 shows the calculated and experimentally observed times to rupture for a variety of monotonic creep-rupture and tensile tests for Type 304 stainless steel at 593°C. The fatigue parameters k and m, which determine the slope of the calculated rupture life, are

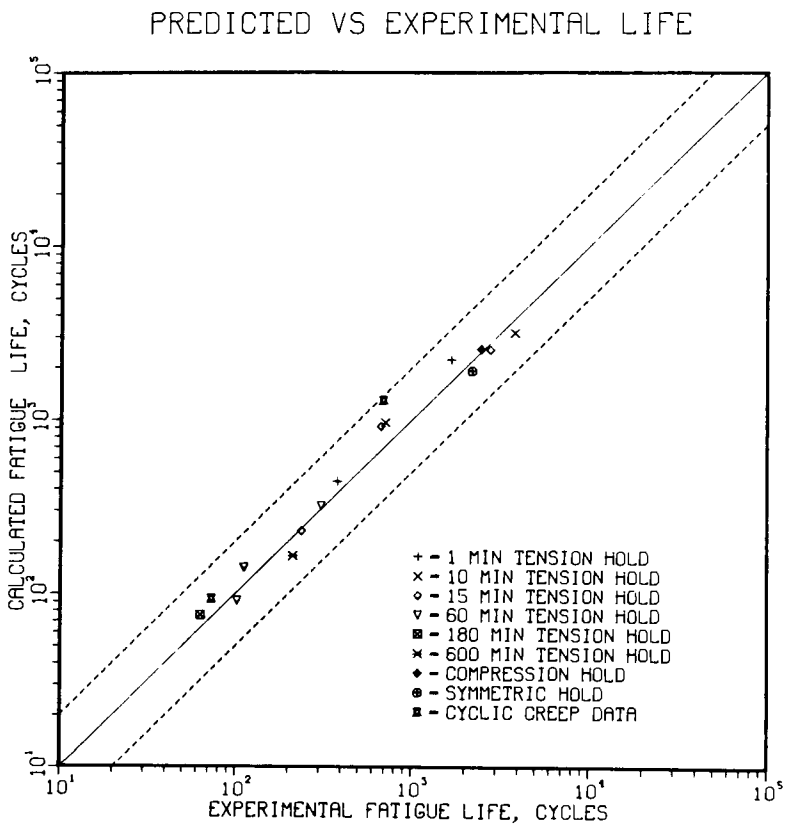

Fig. 2.7. Experimental and Predicted Cycles to Failure for Hold-time Fatigue Tests of Type 304 Stainless Steel at 593°C. Neg. No. MSD-62105.

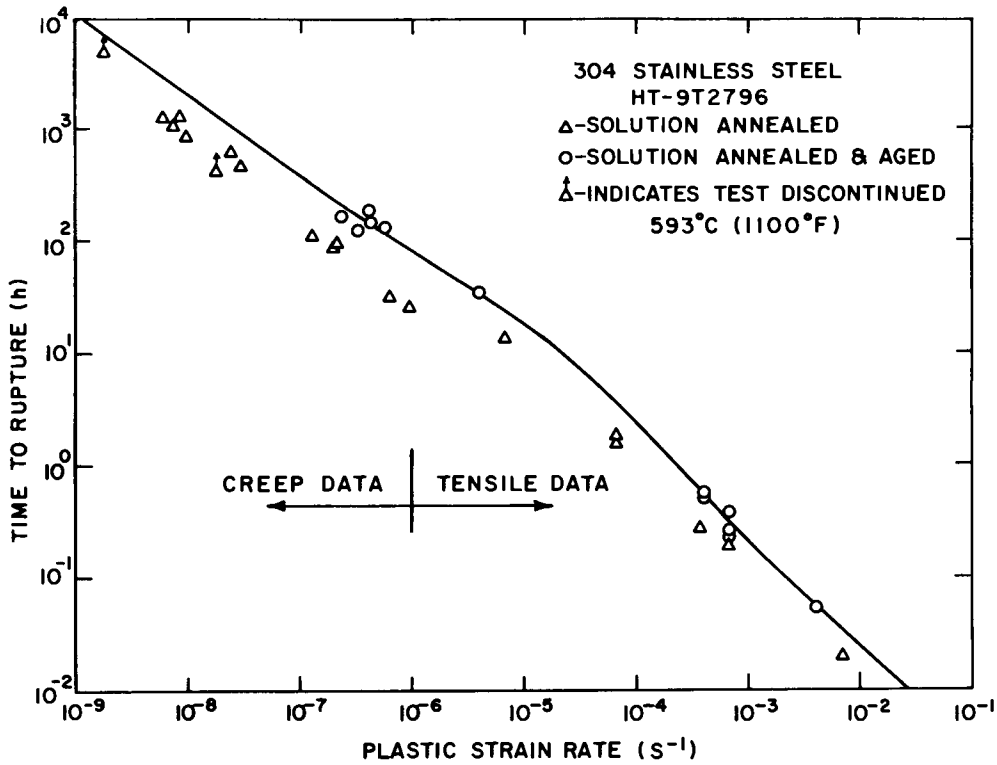

Fig. 2.8 Variation of Time to Rupture with Plastic Strain Rate. Neg. No. MSD-62107.

thus applicable to monotonic loading. However, the value of the coefficient T in Eq. (2) is found to be 15 times smaller for the monotonic case when compared with the cyclic case.

Rising mean strain fatigue tests involve interaction between monotonic extension rate and cyclic loading. Figure 2.9 shows experimental data as well as fatigue lives calculated by means of both the monotonic value, A', and cyclic value, A, of the coefficient. The rising mean strain rates are sufficiently high so that all test data fall close to the lives calculated by means of the monotonic value of the coefficient A'.

2.2.2.4 Conclusions

A creep-fatigue-damage equation that takes into account the effect of plastic strain rate has been presented. Although the basic approach is phenomenological, it can be justified qualitatively from

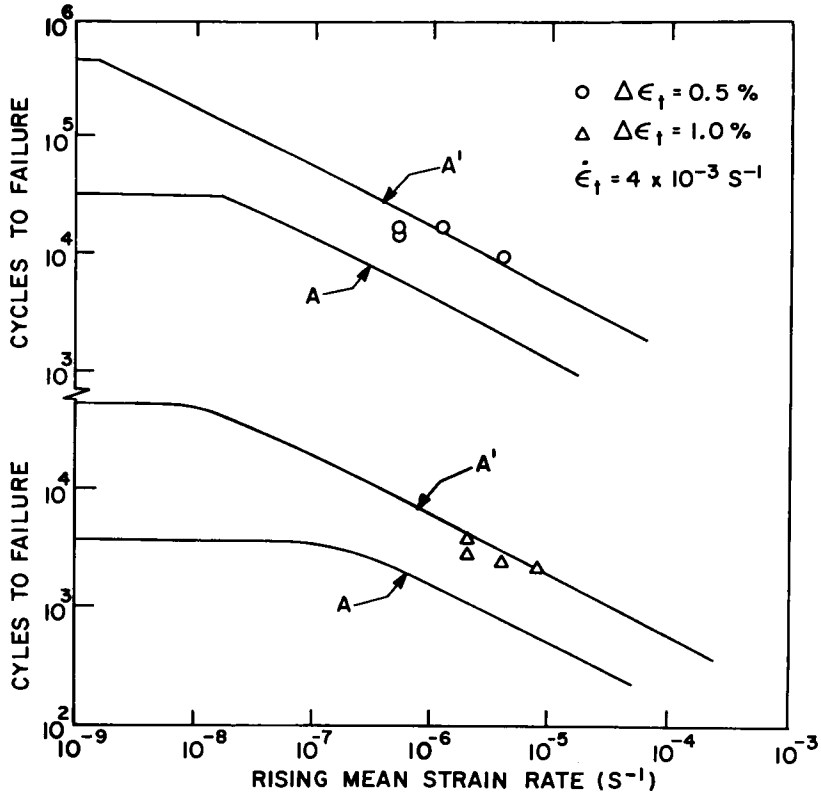

Fig. 2.9. Experimental and Predicted Cycles to Failure for Rising Mean Strain Tests of Type 304 Stainless Steel at 593°C. Neg. No. MSD-62106.

a mechanistic viewpoint. The method has been used to predict the life of Type 304 stainless steel under various monotonic and cyclic loading conditions. Although only data at 593°C have been presented, the approach has also been used successfully to predict data at 538 and 482°C. Additional tests that involve different materials are required to verify the present approach.

2.3 SODIUM EFFECTS ON LMFBR MATERIALS -- T. F. Kassner

2.3.1 Uniaxial Creep-rupture Properties of Austenitic Stainless Steels -- K. Natesan and O. K. Chopra

The effect of carburization on the creep-rupture properties of Types 304, 316, and Ti-modified 316 stainless steel, after exposure to well-characterized sodium at temperatures between 550 and 700°C, is being

determined. The mechanical-property changes in the carburized material will be correlated with the sodium purity, which will be helpful in establishing better design and performance limits for components that operate in a sodium environment.

Data on the uniaxial creep-rupture properties of Type 304 stainless steel specimens in the solution-annealed condition and after exposure to a flowing sodium environment at temperatures of 700, 650, and 600°C have been presented previously[23] in tabular form. Figure 2.10 shows the variations in rupture life and minimum creep rate with applied stress in the temperature range 600-700°C for specimens in both the annealed and sodium-exposed conditions. In general, the data show that, for the range of carbon concentrations attained (0.043-0.046 wt% at 700°C, 0.078-0.195 wt% at 650°C, and 0.145-0.25 wt% at 600°C) in the

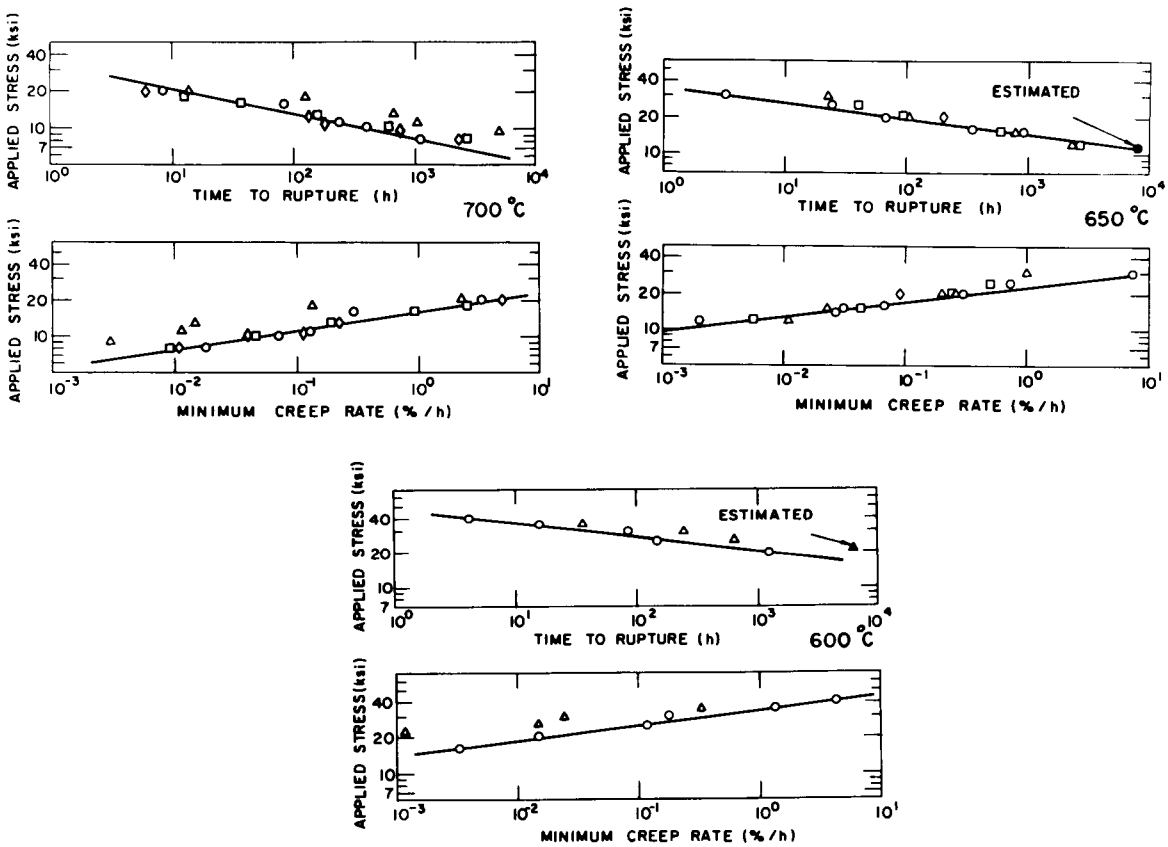

Fig. 2.10. Variation of Time to Rupture and Minimum Creep Rate with Applied Stress at 700, 650, and 600°C. Solution annealed: o; carburization depths: △ = 100 μm, □ = 200 μm, and ◇ = 375 μm; conversion factor: 1 ksi = 6.894 MPa. Neg. No. MSD-62387.

present investigation, the exposure of the stainless steel to the sodium environment resulted in an increase in rupture life and a decrease in minimum creep rate when compared with material in the solution-annealed condition. Creep-rupture correlations that relate rupture life t_r and minimum creep rate $\dot{\varepsilon}_m$ or time to onset of tertiary creep t_2 were also developed for specimens in the annealed and sodium-exposed conditions. These correlations along with values for the exponents and proportionality constants are listed in Table 2.4.

Table 2.4. Creep Correlations

$t_r = C\left(\dot{\varepsilon}_m\right)^{-\alpha}$		
Treatment	α	C
Solution Annealed	0.99	22.16
Na Exposed at 650 and 700°C	0.95	22.45
Na Exposed at 600°C	0.79	17.90
$t_2 = B\left(t_r\right)^{\beta}$		
Treatment	β	B
Solution Annealed	1.025	0.558
Na Exposed (All Temperatures)	1.061	0.475
All Data	1.05	0.501
$\dot{\varepsilon}_2 = D\left(\dot{\varepsilon}_m\right)^{\gamma}$		
Treatment	γ	D
Solution Annealed	0.987	1.072
Na Exposed at 650 and 700°C	0.972	1.079
Na Exposed at 600°C	0.918	1.075

$\dot{\varepsilon}_m = A(\sigma)^n$			
Treatment	Temperature, °C	n	A
Solution Annealed	700	5.60	1.53×10^{-7}
Solution Annealed	650	5.90	5.33×10^{-9}
Solution Annealed	600	6.40	7.31×10^{-11}
Na Exposed	700	6.23	2.74×10^{-8}
Na Exposed	650	6.48	5.26×10^{-10}
Na Exposed	600	10.71	9.22×10^{-18}

Current elevated-temperature design rules[24] require not only a knowledge of rupture behavior and time to onset of tertiary creep but also the time to reach a specified strain. The time to a specified strain limit (currently set at 1% total inelastic membrane strain) has been analyzed by means of isochronous stress-strain curves.[25] This involves analysis of individual strain-time curves for constant-load constant-temperature tests and development of analytical formalisms to describe the strain-time behavior. The experimental strain-time curves generated in the present work were analyzed in terms of the creep equation developed by Booker.[26] The equation is a single rational polynomial and is written as

$$\varepsilon = \frac{dpt}{1 + pt} + \dot{\varepsilon}_m t \,, \tag{4}$$

where ε is the creep strain, d is the intercept strain, $\dot{\varepsilon}_m$ is the minimum creep rate, and t is the time. The parameter p is related to the curvature of the primary portion of the curve. The intercept d was evaluated by the expression

$$d = \varepsilon_2 - \dot{\varepsilon}_m t_2 = \dot{\varepsilon}_2 t_2 - \dot{\varepsilon}_m t_2 \,, \tag{5}$$

where ε_2 and t_2 are the strain and time, respectively, that correspond to the onset of tertiary creep and $\dot{\varepsilon}_2$ is the slope of the line drawn from the origin of the creep curve to the point which corresponds to the onset of tertiary creep. The parameter p was assigned a value of $49/t_2$ since this value resulted in good agreement between the experimental strain-time data for Type 304 stainless steel (Heat 9T2796) and Booker's analysis.[26] An analytical expression that relates the minimum creep rate $\dot{\varepsilon}_m$ and applied stress σ was also developed for temperatures of 700, 650, and 600°C from the creep data generated in the present program on specimens in both the annealed and sodium-exposed conditions. The expression can be written as

$$\dot{\varepsilon}_m = A\,(\sigma)^n \,, \tag{6}$$

where A and n are constants, the values of which are also shown in Table 2.4.

The correlations listed in Table 2.4 were used in Eq. (4) to compute the strain-time curves, and a comparison of the experimental data with the calculated values for specimens in the annealed and sodium-exposed conditions was attempted. Figure 2.11 shows that the calculated values are in good agreement with the experimental data generated on solution-annealed and sodium-exposed specimens at 600 and 650°C. Generally, the agreement was good in the temperature range 600-700°C and stress range 8-35 ksi. Figure 2.12 shows the isochronous stress-creep strain curves that were generated at temperatures of 700, 650, and 600°C for the annealed and sodium-exposed conditions. The results show that the carburization of the steel in the sodium environment, in the range of our investigation, enhances the creep-rupture properties of the material. The beneficial effect is most pronounced at 600°C, where the material has undergone a greater degree of carburization than at 650 and 700°C.

Figure 2.13 shows the stress levels as a function of temperature calculated for the 1% strain limit in a specified time for the steel in the solution-annealed and sodium-exposed conditions. Figure 2.14 shows the stress levels calculated for 10^4 and 10^5 h rupture strengths as a function of temperature.

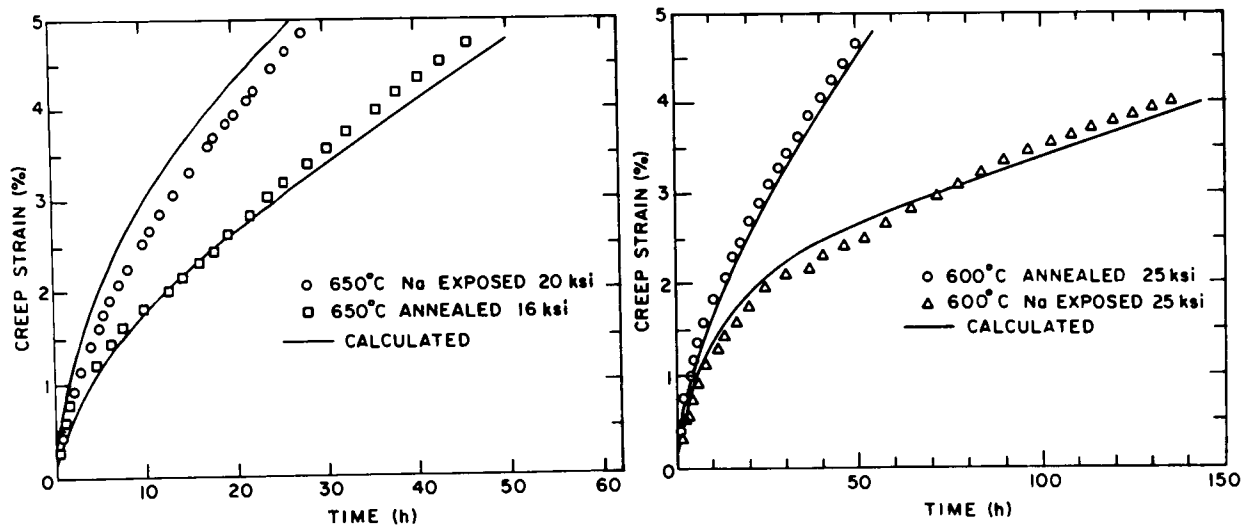

Fig. 2.11. Comparison of Experimental Creep Strain-Time Curves with Calculated Values. Neg. No. MSD-62593.

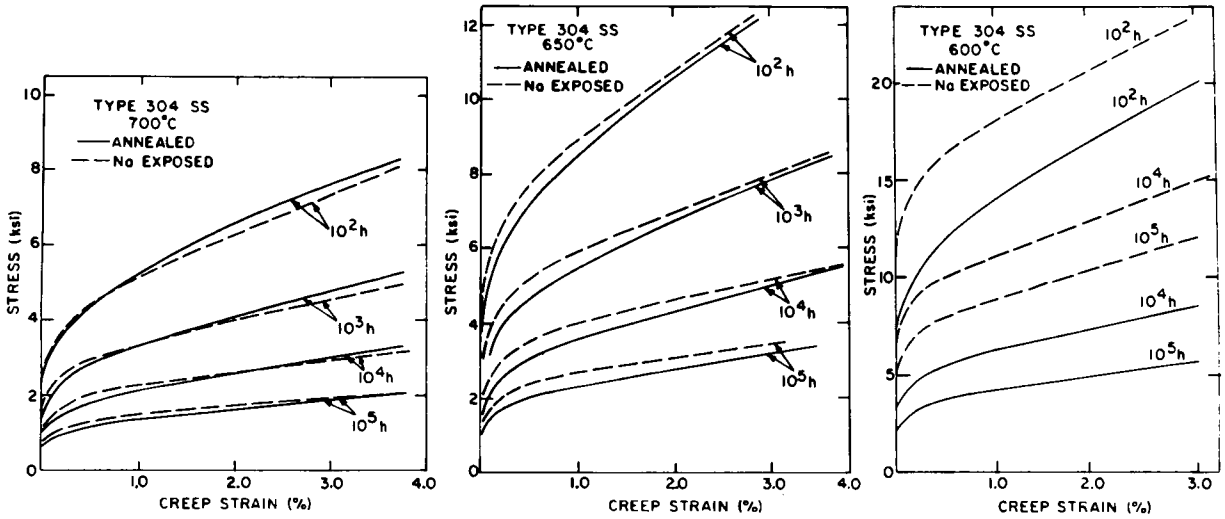

Fig. 2.12. Isochronous Stress-Creep Strain Curves for Specimens in the Solution-annealed and Sodium-exposed Conditions. Conversion factor: 1 ksi = 6.894 MPa. Neg. No. MSD-62594.

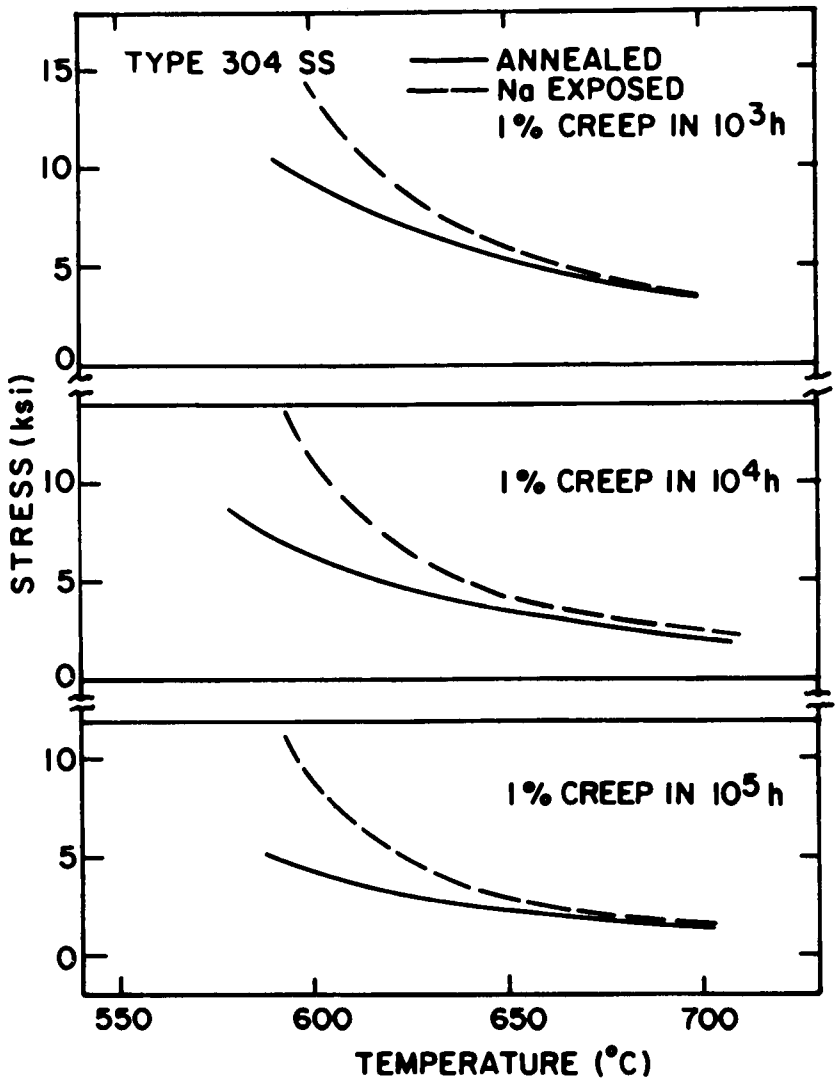

Fig. 2.13. Stress Values to Produce 1% Creep Strain as a Function of Temperature for the Solution-annealed and Sodium-exposed Conditions. Conversion factor: 1 ksi = 6.894 MPa. Neg. No. MSD-62591.

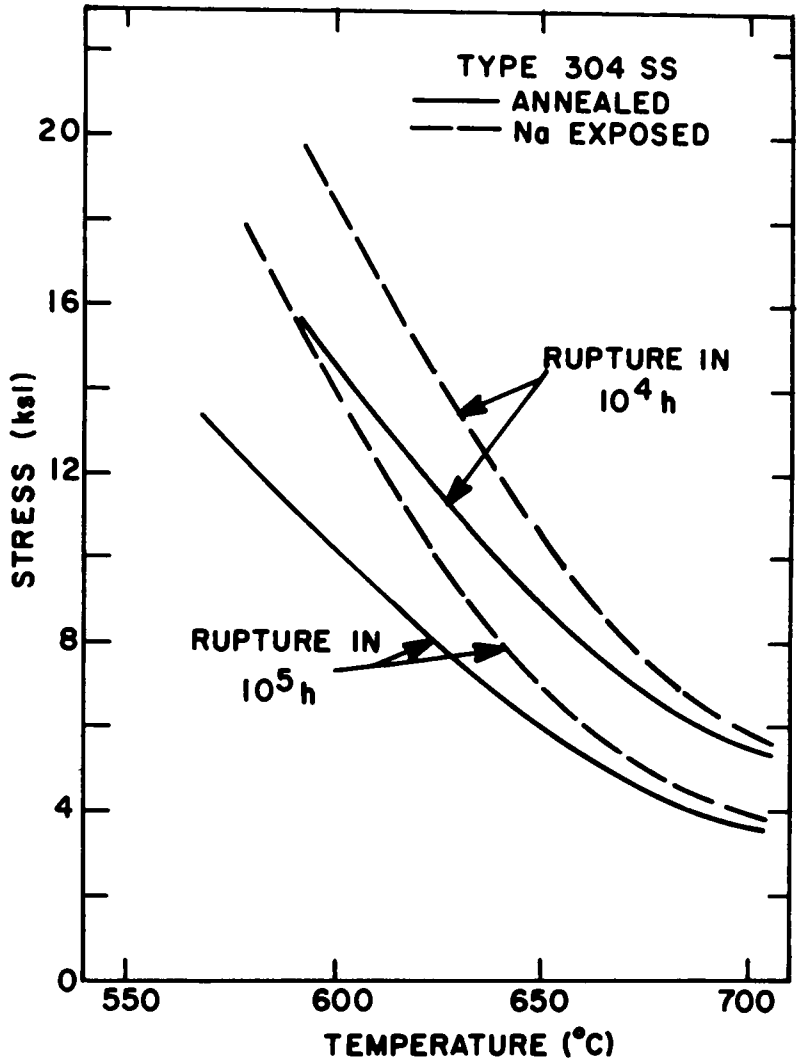

Fig. 2.14. Stress Values for 10^4 and 10^5 h Rupture Strengths as a Function of Temperature for the Solution-annealed and Sodium-exposed Conditions. Conversion factor: 1 ksi = 6.894 MPa. Neg. No. MSD-62592.

2.3.2 Influence of Sodium Environment on the Low-cycle Fatigue Behavior of Austenitic Stainless Steels -- D. L. Smith and G. J. Zeman

Investigations are being conducted to determine the effect of a high-temperature sodium environment on the fatigue behavior of AISI Types 304 and 316 stainless steel. The tests have been formulated to determine the influence of testing in a sodium environment and the effect of long-term sodium exposure on the fatigue properties of the

steels. The fatigue tests are performed in sodium of controlled purity (∿1 ppm oxygen and 0.3 ppm carbon) with a fully reversed triangular waveform and zero mean strain at a strain rate of $\sim 4 \times 10^{-3}\ s^{-1}$.

In the previous report,[23] fatigue data obtained on annealed Type 304 stainless steel in sodium at 600°C were compared with results in air at 593°C. The fatigue lifetime curves were essentially the same for the two environments at strain ranges below ∿1%. It was also reported that a 1512-h exposure of Type 304 stainless steel to sodium at 600°C resulted in a factor of ∿2 to 4 increase for the fatigue life in sodium for strain ranges between 1.4 and 0.7% when compared with that of the annealed material. This is substantially greater than the ∿50% increase in the fatigue lifetime in air for aged material when compared with annealed material.[1,27] Therefore, the greater fatigue life of the sodium-exposed material can be attributed to surface carburization.

During this reporting period, the fatigue properties were determined for specimens exposed to sodium at 600°C for 5012 h. Figure 2.15 shows the relationship between the strain range and the fatigue lifetime in

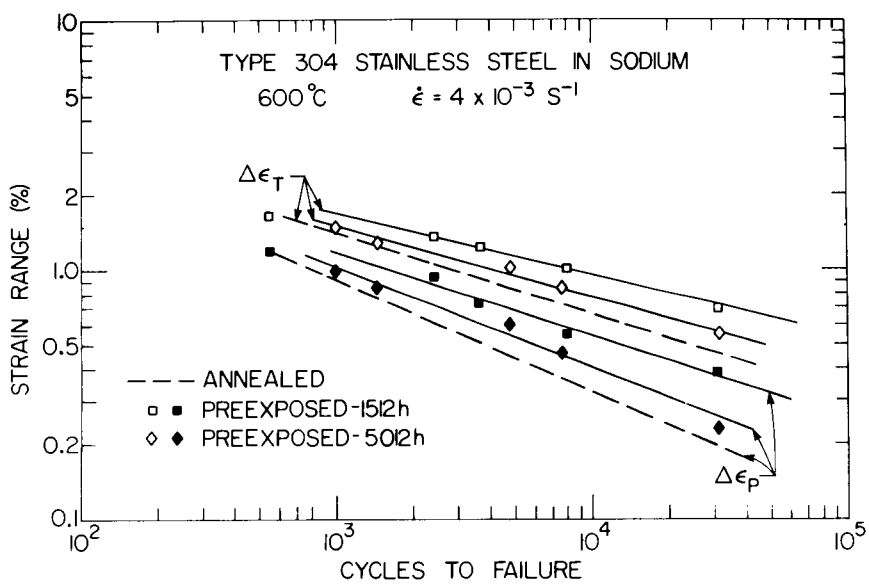

Fig. 2.15. Fatigue Data Obtained in Sodium at 600°C on Type 304 Stainless Steel in the Annealed and Sodium-exposed Conditions. The term $\Delta\varepsilon_T$ is the total strain, and $\Delta\varepsilon_p$ is the plastic strain. Neg. No. MSD-62680.

sodium at 600°C for material in the annealed condition and after exposure to sodium for 1512 and 5012 h at this temperature. The results indicate that the fatigue lifetime decreases with an increase in the exposure time beyond 1512 h; however, the lifetimes for the longer exposures are greater than for the annealed material. The decrease may be a result of the larger carbon penetration depth associated with the longer exposure time, i.e., 0.01 and 0.02 cm at 1512 and 5012 h, respectively, since the surface carbon concentration was ∿0.3 wt% in both cases.

The fatigue properties of annealed and sodium-exposed (1512 h at 700°C) Type 304 stainless steel in sodium at 700°C are shown in Fig. 2.16. Since the initial carbon concentration in the steel was approximately in equilibrium with the carbon concentration in the sodium during the 700°C exposure, no significant carburization or decarburization occurred. Therefore, the modest increase in the lifetime of ∿30 to 50% for the sodium-exposed material when compared with the annealed material can be attributed to thermal aging. Similar increases in the fatigue lifetime have been reported for aged material tested at ∿600 and 650°C in an air environment.[1,27]

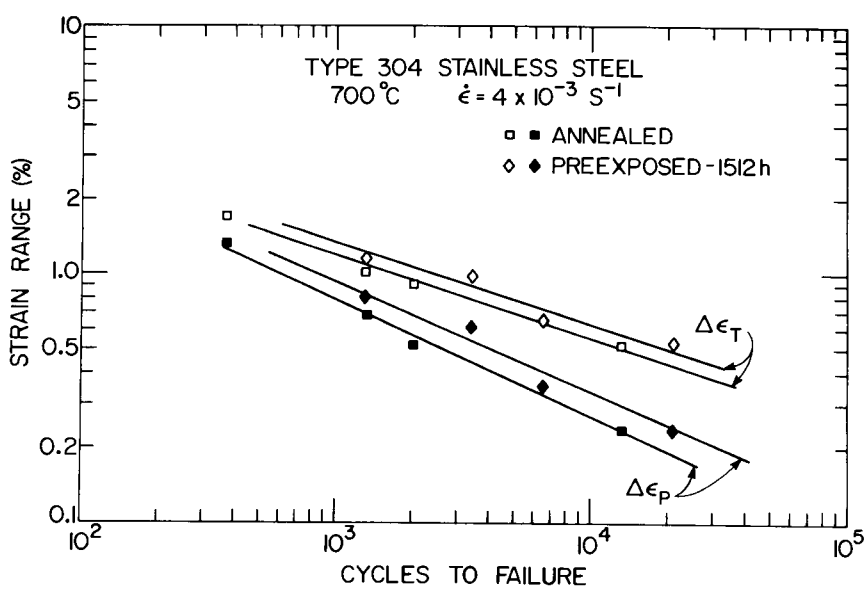

Fig. 2.16. Fatigue Data Obtained in Sodium at 700°C on Type 304 Stainless Steel in the Annealed and Sodium-exposed Conditions. Neg. No. MSD-62683.

2.4 REFERENCES

1. R. W. Weeks, D. R. Diercks, and C. F. Cheng, *ANL Low-cycle Fatigue Studies -- Program, Results, and Analysis,* Argonne National Laboratory, ANL-8009, (November 1973).

2. D. R. Diercks, *Mechanical Properties Test Data for Structural Materials Quart. Progr. Rep. Apr. 30, 1974,* ORNL-4963, pp. 11-18.

3. D. R. Diercks, "The Application of Strainrange Partitioning to the Prediction of Elevated-temperature, Low-cycle Fatigue Life for Type 304 Stainless Steel," pp. 29-38 in *Advances in Design for Elevated Temperature Environment,* ASME, New York, 1975; also in *Mechanical Properties Test Data for Structural Materials Quart. Progr. Rep. Jan. 31, 1975,* ORNL-5104, pp. 3-13.

4. D. R. Diercks, *Mechanical Properties Test Data for Structural Materials Quart. Progr. Rep. July 31, 1975,* ORNL-5106, pp. 19-24.

5. P. S. Maiya, discussion of "Heat-to-heat Variation in Creep Properties of Types 304 and 316 Stainless Steels," by V. K. Sikka, H. E. McCoy, Jr., M. K. Booker, and C. R. Brinkman, *J. Pressure Vessel Technol.* 98(1): 85-86 (February 1976).

6. S. Majumdar and P. S. Maiya, *A Unified and Mechanistic Approach to Creep-fatigue Damage,* Argonne National Laboratory, ANL-76-58, in preparation.

7. Unpublished data, D. R. Diercks, P. S. Maiya, and S. Majumdar, Argonne National Laboratory.

8. J. B. Conway, R. H. Stentz, and J. T. Berling, *Fatigue, Tensile, and Relaxation Behavior of Stainless Steels,* TID-26135, U. S. Atomic Energy Commission, Washington, D. C., 1975.

9. C. R. Brinkman and G. E. Korth, "Heat-to-heat Variations in the Fatigue and Creep-fatigue Behavior of AISI Type 304 Stainless Steel at 593°C," *J. Nucl. Mater.* 48: 293-306 (1973); also Aerojet Nuclear Company, ANCR-1097 (May 1973).

10. C. R. Brinkman, G. E. Korth, and J. M. Beeston, "Influence of Irradiation on the Creep-Fatigue Behavior of Several Austenitic Stainless Steels and Incoloy 800 at 700 C," in *Effects of Radiation on Substructure and Mechanical Properties of Metals and Alloys,* ASTM STP 529, American Society for Testing and Materials, Philadelphia, 1973, pp. 473-492.

11. G. E. Korth and M. D. Harper, "Effects of Neutron Radiation on the Fatigue and Creep/Fatigue Behavior of Type 304 Stainless Steel Weld Metal at Elevated Temperature," to be published in ASTM STP 570.

12. G. E. Korth and M. D. Harper, *Semi-annual Progress Report, Irradiation Effects on Reactor Structural Materials, August 1973-January 1974,* Hanford Engineering Development Laboratory, HEDL-TME 74-9, p. ANC-4.

13. G. E. Korth and M. D. Harper, *Semi-annual Progress Report, Irradiation Effects on Reactor Structural Materials, August 1974-February 1975,* Hanford Engineering Development Laboratory, HEDL-TME 75-23, p. ANC-3.

14. G. E. Korth and M. D. Harper, *Mechanical Properties Test Data for Structural Materials Quart. Progr. Rep. Oct. 31, 1974,* ORNL-5103, pp. 2-5.

15. D. L. Keller, *Progress on LMFBR Cladding, Structural, and Component Materials Studies During July 1970 through June 1971, Annual Report, Final Report,* Battelle-Columbus Laboratories, BMI-1914, 1971.

16. J. Neter and W. Wasserman, *Applied Linear Statistical Models,* Richard D. Irwin, Inc., Homewood, Illinois, 1974, pp. 121-123.

17. Private communication, C. E. Jaske, Battelle-Columbus Laboratories, to D. R. Diercks, Argonne National Laboratory.

18. J. Service, *A User's Guide to the Statistical Analysis System,* Sparks Press, Raleigh, North Carolina, 1972.

19. L. F. Coffin, "Predictive Parameters and Their Application to High Temperature Low-cycle Fatigue," in Proc. 2nd Int. Conf. on Fracture, Brighton, 1969, p. 643.

20. F. Garofalo, *Fundamentals of Creep and Creep-Rupture in Metals,* MacMillan Company, New York, 1965.

21. S. S. Manson, G. R. Halford, and M. H. Hirschberg, "Creep-fatigue Analysis by Strain-range Partitioning," in *Design for Elevated Temperature Environment,* American Society for Mechanical Engineers, New York, 1971, p. 12.

22. E. W. Hart, "A Phenomenological Theory for Plastic Deformation of Poly-crystalline Materials," *Acta. Met.* 18: 599 (1970).

23. K. Natesan and O. K. Chopra, *Mechanical Properties Test Data for Structural Materials Quart. Progr. Rep. Jan. 31, 1976,* ORNL-5112, pp. 21-34.

24. *Interpretations of the ASME Boiler and Pressure Vessel Code,* Case 1592, American Society of Mechanical Engineers (1974).

25. L. D. Blackburn, J. C. Tobin, and R. A. Moen, *Nucl. Technol.* 16: 278 (1972).

26. Private communication, M. K. Booker, Oak Ridge National Laboratory, to K. Natesan, Argonne National Laboratory.

27. C. F. Cheng, C. Y. Cheng, D. R. Diercks, and R. W. Weeks, "Low-Cycle Fatigue Behavior of Types 304 and 316 Stainless Steel at LMFBR Operating Temperature," in *Fatigue at Elevated Temperatures*, ASTM STP 520, American Society for Testing and Materials, 1973, pp. 355-364.

3. OAK RIDGE NATIONAL LABORATORY

W. R. Martin

3.1 INTRODUCTION

The ORNL mechanical properties effort comprises several programs. The program Mechanical Properties and Behavior for Structural Materials deals with materials of general applicability to the LMFBR program. Other programs are concerned with the mechanical properties of weldments in LMFBR components, the specific materials of interest for LMFBR steam generators, collection and correlation of mechanical data needed for design on high-temperature LMFBR systems, and materials for the primary circuit and steam generators of HTGR systems.

3.2 MECHANICAL PROPERTIES AND BEHAVIOR FOR STRUCTURAL MATERIALS — C. R. Brinkman

The objective of this program is to collect mechanical property data and material behavior for LMFBR structural and component materials. Included in the scope of this effort are the following: (1) basic tensile, creep, creep-rupture, and relaxation base-line data that are directly applicable to design criteria and methods for types 304 and 316 stainless steel reference heats and cyclic stress-strain tests performed with emphasis on loading and aging history effects, (2) variations in properties for several heats of types 304 and 316 stainless steel determined to allow establishment of minimum and average values of specific properties and the equation parameters required for design purposes. This work will include determination of property variations of samples from different mill products within a given heat of stainless steel.

3.2.1 Mechanical Property Characterization of Type 316 Stainless Steel Reference Heat — V. K. Sikka and M. K. Booker

3.2.1.1 Rational Polynomial Tensile Stress-Strain Equation for Low-Strain Behavior of Austenitic Type 316 Stainless Steel

The true-stress true-plastic-strain curve up to approximately 0.06 strain for type 316 stainless steel shows a behavior similar to a classical

creep curve before onset of tertiary creep. This is to say that there exists an accelerated initial hardening stage, similar to primary creep. It blends into a steady-state strain hardening, similar to steady-state creep rate. The classical creep behavior of several alloys has been successfully described by a single rational polynomial.[1-3] The details of this equation were described by Booker.[4] The purpose of this section is to show the application of the single rational polynomial equation to describe the true-stress true-plastic-strain behavior of the reference heat of type 316 stainless steel.

The single rational equation for true stress-strain behavior can be written as:

$$\sigma - \sigma_{PL} = \frac{CP\varepsilon_p}{1 + P\varepsilon_p} + \dot{H}\varepsilon_p \ , \tag{1}$$

where

C = a measure of strength level and, as shown later, related to yield strength,

$\dot{H}$ = steady-state hardening,

P = parameter describing the shape of the stress-strain curve before reaching the steady-state hardening,

σ_{PL} = proportional limit or stress below which there is no plastic strain,

ε_p = true plastic strain.

The graphical technique suggested by Oding[3] and successfully applied by Booker[4] to the creep data was used to obtain the values of C, P, and $\dot{H}$. This method requires the use of three stress-strain points from the actual curve. The stress points selected in the present analysis were at strain values of 0.0004, 0.004, and 0.04. The stress-strain data[5,6] used are on the reference heat (297) of type 316 stainless steel. Tests were performed at a crosshead speed of 0.004/min and in the temperature range from room temperature to 760°C (1400°F). Calculated values of $\dot{H}$ are plotted as a function of test temperature in Fig. 3.1 and least squares fitted to the following equation:

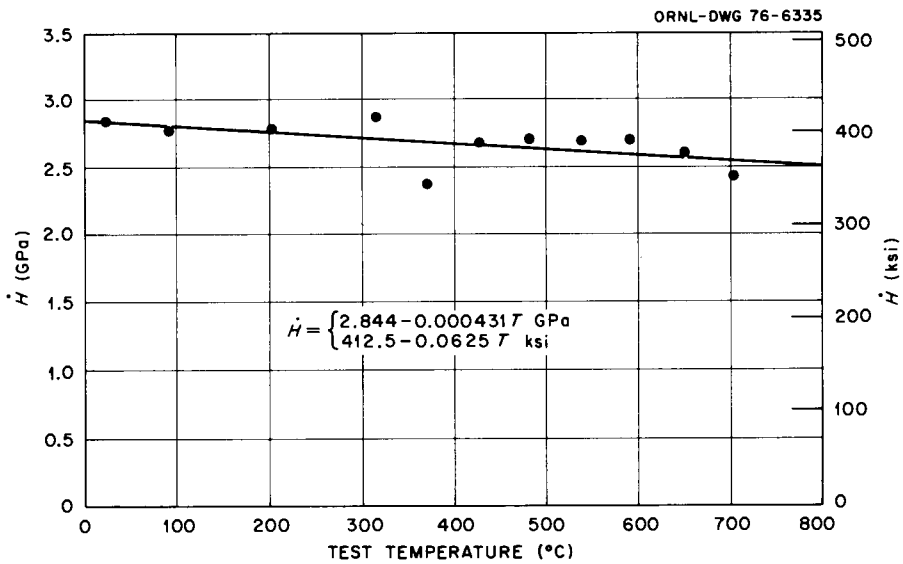

Fig. 3.1. Steady-State Hardening, $\dot{H}$, As a Function of Test Temperature for Reference Heat (Mill-Annealed Condition) of Type 316 Stainless Steel.

$$\begin{aligned} \dot{H} &= 2.844 - 0.000431T \text{ GPa} \\ &= 412.5 - 0.0625T \text{ ksi}, \end{aligned} \tag{2}$$

where T is the temperature (°C).

Although Eq. (2) shows a slight temperature dependence of $\dot{H}$, an average value of 2.76 GPa (400 ksi) independent of temperature has been selected for the present analysis. It will be shown later that this assumption is fairly good, at least at test temperatures of 649°C (1200°F) and below.

Figure 3.2 shows P as a function of C for the whole test temperature range. This figure shows that P and C are possibly related as:

$$\begin{aligned} P &= 72.5C(\text{MPa}) \\ &= 500C(\text{ksi}) \ . \end{aligned} \tag{3}$$

For $\varepsilon_p = 0.002$, $\sigma = \sigma_{ys}$(0.2% yield strength), and therefore Eq. (1) can be solved for values of C:

$$C = [(\sigma_{ys} - \sigma_{PL} - a) + \sqrt{(\sigma_{ys} - \sigma_{PL} - a)^2 + b(\sigma_{ys} - \sigma_{PL} - a)}]/2 \tag{4}$$

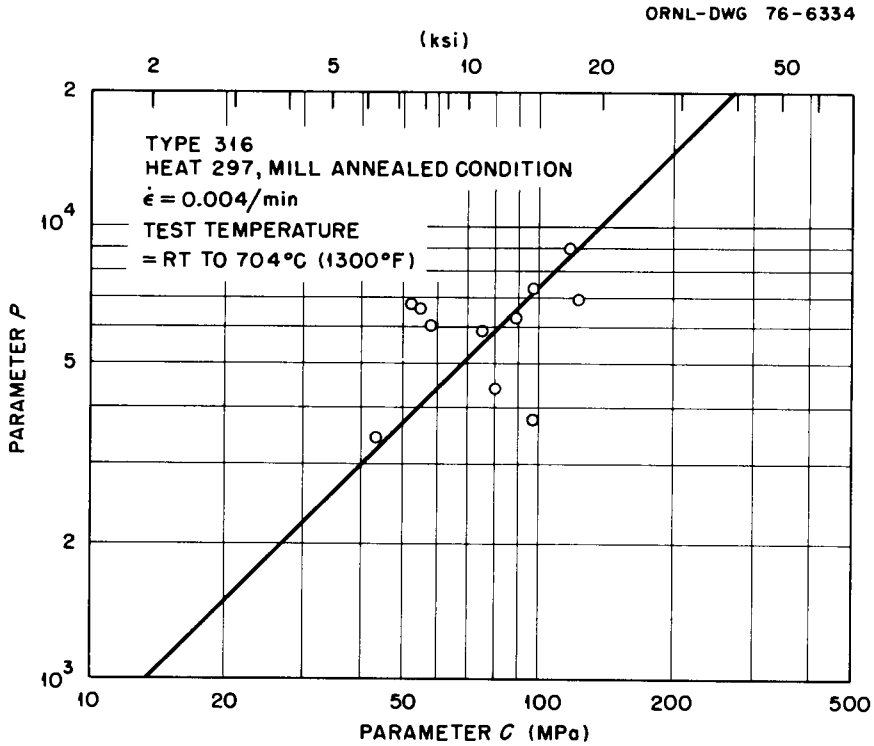

Fig. 3.2 Parameter P As a Function of Parameter C for the Reference Heat of Type 316 Stainless Steel.

where

a = 5.52 MPa = 0.80 ksi,

b = 27.6 MPa = 4.0 ksi.

Values of σ_{PL} are generally very difficult to determine with any significant accuracy. Thus, in an attempt to eliminate σ_{PL} from Eqs. (1) and (4), it was plotted as a function of σ_{ys} in Fig. 3.3. It can be noted that for the mill-annealed condition,

$$\sigma_{PL} = 0.5\sigma_{ys} \ , \tag{5}$$

and for reannealed condition,

$$\sigma_{PL} = 0.76\sigma_{ys} \ . \tag{6}$$

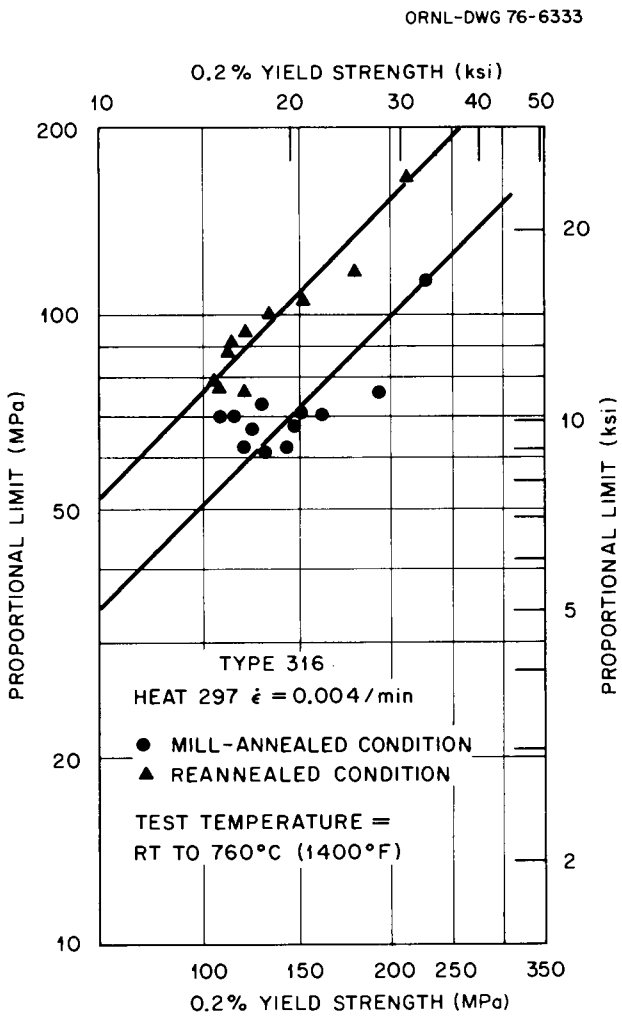

Fig. 3.3. Proportional Limit as a Function of 0.2% Yield Strength for the Reference Heat of Type 316 Stainless Steel.

A comparison between the experimental and computed values for mill-annealed and reannealed conditions suggested that $\sigma_{PL} = 0.5\sigma_{ys}$ is adequate for both conditions. Thus, it appears that instead of plastic strain being zero at the proportional limit, it should be assumed to be zero at $0.5\sigma_{ys}$.

Substituting Eq. (5) in Eqs. (4) and (1) results in:

$$C = [(0.5\sigma_{ys} - a) + \sqrt{(0.5\sigma_{ys} - a)^2 + b(0.5\sigma_{ys} - a)}]/2 \ , \qquad (7)$$

and

$$\sigma = 0.5\sigma_{ys} + \frac{72.5C^2\varepsilon_p}{1 + 72.5C\varepsilon_p} + 2760\varepsilon_p$$

(stresses in MPa)

$$= 0.5\sigma_{ys} + \frac{500C^2\varepsilon_p}{1 + 500C\varepsilon_p} + 400\varepsilon_p \ . \tag{8}$$

(stresses in ksi)

Values of C in Eq. (8) are given by Eq. (7). Thus, Eqs. (7) and (8) can be used to predict true-stress true-plastic-strain behavior if the yield strength is known. The temperature dependence of true-stress and true-plastic-strain behavior can be obtained by substituting the σ_{ys} at the desired temperatures. Figures 3.4 and 3.5 compare the experimental and predicted values for the mill-annealed condition data on the reference heat of type 316 stainless steel. Note the excellent agreement. Furthermore, by definition, predicted values always go through the 0.2% yield strength value.

Since Eqs. (7) and (8) contain only σ_{ys}, we tried to see if they could also be used to predict the true-stress true-plastic-strain behavior of the reannealed type 316 stainless steel. Figures 3.6 and 3.7 compare the experimental and predicted values. The agreement is extremely good except at two higher temperatures, 704 and 760°C (1300 and 1400°F). Thus, it appears that Eqs. (7) and (8) can be used to predict fairly accurately the stress-strain behavior for the reference heat of type 316 stainless steel for both mill-annealed and reannealed conditions.

The model presented above has an advantage that it requires a knowledge of only the yield strength at a given temperature. Thus, it can be used to predict the stress-strain behavior of individual heats at desired temperatures. It should, however, be noted that the accuracy of prediction drops beyond a strain of 5%. This model has several advantages over the present model in the *Nuclear Systems Materials Handbook* (NSMH): it is valid over a temperature range from room temperature to 760°C (1400°F) for both mill- and laboratory-annealed conditions and

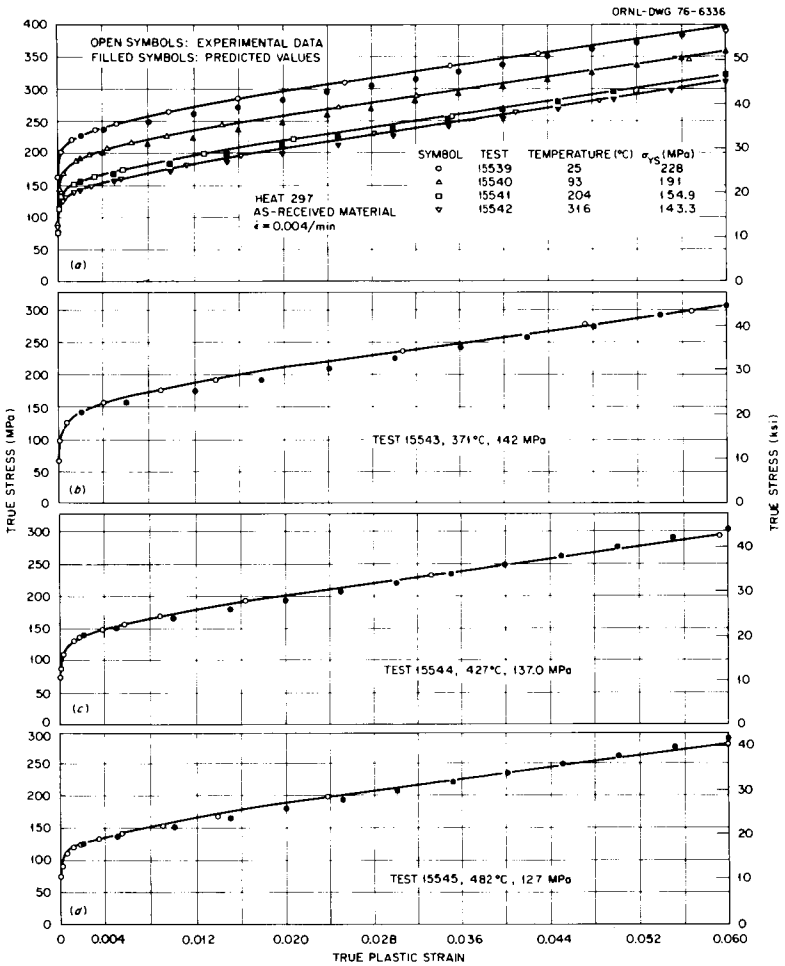

Fig. 3.4. Comparison Between Experimental Data and Predicted Values for Mill-Annealed Reference Heat of Type 316 Stainless Steel, 25 to 482°C (77–900°F).

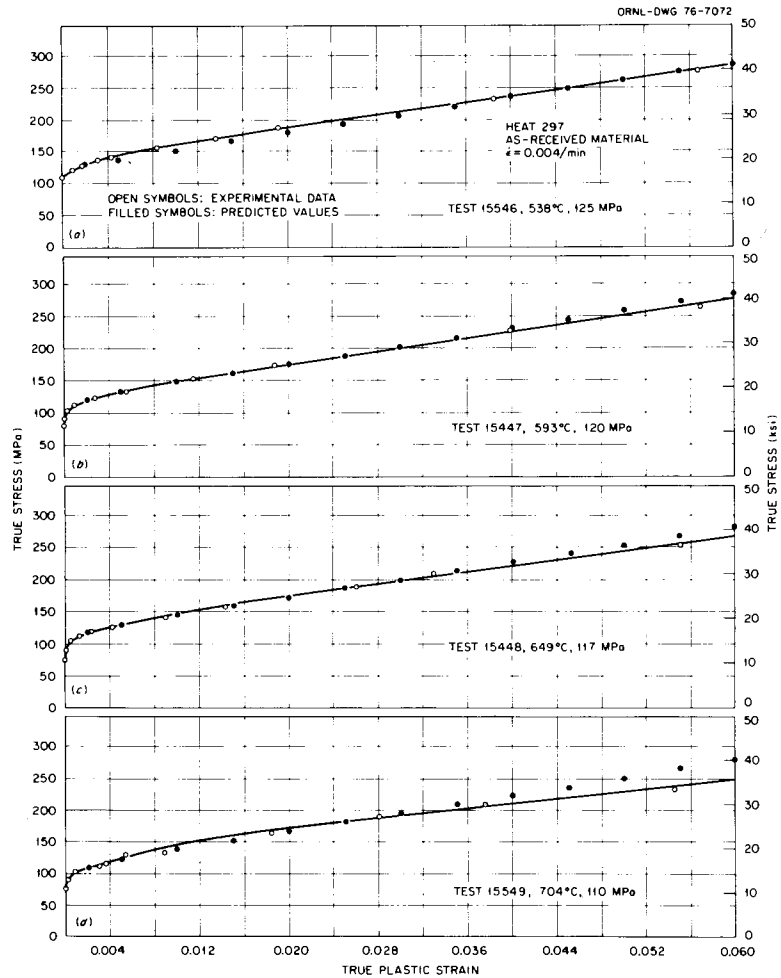

Fig. 3.5. Comparison Between Experimental Data and Predicted Values for Mill-Annealed Reference Heat of Type 316 Stainless Steel, 538 to 704°C (1000–1300°F).

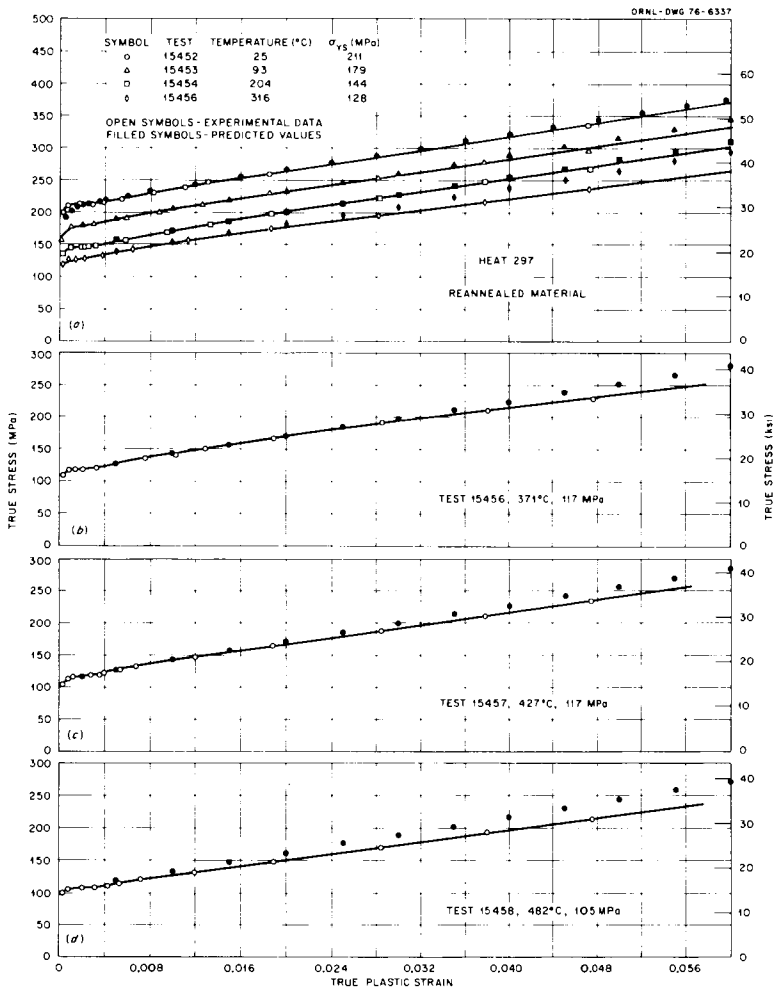

Fig. 3.6. Comparison Between Experimental Data and Predicted Values for Reannealed Reference Heat of Type 316 Stainless Steel, 25 to 482°C (77–900°F).

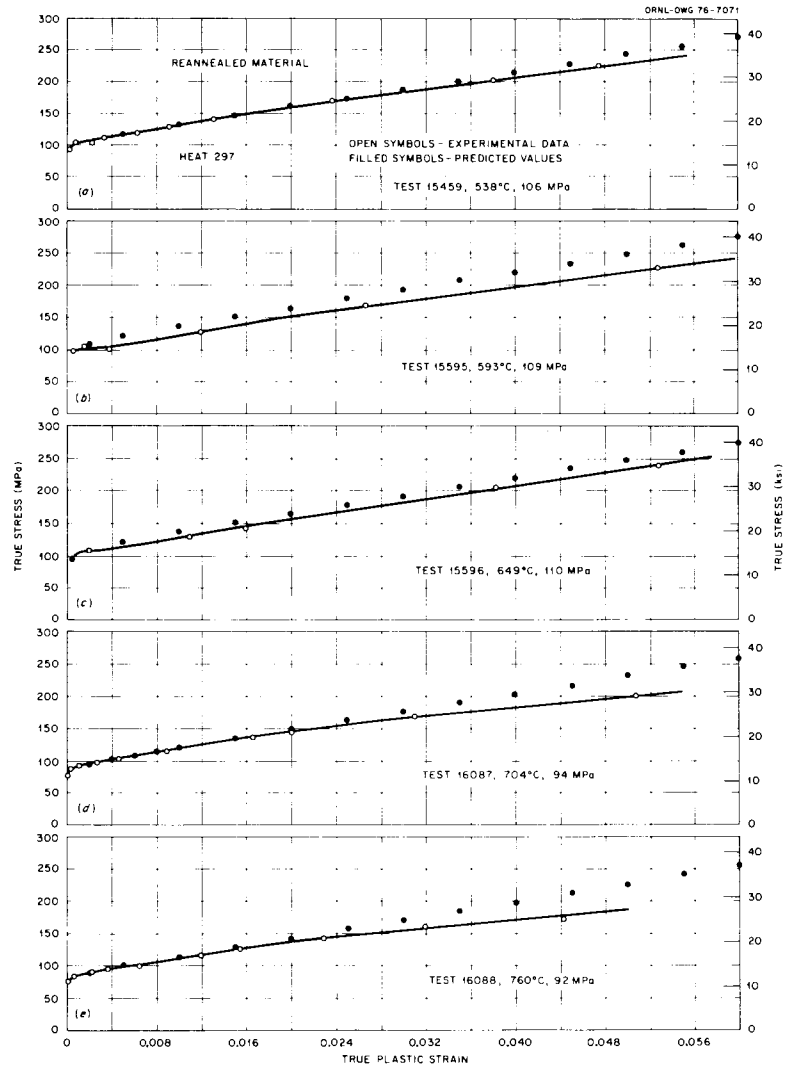

Fig. 3.7. Comparison Between Experimental Data and Predicted Values for Reannealed Reference Heat of Type 316 Stainless Steel, 538 to 760°C (1000–1400°F).

for individual heats. Furthermore, it permits one to calculate the minimum behavior by a mere substitution of minimum yield strength values. The model presented here has been verified for only a single strain rate. Testing it for other strain rates is in progress.

3.2.2 Heat-to-Heat Variations of Mechanical Properties of Austenitic Stainless Steels of Types 304 and 316 — Assessment of Tensile and Creep Data for Types 304 and 316 Stainless Steel — V. K. Sikka and M. K. Booker

Austenitic stainless steels of types 304 and 316 are prime construction materials for nuclear fast breeder reactors. These steels will be used in the temperature range where elevated-temperature tensile, creep, and fatigue properties are required to calculate the design stress limits. This report examines the possible variations in such properties, using data from a wide variety of sources. The first attempt in collecting tensile and creep data from various sources in the United States was made in 1952 by Simmons and Cross.[7] The report contained individual data sheets and graphical representation of the elevated-temperature data for the commercially produced stainless steels. This report was updated by Simmons and Van Echo[8] in 1965. Although additional data and graphs were included in the second report, no attempt was made to describe the scatter or variations in the properties. Smith[9] evaluated the yield, tensile, creep, and rupture strength data of wrought types 304, 316, 321, and 347 stainless steel given in the previous reports.[7,8] Smith[9,10] analyzed yield and tensile strength with a method based on the ratio between elevated-temperature and room-temperature strengths for a given heat of material. This method forms the basis for determination of minimum-value curves for yield and tensile strength and for the evaluation of time-independent stress intensity limit, S_m, in the ASME Code Case 1592 (Ref. 11). However, the ratio method is designed to reduce the variations in a property rather than to describe them. The creep data, on the other hand, were analyzed[9] in various ways, all of which were based on the assumption that at a given temperature, stress is the dependent variable in stress-rupture testing. Unfortunately, this

assumption is incorrect by the nature of the stress-rupture test,[12-14] and as a result variations in rupture life, the true dependent variable, were not analyzed.

Data compilation and evaluation programs have also been followed in Britain,[15] Germany,[16] France,[17] and Japan.[18] All these countries except Japan have compiled the data on commercial steels. Japan's testing program is relatively recent and is being carried out on a large scale at the National Research Institute for Metals (NRIM). Their data have become available in the form of NRIM data sheets, which are updated from time to time. Again, however, little analysis of the variations in various properties has been attempted.

Currently in the United States, large mechanical properties testing programs are under way at Oak Ridge National Laboratory (ORNL), Hanford Engineering Development Laboratory (HEDL), Argonne National Laboratory (ANL), and elsewhere. The ORNL mechanical property program is being conducted primarily on austenitic stainless steels and involves the study of product form characterization,[19,20] heat-to-heat variations,[21] long-term creep testing, and evaluation of effects of thermal aging[22] with and without stress. The ANL programs are on determination of fatigue, creep-fatigue interactions, and environmental effects on the austenitic stainless steels.

The analysis of these elevated-temperature data for determining design stress intensities is complicated by variations in the properties due to product form, heat differences, thermomechanical processing history, and testing laboratory differences. Our purpose is to assess these variations in tensile and creep properties of types 304 and 316 stainless steel. The variations in tensile and creep properties have been compared for data taken from U.S. and foreign data compilations.[8,15,18] The German and French data books could not be obtained in time for their incorporation in this analysis. No attempt is made here to extrapolate the creep data.

3.2.2.1 Data Selection and Characterization

Data for assessment were selected on the basis that the steels and their products for which data are available should meet the American

Society for Testing and Materials (ASTM) or equivalent material specifications. The ASTM specifications[23-25] call for limits on chemical composition and on room-temperature yield and tensile strength minimum values. All the U.S. data[8,26] met chemical composition requirements, and most of them also met the mechanical property specifications. The Japanese steels were purchased in accordance with Japanese specifications (JIS); however, these specifications correspond directly to ASTM specifications. All heats and products forms used in production of NRIM data met both the chemical composition and mechanical property specifications. The purchase specifications for British steels are not known, although the BSCC data book[15] provides detailed information on product, size, melting practice, heat treatment (although no distinction is made between laboratory- and mill-annealed conditions), and chemical composition. Both tensile and creep properties were available for most of the heats, but creep data were not necessarily available for the same heats from which the tensile data were obtained. Thus, BSCC data could only be subjected to a check on chemical composition of different heats, and all data included herein meet the ASTM composition specifications.

The following are the specific characteristics of tensile and creep data from different sources:

1. U.S. Data — Obtained on steels purchased to or otherwise meeting the ASTM materials specifications. Data are relatively old and from several laboratories. Most of the data were obtained for material in the mill-annealed condition. Strain rates were not given for each tensile data source, but tests were performed according to ASTM testing procedures.

2. NRIM Data — Japanese data obtained on 11 heats of type 304 stainless steel and 17 heats of type 316, which meet both ASTM chemical composition and room-temperature mechanical property requirements. These are relatively new data and were obtained at a single laboratory (NRIM). All data are for mill-annealed material. Strain rates for tensile tests were 0.003/min up to 1% extension followed by 0.075/min.

3. BSCC Data — British data obtained from a large number of heats of types 304 and 316 stainless steel. The chemical composition of all

these steels met the ASTM material specifications. These data are relatively (with respect to U.S. data) new and were collected at several different laboratories. Data on mill- and laboratory-annealed materials were not distinguished. The strain rates for tensile tests were not given. The details of test temperatures, product forms, and number of data are included with the tables of results.

3.2.2.2 Method of Analysis

3.2.2.2.1 Tensile Properties. The most common method in use for engineering analysis of the tensile data is the ratioing technique.[9,10] This method suffers from several objections,[27] but the major weakness as far as this report is concerned is that it provides no direct means for determining the variations in the tensile properties. Thus, we have selected to use direct polynomial regression analysis to describe the tensile properties; it can be used to give a direct measure of variation in the data from the expected values.

All properties could be described by a cubic polynomial of the form:

$$P = a_0 + a_1 T + a_2 T^2 + a_3 T^3 \quad , \tag{9}$$

where

P = tensile property, (MPa or ksi) for strength and (%) for ductility indices,

T = test temperature (°C or °F),

a_0, a_1, a_2, a_3 = regression coefficients.

The ability of a model to describe variations in the data is given by the coefficient of determination, denoted R^2 (square of the multiple correlation coefficient):

$$R^2 = 1 - \mathrm{RSS/CTSS} \quad , \tag{10}$$

where

RSS = residual sum of squares,

CTSS = corrected total sum of squares.

The selection of the third-degree polynomial to describe all tensile properties was based on a compromise between only a small further improvement in value of R^2 for higher degree polynomials and simplicity of the model.

The standard error of estimate (SEE) was used as a measure of describing variations in the data from the expected values:

$$\text{SEE} = \sqrt{\Sigma y^2/(n - \nu)} \ , \tag{11}$$

where

n = number of data points,

ν = number of coefficients in the model (here $\nu = 4$),

Σy^2 = sum of squared residuals = $\Sigma(P_{\text{predicted}} - P_{\text{experimental}})^2$,

$P_{\text{experimental}}$ = experimentally observed value of the property,

$P_{\text{predicted}}$ = predicted value of the property.

In the present analysis we assume that the dependent variable (tensile property) is normally distributed about the mean curve and that the variance in the dependent variable is homogeneous in the independent variable (temperature). The detailed analysis in making the above assumption is described in another report.[28] To describe the total variation in the data, upper and lower limit curves were drawn for expected ±2SEE values. The choice of 2SEE for determining upper and lower limit curves was based on visual observation of the data. It will be shown later that such a choice in fact describes the variations in the data. However, it must be realized that these limits have no statistical meaning in terms of the percentage of data falling within the limits. Rather, these limits are merely a convenient way to illustrate the scatter in the data.

3.2.2.2.2 Creep Properties. Based on the nature of the available data, analysis was limited only to variations in time to rupture and in total creep elongation.

3.2.2.2.3 Creep Rupture. Data from each source were separated and treated isothermally for each product form and also for all product forms combined. Because of the nature of the creep rupture test, it is necessary to consider rupture life time (t_r) as the dependent variable and stress as the independent variable. Log-log plots were made for time to rupture as a function of stress. Each isothermal data set was fitted by linear and quadratic models of the forms:

$$\log t_r = \alpha_0 + \alpha_1 \log \sigma \ , \tag{12}$$

$$\log t_r = \alpha_0 + \alpha_1 \log \sigma + \alpha_2 (\log \sigma)^2 \ , \tag{13}$$

where

t_r = time to rupture,

α_0, α_1, α_2 = regression coefficients.

Equation (12) is the most commonly used model, although the engineering community generally plots the data as log σ vs log t_r, rather than log t_r vs log σ. Equation (13) was employed to describe any curvilinearity observed in the data. Although constants in both Eqs. (12) and (13) have been determined in this report, Eq. (12) was found adequate to describe variations in the rupture data. Equation (12) can be rewritten as a power law:

$$t_r = 10^{\alpha_0} \sigma^{\alpha_1}, \tag{14}$$

and the constant α_1 then becomes the commonly known stress exponent.

The variations in time to rupture for a given stress were again described by SEE. The values of SEE were in terms of log t_r. The upper and lower limit lines on rupture plots were also determined by the expected ±2SEE.

3.2.2.2.4 Creep Elongation (e_r). Creep elongation (including loading strain) data commonly show so much scatter that direct analysis is difficult. Booker et al.[29] and Booker and Sikka[30,31] have described methods to minimize the uncertainty in the analysis of such data. This method involves use of the so-called average creep rate to rupture, $\dot{e}_r$, defined by

$$\dot{e}_r = e_r/t_r \ , \tag{15}$$

where e_r is the elongation at rupture. Previous results[30,31] have shown $\dot{e}_r$ and t_r to be related by an equation of the form

$$\dot{e}_r = At_r^{\ B} \ , \tag{16}$$

where A and B are material constants that are functions of temperature. Analysis of the current data using Eq. (16) yields values of R^2 in the range 90 to 100%, indicating an excellent description of the data. Equation (16) can also be used to predict e_r itself, since $e_r = \dot{e}_r t_r$, or

$$e_r = At_r^{\ B+1} \ . \tag{17}$$

Thus the slope of the line for log e_r vs log t_r for a given temperature, while difficult to predict accurately, is given by $B + 1$. The value of B can be accurately predicted from Eq. (16). The upper and lower limits for log e_r vs log t_r were also based on upper and lower limit lines in log $\dot{e}_r$ vs log t_r plots. The latter was based on the common procedure used in this report (expected ±2SEE).

3.2.2.3 Results

3.2.2.3.1 Tensile Properties. Although each tensile property (0.2% yield, ultimate tensile strength, total elongation, or reduction of area) was plotted for separate data on each product and combined data on several products of each type of steel and three different data sources,

only plots for the combined data are presented here. The results of individual and combined treatment of the data have been summarized in Tables 3.1 and 3.2. Plots of the combined data on 0.2% yield, ultimate tensile strength, and total elongation are shown in Figs. 3.8 through 3.10. These plots show typical trends in each property, overall scatter in the data, comparison between types 304 and 316 stainless steel, and comparison of the above quantities for data from three different countries. It should be noted from Figs. 3.8 and 3.9 that the room-temperature 0.2% yield and ultimate tensile strength values for all U.S. and NRIM data were above the ASTM specified values of 207 and 517 MPa (30 and 75 ksi), respectively. For the BSCC data, however, room-temperature ultimate tensile values for all heats were above 517 MPa (75 ksi), but several room-temperature yield strength values fell below 207 MPa (30 ksi).

Tensile property variations for different product forms are shown in Fig. 3.11 and the following are some general observations:

1. U.S. Data — Bar shows maximum variation in the properties and tube shows the least.

2. NRIM and BSCC Data — Bar product shows less scatter than tube.

3. Combined Data — U.S. data show the maximum variation in all tensile properties, and NRIM the least.

4. Relative Variation in Properties — The percent variation is smaller in ultimate tensile strength than in yield strength. Ductility indices (total elongation and reduction of area) show greater variations than strength properties.

5. Different Alloys — From the tensile data analyzed in this report, it is not possible to make a distinction between variations observed for types 304 and 316 stainless steel. However, later we will show that variations in creep properties of type 316 stainless steel are noticeably less than those observed for type 304.

3.2.2.3.2 Creep Properties. The isothermal treatment of the creep rupture, average creep rate, and total elongation produced a large number of plots, and again it is not possible here to show more than one isothermal plot for these properties. The temperature selected was 649°C (1200°F) for the U.S. data and 650°C (1202°F) for the foreign data.

Table 3.1. Summary of Constants for Tensile Data Analysis on Type 304 Stainless Steel

Data Source	Product	Number of Data Points	Regression Coefficients from Eq. (9)[a,b]				SEE	R^2 (%)
			a_0	a_1	a_2	a_3		
				0.2% Yield Strength (ksi)[c]				
BSCC	Tube	203	35.19	-5.12×10^{-2}	5.10×10^{-5}	-1.86×10^{-8}	2.41	82.98
BSCC	Combined	218	35.27	-5.15×10^{-2}	5.18×10^{-5}	-1.90×10^{-8}	2.40	83.16
NRIM	Tube	99	39.14	-3.97×10^{-2}	3.89×10^{-5}	-1.57×10^{-8}	2.35	85.17
U.S.	Tube	117	42.09	-6.61×10^{-2}	7.62×10^{-5}	-3.26×10^{-8}	2.61	86.61
U.S.	Plate	39	41.83	-6.03×10^{-2}	6.59×10^{-5}	-2.70×10^{-8}	4.62	66.21
U.S.	Bar	111	42.05	-3.20×10^{-2}	6.39×10^{-6}	-6.28×10^{-10}	6.84	61.28
U.S.	Combined	267	41.89	-4.98×10^{-2}	4.37×10^{-5}	-1.68×10^{-8}	5.15	66.93
				Ultimate Tensile Strength (ksi)[c]				
BSCC	Tube	203	88.41	-1.04×10^{-1}	1.44×10^{-4}	-7.11×10^{-8}	3.00	91.73
BSCC	Combined	218	89.09	-1.09×10^{-1}	1.51×10^{-4}	-7.40×10^{-8}	2.94	92.24
NRIM	Tube	99	95.44	-1.291	1.90×10^{-4}	-9.55×10^{-8}	2.79	96.94
U.S.	Tube	117	91.33	-1.77×10^{-1}	1.82×10^{-4}	-9.54×10^{-8}	3.17	88.07
U.S.	Plate	39	90.41	-1.31×10^{-1}	2.02×10^{-4}	-1.04×10^{-7}	1.76	96.75
U.S.	Bar	116	93.93	-1.16×10^{-1}	1.53×10^{-4}	-7.33×10^{-8}	4.53	91.23
U.S.	Combined	272	91.93	-1.13×10^{-1}	1.59×10^{-4}	-7.84×10^{-8}	3.98	89.27
				Total Elongation (%)[d]				
BSCC	Tube	203	64.69	-6.30×10^{-2}	5.40×10^{-5}	-1.37×10^{-8}	2.96	80.77
BSCC	Combined	218	65.16	-6.31×10^{-2}	5.15×10^{-5}	-1.17×10^{-8}	3.07	80.68
NRIM	Tube	99	73.13	-6.20×10^{-2}	3.66×10^{-6}	-2.73×10^{-8}	4.85	80.76
U.S.	Tube	117	72.33	-9.65×10^{-2}	1.13×10^{-4}	-4.41×10^{-8}	5.62	67.71
U.S.	Plate	39	70.59	-1.27×10^{-1}	1.72×10^{-4}	-7.66×10^{-8}	5.13	73.98
U.S.	Bar	116	75.98	-1.08×10^{-1}	1.20×10^{-4}	-4.60×10^{-8}	5.34	81.36
U.S.	Combined	272	73.76	-1.07×10^{-1}	1.26×10^{-4}	-5.05×10^{-8}	5.76	72.81
				Reduction of Area (%)[d]				
NRIM	Tube	99	83.16	-1.16×10^{-2}	-8.92×10^{-6}	7.90×10^{-9}	4.08	53.07
U.S.	Tube	105	79.94	-3.99×10^{-2}	4.41×10^{-5}	-1.46×10^{-8}	5.69	23.55
U.S.	Plate	7	82.98	-6.66×10^{-2}	1.13×10^{-4}	-6.43×10^{-8}	1.79	97.09
U.S.	Bar	107	79.07	-5.44×10^{-3}	-1.17×10^{-5}	-1.39×10^{-9}	4.97	74.48
U.S.	Combined	219	80.96	-4.26×10^{-2}	6.31×10^{-5}	-3.55×10^{-8}	5.88	49.24

[a]Regression coefficients are for the temperature range of room-temperature to 816°C (1500°F).

[b]Temperatures for these coefficients were °F.

[c]If a_0', a_1', a_2', and a_3' are the corresponding constants for stress in megapascals as a function of Celsius temperature, they can be obtained from the tabulated coefficients as follows:

$a_0' = 6.895a_0 + 220.63a_1 + 7060a_2 + 2.2593 \times 10^5 a_3$

$a_1' = 12.416a_1 + 794.3a_2 + 38125a_3$

$a_2' = 22.339a_2 + 2144.6a_3$

$a_3' = 40.21a_3$.

Standard estimate of error (SEE) should be multiplied by 6.895 for stress in megapascals.

[d]If a_0', a_1', a_2', and a_3' are the corresponding constants for strain as a function of Celsius temperature, they can be obtained from the tabulated coefficients as follows:

$a_0' = a_0 + 32a_1 + 1024a_2 + 32768a_3$

$a_1' = 1.8a_1 + 115.2a_2 + 5529.6a_3$

$a_2' = 3.24a_2 + 311.04a_3$

$a_3' = 5.832a_3$.

Table 3.2. Summary of Constants for Tensile Data Analysis on Type 316 Stainless Steel

Data Source	Product	Number of Data Points	Regression Coefficient from Eq. (9)[a,b]				SEE	R^2 (%)
			a_0	a_1	a_2	a_3		
			0.2% Yield Strength (ksi)[c]					
BSCC	Bar	58	34.78	-5.05×10^{-2}	4.90×10^{-5}	-1.70×10^{-8}	1.647	92.41
BSCC	Tube	425	37.25	-6.02×10^{-2}	7.61×10^{-5}	-3.31×10^{-8}	4.078	58.36
BSCC	Bar and Tube	482	36.84	-5.82×10^{-2}	7.16×10^{-5}	-3.07×10^{-8}	3.929	51.00
NRIM	Bar	60	37.26	-4.75×10^{-2}	4.66×10^{-5}	-1.65×10^{-8}	1.576	91.92
NRIM	Tube	99	40.12	-4.11×10^{-2}	3.59×10^{-5}	-1.24×10^{-8}	2.780	79.78
NRIM	Bar and Tube	184	38.67	-4.61×10^{-2}	4.49×10^{-5}	-1.62×10^{-8}	2.910	79.59
U.S.	Bar	40	41.22	-3.90×10^{-2}	3.17×10^{-5}	-1.10×10^{-8}	5.153	67.64
U.S.	Tube	32	42.76	-6.98×10^{-2}	7.76×10^{-5}	-2.88×10^{-8}	3.046	84.10
U.S.	Bar and Tube	72	41.79	-5.21×10^{-2}	5.15×10^{-5}	-1.88×10^{-8}	4.347	72.41
			Ultimate Tensile Strength (ksi)[c]					
BSCC	Bar	56	87.47	-9.46×10^{-2}	1.40×10^{-4}	-7.06×10^{-8}	4.18	84.33
BSCC	Tube	424	89.79	-1.06×10^{-1}	1.65×10^{-4}	-8.48×10^{-8}	3.51	86.38
BSCC	Bar and Tube	480	89.43	-1.04×10^{-1}	1.61×10^{-4}	-8.26×10^{-8}	3.61	85.89
NRIM	Bar	60	89.66	-9.93×10^{-2}	1.59×10^{-4}	-8.42×10^{-8}	1.88	98.36
NRIM	Tube	99	90.39	-1.01×10^{-1}	1.66×10^{-4}	-8.86×10^{-8}	2.539	96.75
NRIM	Bar and Tube	184	90.20	-1.02×10^{-1}	1.65×10^{-4}	-8.75×10^{-8}	2.324	97.27
U.S.	Bar	41	87.16	-6.2×10^{-2}	9.42×10^{-5}	-5.36×10^{-8}	4.04	95.04
U.S.	Tube	36	83.58	-6.35×10^{-2}	9.45×10^{-5}	-5.39×10^{-8}	3.94	95.37
U.S.	Bar and Tube	77	85.15	-5.89×10^{-2}	8.84×10^{-5}	-5.13×10^{-8}	4.64	93.29
			Total Elongation (%)[d]					
BSCC	Bar	39	56.26	-3.29×10^{-2}	2.04×10^{-6}	1.23×10^{-8}	5.64	52.96
BSCC	Tube	414	64.26	-5.32×10^{-2}	2.04×10^{-5}	9.57×10^{-9}	6.28	53.01
BSCC	Bar and Tube	452	63.68	-5.36×10^{-2}	2.34×10^{-5}	7.55×10^{-9}	6.00	54.13
NRIM	Bar	60	65.70	-3.97×10^{-2}	-2.42×10^{-6}	2.32×10^{-8}	3.83	80.14
NRIM	Tube	99	66.51	-5.80×10^{-2}	2.00×10^{-5}	1.59×10^{-8}	4.46	77.97
NRIM	Bar and Tube	184	65.87	-4.89×10^{-2}	9.48×10^{-6}	1.90×10^{-8}	4.16	78.19
U.S.	Bar	41	60.98	-5.66×10^{-2}	4.69×10^{-5}	-1.01×10^{-8}	6.62	47.03
U.S.	Tube	36	67.86	-6.04×10^{-2}	2.54×10^{-5}	1.33×10^{-8}	6.34	74.80
U.S.	Bar and Tube	77	64.67	-6.44×10^{-2}	4.80×10^{-5}	-4.44×10^{-9}	9.26	38.88
			Reduction of Area (%)[d]					
NRIM	Bar		77.17	6.83×10^{-3}	-4.00×10^{-5}	2.35×10^{-8}	3.54	51.60
NRIM	Tube	99	81.80	-3.30×10^{-2}	-2.21×10^{-5}	1.34×10^{-8}	3.96	56.60
NRIM	Bar and Tube	179	79.66	2.72×10^{-4}	-2.85×10^{-5}	1.74×10^{-8}	3.96	49.59
U.S.	Bar	23	78.16	-3.00×10^{-2}	1.88×10^{-5}	-5.85×10^{-9}	8.13	43.24
U.S.	Tube	36	82.05	-6.48×10^{-2}	5.50×10^{-5}	-9.69×10^{-9}	7.31	43.47
U.S.	Bar and Tube	59	80.48	-5.06×10^{-2}	4.04×10^{-5}	-8.09×10^{-9}	8.40	30.00

[a]Regression coefficients are for the temperature range of room-temperature to 816°C (1500°F).

[b]Temperatures for these coefficients were °F.

[c]If a_0', a_1', a_2', and a_3' are the corresponding constants for stress in megapascals as a function of Celsius temperature, they can be obtained from the tabulated coefficients as follows:

$a_0' = 6.895a_0 + 220.63a_1 + 7060a_2 + 2.2593 \times 10^5 a_3$

$a_1' = 12.416a_1 + 794.3a_2 + 38125a_3$

$a_2' = 22.339a_2 + 2144.6a_3$

$a_3' = 40.21a_3$.

Standard estimate of error (SEE) should be multiplied by 6.895 for stress in megapascals.

[d]If a_0', a_1', a_2', and a_3' are the corresponding constants for strain as a function of Celsius temperature, they can be obtained from the tabulated coefficients as follows:

$a_0' = a_0 + 32a_1 + 1024a_2 + 32768a_3$

$a_1' = 1.8a_1 + 115.2a_2 + 5529.6a_3$

$a_2' = 3.24a_2 + 311.04a_3$

$a_3' = 5.832a_3$.

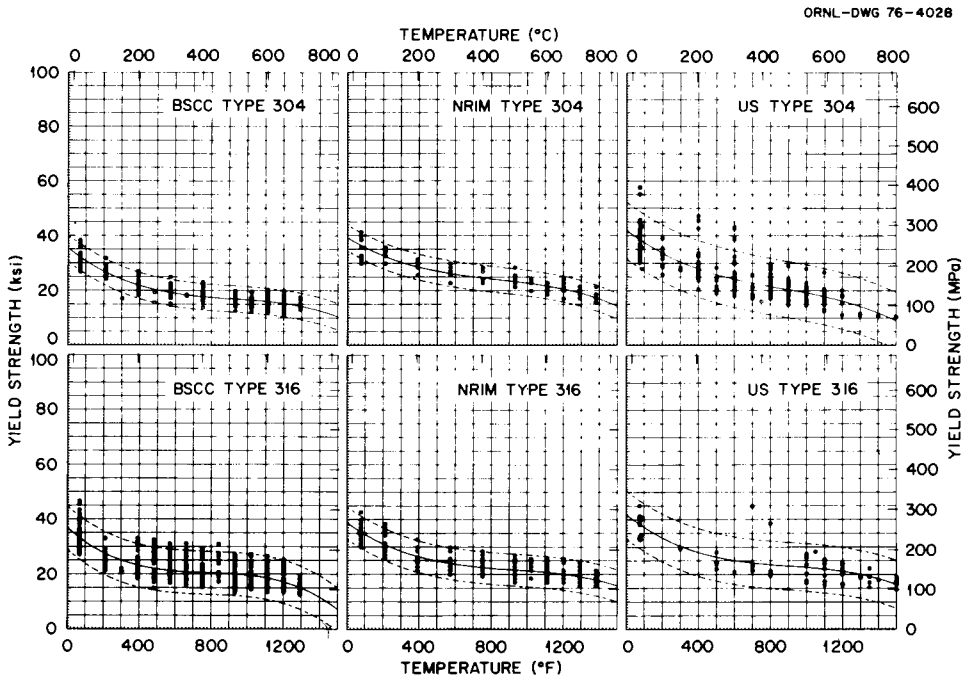

Fig. 3.8. Trends in Variations in 0.2% Yield Strength as a Function of Test Temperature for Types 304 and 316 Stainless Steel Data Obtained in Three Different Countries. Lower and upper limit lines are ±2SEE.

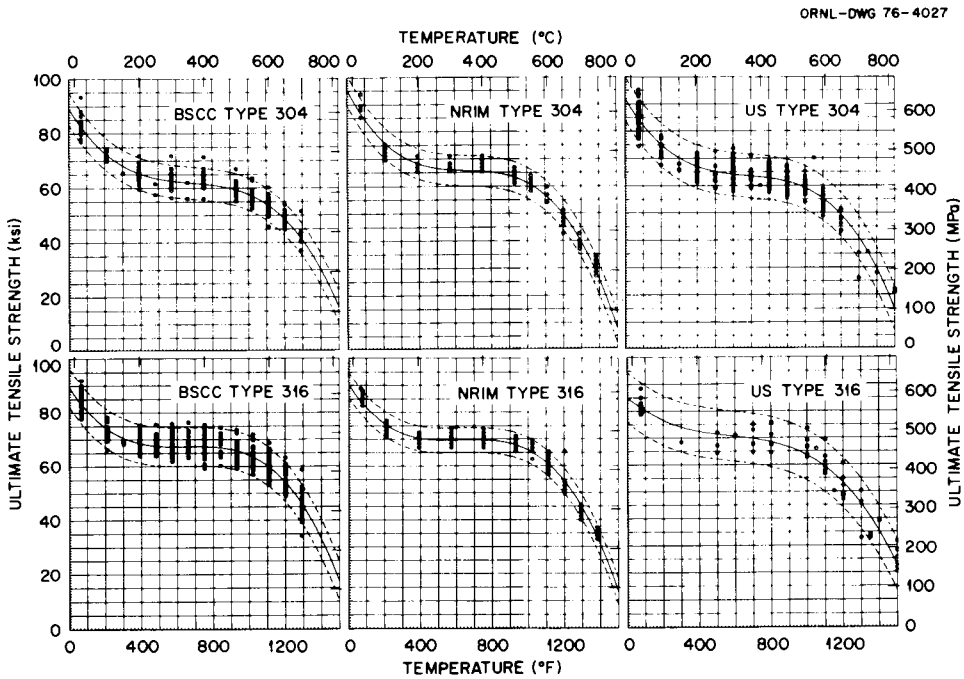

Fig. 3.9. Trends in Variations in Ultimate Tensile Strength as a Function of Test Temperature for Types 304 and 316 Stainless Steel Data Obtained in Three Different Countries. Lower and upper limit lines are ±2SEE.

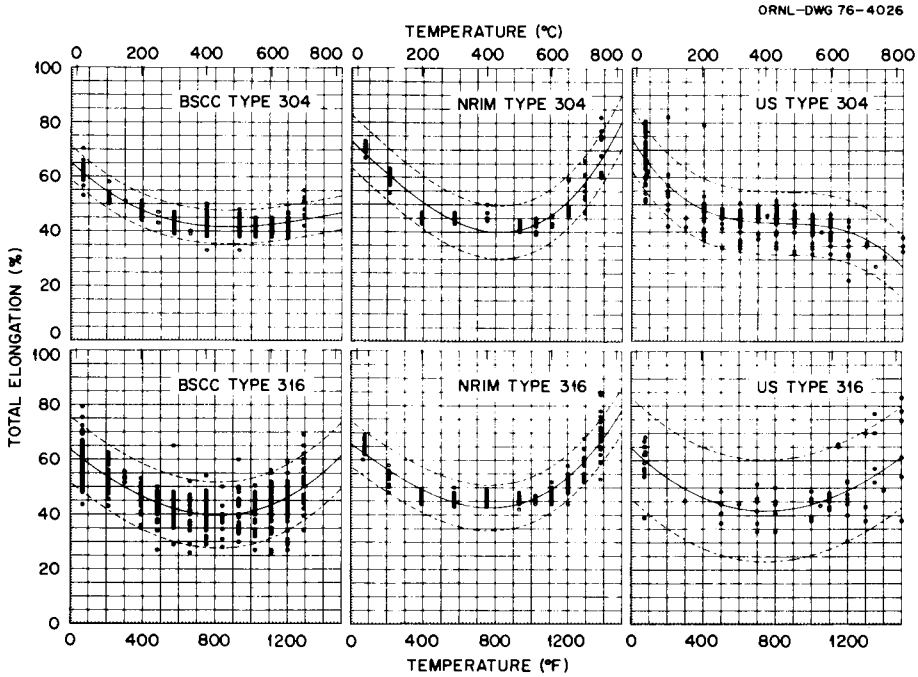

Fig. 3.10. Trends in Variations in Total Elongation as a Function of Test Temperature for Types 304 and 316 Stainless Steel Data Obtained in Three Different Countries. Lower and upper limit lines are ±2SEE.

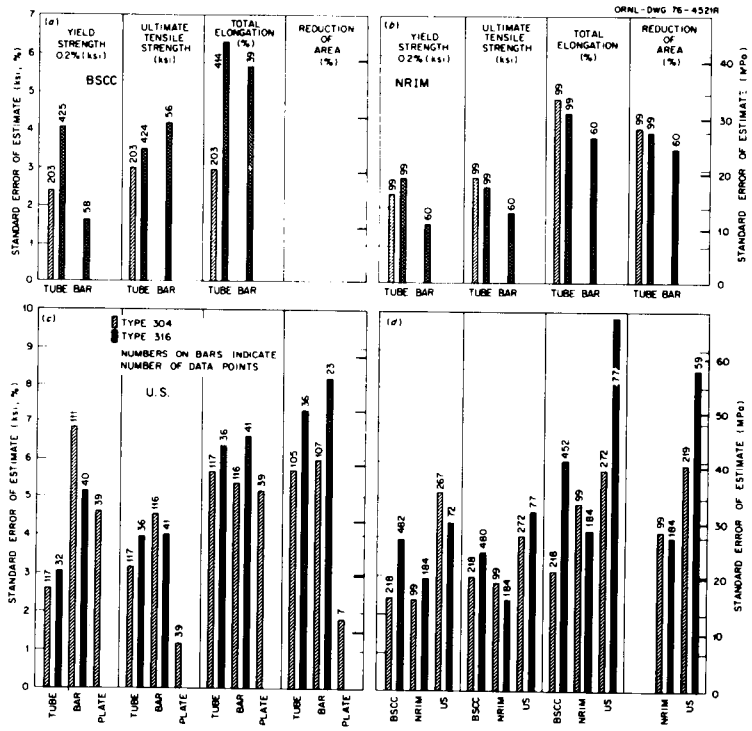

Fig. 3.11. Standard Error of Estimate in Tensile Properties of Several Products of Types 304 and 316 Stainless Steels for Data Collected from U.S. and Two Foreign Countries.

A difference of 1°C (2°F) in test temperature was not expected to change the properties by any significant amount. Figures 3.12 through 3.14 show the plots for rupture time, average creep rate, and total elongation. Regression constants for Eqs. (12), (13), and (16) are summarized in Tables 3.3 through 3.6. Note from Tables 3.3 and 3.4 that going from the linear to the quadratic model improves both R^2 and SEE values. However, the improvement in R^2 depends on the data source. For example, BSCC type 316 data showed the maximum improvement, whereas NRIM and U.S. data showed relatively small improvement. For type 304 stainless steel, U.S. data showed significant improvement in R^2 for the quadratic model, as opposed to relatively small changes observed for NRIM and BSCC data. The BSCC data for type 316 stainless steel were both long-time and large in total number (817), whereas U.S. data for type 304 stainless steel were both long-time and large in total number (298). Both these data sources showed an improvement in R^2 by changing the rupture model from linear to quadratic, and thus it appears that long-time (>10,000 hr) data, when available in sufficient quantity, indicate the start of

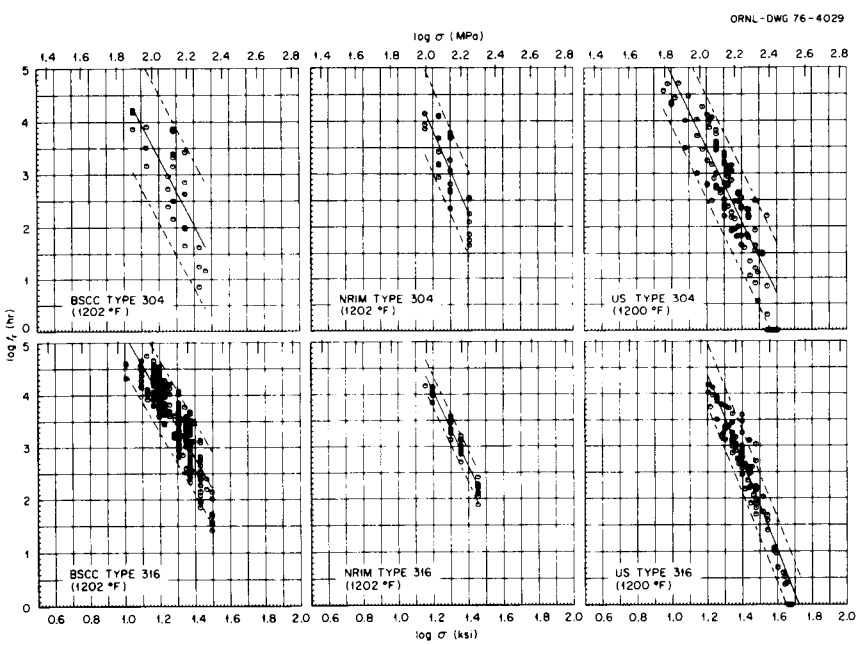

Fig. 3.12. Time to Rupture as a Function of Stress for BSCC and NRIM Data at 650°C (1202°F) and U.S. Data at 649°C (1200°F). The upper and lower limit lines are log t_r ± 2SEE.

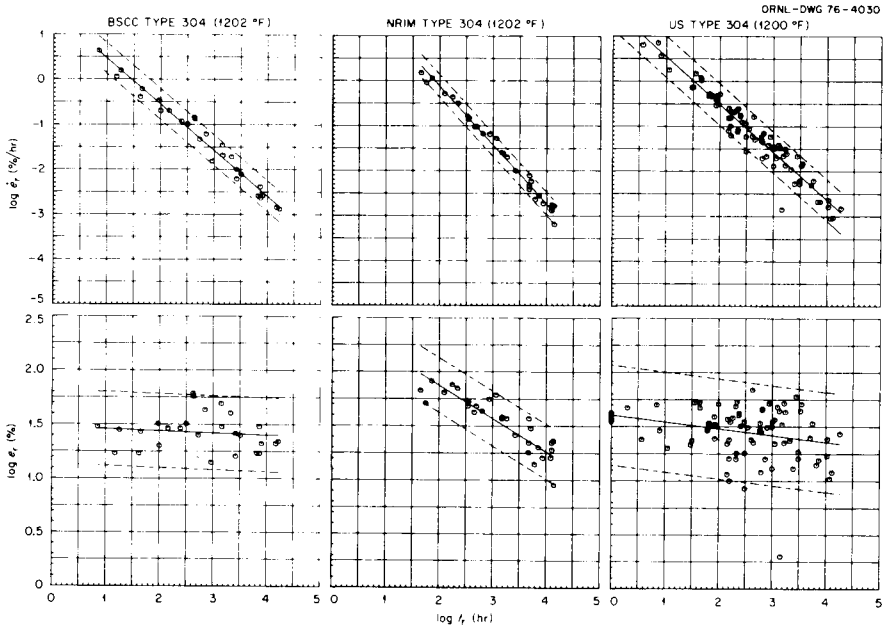

Fig. 3.13. Average Creep Rate and Creep Total Elongation for Type 304 Stainless Steel Data Collected from U.S. and Two Foreign Countries.

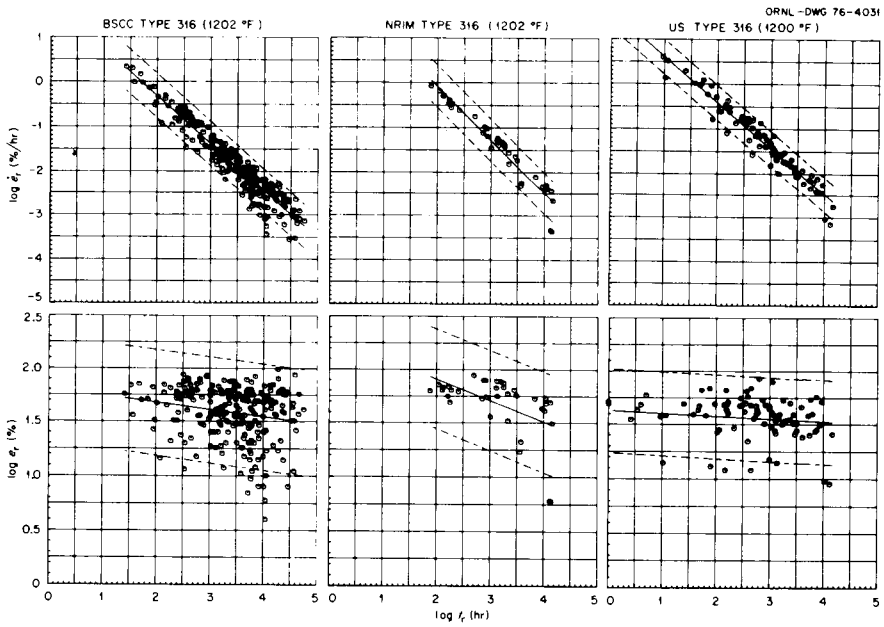

Fig. 3.14. Average Creep Rate and Creep Total Elongation for Type 316 Stainless Steel Data Collected from U.S. and Two Foreign Countries.

Table 3.3. Summary of Constants for Creep Data Analysis of Type 304 Stainless Steel

Data Source	Product Form	Number of Data Points	Test Temperature (°C)	Test Temperature (°F)	Model	Regression Coefficients[a] α_0	α_1	α_2	SEE (log t_r)	R^2 (%)	10^4-hr Creep Rupture Strength (ksi)[b]
BSCC	Tube	15	600	1112	Linear	11.61	−5.82		0.676	2.81	
BSCC	Tube	15	600	1112	Quadratic	8.62×10^{14}	-1.21×10^{15}	4.23×10^{14}	0.665	13.02	
BSCC	Tube	26	625	1157	Linear	15.38	−8.98		0.694	27.71	
BSCC	Tube	26	625	1157	Quadratic	−77.21	1.3×10^{2}	-5.21×10^{1}	0.705	28.50	
BSCC	Tube	14	650	1202	Linear	12.87	−7.57		0.653	15.65	
BSCC	Tube	14	650	1202	Quadratic	6.30×10^{14}	-9.60×10^{14}	3.65×10^{14}	0.635	26.87	
NRIM	Tube	32	600	1112	Linear	12.40	−6.33		0.425	43.43	
NRIM	Tube	32	600	1112	Quadratic	−43.90	73.65	−28.35	0.420	46.72	
NRIM	Tube	32	650	1202	Linear	13.10	−7.71		0.370	78.40	
NRIM	Tube	32	650	1202	Quadratic	−12.76	32.54	−15.59	0.357	80.50	
NRIM	Tube	40	700	1293	Linear	10.97	−7.02		0.206	94.89	
NRIM	Tube	40	700	1293	Quadratic	2.04	8.99	−7.09	0.183	96.08	
NRIM	Tube	27	750	1383	Linear	9.19	−6.22		0.142	94.93	
NRIM	Tube	27	750	1383	Quadratic	4.74	3.24	−4.98	0.143	95.03	
U.S.	Tube	22	593	1100	Linear	9.07	−4.12		0.509	40.78	
U.S.	Tube	22	593	1100	Quadratic	32.17	−34.47	9.89	0.498	46.17	
U.S.	Tube	53	649	1200	Linear	12.08	−6.92		0.336	79.74	
U.S.	Tube	53	649	1200	Quadratic	10.39	−4.42	−0.92	0.339	79.75	
U.S.	Tube	5	732	1350	Linear	11.00	−7.17		0.105	98.03	
U.S.	Tube	5	732	1350	Quadratic	10.86	−6.92	−0.11	0.129	98.03	
BSCC	Bar	15	550	1022	Linear	16.14	−8.74		0.277	91.89	
BSCC	Bar	15	550	1022	Quadratic	−6.37	21.33	−9.999	0.270	92.90	
BSCC	Bar	13	600	1112	Linear	12.81	−7.23		0.246	94.97	
BSCC	Bar	13	600	1112	Quadratic	13.91	−8.81	0.564	0.258	94.98	
BSCC	Bar	14	650	1202	Linear	11.81	−7.33		0.271	95.06	
BSCC	Bar	14	650	1202	Quadratic	8.75	−2.37	−1.98	0.286	95.14	
BSCC	Bar	4	700	1293	Linear	8.72	−5.68		0.101	99.09	
BSCC	Bar	4	700	1293	Quadratic	15.05	−17.03	5.02	0.033	99.95	
U.S.	Bar	43	538	1000	Linear	11.56	−6.02		0.489	79.95	
U.S.	Bar	43	538	1000	Quadratic	20.70	−18.88	4.46	0.481	81.06	
U.S.	Bar	6	566	1050	Linear	16.35	−8.85		0.225	94.66	
U.S.	Bar	6	566	1050	Quadratic	−11.64	28.55	−12.45	0.244	95.28	
U.S.	Bar	7	593	1100	Linear	15.77	−9.14		0.323	90.76	
U.S.	Bar	7	593	1100	Quadratic	26.61	45.85	−17.77	0.294	93.88	
U.S.	Bar	52	649	1200	Linear	12.10	−7.41		0.411	89.65	
U.S.	Bar	52	649	1200	Quadratic	2.204	8.30	−6.14	0.365	92.00	
U.S.	Bar	16	704	1300	Linear	8.82	−5.89		0.359	90.91	
U.S.	Bar	16	704	1300	Quadratic	22.98	6.00	−5.28	0.295	93.34	
U.S.	Bar	13	732	1350	Linear	10.65	−7.35		0.283	92.42	
U.S.	Bar	13	732	1350	Quadratic	29.91	7.33	−6.85	0.269	93.78	
U.S.	Bar	10	760	1400	Linear	7.52	−5.57		0.342	93.54	
U.S.	Bar	10	760	1400	Quadratic	4.48	0.70	−3.08	0.339	94.44	
U.S.	Bar	12	816	1500	Linear	6.63	−5.65		0.425	88.06	
U.S.	Bar	12	816	1500	Quadratic	4.30	−4.23	−3.22	0.435	88.75	

Table 3.3. (Continued)

Data Source	Product Form	Number of Data Points	Test Temperature (°C)	Test Temperature (°F)	Model	Regression Coefficients[a] α_0	α_1	α_2	SEE (log t_r)	R^2 (%)	10^4-hr Creep Rupture Strength (ksi)[b]
BSCC	Combined	15	550	1022	Linear	16.15	−8.74		0.277	91.89	24.56
BSCC	Combined	15	550	1022	Quadratic	−6.37	21.33	−9.999	0.270	92.90	
BSCC	Combined	28	600	1112	Linear	12.87	−6.96		0.654	51.75	18.81
BSCC	Combined	28	600	1112	Quadratic	−17.89	37.20	−15.78	0.620	58.35	
BSCC	Combined	26	625	1147	Linear	15.38	−8.98		0.694	27.71	18.50
BSCC	Combined	26	625	1147	Quadratic	−77.21	130.02	−52.10	0.705	28.50	
BSCC	Combined	28	650	1202	Linear	10.91	−6.34		0.603	60.98	12.30
BSCC	Combined	28	650	1202	Quadratic	−12.86	32.29	−15.54	0.567	66.84	
BSCC	Combined	4	700	1293	Linear	8.72	−5.68		0.101	99.09	6.78
BSCC	Combined	4	700	1293	Quadratic	15.05	−17.03	5.02	0.033	99.95	
NRIM	Combined	10	550	1022	Linear	19.58	−9.89		0.074	97.57	37.61
NRIM	Combined	10	550	1022	Quadratic	−46.11	68.82	−23.56	0.063	98.49	
NRIM	Combined	10	575	1067	Linear	17.82	−9.63		0.137	96.13	27.23
NRIM	Combined	10	575	1067	Quadratic	−21.97	43.02	−17.39	0.123	97.27	
NRIM	Combined	41	600	1112	Linear	9.81	−4.59		0.433	36.34	18.44
NRIM	Combined	41	600	1112	Quadratic	−23.17	43.12	−17.20	0.428	39.34	
NRIM	Combined	34	650	1202	Linear	12.92	7.60		0.397	74.35	14.92
NRIM	Combined	34	650	1202	Quadratic	−3.98	18.70	−10.18	0.396	75.27	
NRIM	Combined	40	700	1293	Linear	10.97	−7.02		0.206	94.89	9.84
NRIM	Combined	40	700	1293	Quadratic	2.04	8.99	−7.09	0.183	96.08	
NRIM	Combined	27	750	1383	Linear	9.49	−6.22		0.141	94.93	7.63
NRIM	Combined	27	750	1383	Quadratic	4.74	3.24	−4.98	0.143	95.03	
U.S.	Combined	20	538	1000	Linear	16.28	−8.78		0.467	67.32	25.04
U.S.	Combined	20	538	1000	Quadratic	20.06	−13.64	1.56	0.480	67.34	
U.S.	Combined	9	565	1050	Linear	17.11	−9.28		0.269	90.40	25.87
U.S.	Combined	9	565	1050	Quadratic	−42.48	70.23	−26.44	0.246	93.10	
U.S.	Combined	64	593	1100	Linear	12.01	−6.40		0.582	68.73	17.85
U.S.	Combined	64	593	1100	Quadratic	20.58	−18.42	4.17	0.578	69.65	
U.S.	Combined	114	649	1200	Linear	11.77	−6.90		0.482	78.99	13.37
U.S.	Combined	114	649	1200	Quadratic	−4.86	11.60	−7.16	0.448	82.04	
U.S.	Combined	29	704	1300	Linear	9.05	−6.06		0.362	90.51	6.81
U.S.	Combined	29	704	1300	Quadratic	1.93	6.52	−5.42	0.304	93.54	
U.S.	Combined	23	732	1350	Linear	9.08	−5.78		0.348	85.64	7.57
U.S.	Combined	23	732	1350	Quadratic	1.61	9.12	−7.30	0.295	90.17	
U.S.	Combined	12	760	1400	Linear	7.47	−5.47		0.332	92.92	4.31
U.S.	Combined	12	760	1400	Quadratic	4.17	1.28	−3.31	0.322	94.02	
U.S.	Combined	27	816	1500	Linear	6.98	−5.86		0.376	89.28	3.23
U.S.	Combined	27	816	1500	Quadratic	3.39	2.68	−4.86	0.354	90.88	

[a]Coefficients of the linear model, $\log t_r = \alpha_0 + \alpha_1 \log \sigma$, and the quadratic model, $\log t_r = \alpha_0 + \alpha_1 \log \sigma + \alpha_2 (\log \sigma)^2$, where σ is the stress in ksi. To obtain t_r in terms of stress in MPa, in the linear model subtract $0.83842\alpha_1$ from α_0; in the quadratic model subtract $1.67684\alpha_2$ from α_1 and add $0.70312\alpha_2 - 0.83852\alpha_1$ to α_0.

[b]To convert to MPa, multiply by 6.895.

Table 3.4. Summary of Constants for Creep Data Analysis of Type 316 Stainless Steel

Data Source	Product Form	Number of Data Points	Test Temperature (°C)	Test Temperature (°F)	Model	Regression Coefficients[a] α_0	α_1	α_2	SEE (log t_r)	R^2 (%)	10^4-hr Creep Rupture Strength (ksi)[b]
BSCC	Tube	9	550	1022	Linear	17.46	−8.93		0.201	94.41	
BSCC	Tube	9	550	1022	Quadratic	21.01	−13.38	1.39	0.217	94.42	
BSCC	Tube	129	600	1112	Linear	17.14	−9.28		0.394	67.16	
BSCC	Tube	129	600	1112	Quadratic	−40.72	71.09	−27.86	0.372	70.92	
BSCC	Tube	112	625	1157	Linear	13.22	−6.92		0.412	60.17	
BSCC	Tube	112	625	1157	Quadratic	−54.71	92.81	−36.50	0.378	66.85	
BSCC	Tube	180	650	1202	Linear	11.14	−5.95		0.338	74.62	
BSCC	Tube	180	650	1202	Quadratic	−8.62	25.02	−12.07	0.308	79.01	
BSCC	Tube	29	675	1247	Linear	10.28	−5.74		0.278	88.38	
BSCC	Tube	29	675	1247	Quadratic	4.63	3.79	−3.97	0.281	88.53	
BSCC	Tube	63	700	1293	Linear	9.54	−5.63		0.263	88.93	
BSCC	Tube	63	700	1293	Quadratic	1.95	8.03	−6.06	0.237	91.14	
NRIM	Tube	35	600	1112	Linear	16.00	−8.50		0.177	85.28	
NRIM	Tube	35	600	1112	Quadratic	−46.81	77.43	−29.36	0.164	87.75	
NRIM	Tube	36	650	1202	Linear	12.52	−7.08		0.152	95.48	
NRIM	Tube	36	650	1202	Quadratic	0.571	11.13	−6.90	0.141	96.20	
NRIM	Tube	38	700	1293	Linear	10.08	−6.07		0.159	94.78	
NRIM	Tube	38	700	1293	Quadratic	1.640	8.78	−6.47	0.144	95.89	
NRIM	Tube	26	750	1383	Linear	8.64	−5.61		0.173	90.15	
NRIM	Tube	26	750	1383	Quadratic	4.10	3.58	−4.62	0.175	90.40	
U.S.	Tube	16	593	1100	Linear	14.10	−7.39		0.421	55.89	
U.S.	Tube	16	593	1100	Quadratic	−56.2	83.36	−29.24	0.417	59.71	
U.S.	Tube	61	649	1200	Linear	12.67	−7.08		0.293	83.12	
U.S.	Tube	61	649	1200	Quadratic	−4.45	17.58	−8.84	0.276	85.24	
U.S.	Tube	3	704	1300	Linear	10.69	−6.65		0.391	99.93	
U.S.	Tube	3	704	1300	Quadratic						
U.S.	Tube	17	732	1350	Linear	8.96	−5.63		0.167	93.39	
U.S.	Tube	17	732	1350	Quadratic	5.90	−0.084	−2.49	0.172	93.72	
U.S.	Tube	8	816	1500	Linear	6.83	−4.99		0.085	98.66	
U.S.	Tube	8	816	1500	Quadratic	6.57	−4.32	−4.05	0.093	98.67	
BSCC	Bar	8	550	1022	Linear	17.96	−9.20		0.445	73.71	
BSCC	Bar	8	550	1022	Quadratic	−13.33	29.54	−11.97	0.473	74.10	
BSCC	Bar	71	600	1112	Linear	15.76	−8.49		0.485	74.05	
BSCC	Bar	71	600	1112	Quadratic	−23.34	46.14	−19.00	0.433	78.60	
BSCC	Bar	39	625	1157	Linear	14.19	−7.87		0.450	74.58	
BSCC	Bar	39	625	1157	Quadratic	20.80	43.36	−18.66	0.391	81.33	
BSCC	Bar	81	650	1202	Linear	10.71	−5.70		0.361	77.67	
BSCC	Bar	81	650	1202	Quadratic	−3.50	17.13	−9.09	0.335	80.99	
BSCC	Bar	33	675	1247	Linear	9.87	−5.46		0.290	79.49	
BSCC	Bar	33	675	1247	Quadratic	−5.13	19.50	−10.31	0.279	81.61	
BSCC	Bar	57	700	1293	Linear	8.26	−4.49		0.306	83.52	
BSCC	Bar	57	700	1293	Quadratic	1.71	7.59	−5.47	0.268	87.59	
NRIM	Bar	40	700	1293	Linear	9.33	−5.62		0.102	98.12	
NRIM	Bar	40	700	1293	Quadratic	6.11	0.385	−2.75	0.0926	98.50	
NRIM	Bar	31	750	1383	Linear	7.41	−4.69		0.209	92.10	
NRIM	Bar	31	750	1383	Quadratic	7.32	−4.48	−0.11	0.213	92.10	
NRIM	Bar	21	800	1473	Linear	6.45	−4.31		0.061	98.37	
NRIM	Bar	21	800	1473	Quadratic	5.23	−0.91	−2.33	0.057	98.64	
NRIM	Bar	19	850	1563	Linear	4.76	−2.43		0.224	82.06	
NRIM	Bar	19	850	1563	Quadratic	6.46	−7.06	2.75	0.150	92.40	
U.S.	Bar	13	538	1000	Linear	16.32	−8.18		0.390	71.81	
U.S.	Bar	13	538	1000	Quadratic	−22.75	37.82	−13.51	0.405	72.36	
U.S.	Bar	48	593	1100	Linear	19.13	−10.97		0.370	83.10	
U.S.	Bar	48	593	1100	Quadratic	74.41	−81.16	22.24	0.349	85.18	
U.S.	Bar	29	649	1200	Linear	15.82	−9.34		0.251	96.26	
U.S.	Bar	29	649	1200	Quadratic	4.41	6.25	−5.28	0.229	96.99	
U.S.	Bar	48	704	1300	Linear	9.64	−6.03		0.273	92.93	
U.S.	Bar	48	704	1300	Quadratic	4.87	1.78	−3.14	0.257	93.89	
U.S.	Bar	13	760	1400	Linear	9.34	−6.30		0.131	98.88	
U.S.	Bar	13	760	1400	Quadratic	9.05	−5.80	−0.21	0.137	98.88	
U.S.	Bar	51	816	1500	Linear	5.80	−3.82		0.603	66.46	
U.S.	Bar	51	816	1500	Quadratic	3.03	2.85	−3.76	0.573	70.33	

Table 3.4. (Continued)

Data Source	Product Form	Number of Data Points	Test Temperature (°C)	Test Temperature (°F)	Model	Regression Coefficients[a] α_0	α_1	α_2	SEE (log t_r)	R^2 (%)	10^4-hr Creep Rupture Strength (ksi)[b]
BSCC	Combined	17	550	1022	Linear	17.59	−8.99		0.315	84.52	32.48
BSCC	Combined	17	550	1022	Quadratic	−33.35	60.48	−24.07	0.397	74.47	
BSCC	Combined	200	600	1112	Linear	16.38	−8.81		0.437	69.00	25.42
BSCC	Combined	200	600	1112	Quadratic	−33.35	60.48	−24.07	0.397	74.47	
BSCC	Combined	151	625	1157	Linear	13.79	−7.40		0.446	63.73	21.04
BSCC	Combined	151	625	1157	Quadratic	−37.10	67.18	−27.22	0.396	71.48	
BSCC	Combined	261	650	1202	Linear	10.99	−5.86		0.348	75.38	15.59
BSCC	Combined	261	650	1202	Quadratic	−6.48	21.78	−10.86	0.317	79.61	
BSCC	Combined	62	675	1247	Linear	10.14	−5.65		0.283	84.60	12.21
BSCC	Combined	62	675	1247	Quadratic	2.94	6.42	−5.02	0.281	85.03	
BSCC	Combined	120	700	1293	Linear	8.84	−5.01		0.293	85.41	9.25
BSCC	Combined	120	700	1293	Quadratic	1.60	8.19	−5.92	0.258	88.82	
BSCC	Combined	6	750	1383	Linear	5.73	−2.90		0.116	97.92	3.95
BSCC	Combined	6	750	1383	Quadratic	6.89	−5.35	1.22	0.100	98.84	
NRIM	Combined	35	600	1112	Linear	16.00	−8.53		0.177	85.28	25.52
NRIM	Combined	35	600	1112	Quadratic	−46.81	77.43	−29.36	0.164	87.75	
NRIM	Combined	36	650	1202	Linear	12.52	−7.08		0.152	95.48	15.97
NRIM	Combined	36	650	1202	Quadratic	0.571	11.13	−6.90	0.141	96.20	
NRIM	Combined	91	700	1293	Linear	9.29	−5.47		0.169	94.44	9.27
NRIM	Combined	91	700	1293	Quadratic	3.78	4.59	−4.53	0.154	95.46	
NRIM	Combined	67	750	1383	Linear	7.43	−4.56		0.235	88.31	5.65
NRIM	Combined	67	750	1383	Quadratic	5.09	0.71	−2.90	0.230	88.93	
NRIM	Combined	28	800	1473	Linear	6.45	−4.32		0.060	98.40	3.69
NRIM	Combined	28	800	1473	Quadratic	4.98	−2.36	−2.78	0.053	98.79	
NRIM	Combined	23	850	1563	Linear	4.75	−2.49		0.225	80.14	2.00
NRIM	Combined	23	850	1563	Quadratic	6.48	−7.19	2.84	0.150	91.64	
U.S.	Combined	13	538	1000	Linear	16.32	−8.18		0.390	71.81	32.07
U.S.	Combined	13	538	1000	Quadratic	−22.75	37.82	−13.51	0.405	72.36	
U.S.	Combined	71	593	1100	Linear	16.66	−9.27		0.471	72.79	23.21
U.S.	Combined	71	593	1100	Quadratic	62.96	−67.45	18.22	0.453	75.28	
U.S.	Combined	94	649	1200	Linear	14.35	−8.32		0.303	91.04	17.54
U.S.	Combined	94	649	1200	Quadratic	7.77	14.18	−7.80	0.272	92.87	
U.S.	Combined	56	704	1300	Linear	9.52	−5.88		0.301	92.12	8.69
U.S.	Combined	56	704	1300	Quadratic	5.51	0.585	−2.56	0.291	92.19	
U.S.	Combined	23	732	1350	Linear	8.68	−5.35		0.161	95.07	7.49
U.S.	Combined	23	732	1350	Quadratic	8.14	−4.34	−0.46	0.164	95.08	
U.S.	Combined	13	760	1400	Linear	9.34	−6.30		0.131	98.88	7.04
U.S.	Combined	13	760	1400	Quadratic	9.05	−5.79	−0.21	0.137	98.88	
U.S.	Combined	69	816	1500	Linear	6.06	−4.13		0.541	73.33	3.16
U.S.	Combined	69	816	1500	Quadratic	3.36	2.23	−3.50	0.507	76.89	

[a]Coefficients of the linear model, $\log t_r = \alpha_0 + \alpha_1 \log \sigma$, and the quadratic model, $\log t_r = \alpha_0 + \alpha_1 \log \sigma + \alpha_2 (\log \sigma)^2$, where σ is the stress in ksi. To obtain t_r in terms of stress in MPa, in the linear model subtract $0.83842\alpha_1$ from α_0; in the quadratic model subtract $1.67684\alpha_2$ from α_1 and add $0.70312\alpha_2 - 0.83852\alpha_1$ to α_0.

[b]To convert to MPa, multiply by 6.895.

Table 3.5. Summary of Constants for Average Creep Rate and Creep Total Elongation Data Analysis of Type 304 Stainless Steel

Data Source	Product	Number of Data Points	Temperature (°C)	Temperature (°F)	Regression Coefficients A	Regression Coefficients B	SEE (log $\dot{e}_T$)	R^2 (%)	10^4-hr Creep Total Elongation (%)
BSCC	Tube	13	600	1112	1.69	−1.11	0.144	95.74	
BSCC	Tube	23	625	1157	1.81	−1.17	0.127	98.08	
BSCC	Tube	13	650	1202	1.82	−1.11	0.186	94.98	
NRIM	Tube	32	600	1112	2.19	−1.22	0.138	96.16	
NRIM	Tube	32	650	1202	2.46	−1.30	0.126	98.54	
NRIM	Tube	40	700	1273	2.41	−1.30	0.249	95.77	
NRIM	Tube	27	750	1383	2.20	−1.25	0.274	89.24	
U.S.	Tube	22	593	1100	1.46	−1.05	0.194	92.81	
U.S.	Tube	53	649	1200	1.73	−1.10	0.267	90.40	
U.S.	Tube	5	732	1350	1.03	−0.93	0.248	88.71	
BSCC	Bar	15	550	1022	1.52	−1.14	0.105	99.11	
BSCC	Bar	13	600	1112	1.47	−1.05	0.256	95.27	
BSCC	Bar	14	650	1202	1.35	−1.00	0.111	99.17	
BSCC	Bar	4	700	1293	1.62	−0.92	0.154	97.56	
U.S.	Bar	14	538	1000	1.73	−1.22	0.060	99.60	
U.S.	Bar	5	565	1050	1.72	−1.23	0.065	99.61	
U.S.	Bar	16	593	1100	1.50	−1.13	0.099	99.04	
U.S.	Bar	35	649	1200	1.57	−1.06	0.159	98.49	
U.S.	Bar	15	704	1300	1.52	−1.07	0.226	97.05	
U.S.	Bar	12	732	1350	1.72	−1.06	0.159	96.26	
U.S.	Bar	9	760	1400	1.50	−1.05	0.178	98.52	
U.S.	Bar	10	816	1500	1.42	−1.04	0.178	97.67	
BSCC	Combined	15	550	1022	1.52	−1.14	0.105	99.11	9.12
BSCC	Combined	26	600	1112	1.53	−1.08	0.202	96.13	16.22
BSCC	Combined	23	675	1157	1.81	−1.17	0.127	98.08	13.49
BSCC	Combined	27	650	1202	1.48	−1.02	0.170	97.17	25.12
BSCC	Combined	4	700	1293	1.62	−0.92	0.154	97.56	87.10
NRIM	Combined	10	550	1022	1.90	−1.16	0.087	97.54	18.20
NRIM	Combined	10	575	1067	1.74	−1.08	0.163	95.47	26.30
NRIM	Combined	41	600	1112	2.17	−1.21	0.153	94.84	21.38
NRIM	Combined	34	650	1202	2.49	−1.31	0.126	98.51	17.78
NRIM	Combined	40	700	1293	2.41	−1.30	0.249	95.77	16.22
NRIM	Combined	27	750	1383	2.20	−1.25	0.274	89.24	17.78
U.S.	Combined	17	538	1000	1.61	−1.17	0.086	99.29	8.51
U.S.	Combined	5	565	1050	1.72	−1.23	0.065	99.61	6.31
U.S.	Combined	44	593	1100	1.49	−1.08	0.181	95.86	14.79
U.S.	Combined	91	649	1200	1.60	−1.06	0.231	95.21	22.91
U.S.	Combined	26	704	1300	1.59	−1.04	0.266	95.75	26.92
U.S.	Combined	17	732	1350	1.35	−0.97	0.226	90.99	29.51
U.S.	Combined	9	760	1400	1.50	−1.05	0.178	98.52	19.95
U.S.	Combined	21	816	1500	1.58	−1.02	0.254	95.03	31.63

Table 3.6. Summary of Constants for Average Creep Rate and Creep Total Elongation Data Analysis of Type 316 Stainless Steel

Data Source	Product	Number of Data Points	Temperature (°C)	Temperature (°F)	Regression Coefficients A	Regression Coefficients B	SEE (log $\dot{e}_r$)	R^2 (%)	10^4-hr Creep Total Elongation (%)
BSCC	Tube	9	550	1022	2.07	−1.21	0.081	99.38	
BSCC	Tube	124	600	1112	1.42	−1.00	0.222	90.52	
BSCC	Tube	96	625	1157	1.54	−1.01	0.224	89.35	
BSCC	Tube	165	650	1202	1.91	−1.10	0.240	90.40	
BSCC	Tube	29	675	1247	2.10	−1.13	0.232	94.00	
BSCC	Tube	62	700	1293	2.28	−1.19	0.275	92.20	
NRIM	Tube	35	600	1112	1.61	−0.99	0.103	95.16	
NRIM	Tube	36	650	1202	2.31	−1.20	0.234	93.10	
NRIM	Tube	38	700	1293	2.91	−1.43	0.345	89.35	
NRIM	Tube	26	750	1383	3.08	−1.51	0.378	82.98	
U.S.	Tube	16	593	1100	1.52	−1.03	0.101	97.66	
U.S.	Tube	60	649	1200	1.86	−1.09	0.142	96.81	
U.S.	Tube	17	732	1350	2.20	−1.21	0.182	95.07	
U.S.	Tube	8	816	1500	2.02	−1.16	0.130	97.72	
BSCC	Bar	8	550	1022	1.96	−1.17	0.095	99.14	
BSCC	Bar	71	600	1112	1.13	−0.91	0.206	94.42	
BSCC	Bar	39	625	1157	1.23	−0.89	0.260	90.31	
BSCC	Bar	81	650	1202	1.66	−1.02	0.260	90.00	
BSCC	Bar	33	675	1247	2.16	−1.12	0.217	91.68	
BSCC	Bar	57	700	1293	2.05	−1.11	0.272	90.43	
NRIM	Bar	40	700	1293	2.43	−1.21	0.149	97.38	
NRIM	Bar	31	750	1383	2.35	−1.19	0.139	97.58	
NRIM	Bar	21	800	1473	2.68	−1.30	0.130	95.78	
NRIM	Bar	19	850	1563	2.40	−1.24	0.111	97.18	
U.S.	Bar	8	538	1000	2.09	−1.30	0.071	99.16	
U.S.	Bar	5	565	1050	1.94	−1.30	0.101	99.40	
U.S.	Bar	47	593	1100	1.48	−1.06	0.091	99.10	
U.S.	Bar	29	649	1200	1.60	−1.04	0.204	97.74	
U.S.	Bar	48	704	1300	1.90	−1.03	0.203	96.42	
U.S.	Bar	6	732	1350	2.42	−1.26	0.081	99.62	
U.S.	Bar	12	760	1400	1.78	−1.07	0.236	97.10	
U.S.	Bar	51	816	1500	1.96	−1.09	0.171	97.77	
BSCC	Combined	17	550	1022	1.92	−1.19	0.088	99.15	14.19
BSCC	Combined	195	600	1112	1.27	−0.95	0.217	92.21	29.51
BSCC	Combined	135	625	1157	1.44	−0.97	0.240	89.84	36.31
BSCC	Combined	246	650	1202	1.81	−1.07	0.247	90.20	33.89
BSCC	Combined	62	675	1247	2.16	−1.13	0.223	93.02	43.65
BSCC	Combined	119	700	1293	2.17	−1.15	0.273	91.31	37.15
BSCC	Combined	6	750	1383	2.26	−1.35	0.436	86.19	7.24
NRIM	Combined	35	600	1112	1.61	−0.99	0.103	95.16	44.67
NRIM	Combined	36	650	1202	2.31	−1.20	0.234	93.11	32.36
NRIM	Combined	91	700	1293	2.52	−1.27	0.282	91.26	27.54
NRIM	Combined	67	750	1383	2.42	−1.24	0.303	88.76	28.84
NRIM	Combined	28	800	1473	2.67	−1.29	0.129	95.70	32.36
NRIM	Combined	23	850	1563	2.43	−1.24	0.118	96.56	29.51
U.S.	Combined	13	538	1000	1.94	−1.25	0.107	98.67	8.71
U.S.	Combined	70	593	1100	1.46	−1.04	0.113	98.59	19.95
U.S.	Combined	93	649	1200	1.63	−1.03	0.196	96.60	32.36
U.S.	Combined	56	704	1300	1.86	−1.01	0.192	96.96	66.07
U.S.	Combined	23	732	1350	2.27	−1.23	0.162	96.76	22.39
U.S.	Combined	12	760	1400	1.78	−1.07	0.236	97.10	31.62
U.S.	Combined	69	816	1500	1.93	−1.09	0.176	97.68	37.15

curvilinearity for type 304 stainless steel at a test temperature of 649°C (1200°F) and for type 316 stainless steel at 593°C (1100°F).

To compare variations in creep-rupture properties of types 304 and 316 stainless steels, we selected the linear model. Using this model, 10^4-hr creep rupture strength values were computed and listed in Tables 3.3 and 3.4. Our choice of 10^4-hr creep-rupture strength for comparison between the data collected in three different countries was based on the following reasons: (1) 10^4-hr creep-rupture strength did not require any extrapolation of the data; (2) errors due to curvilinearity in computing creep-rupture strength values are expected for time-to-rupture periods greater than 10^4 hr.

To check variations in creep elongation (e_r), we computed 10^4-hr creep elongation using Eq. (17), based on values of constants A and B determined from Eq. (16). These values of 10^4-hr creep total elongation are included in Tables 3.5 and 3.6.

The variations in rupture time, the stress-rupture exponent (α_1) from Eq. (12), and 10^4-hr creep-rupture strength and creep total elongation for types 304 and 316 stainless steels can be observed from the composite plots in Fig. 3.15. The SEE in log t_r for the combined data on all products of types 304 and 316 stainless steel are compared in Fig. 3.13(a). Consistent with observations on tensile properties, NRIM data showed the least variations for a given type of steel. However, a comparison of variations of log t_r for types 304 and 316 stainless steel clearly shows that type 316 has less variation in the data.

In Fig. 3.15(b), the stress exponent values for both types 304 and 316 stainless steel are plotted as a function of test temperature. It can be noted again that α_1 values computed for type 316 stainless steel data from three different countries show less variation than corresponding values for type 304.

In Fig. 3.15(c) are plotted the 10^4-hr creep-rupture strength values as a function of test temperature. Included is the ASME Code Case 1592 minimum stress to cause rupture in 10^4 hr. For comparison, "minimum" stresses from the current analysis of the U.S. data are also shown in the figure. These values were defined as the stress to cause a "minimum"

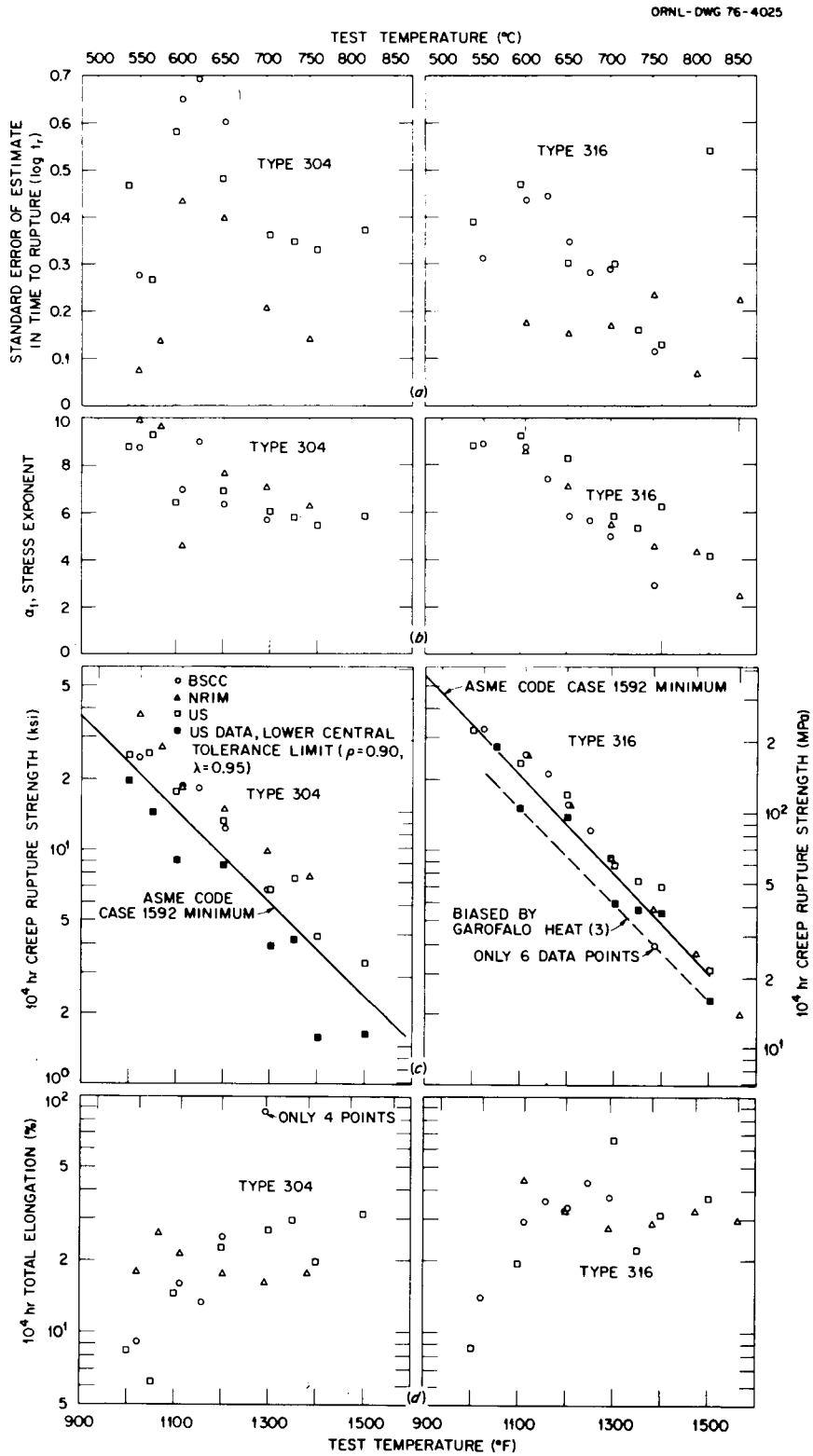

Fig. 3.15. Plots of SEE in log t_r, Stress Exponent (α_1), and 10^4-hr Creep Rupture Strength and Total Elongation as Functions of Test Temperature for Types 304 and 316 Stainless Steel Data Collected from U.S. and Two Foreign Countries.

rupture life of 10^4 hr. The minimum t_r values were defined by the lower central tolerance limit (P = 0.90, λ = 0.95) about the predicted line for log t_r. At a P = 0.90, 95% of the observations of log t_r are expected to fall above the lower limit. While this method is not that used for the ASME "minimum" values, it is a well-defined statistical procedure. Still, it is not our purpose here to compare various methods for setting allowable stresses.

It can be noted from Fig. 3.15(c) that 10^4-hr creep-rupture strength values for type 316 stainless steel show less scatter than similar values for type 304. It is also worth noting that no significant differences can be observed between the 10^4-hr creep-rupture strengths for type 316 stainless steel produced in three different countries. For type 304, scatter in 10^4-hr creep-rupture strength is too large to permit a similar conclusion.

A comparison [Fig. 3.15(c)] of minimum values of 10^4-hr creep-rupture strength from ASME Code Case 1592 with lower central tolerance limits (P = 0.90, λ = 0.95) evaluated for the combined U.S. data showed the following results:

1. For type 304 stainless steel, 10^4-hr code minimum rupture strength values fall above the lower tolerance limit.

2. For type 316 stainless steel, 10^4-hr code minimum rupture strength values appear consistent with lower tolerance limit except at 593, 704, and 816°C (1100, 1300, and 1500°F). This anomaly is due to the Garofalo data,[8] which were on an extremely weak heat and were excluded from the data analyzed for code minimum values. The Garofalo data were included in this investigation to allow an assessment of total variations in the data.

In Fig. 3.15(d) is plotted the 10^4-hr creep total elongation as a function of test temperature. Consistent with the previous observations, creep elongation values for type 316 stainless steel from three different countries again showed less variation than did corresponding values for type 304. Furthermore, at any given test temperature, type 316 stainless steel shows higher creep total elongation, which is consistent with the earlier work of Booker et al.[29] and Booker and Sikka.[30,31]

3.2.2.4 Discussion

The variations determined in tensile and creep properties of types 304 and 316 stainless steel can be due to any or all of the following factors:

1. heat-treatment, mill- or laboratory-annealed;
2. product forms;[19,20,32]
3. heat-to-heat variability;[21,32–34]
4. thermomechanical processing history;[35]
5. laboratory-to-laboratory testing variability;[36]
6. scatter inherent in type of test and magnitude of the independent variable.

The results analyzed in the present investigation cover variabilities due to all six factors listed above. An example of variability due to heat treatment can be observed in the BSCC tensile data. The room-temperature yield strength values of several heats (meeting ASTM composition specifications) of types 304 and 316 stainless steel fell below the ASTM specified minimum value of 207 MPa (30 ksi). All U.S. and Japanese steels that met ASTM composition specifications met the room-temperature mechanical property requirement in the mill-annealed condition. Sikka et al.[30,35] have recently shown that laboratory annealing of mill-annealed products can lower their yield strength by approximately 34 MPa (5 ksi) for the plate and pipe products and by even greater amounts for the bar product. Thus, a possible reason for BSCC heats (meeting composition requirements) falling below the ASTM mechanical properties lower limit can be the laboratory annealing for these heats. This also suggests that the total BSCC data population in fact might be a mixture of mill- and laboratory-annealed properties. A comparison between the variation in ORNL yield strength data[37] on 20 heats of type 304 stainless steel in mill- and laboratory-annealed condition showed for the same number of data points an improvement in SEE from 2.52 to 1.59 upon laboratory annealing. Although a comparison of all mill-annealed data with all laboratory-annealed data shows a decrease in variation, a mixed population of data in these two conditions would be expected to show greater total scatter.

The example of variability due to different product forms has been observed in the U.S. data, where the bar showed significantly larger variations than the plate and tube. However, the NRIM and BSCC bar data have shown opposite trends. Reasons for such differences are not clear, although U.S. bar in general shows higher tensile properties[35,37] than other products, whereas BSCC and NRIM bar is lower in tensile properties than the tube. Such differences may be due to differences in the fabrication techniques of the various countries.

An example of heat-to-heat variability can be best seen from the NRIM tube data. These data were obtained at one laboratory on nine heats of both types 304 and 316 stainless steel of a single product form (tube) in the mill-annealed condition. The yield strength variations (SEE) in tubes of nine heats of types 304 and 316 stainless steel were 16.20 and 19.17 MPa (2.35 and 2.78 ksi), respectively. At a mean rupture life value of 10^4 hr, the band of log t_r ± SEE at 600°C (1112°F) yields rupture life values that vary from 3758 to 26,607 hr for type 304 and from 6653 to 15,031 hr for type 316 stainless steel tubes. Note that these variations almost certainly have to be associated with heat-to-heat variability, because all other factors contributing to variability were kept to a minimum in the NRIM data. Heat-to-heat variability observed[21] at ORNL in creep properties of 20 heats of type 304 stainless steel was of a similar magnitude to that reported for NRIM data. For example, at a stress of 207 MPa (30 ksi) at 593°C (1100°F), rupture times varied from 100 to 3000 hr. Variations at 117 MPa (17 ksi) and the same temperature were from 10,000 to 37,000 hr. The variability in creep properties increases as more heats are added. This is clearly demonstrated by the increase in variability for BSCC and U.S. data, where the numbers of heats investigated were many more than the nine heats used by NRIM. However, a part of the increased variability in BSCC and U.S. data is probably a result of the greater number of laboratories performing tests.

One of the most interesting observations emerging from the present investigation is that variability in creep properties of type 316 stainless steel is significantly less than corresponding variations in type 304. Such results may be expected from the relative strength differences

between the two steels. Type 316 stainless steel is stronger in tensile and creep properties than type 304. The increased strength of type 316 stainless steel is associated with the presence of 2 to 3% Mo in this steel as opposed to only 0.2 to 0.3% in type 304. The heat-to-heat variations in commercial steels have been suggested[21,32,33,37,38] to result from variations in contents of chemical elements such as C, N, P, B, Nb, Ti, etc. Because of the higher strength, the percent variations in type 316 stainless steel caused by small variations in chemical elements mentioned above are expected to be small. On the other hand, relatively weak type 304 stainless steel can change its strength character by fluctuation in chemical elements.

Sikka and Brinkman[21,39] have shown that variations in creep-rupture strength can be related to corresponding variations in ultimate tensile strength by a relationship of the form

$$S_R = \alpha \exp(\beta S_u) \ , \tag{18}$$

where

S_R = creep rupture strength,

S_u = ultimate tensile strength at the creep test temperature and a fixed strain rate,

α, β = constants.

Since the first two papers,[21,39] modification of Eq. (12) has explained direct variations in time to rupture. The modified version of Eq. (12) is written as

$$\log t_r = \alpha_0 + \alpha_1(\log \sigma + \beta S_u) \ . \tag{19}$$

Figure 3.16 shows plots of combined U.S. and ORNL creep data on 20 heats of type 304 stainless steel that are fitted in accordance with Eq. (19). Visual examination shows a clear improvement in variation of the data when expressed by Eq. (19). The improvements in SEE in $\log t_r$ at 593 and 649°C (1100 and 1200°F) were from 0.52 to 0.39 and

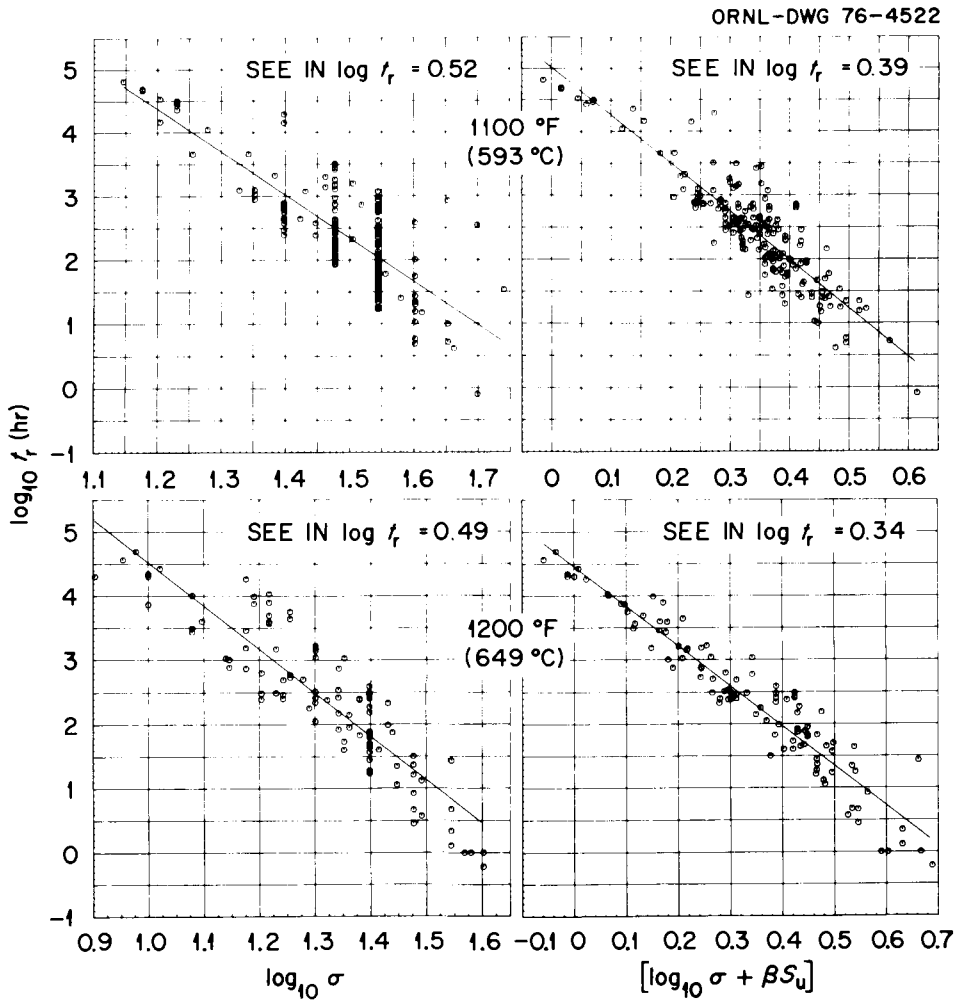

Fig. 3.16. Plots of log t_r as Functions of log σ and log $\sigma + \beta S_u$ for ORNL Data on 20 Heats of Type 304 Stainless Steel. Note an improvement in SEE from 0.52 to 0.39 in log t_r at 593°C (1100°F) and from 0.49 to 0.34 for 649°C (1200°F).

from 0.49 to 0.34, respectively. Thus, it appears that if weak and strong heats could be characterized by their ultimate tensile strength, variations in creep-rupture data can be minimized. For type 316 stainless steel, Eq. (19) was also obeyed, but improvement required in minimizing variation was relatively small (because these steels have very small variations), and thus the use of Eq. (19) is not even necessary. This result is consistent with the above observation that heat-to-heat variations are relatively smaller in type 316 stainless steel.

3.2.2.5 Summary and Conclusion

This report represents an attempt at evaluating variations in tensile and creep properties of types 304 and 316 stainless steel for U.S. data, including comparisons with the variations in data from two foreign countries, Japan and Britain. Variations were evaluated for the data on different products separately and for the combined data on all products. The following are some important conclusions from this work.

1. All steels used in U.S. and NRIM data collection met ASTM material specifications for both chemical composition and minimum values for room-temperature mechanical properties. Stainless steels used in BSCC data generation, although meeting the ASTM chemical composition requirement, included several steels showing room-temperature yield strength values below 207 MPa (30 ksi). This drop in room-temperature yield strength for BSCC steels was suggested to have resulted from a mixed population of mill-annealed and laboratory-annealed data.

2. United States tensile data showed maximum variations in the bar product and least in the tube product.

3. Compared with other countries, U.S. data showed maximum variations in both tensile and creep properties.

4. For a given country, no clear distinction could be made between the variations in tensile properties of types 304 and 316 stainless steel.

5. Variations in ultimate tensile strength were smaller than in yield strength. The ductility indices (total elongation and reduction of area) showed greater variations than did strength properties.

6. Variations in SEE in log t_r, stress exponent, and 10^4-hr creep-rupture strength and creep total elongation for the combined data on type 316 stainless steel were significantly lower than corresponding variations for type 304 stainless steel.

7. The 10^4-hr creep-rupture strength of type 316 stainless steel was indistinguishable for steels produced in the U.S. and the foreign countries investigated. Variations in creep-rupture strengths of type 304 stainless steel were too large to permit a similar conclusion.

8. Results of the analysis performed in this paper suggest that U.S. and NRIM data might be combined in future analyses, because heats used in both studies meet both chemical composition and room-temperature mechanical properties requirement. BSCC data can also possibly be used if heats showing room-temperature yield strength values below 207 MPa (30 ksi) are separated from those meeting this condition.

3.2.3 Materials Behavior in Support of Development and Evaluation of Failure Criteria for Materials

3.2.3.1 Development of Creep Equation — M. K. Booker

Design of elevated-temperature operating systems requires an accurate means of predicting the creep strain response of structural materials under the expected operating conditions. A first step in such predictions is the expression of strain as a function of time (t), stress (σ), and temperature (T) in uniaxial, constant-load (or constant-stress), isothermal laboratory tests. However, even under these simplified conditions, analysis can be complicated and difficult. In addition to the occurrence of complex interrelationships among t, σ, and T, the problem of heat-to-heat variations can often be large.[21] Also, as is usually the case with creep data, design applications generally require extrapolation of results. This report describes a promising new technique for predicting the creep strain-time behavior of types 304 and 316 austenitic stainless steel, including estimates of heat-to-heat variations. Predictions are compared with experimental data for several heats, with good results.

3.2.3.1.1 Previous Work. In the past,[40-42] the creep strain-time behavior of structural materials has been estimated as follows. First, available experimental creep curves for the material are individually fitted to some equation form for strain as a function of time, such as the recently popular rational polynomial equation.[41-43] Then, the individual equation parameters are themselves expressed as functions of stress and temperature. Although this method has met with some success, it suffers from several shortcomings, enumerated below.

1. Often, the number of available creep curves is quite small in comparison with rupture and other data.

2. Experimental variations and complex interrelationships between equation parameters can cause considerable scatter in the values of these parameters. As a result, the correlations between these parameters and the test conditions (σ, T) can be very poor. This problem becomes particularly large when extrapolation in one or more of the independent variables is necessary.

3. Separate analysis of the equation parameters as functions of stress and temperature can cause problems when the parameters are recombined into a unified equation, since they are actually interrelated.

4. It is extremely difficult to account for heat-to-heat variations with this method.

3.2.3.1.2 Alternate Method. Using a single rational polynomial creep equation, a method which largely eliminates the above objections has been developed. The creep equation is expressed as

$$e_c = \frac{Cpt}{1 + pt} + \dot{e}_m t \ , \tag{20}$$

where e_c is the creep strain, t the time, C the transient intercept strain, and $\dot{e}_m$ the minimum creep rate. The parameter p is related to the curvature of the primary portion of the curve. Figure 3.17 illustrates the properties of this equation, which are more fully discussed elsewhere.[43]

That Eq. (20) adequately describes individual strain-time curves for types 304 and 316 stainless steel is shown elsewhere.[42,43] The remaining problem is to evaluate the stress and temperature dependence of the parameters C, p, and $\dot{e}_m$. One of the advantages of the current equation form is the explicit minimum creep rate term. While fits of Eq. (20) to experimental curves will in general yield slightly different values of $\dot{e}_m$ than graphical measurements, this difference is insignificant in comparison with the overall uncertainty in creep strain-time predictions. Thus all available minimum creep rate data can be used to determine $\dot{e}_m$ as a function of stress and temperature. Many methods are available for

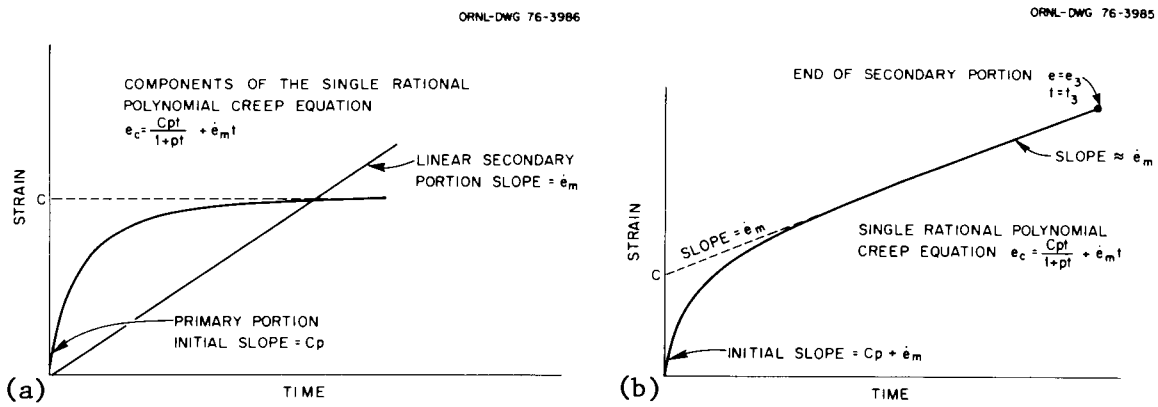

Fig. 3.17. Schematic Illustration of the Properties of the Rational Polynomial Creep Equation. (a) Primary and secondary components. (b) Combined equation.

this analysis, such as standard time-temperature parameters.[44] In some cases, $\dot{e}_m$ can be estimated as a function of rupture life.[45] At any rate, many methods for the analysis of minimum creep rate data are available, but their relative evaluation is not the purpose of this report.

From Fig. 3.17, it can easily be verified that the value of C is given by

$$C = e_3 - \dot{e}_m t_3 \ , \tag{21}$$

where e_3 and t_3 are the strain and time to the onset of tertiary creep, respectively. Methods for the calculation of e_3 and t_3 have been previously established.[30,46] Those results, as illustrated in Figs. 3.18 and 3.19, used the relationships

$$t_3 = A t_r^{\beta} \ , \tag{22}$$

and

$$\dot{e}_3 = e_3/t_3 = B\dot{e}_m^{\alpha} \ , \tag{23}$$

where A, B, α, and β are material constants. Equations (22) and (23), in turn, yield

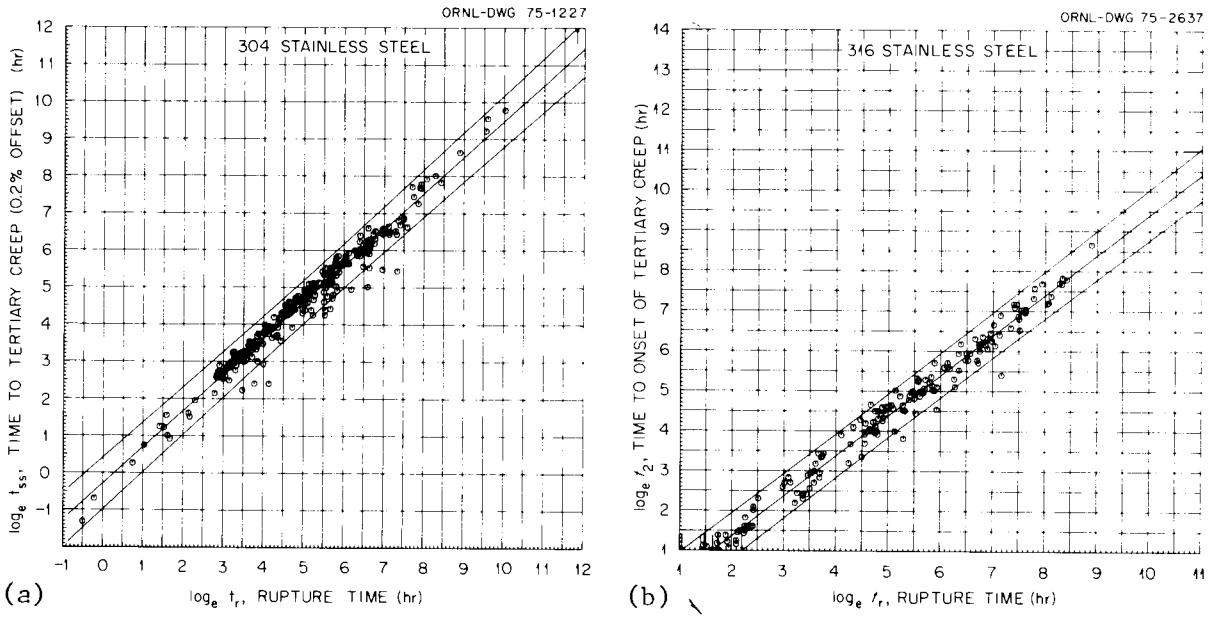

Fig. 3.18. Relationship Between Rupture Life and Time to Tertiary Creep for Annealed Stainless Steel. (a) Type 304. (b) Type 316.

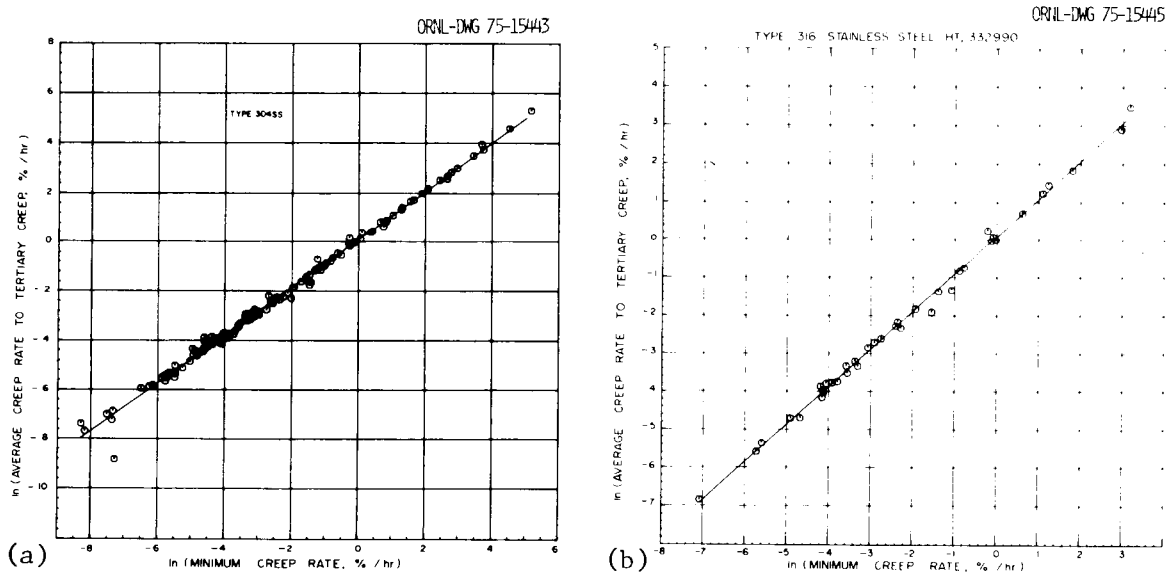

Fig. 3.19. Relationship Between Minimum Creep Rate and Average Creep Rate to Tertiary Creep for (a) Type 304 Stainless Steel and (b) Type 316 Stainless Steel Heat 332990.

$$e_3 = AB\dot{e}_m^{\alpha} t_r^{\beta} \ . \tag{24}$$

Thus, a knowledge of t_r and $\dot{e}_m$ yields e_3 and t_3, which in turn yield C.

Another approach that might be used is that suggested by Ivanova,[47] who estimated e_3 by use of the "plasticity resource," $e_s = \dot{e}_m t_r$. The results of ref. 30 indicate that, within the data scatter, e_s does provide a reasonable estimate of e_3 for the current data. Using this approach, Eq. (21) becomes

$$C = \dot{e}_m(t_r - t_3) \ . \tag{25}$$

The quantity p is perhaps the most difficult to estimate, but fortunately it is also the least important. From Eq. (20), at a time when a given fraction $F = pt/(1 + pt)$ of the total transient creep strain component, C, has been exhausted, p is given by

$$p = F/(1 - F)t \ . \tag{26}$$

On an individual curve basis, probably the best choice of F is 0.5, where $p = 1/t$. However, the sheer scatter in creep data makes this precision unnecessary and possibly meaningless. The value of p has no effect on the creep curve after the onset of secondary creep, but merely influences the curvature of the primary creep region. Certainly, this curvature can be an important factor, but data scatter probably make it impossible to predict this curvature very precisely by any method. Thus, since t_3 has already been estimated, it is felt to be sufficient to choose $t = t_3$ in Eq. (26). At t_3, F should be near unity (F will actually be unity only at $t = \infty$), and the exact value can be estimated by trial and error. Thus, the entire creep equation is determined from $\dot{e}_m$ and t_r.

3.2.3.1.3 Results. Exploratory application of the above approach has been carried out for several heats of types 304 and 316 stainless steel, which are characterized in Tables 3.7 and 3.8. The 25-mm and

Table 3.7. Compositions and Product Forms of Materials Investigated

Heat	Reference	Product Form	Content, wt %[a]										
			C	Mn	P	S	Si	Cr	Ni	Co	Mo	Cu	N
					Type 304 Stainless Steel								
9T2796	48	25.4-mm plate	0.051	1.37	0.041	a	0.4	18.5	9.87	0.1	0.3	0.24	0.031
9T2796	21	50.8-mm plate	0.047	1.22	0.029	0.012	0.47	18.5	9.58	0.05	0.10	0.10	0.031
55697	40	7-mm rod	0.052	1.1	0.011	0.01	0.52	18.92	9.52	0.035	0.12	0.10	0.052
8043813	49	25.2-mm plate	0.062	1.87	0.04	0.0043	0.48	17.8	8.95	0.20	0.32	0.20	0.033
ASTM A 240, 479	23, 25	Plate, rod	0.08[c]	2.0[c]	0.045[c]	0.03[c]	1.0[c]	17–19	8–10				
					Type 316 Stainless Steel								
332990	40	7-mm rod	0.052	1.72	0.012	0.02	0.38	17.8	13.55	0.14	2.33	0.20	0.041
Garofalo et al.	50, 51	12.7-mm bar	0.07	1.94	0.01	0.021	0.38	18.0	11.4	b	2.15	b	0.043
ASTM A 240, 479	23, 25	Plate, rod	0.08[c]	2.0[c]	0.045[c]	0.03[c]	1.0[c]	16–18	10–14		2–3		

[a]All analyses include balance iron.

[b]Not reported.

[c]Maximum allowed.

Table 3.8. Heat Treatments and Specimen Gage Lengths of Materials Studied

Heat, Description	Initial Gage Length (mm)	Treatment	Time (hr)	Temperature (°C)	Cooling Method
		Type 304 Stainless Steel			
9T2796, 25-mm plate	57.2[a]	Anneal	0.5	1093	Air cool
9T2796, 51-mm plate	57.2	Anneal	0.5	1093	Air cool
8043813	57.2[a]	Anneal	0.5	1065	Air cool
55697	31.8	Anneal	1.0	1066	Rapid air cool
		Type 316 Stainless Steel			
332990	31.8	Anneal	1.0	1066	Rapid air cool
Garofalo et al.	38.1	Anneal	0.5	1093	Water quench

[a]Some high-stress and/or low-temperature tests were run on 31.8-mm-gage-length specimens.

51-mm plates of heat 9T2796 of type 304 stainless steel were analyzed separately since they appeared to exhibit slightly different properties. Of the heats used, 9T2796 and 55697 of type 304 are relatively weak, while 8043813 is an unusually strong heat. The type 316 stainless steel data of Garofalo et al.[50,51] are for a weak heat, while heat 332990 is of approximately average strength for this material.

In the current analysis, rupture life data for individual heats of material were first analyzed using a form of the Orr-Sherby-Dorn time-temperature parameter,[52]

$$\log t_r = \alpha_0 + \alpha_1\sigma + \alpha_2 \log \sigma + \alpha_3/T \ . \tag{27}$$

Least squares best fits of the constants α_0 through α_3 are given in Table 3.9, where the values of RMS indicate that Eq. (27) provides excellent fits to the data, as shown in Fig. 3.20.

Next, $\dot{e}_m$ was expressed as a function of t_r in hours by use of a temperature-modified form[30] of the Monkman-Grant relationship[45]

Table 3.9. Results of Rupture Life Correlations[a]

Data Set	Constants of Eq. (27)				RMS	Number of Points
	α_0	α_1	α_2	α_3		
		Type 304 Stainless Steel				
Heat 55697	2.037	-6.222×10^{-5}	−3.987	1.722×10^4	0.021	45
Heat 9T2796, 25-mm plate	3.626	-5.718×10^{-5}	−4.822	1.874×10^4	0.015	58
Heat 9T2796, 51-mm plate	3.066	-5.393×10^{-5}	−4.966	1.962×10^4	0.014	20
Heat 8043813	−5.312	-1.067×10^{-4}	−4.233	2.667×10^4	0.023	24
		Type 316 Stainless Steel				
Garofalo et al.	−3.488	-1.018×10^{-4}	−2.813	1.895×10^4	0.018	132
Heat 332990	6.123	-4.248×10^{-5}	−5.414	1.962×10^4	0.027	39

[a]Constants of $\log t_r = \alpha_0 + \alpha_1\sigma + \alpha_2 \log \sigma + \alpha_3/T$, where σ is stress in psi (1 psi = 6.895 kPa) and T is the temperature in Kelvins.

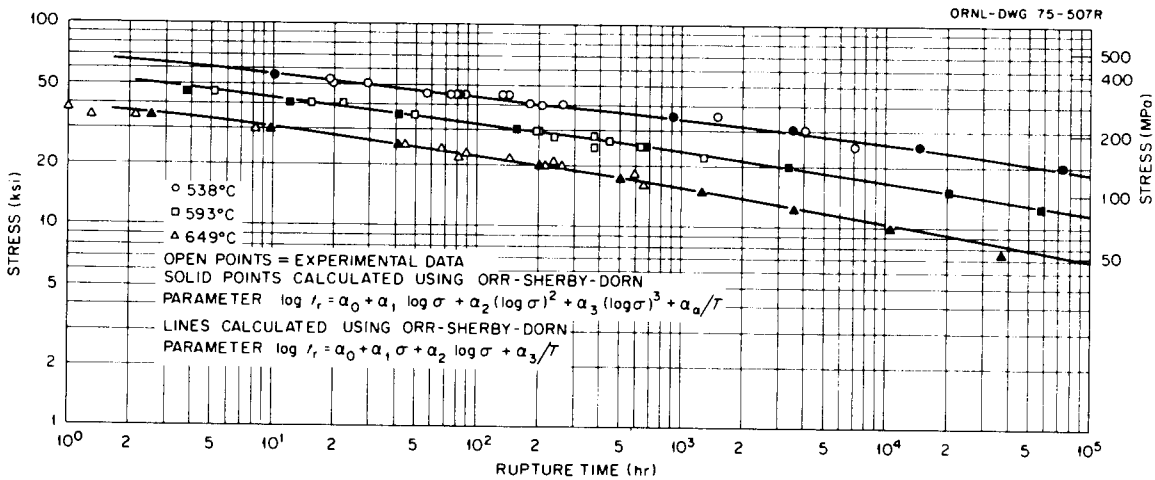

Fig. 3.20. Comparison of Predicted Rupture Life Values with Experimental Data for Heat 55697 of Type 304 Stainless Steel.

$$\dot{e}_m = F_0\, e^{-Q/RT}\, t_r^{-\lambda_0} \ \%/\text{hr} \ , \tag{28}$$

where T is the Kelvin temperature, R is the gas constant 8.31 J mole^{-1} K^{-1}, and F_0, Q, and λ_0 are given in Table 3.10. Again, the tabulated values of R^2 indicate a good description of the experimental data (see Figs. 3.21 and 3.22).

Table 3.10. Results of Correlation Among Minimum Creep Rate, Rupture Life, and Temperature[a]

Data Set	Temperature Range	Number of Points	F_0	Q	λ_0	RMS[b]	R^2[c]
Type 304 Stainless Steel	482–816	144	56,552	60,768	1.133	0.0424	97.3
Type 316 Stainless Steel	538–760	159	15,999	54,384	1.020	0.0344	97.0

[a]Minimum creep rate, $\dot{e}_m$ (%/hr), has been expressed as a function of rupture life in hours, t_r, and temperature (K), T, by $\dot{e}_m = F_0 e^{-Q/RT}$, where R is the gas constant, 8.31 J mole^{-1} K^{-1}.

[b]RMS is expressed in terms of log ($\dot{e}_m$)

[c]Coefficient of determination.

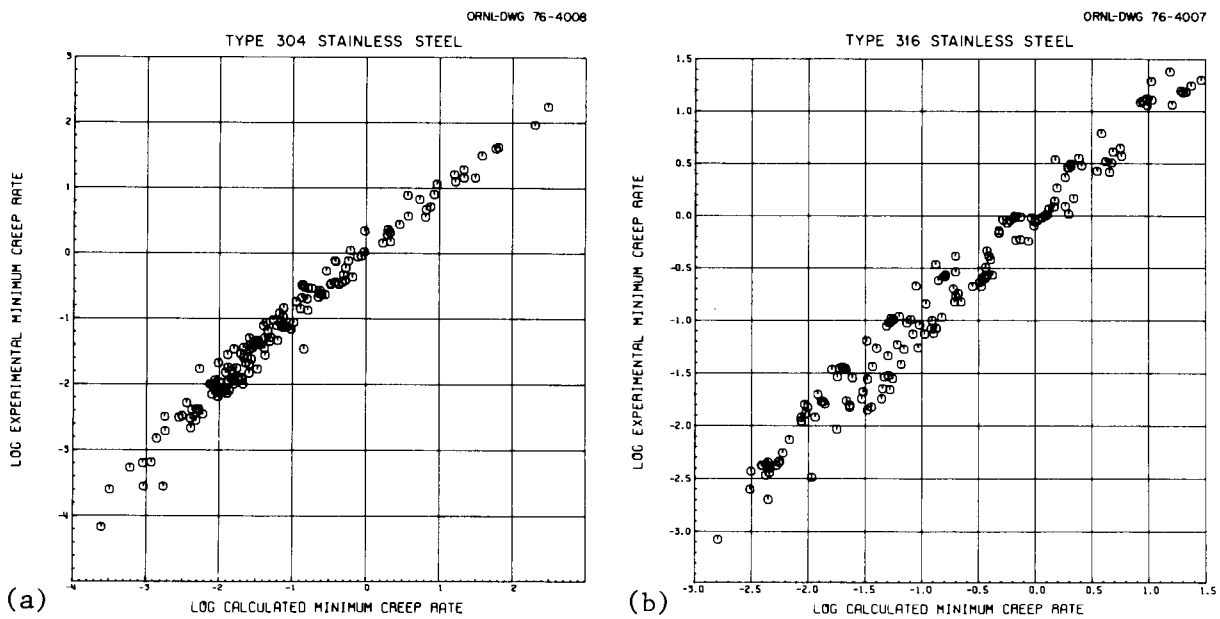

Fig. 3.21. Comparison Between Experimental and Predicted Values of Minimum Creep Rate, Where $\dot{e}_m$(Predicted) = $F_2 e^{-Q/RT}\ t_r^{-\lambda_0}$. (a) Type 304 stainless steel. (b) Type 316 stainless steel.

Having thus established t_r and, indirectly, $\dot{e}_m$ as functions of stress and temperature, we then applied Eqs. (22) and (23) with the resulting values of A, B, α, and β given in Tables 3.11 and 3.12. Fits to data were again quite good. It should be noted, however, that for heats 9T2796 and 8043813 of type 304 stainless steel, onset of tertiary creep

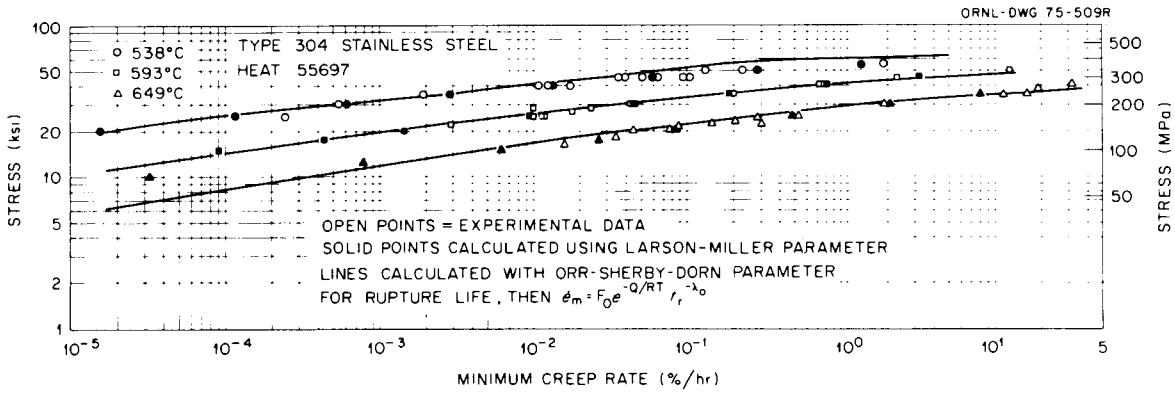

Fig. 3.22. Comparison of Predicted Minimum Creep Rate Values with Experimental Data for Heat 55697 of Type 304 Stainless Steel.

Table 3.11. Results of Correlation Between Rupture Life and Time to Tertiary Creep[a]

Data Set	Number of Points	A	β	RMS[b]	R^2[c]	Temperature Range of Data (°C)
Type 304 Stainless, t_{ss}	277	0.752	0.977	0.090	96.6	482–816
Type 316 Stainless, t_2	183	0.526	1.004	0.071	93.5	538–816

[a]Time to tertiary creep, t_3, and rupture life, t_r, have been related by $t_3 = At_r^{\beta}$; t_3 may be t_{ss} (0.2% offset time to tertiary creep) or t_2 (time to first deviation from linear secondary creep).

[b]RMS = $\Sigma Y^2/(n - \nu)$ where n = number of data points and ν = number of coefficients in the model (here $\nu = 2$); ΣY^2 is the sum of squared residuals: $\Sigma Y^2 = \Sigma(\ln t_{3_{pred}} - \ln t_{3_{exp}})^2$.

[c]R^2 = coefficient of determination; R^2 describes how well a regression model describes variations in the data. $R^2 = 100$ signifies complete description, $R^2 = 0.0$ signifies no description. $\sqrt{R^2/100} = r$, the linear correlation coefficient.

was defined by a 0.2% strain offset from the linear secondary creep line. This use causes no special difficulties, except that e_3 in Eq. (21) is replaced by $e_3 - 0.2$. Also, because of constraints of data availability, Eq. (23) for type 316 stainless steel can be used for heat 332990 only since the e_3 values reported by Garofalo et al.[50] refer to total strain, not merely creep strain. Figs. 3.18 and 3.19 illustrate these results.

Finally, a simple trial and error approach showed that F from Eq. (25) was approximately 0.98 for both steels examined at $t = t_3$.

Table 3.12. Results of Correlation Between Minimum Creep Rate and Average Creep Rate to Tertiary Creep[a]

Data Set	Number of Points	B	α	RMS[b]	R^2[c]	Temperature Range of Data (°C)
304 Stainless	138	1.110	0.974	0.050	99.3	482–816
316 Stainless G[d]	120	1.602	0.995	0.269	95.6	593–816
316 Stainless H[e]	38	1.092	0.991	0.0235	99.6	538–760

[a]Minimum creep rate, $\dot{e}_m$, and average creep rate to tertiary creep, $\dot{e}_3$, have been related by $\dot{e}_3 = B\dot{e}_m^{\alpha}$.

[b]RMS = $\Sigma Y^2/(n - \nu)$, where n = number of data points and ν = number of coefficients in the model (here $\nu = 2$); ΣY^2 = sum of squared residuals, $\Sigma Y^2 = \Sigma(\ln \dot{e}_{3pred} - \ln \dot{e}_{3exp})^2$ where $\ln \dot{e}_{3pred}$ = ln [predicted rate (%/hr)] and $\ln \dot{e}_{3exp}$ = ln [experimentally observed rate (%/hr)].

[c]R^2 = coefficient of determination; R^2 describes how well a regression model describes variations in the data. $R^2 = 100$ signifies complete description, $R^2 = 0.0$ signifies no description. $\sqrt{R^2/100} = r$, the linear correlation coefficient.

[d]Data for total strain, from Ref. 50.

[e]Data for creep strain only, from Ref. 40.

This value of F implies that p is given by

$$p = 49/t_3 \ , \tag{29}$$

where t_3 is given by Eq. (22). It might be noted that Eq. (20) with the above defined parameters would be slightly more accurate if the primary term $Cpt/(1 + pt)$ were multiplied by $1/F$. However, F is so near unity that this correction was ignored as insignificant.

Figures 3.23 and 3.24 show isochronous stress creep-strain curves constructed from the above equations. Note the prediction of heat-to-heat variations. Most importantly, the results provided excellent fits to experimental creep data, as illustrated in Figs. 3.25 and 3.26. The predictions for heat 9T2796 51-mm plate of type 304 stainless steel in Fig. 3.25 appear slightly overconservative. However, most of these data are from long-term creep tests, which have yet to rupture. Thus,

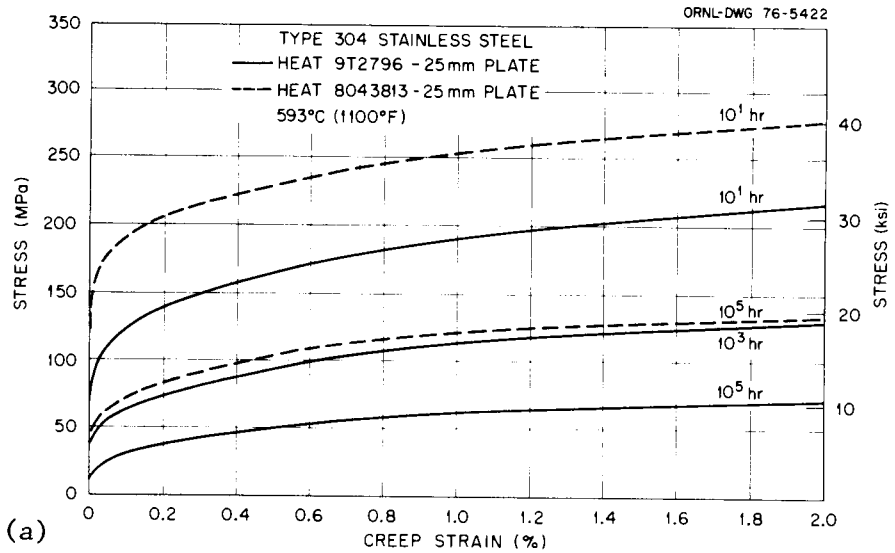

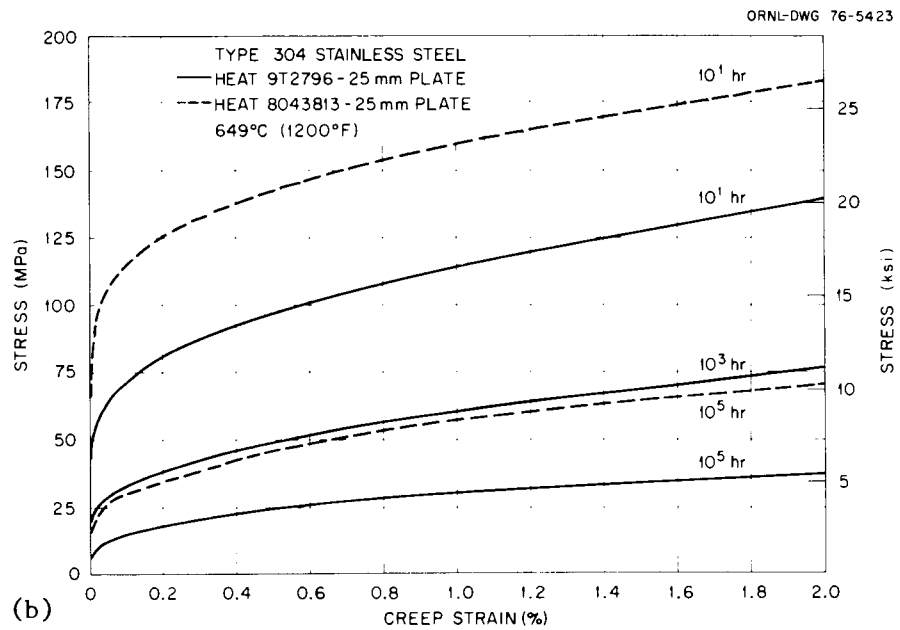

Fig. 3.23. Predicted Isochronous Stress Strain Curves for 2 Heats of Type 304 Stainless Steel. (a) 593°C. (b) 649°C.

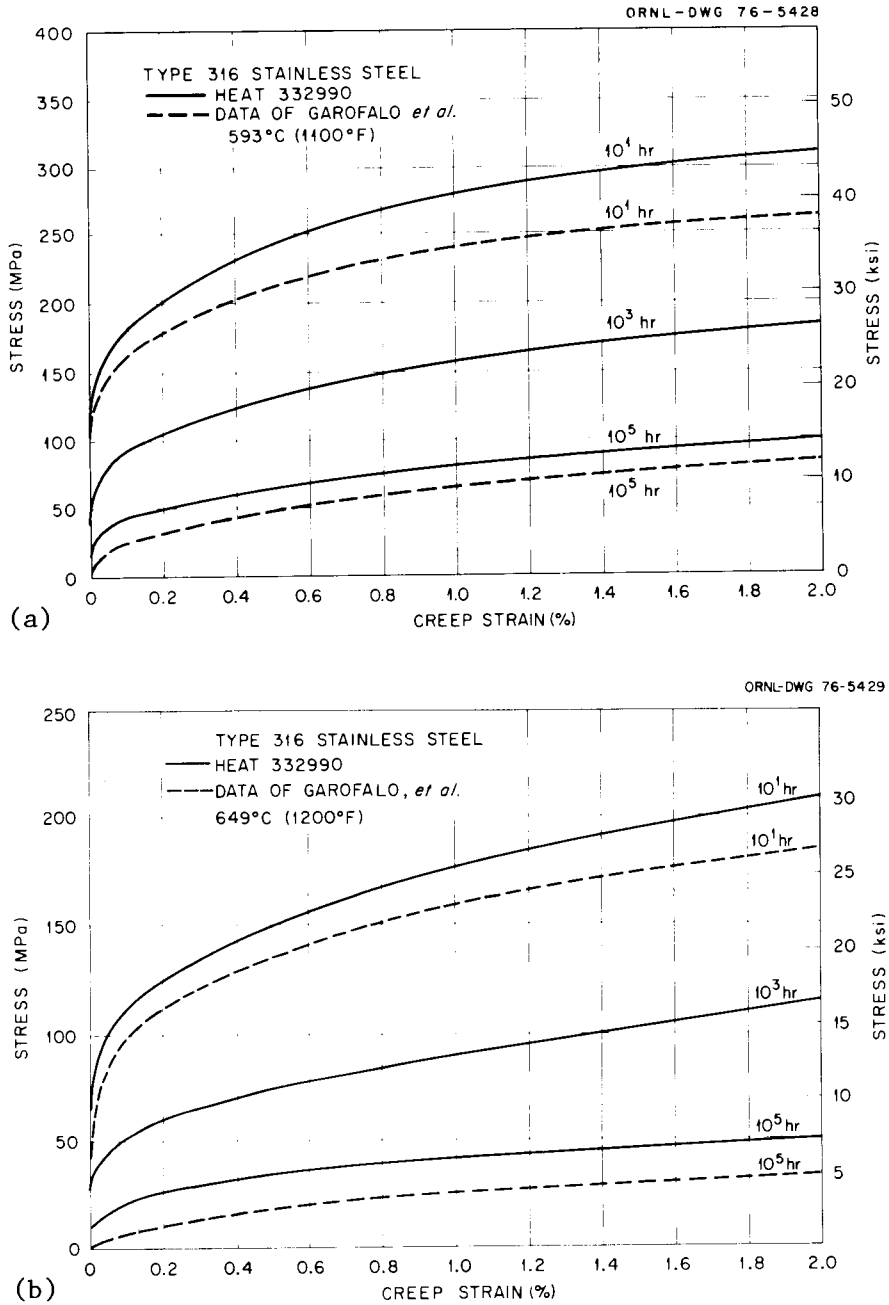

Fig. 3.24. Predicted Isochronous Stress Strain Curves for 2 Heats of Type 316 Stainless Steel. (a) 593°C. (b) 649°C.

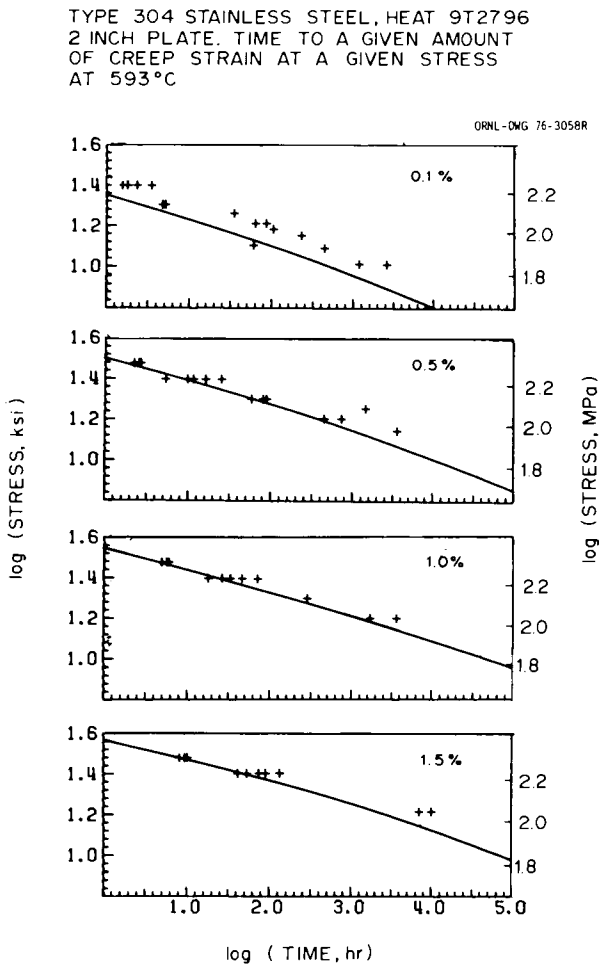

Fig. 3.25. Comparison of Predicted Creep Strength Values with Experimental Data for Type 304 Stainless Steel at 593°C.

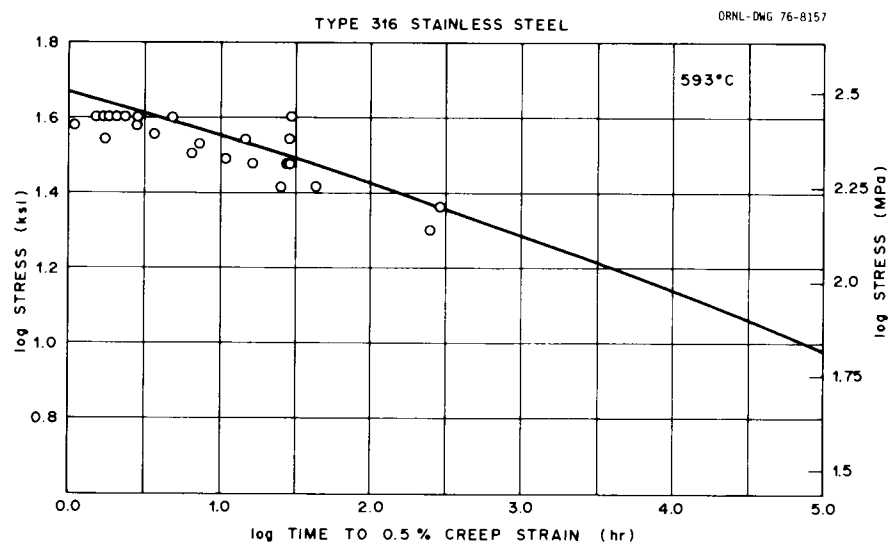

Fig. 3.26. Comparison of Predicted Creep Strength Values with Experimental Data for Type 316 Stainless Steel at 593°C.

most of the data shown in Fig. 3.25 were not used in making the predictions shown. Considering this fact, the predictions are more than satisfactory.

3.2.3.1.4 Discussion. The empirical method described above greatly alleviates the four problems discussed earlier in connection with previous methods for predicting creep strain response. The ways in which each of these problems is overcome are discussed below in turn.

First, the method relies heavily on rupture life and minimum creep rate data, which are the most widely available of all creep data. However, one still clearly needs experimental curves. First, the application of Eqs. (22) through (24) requires the existence of data for e_3 and t_3, which are largely unavailable except through actual curves. Second, unless one has actual experimental curves for comparison, there is no way of verifying the prediction method. Still, the method does not rely wholly on complete experimental curves as sources of information. Moreover, as will be shown below, the current method inherently requires fewer data to establish accurate predictions than did previous methods.

Objection (2) above is clearly avoided, as shown by the high degree of correlation involved in the various steps of the current analysis (Tables 3.9—3.11). The first step here is to evaluate rupture data, and much study has gone into such evaluations, such as the use of time-temperature parameters,[44] the minimum commitment method,[53] or generalized algebraic models.[54] In any case, such data can usually be analyzed successfully, especially for reasonably stable materials such as those used here. The problem of extrapolation is more difficult, but the extrapolation of rupture data is probably the best understood of all extrapolations of time-dependent behavior.

Minimum creep rate is predicted here from rupture life only for demonstration. Certainly, the minimum creep rate data themselves may be analyzed by methods similar to those used for rupture life. In fact, such analyses for the same data used here have been reported elsewhere with good results.[55] The Monkman-Grant type relation does, however, fit

the data well and, in fact, yields similar results to direct analysis, as shown in Fig. 3.21. Direct extrapolation of minimum creep rate data is similar to extrapolation of rupture data. Extrapolation of the Monkman-Grant relationship is straightforward since it involves a linear relationship between log t_r and log $\dot{e}_m$. The excellent fit of the equation over a wide range of times and rates indicates that such extrapolation on a limited basis is justified (say to at least $t_r = 10^5$ hr). However, extrapolation of $\dot{e}_m$ by this method does involve a double extrapolation and should be done carefully. Still, such extrapolations probably suffer less risk of misrepresenting material behavior than extrapolations of best fit values from individual curves. Such best fit values are likely to be less numerous than the total amount of minimum creep rate data available, and are likely to show more scatter in stress and temperature. (See Refs. 40—42).

Prediction of parameters other than $\dot{e}_m$ using individual best fit values can be even more difficult. Equations (22) and (23) of the current method are simple and easy to apply. Moreover, being inherently normalization-type procedures, these equations describe the data quite well, independently of heat-to-heat, experimental, and other variations. Again, they involve linear log-log relationships, which fit a wide range of data and thus are probably safely extrapolable at least on a limited basis. Moreover, the very simplicity of Eqs. (22) and (23) means that fewer data are required to establish them. Clearly, use of Eq. (25) requires even fewer data.

Using Eq. (29) for p is clearly a simplification. However, we feel that this equation predicts p at least as accurately as does direct analysis and is much simpler. Unfortunately, a precise knowledge of the value of p at a given stress and temperature is not possible. Thus, the most practical approach is to obtain the simplest approximation to its value. Note that Eq. (22) allows expression of p directly as a function of t_r.

The very nature of the current method involves interrelationships among the different parameters. For instance, in the current analysis, both $\dot{e}_m$ and p are calculated from the predicted value of t_r. Equation (21) then utilizes the value of $\dot{e}_m$ to calculate C. Therefore, objection 3 in Sect. 3.2.3.1.1 is avoided.

One of the most promising aspects of the current approach is that it allows some measure of heat-to-heat variation to be built into the creep equation, thus alleviating objection 4 above. Since Eqs. (22) through (24) and (29) are relatively independent of such variations, the problem is reduced to heat-to-heat variations in t_r and $\dot{e}_m$. In fact, if Eq. (28) is independent of heat-to-heat variations, then one need only consider variations in t_r. Thus, one can obtain a good idea of variations in creep strain response in many cases by analyzing individual heat t_r and $\dot{e}_m$ data for weak, medium, and strong heats to gage the magnitude of possible strength effects. Alternatively, t_r and $\dot{e}_m$ can be directly expressed as functions of σ, T, and relative heat strength by use of some parameter such as ultimate tensile strength (UTS). Successful correlations of this type have been recently reported.[39,54] However, it should be noted that the indications of Ref. 54 are that for type 316 stainless steel $\dot{e}_m$ depends more strongly upon UTS than does t_r. If this is the case, then Eq. (28) may be a function of UTS. Unfortunately, the present data do not allow a quantitative analysis of this effect, since the data for Garofalo et al. and for heat 332990 were generally taken at different temperatures. [Only 593°C (1100°F) is a common temperature.] Thus, it is difficult to separate the effects of temperature and heat-to-heat variations.

At the very least, average t_r values can be used in conjunction with the current methods to calculate creep behavior, and minimum t_r values can be used in calculating the creep strain response of minimum strength material. Even this capability somewhat surpasses that of previous methods.

3.2.3.1.5 Summary. A method has been presented through which rupture life and minimum creep rate data can be used to predict creep strain as a function of stress, temperature, and time in uniaxial, constant-load, isothermal creep tests. In addition, the method contains capabilities for predicting the magnitude of heat-to-heat variations. Application of the method to several heats of types 304 and 316 stainless steel has yielded good results. It must be remembered that the relationships used are totally empirical and are not claimed to have fundamental

significance. As such, the current method cannot be expanded to other materials without verification. However, all evidence currently available shows that this method represents a promising new analytical technique. Effects of extrapolation to very low stress-temperature combinations (corresponding to $t_r > 10^6$ hr) need to be investigated.

3.2.3.2 Creep Evaluation for Type 316 Stainless Steel — W. E. Stillman*

3.2.3.2.1 Equation Form Selection. Various equation forms were used to fit, by a nonlinear least squares procedure, creep-time experimental data for type 316 stainless steel. They are single and double exponential and single and double rational polynomial equations, as follows:

$$\varepsilon_c = \varepsilon_t(1 - e^{-rt}) + \dot{\varepsilon}_m t \ , \tag{30}$$

$$\varepsilon_c = \varepsilon_t(1 - e^{-rt}) + \varepsilon_x(1 - e^{-st}) + \dot{\varepsilon}_m t \ , \tag{31}$$

$$\varepsilon_c = \frac{at}{1 + bt} + ct \ , \tag{32}$$

$$\varepsilon_c = \frac{at}{1 + bt} + \frac{ct}{1 + dt} + et \ . \tag{33}$$

The data base consisted of the following numbers of tests: Hanford Engineering Development Laboratory (HEDL), 38; Oak Ridge National Laboratory (ORNL), 18; Babcock and Wilcox (B&W), 44; total, 100.

Single primary term equations [both rational polynomial Eq. (32) and exponential, Eq. (30)] were obtained for the tests denoted above. Four of the ORNL tests were discarded as being derived from material far stronger than standard specification type 316 stainless steel. Further efforts were made to fit two-primary-term equations [Eqs. (31) and (33)] to the data. These were much less successful, yielding results only for tests as follows: 10 HEDL, 7 ORNL, and 17 B&W, total 34. It

*Consultant from the University of Tennessee.

is quite significant that less than half the tests were amenable to double-term equation fitting. The suggestion appears reasonable that, in general, the data do not exhibit a pattern that is conductive to a two-term fit.

Average rms errors resulting from the curve-fitting exercise are shown in Table 3.13. Cases 2 and 4 refer to exact fits to exponential-form equations. This is a consequence of the fact that the HEDL strain-time data were generated from the parameters listed by Blackburn,[40] thus giving exact fits to the appropriate exponential equation in each case. Note also the zero error for the fourth equation in case 5, the expected result. All four equation forms can best be compared by referring to case 4. Here it is seen that the best fit is obtained by the fourth equation form. However, the first equation form is much superior to the second form and not unacceptably worse (an opinion, of course) than the fourth form. When all the data are evaluated it is seen that the single rational polynomial form consistently excels the corresponding exponential form.

Table 3.13. Average rms Error Comparison for Different Creep Equation Formulation

Case	rms Error for Each Equation				Number of Fits	
	Single Rational[a]	Single Exponential[b]	Double Rational[c]	Double Exponential[d]	Single Forms	Double Forms
1. All tests	0.165064	0.177604	0.029997	0.025228	100	34
2. All tests less exact single exponential fits	0.199779	0.218590	0.029997	0.025228	82	34
3. All test yielding four equations	0.064456	0.121721	0.029997	0.025228	34	34
4. Case 3 less exact double exponential fits	0.057237	0.087569	0.04044	0.035731	24	
5. HEDL only	0.03239	0.06088	0.04933	0	38	10
6. ORNL only	0.052142	0.052879	0.026811	0.022842	14	7
7. B&W only	0.328121	0.33073	0.046052	0.04105	44	17

[a] $\varepsilon_c = \frac{at}{1 + bt} + ct$.

[b] $\varepsilon_c = \varepsilon_t(1 - e^{-rt}) + \dot{\varepsilon}_m t$.

[c] $\varepsilon_c = \frac{at}{1 + bt} + \frac{ct}{1 + dt} + et$.

[d] $\varepsilon_c = \varepsilon_t(1 - e^{-rt}) + \varepsilon_x(1 - e^{-st}) + \dot{\varepsilon}_m t$.

Typical comparisons are illustrated in Figs. 3.27 through 3.31. The parameters for each equation are listed in Table 3.14. Note that only Fig. 3.30 indicates any significant difference between equation forms. We conclude that Eq. (32) (single rational polynomial) is the appropriate form to use for creep-time response up to the beginning of the tertiary creep stage.

3.2.3.2.2 Curve Parameter Fit. The Eq. (32) parameters a, b, and c, having been computed for each of the above-mentioned 96 tests, are in turn subjected to least squares curve fitting procedures. Each of the three parameters is defined by equations as applied to three different sets of data. The results are for:

1. HEDL data only.

$$\ln a = 35.154 - 45{,}677/T + 0.7366\sigma - 0.00847\sigma^2$$

$$\ln b = 35.088 - 45{,}683/T + 0.7355\sigma - 0.00868\sigma^2 \qquad (34)$$

$$\ln c = 45.105 - 59{,}365/T + 0.2562\sigma + 2.832 \ln \sigma$$

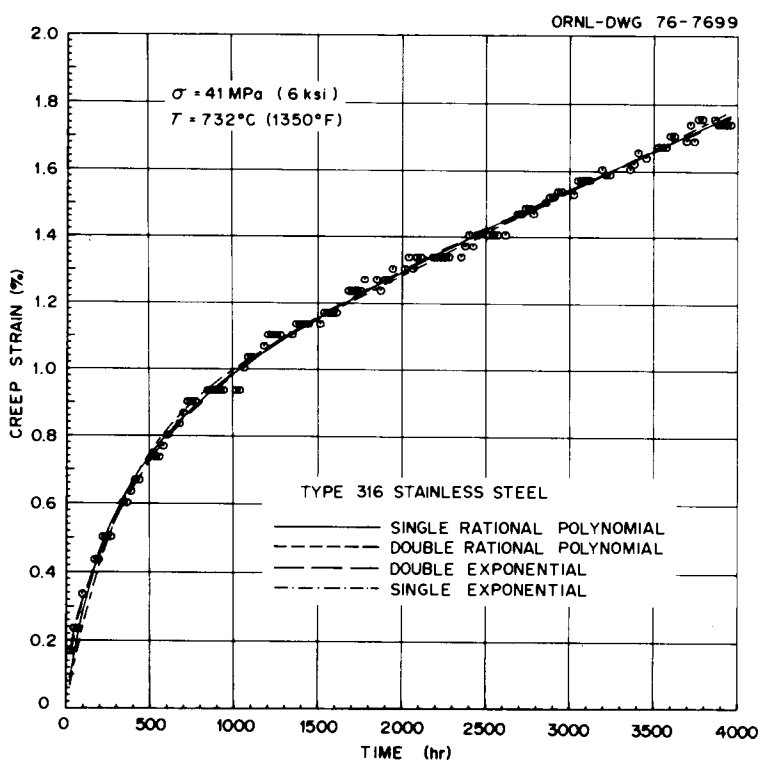

Fig. 3.27. Fit of Four Equation Corms to Creep at 732°C (1350°F), and 41 MPa (6 ksi).

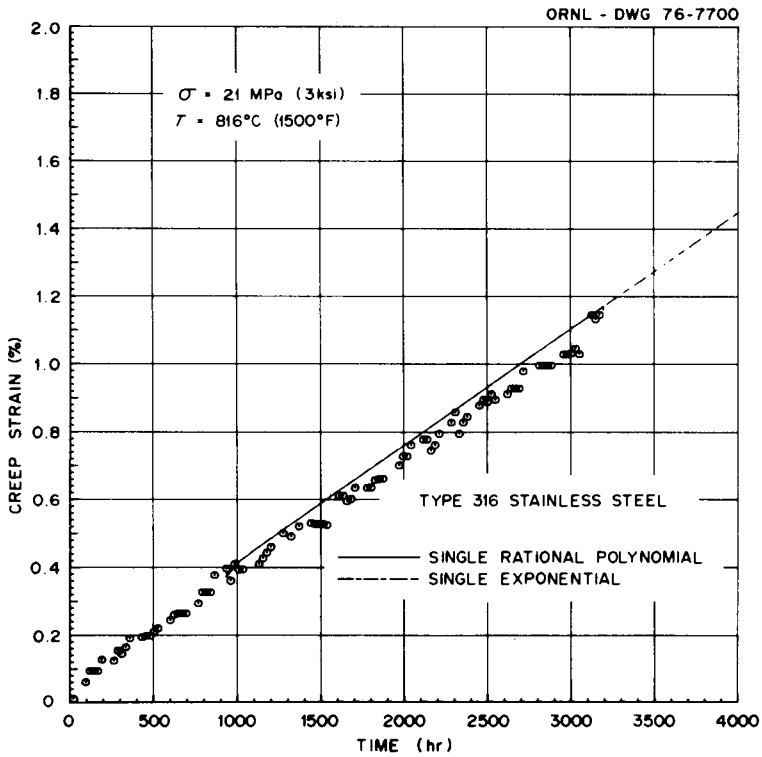

Fig. 3.28. Fit of Two Equation Forms to Creep at 816°C (1500°F) and 21 MPa (3 ksi).

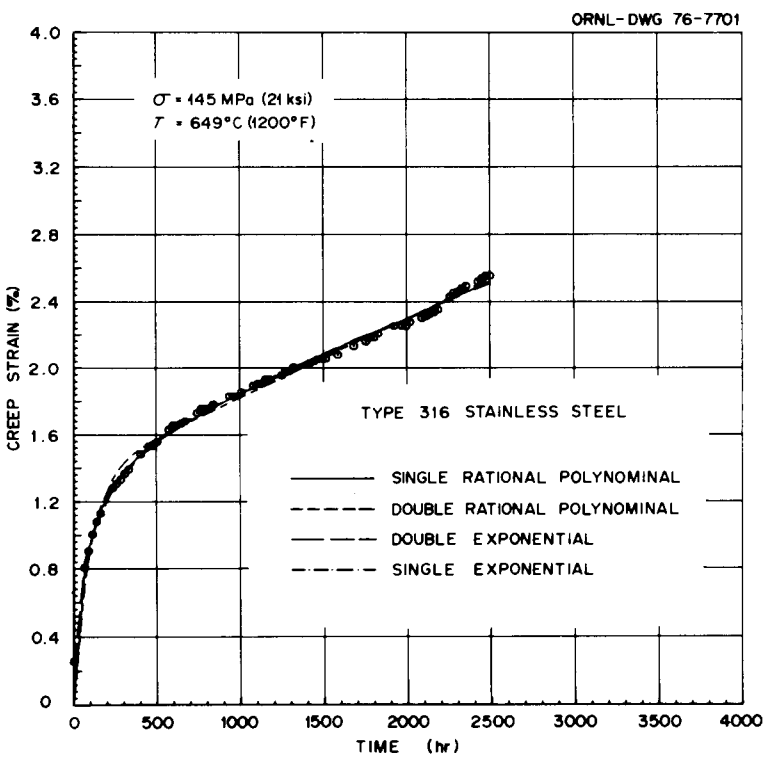

Fig. 3.29. Fit of Four Equation Forms to Creep at 649°C (1200°F) and 145 MPa (21 ksi).

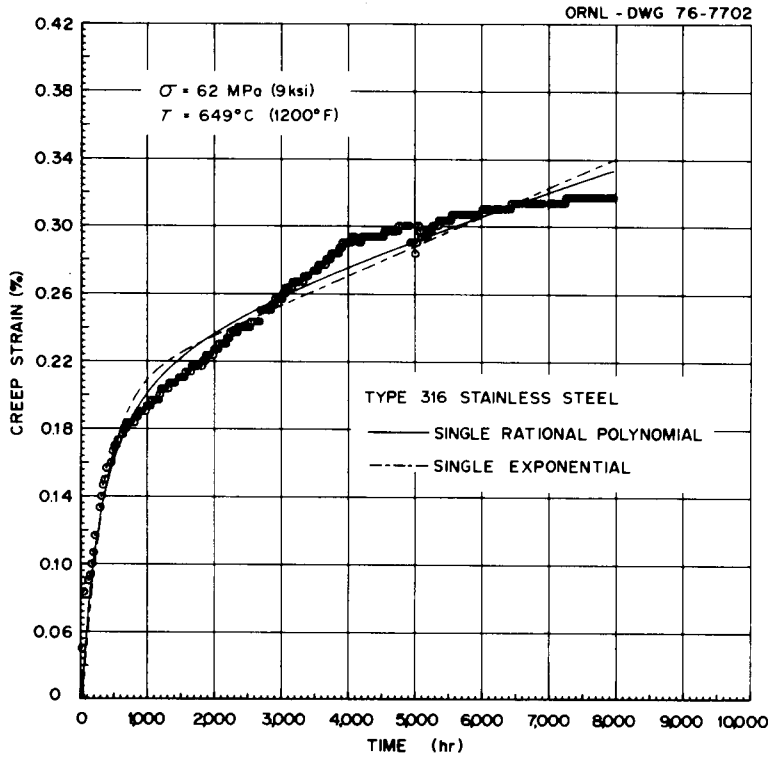

Fig. 3.30. Fit of Two Equation Forms to Creep Data at 649°C (1200°F) and 62 MPa (9 ksi).

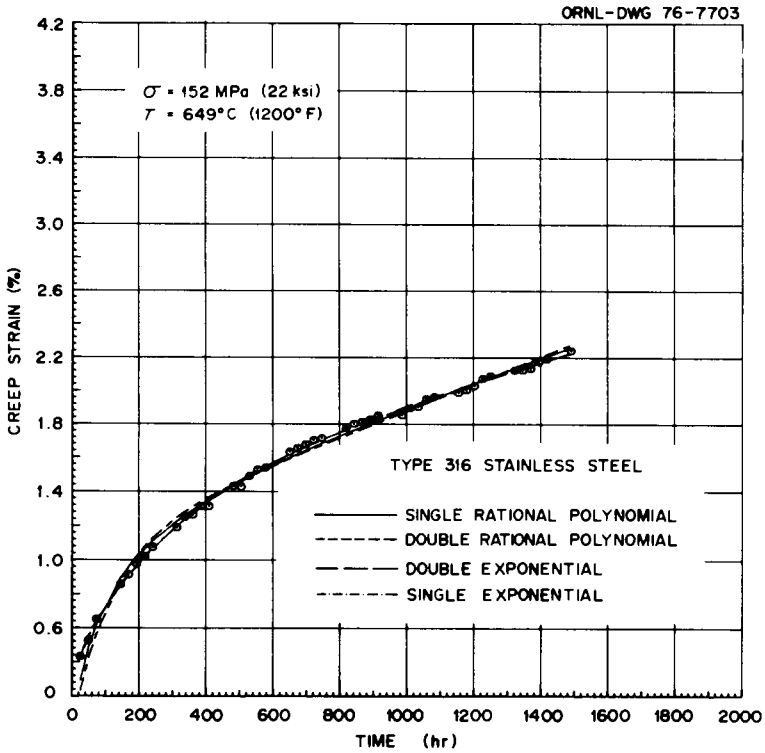

Fig. 3.31. Fit of Four Equation Forms to Creep at 649°C (1200°F) and 152 MPa (22 ksi).

Table 3.14. Equation Parameters for Examples Plotted

Parameter	Value for Curve Plotted in Each Figure				
	3.27	3.28	3.29	3.30	3.31
			Single Rational		
a	0.00361	0.002527	0.02282	0.000899	0.0137
b	0.003678	0.06340	0.01498	0.003768	0.01031
c	0.00021215	0.0003425	0.0004122	0.0000128	0.000676
			Single Exponential		
ε_t	0.77617	0.03906	1.34	0.2008	1.0636
r	0.003273	0.02095	0.0102	0.00313	0.008715
$\dot{\varepsilon}_m$	0.000252	0.0003427	0.0004798	0.0000174	0.000813
			Double Rational		
a	0.01		0.09934		0.0685
b	0.06546		0.20415		0.1743
c	0.00203		0.008032		0.00395
d	0.002194		0.007255		0.00254
e	0.0001943		0.000389		0.000413
			Double Exponential		
ε_t	0.1667		0.5533		0.37016
r	0.05237		0.20416		0.0734
ε_x	0.6571		0.84172		0.9207
s	0.002223		0.005368		0.003508
$\dot{\varepsilon}_m$	0.0002369		0.0004507		0.0006168

2. B&W data only.

$$\ln a = 10.114 - 17{,}359/T + 0.2573\sigma - 0.002305\sigma^2$$

$$\ln b = 6.07 - 10{,}761/T + 0.0483\sigma + 0.000865\sigma^2 \qquad (35)$$

$$\ln c = 32.02 - 45{,}995/T + 0.1614\sigma + 2.245 \ln \sigma$$

3. HEDL, B&W, and ORNL data.

$$\ln a = 31.11 - 39{,}761/T + 0.50708\sigma - 0.004618\sigma^2$$

$$\ln b = 31.00 - 37{,}396/T + 0.33064\sigma - 0.001885\sigma^2 \qquad (36)$$

$$\ln c = 43.69 - 59{,}108/T + 0.2943\sigma + 2.596 \ln \sigma$$

where

T = Kelvin temperature,

σ = stress, ksi (1 ksi = 6.89 MPa).

The range of ORNL data is considered to be too restricted to be of value when considered alone.

Now the three equation systems are compared with experimental data from Refs. 8 and 40. Figure 3.32 shows such a comparison for minimum creep rate at four temperatures. Note that the HEDL-based curves give the best fit to HEDL data (certainly no surprise). The B&W-based curves indicate the material to be, by comparison, stronger at high stresses, weaker at low stresses. The curves using all three data sets show the material to be consistently stronger in these cases than do the HEDL-based curves. In addition, these curves (combined data base) appear to give the best overall fit.

As a further exercise the three derived equations, together with the *Nuclear Systems Materials Handbook* (NSMH) equation,[56] are compared in Figs. 3.33 and 3.34 with experimental strain-time data obtained from the ORNL reference heat. These test results were not contained in the data base used to obtain the equations. Here the NSMH equation fits somewhat the best in Fig. 33(a), (b), and (c) [if one excepts the HEDL-only curve in Fig. 3.33(b)]. These cases are all at relatively high stresses and at even 55°C (100°F) temperature increments, exactly corresponding to the original HEDL data base, which underlies the NSMH equation. It is argued, however, that the equation based on all data gives acceptable fits in Fig. 3.33(a) and (b), though not in (c), which indicates a very high-strain response.

In Figs. 3.33(d) and 3.34(a) the combined data base equation gives a somewhat superior fit for two tests at low stress. Figure 3.34(b) shows the marked improvement given by the new equation for a test at 566°C (1050°F).

Finally, consider plots of parameter isotherms compared with experimental data in Figs. 3.35 through 3.37. These contours appear to be reasonably well behaved. The minimum creep rate, $\dot{\epsilon}$, extrapolated to

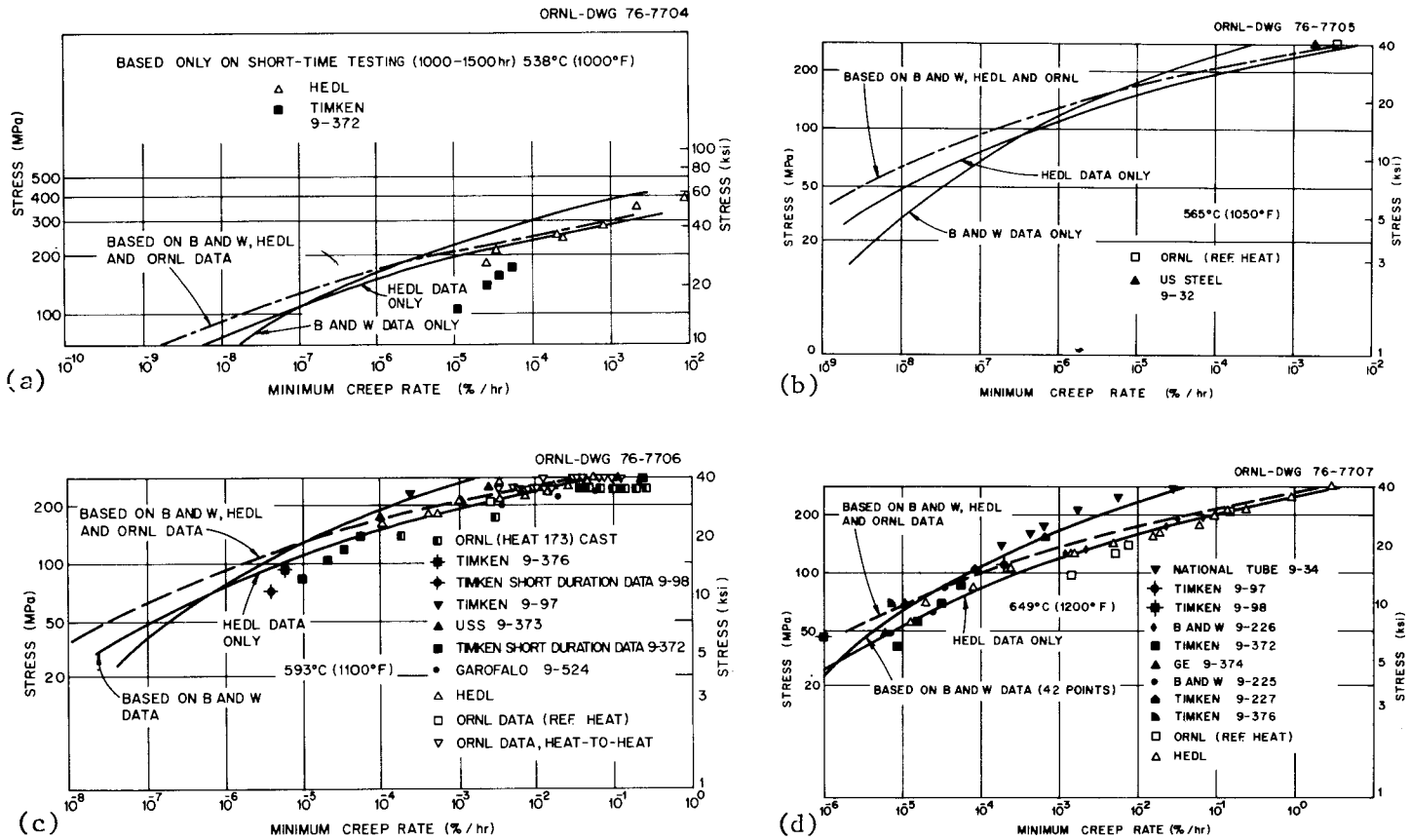

Fig. 3.32. Stress as a Function of Minimum Creep Rate: Comparisons of Curves Fitted in Three Data Sets with Experimental Data, at Four Temperatures. (a) 538°C (1000°F). (b) 565°C (1050°F). (c) 593°C (1150°F). (d) 649°C (1200°F).

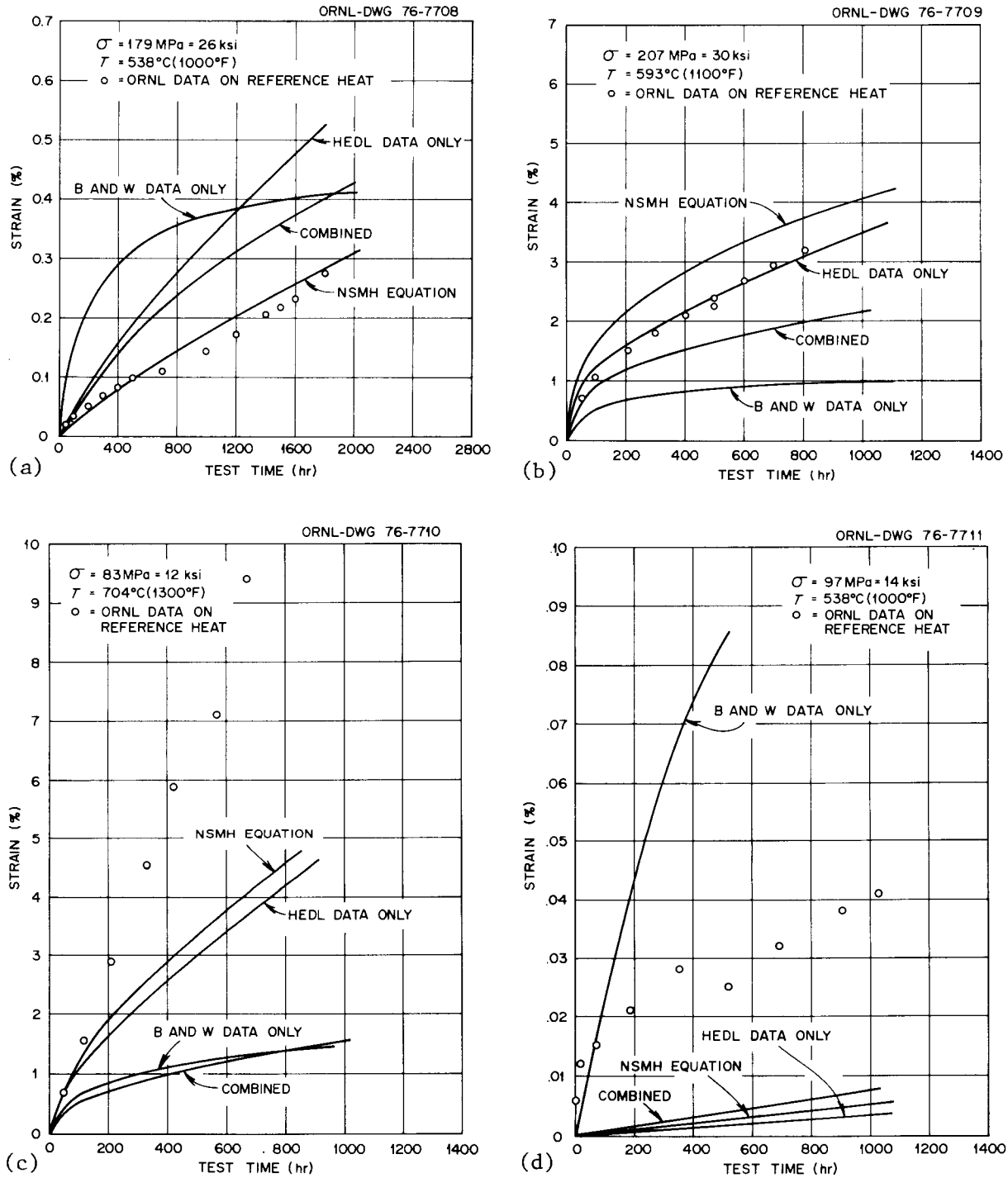

Fig. 3.33. Comparison of ORNL Reference Heat Data Under Four Sets of Conditions with Creep Curves Calculated by the Single Rational Polynomial Equation Based on Three Data Sets and with the NSMH Equation.

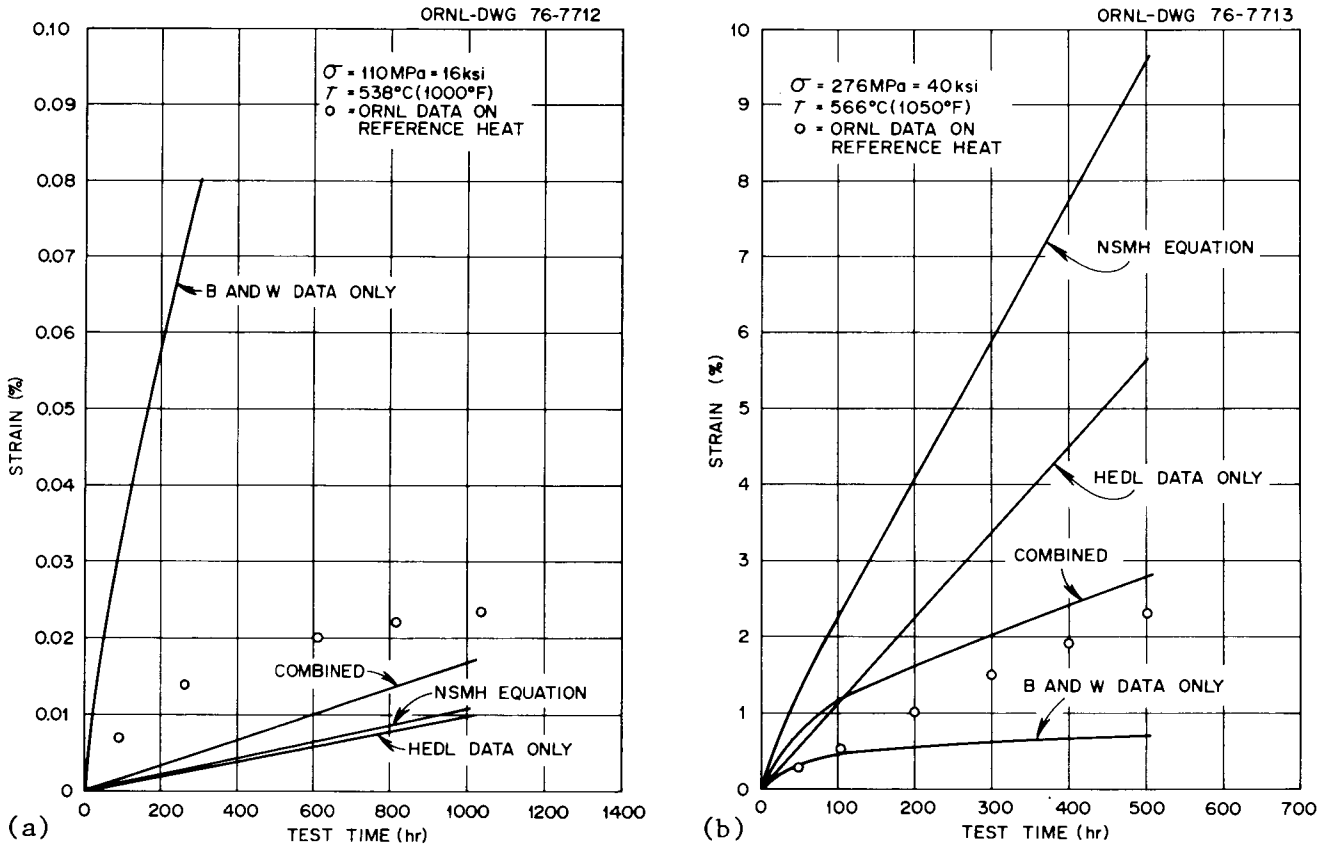

Fig. 3.34. Comparison of ORNL Reference Heat Data Under Two Sets of Conditions with Creep Curves Calculated by the Single Rational Polynomial Equation Based on Three Data Sets and with the NSMH Equation.

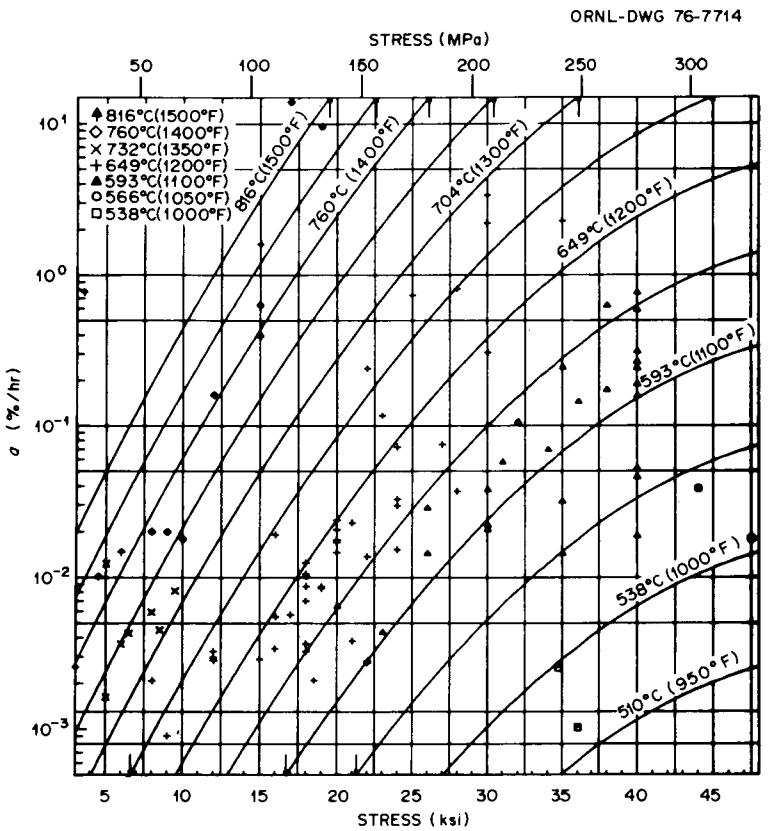

Fig. 3.35. Fit of Eq. (36) for Constant a of Eq. (32) for the Combined Data Set.

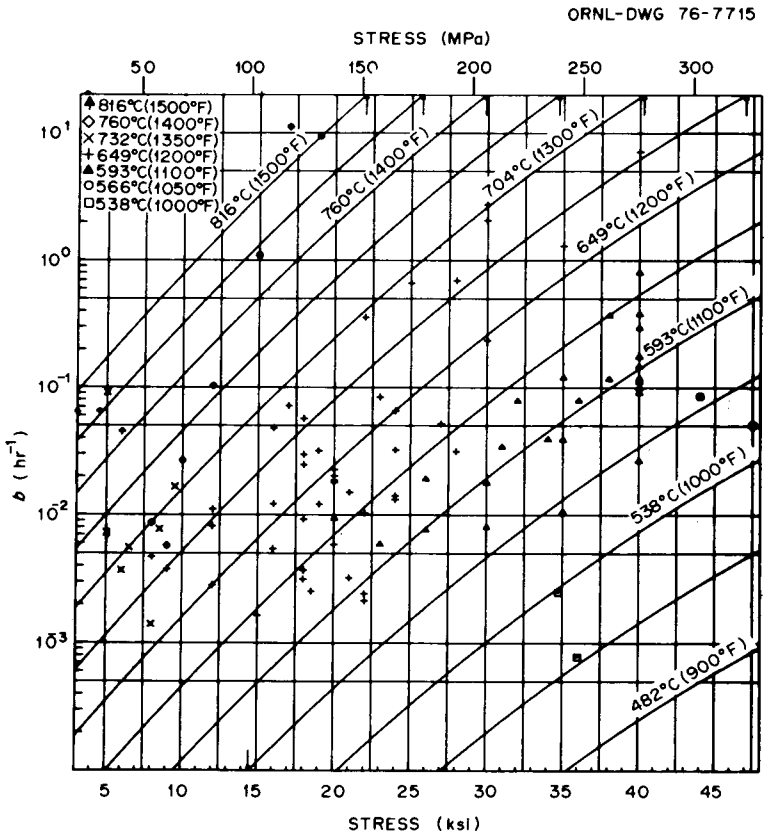

Fig. 3.36. Fit of Eq. (36) for Constant b of Eq. (32) for the Combined Data Set.

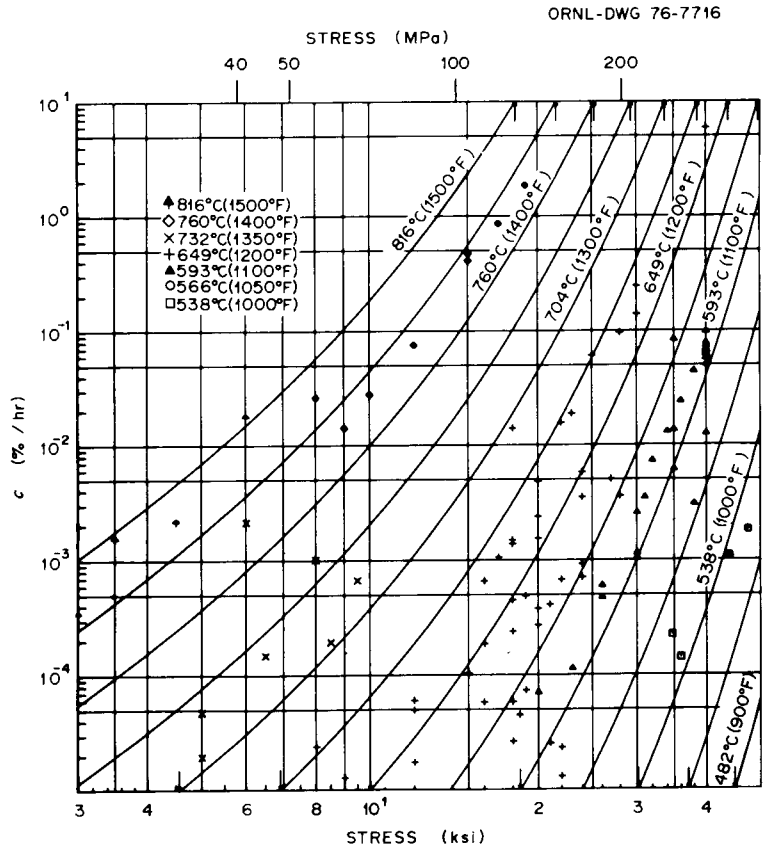

Fig. 3.37. Fit of Eq. (36) for Constant c of Eq. (32) for the Combined Data Set.

low stresses at low temperatures, may predict too low, but additional test data are necessary to evaluate properly this tendency. An unexpected bonus is the much reduced scatter of a and b, as compared with the corresponding single exponential equation parameters, ε_t and r. The large scatter in ε_t, in particular, was demonstrated previously.[2]

It would be useful to modify Eq. (32) to the form

$$\varepsilon_c = \frac{a'bt}{1 + bt} + ct \ . \tag{37}$$

This slight change enables the direct evaluation of primary creep as having a limiting value of a'. Using the same notation, a curve fit gives

$$\ln a' = -1.35035 - 3122.2/T - 0.05062\sigma + 1.91818 \ln \sigma \ . \tag{38}$$

Figure 3.38 compares isotherms with input parameters.

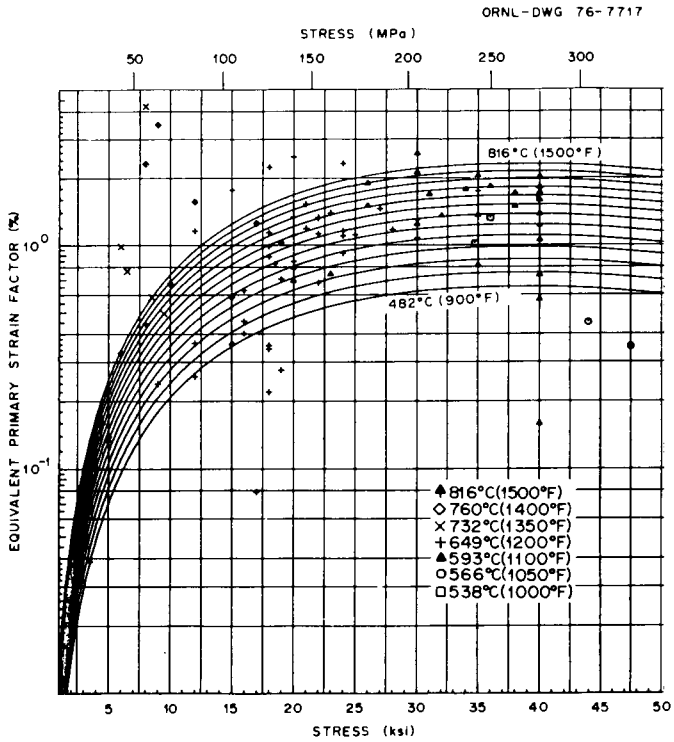

Fig. 3.38. Fit of Eq. (38) for Constant a' of Eq. (37) for the Combined Data Set.

3.2.3.2.3 Recommended Equations. Based on all the above the recommended equation form is

$$\varepsilon_c = \frac{at}{1 + bt} + ct \quad . \tag{39}$$

The parameters are given by

$$\ln a = 31.11 - 39{,}761/T + 0.07355\sigma - 9.7144(10)^{-5}\,\sigma^2 \ ,$$

$$\ln b = 31.00 - 37{,}396/T + 0.047955\sigma - 3.9653(10)^{-5}\,\sigma^2 \ , \tag{40}$$

$$\ln c = 41.76 - 59{,}108/T + 0.042685\sigma + 2.596 \ln \sigma \ ,$$

where

T = Kelvin temperature,

σ = stress in MPa

or by

$$\ln a = 31.11 - 71{,}570/T + 0.50708\sigma - 0.004618\sigma^2 ,$$

$$\ln b = 31.00 - 67{,}313/T + 0.33064\sigma - 0.001885\sigma^2 , \qquad (41)$$

$$\ln c = 43.69 - 106{,}394/T + 0.2943\sigma + 2.596 \ln \sigma ,$$

where

T = Rankine temperature,

σ = stress in ksi.

Note that ε_c is in percent and the time, t, in hours.

Figure 3.39 compares, without comment, the minimum creep rates predicted by the recommended and NSMH equations against stress and temperature. Figure 3.40 does likewise for total primary creep strain amplitude.

Figures 3.41 through 3.43 compare isochronous stress-strain curves based on the NSMH and the proposed equation. All curves based on the proposed equation are dashed.

Figure 3.44 compares predicted and measured uniaxial relaxation response at 593°C (1100°F). It is seen that excellent agreement is obtained with the two tests available.

3.2.4 Computerized Data Management System — M. K. Booker and B.L.P. Booker*

Computer programs are being developed to aid in the processing and analysis of mechanical properties data as part of the ORNL computerized data management system. Development of the APEND program (Analytical Program for Edited Numerical Datasets) was reported[57] last quarter. This program allows retrieval and analysis of data from the Mechanical Properties Data Storage and Retrieval System (DSRS), including graphical display of results. However, APEND is limited to cases involving one

---

*Consultant.

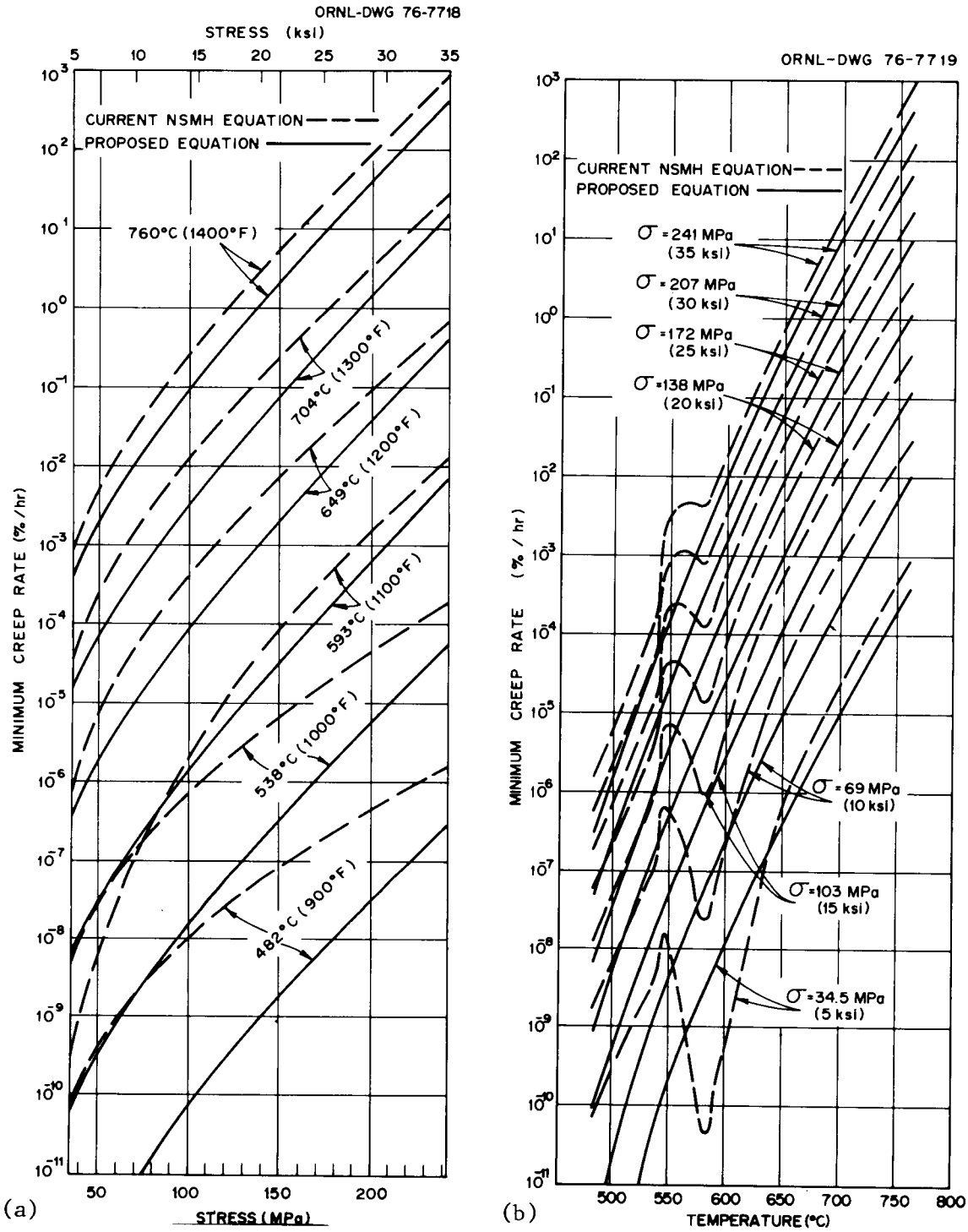

Fig. 3.39. Comparison of Minimum Creep Rates Predicted by the Recommended and NSMH Equations.

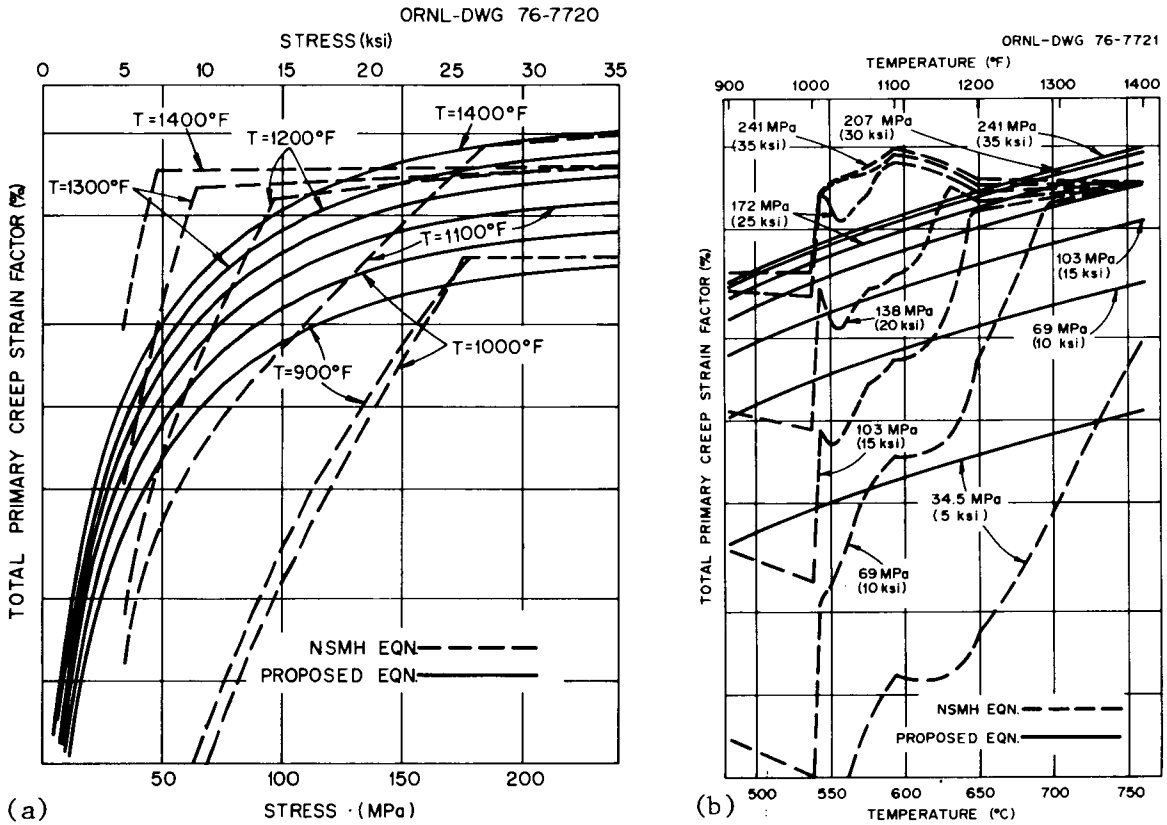

Fig. 3.40. Comparison of Total Primary Creep Strain Predicted by the Recommended and NSMH Equations.

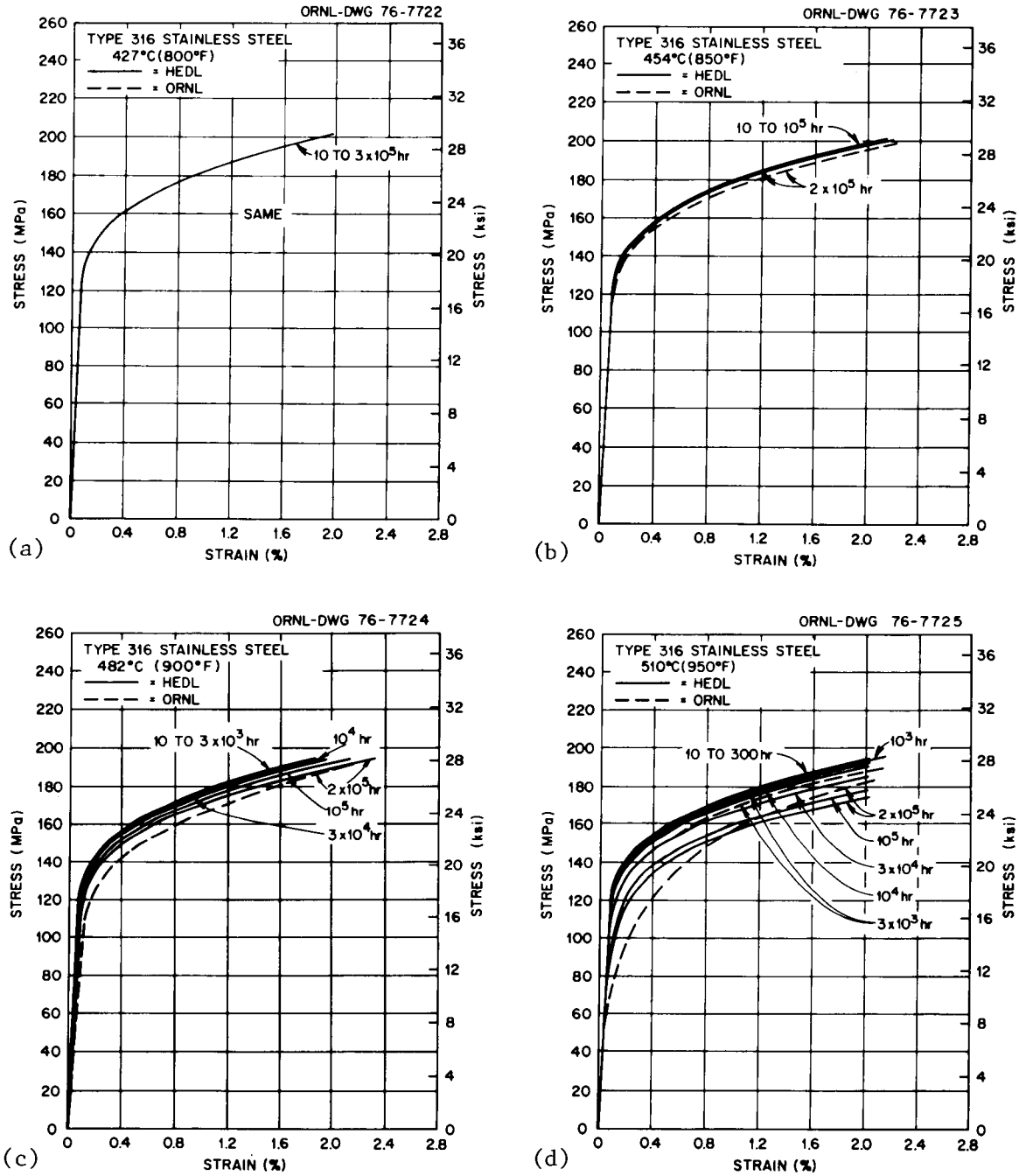

Fig. 3.41. Isochronous Stress-Strain Curves for Type 316 Stainless Steel at 427 to 510°C (800–950°F). Solid lines are for NSMH equation; dashed lines for proposed equation.

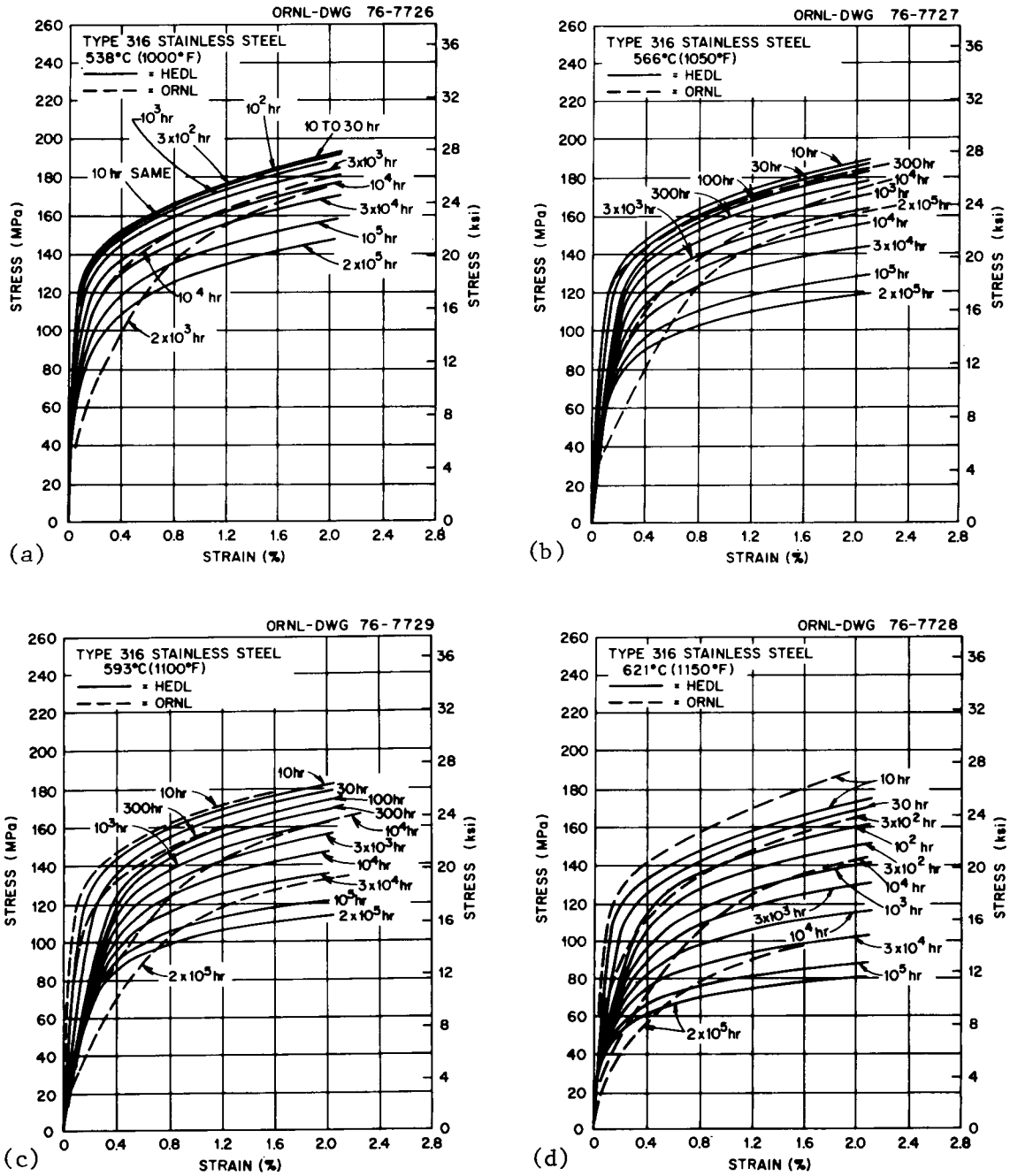

Fig. 3.42. Isochronous Stress-Strain Curves for Type 316 Stainless Steel at 538 to 621°C (1000—1150°F). Solid lines are for NSMH equation; dashed lines for proposed equation.

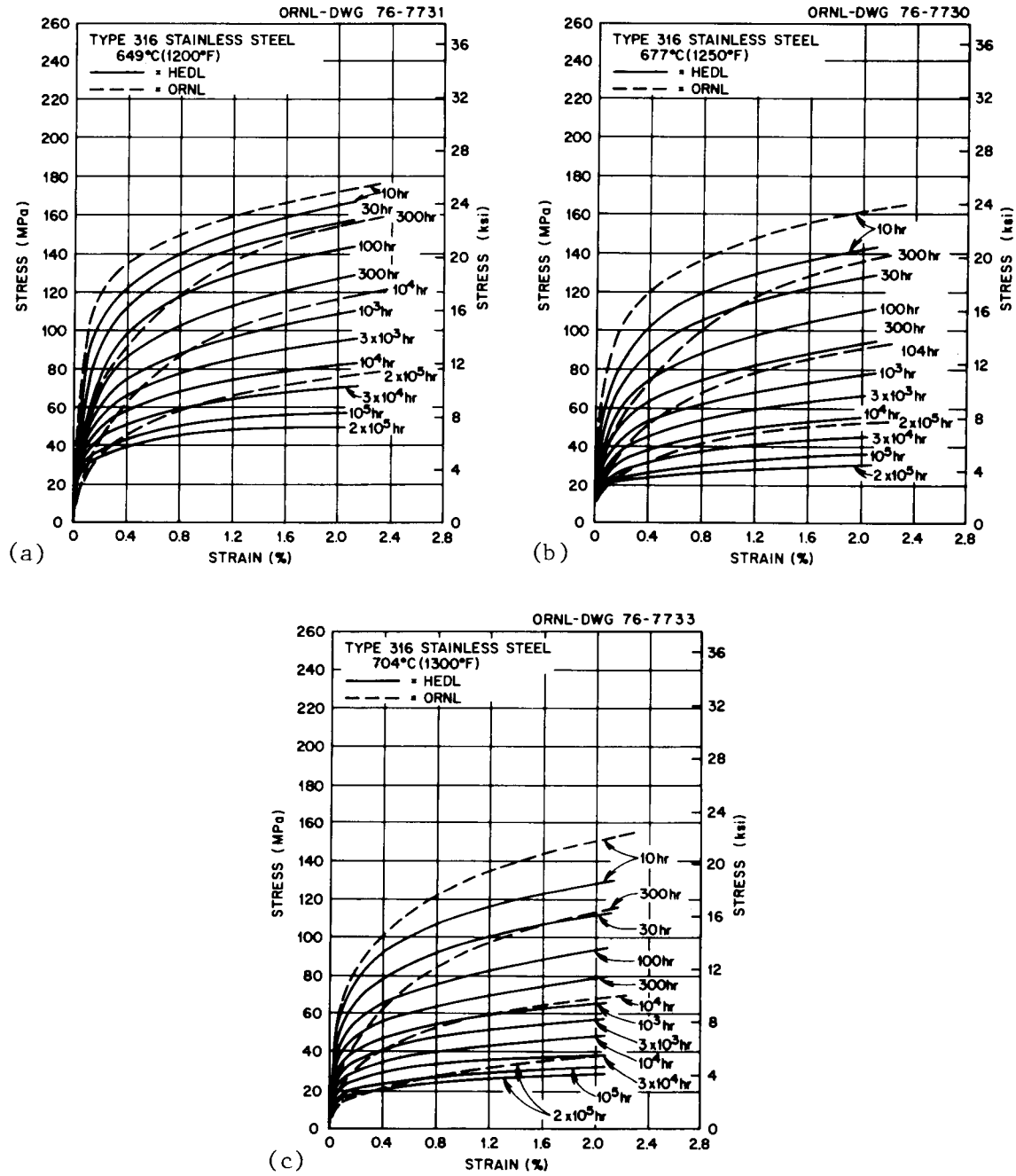

Fig. 3.43. Isochronous Stress-Strain Curbes for Type 316 Stainless Steel at 649 to 704°C (1200—1300°F). Solid lines are for NSMH equation; dashed lines for proposed equation.

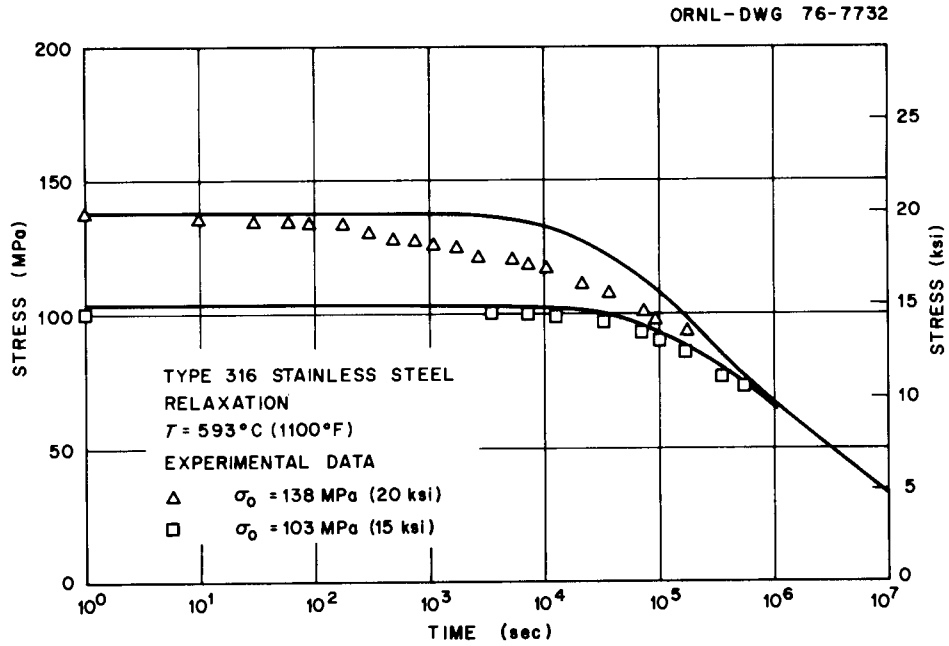

Fig. 3.44. Predicted and Measured Relaxation of Type 316 Stainless Steel at 593°C (1100°F).

independent variable. A second program ASEND (Analytical System for Edited Numerical Datasets), is being developed to handle the more general case of multiple regression analysis involving several variables. During this past quarter, the initial phase of ASEND was completed.

The ASEND program is particularly useful in the analysis of creep or other data in which there are inherently more than one independent variable. For example, ASEND allows analysis of creep-rupture data by any model in which rupture life, the inherently dependent variable, can be expressed as a linear function of stress and temperature, including cross-terms, higher-order terms, logarithmic terms, etc. Clearly, this capability provides a powerful, flexible tool for data analysis. For example, the commonly used Larson-Miller parameter may be expressed as

$$\log t_r = P(\sigma)/T - C \quad , \tag{42}$$

where C is the so-called Larson-Miller constant, and $P(\sigma)$ is some generalized function of stress. Figure 3.45 illustrates the analysis of creep-rupture data for annealed 2 1/4 Cr-1 Mo steel using this model

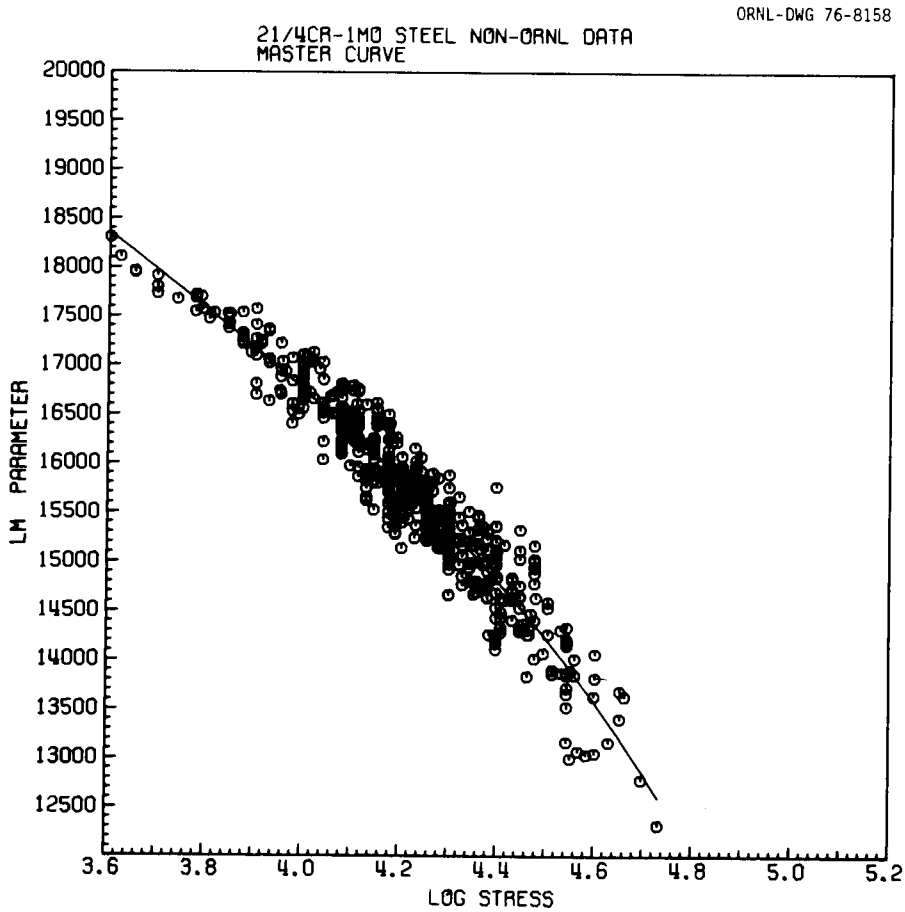

Fig. 3.45. Sample Larson-Miller Analysis of Creep-Rupture Data for 2 1/4 Cr-1 Mo Steel.

with $P(\sigma) = \alpha_0 + \alpha_1\sigma + \alpha_2 \log \sigma$, where α_0, α_1, and α_2, along with C, were estimated by the least squares fitting procedures of ASEND.

At present, ASEND and APEND calculate best fit values of regression constants, standard errors of estimate(s), and coefficients of determination. Figure 3.46 illustrates a fit and plot obtained through APEND. The dashed lines represent offsets of $\pm 2s$ from the predicted mean curve. Current work is centering on the development of additional statistical capabilities in the programs such as analysis of variance and calculation of tolerance limits.

The basic routines through which ASEND and APEND obtain data from DSRS potentially form the basis for a complete library of analytical programs. Once read from the DSRS on-line file, the data are no different from data read from punched cards or other input devices. Thus, any of

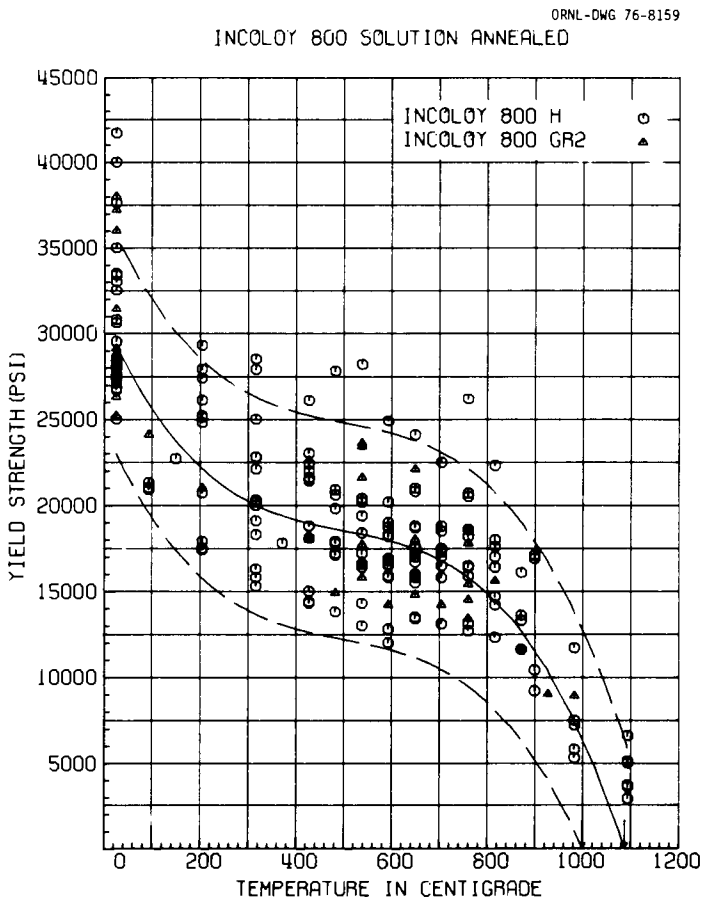

Fig. 3.46. Sample Analysis of Tensile Data for Incoloy Alloy 800H, Including a Best Fit Mean Curve and ±2 Standard Error Limits.

the wide variety of computer routines available can be potentially applied to the data stored in DSRS. The system then will provide not only a convenient means for storage and retrieval of data, but also will bring forth the full power of the modern digital computer in the analysis of those data.

3.2.5 Elastic Properties of Engineering Construction Materials — J. P. Hammond

Precise measurements show that for metals the "elastic" stress-strain relationships are not perfectly linear, even at low stresses and strain levels, and they become progressively more nonlinear as stress increases. Discrepancies thus often occur between elastic constants determined at different strain levels and rates of strain (for example, constants determined by dynamic and static techniques).

The purpose of this program is to correlate the two separate categories of elastic constants (dynamic and static) for reactor materials of interest, giving specific attention to temperature and other significant test variables. In addition to elastic constants (Young's modulus, E; shear modulus, G; and Poisson's ratio, ν), elastic and proportional limits (E.L. and P.L.) will be determined. This information is needed to enable more exact and enlightened use of this class of information in engineering design and structural verification work.

3.2.5.1 Elastic Properties Determined by Dynamic Tests — J. P. Hammond and M. W. Moyer*

Dynamic (sonic) elastic constants (E, G, and ν) are being established at room temperature on bulk samples by the pulse-echo method (5 MHz) and at elevated temperatures on wires by the remote magnetostrictive technique (0.2 MHz). The methods of determining elastic constants from sound velocities were recently reported.[58] The modulus data, which consist of sets of 52 or more points from room temperature to 650°C (1200°F) or higher, are fitted with cubic polynomials by regression analysis. The equations are of a form that normalizes the high-resolution but less accurate elevated-temperature data to the accurate (0.1–0.4% standard error) room-temperature values. Results are obtained as computer readout graphs that give best estimates of the elastic property as a function of temperature.

During the last quarter dynamic elastic constants were determined for type 316 stainless steel (heat 8092297) and Incoloy Alloy 800H (heat HH6758A). For each the elastic properties were determined on 25-mm (1-in.) plate in the solution-annealed condition, parallel to the rolling direction.

Cubic polynomials of the following form are established for E, G, and ν:

$$X = X_0[1 + A_x(T - T_0) + B_x(T - T_0)^2 + C_x(T - T_0)^3] ,$$

*Laboratory Development, Oak Ridge Y-12 Plant.

where

X = the property (E, G, or ν),

X_0 = same at 24°C (75°F),

T = temperature in °C or °F,

T_0 = 24°C (75°F), and

A_x, B_x, and C_x = constants.

The coefficients for the polynomials and standard deviations of fit of data to the polynomials are given in Table 3.15. Graphical displays of the equations with the data points superimposed are presented in Figs. 3.47 and 3.48.

The room-temperature elastic constants of the respective materials with standard deviations, to which the elevated-temperature properties were normalized, are given below:

Type 316 Stainless Steel

E = 198.0 ± 0.8 GPa

= (28.72 ± 0.12) × 10^6 psi

G = 76.74 ± 0.16 GPa

= (11.13 ± 0.02) × 10^6 psi

ν = 0.2901

Table 3.15. Coefficients for Polynomial Fit to Elastic Constants[a]

Constant	Values of Coefficients				
	x_0	A_x, °C^{-1}	B_x, °C^{-2}	C_x, °C^{-3}	Std Dev of Fit
			Type 316 Stainless Steel, Heat 8092297		
E	2.872 × 10^7 psi	−3.93625 × 10^{-4}	−8.37648 × 10^{-8}	9.26214 × 10^{-11}	9.27 × 10^4 psi
G	1.113 × 10^7 psi	−4.72563 × 10^{-4}	−4.05496 × 10^{-9}	5.80860 × 10^{-11}	8.25 × 10^4 psi
ν	0.2901	3.55518 × 10^{-4}	−2.20321 × 10^{-7}	1.18177 × 10^{-10}	4.93 × 10^{-5}
			Incoloy 800H, Heat HH6758A		
E	2.817 × 10^7 psi	−3.64822 × 10^{-4}	7.06294 × 10^{-8}	−6.53397 × 10^{-11}	9.50 × 10^4 psi
G	1.086 × 10^7 psi	−2.50350 × 10^{-4}	−4.31878 × 10^{-7}	3.39907 × 10^{-10}	9.04 × 10^4 psi
ν	0.2969	−6.05000 × 10^{-4}	2.66177 × 10^{-6}	−2.10991 × 10^{-9}	1.16 × 10^{-3}

[a] T_0 = 24°C. For moduli (E, G) in pascals, x_0 should be multiplied by 6895.

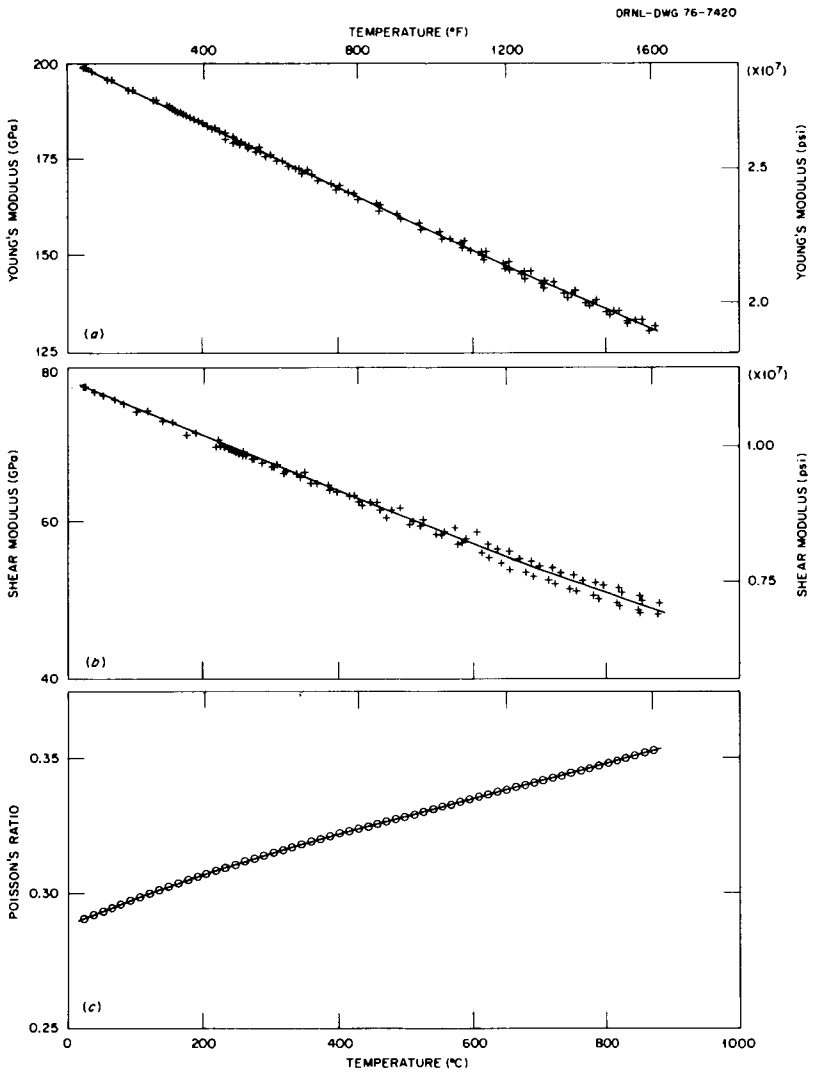

Fig. 3.47. Elastic Constants of Type 316 Stainless Steel, Heat 8092297.

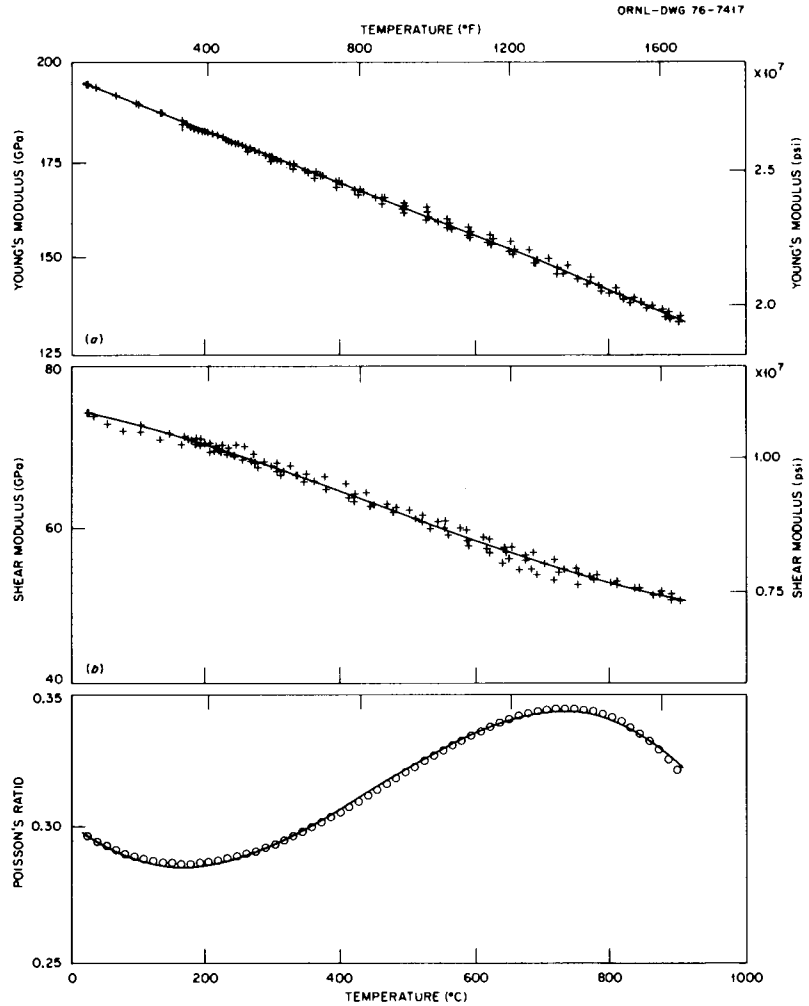

Fig. 3.48. Elastic Constants of Incoloy 800H, Heat HH6758A.

Incoloy 800H

E = 194.2 ± 1.2 GPa

= (28.17 ± 0.18) × 10^6 psi

G = 74.87 ± 0.55 GPa

= (10.86 ± 0.08) × 10^6 psi

ν = 0.2969

Estimates of the elastic properties established with the polynomials at 24°C (75°F) and at 28°C (50°F) intervals from 38°C (100°F) to 871 or 899°C (1600 or 1650°F) are given in Tables 3.16 and 3.17.

Table 3.16. Dynamic Elastic Constants of Type 316 Stainless Steel, Heat 8092297

Temperature		Young's Modulus		Shear Modulus		Poisson's Ratio
(°C)	(°F)	(GPa)	(psi)	(GPa)	(psi)	
24	75	198.2	28.74 × 10^6	76.81	11.14 × 10^6	0.291
38	100	197.1	28.59	76.26	11.06	0.292
66	150	194.9	28.27	75.29	10.92	0.295
93	200	192.7	27.95	74.26	10.77	0.297
121	250	190.4	27.62	73.22	10.62	0.300
149	300	188.2	27.30	72.26	10.48	0.303
177	350	185.9	26.97	71.22	10.33	0.305
204	400	183.7	26.64	70.26	10.19	0.307
232	450	181.4	26.31	69.22	10.04	0.310
260	500	179.1	25.97	68.26	9.90	0.312
288	550	176.8	25.64	67.29	9.76	0.314
316	600	174.5	25.31	66.26	9.61	0.316
343	650	172.2	24.97	65.29	9.47	0.318
371	700	169.9	24.64	64.33	9.33	0.320
399	750	167.5	24.30	63.36	9.19	0.322
427	800	165.3	23.97	62.40	9.05	0.324
454	850	163.0	23.64	61.43	8.91	0.326
482	900	160.7	23.31	60.54	8.78	0.328
510	950	158.4	22.98	59.57	8.64	0.330
538	1000	156.2	22.66	58.67	8.51	0.332
566	1050	154.0	22.33	57.78	8.38	0.333
593	1100	151.8	22.01	56.81	8.24	0.335
621	1150	149.6	21.70	55.99	8.12	0.337
649	1200	147.4	21.38	55.09	7.99	0.339
677	1250	145.3	21.07	54.19	7.86	0.340
704	1300	143.2	20.77	53.37	7.74	0.342
732	1350	141.1	20.47	52.54	7.62	0.344
760	1400	139.1	20.17	51.71	7.50	0.346
788	1450	137.1	19.88	50.88	7.38	0.347
816	1500	135.1	19.60	50.06	7.26	0.349
843	1550	133.2	19.32	49.30	7.15	0.351
871	1600	131.3	19.05	48.54	7.04	0.353

Table 3.17. Dynamic Elastic Constants of Incoloy 800H, Heat HH6758A

Temperature		Young's Modulus		Shear Modulus		Poisson's Ratio
(°C)	(°F)	(GPa)	(psi)	(GPa)	(psi)	
24	75	194.3	28.18×10^6	74.88	10.86×10^6	0.297
38	100	193.3	28.04	74.60	10.82	0.295
66	150	191.3	27.75	74.05	10.74	0.292
93	200	189.4	27.47	73.43	10.65	0.290
121	250	187.6	27.20	72.81	10.56	0.288
149	300	185.6	26.92	72.12	10.46	0.287
177	350	183.7	26.65	71.36	10.35	0.287
204	400	181.9	26.38	70.60	10.24	0.288
232	450	180.0	26.11	69.84	10.13	0.289
260	500	178.2	25.84	69.02	10.01	0.291
288	550	176.3	25.57	68.19	9.89	0.293
316	600	174.6	25.31	67.29	9.76	0.296
343	650	172.6	25.04	66.47	9.64	0.299
371	700	170.8	24.77	65.57	9.51	0.303
399	750	169.0	24.51	64.67	9.38	0.306
427	800	167.1	24.24	63.78	9.25	0.310
454	850	165.3	23.98	62.88	9.12	0.315
482	900	163.5	23.71	61.98	8.99	0.319
510	950	161.6	23.44	61.09	8.86	0.323
538	1000	159.7	23.17	60.19	8.73	0.327
566	1050	157.9	22.90	59.29	8.60	0.331
593	1100	156.0	22.63	58.47	8.48	0.335
621	1150	154.2	22.36	57.57	8.35	0.338
649	1200	152.2	22.08	56.74	8.23	0.341
677	1250	150.4	21.81	55.99	8.12	0.343
704	1300	148.4	21.53	55.23	8.01	0.345
732	1350	146.4	21.24	54.47	7.90	0.345
760	1400	144.5	20.96	53.71	7.79	0.345
788	1450	142.5	20.67	53.09	7.70	0.343
816	1500	140.5	20.38	52.40	7.60	0.340
843	1550	138.4	20.08	51.85	7.52	0.336
871	1600	136.4	19.78	51.30	7.44	0.330
899	1650	134.3	19.48	50.81	7.37	0.322

The dynamic and shear Young's moduli of the type 316 stainless steel and Incoloy 800H [Figs. 3.47(a) and 3.48(a)] decrease almost linearly with temperature, as was observed earlier[59] for type 304 stainless steel. The dynamic Young's modulus of type 316 stainless steel was about 2% higher than that of Incoloy 800 at room temperature and 3.5% lower at 871°C (1600°F). The curve for Poisson's ratio of Incoloy 800H [Fig. 3.48(c)] is distinctly sinusoidal, whereas that for type 316 stainless steel [Fig. 3.47(c)] is much more linear, increasing in value with temperature.

The ASME pressure vessel code values[11] (case 1592) for the Young's modulus of type 316 stainless steel, which pressumably are static, generally fall just below the present dynamic values. The code value is about 1.5% below at room temperature, nearly coincident between 316 and 510°C (600 and 950°F), and about 5% below at 760°C (1400°F). On theoretical grounds the static values should be below the dynamic.

3.3 MECHANICAL AND METALLURGICAL BEHAVIOR OF WELDMENTS FOR LMFBR — P. Patriarca, G. M. Slaughter, W. R. Martin, and C. R. Brinkman

3.3.1 Structure and Properties of a 16-8-2 Submerged-Arc Weld — R. T. King and D. P. Edmonds

The type 16-8-2 (16% Cr—8% Ni—2% Mo) stainless steel weld filler metal was developed by Babcock and Wilcox in the 1950s for high-temperature, high-pressure piping welds.[60] Data and an experience base exist for 16-8-2 welds made by the gas tungsten-arc and shielded metal-arc processes,[61] but little is presently known about 16-8-2 welds made by the submerged-arc process. Since submerged-arc welding is economically attractive for making large shells and vessels, and because the 16-8-2 data base is thus far attractive for high-temperature nuclear service, the Babcock and Wilcox Company has made a series of 16-8-2 trial welds in 25-mm-thick (1-in.) type 316 stainless steel plate for characterization. This report gives the results from a program in progress.

The test welds were all made by identical procedures at Babcock and Wilcox facilities in plate from reference heat 8092297. Analyses of the chemical composition supplied by the vendor and obtained at ORNL are given in Table 3.18. The welds were made in a single-V joint with a 19-mm root opening and a 20° included angle. Arcos S-11 flux was used. All the tensile and creep tests performed to date at ORNL have been on specimens from 0.298 by 0.311-m test plates DEV 77-5 and DEV 77-6. The 0.305 × 0.61-m test plates DEV 77-7, -8, -9, and -10 have been received at ORNL, and one of them has been transferred to Argonne National Laboratory to make fatigue specimens.

Table 3.18. Chemical Composition of Type 316 Stainless Steel Reference Heat 25-mm-Thick Plate, 16-8-2 Electrodes, and 16-8-2 Weld Deposits

Element	Amount Present, wt %						
	Type 316 Plate			16-8-2			
	Vendor Analysis		ORNL Analysis	Filler Metal		Weld Metal	
	Lot 465	Lot 596		Vendor	Check	$T/2$	Final Pass
C	0.059	0.060	0.064	0.042	0.045	0.047	0.047
Mn	1.84	1.86	0.40	1.38	1.41	1.48	1.39
P	0.024	0.024	0.0220	0.020	0.020	0.026	0.029
S	0.018	0.018	0.0188	0.022	0.015	0.012	0.014
Si	0.58	0.57	0.51	0.33	0.35	0.89	0.87
Cu	0.10	0.10	0.12		0.08	0.09	0.04
Ni	13.40	13.45	13.86	9.13	9.36	10.03	9.27
Cr	17.15	17.15	16.46	15.99	15.93	14.85	14.43
Mo	2.34	2.34	2.44	1.76	1.82	1.76	1.8
Ti	0.00	0.00	<0.01		0.01	0.01	0.013
Nb	0.00	0.00	0.0004		0.005	0.03	0.003
Ta	0.00	0.00	0.001		0.03	0.03	0.03
Co	0.02	0.02	0.01		0.10	0.09	0.09
N	0.032	0.031	0.0305		0.06	0.028	0.028
B	0.0005	0.0006	0.0005		<0.001	<0.001	<0.001
Al			<0.02				
W			0.002	0.03			
Sn			<0.02				
Pb			<0.02				
H			0.0007				
O			0.0043				
V					0.04	0.04	0.04

The vendor's analyses of the welding wire, a check analysis performed by Babcock and Wilcox, and B and W analyses of the weld deposit at half the plate thickness and in the final surface pass region are given in Table 3.18.

A section of test weld DEV 77-5 has been polished and etched to reveal its structure. The overall macrostructure is shown in Fig. 3.49. The weld has about 20 passes, and is two passes wide in the root and three passes wide at the crown. Micrographs taken from typical regions of

Fig. 3.49. Macrostructure of Weld DEV 77-5. 2.8×.

the root, intermediate, and surface passes are shown in Fig. 3.50. The structure is essentially cellular dendritic with elongated austenite subgrains and a small amount of δ-ferrite present. The ferrite numbers measured by Ferritescope on several of the test welds are compared with the ferrite content predicted from the Delong constitution diagram in Tables 3.19 and 3.20. Note, however, that the local structure varies greatly with location in any small region.

A diamond pyramid hardness traverse was run up the center of the weld, and additional traverses were run at 6-mm intervals into the heat-affected zone (see Fig. 3.51). While the traverses have local perturbations that can be attributed to local heterogeneities of structure revealed by a relatively fine indenter, there is a clear trend for increasing hardness up the center of the weld from root to crown, and decreasing hardness from the center of the weld toward the base metal. A similar pattern has been reported[62,63] for a type 308 stainless steel shielded metal-arc weld in 60-mm-thick type 304 stainless steel base plate, where the observations could be related to the effects of solidification processes on the local microstructure. An in-depth transmission electron microscopy study of this structure has not yet been planned for these welds.

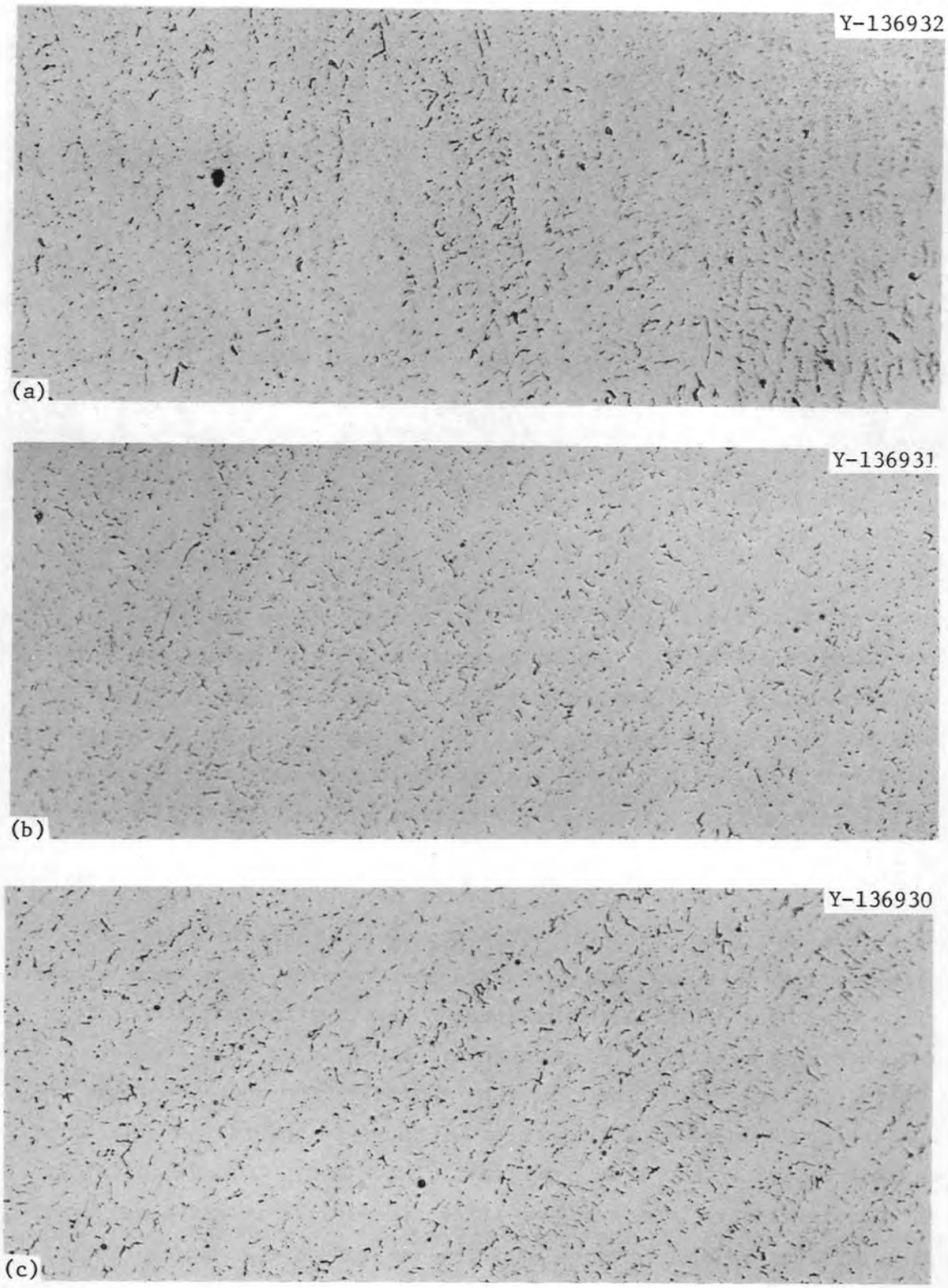

Fig. 3.50. Representative Microstructures of Type 16-8-2 Stainless Steel Submerged-Arc Test Welds with Sections from the (a) Root, (b) Intermediate Pass, and (c) Crown Pass Regions. Dark areas are ferrite. Etchant selected to reveal ferrite. 200×.

Table 3.19. Measured Ferrite Numbers in Type 16-8-2 Stainless Steel Submerged-Arc Welds Made in 25-mm-Thick Type 316 Stainless Steel Base Metal

Weld	Pass	Ferrite Number
DEV 77-5	Root	1.0–1.6
	Intermediate	≈1.5
	Surface	2.5–3.0
DEV 77-6	Root	0.8–1.4
	Intermediate	≈1.5
	Surface	1.5–1.8

Table 3.20. Calculated Ferrite Contents of Type 16-8-2 Stainless Steel Submerged-Arc Welds

Analysis Used	Equivalents, %		Ferrite Content (%)
	Cr	Ni	
Vendor wire	18.25	12.88	1
B and W wire	18.27	13.2	0
T/2 deposit	17.96	13.02	0
Surface pass	17.54	12.22	1

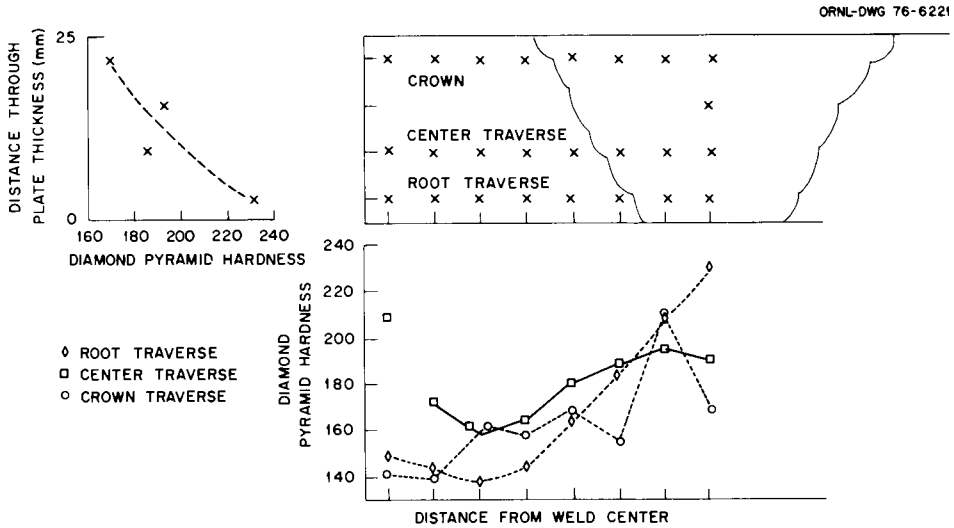

Fig. 3.51. Diamond Pyramid Hardness Traverses of 16-8-2 Submerged-Arc Weld, 100 kg Load.

The tensile specimens that were prepared for characterization of the weld all had a common geometrical design that involves welding end grips to a section, into which a cylindrical tensile gage section is later machined.[64] In one test series, specimens were prepared with 31.7-mm-long by 6.3-mm-diam (1.25 × 0.25-in.) gage sections parallel to the welding direction [Fig. 3.52(a)], including five all-weld-metal specimens, one that contained the fusion line, and the balance of type 316 stainless steel from the heat-affected zone. Specimens with center lines about 5 mm below the crown surface are designated L1 (specimens 1–8) and those with center lines about 5 mm above the root surface are designated L2 specimens (specimens 9–16). In addition, two transverse specimens were prepared, as shown in Fig. 3.52(b). The T1 specimen had a 31.7-mm long by 6.3-mm-diam gage section, while the T2 specimen had a 19-mm-long by 3.8-mm-diam (0.75 × 0.15 in.) gage section (which unfortunately was damaged in fabrication).

All these specimens were tested at room temperature at 0.127 mm/min crosshead speed on an Instron tensile testing machine, resulting in a 0.004/min strain rate for the 31.7-mm gage lengths. While the stress-strain behavior was monitored at small strains by extensometers fitted with LVDTs and an in-line load cell, we include only the engineering

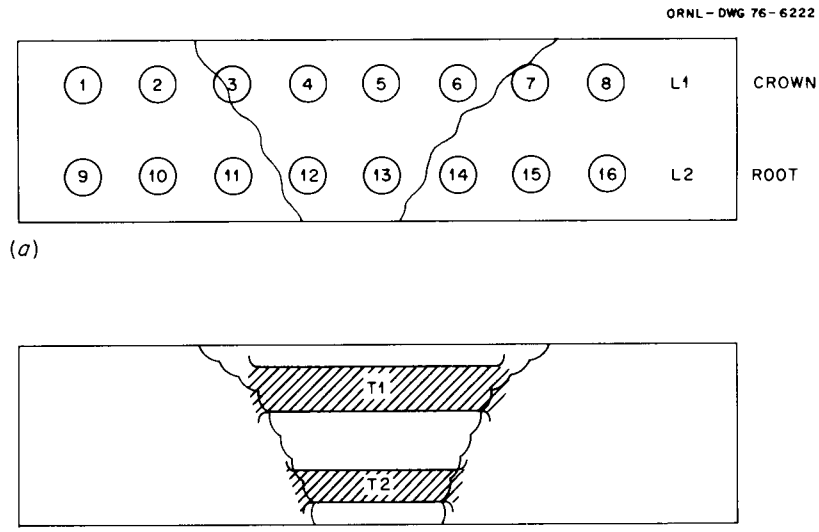

Fig. 3.52. Location of Specimens in 16-8-2 Submerged-Arc Weld and Weldments.

data in this preliminary report. (Table 3.21). The following observations are consistent with those made previously[62] for a type 308 CRE stainless steel multipass weld made by the shielded metal-arc process:

1. The yield strength of the crown pass region weld metal is less than that of the root pass region by about 70 MPa (10 ksi).

2. The yield strength of the base metal tends to decrease as the specimen distance from the fusion line increases.

Data for as-received 16-mm-thick plate from the same heat of type 316 stainless steel are included for comparison in Table 3.21. The most obvious effect of welding on the base metal is an increase of the proportional elastic limit and the yield strength in the immediate vicinity of the fusion line.

Other specimens were prepared from the weld in the manner described above and tensile tested at temperatures to 650°C. These tests included a basic matrix of L1 type specimens, with spot-checks on effects of strain rate, location, and orientation on properties for selected test conditions. The data are listed in Table 3.22. The tensile strength and yield strength values are plotted in Fig. 3.53 for comparison with Smith's minimum trend curves[9] for type 316 stainless steel base metal

Table 3.21. Engineering Tensile Properties of Type 16-8-2 Stainless Steel Weld Metal and Fusion Line and Heat-Affected Type 316 Base Metal at Room Temperature and a 0.004/min Strain Rate

Specimen Type and Number		Proportional Limit		0.2% Offset Yield Strength		Ultimate Strength		Elongation, %		Reduction of Area (%)
		(MPa)	(ksi)	(MPa)	(ksi)	(MPa)	(ksi)	Uniform	Total	
Base L1	1	110	15.9	208	30.1	578	83.8	68.9	82.0	71.4
Base L1	2	118	17.1	221	32.1	581	84.2	61.9	73.6	74.4
Fusion L1	3	179	26.0	260	37.7	590	85.6	65.4	70.7	62.6
Weld L1	4	92	13.4	322	46.7	585	84.8	60.5	61.1	47.3
Weld L1	5	260	37.7	323	46.9	587	85.1	46.3	47.3	40.4
Weld L1	6	145	21.1	316	45.9	585	84.9	55.7	62.1	51.1
Base L1	7	169	24.5	345	50.1	590	85.5	58.4	69.7	68.7
Base L1	8	92	13.4	291	42.2	572	83.0	63.6	74.4	70.3
Base L2	9	152	22.0	271	39.3	571	82.8	63.8	75.8	70.7
Base L2	10	155	22.5	294	42.6	579	84.0	62.5	74.0	65.0
Base L2	11	190	27.6	378	54.8	597	86.6	56.0	66.9	65.2
Weld L2	12	232	33.7	395	57.3	614	89.1	46.4	47.0	33.6
Weld L2	13	197	28.6	383	55.5	601	87.1	59.8	70.8	31.4
Base L2	14	203	29.4	401	58.2	570	82.7	53.8	63.4	56.2
Base L2	15	158	22.9	301	43.7	577	83.7	62.4	73.3	71.2
Base L2	16	123	17.8	256	37.2	570	82.6	63.6	75.9	69.6
T1[a]		201	29.2	324	47.0	641	93.0	50.9	51.5	30.9
Unwelded[b]		115	16.7	228	33.0	583	84.5	60.1	73.9	79.6

[a]T2 specimen damaged in fabrication, not tested.

[b]Properties supplied by V. K. Sikka, ORNL, for as-received 16-mm-thick base metal.

Table 3.22. Tensile Properties of Type 16-8-2 Stainless Steel Weld Metal Specimens at Elevated Temperatures

Test Temperature		Strain Rate (min^{-1})	Specimen Type and Number	Proportional Limit		0.2% Offset Yield Strength		Ultimate Strength		Elongation, %		Reduction of Area (%)
(°C)	(°F)			(MPa)	(ksi)	(MPa)	(ksi)	(MPa)	(ksi)	Uniform	Total	
204	400	0.004	L1 775-L13	81	11.7	256	37.2	444	64.4	32.9	38.4	45.5
315	600		L1 775-L12	119	17.2	234	34.0	438	63.5	35.4	40.0	42.1
426	800		L1 775-L11	145	21.0	227	32.9	439	63.7	36.4	40.7	43.1
565	1050	0.004	L1 776-L33	99	14.3	203	29.5	371	53.9	33.2	39.4	50.7
		0.0004	L1 775-L8	139	20.1	197	28.6	366	53.1	32.7	41.3	43.1
		0.004	L2 776-L36	169	24.5	256	37.2	383	55.5	27.2	33.7	36.6
		0.007	T1 776-T5	77	11.2	233	33.8	396	57.4	22.0	24.6	53.2
649	1200	0.04	L1 775-L7	63	9.1	172	24.9	238	34.5	23.1	50.2	58.7
			L2 775-L15	157	22.8	205	29.8	252	36.5	17.6	56.3	46.1
		0.007	T1 775-T11	77	11.1	195	28.3	272	39.5	18.4	35.5	50.9
			T1 775-T12	142	20.6	245	35.6	292	42.4	5.9	15.5	41.8

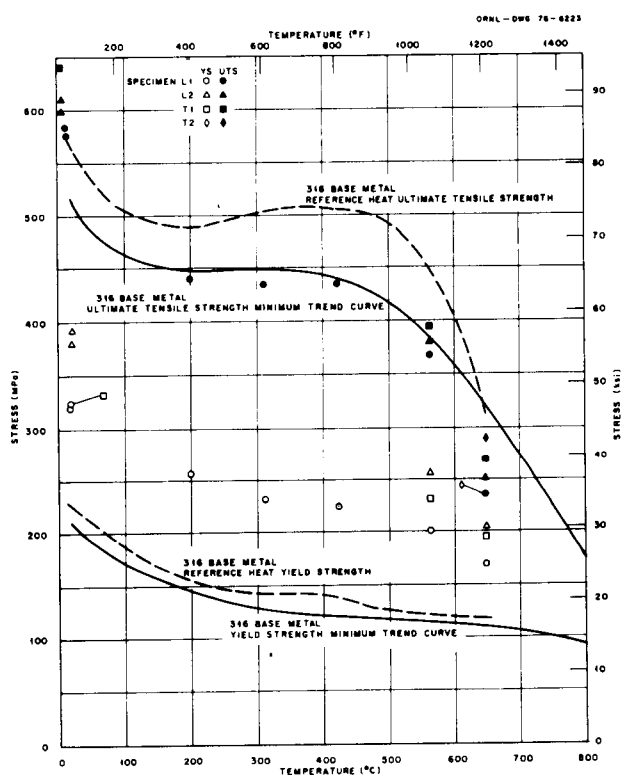

Fig. 3.53. Tensile Properties of Type 16-8-2 Submerged-Arc Weld Metal and Weldments at 0.004/min Strain Rate.

and recent ORNL data on 16-mm-thick plate from the type 316 stainless steel reference heat. While the yield strength of the weld metal at elevated temperatures exceeds the values measured for the base material and the minimum trend curve for base metal, the tensile strength of the weld metal tends to be below both these measures of base metal tensile strength.

The creep and creep-rupture properties of weld metal specimens are being investigated at 566 and 649°C (1050 and 1200°F). The engineering data obtained to date are summarized in Table 3.23. Most of the data are for rupture times near 100 hr for both longitudinal and transverse weld specimens from the root and crown pass regions. Lower stress tests are in progress.

Table 3.23. Creep-Rupture Test Data for Babcock and Wilcox Type 16-8-2 Submerged-Arc Welds

Stress (MPa)	Stress (ksi)	Specimen Type and Number	Test	Rupture Time (hr)	Time to Tertiary Creep: Linearity	Time to Tertiary Creep: Offset	Strain, %: Onset of Tertiary Creep: Linearity	Strain, %: Onset of Tertiary Creep: Offset	Strain, %: Total at Rupture	Reduction of Area (%)
				Tests at 649°C (1200°F)						
172	25	L1	776-L35 FWB-239	31.5	1.7	∿2	2.1	∿2.3	55.3	58.4
138	20	L1	775-1L FWB-249	>258.5					>9	
110	16	L1	775-L6 FWB-250	>162.4					>0.078	
172	25	L2	776-L37 FWB-237	73.9	1.6 14.4	5 18.3	0.72 4.3	1.1 5.7 [a]	60.6	50.1
138	20	L2	775-L14 FWB-254	>64.8					>1.2	
172	25	T1	776-T3 FWB-240	121.3					38.3	37.7
138	20	T1	775-T1 FWB-252	>114.3					>1.55	
110	16	T1	775-T5 FWB-253	>89.9					>2.7	
345	50	T2	776-T4	∿0						
172	25	T2	776-T6 FWB-246	111.8	11.4	18	0.71	1.2	24.0	49.0
				Tests at 566°C (1050°F)						
310	45	L1	776-L34 FWB-241	45.1	27.0	30	26.9	28	55.1	45.3
276	40	L1	775-L2 FWB-255	>24					>4	
310	45	L2	775-L5 FWB-248	78.8	21	33.5	9.4	11.1	43.4	36.2
310	45	T1	776-T1 FWB-238	75.3	31.3	41.8	13.8	15.9	32.1	25.0
310	45	T2	776-T2 FWB-245	109.6	9.2	33.5	1.95	2.25	9.2	13.9
241	35	T2	775-T8 FWB-247	>331.5					>0.06	

[a]There were two linear segments of the strain-time curve, and either set of results might be interpreted as being correct.

The weld metal creep-rupture times are plotted together with average and −1.65 standard deviation base metal stress-rupture time curves derived from Blackburn's analysis of type 316 stainless steel data[40] in Fig. 3.54. Nearly all the weld metal rupture data at both 566 and 649°C fall below the −1.65 standard deviation "minimum" curves for base metal. Some data are available from creep-rupture tests at 566 and 650°C performed on the as-received reference heat base metal in which these welds were made; the rupture times tend to be near the average values of Blackburn.

Only one weld creep-rupture specimen strained less than 10% at failure, a transverse specimen tested at 566°C. The fracture surface was examined by scanning electron microscopy. While much of the fracture surface had the dimpled appearance characteristic of ductile failures [Fig. 3.55(a)], there were regions where the local substructure of the weld appeared to influence the fracture morphology [Fig. 3.55(b)].

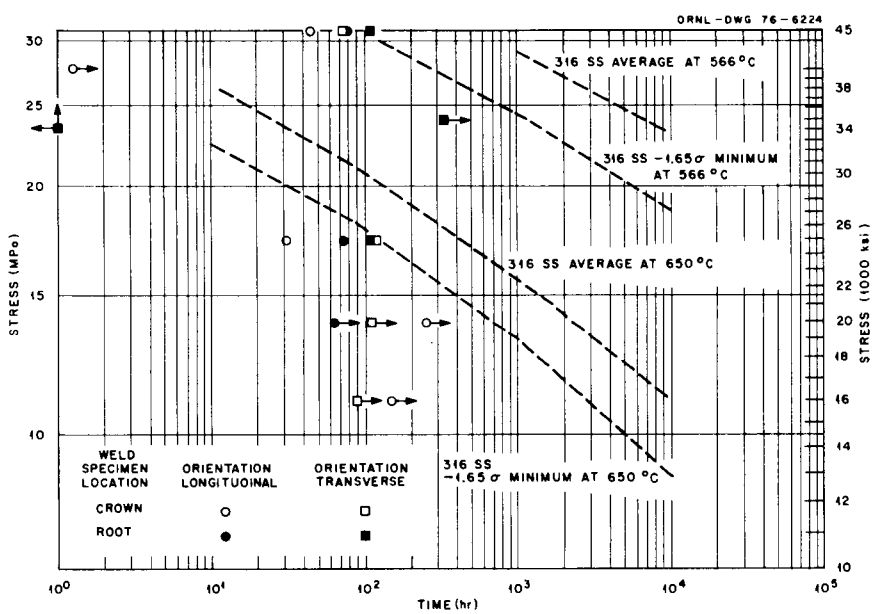

Fig. 3.54. Comparison of Creep-Rupture Properties of Type 16-8-2 Stainless Steel Submerged-Arc Weld Specimens with Type 316 Stainless Steel Base Metal (after Blackburn).

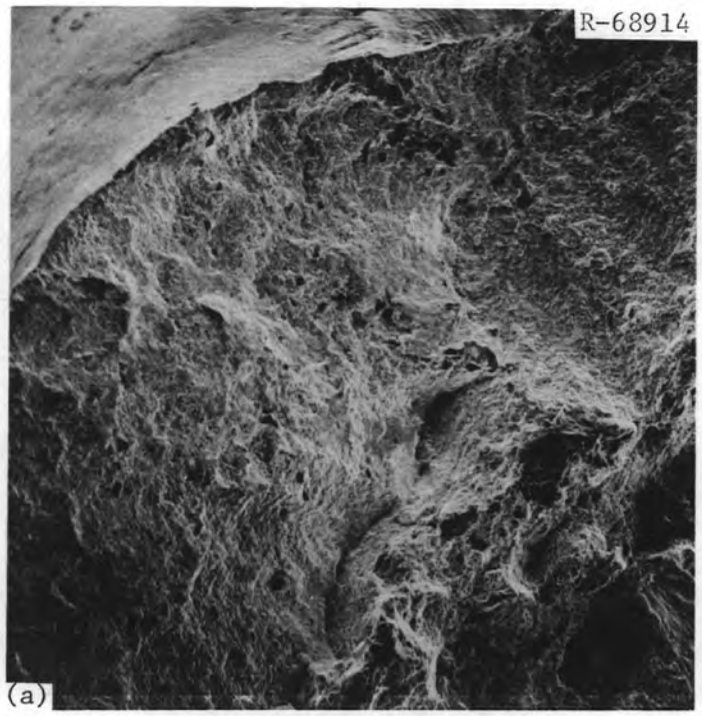

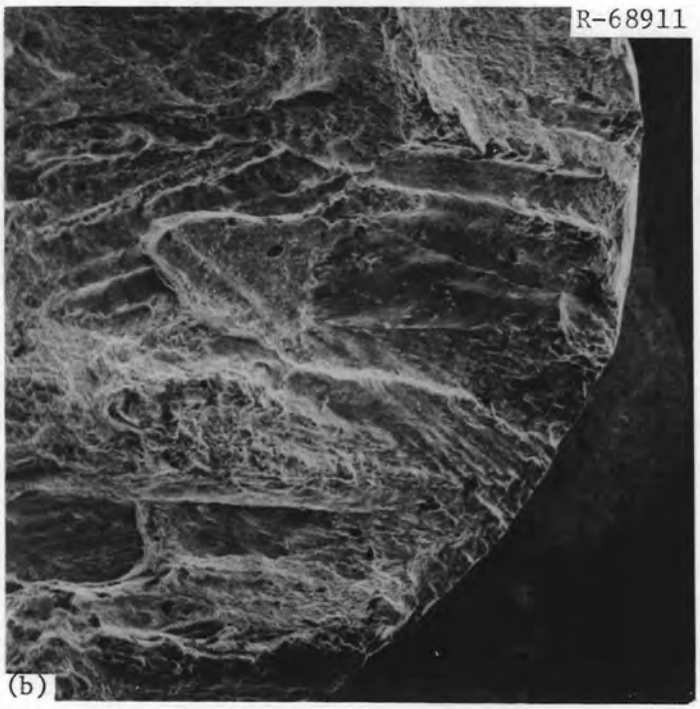

Fig. 3.55. Fracture Surface of Type 16-8-2 Stainless Steel Submerged-Arc Weld That Had Been Creep Tested in the Transverse Direction at 566°C and Failed after 109.6 hr. In most regions, the fracture morphology is transsubstructural with dimples characteristic of ductile shear failures (a), but areas were found where the fracture morphology appeared to be related to the substructure of the weld (b). 50×.

3.4 MECHANICAL PROPERTIES OF STEAM GENERATOR MATERIALS — C. R. Brinkman

3.4.1 High-Strain-Rate Properties of 2 1/4 Cr-1 Mo Steel — R. L. Klueh

We have completed our studies on the high-strain-rate tensile properties (0.16 to 144/sec) of normalized-and-tempered 2 1/4 Cr-1 Mo steel.[65] Although the steel is to be used in the CRBRP steam generator in the annealed condition, the normalized-and-tempered data should have relevance for welds. These high-strain-rate data have been combined with previous data obtained at lower strain rates. A report has been prepared[66] and is summarized here.

The tensile properties of a normalized-and-tempered 2 1/4 Cr-1 Mo steel were studied over the temperature range 25 to 566°C and the strain rate range 2.67×10^{-6} to 144/sec. In this heat-treated condition, the microstructure was entirely bainite.

The yield stress for a given strain rate decreased continuously with increasing temperature. Except at 25 and 566°C, there was relatively little change in yield strength with strain rate at a constant temperature. At 25 and 566°C, the yield stress increased with increasing strain rate. The topography of the relationship between ultimate tensile strength, temperature, and strain rate was somewhat more complicated. For a given strain rate, plots of ultimate tensile strength as a function of temperature had strength peaks, which were the result of hardening due to dynamic strain aging. These strength peaks moved to higher temperatures with increasing strain rate. When these peaks were compared with those previously observed in this same heat of steel in the annealed condition, differences in dynamic strain aging effects were noted and attributed to the different carbides in the microstructures of the two steels. The total elongation and reduction of area were little affected by strain rate and temperature except at 566°C, where these quantities increased as the strain rate decreased. Uniform elongation was affected at 510 and 566°C, where it decreased with decreasing strain rate.

3.4.2 Creep-Rupture Properties of 2 1/4 Cr-1 Mo Steel — R. L. Klueh

We previously reported[67] on the effect of heat treatment on the creep rupture properties of sections of 25-mm-thick (1-in.) plate (heat 20017) that had been annealed differently. Two sections of plate were furnace cooled (fully annealed) at different rates after austenitization [1 hr at 927°C (1700°F)]. These two plates were referred to as AN-1 and AN-2; AN-1 was cooled to 700°C (1292°F) (most of the transformation to proeutectoid ferrite is complete by the time the temperature reaches 700°C) in about 3.5 hr, AN-2 in about 4.8 hr. We also tested a section of plate that had been isothermally annealed [after 1 hr at 927°C it was cooled at about 83°C/hr (150°F/hr) to 704°C (1300°F), held for 2 hr, then furnace cooled]; this heat treatment was referred to as IA.

Figure 3.56 shows the creep-rupture curves for the plates given these different heat treatments. Two types of creep curves were observed:[68] a classical creep curve with single primary, secondary, and tertiary creep stages; a nonclassical creep curve with two steady-state stages (i.e., instead of increasing to rupture after the first steady-state stage, as in classical creep, the creep rate again decreases, becomes constant, then increases to rupture).

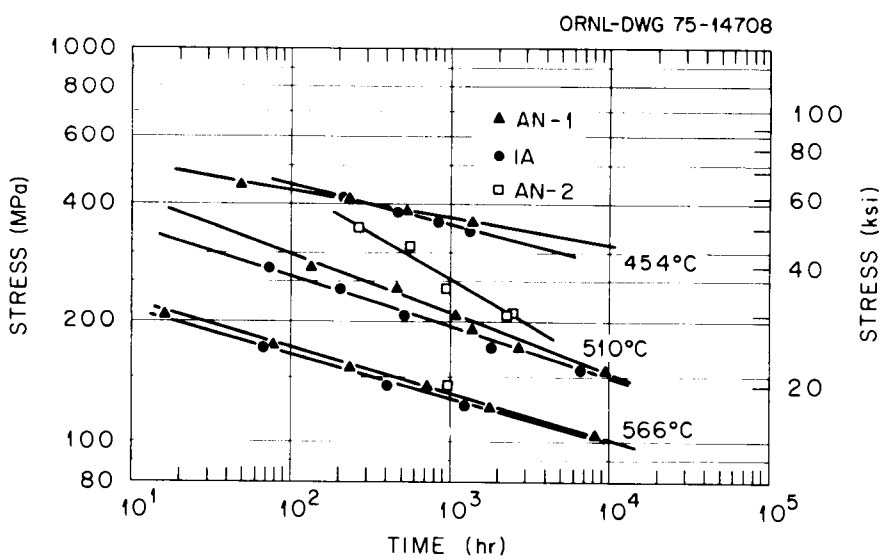

Fig. 3.56. Creep Rupture Curves for 2 1/4 Cr-1 Mo Steel at 454, 510, and 566°C (850, 950, and 1050°F).

When the creep rates were plotted as a function of stress, it was concluded that the second steady-state stage was the one that should be used to define the creep strength. It is felt that during the first steady-state stage interaction solid solution hardening controls the creep rate,[68,69] and during the second steady-state stage, the creep rate is controlled by the movement of dislocations through the Mo_2C precipitate in the proeutectoid ferrite. Next quarter we intend to discuss interaction solid solution hardening in some detail and explore the implications of this process on secondary and tertiary creep. In this report we intend to give a general discussion of the rupture and minimum creep rate results.

From an examination of the creep rupture curves at 510°C given in Fig. 3.56, the large data scatter observed when data are collected from various sources[70] is now easily understood. These data show that for the slight difference in cooling rate used in this study, a considerable variation in properties can result. When data are compiled from different sources,[70] not only do differences in heat treatment affect the properties but heat-to-heat variations in composition can also play a role. In reality, these chemical differences also give rise to heat treatment effects: composition changes affect the hardenability of the steel, which in turn affects the type of microstructure acheived during an anneal.

The approach of properties for all three heat treatments at 510°C is to be expected. The early difference is the result of the difference in interaction solid solution strengthening in the different heat treatments. At longer rupture times the properties are determined more and more by the Mo_2C-strengthtned matrix. With time these microstructures become similar, and the properties for each approach one another. If we could determine the minimum creep rate for the second steady-state stage for AN-2 at 510°C, it should also approach that for the other two heat treatments as the stress is lowered. Indeed, such an approach of properties for all three heat treatments is observed at 566°C (Fig. 3.56). Because diffusion is more rapid at the higher temperature, the approach of properties occurs more rapidly. The

divergence of properties for AN-1 and IA at 454°C indicates that the stronger interaction solid solution strengthening effect noted for AN-1 at 510 and 566°C has a considerable effect at this lower temperature.

This discussion ignores the eventual transformation of the Mo_2C to the eta carbide. Such a change from dispersion strengthening by a high density of small needle- and platelike precipitate particles to much fewer large globular particles could affect the properties. However, this effect, if it occurs, should occur at times somewhat beyond those of the present tests.[71,72]

The effect of stress on creep rate is generally analyzed according to the power law equation

$$\dot{\varepsilon} = A\sigma^n \exp(-Q/RT) \ ,$$

where A and n are constants, Q the activation energy for creep, R the gas constant, and T the absolute temperature. Examination of the minimum creep rate curves previously given[67] indicates that, for a given temperature, n is a constant for each steady-state stage. However, n varies with temperature and heat treatment, and n is different for the two steady-state stages.

It is interesting to note that n appears to go through a minimum as the temperature is decreased from 566 to 454°C. The n values determined from these tests are given in Table 3.24. Generally n decreases with decreasing temperature.[72] The reason for the minimum is not understood, but it must involve the interaction solid solution hardening. We must therefore agree with Baird et al.,[73] who concluded that an examination of the stress dependence and activation energy for creep to determine mechanisms can "give valuable information on alloys which are stable during the creep test, but for the type of alloys examined in the present work, where metallurgical changes occur during creep, measurements of stress dependence and activation energy are unlikely to give meaningful results."

Table 3.24. Stress Exponents for 2 1/4 Cr-1 Mo Steel Given Different Anneals

Heat Treatment	n, Stress Exponent				
	454°C	510°C		566°C	
		Stage 1	Stage 2	Stage 1	Stage 2
AN-1	20.6	8.3	5.6	12.1	11.1
IA	10.3	8.9	7.4	12.1	14.3
AN-2		6.7			

3.4.3 Observations of Curvature in Elevated-Temperature Stress-Rupture Isotherms — R. L. Klueh and V. K. Sikka

Although the rupture-life model submitted[74] for the *Nuclear Systems Materials Handbook* (NSMH) for annealed 2 1/4 Cr-1 Mo steel for the temperature range 371 to 593°C (700–1100°F) is linear in log σ_R vs log t_R (σ_R is the stress to cause rupture in time t_R), it is well known that such plots can be curved. Some possible reasons for curvature in 2 1/4 Cr-1 Mo steel are: a change in fracture mechanism from transgranular to intergranular, precipitation reactions, and oxidation. The effects of a change in fracture mechanism and specimen oxidation on curvature are easily understood. Several precipitation effects could affect curvature. The first precipitate to form in proeutectoid ferrite is a high density of Mo_2C, which forms early in the test (or during heat treatment) and enhances the creep strength. During elevated-temperature exposure, however, Mo_2C transforms to $M_{23}C_6$ and M_6C. These latter carbides form as coarse, globular particles and provide very little dispersion strengthening. Simultaneously, molybdenum and chromium are lost from solution to form the molybdenum-rich M_6C and the chromium-rich $M_{23}C_6$. The loss of these solid solution elements — especially molybdenum — will further lower the creep strength.[73,75] Precipitation effects have been used[76] to explain the curvature in the creep-rupture curves of a bainitic 2 1/4 Cr-1 Mo steel.

In general, the processes described above lead to a concave downward slope in the curve: the actual rupture life after such a downward curvature is less than would be predicted from an extrapolation of the short-time curve. Since the mechanisms that lead to such changes in curvature are generally thermally activated processes, the tendency toward curvature is more easily detected at higher temperatures, where the curvature becomes apparent in the shortest times.

In the development of the creep-rupture model given in the NSMH, all the available data (includes all U.S. and Japanese data apparently meeting Code requirements) between 454 and 600°C (850 and 1112°F) were fitted with various appropriate empirical models, and the model that best fit the data was chosen to represent the data and make the appropriate extrapolations. When the resulting calculated isothermals were examined with all the included data and its inherent scatter, the ability of the model to represent the data was apparent.[74] Furthermore, when the data were presented in this form, no curvature was readily apparent.

To determine whether curvature was inherent in individual heats, since it might be obscured by the scatter that results when the data from all heats were combined, creep-rupture curves for individual heats were examined. For temperatures up to and including 593°C (1100°F), no curvature could be detected.

In the case of the Japanese data (data were available from Sumitomo and Nippon Kokan) package used for this correlation, rupture data were also available at 600°C (1112°F). Since this temperature is only slightly above the upper limit of the temperature range for which the correlation was required [593°C (1100°F)], these data were included in the analysis. The Japanese data are summarized in Table 3.25 and compared with the American data in Table 3.26. Examination of these data as a whole and on an individual heat basis indicated that there was apparently curvature beyond 10^4 hr at 600°C (1112°F). As seen in Fig. 3.57, however, the curvature is generally determined by only one — or at most two — data points. Two straight line segments have been drawn through several of the heats to represent the change in slope on the log t_R vs log σ_R plots.

Table 3.25. Summary of Japanese Creep-Rupture Data on 2 1/4 Cr-1 Mo Steel

Test Temperature (°C)	Source	Number of Heats		Number of Points			Longest Time, hr	
		Bar	Tube, Pipe	Bar	Tube, Pipe	Total	Bar	Tube, Pipe All Forms
500	NKK[a]	2	4	6	16	22	9,670	34,830
	Sumitomo[b]		4		39	39		7,846
550	NKK	3	5	11	20	31	18,445	50,190
	Sumitomo		4		16	16		14,584
600	NKK	3	6	15	32	47	23,590	28,270
	Sumitomo		4		21	21		10,443
650	NKK	2	4	7	22	29	3,014	4,917
	Sumitomo		4		22	22		11,001
700	NKK	2	2	5	9	14	501	1,080

[a]Room-temperature ultimate tensile strength varied from 455 to 517 MPa (66–75 ksi). Carbon varied from 0.09 to 0.12%. Specimen size not specified.

[b]Room-temperature ultimate tensile strength varied from 503 to 517 MPa (73–75 ksi). Carbon varied from 0.1 to 0.15%. Specimen size = 10 by 35 mm (0.39 by 1.38 in.) round bar.

Table 3.26. Comparison Between United States and Japanese Creep Rupture Data on 2 1/4 Cr-1 Mo Steel

Test Temperature		United States					Japanese				Estimated[b] Break Time (hr)
		Number of Data				Longest Time (hr)	Number of Data			Longest Time (hr)	
(°C)	(°F)	Bar/Rod	Plate	Tube/Pipe	Total		Bar/Rod	Tube/Pipe	Total		
454	850		4		4	1,435					3×10^7
482	900										5×10^6
500	932						6	55	61	34,830	1.6×10^6
510	950		6	5	11	4,902					9.2×10^5
538	1000	6		75	81	22,242					1.9×10^5
550	1022						11	36	47	50,190	1×10^5
566	1050		4	58	62	10,673					4.4×10^5
593	1100	41		132	136	29,286					1.2×10^4
600	1112						15	53	68	28,270	8.5×10^3
621	1150			15	15	1,465					3.3×10^3
649	1200	20		47	67	16,182					9.8×10^2
650	1202						7	44	51	11,001	9.4×10^2
700	1292						5	9	14	1,080	1.3×10^2
704	1300			1	1	49					1.12×10^2
TOTAL DATA POINTS					377				241		

[a]ORNL linear model included rupture data on test temperatures up to 600°C (1112°F).

[b]Break time is the time at which stress-rupture time isotherm plot is expected to show a downward curvature.

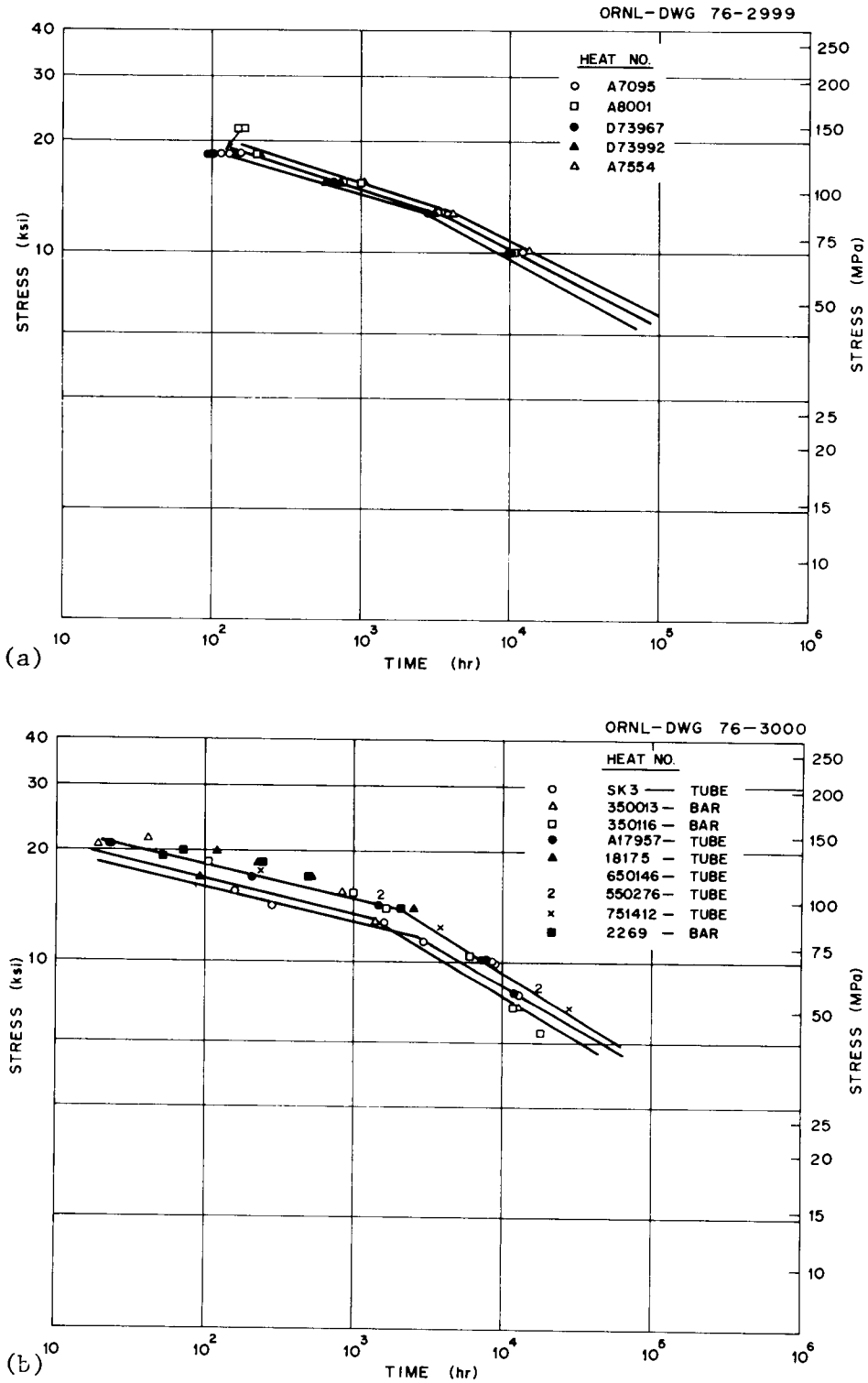

Fig. 3.57. Japanese Rupture-Life Data at 600°C. Selected visual-fit lines have been drawn. (a) Sumitomo. (b) Nippon Kokan.

After curvature was detected at 600°C (1112°F) on the Japanese data, the American data at 593°C (1200°F) were reexamined, and we concluded that the reason no curvature was detected in these data was that the tests, for a given heat, were usually not conducted at stresses below which significant curvature existed. In some instances, curvature could be implied, but because of the sparse data, the existence of such curvature was dubious.

Several points are obvious from these observations on curvature. Downward curvature for times up to 10^4 hr apparently becomes important only at about 600°C (1112°F). To establish curvature at 593 and 600°C (1100 and 1112°F), more data are required beyond 10^4 hr. With the exception of the Japanese tests, such data were not available. When the data in either Fig. 3.57(a) or (b) are considered as a whole, scatter makes the curvature less apparent. This becomes even more obvious when the data of Fig. 3.57(a) and (b) are combined. Given the method of analysis for the NSMH, the reason for the arrival at a linear model is not difficult to understand.

In addition to the significant amount of long-time data available at 600°C (1112°F) in the Japanese data, data were also available at 650 and 700°C (1202 and 1292°F). In an effort to determine the nature of the kinetics of the process that causes the curvature, the data at 600°C (1112°F) along with those at 650 and 700°C (1202 and 1292°F) were represented by two straight line segments on a logarithmic plot [the Sumitomo and Nippon Kokan data were treated separately, although all heats were combined, that is, only one curve was fitted to the data corresponding to Fig. 3.57(a) and (b)]. Hence, rupture life, t_R, can be represented as a function of rupture stress, σ_R:

$$t_R = A\sigma_R^n \ , \tag{43}$$

where A and n are constants. On a logarithmic plot, two straight line segments result at high temperatures. At high stresses, $n \approx -8$ to -10 [at temperatures below 600°C (1112°F), this line should represent all the data], while at stresses below the break, $n \approx -2.5$ to -3.5.

Assuming that the process that causes the change in curvature is thermally activated, we can express the time at which the break occurs, t_B, as a function of the absolute temperature, T:

$$1/t_B = Be^{-Q/RT} , \tag{44}$$

where B is a constant, Q the activation energy, and R the gas constant. Figure 3.58 shows t_B as a function of $1/T$, from which, by methods of least squares, B and Q were found to have values of 1.8×10^{-14}/hr and 297.3 kJ/mole (71,060 cal/mole), respectively.

From these results we can estimate the position of the break at other temperatures. An estimate for t_B at 566°C (1050°F) gave values

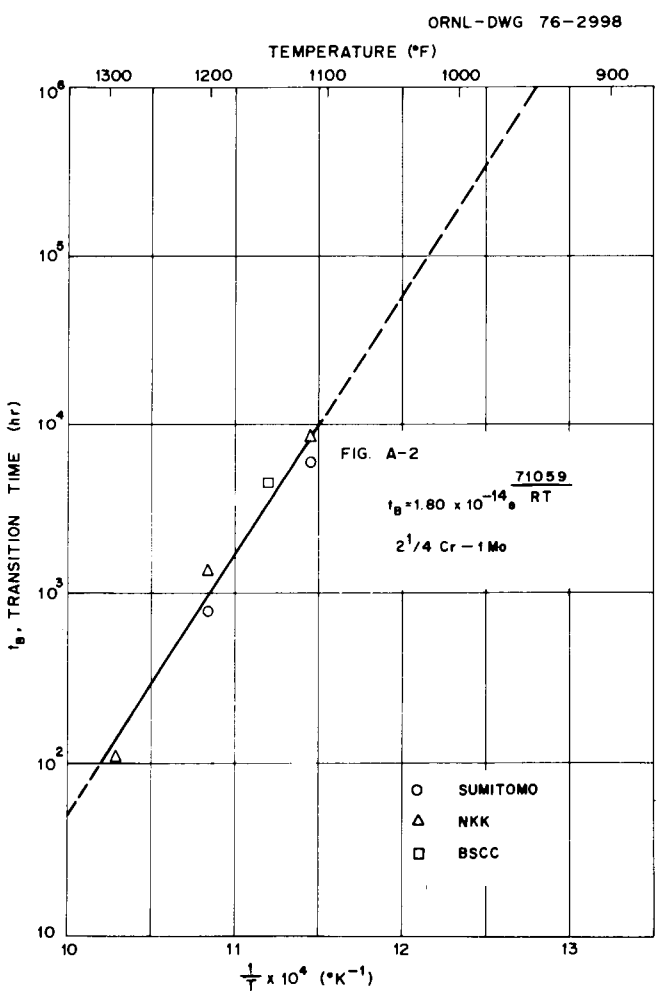

Fig. 3.58. The Estimated Time at Which a Break (Slope Change) Occurs in the Creep-Rupture Curves as a Function of the Reciprocal of Absolute Temperature. Activation energy shown in equation for t_B is in cal/mole; it is 297.3 kJ/mole.

approaching 5×10^4 hr, indicating that a straight line should adequately represent the data to 5×10^4 hr. At lower temperatures, a similar break should occur, but at times greater than 10^5 hr.

Equation (44), which was derived from the Japanese data, gave very good predictions for similar behavior that was detected in British long-time data[77] at elevated temperatures (these data were not used in the NSMH correlation). Hence, this break appears to be well defined at elevated temperatures, and at temperatures below about 550°C (1022°F), a straight line should adequately represent the creep-rupture behavior to beyond 1×10^5 hr.

We believe that the break in the creep-rupture curves is the result of oxidation, which decreases the specimen cross sectional area, thus raising the effective stress. Murphy and Branch[78] have shown that at 593°C (1200°F) the metal loss due to oxidation can result in the equivalent of an increase in stress of about 10% over 50,000 hr. At 566°C (1050°F) they found no effect of oxidation over a similar time period. Such a change in stress could explain our observations. We are presently conducting tests to confirm this conclusion.

Murphy has pointed out that oxidation under restricted air conditions of the creep rupture tests was an insignificant factor in terms of metal wastage over times of up to 50,000 hr at 566°C (1050°F), but a significant factor over similar times at 593°C (1100°F). In a recent (Oct. 23, 1975) telephone conversation, Murphy again pointed out that the metal wastage at 593°C (1100°F) and higher temperatures could be very important and should be incorporated in design.

To determine the effect of this curvature on the model presented in NSMH, Fig. 3.59 shows the straight line model at 600°C (1112°F), and it is compared with the two straight lines determined from the analysis of the Japanese data (the combined data from Fig. 3.57). As seen, the proposed linear model adequately represents the data that display curvature, at least to about 10^5 hr. Certainly, the lower limits, which reflect our uncertainty in the linear model, account for the error caused by the downward curvature.

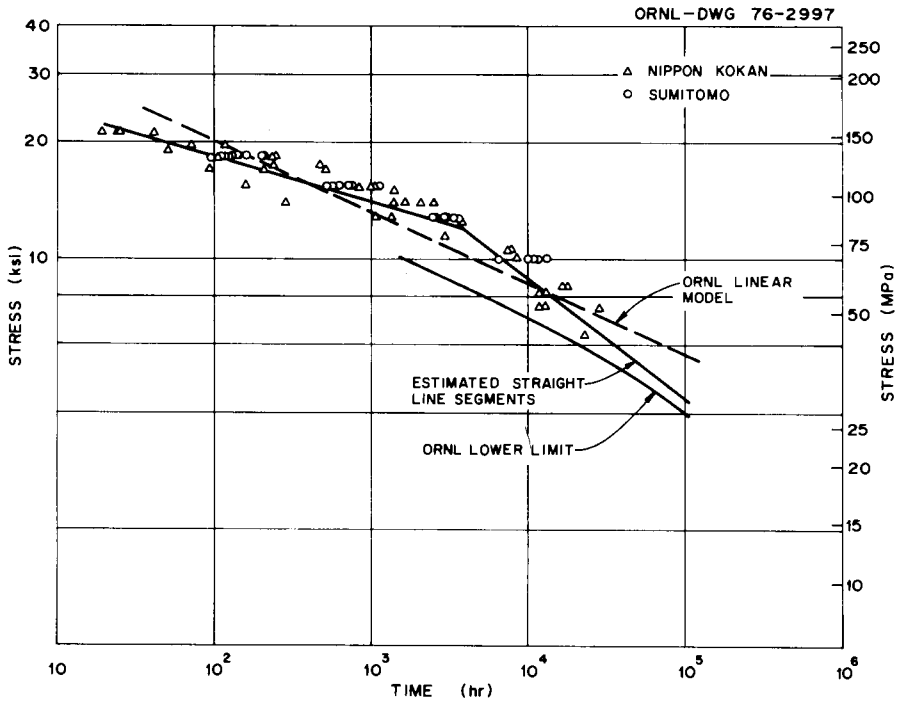

Fig. 3.59. A Comparison of the ORNL Linear Rupture Life Model with the Two Straight-Line Segments Fit to the Japanese 600°C Data. Also shown is the ORNL lower limit.

3.4.4 Fatigue Behavior of 2 1/4 Cr-1 Mo Steel — C. R. Brinkman

3.4.4.1 Time-Dependent Fatigue — Estimates of Worst Effects — M. K. Booker

Data are currently being obtained to assess the effects of hold periods at peak strain in strain-controlled fatigue tests of 2 1/4 Cr-1 Mo steel. Unfortunately, obtaining such data is tedious, expensive, and time-consuming. Practical considerations dictate that only very short ($\leq$0.5 hr) hold periods be applied. Efforts are under way to analyze the data to allow estimates of behavior over the long periods of time incurred in real situations. To provide information for preliminary design procedures, the "worst effects" due to hold periods have been estimated.

The extrapolation technique used is based on the method of strain range partitioning,[79] which involves partitioning the inelastic strain range traversed by a cycling specimen into four types:

$\Delta\varepsilon_{pp}$ = tensile plastic strain reversed by compressive plastic strain.

$\Delta\varepsilon_{cc}$ = tensile creep strain reversed by compressive creep strain,

$\Delta\varepsilon_{cp}$ = tensile creep strain reversed by compressive plastic strain,

$\Delta\varepsilon_{pc}$ = tensile plastic strain reversed by compressive creep strain.

Here, "plastic" strain is defined as time-independent inelastic strain, while "creep" strain is defined as time-dependent inelastic strain. Results of analysis of the current data by this technique were reported earlier.[80] Briefly, the method involves two steps. First, the four types of strain are related respectively, by "life relationships," to N_{pp}, N_{cc}, N_{cp}, and N_{pc}, where N_i is the expected cyclic life of a specimen cycled in pure $\Delta\varepsilon_i$ strain. Then, for a given loading situation (and a given set of partitioned strain ranges), the expected life, N, is given by

$$\frac{F_{cp}}{N_{cp}} + \frac{F_{pc}}{N_{pc}} + \frac{F_{cc}}{N_{cc}} + \frac{F_{pp}}{N_{pp}} = \frac{1}{N} , \tag{45}$$

where, for example $F_{cp} = \Delta\varepsilon_{cp}/\Delta\varepsilon_{\text{inel}}$, $\Delta\varepsilon_{\text{inel}}$ being the total inelastic strain range.

This procedure yielded good results in predicting the data obtained thus far. If the method is still applicable to tests with longer hold periods, then it should be possible to predict the life with such hold periods. A method for doing this is described below.

The goal is to calculate N_f at a given temperature, total strain range ($\Delta\varepsilon_t$), and hold period. Clearly, if one can estimate the total stress range ($\Delta\sigma$) associated with the given loading conditions, then

$$\Delta\varepsilon_{\text{inel}} = \Delta\varepsilon_t - \Delta\sigma/E , \tag{46}$$

where E is Young's modulus. Note here that $\Delta\sigma$ is the maximum stress range traversed and does not include a reduction for the effects of relaxation during the hold period. (Fig. 3.60). Figure 3.61 illustrates the data obtained thus far at 482°C (900°F) plotted in terms of stress amplitude, $\Delta\sigma/2$. No significant mean stresses have been observed. The data exhibit quite a bit of scatter, but trends can be observed. For instance, there is no discernible difference between tests with tensile holds and those with compressive holds. It appears that the inposition of a brief hold period results in a decrease in $\Delta\sigma$ from the continuous cycling tests. However, the effect appears to saturate rapidly, with little additional decreases in $\Delta\sigma$ seen by extending the hold period past 0.01 hr. Clearly, data from tests with longer hold periods are desirable. While it is impractical to run failure tests, cyclic stress-strain tests with longer hold periods and at lower strain ranges are currently planned. The curves shown in Fig. 3.61 are visual estimates based on the present data. They allow one to estimate $\Delta\sigma$ and thus $\Delta\varepsilon_{inel}$ for a given $\Delta\varepsilon_t$ and hold time.

The next step is to estimate the individual strain range components. At present, too few data are available to allow quantitative analysis of tests involving both tensile and compressive holds. Tests with tensile or compressive holds can be treated very similarly, however, except that

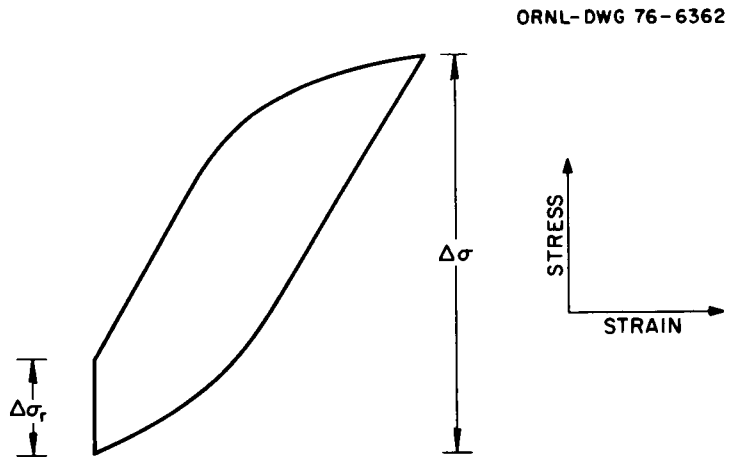

Fig. 3.60. Hysteresis Loop for a Test Involving a Hold Period at Peak Compressive Strain.

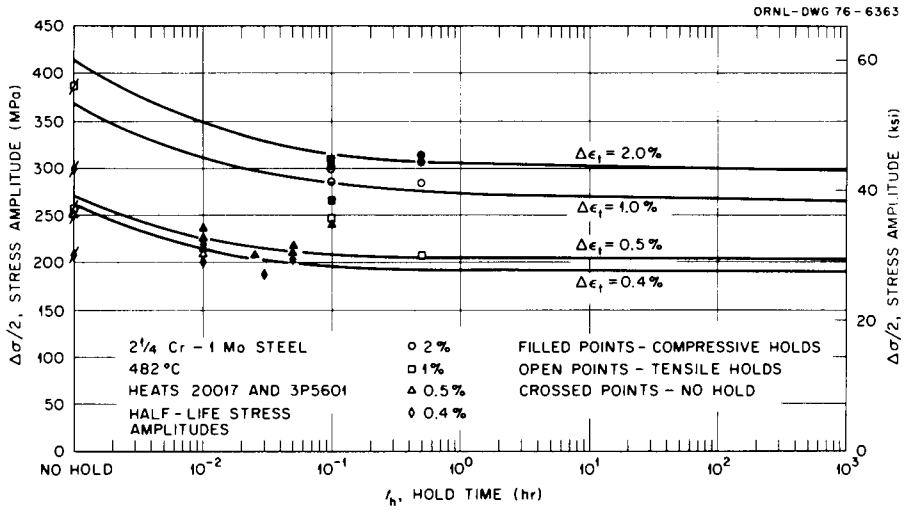

Fig. 3.61. Variation of Half-Life Stress Amplitude with Hold Time for Two Heats of Isothermally Annealed 2 1/4 Cr-1 Mo Steel at 482°C (900°F).

one involves $\Delta\varepsilon_{cp}$ strain, and the other $\Delta\varepsilon_{pc}$ strain. Previous results[80] have shown that compressive holds are the most damaging type for 2 1/4 Cr-1 Mo steel, so these will be treated as an example. Also, the discussion below applies to tests at 482°C (900°F). If $\Delta\sigma_r$ is the magnitude of the total stress decrease during relaxation (Fig. 3.60), $\Delta\varepsilon_{pc}$ and $\Delta\varepsilon_{pp}$ are given by

$$\Delta\varepsilon_{pc} = \Delta\sigma_r/E \tag{47}$$

and

$$\Delta\varepsilon_{pp} = \Delta\varepsilon_{\text{inel}} - \Delta\varepsilon_{pc} \ . \tag{48}$$

Examinations of relaxation curves obtained from the hold period tests performed to date indicate that the curves can be well approximated by a form of the Gittus equation,[81] expressed as

$$\ln(\sigma_0/\sigma) = Ct^m \ , \tag{49}$$

where σ_0 is the stress at the beginning of the relaxation ($\sigma_0 = \Delta\sigma/2$), and σ and t are the instantaneous stress and time during relaxation. Figure 3.62 illustrates the behavior of the constants C and m from data obtained thus far. Note that Eq. (49) can be extrapolated in time if the values of the constants are known. The scatter in their values is great. Within the limits of data availability, these values have been approximated by

$$C = 0.47 \qquad (\Delta\varepsilon_t \geqslant 1.0\%) \ , \tag{50}$$

$$C = 0.3 \qquad (\Delta\varepsilon_t \leqslant 0.5\%) \ , \tag{51}$$

$$m = 0.14 \ . \tag{52}$$

Values of C for $\Delta\varepsilon_t$ between 0.5 and 1.0% may be obtained by linear interpolation. Clearly more data at lower strain ranges and for longer hold periods are needed to verify these equations, which are merely interim approximations. Curves constructed by use of these equations do appear representative of available data, however.

Now $\Delta\sigma/2$ (and thus σ_0) can be estimated from Fig. 3.61 for the situation of interest. If t_h is the hold time of interest, substituting t_h for t in Eq. (49) allows one to calculate σ_h, the stress at the end of the hold period. Then, $\sigma_0 - \sigma_h$ yields $\Delta\sigma_r$, from which Eqs. (47) and (48) allow one to calculate $\Delta\varepsilon_{pc}$ and $\Delta\varepsilon_{pp}$. Finally, Eq. (45) allows one to predict N_f under these conditions. Figure 3.63 shows an estimated relationship between $\Delta\varepsilon_t$ and N_f at 482°C with a 100-hr compressive hold period, along with experimental data for shorter hold periods. The prediction appears quite reasonable, although it is an approximation.

Using the strain range partitioning approach, one can very simply construct a worst-effects curve without most of the above approximations. Since $\Delta\varepsilon_{pc}$ is the most damaging strain component, simply let $\Delta\varepsilon_{\text{inel}} = \Delta\varepsilon_{pc}$. Then, N_f is merely N_{pc}, and one has a curve such as that also shown in Fig. 3.63, which should represent the lowest expected cyclic life due to hold periods.

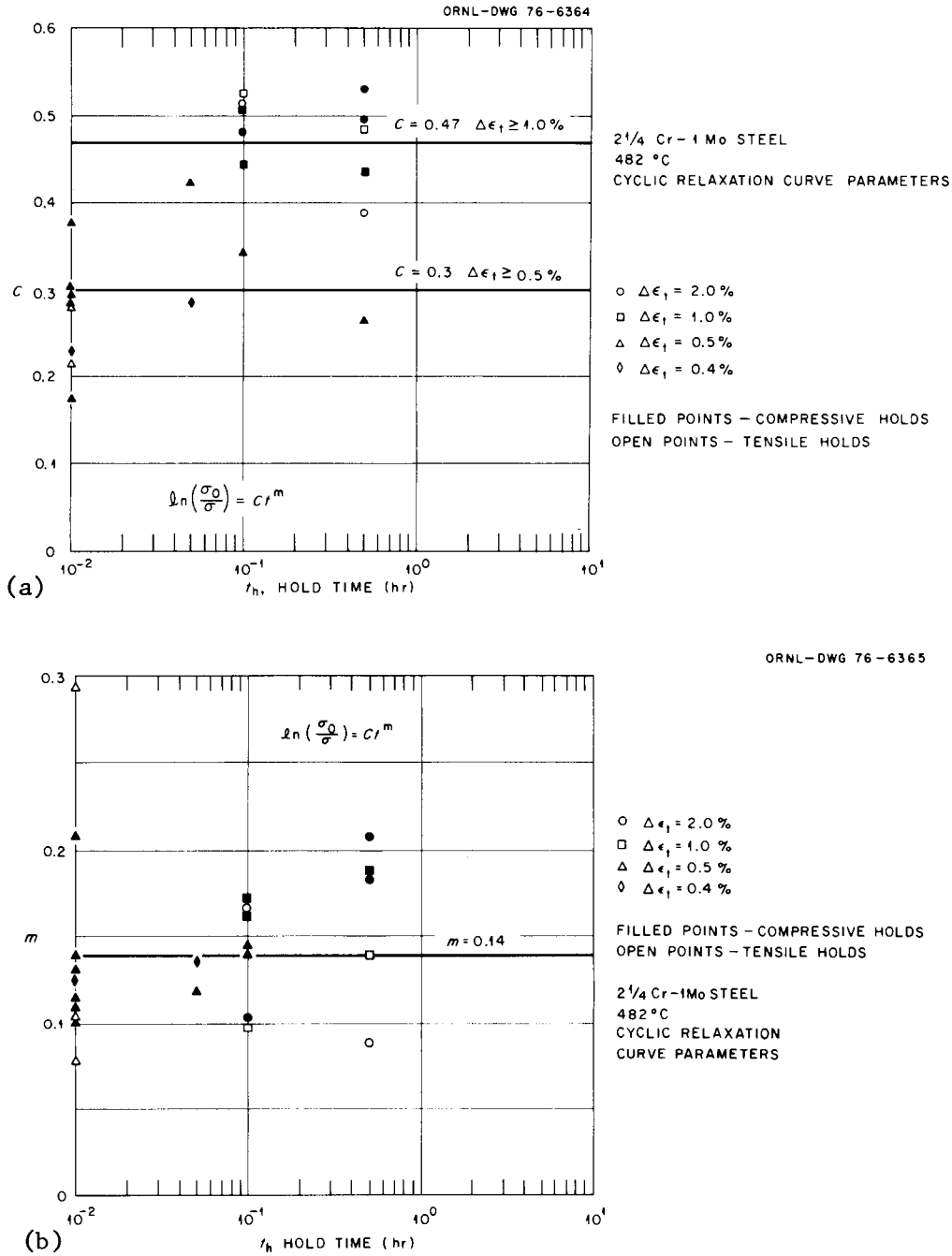

Fig. 3.62. Variation of Gittus Equation Constants with Hold Time at 482°C for Isothermally Annealed 2 1/4 Cr-1 Mo Steel at Various Strain Ranges.

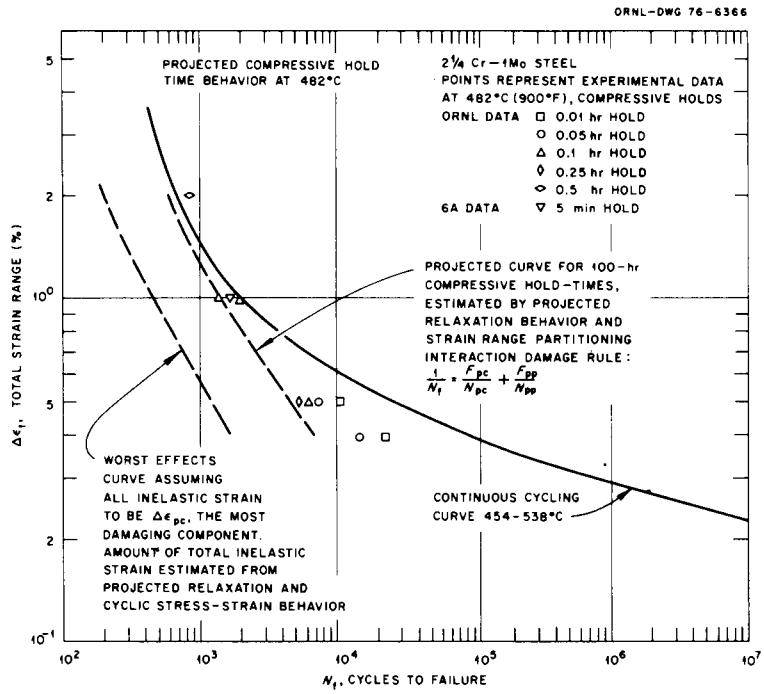

Fig. 3.63. Estimated Worst Effects of Hold Periods on the Fatigue Life of Isothermally Annealed 2 1/4 Cr-1 Mo Steel at 482°C (900°F).

Clearly, more data are needed to verify the analysis presented above. This approach does, however, seem promising to aid in many design procedures, and allows one to make maximum use of the available data.

3.4.4.2 Cyclic Stress-Strain Behavior — M. K. Booker, B.L.P. Booker* and J. P. Strizak

Three heats of isothermally annealed plate of 2 1/4 Cr-1 Mo steel have been examined in the ORNL study of the fatigue properties of this material. The data being obtained provide important information on the fatigue life of this material, but other information can also be derived from these tests. For example, reliable inelastic stress analyses require a knowledge of stress-strain response under cyclic loading conditions. This report presents results of the examination of the cyclic stress-strain behavior of 2 1/4 Cr-1 Mo steel during

*Consultant.

strain-controlled fatigue testing. Measurements of the stress range required to maintain an imposed axial strain range were used to indicate cyclic stress-strain response.

All material used came from 25.4-mm-thick plates from commercial heats of 2 1/4 Cr-1 Mo steel. Table 3.27 lists the chemical compositions of the heats tested. Sections of the plates were heat-treated in air according to the following isothermal annealing schedule:

> Austenitize at 927 ± 14°C (1700 ± 25°F) for 1 hr; cool to 704 ± 14°C (1300 ± 25°F) at a maximum cooling rate of 83°C/hr (150°F/hr); hold at 704 ± 14°C for 2 hr; cool to room temperature at a rate not to exceed 6°C/min (11°F/min).

Table 3.27. Chemical Composition of 2 1/4 Cr-1 Mo Steel

Heat Number	Chemical Composition, wt %								
	C	Mn	Si	Cr	Mo	Ni	S	P	N
20017	0.135	0.57	0.37	2.2	0.92	0.16	0.016	0.012	
3P5601	0.12	0.35	0.27	2.3	0.96	0.20	0.022	0.009	0.0135
50557	0.026	0.50	0.27	2.45	1.0		0.009	0.012	0.0125

Fully reversed axial push-pull cyclic tests were conducted in air on hourglass-type specimens using closed-loop electrohydraulic testing machines. Heat 20017 was tested in continuous cycling ($\dot{\varepsilon} = 4 \times 10^{-5}$ to 4×10^{-3}/sec) from room temperature to 538°C (1000°F); heat 3P5601 from 316 to 593°C (600–1100°F), and heat 50557 from 93 to 593°C (200–1100°F). Heats 20017 and 3P5601 were tested at 371°C (700°F) and above with hold periods at maximum strain in tension, compression, or both. Complete experimental details are given elsewhere.[82]

Cycled specimens generally displayed rapid initial hardening. The low-carbon heat exhibited continual hardening at high strain ranges (≈2.0%). At lower strain ranges (<1.0%), it generally maintained stable stress levels throughout most of the test, with some secondary hardening

near the end of the test. Heat 3P5601 maintained essentially stable stress ranges after initial hardening at high strain ranges (≈2.0%). However, for temperatures of 427 to 538°C (800–1000°F), tests at lower strain ranges involved slight cyclic softening after the initial hardening. Higher strain range tests for heat 20017 tended to exhibit continuous hardening below 427°C and relative stability (after initial hardening) at higher temperatures, although some softening occurred after initial hardening at 538°C. Lower strain range tests showed softening after initial hardening at 427–538°C, with half-life stress range dropping to as low as about three-fourths of the maximum value achieved near one-tenth of the cyclic life. Figures 3.64 and 3.65 illustrate the behavior of these three heats in concinuous cycling at a strain rate of 4×10^{-3}/sec.

The above behavior was qualitatively independent of strain rate and brief hold periods (≤0.5 hr). These results are illustrated in Figs. 3.66 through 3.69.

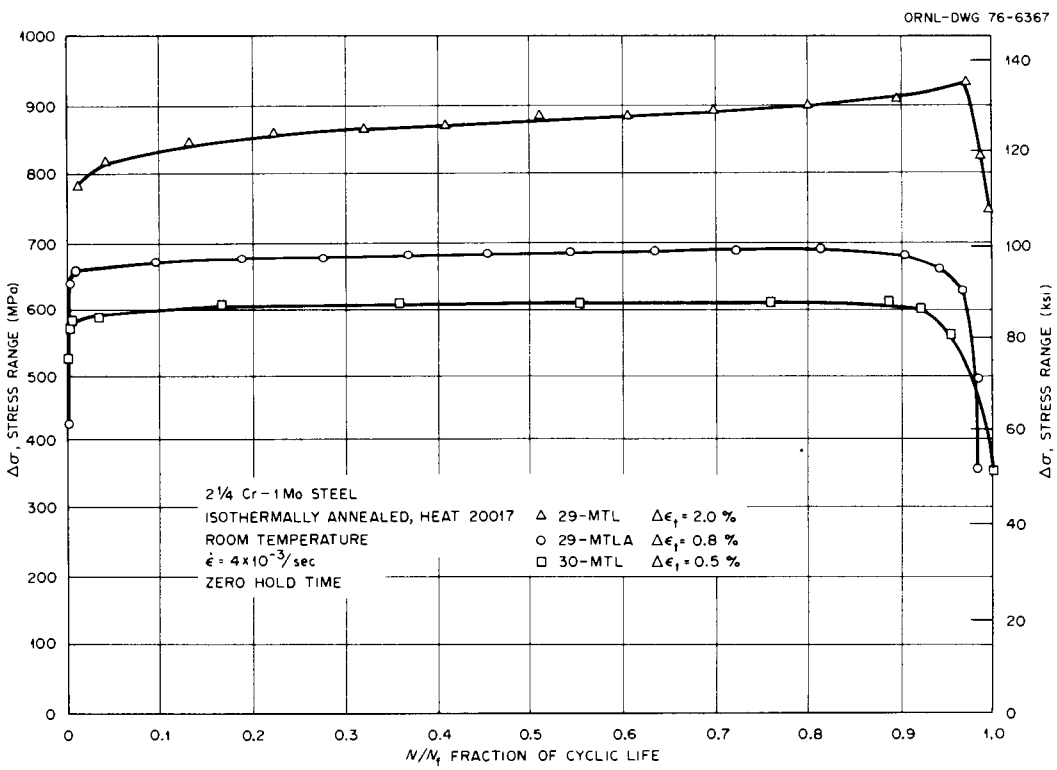

Fig. 3.64. Measured Stress Response During Cycling of Heat 20017 of Isothermally Annealed 2 1/4 Cr-1 Mo Steel at Room Temperature.

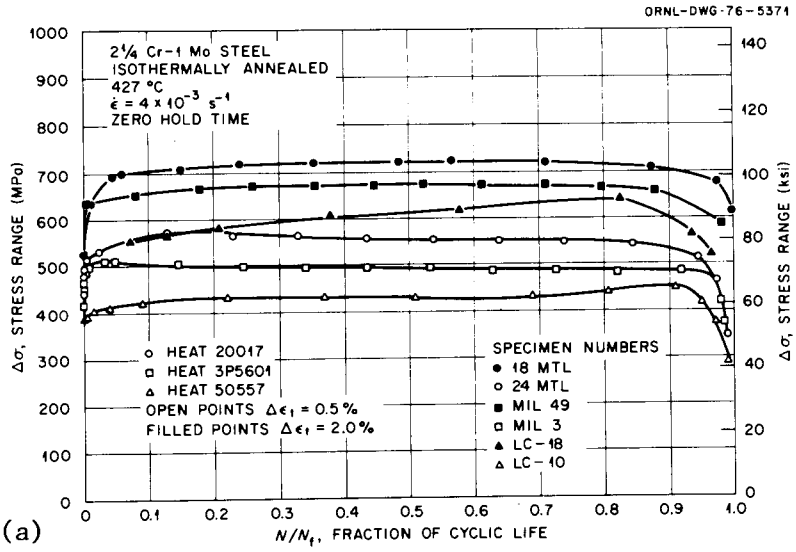

(a)

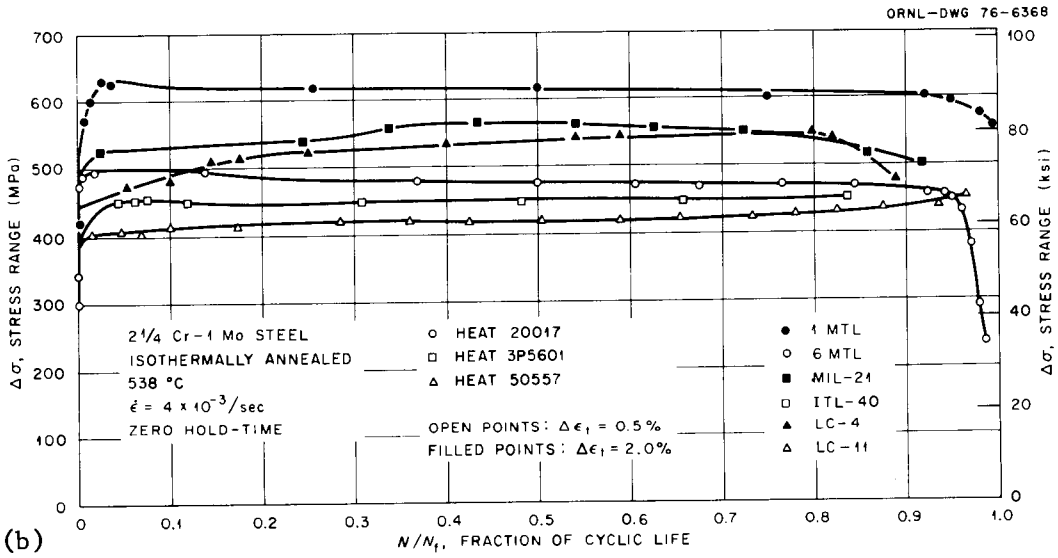

(b)

Fig. 3.65. Measured Stress Response During Cycling of Three Heats of Isothermally Annealed 2 1/4 Cr-1 Mo Steel at (a) 427°C (800°F) and (b) 538°C (1000°F).

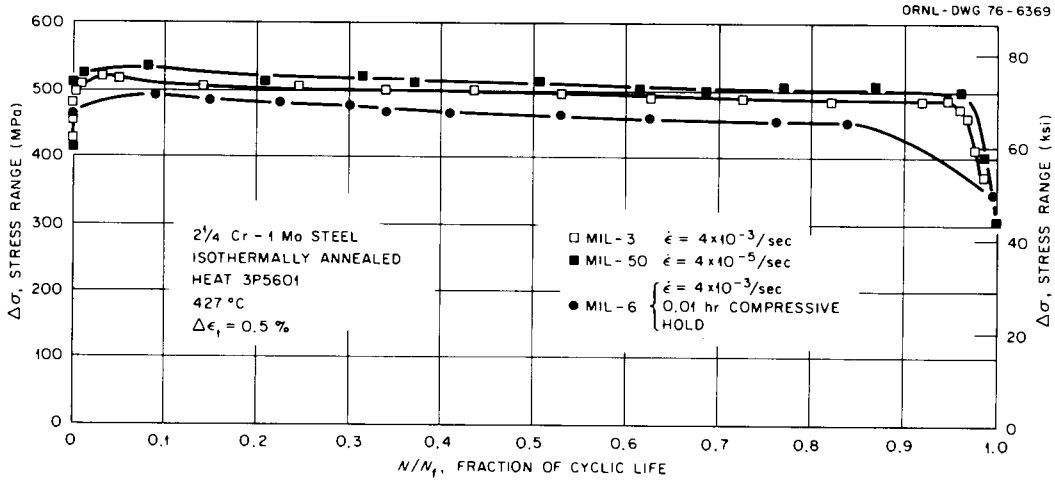

Fig. 3.66. Effects of Strain Rate and Hold Time on the Stress Range of Heat 3P5601 of Isothermally Annealed 2 1/4 Cr-1 Mo Steel at a Strain Range of 0.5% at 427°C (800°F).

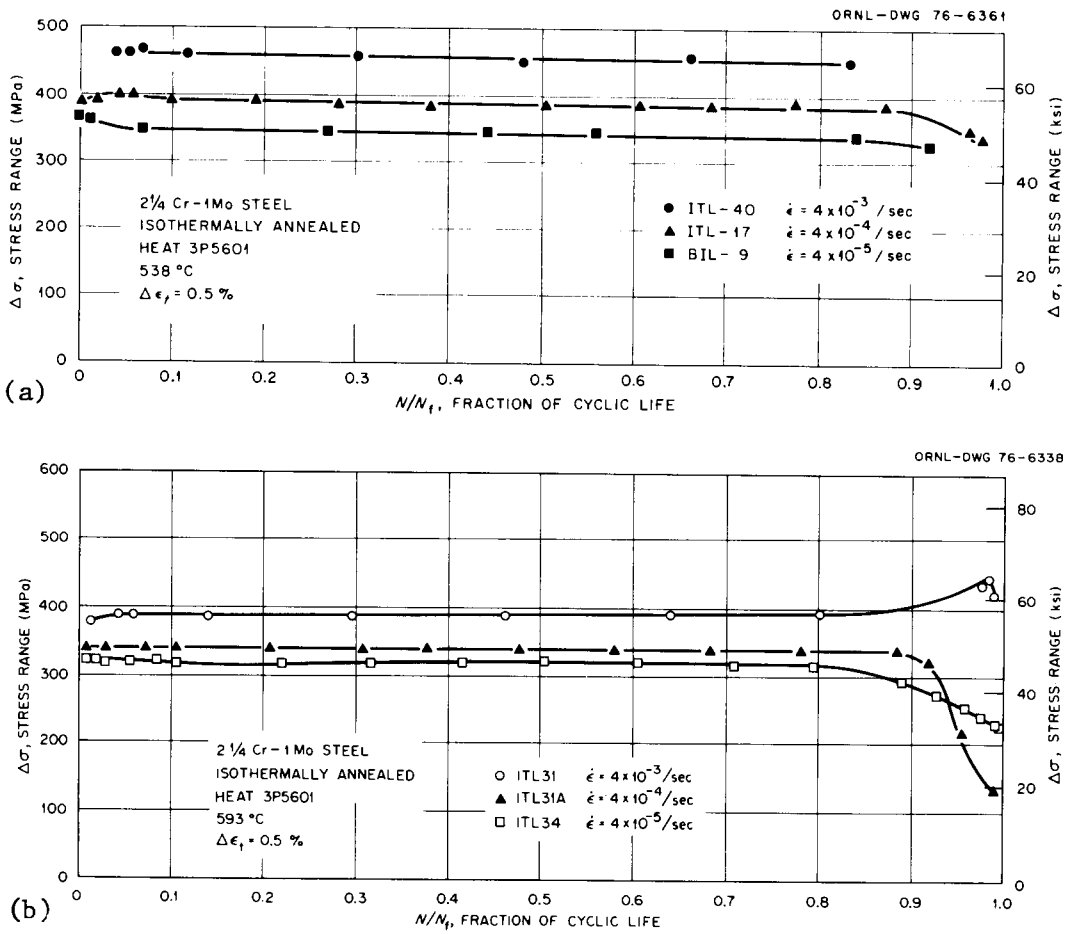

Fig. 3.67. Effects of Strain Rate on the Stress Range of Heat 3P5601 of Isothermally Annealed 2 1/4 Cr-1 Mo Steel at a Strain Range of 0.5% at (a) 538°C (1000°F) and (b) 593°C (1100°F).

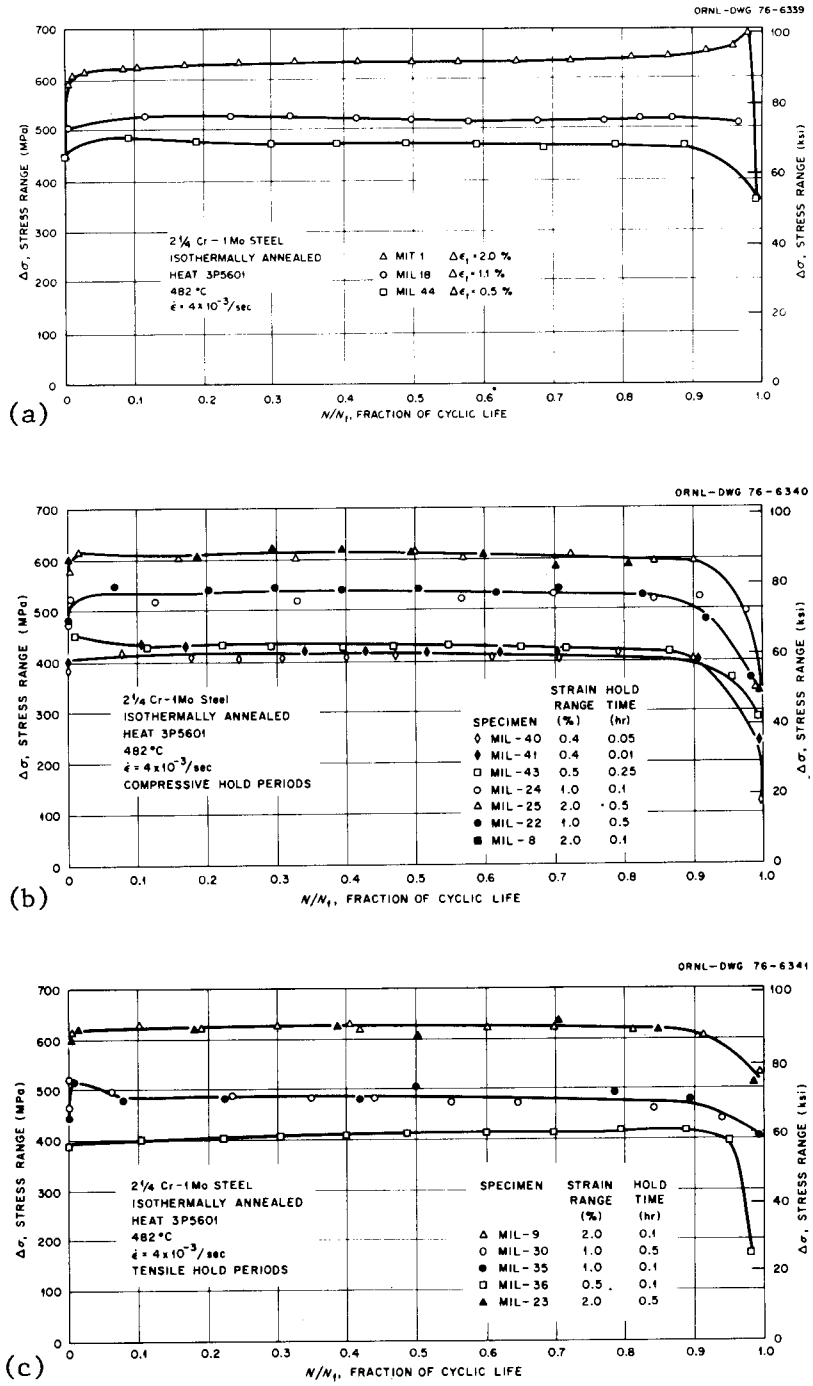

Fig. 3.68. Stress Range as a Function of Fraction of Cyclic Life for Isothermally Annealed Heat 3P5601 of 2 1/4 Cr-1 Mo Steel at 482°C; $\dot{\varepsilon} = 4 \times 10^{-3}$/sec. (a) Continuous cycling. (b) Compressive hold periods. (c) Tensile hold periods.

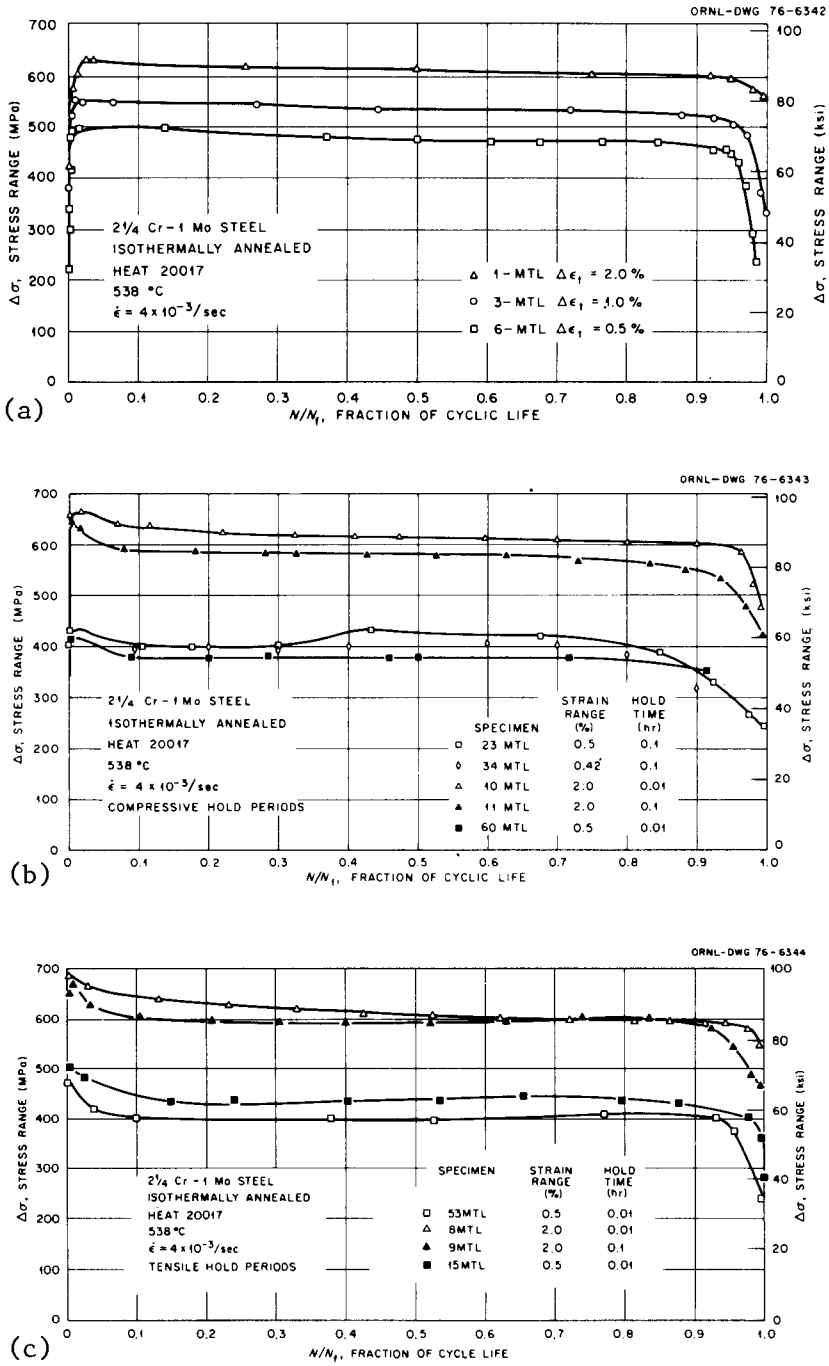

Fig. 3.69. Stress Range as a Function of Fraction of Cyclic Life for Isothermally Annealed Heat 20017 of 2 1/4 Cr-1 Mo Steel at 538°C; $\dot{\varepsilon} = 4 \times 10^{-3}$/sec. (a) Continuous cycling. (b) Compressive hold periods. (c) Tensile hold periods.

Cyclic stress-strain curves[83] were constructed with half-life stress-strain amplitude values used as coordinates. Such curves could be adequately represented by

$$\Delta\sigma/2 = K(\Delta\varepsilon_p/2)^n \ , \tag{50}$$

where $\Delta\sigma/2$ and $\Delta\varepsilon/2$ are the half-life stress and plastic strain amplitudes, respectively. Best-fit values of K and n are given in Table 3.28. The n values at each temperature were obtained from data for heat 20017 only and were assumed to be the same for all three heats at a given temperature.

Table 3.28. Cyclic Stress-Strain Curve Coefficients

Temperature		n	K, MPa, for Each Heat		
(°C)	(°F)		20017	3P5601	50557
Room Temp.		0.136	415	No Data	No Data
316	600	0.130	375	318	256
371	700	0.167	404	372	296
427	800	0.112	354	310	283
538	1000	0.120	314	271	241

Figure 3.70 illustrates fits of Eq. (50) to the data for heat 20017. Since n does not vary widely, the values of K provide a comparison of the strengths of the three heats at various temperatures. Examination of actual half-life hysteresis loops (scaled down by a factor of two) showed that, while the loop tips fell on the cyclic stress-strain curves, the tension-going portions of high-strain-range loops generally fell above the predicted curves. Low-strain-range loops generally fell below the cyclic stress-strain curves. Hold periods decreased the cyclic strength level at 427°C (800°F) and above. This effect appeared to saturate rapidly, however, with little evident difference between tests with hold periods of 0.01 and 0.1 hr. There were no discernible differences due to hold mode. A decrease in cyclic strain rate caused

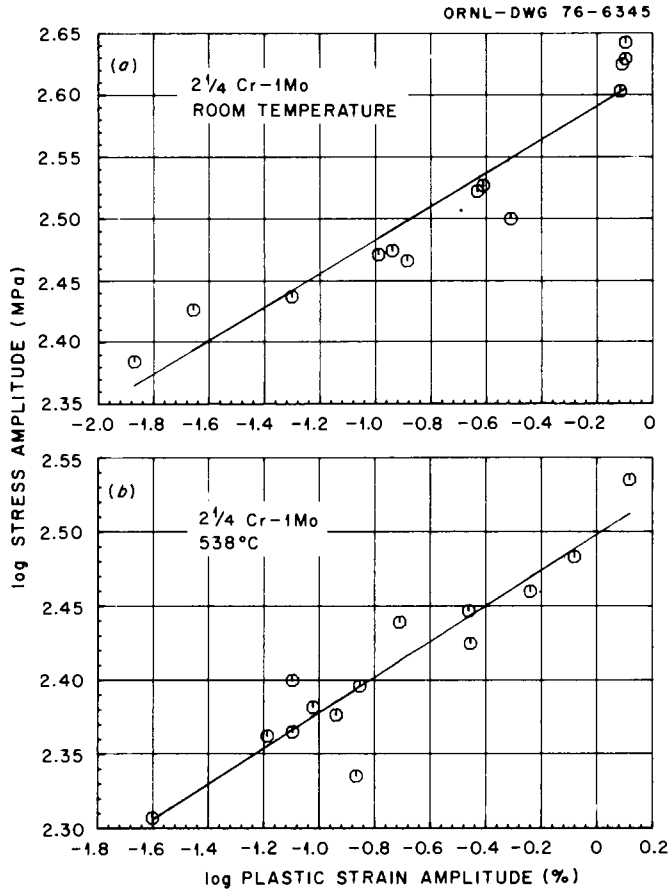

Fig. 3.70. Relationship Between Half-Life Stress Amplitude and Strain Amplitude for Heat 20017 of Isothermally Annealed 2 1/4 Cr-1 Mo Steel. Continuous cycling, $\dot{\varepsilon} = 4 \times 10^{-3}$/sec. (a) Room temperature. (b) 538°C (1000°F).

effects similar to hold periods above 427°C. Figure 3.71 and 3.72 illustrate the above results. At 371°C, hold periods tended to increase cyclic strength.

3.4.4.2.1 Bilinear Cyclic Stress-Strain Curves. Attempts to construct cyclic stress-strain curves according to the recommended[84] bilinear model have been described earlier.[85,86] Work this quarter has centered on further simplification and quantification of the earlier results. For instance, it is reasonable to expect that the κ values reported earlier, being a measure of yield strength, might be related to the stress range required to maintain an imposed strain range. In particular, κ_3 (where the half-life bilinear yield strength is $\sqrt{3\kappa_3}$) has been related

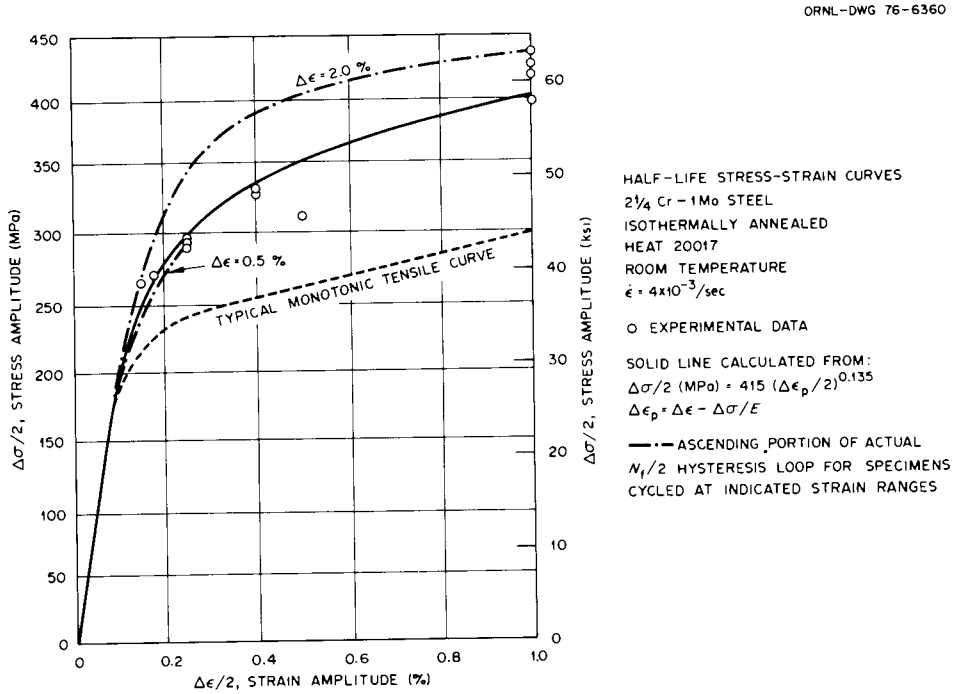

Fig. 3.71. Half-Life Cyclic Stress-Strain Curves for Heat 20017 of Isothermally Annealed 2 1/4 Cr-1 Mo Steel at Room Temperature.

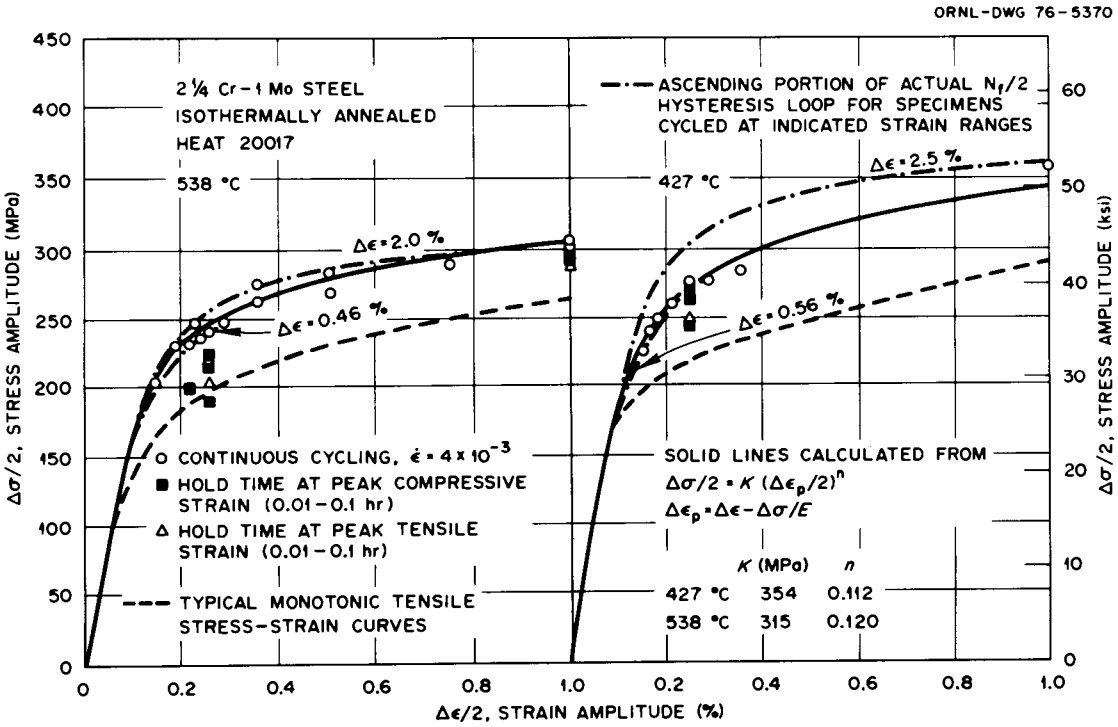

Fig. 3.72. Half-Life Cyclic Stress-Strain Curves for Heat 20017 of Isothermally Annealed 2 1/4 Cr-1 Mo Steel at 427 and 538°C (800 and 1000°F).

to the half-life stress amplitude $\Delta\sigma/2$. Figure 3.73 illustrates the relationship found for continuous cycling tests ($\dot{\varepsilon} = 4 \times 10^{-3}$/sec), where

$$\kappa_3 = 0.07(\Delta\sigma/2)^{2.21} \tag{51}$$

for κ_3 in $(\text{MPa})^2$ and $\Delta\sigma/2$ in MPa. The coefficient of this determination was 94.7% for this relationship, which appears to be independent of temperature. Note that Eqs. (50) and (51) together allow expression of κ_3 as a function of $\Delta\varepsilon_p$ or of $\Delta\varepsilon_t$, which is merely $\Delta\varepsilon_p + \Delta\sigma/E$, where E is Young's modulus.

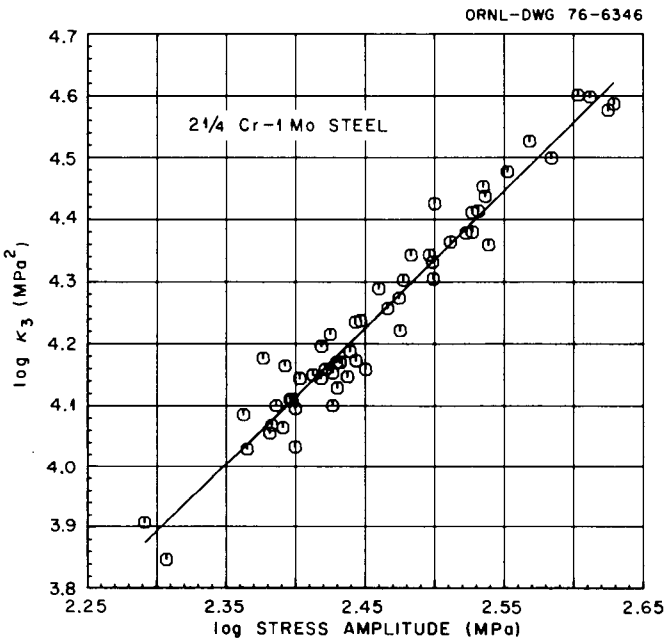

Fig. 3.73. Relationship Between Half-Life Stress Amplitude and Bilinear Parameter κ_3 for Isothermally Annealed Heats 20017 and 3P5601 of 2 1/4 Cr-1 Mo Steel. Room temperature to 538°C; continuous cycling, $\dot{\varepsilon} = 4 \times 10^{-3}$/sec.

3.4.4.2.2 Discussion. An examination of the values given in Table 3.28 immediately shows that the 2 1/4 Cr-1 Mo steel in this study undergoes a peak in half-life cyclic strength with temperature near 371°C (700°F). Studies of the monotonic tensile test data for this

material revealed a similar peak in ultimate tensile strength at about the same temperature, attributing the phenomenon to the effects of dynamic strain aging. Recent studies have looked at the effects of strain aging on various properties of this material,[87–89] explaining anomalies in the tensile, creep, and relaxation behavior of 2 1/4 Cr-1 Mo steel in terms of the "interaction solid-solution hardening" mechanism of Baird and Jamieson.[90] Briefly, this mechanism proposes that strain aging occurs through the interaction of dislocations with carbon and molybdenum (or possibly chromium) in solution. Details may be found in Refs. 87 through 90.

No conclusive evidence is available, but many of the current effects can be similarly explained. For instance, the peak in cyclic strength at about 371°C (700°F) is consistent with this form of dynamic strain aging. The cyclic softening, most prominent in the highest carbon heat and absent in the low-carbon heat, could be due to precipitation of Mo_2C particles at higher temperatures, which have tentatively been identified from transmission electron micrographs of fatigued specimens. Such precipitation, by decreasing the concentration of molybdenum and carbon in solution, decreases the strain aging effect. The peak in hardening early in life may be contributed to by the clustering of molybdenum and carbon atoms in solution before precipitation. Such clustering should increase the effectiveness of interaction solid-solution hardening. The weakening caused by imposition of hold periods at higher temperatures may be due to enhanced precipitation processes. Further attempts at explaining the above effects, including comparisons with data from other sources, are now under way.

3.4.5 Mechanical Properties of Transition Weld Joint Materials — R. L. Klueh and J. F. King

The intermediate heat exchanger of the CRBRP is to be constructed of an austenitic stainless steel and the steam generator from the low-alloy ferritic 2 1/4 Cr-1 Mo steel. Thus, a welded transition joint between these two units will be required. Since a number of failures of these types of joints has occurred in fossile-fired plants, we are presently developing transition weld procedures for the CRBRP steam generator

circuit. Included in these studies will be the determination of the mechanical properties of filler metals and transverse weldments that are appropriate for such transition joints.

To make a transition joint between type 316 stainless steel and 2 1/4 Cr-1 Mo steel, the present procedure calls for the use of Inconel 82 filler metal. Because of the differences in thermal coefficients of expansion between the materials in such a joint, a transition piece is being considered. Instead of making the transition between type 316 stainless steel and 2 1/4 Cr-1 Mo steel directly, using Inconel 82 weld metal, an intermediate spool piece of Incoloy alloy 800 would be used. Regardless of whether such a transition piece is used or not, Inconel 82 filler metal will undoubtedly be used (between the Incoloy alloy 800 and 2 1/4 Cr-1 Mo steel if a transition piece is used). For this reason, our first mechanical properties studies are being made on Inconel 82 weld metal. A limited number of tensile tests are also being done on transverse weldments that contain type 316 stainless steel, Inconel 82 weld metal, and 2 1/4 Cr-1 Mo steel in the gage section.

One problem with testing weld metal is the fabrication of sufficient welds to obtain the required number of specimens for the test program. Initially it was decided to make the Inconel 82 welds between two 13-mm-thick (1/2-in.) plates — one plate of Incoloy alloy 800, the other of 2 1/4 Cr-1 Mo steel. A 90°-included-angle V-groove joint geometry was used. The welding was performed by the automatic gas tungsten-arc process with cold wire filler additions. A root pass and seven fill passes were required to complete the weld. One such weld was also made with 13-mm plates of 2 1/4 Cr-1 Mo steel and type 316 stainless steel.

Since the number of specimens that could be obtained from such welds was quite limited, a larger weld geometry was designed to produce a large deposit of Inconel 82 filler metal. Plates of 19-mm-thick (3/4-in.) 2 1/4 Cr-1 Mo steel were used as base material. These were prepared with a 30°-included-angle V-groove joint geometry with a 32-mm (1 1/4-in.) root opening and a backing strip. Weld deposits were made by the automatic gas tungsten-arc welding process with cold wire filler additions. Filling this joint required 40 weld passes.

Before specimens were taken from the welds, they were nondestructively examined by radiography. No defects could be detected. As a result of some premature creep failures, several of the specimens taken from these welds were also radiographed. Again, no defects could be detected.

Mechanical property test specimens were of a buttonhead type with a 3.18-mm-diam (0.125-in.) and 28.6-mm-long (1.125-in.) gage section. Most of the specimens tested to date were longitudinal all-weld-metal specimens, but some tensile tests were also made on transverse weldment specimens that contained type 316 stainless steel, Inconel 82 weld metal, and 2 1/4 Cr-1 Mo steel in the gage length of the specimen.

Tensile tests were made on an Instron test machine with a crosshead speed of 8.5 mm/sec (0.02 in./min). The creep rupture tests were done in air on lever-arm creep machines. During test the specimens were heated with a resistance tube furnace, and the temperature was monitored and controlled by three Chromel vs Alumel thermocouples attached on the specimen gage length. Temperatures were controlled to ±1°C (±2°F) with the temperature variation along the gage length of less than ±3°C (±5°F). Elongation was determined with a mechanical extensometer attached to the specimen grips and the specimen elongation read periodically on a dial gage.

3.4.5.1 Tensile Properties of Inconel 82 Weld Metal

The tensile properties of the Inconel 82 weld metal specimens over the range 25 to 732°C (75—1350°F) are given in Table 3.29. Specimens taken from the welds made on the 19-mm-thick (3/4-in.) plates were tested over the entire temperature range. Specimens taken from welds made on the 13-mm-thick (1/2-in.) plates were tested only at 25, 454, 510, 566, and 621°C. In Fig. 3.74 the 0.2% yield stress and the ultimate tensile strength are shown as functions of temperature, while Fig. 3.75 shows the elongation and reduction of area as functions of temperature.

Figure 3.74 shows that there is a definite difference in the properties for the welds made on the different thickness plates; the thicker have higher yield and ultimate tensile strengths. The elongation (Fig. 3.75) of the specimens from the 13-mm plates are somewhat greater

Table 3.29. Tensile Properties of Inconel 82 Weld Metal[a]

Temperature		Strength, MPa (ksi)			Elongation, %		Reduction of Area
(°C)	(°F)	Yield	Tensile	Fracture	Uniform	Total	(%)
			19-mm (3/4-in.) Plates				
25	75	335 (51.3)	658 (95.5)	476 (69.1)	30.4	34.7	44.1
204	400	305 (44.3)	575 (83.4)	473 (68.7)	34.3	36.7	45.6
316	600	298 (43.2)	548 (79.6)	452 (65.6)	26.4	29.9	45.5
454	850	282 (41.0)	542 (78.7)	474 (68.9)	36.8	40.6	43.7
510	950	267 (38.8)	501 (72.7)	369 (53.5)	33.9	37.1	40.1
566	1050	259 (37.6)	486 (70.6)	371 (53.9)	33.6	37.6	51.5
621	1150	258 (37.4)	451 (65.4)	265 (38.4)	25.8	29.4	50.4
677	1250	256 (37.1)	405[b] (58.8)	62[b] (9.0)	15.3	19.0	30.9
677	1250	247 (35.8)	422 (61.2)	141 (20.4)	19.9	28.3	46.9
732	1350	261 (37.9)	327 (47.5)	124 (18.0)	4.1	29.9	53.7
			13-mm (1/2-in.) Plates				
25	75	295 (42.9)	610 (88.6)	483 (70.1)	39.1	43.9	45.8
25	75	311 (45.2)	622 (90.3)	474 (68.8)	33.3	37.6	44.4
454	850	219 (31.8)	507 (73.6)	442 (64.1)	41.8	46.8	47.7
510	950	229 (33.3)	488 (70.8)	413 (59.9)	35.8	38.9	40.0
566	1050	220 (32.0)	478 (69.4)	377 (54.6)	39.2	43.0	51.6
621	1150	203 (29.5)	422 (61.3)	237 (34.2)	32.8	38.0	47.0

[a]Postweld heat treated for 1 hr at 732°C (1350°F); tested at 8.5 mm/sec (0.02 in./min).

[b]Failed near end of gage section at point where extensometer was attached.

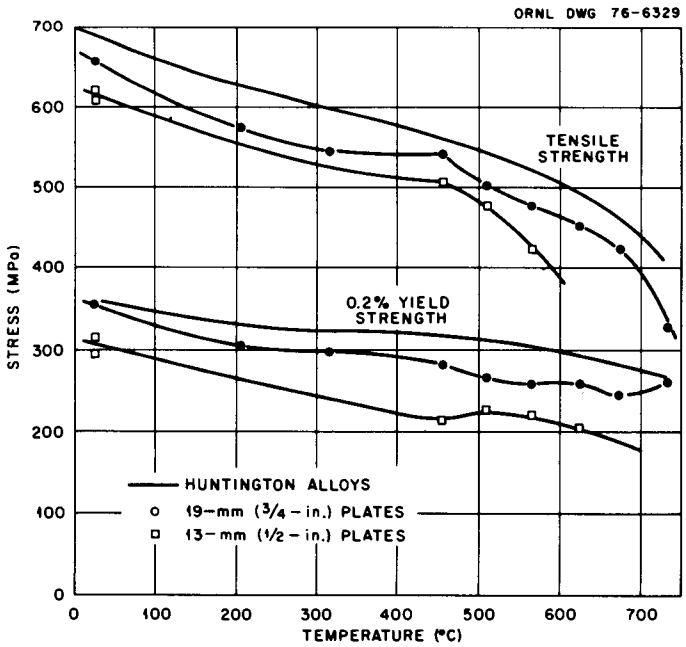

Fig. 3.74. The 0.2% Yield Stress and the Ultimate Tensile Strength as Functions of Temperature for Inconel 82 Weld Metal. Also shown are curves obtained by Huntington Alloys.

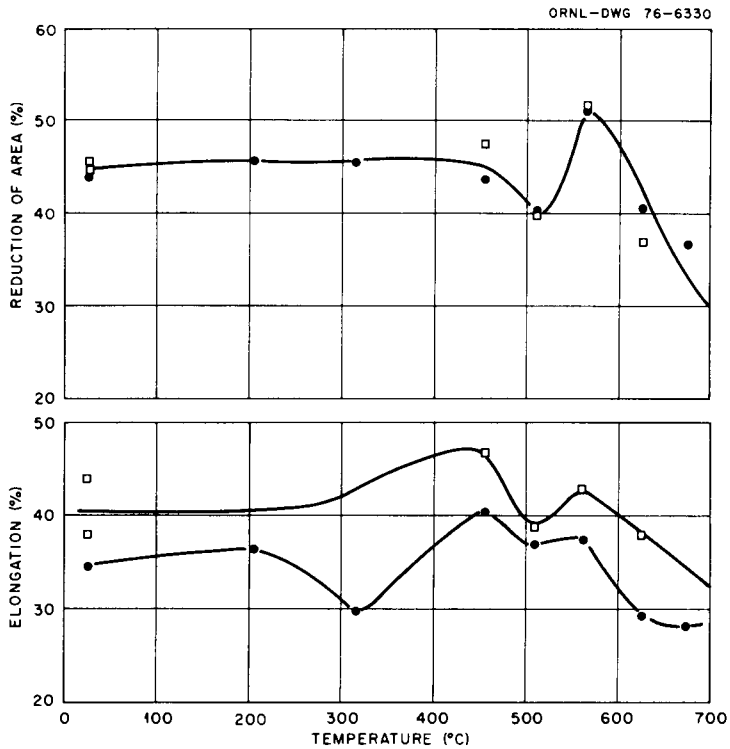

Fig. 3.75. Elongation and Reduction of Area as Functions of Temperature for Inconel 82 Weld Metal.

than those from the 19-mm plate, but there was no difference in the reduction of area. Curves put through the points, in both figures, are meant only to show the trends in the data. In Fig. 3.74 the yield stress and the ultimate tensile strength for Inconel 82 taken from Huntington Alloys literature[91] is also shown. The Huntington Alloys material is somewhat stronger than the weld metal tested in the present studies. However, the general trends for all three curves are similar.

Two tests were made at 677°C (1250°F) on specimens taken from the welds made on the 19-mm-thick (3/4-in.) plates. The first failed near the end of the gage length where the extensometer was attached. As seen in Table 3.29, the ultimate tensile strength, fracture stress, and ductility measurements for this specimen fell significantly below those for the other specimen (the results for this test are not given in Figs. 3.74 and 3.75).

When the specimens were examined after deformation, two types of anisotropic deformation were noted: (1) the cross section deformed to

an ellipse, rather than a circle, and (2) the specimen had a "knobby" appearance after test; that is, usually one or more points on the specimen gage section, in addition to the point that necked to failure, appeared to be in the process of neck formation.

The different properties for the different weld geometries are probably the result of different dilution effects. The smaller the weld, the greater the amount of dilution by the base materials. To minimize dilution, Huntington Alloys used a base metal of composition similar to the weld metal.

We are presently examining selected specimens by metallography. The results of these studies will be presented later.

3.4.5.2 Tensile Properties of Transverse Weldment Specimens

A limited number of tensile tests were also made on transverse weldment specimens that contained type 316 stainless steel, Inconel 82 weld metal, and 2 1/4 Cr-1 Mo steel in the gage section. Initially, tests were made at 25 and 566°C (75 and 1050°F) on materials as welded and at 25, 316, 454, 510, and 566°C (75, 600, 850, 950, and 1050°F) after a 1-hr postweld heat treatment at 732°C (1350°F). The results are given in Table 3.30. Except at 316°C, all failures occurred in the 2 1/4 Cr-1 Mo steel. However, even though failure occurred in the 2 1/4 Cr-1 Mo steel, both the Inconel 82 weld metal and the type 316 stainless steel portions of the gage sections were deformed during test. At 316°C (600°F), failure occurred in the type 316 stainless steel. In this specimen, the Inconel 82 weld metal was also deformed, but the 2 1/4 Cr-1 Mo steel portion of the gage length was essentially undeformed.

The observation that the test at 316°C (600°F) failed in the type 316 stainless steel instead of the 2 1/4 Cr-1 Mo steel was concluded to be the result of dynamic strain aging in 2 1/4 Cr-1 Mo steel. To verify this result, the test at 316°C was repeated, and since previous work[87] has shown that dynamic strain aging is a maximum in the range 300 to 400°C (570–750°F), a test was also made at 371°C (700°F) (Table 3.30). The results for these last two tests were similar: both failed in the

Table 3.30. Tensile Properties of Type 316 Stainless Steel — Inconel 82 Weld Metal — 2 1/4 Cr-1 Mo Steel Transverse Weldments[a]

Temperature		Strength, MPa (ksi)			Total Elongation (%)	Reduction of Area (%)
(°C)	(°F)	Yield	Ultimate	Fracture		
			As Welded			
25	75	334 (48.5)	548 (79.5)	390 (56.6)	20.9	58.4
566	1050	248 (36.0)	447 (64.8)	272 (39.4)	22.2	61.6
		Postweld Heat-Treated for 1 hr at 732°C (1350°F)				
25	75	304 (44.1)	502 (72.8)	302 (43.9)	18.7	73.3
316	600	227 (32.9)	488 (70.8)	336 (48.8)	24.5	61.1
316	600	228 (33.1)	479 (69.5)	333 (48.3)	22.8	64.8
371	700	227 (32.9)	497 (72.2)	354 (51.3)	26.1	54.9
454	850	218 (31.7)	479 (69.5)	294 (42.7)	25.5	61.1
510	950	208 (30.2)	418 (60.6)	215 (31.2)	21.0	64.7
566	1050	196 (28.5)	335 (48.6)	124 (18.0)	18.7	76.9

[a]Teated at a crosshead speed of 0.02 in./min (nominal strain rate 0.0178/min).

type 316 stainless steel, with some deformation occurring in the Inconel 82 weld metal, but essentially no deformation occurring in the 2 1/4 Cr-1 Mo steel.

The reason for the type of behavior noted here can be understood by reference to Fig. 3.75, where the ultimate tensile strength is shown as a function of temperature for type 316 stainless steel, 2 1/4 Cr-1 Mo steel, and Inconel 82 weld metal (the weld metal data is that for the welds in 19-mm-thick (3/4-in.) plates shown in Fig. 3.74). The data for the type 316 stainless steel and the 2 1/4 Cr-1 Mo steel are average values taken from data compilations of Smith.[9,70] We see that between about 200 and 500°C (400 and 930°F) the ultimate tensile strength of the 2 1/4 Cr-1 Mo steel exceeds that of the type 316 stainless steel. At all temperatures, the strength of the Inconel 82 weld metal is greater than that of the other two materials. It is in the temperature range of the 2 1/4 Cr-1 Mo steel peak that the failures occurred in the type 316 stainless steel. Thus, dynamic strain aging in the 2 1/4 Cr-1 Mo

steel is apparently the cause of the change from fracture in the 2 1/4 Cr-1 Mo steel to the type 316 stainless steel. Note that since the properties given in Fig. 3.76 are average values (taken from various heats), the temperature range where the ultimate tensile strength values for the 2 1/4 Cr-1 Mo steel exceed those for the type 316 stainless steel only approximate those for the materials used in this study. To do an accurate analysis of this behavior, data would need to be collected from the actual heats of base materials used to make these welds. In addition to analysis of the ultimate tensile strength relationships, the total flow behavior of the materials involved would also be required.

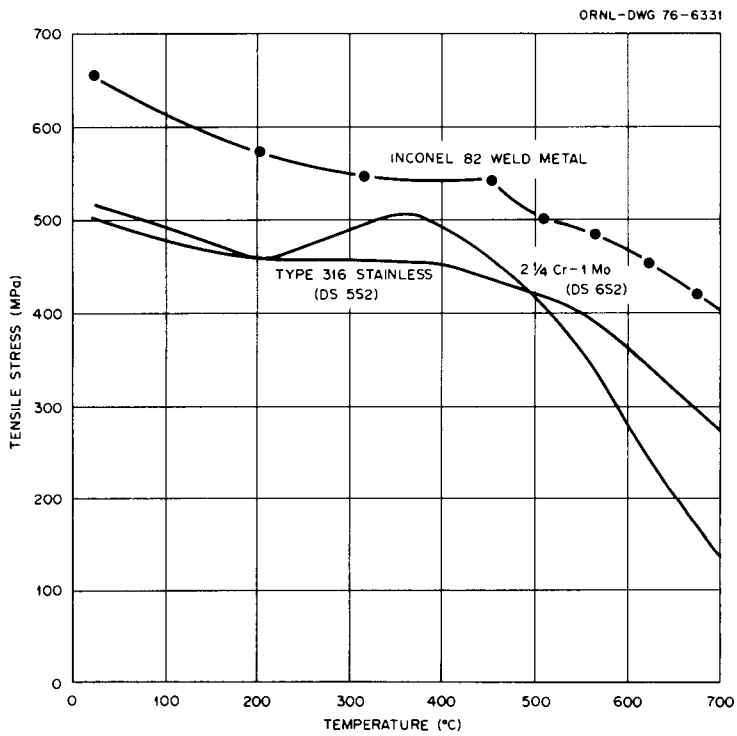

Fig. 3.76. The Ultimate Tensile Strength as a Function of Temperature for Inconel 82 Weld Metal, Type 316 Stainless Steel, and 2 1/4 Cr-1 Mo Steel.

3.4.5.3 Creep and Rupture Behavior of Inconel 82 Weld Metal

The creep and rupture behavior of Inconel 82 weld metal is to be investigated over the range 454 to 732°C (850–1350°F). At present, tests are under way at 454, 510, and 566°C (850, 950, and 1050°F). The

results for the completed tests and those presently under way are shown in Table 3.31. The first welds made were on the 13-mm-thick (1/2-in.) plates and the tests at 510 and 566°C (950 and 1050°F) were made on specimens taken from such welds. The tests at 454°C (850°F) are being made on specimens taken from the large welds made on the 19-mm-thick (3/4-in.) plates.

Table 3.31. Creep-Rupture Properties of Inconel 82 Weld Metal

Stress (MPa)	Stress (ksi)	Rupture Life (hr)	Elongation (%)	Reduction of Area (%)	Minimum Creep Rate (%/hr)
Tests at 454°C (850°F) on Welds in 19-mm (3/4-in.) Plate					
414	60	a			
434	63	a			
455	66	a			
483	70	a			
483	70	75.1	33.4		0.0187
496	72	1012.6	36.0	38.5	0.000769
510	74	142.3	40.2	52.5	0.013
517	75	3.2	33.7	53.0	0.125
Tests at 510°C (950°F) on Welds in 13-mm (1/2-in.) Plate					
379	55	a			
396	57.5	a			
414	60	1645.4	23.6	19.7	0.000463
434	63	1205.1	33.7	29.3	0.000536
448	65	357.1	39.1	35.9	0.00459
455	66	4.0	40.4	39.0	0.150
455	66	39.4	38.7	42.9	0.138
465	67.5	37.1	48.4	51.8	0.209
483	70	10.9	48.4	53.7	0.395
Tests at 566°C (1050°F) on Welds in 13-mm (1/2-in.) Plate					
328	47.5	b			0.000149
345	50	778.8	14.5	15.6	0.000324
345	50	a			
365	53	1087.5	17.2	18.2	0.000611
379	55	841.1	18.9	18.9	0.00105
396	57.5	448.2	21.4	19.6	0.00280
396	57.5[c]	124.6	21.9		0.0652
396	57.5[c]	63.8	22.2		0.133
414	60	112.8	29.7	27.4	0.0331
434	63	29.5	37.6	36.8	0.231

[a]Test in progress.

[b]Test discontinued before rupture.

[c]Tests made on 19-mm (3/4-in.) plates.

Since many of the tests at 566°C are complete at this time, most of this discussion will be directed toward the results at that temperature. Figure 3.77 shows the creep-rupture behavior of Inconel 82 weld metal at 566°C; for comparison, the average creep-rupture curves for type 316 stainless steel and 2 1/4 Cr-1 Mo steel are also given.[9,74] The Inconel 82 weld metal is stronger than either of these materials. Huntington Alloys[92] has a limited amount of data on Inconel 82, but none are at 454, 510, or 566°C (850, 950, and 1050°F). It has two datum points at 538°C (1000°F), which fall on the line shown in Fig. 3.77 for the 566°C tests. Thus, although the tensile properties for these same welds fell considerably below Huntington Alloys' tensile data,[91] the creep-rupture properties were better than those tested by Huntington Alloys.

Figure 3.77 also shows two typical creep curves for Inconel 82 weld metal. In general, the initial creep rate is quite high; the rate then rapidly flattens out into a steady-state stage. Generally, there

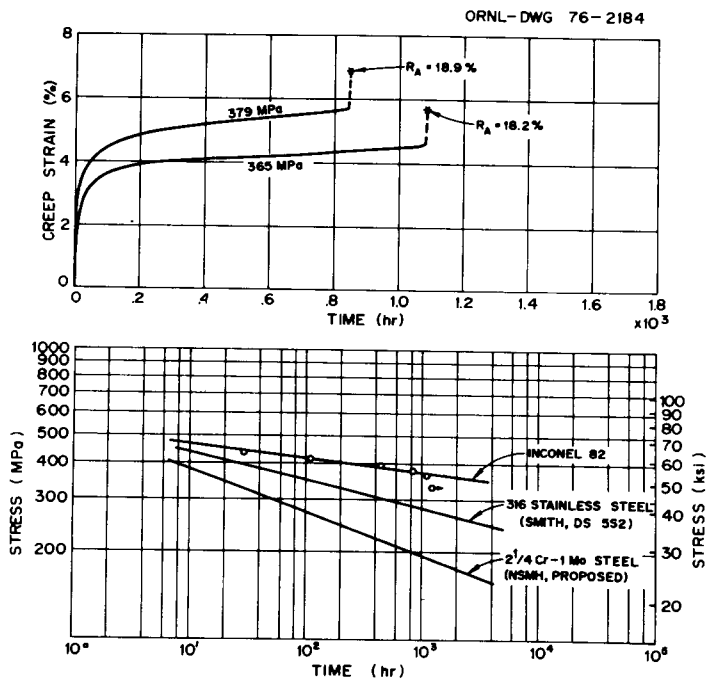

Fig. 3.77. The Creep and Rupture Behavior of Inconel 82 Weld Metal at 566°C (1050°F). Top: representative creep curves. Bottom: the creep rupture curve for Inconel 82 weld metal compared with curves for type 316 stainless steel and 2 1/4 Cr-1 Mo steel.

is very little tertiary creep. The specimen abruptly fails, usually without any pronounced deviation from the steady-state stage (the dotted lines in Fig. 3.77 are to indicate that no readings were made between the steady-state stage and rupture).

In most cases the fractures were quite flat with little neck formation. This is indicated by the fact that the reduction of area and elongation values are quite similar in magnitude (Table 3.31). Visual inspection of the failed specimens indicated that creep deformation was also anisotropic. Specimens tested at all three temperatures had a "knobby" appearance similar to that described for the tensile behavior. At 454 and 510°C (850 and 950°F), the high-stress specimens that failed had eliptical cross sections, similar to the tensile specimens. At 566°C (1050°F), the cross sections were essentially circular.

Two unusual types of behavior were noted. Several of the specimens failed prematurely [viz., the 483-MPa (70-ksi) test at 454°C (850°F), 434 and 455-MPa (63- and 66-ksi) tests at 510°C (950°F), and 345- and two 396-MPa (50- and 57.5-ksi) tests at 566°C (1050°F)]. The second type of unusual behavior is illustrated by the creep curve shown in Fig. 3.78. For no apparent reason, a specimen rather abruptly makes a large jump in strain — a "strain burst" — without rupture. When such a strain burst occurred during the steady-state stage, as shown in Fig. 3.78, the creep rate after the strain burst was usually quite similar to that before the burst. In some instances a strain burst occurred quite soon after the load was applied, but again, the curve appeared "normal" thereafter.

The tests at 396 MPa (57.5 ksi) at 566°C (1050°F) are rather interesting. Since there was a difference between the tensile properties of welds taken from the 13-mm-thick (1/2-in.) and 19-mm-thick (3/4-in.) plates, we decided to test a specimen from the 19-mm-thick plate at 566°C and 396 MPa. The specimen that was used for this test was radiographically inspected and found to have no detectable flaws. It failed prematurely: 63.8 hr as opposed to 448.2 hr. The test was repeated, and failure occurred in 124.6 hr, again considerably sooner than the specimen taken from the 13-mm-thick plate.

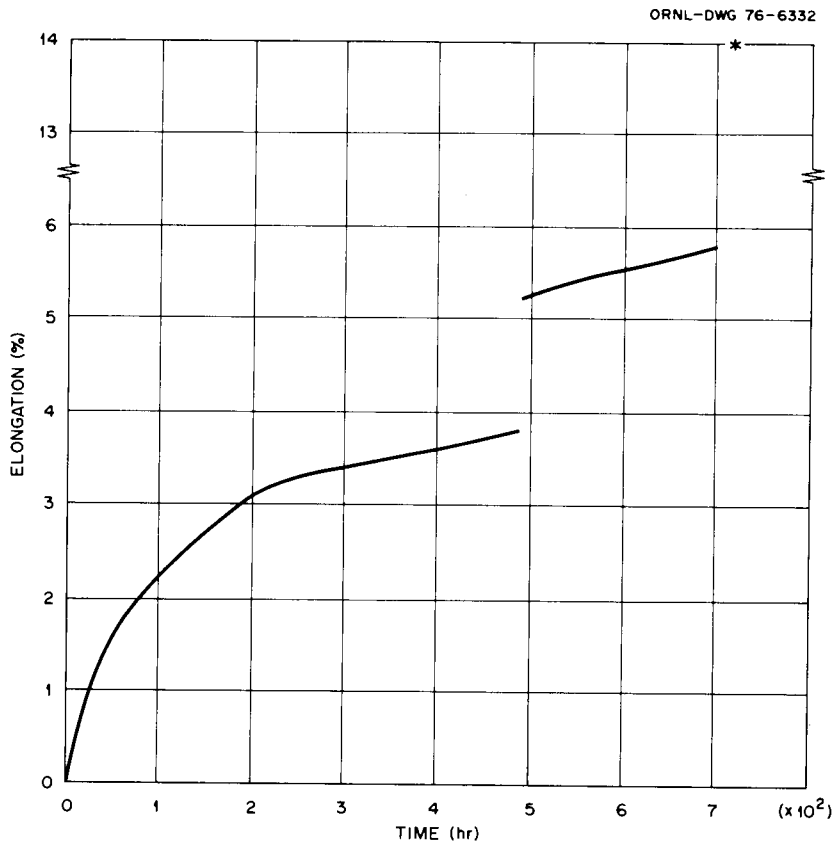

Fig. 3.78. Creep Curve for Inconel 82 Weld Metal at 496 MPa (72 ksi) and 454°C (850°F) Showing the "Strain Burst" Phenomenon.

At present we will offer no explanation for the "abnormal" behavior. With one exception, no unusual observations were made on the fracture surfaces of the failed specimens at 566°C (1050°F), either by visual inspection or with a stereographic microscope. The exception was the specimen that failed prematurely at 345 MPa (50 ksi). There appeared to be a "hole" visible on the fracture surface of this particular specimen. To verify this, scanning electron microscopy is required. We are presently conducting a metallographic examination on selected specimens. Since the examination at 566°C is only partially complete, the discussion on this aspect of the study will be delayed until the next quarterly report. In the future we also hope to stop a test for examination immediately after a "strain burst."

3.5 HIGH-TEMPERATURE DESIGN — J. M. Corum* and C. E. Pugh*

These programs now report semiannually so there is no report this quarter.

3.6 MECHANICAL PROPERTIES OF HTGR STEAM GENERATOR AND PRIMARY CIRCUIT MATERIALS — J. R. DiStefano

The major overall objectives of this program are to (1) determine the compatibility of alloys planned for use in the HTGR steam-cycle system with their environment and (2) determine, compile, and analyze materials design data for the commercial HTGR. To achieve these objectives it is necessary to study the mechanical behavior (tensile, creep, low-cycle fatigue, and crack growth) of HTGR alloys at temperatures and in environments (helium and steam) appropriate to their service in the reactor.

3.6.1 Tensile Testing — A. Lystrup†

Tensile tests have been performed on Inconel 617 (Heat XX01A3US). Background data on the material are given in Table 3.32 and the results of the tensile tests are reported on Table 3.33. The rod-type specimens

Table 3.32. Data on Inconel 617 Used for Tensile Tests

Heat	XX01A3US
Source	The International Nickel Company, Inc. Huntington Alloy Products Division
Product form	12.7-mm (0.5-in.) plate
Heat treatment	Solution annealed
Hardness	Rockwell B 83
Chemical Composition, wt %	
Ni	57.35
Cr	20.30
Co	11.72
Mo	8.58
Fe	1.01
Al	0.76
Si	0.16
C	0.07
Mn	0.05
S	0.004

*Reactor Division.

†On assignment from Risö, Denmark.

Table 3.33. Tensile Properties of Inconel 617 (Heat XX01A3US)

Test	Temperature		Yield Strength (0.2%)		Ultimate Tensile Strength		Elongation in 31.8 mm (1.25 in.)		Reduction of Area (%)	Remarks[a]
	(°C)	(°F)	(MPa)	(ksi)	(MPa)	(ksi)	Uniform (%)	Total (%)		
16545	22	72	303	43.9	747	108.3	54.1	54.3	36.2	
16546	22	72	301	43.7	757	109.8	59.6	60.9	40.7	
16547	22	72	305	44.3	754	109.3	57.4	57.9	38.4	
16548	149	300	260	37.7	698	101.2	61.3	61.7	40.9	
16549	149	300	251	36.4	698	101.2	60.2	61.4	44.0	
16550	288	550	225	32.6	671	97.3	63.2	64.8	46.0	
16551	288	550	221	32.0	663	96.2	66.7	68.7	49.6	
16552	288	550	217	31.5	665	96.5	60.7	61.9	44.0	
16553	427	800	222	32.2	640	92.8	63.1	65.4	45.7	
16554	427	800	223	32.3	635	92.1	62.3	64.2	40.1	BGM
16654	482	900	216	31.3	626	90.8	65.0	67.5	47.0	
16655	482	900	217	31.5	634	91.9	63.6	64.9	44.5	
16656	482	900	225	32.7	625	90.7	63.1	64.9	47.7	
16657	538	1000	216	31.3	610	88.5	64.7	67.3	49.8	
16658	538	1000	207	30.0	606	87.9	61.1	64.4	46.1	
16659	593	1100	201	29.1	589	85.4	59.3	60.4	43.1	BGM, SBY
16660	593	1100	203	29.5	589	85.4	57.6	58.7	42.3	SBY
16661	593	1100	206	29.9	596	86.4	61.3	62.6	39.2	BGM, SBY
16662	649	1200	210	30.4	539	78.2	51.6	59.2	39.2	BGM
16663	649	1200	210	30.4	545	79.1	53.7	62.4	39.8	BGM
16664	704	1300	199	28.8	466	67.6	29.3	68.0	49.3	
16665	704	1300	196	28.4	443	64.2	25.9	69.9	53.1	
16666	704	1300	196	28.4	454	65.9	29.9	74.7	52.5	
16667	760	1400	210	30.5	368	53.4	10.3	86.3	69.1	SBY
16668	760	1400	208	30.2	370	53.6	11.0	86.2	68.9	BGM, SBY
16669	816	1500	210	30.4	263	28.1	4.6	111.1	87.0	BGM, SBY
16670	816	1500	210	30.5	269	39.0	4.9	108.4	82.6	SBY
16671	816	1500	211	30.6	270	39.1	5.8	95.8	82.6	BGM, SBY
16672	871	1600	181	26.3	194	28.1	3.2	88.0	87.8	BGM
16673	871	1600	189	27.4	194	28.1	3.2	91.6	86.0	
16674	927	1700	127	18.4	139	20.2	2.2	99.2	88.8	
16675	927	1700	125	18.1	136	19.7	2.1	110.3	90.3	BGM
16676	927	1700	123	17.9	134	19.5	3.2	96.4	89.1	BGM
16677	982	1800	97	14.0	101	14.7	1.9	75.0	73.9	
16678	982	1800	89	12.9	99	14.3	3.2	91.5	83.0	BGM

[a]BGM = Broke at Gage Mark. SBY = Serration Occurred Before 0.2% Yield.

had a gage length of 31.8 mm (1.25 in.) and a gage diameter of 6.35 mm (0.25 in.). All the tests were run to failure at a strain rate of 0.4%/min. Ultimate tensile strengths were calculated from the load-crosshead movement curves, and the yield strengths were calculated from load-strain curves obtained by an extensometer attached to a 25.4 mm (1 in.) gage length.

Yield strength of this material appeared to be very little affected by the temperature in the range 288 to 816°C (550–1500°F). Above 816°C (1500°F) the yield strength dropped very fast. Also, ultimate tensile strength decreased with increasing temperature; above 593°C (1100°F) the strength and amount of uniform elongation dropped rapidly.

3.6.2 Environmental Creep Testing — A. Lystrup†

The environmental creep tests of HTGR structural alloys in simulated primary coolant helium and the tests in air for comparison have continued during the quarter. Four tests were completed during this period, and the results are shown in Table 3.34. Three of those tests have been examined metallographically, and cross sections of the specimens are shown in Figs. 3.79 through 3.81. In each of the figures (a) shows the edge of a cross section very close to the fracture and (b) shows the edge of a cross section at the shoulder of the specimen (where the stress is one-fourth that at the gage section). Test 15047 [2 1/4 Cr-1 Mo, 593°C (1100°F), 69 MPa (10 ksi), 7784 hr, He] shows a uniform surface penetration, which is 20 μm deep at the gage section and 15 μm deep at the shoulder. Test 16266 [2 1/4 Cr-1 Mo, 593°C (1100°F), 103 MPa (15 ksi), 388 hr, air] shows a 30-μm-thick oxide layer both at the gage section and at the shoulder. Test 16125 [Hastelloy X, 760°C (1400°F),

Table 3.34. Results of Creep Tests Completed

Material and Heat	Test	Temperature		Stress		Rupture Life	Elongation at Rupture
		(°C)	(°F)	(MPa)	(ksi)	(hr)	(%)
			He Environment Tests				
2 1/4 Cr-1 Mo X-6216	15047	593	1100	69	10	7784	27
Hastelloy X 2600-3-4936	15792	704	1300	138	20	4588	23
Hastelloy X 2600-3-4936	16125	760	1400	138	20	305	39
			Air Test				
2 1/4 Cr-1 Mo 72768	16266	593	1100	103	15	388	53

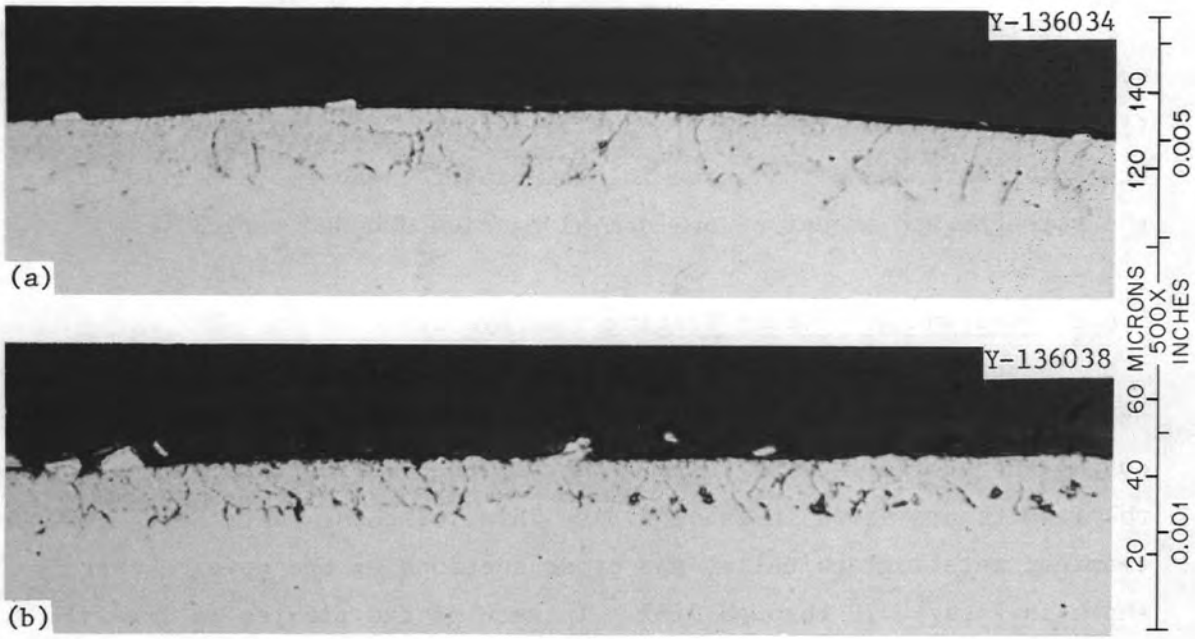

Fig. 3.79. Test 15047: 2 1/4 Cr-1 Mo Steel Explsed in HTGR Helium at 593°C (1100°F) for 7784 hr. 500×. (a) Gage section. (b) Shoulder of the specimen.

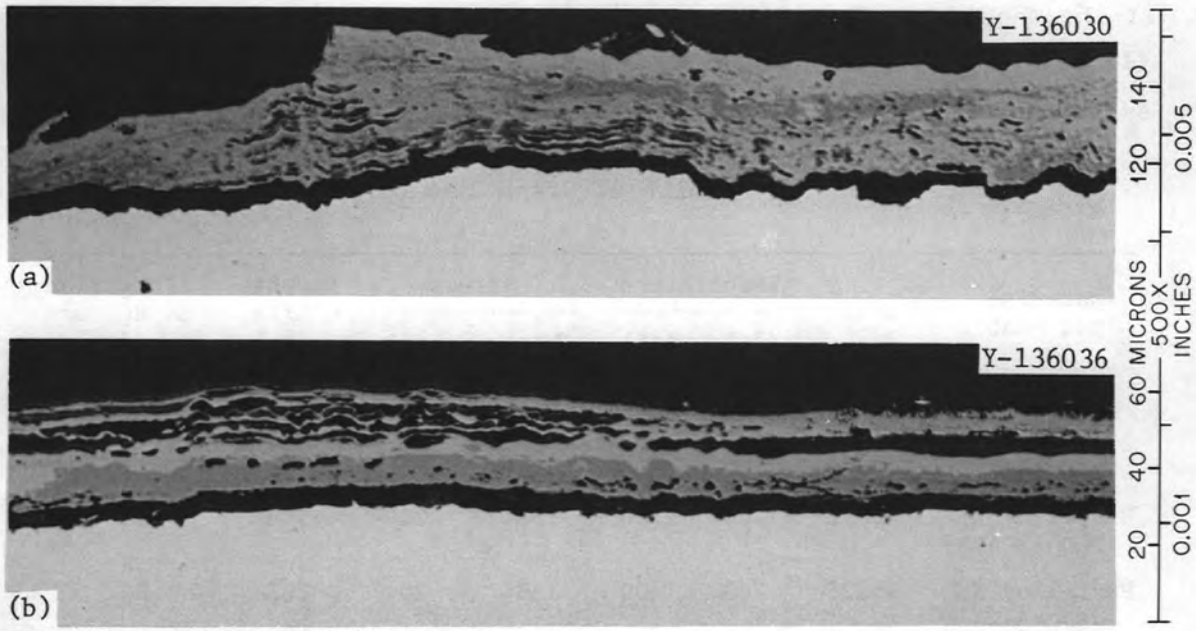

Fig. 3.80. Test 16266: 2 1/4 Cr-1 Mo Steel Exposed in Air at 593°C (1100°F) for 388 hr. 500×. (a) Gage section. (b) Shoulder of the specimen.

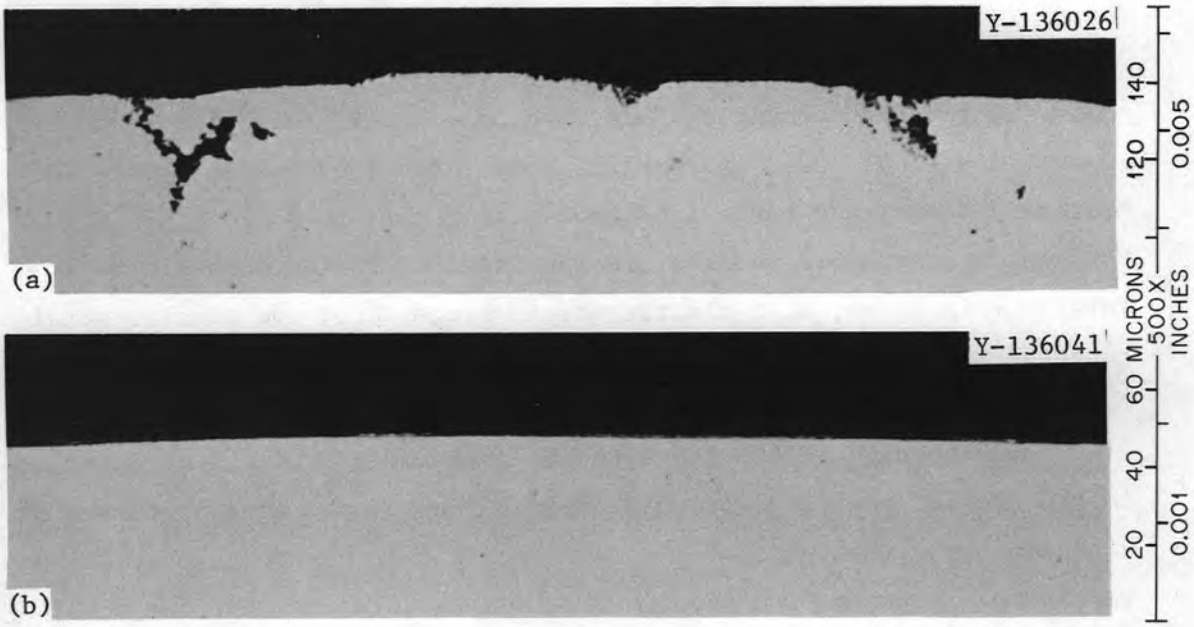

Fig. 3.81. Test 16125: Hastelloy X Exposed in HTGR Helium at 760°C (1400°F) for 305 hr. 500×. (a) Gage section. (b) Shoulder of the specimen.

138 MPa (20 ksi), 305 hr, He] has some 30-μm-deep penetration at the stressed part of the specimen and no corrosion attack at the low-stressed part. The matrix of our current creep tests is shown on Table 3.35. Maximum time in test is approaching 9600 hr (e.g., tests 15023 and 15046).

Table 3.35. Current Environmental and Air Creep Tests

Test	Test Frame	Material	Heat	Temperature (°C)	Temperature (°F)	Stress (MPa)	Stress (ksi)
			He Environment Tests				
16490	I-160	Hastelloy X	2600-3-4936	760	1400	103	15
15046	I-161	2 1/4 Cr-1 Mo	X-6216	538	1000	103	15
Being Loaded	I-162	Hastelloy X	2600-3-4936	704	1300	103	15
15363	I-163	9 Cr-1 Mo	316381-1A	538	1000	103	15
15369	I-164	2 1/4 Cr-1 Mo	36202	538	1000	103	15
15374	I-165	2 1/4 Cr-1 Mo	36202	482	900	172	25
16126	I-166	Hastelloy X	2600-3-4936	871	1600	34	5
15772	I-167	Hastelloy X	2600-3-4936	649	1200	172	25
15023	I-168	2 1/4 Cr-1 Mo	X-6216	593	1100	69	10
Being Loaded	I-169	2 1/4 Cr-1 Mo	36202	593	1100	103	15
			Air Tests				
16263	I-170	2 1/4 Cr-1 Mo	36202	482	900	207	30
16264	I-171	2 1/4 Cr-1 Mo	36202	538	1000	103	15
16360	I-172	2 1/4 Cr-1 Mo	72768	593	1100	69	10
16267	I-173	Hastelloy X	2600-3-4936	649	1200	172	25
16268	I-174	Hastelloy X	2600-3-4936	704	1300	138	20
16269	I-175	Hastelloy X	2600-3-4936	816	1500	69	10

3.6.3 Fatigue-Life Testing — J. P. Strizak

Fully reversed isothermal uniaxial strain-controlled fatigue tests employing testing techniques described previously[93] have been conducted in air on a single heat and product form (Heat 2600-3-4936, plate) of Hastelloy X over the range from room temperature to 871°C (1600°F). Fatigue data obtained to date are tabulated in Tables 3.36 and 3.37. Total strain range, $\Delta\varepsilon_t$; plastic strain range, $\Delta\varepsilon_p$; and elastic strain range, $\Delta\varepsilon_e$, versus cycles to failure, N_f, are plotted for room temperature, 538, 649, 760, and 871°C (1000, 1200, 1400, and 1600°F) in Figs. 3.82 through 3.84. The data of Jaske and Porfilio[94] were included in the plot of the 760°C (1400°F) data. These tests were conducted at a continuous strain rate of 4×10^{-3}/sec, except as noted, using a ramp wave form. Figures 3.82 through 3.84 demonstrate that the components of the total strain range, $\Delta\varepsilon_t$, namely the plastic, $\Delta\varepsilon_p$, and elastic, $\Delta\varepsilon_e$, strain ranges can be expressed as simple power law relationships, thus:

$$\Delta\varepsilon_t = \Delta\varepsilon_p + \Delta\varepsilon_e \,, \tag{52}$$

$$\Delta\varepsilon_t = AN_f^{-a} + BN_f^{-b} \,. \tag{53}$$

Values of the coefficients and exponents in the above equation have been determined by linear least squares analysis and are summarized in Table 3.38.

In Fig. 3.85 a summary comparison plot is given of the various isothermal best fit lines of total strain range versus cycles to failure. Generally, increasing the temperature decreases the continuous cycling fatigue life of Hastelloy X, as shown. Several tests at 871°C (1600°F) were conducted at a strain rate of 1×10^{-2}/sec to determine if fatigue life depended on strain rate within the creep range at strain rates greater than 4×10^{-3}/sec. As shown in Fig. 3.84(b) the higher strain rate tests showed essentially identical cyclic lives, indicating strain rate independence over the range covered.

Table 3.36. Results of Strain-Controlled Fatigue Tests on Hastelloy X [Heat 2600-3-4936 13-mm (1/2-in.) Plate] Tested in Air[a]

Specimen[b]	Poisson's Ratio, ν	Total Strain Range, $\Delta\varepsilon_t$	Strain Range at $N_f/2$, % Elastic, $\Delta\varepsilon_e$ Measured	Elastic, $\Delta\varepsilon_e$ Calculated[c]	Inelastic, $\Delta\varepsilon_{in}$ Measured	Inelastic, $\Delta\varepsilon_{in}$ Calculated[d]	Cycles to Failure, N_f	Time to Failure, t_f	Stress Range at 10th Cycle, $\Delta\sigma_{10}$ (MPa)	Stress Range at 10th Cycle, $\Delta\sigma_{10}$ (ksi)	Properties of $N_f/2$, MPa (ksi) Stress Range[c]	Tensile Stress Amplitude, σ_t	Compressive Stress Amplitude, σ_c
Tested at 22°C (72°F) (Young's Modulus E = 199 GPa = 28.87 × 10^6 psi)													
HXL-51	0.315	4.10	0.79	0.72	3.31	3.38	439	146	1292	187.4	1425 (206.7)	698 (101.3)	727 (105.4)
HXL-29	0.265	3.04	0.76	0.70	2.28	2.34	591	148	1237	179.5	1392 (201.9)	681 (98.8)	711 (103.1)
HXL-28	0.285	2.11	0.62	0.59	1.49	1.51	1,494	249	1087	157.7	1177 (170.8)	584 (84.8)	593 (86.0)
HXL-27	0.280	1.50	0.49	0.49	1.02	1.02	6,101	763	956	138.6	968 (140.4)	478 (69.3)	490 (71.1)
HXL-23	0.278	0.99	0.46	0.43	0.53	0.56	10,245	854			862 (125.0)	427 (62.0)	435 (63.1)
HXL-47	0.261	0.89	0.48	0.42	0.41	0.47	15,796	1,185	815	118.1	829 (120.3)	407 (59.1)	422 (61.2)
HXL-22	0.269	0.80	0.46	0.42	0.33	0.38	49,664	3,311			837 (121.4)	406 (58.9)	431 (62.5)
Tested at 538°C (1000°F) (Young's Modulus E = 162 GPa = 23.54 × 10^6 psi)													
HXL-46	0.299	4.06	0.89	0.94	3.18	3.12	177	59	1084	157.2	1530 (221.9)	748 (108.4)	782 (113.5)
HXL-16	0.306	3.02	0.73	0.83	2.94	2.19	418	104	847	122.8	1353 (196.3)	665 (96.5)	688 (99.8)
HXL-20	0.274	1.56	0.65	0.70	0.91	0.86	1,181	148	764	110.8	1141 (165.5)	562 (81.6)	579 (83.9)
HXL-30	0.302	0.99	0.62	0.63	0.37	0.36	5,182	432	666	96.6	1015 (147.3)	494 (71.7)	521 (75.6)
HXL-3	0.268	0.79	0.73	0.67	0.06	0.12	7,596	501			1084 (157.2)	493 (71.5)	591 (85.8)
HXT-2	0.290	0.71	0.57	0.53	0.13	0.18	14,240	831	577	83.7	855 (124.0)	405 (58.7)	450 (65.3)
HXT-4	0.320	0.65	0.48	0.56	0.17	0.08	13,675	741	542	78.6	917 (133.0)	446 (64.7)	471 (68.3)
HXL-19	0.341	0.60	0.56	0.54	0.04	0.06	225,000	11,250			877 (127.2)	444 (64.4)	433 (62.8)
Tested at 649°C (1200°F) (Young's Modulus E = 154 GPa = 22.4 × 10^6 psi)													
HXL-6	0.312	4.17	0.80	0.96	3.37	3.21	94	31	1118	162.3	1476 (214.0)	719 (104.2)	757 (109.8)
HXL-14	0.323	3.00	0.76	0.91	2.24	2.09	133	33	1059	153.6	1412 (204.8)	693 (100.6)	719 (104.2)
HXL-42	0.316	2.03	0.72	0.82	1.31	1.21	318	53	872	126.5	1258 (182.5)	611 (88.6)	647 (93.8)
HXL-44	0.334	1.52	0.63	0.72	0.89	0.80	713	89	711	103.1	1119 (162.3)	547 (79.3)	572 (83.0)
HXL-8	0.305	1.00	0.63	0.63	0.38	0.37	1,617	135			972 (141.0)	478 (69.3)	494 (71.7)
HXT-3	0.270	0.80	0.64	0.59	0.16	0.22	5,147	343	628	91.1	909 (131.8)	438 (63.5)	471 (68.3)
HXL-10	0.308	0.70	0.55	0.54	0.15	0.16	11,764	686			831 (120.5)	406 (58.9)	425 (61.6)
HXL-7	0.325	0.50	0.45	0.47	0.05	0.03	19,262	802			731 (106.2)	371 (53.9)	360 (52.3)
HXL-1	0.258	0.50	0.46	0.46	0.04	0.04	17,820	742			715 (103.8)	382 (55.5)	333 (48.3)
HXL-15	0.381	0.44	0.42	0.45	0.02		148,497	5,445	454	65.9	700 (101.6)	351 (51.0)	349 (50.6)
Tested at 760°C (1400°F) (Young's Modulus E = 146 GPa = 21.16 × 10^6 psi)													
HXL-13	0.321	4.48	0.54	0.70	3.94	3.78	56	21	966	140.1	1016 (147.4)	494 (71.7)	522 (75.7)
HXL-11	0.305	3.00	0.55	0.64	2.45	2.36	154	38	848	123.0	935 (135.7)	465 (67.4)	470 (68.2)
HXL-48	0.282	2.07	0.55	0.62	1.52	1.45	280	46	725	105.2	902 (130.8)	449 (65.2)	453 (65.6)
HXL-50	0.316	1.50	0.50	0.55	1.00	0.95	598	75	663	96.2	800 (116.1)	396 (57.4)	404 (58.7)
HXL-2	0.294	1.0	0.48	0.47	0.52	0.53	1,582	132			684 (99.2)	339 (49.2)	345 (50.0)
HXL-17	0.320	0.70	0.42	0.45	0.28	0.25	3,351	195			655 (95.0)	323 (46.9)	332 (48.1)
HXL-18	0.369	0.51	0.37	0.40	0.14	0.11	8,362	348	434	63.0	586 (85.0)	293 (42.5)	293 (42.5)
HXT-5	0.267	0.45	0.38	0.35	0.07	0.10	102,168	3,831	460	66.7	518 (75.1)	256 (37.2)	262 (38.0)
HXL-5	0.308	0.35	0.34	0.32	0.02	0.03	215,747	6,293	363	52.7	476 (69.0)	213 (30.9)	263 (38.1)
Tested at 871°C (1600°F) (Young's Modulus E = 137 GPa = 19.86 × 10^6 psi)													
HXL-41	0.311	4.00	0.42	0.53	3.58	3.47	96	32	702	101.8	720 (104.7)	347 (50.4)	373 (54.0)
HXL-40	0.326	3.01	0.41	0.52	2.60	2.49	138	34	690	100.1	715 (103.7)	343 (49.7)	372 (54.0)
HXL-33	0.337	2.01	0.34	0.44	1.67	1.57	312	52	536	77.8	610 (88.5)	298 (43.2)	312 (45.3)
HXL-53[e]	0.319	2.00	0.35	0.44	1.65	1.56	280	19	609	88.4	682 (99.0)	333 (48.3)	349 (50.7)
HXL-34[f]	0.298	2.00		0.47		1.53	216	1,332	566	82.0	638 (92.6)	318 (46.1)	320 (46.4)
HXL-35[g]	0.329	2.00		0.48		1.52	185	1,141	536	77.7	655 (95.0)	333 (48.2)	322 (46.8)
HXL-37[f,g]	0.320	2.00		0.47		1.53	196	2,384	521	75.6	644 (93.4)	319 (46.3)	325 (47.1)
HXT-7	0.307	1.50	0.34	0.44	1.16	1.06	466	58	542	78.6	604 (87.5)	297 (43.1)	307 (46.5)
HXL-36	0.305	1.00	0.38	0.38	0.62	0.62	1,156	96	486	70.4	523 (75.8)	257 (37.2)	266 (38.6)
HXL-54[h]	0.274	0.99		0.389		0.601	618	9,322	417	60.5	533 (77.3)	275 (39.8)	258 (37.4)
HXL-43	0.307	0.80	0.32	0.35	0.48	0.45	2,002	133			479 (69.5)	236 (34.2)	243 (35.2)
HXL-21	0.270	0.59	0.34	0.33	0.25	0.26	3,433	172	408	59.2	452 (65.6)	229 (33.2)	223 (32.4)
HXL-24[e]	0.279	0.59	0.34	0.34	0.25	0.25	3,494	70			460 (66.8)	232 (33.6)	228 (33.2)
HXL-26[f,i]	0.253	0.60		0.37		0.23	2,191	13,255	385	55.8	509 (73.8)	219 (31.8)	290 (42.1)
HXL-32[g,i]	0.315	0.60		0.37		0.23	1,084	6,558	383	55.5	510 (74.1)	274 (39.8)	236 (34.3)
HXL-38[f,g]	0.283	0.60		0.36		0.24	984	11,857	394	57.2	495 (71.8)	247 (35.9)	248 (35.9)
HXT-6	0.255	0.50	0.34	0.28	0.16	0.22	13,234	551	374	54.3	392 (56.9)	195 (28.3)	197 (28.6)

[a]Strain rate 4 × 10^{-3}/sec unless otherwise noted.

[b]L in specimen number implies specimen axis parallel to rolling direction; T transverse.

[c]$\Delta\sigma/E$.

[d]$\Delta\varepsilon_t - \Delta\sigma/E$.

[e]Strain rate 10 × 10^{-3}/sec.

[f]0.1-hr tensile hold period.

[g]0.1-hr compressive hold period.

[h]0.25-hr compressive hold period.

[i]Strain rate 9 × 10^{-3}/sec.

Table 3.37. Strain-Range Partitioning in Strain-Controlled Fatigue Tests on Hastelloy X in Air at 871°C (1600°F)

Specimen	Strain Rate (sec^{-1})	Hold Period, hr		Relaxed Stress, MPa (ksi)		Partitioned Inelastic Strain Range,[a] %		Associated Cycle Lifetimes, hr	
		Tensile	Compressive	Tensile, σ_{t_r}	Compressive, σ_{c_r}	$\Delta\varepsilon_{pp}$	Other	N_{pp}	Other
HXL-34	4×10^{-3}	0.1		48 (7.0)		1.34	$\Delta\varepsilon_{cp}$ = 0.20	312	N_{cp} = 70
HXL-35	4		0.1		38 (5.6)	1.31	$\Delta\varepsilon_{pc}$ = 0.21	320	N_{pc} = 50
HXL-37	4	0.1	0.1	33 (4.8)	33 (4.8)	1.32	$\Delta\varepsilon_{cc}$ = 0.21	318	N_{cc} = 58
HXL-54	4		0.25		38 (5.6)	0.44	$\Delta\varepsilon_{pc}$ = 0.16	1,746	N_{pc} = 222
HXL-26	9	0.1		57 (8.3)		0.11	$\Delta\varepsilon_{cp}$ = 0.11	15,039	N_{cp} = 1221
HXL-32	9		0.1		49 (7.1)	0.090	$\Delta\varepsilon_{pc}$ = 0.14	20,604	N_{pc} = 669
HXL-38	4	0.1	0.1	26 (3.9)	30 (4.3)	0.079	$\Delta\varepsilon_{cc}$ = 0.16	25,228	N_{cc} = 667

[a]Based on calculated inelastic strain range.

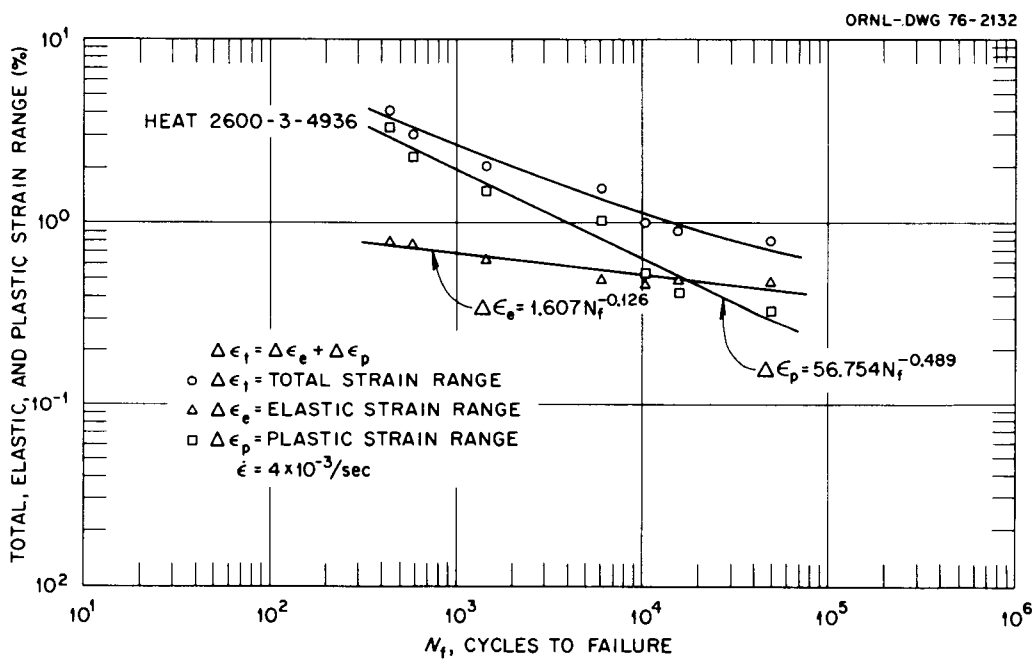

Fig. 3.82. Total, Elastic, and Plastic Strain Range vs Cycles to Failure for Hastelloy X Tested in Air at Room Temperature.

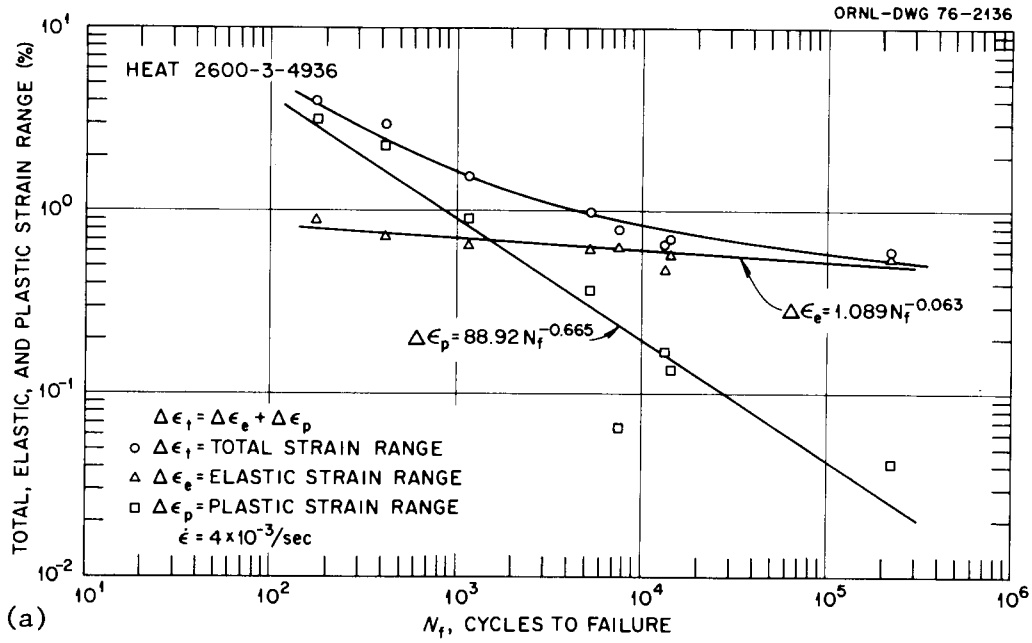

(a)

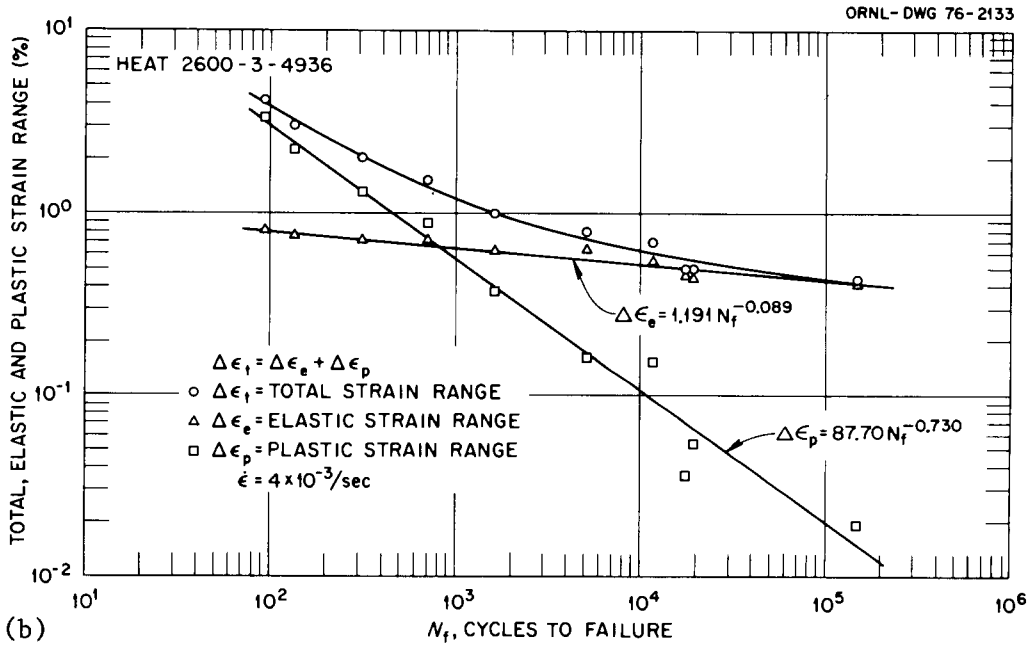

(b)

Fig. 3.83. Total, Elastic, and Plastic Strain Range vs Cycles to Failure for Hastelloy X Tested in Air at (a) 538°C (1000°F) and (b) 649°C (1200°F).

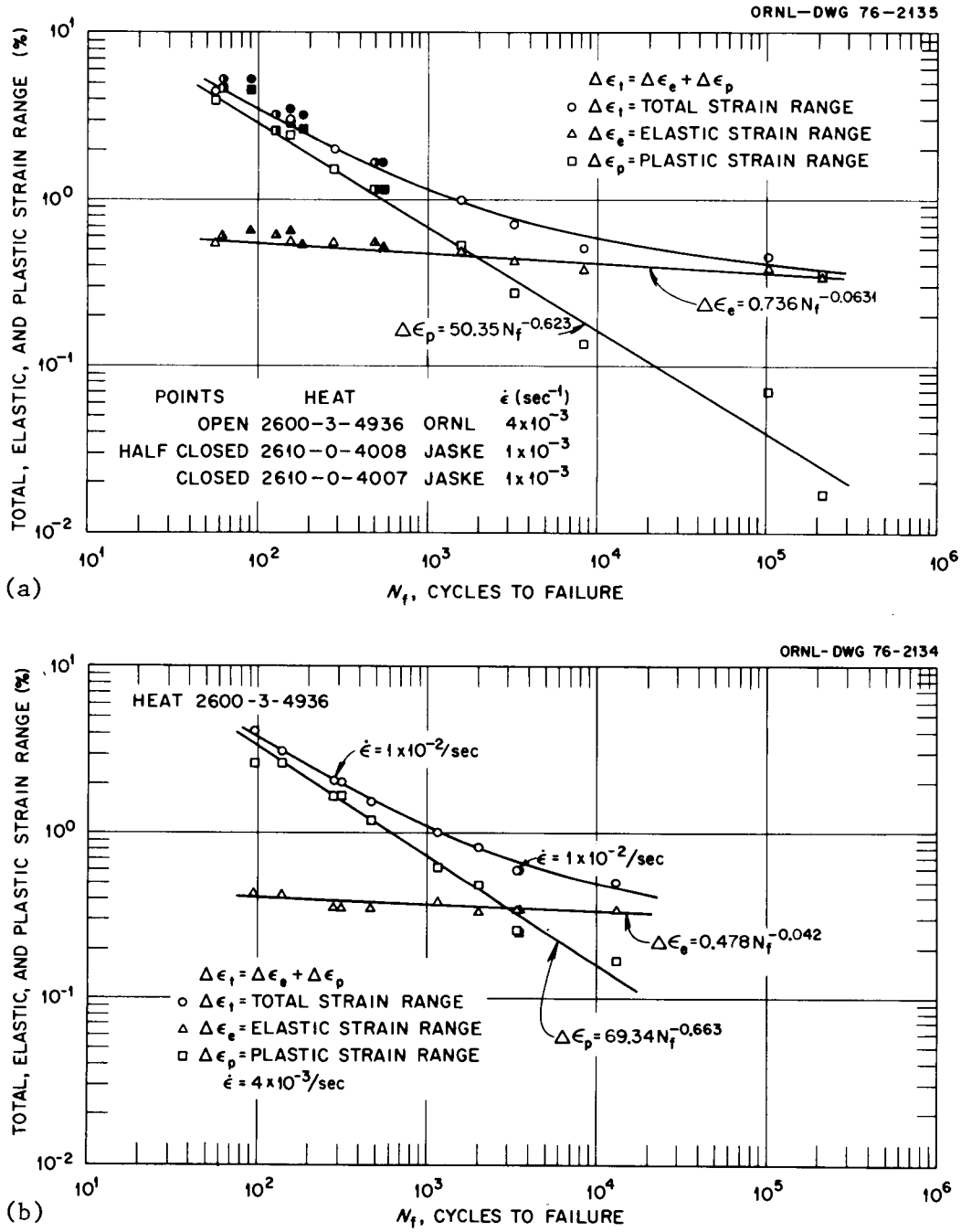

Fig. 3.84. Total, Elastic, and Plastic Strain Range vs Cycles to Failure for Hastelloy X Tested in Air at (a) 760°C (1400°F) and (b) 871°C (1600°F).

Table 3.38. Values for the Elastic and Plastic Strain Range Constants for Strain-Controlled Fatigue Tests Conducted on Hastelloy X (Heat 2600-3-4936) at a Strain Rate of 4×10^{-3}/sec

Temperature		Values of Constants in $\Delta\varepsilon_t = AN_f^{-a} + BN_f^{-b}$			
(°C)	(°F)	A	a	B	b
Room		56.75	0.489	1.607	0.126
538	1000	88.92	0.665	1.089	0.0633
649	1200	87.70	0.730	1.191	0.0890
760	1400	50.35	0.623	0.736	0.0631
871	1600	69.34	0.663	0.478	0.0420

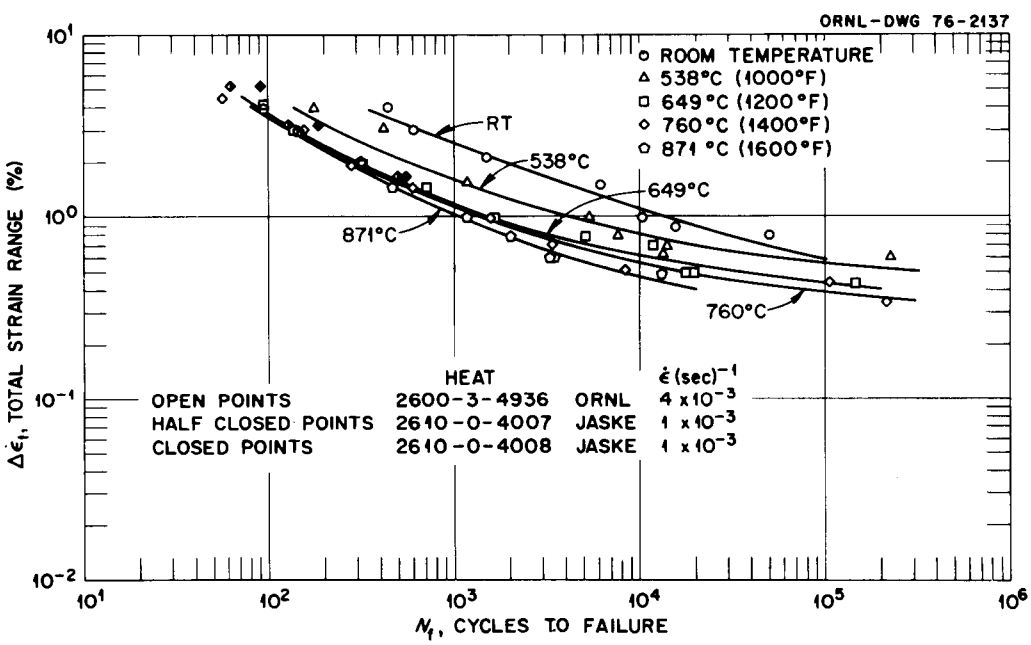

Fig. 3.85. Total Strain Range vs Cycles to Failure for Hastelloy X Tested in Air.

Since other structural materials[95,96] will be used for various components within HTGR systems, comparisons between the continuous cycling fatigue properties of Hastelloy X and a number of these materials would be instructive. These materials include Inconel alloy 718,[97] Incoloy alloy 800,[98—101] 2 1/4 Cr-1 Mo steel,[82] AISI 1010 steel,[102] type 304 stainless steel,[98—101,103,104] and type 316 stainless steel.[98,100,105] Product forms for which the data were obtained along with several tensile properties of interest in fatigue analysis at temperatures where comparisons can be made are given in Table 3.39. All data were obtained in air at a continuous cycling strain rate of 4×10^{-3}/sec. Comparative plots are given in Figs. 3.86 through 3.88. Values of the constants defining equations for Hastelloy X are given in Table 3.38, while equations for other materials are given in Tables 3.40 and 3.41. The coefficients and exponents given in Tables 3.40 and 3.41 define best fit equations having either of the following forms:

$$\Delta\varepsilon_t = AN_f^{-a} + BN_f^{-b} \quad , \tag{53}$$

or

$$\log N_f = \alpha_0 - \alpha_1 \log \Delta\varepsilon_t + \alpha_2(\log \Delta\varepsilon_t)^2 - \alpha_3(\log \Delta\varepsilon_t)^3 \quad , \tag{54}$$

where

$\Delta\varepsilon_t$ = total strain range (%), and
N_f = cycles to failure.

Figure 3.86 includes a mean curve for austenitic stainless steels (types 304, 310, 316, 347, and 348) from room temperature to 427°C (800°F), which is defined[106] by

$$\Delta\varepsilon_t(\%) = 64.0N_f^{-0.5} + 0.223 \quad . \tag{55}$$

Table 3.39. Comparison of Several Tensile Properties (Average Values) of Several Structural Materials Used in Nuclear Reactor Construction

Material and Heat Treatment	Temperature (°C)	Temperature (°F)	Strength, MPa (ksi) Ultimate	Strength, MPa (ksi) Yield	Reduction of Area (%)
Inconel alloy 718 (plate)	20	70	1372 (199)	1034 (150)	28
954°C (1750°F) solution anneal	538	1000	1193 (173)	965 (140)	27
718°/621°C (1325°/1150°F)	649	1200	1069 (155)	903 (131)	23
Duplex age					
Hastelloy alloy X (plate)	20	70	758 (110)	358 (52)	60
solution annealed at 1176°C	538	1000	593 (86)	227 (33)	38
(2150°F) followed by rapid	649	1200	510 (74)	221 (32)	38
air cool or water quench					
Incoloy alloy 800, Grade 2 (bar)	20	70	545 (79)	228 (33)	73
and H, solution annealed	538	1000	448 (65)	131 (19)	55
1148°C (2100°F)	649	1200	379 (55)	117 (17)	53
Type 316 stainless steel (bar)	20	70	593 (86)	290 (42)	72
solution annealed	538	1000	455 (66)	172 (25)	66
	649	1200	365 (53)	165 (24)	69
Type 304 stainless steel (bar)	20	70	593 (86)	248 (36)	81
solution annealed	538	1000	393 (57)	131 (19)	69
	649	1200	290 (42)	117 (17)	58
2 1/4 Cr-1 Mo steel, plate and	20	70	500 (73)	260 (37)	70
pipe, annealed or isothermally	538	1000	380 (55)	195 (28)	75
annealed					
AISI 1010 steel (bar)	20	70	407 (59)	209 (30)	25
	538	1000	153 (22)	92 (13)	59

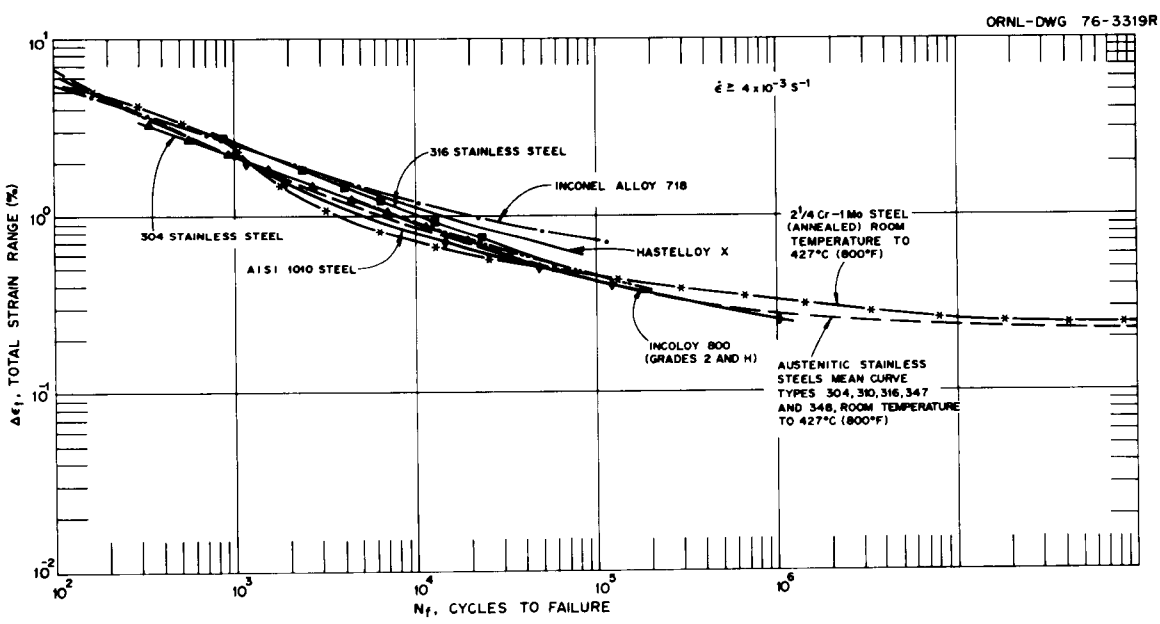

Fig. 3.86. Comparison of the Fatigue Behavior of Several Materials at Room Temperature (Except as Indicated). Lines represent best fit values of actual data.

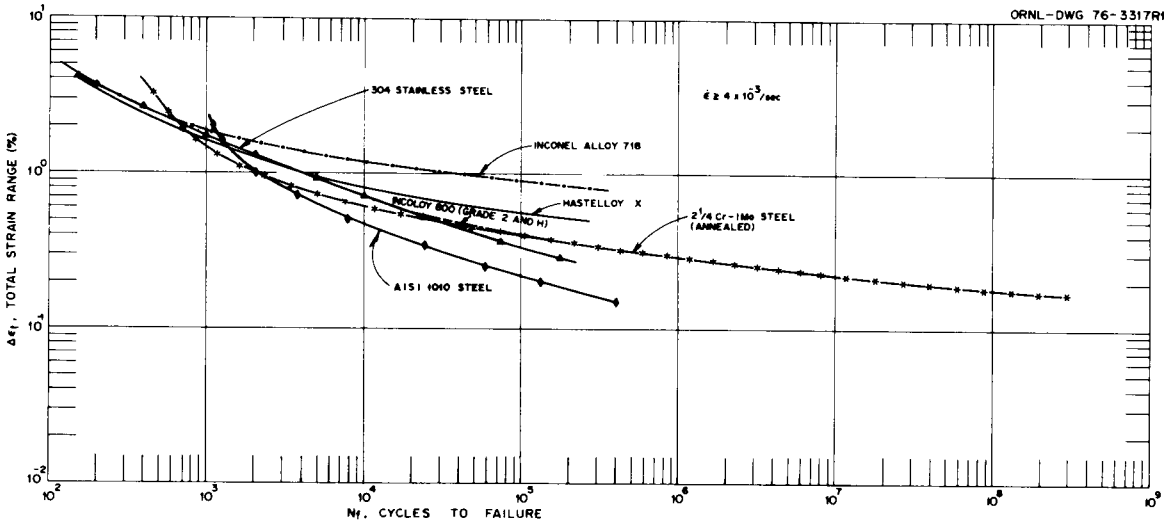

Fig. 3.87. Comparison of the Fatigue Behavior of Several Materials at 538°C (1000°F). Lines represent best fit values of actual data. Data for type 304 stainless steel include tests conducted at 538 and 566°C (1000–1050°F).

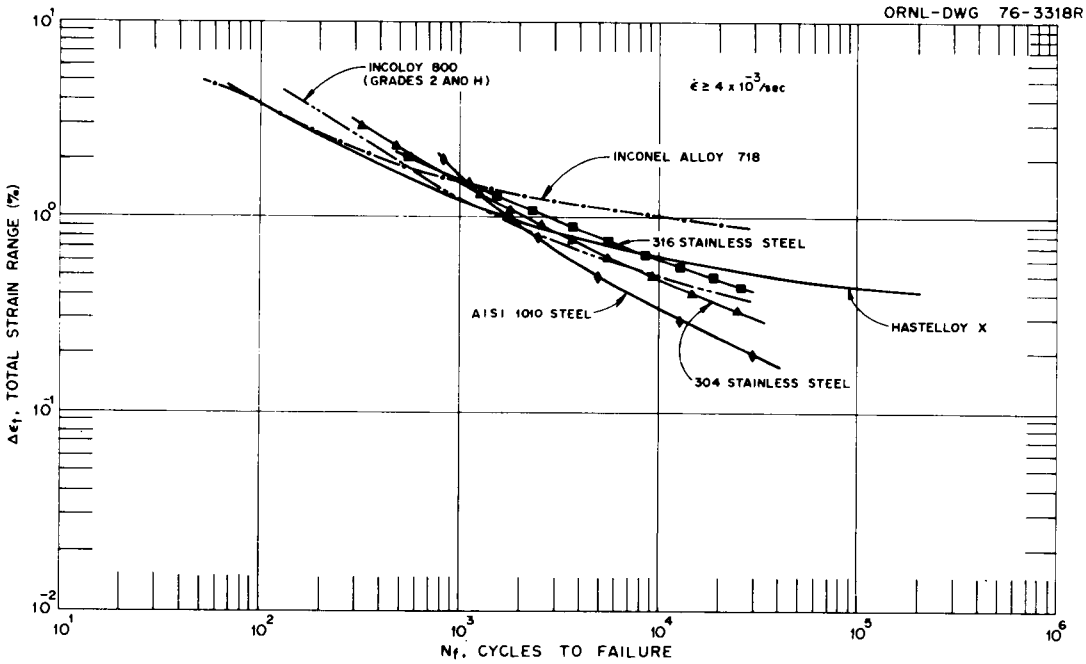

Fig. 3.88. Comparison of the Fatigue Behavior of Several Materials at 649°C (1200°F). Lines represent best fit values of actual data.

Table 3.40. Constants for Defining Best Fit Equations of Fatigue Curves for Structural Materials Following Eq. (54)

Material	Temperature (°C)	Temperature (°F)	Values of Constants α_0	α_1	α_2	α_3
Inconel alloy 718, 954°C (1750°F) Solution Annealed	20	70	4.317	4.184	3.295	2.562
	538	1000	4.590	8.673	12.178	7.048
	649	1200	4.082	7.872	12.364	8.494
Inconoy alloy 800, Grades 2 and H	20	70	3.903	2.903	0.831	0.177
	538	1000	3.485	2.391	2.272	3.009
	649	1200	3.191	2.099	1.495	1.295
AISI 1010 Steel	20	70	3.77	2.71	1.91	0
	538	1000	3.32	1.41	1.67	0
	649	1200	3.25	1.28	0.681	0
2 1/4 Cr-1 Mo[a]	20—427	70—800	3.578 ±0.044	2.358 ±0.176	3.506 ±0.274	4.197 ±0.663
	538	1000	3.302 ±0.081	2.388 ±0.296	3.521 ±0.592	2.577 ±1.122
	593	1100	3.153 ±0.051	1.803 ±0.273	2.613 ±0.466	3.738 ±1.250

[a]Standard error shown. Applicable for cyclic strain rates near 4×10^{-3}/sec. Applicable for product forms: plate, pipe, bar in annealed or isothermally annealed condition. Limitations: 0.07—0.15 wt % C; 2.0—2.5 wt % Cr; 0.9—1.1 wt % Mo; minimum room-temperature ultimate tensile strength, 414 MPa (60 ksi); minimum room-temperature (0.2% offset) yield strength, 207 MPa (30 ksi).

Table 3.41. Constants for Defining Best Fit Equations of Fatigue Curves for Stainless Steels Following Eq. (53)

Stainless Steel	Temperature (°C)	Temperature (°F)	Values of Constants A	a	B	b
Type 316	20	70	0.667	0.499	0.018	0.179
	649	1200	0.545	0.560	0.012	0.153
Type 304	20	70	0.247	0.403	0.050	0.303
	538 560	1000 1050	46.77	0.515	1.176	0.149
	649	1200	36.308	0.506	1.044	0.151

Comparing the continuous cycling fatigue behavior of these materials in Figs. 3.86 through 3.88 indicates similar behavior in the low-cycle range, even though the materials show wide differences in ductility, particularly at room temperature. However, as the total strain range is reduced marked differences in fatigue life occur and are accentuated by increasing the temperature. High-cycle fatigue resistance is a function of the ultimate tensile strength, and, therefore, Inconel alloy 718, having the highest value, shows the best high-cycle fatigue resistance, with Hastelloy X falling second.

In addition to continuous cycling fatigue tests, a limited number of hold-time tests have been conducted to date at 871°C (1600°F) to determine the influence of creep-fatigue and environment interaction on the flow and failure behavior of Hastelloy X. Constant-strain hold periods were introduced each cycle at peak cyclic strain amplitudes (tensile, compressive, and both). Generally the technique of strain range partitioning[107,108] is being used as a guide in developing the necessary data such that the fatigue life of any complex cycle at temperatures within the creep range might be predicted. Interim preliminary data for Hastelloy X are reported in Tables 3.36 and 3.37. Shapes of hysteresis loops at roughly half the cycle life for two strain ranges (i.e., 2% and 0.6%) are compared in Fig. 3.89 with hysteresis loops that were generated without hold periods. For the 0.6% total strain range tests, tests conducted with a tensile hold only developed a mean compressive stress and tests conducted with only a compressive hold period developed a mean tensile stress, while for tests generated with both a tensile and a compressive hold, little or no mean stress was developed. Figure 3.89 also shows that compressive hold times tend to be more damaging.

Lord and Coffin[109] characterized the low-cycle fatigue and hold time behavior of cast René 80 and found that compressive hold times were more damaging than tensile hold times. They qualitatively explained this behavior in terms of the ability of the material to sustain a mean stress at cycle lives beyond the transition fatigue life (i.e., the elastic strain range was greater than the plastic strain range). They

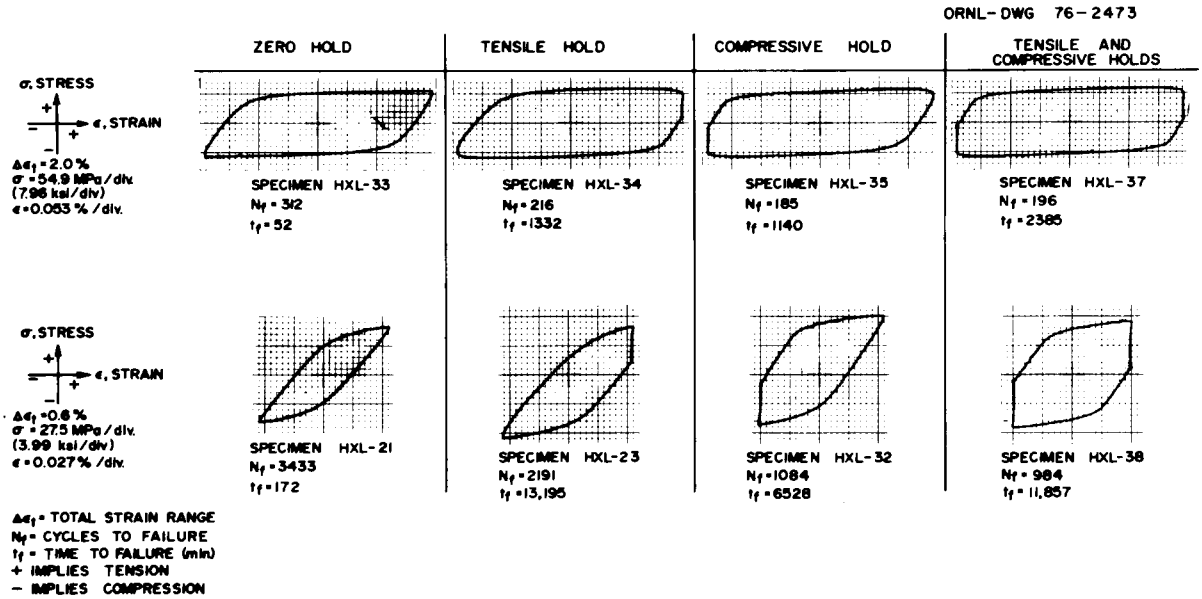

Fig. 3.89. Comparison of Actual Hysteresis Loops from Strain-Controlled Low-Cycle Fatigue Tests Involving Zero Hold Periods or 0.1-hr Hold Periods at Peak (Maximum, Minimum, or Both) Strain Amplitudes. Tests were conducted on Hastelloy X (Heat 2600-3-4936) at 871°C (1600°F) in air.

postulated that in this material compressive hold times were particularly deleterious at low strain ranges because tensile mean stresses could be maintained and enhanced crack growth rates. For Hastelloy X tested at 871°C (1600°F), the cycle life of a continuously cycled specimen tested at 0.6% total strain range is greater than the transition fatigue life. Therefore, the above explanation as to why compressive hold times are more damaging than tensile hold times is plausible.

The strain range partitioning concept was used to partition inelastic strain into four components (i.e., $\Delta\varepsilon_{pp}$, $\Delta\varepsilon_{cp}$, $\Delta\varepsilon_{pc}$, and $\Delta\varepsilon_{cc}$), where:

$\Delta\varepsilon_{pp}$ = Range of tensile plasticity reversed by compressive plastic strain or width of the hysteresis loop generated at high enough strain rates to preclude creep or strain rate effects. In Hastelloy X over the temperature range of interest, strain rates of at least 4×10^{-3}/sec were shown to be acceptable for this purpose.

$\Delta\varepsilon_{cp}$ = Range of tensile creep reversed by compressive plastic strain generated in work to date by tensile strain hold time tests. However, other tests imposing load holds will also be conducted.

$\Delta\varepsilon_{pc}$ = Range of tensile plastic strain reversed by compressive creep strain, obtained from compressive hold time tests. To date only strain hold time tests have been conducted.

$\Delta\varepsilon_{cc}$ = Range of tensile creep reversed by compressive creep. Obtained from tests in which a hold is introduced during both tensile and compressive halves of each cycle. Only strain holds have been employed to date.

Plots of the inelastic strain components from tests conducted to date are given in Fig. 3.90. Only data in the range from 649 to 871°C (1200–1600°F) are included in this plot. The $\Delta\varepsilon_{pp}$ plastic strain data obtained from tests conducted at temperatures of 538°C (1000°F) and lower were excluded from the plot since values clearly fell above the high-temperature data.

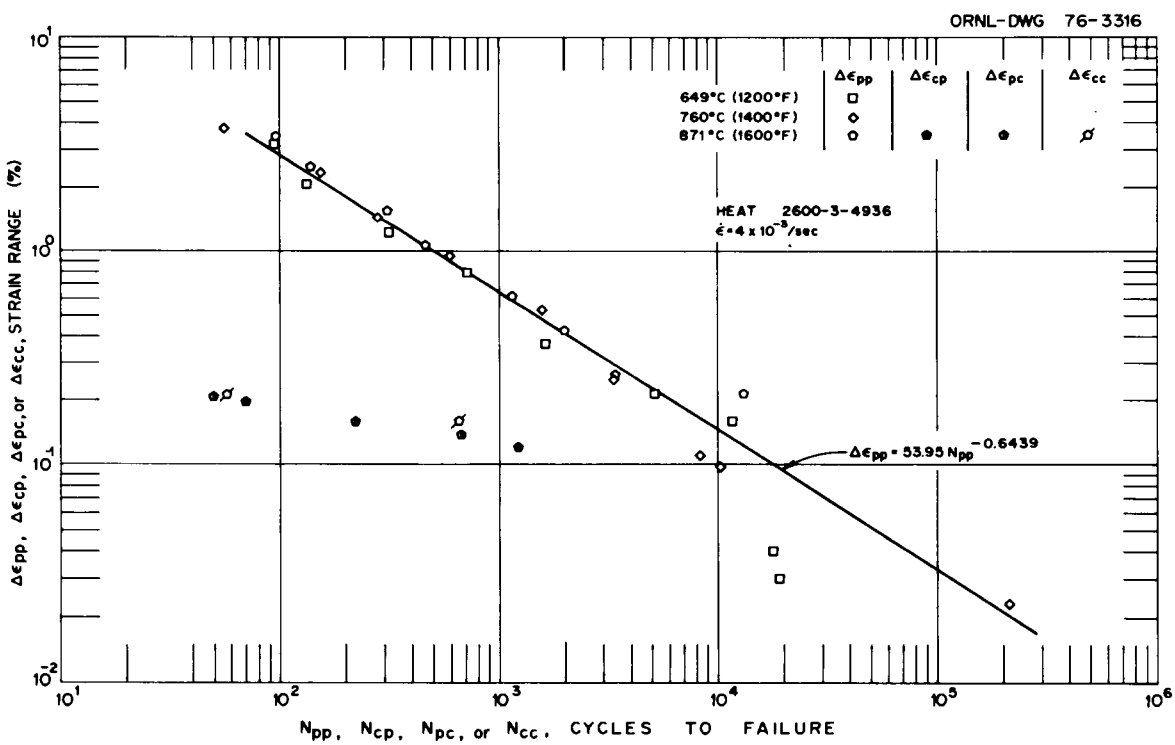

Fig. 3.90. Partitioned Inelastic Strain Components vs Associated Failure Lifetimes for Hastelloy X.

Cyclic lives associated with the various components of time-dependent inelastic strain (i.e., N_{cp}, N_{pc}, and N_{cc}) plotted in Fig. 3.90 were calculated by use of the interaction damage rule:[110]

$$\frac{F_{pp}}{N_{pp}} + \frac{F_{pc}}{N_{pc}} + \frac{F_{cp}}{N_{cp}} + \frac{F_{cc}}{N_{cc}} = \frac{1}{N_f} ,$$

where

$F_{pp} = \Delta\varepsilon_{pp}/\Delta\varepsilon_{in}$,

$F_{pc} = \Delta\varepsilon_{pc}/\Delta\varepsilon_{in}$,

$F_{cp} = \Delta\varepsilon_{cp}/\Delta\varepsilon_{in}$,

$F_{cc} = \Delta\varepsilon_{cc}/\Delta\varepsilon_{in}$,

$\Delta\varepsilon_{in}$ = total inelastic strain range associated with the particular cycle being analyzed.

Tests in air will continue and tests conducted in simulated HTGR primary coolant helium environment will begin in the near future. Completed fabrication of the environmental chamber design described previously[93] is projected for August 14, 1976.

3.6.4 Subcritical Crack Growth Studies — W. R. Corwin

The materials used in this study are two Babcock and Wilcox heats of 2 1/4 Cr-1 Mo ferritic steel, 20017 and 3P5601, and one heat of Hastelloy X, 2600-3-4936, from Cabot. Their mechanical properties have been reported in previous quarterlies.

3.6.4.1 Testing of 2 1/4 Cr-1 Mo Steel

In experimental work in air, the following areas were emphasized this quarter: heat-to-heat effects, frequency effects, and an examination of possible effects of specimen geometry.

Last quarter we reported[111] no difference in the fatigue crack propagation (FCP) behavior of heats 3P5601 and 20017 in air at 510°C (950°F), 0.67 Hz (40 cpm); yet a difference was noted at 371°C (700°F), presumably due to dynamic strain aging. Tests this quarter at room

temperature in air with R = 0.05 and a frequency of 40 Hz (2400 cpm) reveal a small difference in crack growth rates between the two heats, as shown in Fig. 3.91. The growth rate of heat 3P5601 is approximately 20% greater than that of 20017 at any ΔK level investigated. While this difference appears genuine it is well within the standard experimental error of a factor of 2, which exists even in round robin conditions.[112]

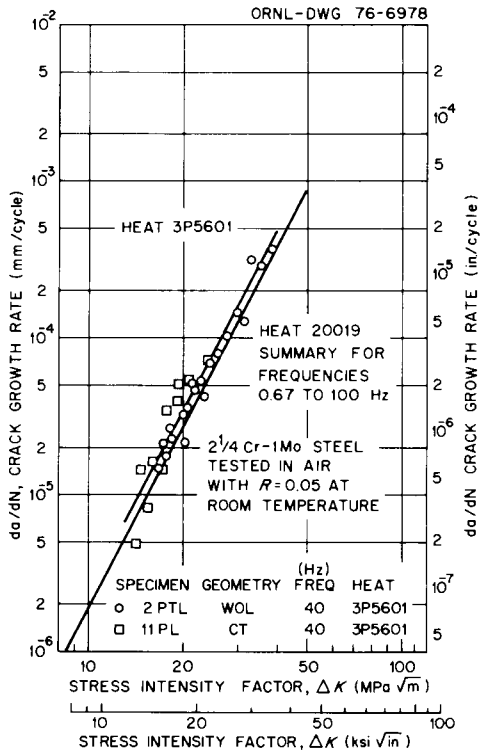

Fig. 3.91. Heat-to-Heat Variation in Fatigue Crack Growth Rate of 2 1/4 Cr-1 Mo Steel.

No other identical comparison tests in air have been performed at conditions besides those reported; however, similar tests in steam and HTGR helium indicate similar behavior and will be discussed subsequently.

Results from tests on Hastelloy X (see Sect. 3.6.4.2) evoked concern on possible effects of test specimen geometry and prompted comparison tests at room temperature and 510°C (950°F). The data from comparison tests at room temperature shown in Fig. 3.91 for heat 3P5601 show no difference in behavior between the compact tension (CT) and wedge opening load (WOL) specimens[82] used in this study. However, the tests at 510°C did show a small but reproducible difference between

the geometries, with the CT specimens yielding growth rates approximately 30% higher than the WOL specimens, as seen in Fig. 3.92. This effect appears real, and may be due to thickness effects, macroscopic stress levels, and/or creep effects. Investigations into possible suprious effects giving rise to the observed behavior are under way. In the interim, comparisons of test parameters, particularly effects of environment, will be made, where possible and appropriate, between specimens of similar geometry.

Frequency effects at elevated temperatures were further investigated this quarter at 510°C (950°F) with the completion of tests at 6.7 mHz (0.4 cpm) and the initiation of testing at 0.67 mHz (0.04 cpm). These tests will allow a representation of crack growth rate over five orders of magnitude of test frequency. The results will be reported later.

Testing in steam was completed at 593°C, 0.67 Hz with R = 0.05. The results shown in Fig. 3.93 follow the same general trends observed at 510°C (950°F). The crack growth rate of 2 1/4 Cr-1 Mo steel at lower ΔK levels is reduced below that in air. Furthermore, the da/dN vs ΔK slope is significantly higher in steam than in air, with the two

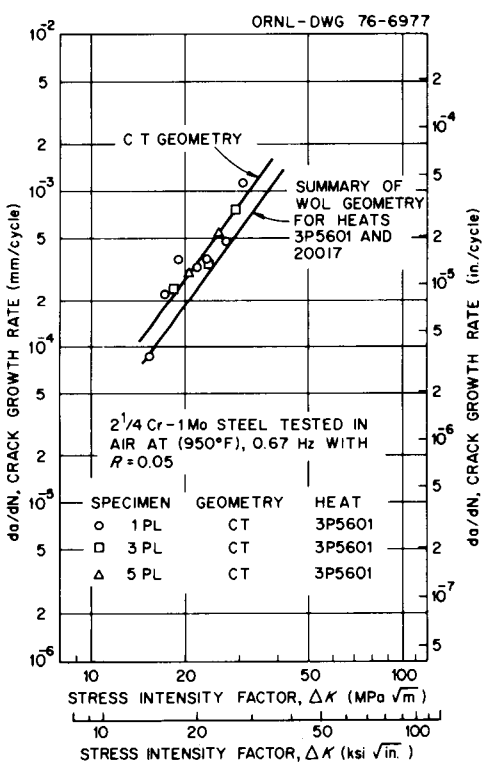

Fig. 3.92. Effects of Specimen Geometry on Fatigue Crack Growth Rate.

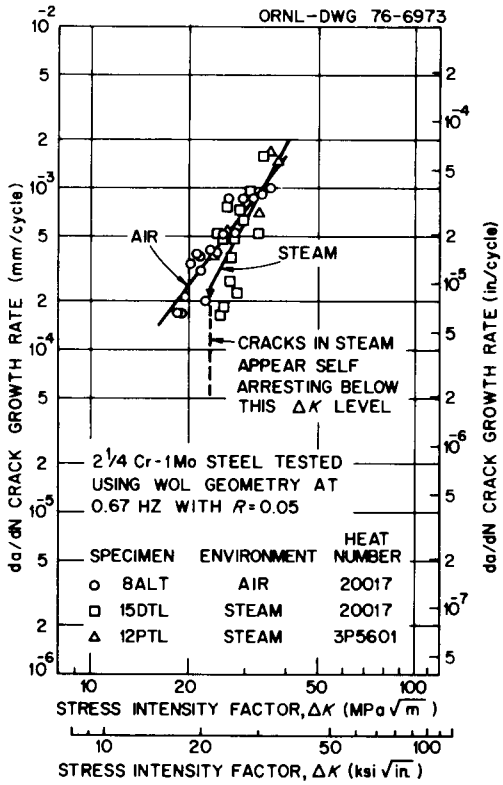

Fig. 3.93. Effect of Super Heated Steam on Fatigue Crack Growth Rate at 593°C (1100°F).

data sets coalescing at ΔK levels around 35 MPa $\sqrt{m}$ (32 ksi $\sqrt{in.}$). This is indicative of a stronger environmental effect at the slower growth rates, where (1) environmental effects have longer times to operate and (2) purely mechanical fracture processes (i.e., ligament rupture, void formation, etc.) contribute less.

Further, we noted for the test conditions examined that growing cracks would self-arrest at ΔK levels below about 23 MPa $\sqrt{m}$ (21 ksi $\sqrt{in.}$). This tendency had been noted in our earlier tests at 510°C (950°F) in steam but was not consistent enough to allow any quantitative assessment. In an additional test at 593°C (1100°F) with a frequency of 67 mHz (4cpm) cracks appeared to self-arrest at about 20 MPa $\sqrt{m}$ (18 ksi $\sqrt{in.}$), although further testing under these conditions is still to be performed.

Results of testing both heats 20017 and 3P5601 in helium at 510°C (950°F), 0.67 Hz (40 cpm) are shown in Fig. 3.94 and compared with the results of similar tests on CT specimens in air. Even with the scatter in the data, a clear reduction in crack growth rate in HTGR helium is observed.

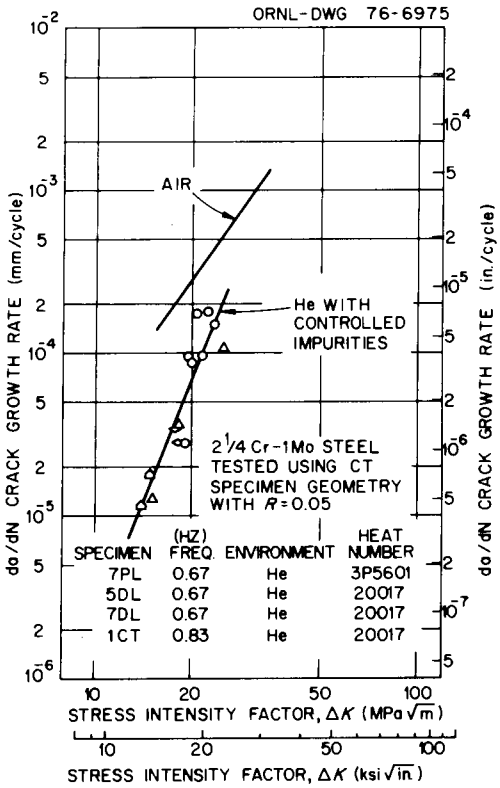

Fig. 3.94. Effect of Simulated HTGR Primary Coolant on Crack Growth Rate.

Cracks in heat 3P5601 may grow somewhat faster under the test conditions in helium, although the present data are inconclusive. The similarity of behavior of the two heats in air at 510°C (950°F) may well exist in the simulated HTGR coolant.

3.6.4.2 Testing of Hastelloy X

Limited testing to determine effects of simulated HTGR primary coolant on the fatigue crack propagation (FCP) behavior of Hastelloy X was performed by first testing in air at 25, 538, and 649°C (77, 1000, and 1200°F) and then running comparative tests in HTGR helium at the elevated temperatures. All tests had an R ratio of 0.05 and were run at a frequency of 1 Hz (60 cpm) at the elevated temperatures and 40 Hz (2400 cpm) at room temperatures, where thermal processes are largely inactive. The results are shown in Figs. 3.95 and 3.96. No difference in crack growth rate was observed in simulated HTGR helium at either of the elevated test temperatures when compared with results obtained in air with specimens of similar geometry. However, a systematic, reproducible

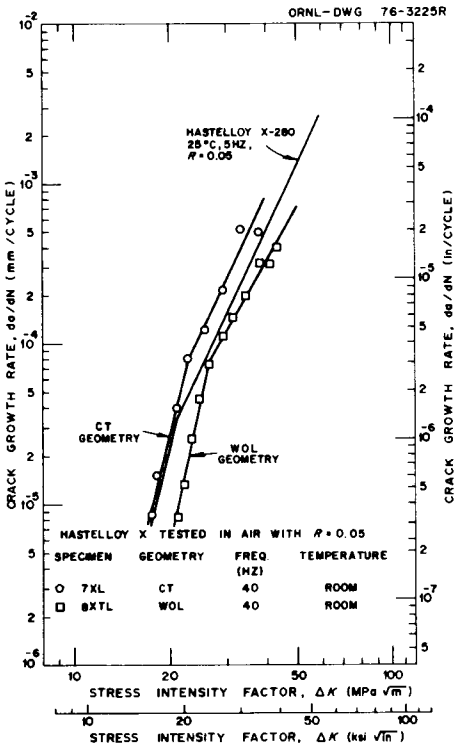

Fig. 3.95. Effect of Specimen Geometry on Fatigue Crack Growth Rate at Room Temperature.

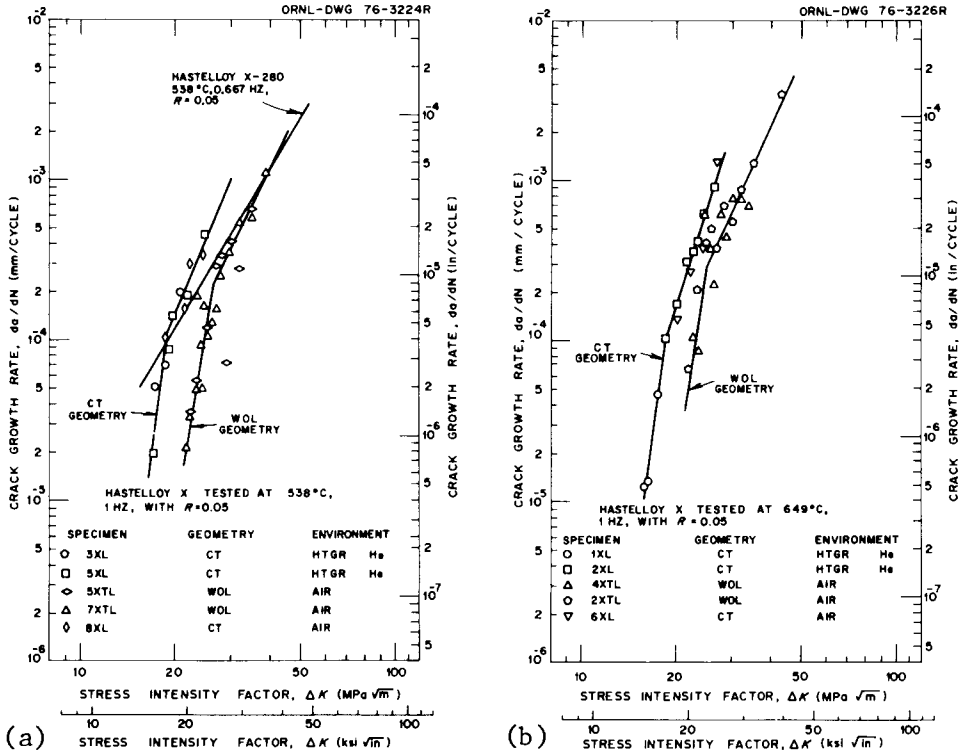

Fig. 3.96. Effect of Simulated HTGR Primary Coolant and Specimen Geometry on Fatigue Crack Growth Rate at (a) 538°C (1000°F) and (b) 649°C (1200°F).

difference was observed at all temperatures between the CT and WOL specimens. Since no similar effect had been noted in our work on 2 1/4 Cr-1 Mo steel to date using the same equipment and techniques, this difference may be attributed to inhomogeneities in the material or anomalies in specimen manufacture. As mentioned earlier, this is being investigated.

Averaged results of both test geometries are given in Fig. 3.97 for all test temperatures. Crack growth rate is plainly shown to increase with increasing temperature at a constant level of ΔK. Further work on Hastelloy X has been suspended to allow further investigations on 2 1/4 Cr-1 Mo steel.

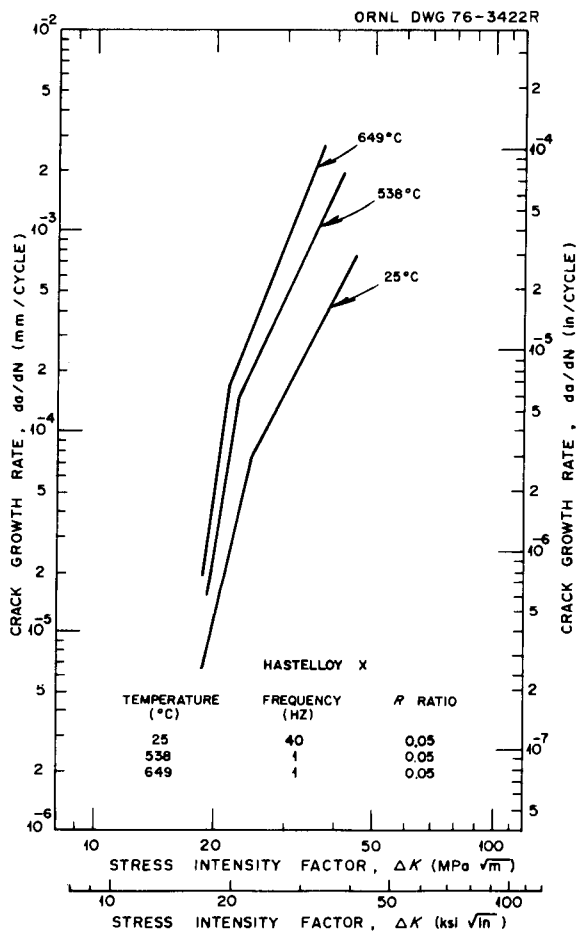

Fig. 3.97. Effect of Temperature on the Averaged Fatigue Crack Growth Behavior of Hastelloy X.

3.7 REFERENCES

1. M. K. Booker, T. L. Hebble, D. O. Hobson, and C. R. Brinkman, "Mechanical Property Correlations for 2 1/4 Cr-1 Mo Steel in Support of Nuclear Reactor Systems Design," paper F 8/9 in *Transitions of the 3rd International Conference on Structural Mechanics in Reactor Technology* (London, UK, 1–5 Sept. 1975), Vol. 2, Part F, Commission of the European Communities, Luxembourg.
2. W. E. Stillman, "Development of Creep Equation for Type 316 Stainless Steel," *Mechanical Properties Test Data for Structural Materials Quart. Progr. Rep. Oct. 31, 1975*, ORNL-5107, pp. 81–93.
3. I. A. Oding, ed., *Creep and Stress Relaxation in Metals*, transl. by E. Bishop, ed. by A. J. Kennedy, Oliver and Boyd, London, 1959, pp. 78–82.
4. M. K. Booker, "Development of Creep Equation for Type 304 Stainless Steel," *Mechanical Properties Test Data for Structural Materials Quart. Progr. Rep. Jan. 31, 1976*, ORNL-5112, pp. 67–74.
5. V. K. Sikka, "Mechanical Property Characterization of Type 316 Stainless Steel Reference Heat," *Mechanical Properties Test Data for Structural Materials Quart. Progr. Rep. July 31, 1975*, ORNL-5106, pp. 50–64.
6. Ibid., *Oct. 31, 1975*, ORNL-5107, pp. 34–46.
7. W. F. Simmons and H. C. Cross, *Report on the Elevated-Temperature Properties of Stainless Steels*, ASTM Special Technical Publication 124, American Society for Testing and Materials, Philadelphia, 1952.
8. W. F. Simmons and J. A. Van Echo, *Report on the Elevated-Temperature Properties of Stainless Steels*, ASTM Data Series DS 5 S1, American Society for Testing and Materials, Philadelphia, 1955.
9. G. V. Smith, *An Evaluation of the Yield, Tensile, Creep, and Rupture Strengths of Wrought 304, 316, 321, and 347 Stainless Steels at Elevated Temperatures*, ASTM Data Series DS 5 S2, American Society for Testing and Materials, Philadelphia, February 1969.
10. G. V. Smith, "The Temperature Dependence of Yield Strength and Tensile Strength of Several Austenitic Stainless Steels," pp. 79–95 in *Symposium on Elevated Temperature Properties of Austenitic Stainless Steels*, ASME, New York, 1974.

11. *Interpretations of the ASME Boiler and Pressure Vessel Code, Code Case 1592,* American Society of Mechanical Engineers, New York, 1974.

12. T. Kowada, et al., "Statistical Analysis of Creep Data," *Trans. Iron Steel Inst. Japan* 11: 167–75 (1971).

13. T. Prnka and V. Foldyna, "The Creep Properties of Low-Alloy Cr-Mo-V Steels with Low Carbon Content," pp. 115–30 in *High-Temperature Properties of Steels, Proceedings of the Joint Conference Organized by the British Iron and Steel Research Association and the Iron and Steel Institute,* ISI Publication 97, 1967.

14. T. L. Hebble, Oak Ridge National Laboratory, private communication, 1976.

15. The British Steelmakers Creep Committee, *BSCC High Temperature Data, British Long Term Creep Rupture and Elevated Temperature Tensile Data on Steels for High Temperature Service,* The Iron and Steel Institute, London.

16. *Ergebnisse deutscher Zeitstandversuche Länger Dauer,* Verein Deutscher Eisenhüttenleute, Verlag Stahleisen M.B.H., Düsseldorf, 1969.

17. *Results of High-Temperature Creep Tests in French Steels,* IRSID, 185, Rue du President Roosevelt, 78-Saint-German-en-laye, France, 1972.

18. *NRIM Creep Data Sheets: Elevated-Temperature Materials Manufactured in Japan, 1973,* National Research Institute for Metals, Tokyo, 153, Japan.

19. H. E. McCoy, Jr. and R. D. Waddell, Jr., "Mechanical Properties of Several Product Forms of a Single Heat of Type 304 Stainless Steel," *J. Eng. Mater. Technol.* 97: 343–49 (1975).

20. R. W. Swindeman, W. J. McAfee, and V. K. Sikka, *Product Form Variability in the Mechanical Behavior of Type 304 Stainless Steel at 593°C,* report in preparation, 1976.

21. V. K. Sikka, H. E. McCoy, M. K. Booker, and C. R. Brinkman, "Heat-to-Heat Variations in Creep Properties of Types 304 and 316 Stainless Steels," *J. Pressure Vessel Technol.* 97: 243–51 (1975).

22. V. K. Sikka, C. R. Brinkman, and H. E. McCoy, "Effect of Thermal Aging on Tensile and Creep Properties of Types 304 and 316 Stainless Steel," pp. 316–50 in *Symposium on Structural Materials for Service at Elevated-Temperatures in Nuclear Power Generation*, MPC-1, ed. by A. O. Schaefer, American Society of Mechanical Engineers, New York, 1975.

23. ASTM Designation: A 240-71, "Standard Specification for Stainless and Heat-Resisting Chromium and Chromium-Nickel Steel Plate, Sheet and Strip for Fusion Welded Unfired Pressure Vessels," *Annual Book of ASTM Standards, Part 3*, American Society for Testing and Materials, Philadelphia, April 1972.

24. ASTM Designation: A 312-71, "Standard Specification for Seamless and Welded Austenitic Stainless Steel Pipe, *Annual Book of ASTM Standards, Part 1*, American Society for Testing and Materials, Philadelphia, April 1972.

25. ASTM Designation: A 479-71, "Standard Specification for Stainless Steel and Heat-Resisting Steel Bars and Shapes for Use in Boilers and Other Pressure Vessels," *Annual Book of ASTM Standards, Part 3*, American Society for Testing and Materials, Philadelphia, April 1972.

26. L. D. Blackburn, Hanford Engineering Development Laboratory, private communication, November 1973.

27. V. K. Sikka, T. L. Hebble, M. K. Booker, and C. R. Brinkman, *Influence of Reannealing (Laboratory Annealing) on Tensile Properties and Time-Independent Design Stress Intensity Limits for Type 304 Stainless Steel*, report in preparation.

28. V. K. Sikka and T. L. Hebble, report in preparation.

29. M. K. Booker, C. R. Brinkman, and V. K. Sikka, "Correlation and Extrapolation of Creep Ductility Data for Four Elevated-Temperature Structural Materials," pp. 108–45 in *Symposium on Structural Materials for Service at Elevated Temperature in Nuclear Power Generation*, American Society for Mechanical Engineers, New York, 1975.

30. M. K. Booker and V. K. Sikka, *Predicting the Strain to Tertiary Creep for Elevated-Temperature Structural Materials*, ORNL/TM-5403 (in preparation).

31. M. K. Booker and V. K. Sikka, *Empirical Relationships Among Creep Properties of Four Elevated-Temperature Structural Materials*, ORNL/TM-5399, (in preparation).

32. G. V. Smith et al., "Creep-Rupture Strength of Austenitic Cr-Ni-Mo Steels in Sheet and Bar Form," *J. Basic Eng.* 81: 610–16 (1959).

33. T. Shinoda, T. Matsuo, and R. Tanaka, "Method for Improving the Creep Strength in Austenitic Heat-Resisting Steel," paper presented at the International Conference on Creep and Fatigue in Elevated-Temperature Applications, Philadelphia, 1973, and Sheffield, UK, (April 1974).

34. C. R. Brinkman and G. E. Korth, "Heat-to-Heat Variations in the Fatigue and Creep-Fatigue Behavior of AISI Type 316 Stainless Steel at 593°C," *J. Nucl. Mater.* 48: 293–306 (1973).

35. V. K. Sikka, R. W. Swindeman, C. R. Brinkman, and M. K. Booker, "Residual Cold Work and Its Influence on Tensile and Creep Properties of Types 304 and 316 Stainless Steels," paper accepted for publication by *Nuclear Technology*, 1976.

36. W. Ruttmann, M. Krause, and K. J. Kremer, "International Community Tests on Long-Term Behavior of 2 1/4 Cr-1 Mo Steel," pp. 23–30 in *High-Temperature Properties of Steels, Proceedings of the Joint Conference Organized by the British Iron and Steel Research Association and the Iron and Steel Institute*, ISI Publication 97, 1967.

37. V. K. Sikka, "Heat-to-Heat Variation and Its Relation with Chemical Composition," *Mechanical Properties Test Data for Structural Materials Quart. Progr. Rep. Apr. 30, 1975*, ORNL-5105, pp. 95–101.

38. C. E. Spaeder, Jr. and J. D. Defilippi, "A Statistical Study of the Effect of Composition on the Creep-Rupture Properties of AISI Type 304 Stainless Steel," pp. 65–77 in *Symposium on Elevated-Temperature Properties of Austenitic Stainless Steels*, American Society of Mechanical Engineers, New York, 1974.

39. V. K. Sikka and C. R. Brinkman, "Relation Between Short- and Long-Term Elevated-Temperature Properties of Several Austenitic Stainless Steels," *Scr. Metall.* 10: 25–28 (1976).

40. L. D. Blackburn, "Isochronous Stress-Strain Curves for Austenitic Stainless Steels," pp. 15–48 in *The Generation of Isochronous Stress-Strain Curves*, ed. by A. O. Schaefer, American Society of Mechanical Engineers, New York, 1972.

41. M. K. Booker, T. L. Hebble, D. O. Hobson, and C. R. Brinkman, "Mechanical Property Correlations for 2 1/4 Cr-1 Mo Steel in Support of Nuclear Reactor Systems Design," paper F 8/9 in *Transactions of the 3rd International Conference on Structural Mechanics in Reactor Technology*, (London, September 1975), Vol. 2, Pt. F, Commission of the European Communities, Luxembourg, 1975.

42. W. E. Stillman, M. K. Booker, and V. K. Sikka, "Mathematical Description of the Creep Strain-Time Behavior of Type 316 Stainless Steel," submitted to Second International Conference on Mechanical Behavior of Materials, Boston, August 16–20, 1976.

43. D. O. Hobson, M. K. Booker, and T. L. Hebble, *Advantages and Applications of a Simple Rational Polynomial Creep Equation*, report in preparation.

44. J. B. Conway, *Stress-Rupture Parameters: Origin, Calculation, and Use*, Gordon and Breach, New York, 1969.

45. F. C. Monkman and N. J. Grant, "An Empirical Relationship Between Rupture Life and Minimum Creep Rate in Creep-Rupture Tests," *Proc. ASTM* 56: 593–605 (1956).

46. M. K. Booker and V. K. Sikka, *Interrelationships Between Creep Life Criteria for Four Nuclear Structural Materials*, ORNL-TM-4997 (August 1975).

47. V. S. Ivanova, "Creep Ductility Criterion for Metals," *Zavod. Labor.* 21(2): 212–16 (1955); Brutcher Translation No. 4210.

48. R. W. Swindeman, "Creep-Rupture Correlations for Type 304 Stainless Steel (Ht. 9T2796)," *Symposium on Structural Materials for Elevated Temperature Nuclear Power Generation Service*, Metal Properties Council, New York, 1975.

49. R. W. Swindeman and C. E. Pugh, *Creep Studies on Type 304 Stainless Steel (Heat 8043813) Under Constant and Varying Loads*, ORNL-TM-4427 (June 1974).

50. F. Garofalo et al., "Creep and Creep-Rupture Relationships in an Austenitic Stainless Steel," *Trans. Metall. Soc. AIME* 221: 310–19 (1961).

51. F. Garofalo et al., "Strain-Time, Rate-Stress, and Rate-Temperature Relations During Large Deformations in Creep," pp. 1-31–1-39 in *Joint International Conference on Creep*, The Institute of Mechanical Engineers, London, 1963.

52. R. L. Orr, O. D. Sherby, and J. E. Dorn, "Correlations of Rupture Data for Metals at Elevated Temperatures," *Trans. ASM* 46: 113–28 (1954).

53. S. S. Manson and C. R. Ensign, *A Specialized Model for Analysis of Creep-Rupture Data by the Minimum Commitment, Station-Function Approach*, NASA-TM-X-52999 (1971).

54. V. K. Sikka and M. K. Booker, "Use of Ultimate Tensile Strength in Correlating and Predicting Creep and Creep Rupture Behavior of Types 304 and 316 Stainless Steel," abstract submitted to *3rd International Conference on Pressure Vessel Technology*, Tokyo, 1977.

55. M. K. Booker, C. R. Brinkman, and V. K. Sikka, "Correlation and Extrapolation of Creep Ductility Data for Four Elevated-Temperature Structural Materials," pp. 108–45 in *Structural Materials for Service at Elevated Temperatures in Nuclear Power Generation*, American Society of Mechanical Engineers, New York, 1975.

56. Hanford Engineering Development Laboratory, *Nuclear Systems Materials Handbook*, TID-26666 (continually revised).

57. M. K. Booker and B.L.P. Booker, "Computerized Data Management System," *Mechanical Properties Test Data for Structural Materials Quart. Progr. Rep. Jan. 31, 1976*, ORNL-5112, pp. 74–76.

58. M. W. Moyer and J. P. Hammond, *Ultrasonic Measurement of Elastic Constants at Temperatures from 20°C to 1100°C*, Y-2047 (March 1976).

59. J. P. Hammond and M. W. Moyer, "Elastic Properties Determined by Dynamic Tests," *Mechanical Properties Test Data for Structural Materials Quart. Progr. Rep. Oct. 31, 1974*, ORNL-5103, pp. 164–67.

60. O. R. Carpenter and R. D. Wylie, "16-8-2 Cr-Ni-Mo for Welding Electrode," *Met. Progr.* 70(5): 65–73 (November 1956).

61. R. T. King, N. C. Cole, R. G. Berggren, and G. M. Goodwin, "Properties and Structure of 16-8-2 Stainless Steel Weld Metal," 75-PVP-45, paper presented at Second National Congress on Pressure Vessels and Piping, San Francisco, June 23–27, 1975, American Society of Mechanical Engineers, New York.

62. R. T. King, J. O. Stiegler, and G. M. Goodwin, *Creep Properties of a Type 308 Stainless Steel Pressure Vessel Weld with Controlled Residual Elements*, ORNL-TM-4131 (May 1973).

63. R. T. King and R. E. Gehlbach, "Characterization of FFTF Vessel-Type Weldments," *Fuels and Materials Development Program Quart. Progr. Rep. Sept. 30, 1971*, ORNL-TM-3550, pp. 187–93.

64. R. T. King and G. M. Goodwin, "Tensile Properties," *Fuels and Materials Development Program Quart. Progr. Rep. Dec. 31, 1971*, ORNL-TM-3703, pp. 209–17; note Fig. 9.11(b), p. 210.

65. R. L. Klueh, "High-Strain-Rate Tensile Properties of 2 1/4 Cr-1 Mo Steel," *Mechanical Properties Test Data for Structural Materials Quart. Progr. Rep. July 31, 1975*, ORNL-5106, pp. 121–31.

66. R. L. Klueh and R. E. Oakes, *Strain Rate Effects on the Tensile Properties of a Bainitic (Normalized-and-Tempered) 2 1/4 Cr-1 Mo Steel*, ORNL-5134 (April 1976).

67. R. L. Klueh, "Creep-Rupture Properties of 2 1/4 Cr-1 Mo Steel," *Mechanical Properties Test Data for Structural Materials Quart. Progr. Rep. Oct. 31, 1975*, ORNL-5107, pp. 141–54.

68. J. D. Baird and A. Jamieson, "Creep Strength of Some Synthesized Iron Alloys Containing Manganese, Molybdenum, and Chromium," *J. Iron Steel Inst.* 210: 847–56 (1972).

69. R. L. Klueh, "Heat-to-Heat Variation of 2 1/4 Cr-1 Mo Steel," *Mechanical Properties Test Data for Structural Materials Quart. Progr. Rep. Jan. 31, 1976*, ORNL-5112, pp. 92–101.

70. G. V. Smith, *Supplemental Report on the Elevated-Temperature Properties of Chromium-Molybdenum Steels (An Evaluation of 2 1/4 Cr-1 Mo Steel)*, ASTM Data Ser. Publ., DS 6 S2, American Society for Testing and Materials, Philadelphia, March 1971.

71. R. G. Baker and J. Nutting, "The Tempering of 2 1/4 Cr-1 Mo Steel After Quenching and Normalizing," *J. Iron Steel Inst.* 192: 257–68 (1959).

72. R. Lagneborg, "Dislocation Mechanisms in Creep," *Intern. Metall. Rev.* 17: 130–46 (1972).

73. J. D. Baird et al., "Strengthening Mechanisms in Ferritic Creep Resistant Steels," pp. 207–16 in *Creep Strength in Steels and High-Temperature Alloys*, The Metals Society, London, 1972.

74. T. L. Hebble, "Rupture Life," *Mechanical Properties Test Data for Structural Materials Quart. Progr. Rep. Jan. 31, 1976*, ORNL-5112, pp. 103–21.

75. R. L. Klueh and J. M. Leitnaker, "An Analysis of the Decarburization and Aging Processes in 2 1/4 Cr-1 Mo Steel," *Metall. Trans.* 6A: 2089–93 (November 1975).

76. R. L. Klueh, "The Effect of Carbon on 2.25 Cr-1 Mo Steel (II). Creep-Rupture Properties," *J. Nucl. Mater.* 54(1): 55–63 (November 1974).

77. The British Steelmakers Creep Committee, *BSCC High Temperature Data, British Long Term Creep Rupture and Elevated Temperature Tensile Data on Steels for High Temperature Service*, The Iron and Steel Institute, London, pp. 355–400.

78. M. C. Murphy and G. D. Branch, "Metallurgical Changes in 2.25 CrMo Steels During Creep-Rupture Tests," *J. Iron Steel Inst.* 209: 546–61 (1971).

79. S. S. Manson, G. R. Halford, and M. H. Hirschberg, *Creep-Fatigue Analysis by Strain-Range Partitioning*, NASA-TM-X-67838 (1971).

80. M. K. Booker, "Creep-Fatigue Data Analysis," *Mechanical Properties Test Data for Structural Materials Quart. Progr. Rep. Oct. 31, 1975*, ORNL-5107, pp. 154–58.

81. J. H. Gittus, "Implications of Some Data on Relaxation Creep in Nimonic 80A," *Phil. Mag.* 9: 749 (1964).

82. C. R. Brinkman, M. K. Booker, J. P. Strizak, W. R. Corwin, J. L. Frazier, and J. M. Leitnaker, *Interim Report on the Continuous Cycling Elevated-Temperature Fatigue and Subcritical Crack Browth Behavior of 2 1/4 Cr-1 Mo Steel*, ORNL-TM-4993 (December 1975).

83. J. Morrow, "Cyclic Plastic Strain Energy and Fatigue of Metals," *Internal Friction, Damping, and Cyclic Plasticity,* ASTM STP 378, American Society for Testing and Materials, Philadelphia, 1965, pp. 45–87.

84. C. E. Pugh et al., *Interim Guidelines and Background Information for Inelastic Analysis of High-Temperature Reactor System Components Made of 2 1/4 Cr-1 Mo Steel,* ORNL-TM-5226 (December 1975).

85. M. K. Booker, "Bilinear Cyclic Stress-Strain Constants," *Mechanical Properties Test Data for Structural Materials Quart. Progr. Rep. Oct. 31, 1975,* ORNL-5107, pp. 158–71.

86. Ibid., *Jan. 31, 1976,* ORNL-5112, pp. 103–08.

87. R. L. Klueh and R. E. Oakes, Jr., *High-Strain-Rate Tensile Properties of Annealed 2 1/4 Cr-1 Mo Steel,* ORNL-TM-5028 (October 1975).

88. R. L. Klueh, *Effects of Heat Treatment on the Creep and Rupture Properties of 2 1/4 Cr-1 Mo Steel,* report in preparation.

89. R. W. Swindeman and R. L. Klueh, "Relaxation of 2 1/4 Cr-1 Mo Steel under Multiple Loading Conditions," paper to be presented at the Second International Conference on Mechanical Behavior of Materials, Boston, Aug. 16–20, 1976.

90. J. D. Baird and A. Jamieson, "High-Temperature Tensile Properties of Some Synthesized Iron Alloys Containing Molybdenum and Chromium," *J. Iron Steel Inst.* 210(11): 841–46 (1972).

91. Huntington Alloys, *Incoloy Alloys,* International Nickel Company, Inc.

92. S. Kiser, Huntington Alloys, private communication.

93. J. P. Strizak, "Fatigue-Life Testing," *Mechanical Properties Test Data for Structural Materials Quart. Progr. Rep. Jan. 31, 1976,* ORNL-5112, pp. 162–68.

94. C. E. Jaske and T. L. Porfilio, *Low-Cycle Fatigue of Type 347 Stainless Steel and Hastelloy X in Hydrogen Gas Environment,* TID/SNA-2047 (1971).

95. P. L. Rittenhouse, *Initial Assessment of the Status of HTGR Metallic Structural Materials Technology,* ORNL-TM-4760 (December 1974).

96. P. L. Rittenhouse and C. S. Morgan, *Status Report on Structural Materials of HTGR Primary System Components*, ORNL-TM-5136 (January 1976).

97. C. R. Brinkman and G. E. Korth, "Strain Fatigue and Tensile Behavior of Inconel 718 from Room Temperature to 650°C," *J. Test. Eval.* 2(4): 249–59 (July 1974).

98. J. B. Conway, R. H. Stentz, and J. T. Berling, *Fatigue, Tensile, and Relaxation Behavior of Stainless Steels*, TID-26135 (1975).

99. D. L. Keller, *Progress on LMFBR Cladding, Structural, and Component Material Studies During July 1971 Through June 1972 — Final Report Task 32*, BMI-1928 (July 1972).

100. D. L. Keller, *Progress on LMFBR Cladding, Structural, and Component Materials Studies During July 1970 Through June 1971 — Annual Report Task 32, Final Report Task 14*, BMI-1914 (July 1971).

101. General Atomic Company, *Component and Systems Development Program*, Quarterly Progress Report for the Period Ending June 30, 1975, GA-A-13512.

102. C. E. Jaske, "Low-Cycle Fatigue of AISI 1010 Steel at Temperatures up to 1200°F (649°C)," Battelle Columbus Laboratory, Columbus, Ohio, to be published.

103. D. R. Diercks, Argonne National Laboratory, personal communication, January 1976.

104. C. R. Brinkman and G. E. Korth, *Heat-to-Heat Variations in the Fatigue and Creep-Fatigue Behavior of AISI Type 304 Stainless Steel, and the Fatigue Behavior of Type 308 Stainless Steel Weld Materials*, ANCR-1097, Aerojet Nuclear Company (May 1973).

105. C. R. Brinkman, G. E. Korth, and R. R. Hibbins, "Estimates of Creep-Fatigue Interaction in Irradiated and Unirradiated Austenitic Stainless Steels," *Nucl. Technol.* 16: 297–307 (October 1972).

106. C. E. Jaske, Battelle Columbus Laboratory, personal communication, June 16, 1975.

107. S. S. Manson, G. R. Halford, and M. H. Hirshberg, "Creep-Fatigue Analysis by Strain-Range Partitioning," pp. 12–28 in *First Symposium on Design for Elevated Temperature Environments, Am. Soc. Mech. Engrs.*, New York, 1971.

108. M. H. Hirshberg and G. R. Halford, "Use of Strainrange Partitioning to Predict High-Temperature Low-Cycle Fatigue Life," NASA Lewis Research Center, Cleveland, Ohio, to be published.

109. D. C. Lord and L. F. Coffin, Jr., "Low-Cycle Fatigue Hold Time Behavior of the Cast René 80," *Metall. Trans.* 4: 1647 (1973).

110. S. S. Manson, *The Challenge to Unify Treatment of High Temperature Fatigue — A Partisan Proposal Based on Strain Range Partitioning*, ASTM STP 520, American Society for Testing Materials, Philadelphia, 1973, pp. 744–75.

111. W. R. Corwin, "Subcritical Crack Growth Studies," *Mechanical Properties Test Data for Structural Materials Quart. Progr. Rep. Jan. 31, 1976*, ORNL-5112, pp. 168–72.

112. W. G. Clark, Jr. and S. J. Hudak, Jr., *Variability in Fatigue Crack Growth Rate Testing* (an ASTM E-24.04.01 Task Group report), Scientific Paper 74-1E7-MSLRA-P2, Westinghouse Research Laboratories, Pittsburgh, Pa. (Sept. 18, 1974).

4. NAVAL RESEARCH LABORATORY

L. E. Steele

4.1 INTRODUCTION - L. E. Steele

The research program of the NRL Engineering Materials Division, Thermostructural Materials Branch, includes the study of the behavior of structural materials useful in reactor construction. Within the scope of the title above much unirradiated data are developed. This report is developed using such data to support the USERDA and USNRC objective of compiling structural materials properties data for use in national reactor development programs. The NRL program is sponsored by the Office of Naval Research, the U. S. Energy Research and Development Administration, the U. S. Nuclear Regulatory Commission, and the U. S. Army Engineer Power Group. The unirradiated materials properties data contributed here include that developed in the course of research in the areas of high temperature materials, radiation damage, and fracture mechanics.

4.2 RESPONSE OF AUSTENITIC STAINLESS STEEL WELDMENTS TO THERMAL CONDITIONING AS A FUNCTION OF DELTA FERRITE CONTENT - J. R. Hawthorne

4.2.1 Background

Welded austenitic stainless steel has been used for selected primary system components of water-cooled nuclear power reactors and is a major design consideration for forthcoming liquid metal-cooled (fast breeder) reactors. Studies of representative weld deposits in pre- and postirradiation conditions have revealed significant differences in notch toughness behavior among welds. The observations prompted detailed investigations of contributing factors. Delta ferrite content is one of several suspect factors being qualified by NRL for Army and ERDA sponsors.

From results given in a previous report[1], it was concluded that delta ferrite content does not have a major effect on either weld strength or notch toughness in the as-welded (unirradiated) condition for the delta ferrite content and temperature ranges studied. The

report emphasized, however, that this determination did not preclude the original concern for a major influence of this variable on irradiation response. The current report presents the results of further investigations on as-welded condition notch ductility trends and exploratory studies of long term thermal conditioning behavior.

4.2.2 Materials

The series of four 2-1/2 in. thick shielded metal arc weldments (Type 304 base plate, Type 308 filler) made for the investigation were fully described in reference 1. For quick referral, the chemical compositions of the weld deposits are reproduced in Table 4.1. Delta ferrite contents in ferrite number, determined by Magne-Gage measurements on actual weld cross sections, were 5.2, 10.4, 15.7, and 19.0 respectively. It is noted that these values differ significantly from the values originally reported that were based on WRC test pads for the same four lots of electrodes. Significant disagreement in delta ferrite determinations has since been confirmed for the WRC test pads vs a second series of test pads made for the Metal Properties Council (MPC) program. The observed noncorrespondence has significant implications and is under intensive investigation by the MPC Task Group on the Properties of Weldments in Elevated Temperature Service.

Test specimens, including the 5/8 in. thick dynamic tear (DT) specimens for the present study, were taken through the weld thickness with the long dimension of the specimen perpendicular to the welding direction. Specimen orientation was based on the need to conserve the test stock. The notch of the DT specimens was made perpendicular to the weldment surface; the width of the weld deposit about the notch was at least 0.75 inches.

4.2.3 Experimental Results

The further definition of as-welded notch ductility trends involved determinations at 700°F (371°C). In Fig. 4.1, the latest DT results are compared to previous DT determinations at 75, 500, and 900°F (24, 260, and 482°C), and denote a peak in notch toughness at this temperature. Unlike the rise in energy absorption values found between 75 and 500°F

Table 4.1

Chemical Compositions of AISI Type 308 Shielded Metal Arc Weld Series With Variable Delta Ferrite Content

NRL Weld Code	Delta Ferrite Content[a]	Chemical Composition (wt-%)[b]								
		C	Mn	Si	P	S	Cr	Ni	Mo	N
V41 (178 AA)[c]	5.2	.056	1.88	.32	.024	.011	19.71	10.35	.05	.068
V42 (179 A)	10.4	.060	1.54	.31	.029	.009	19.90	9.25	.05	.074
V43 (180 A)	15.7	.060	1.65	.32	.029	.011	20.89	9.11	.06	.079
V44 (181 KA)	19.0	.060	1.38	.43	.028	.010	21.08	8.93	.08	.084

[a] Weld deposit ferrite number (avg); Magne-Gage determination.
[b] Composition based on standard WRC weld test pad (courtesy Arcos Corporation); core wire for all electrodes from same steel melt.
[c] Arcos Corporation sample number.

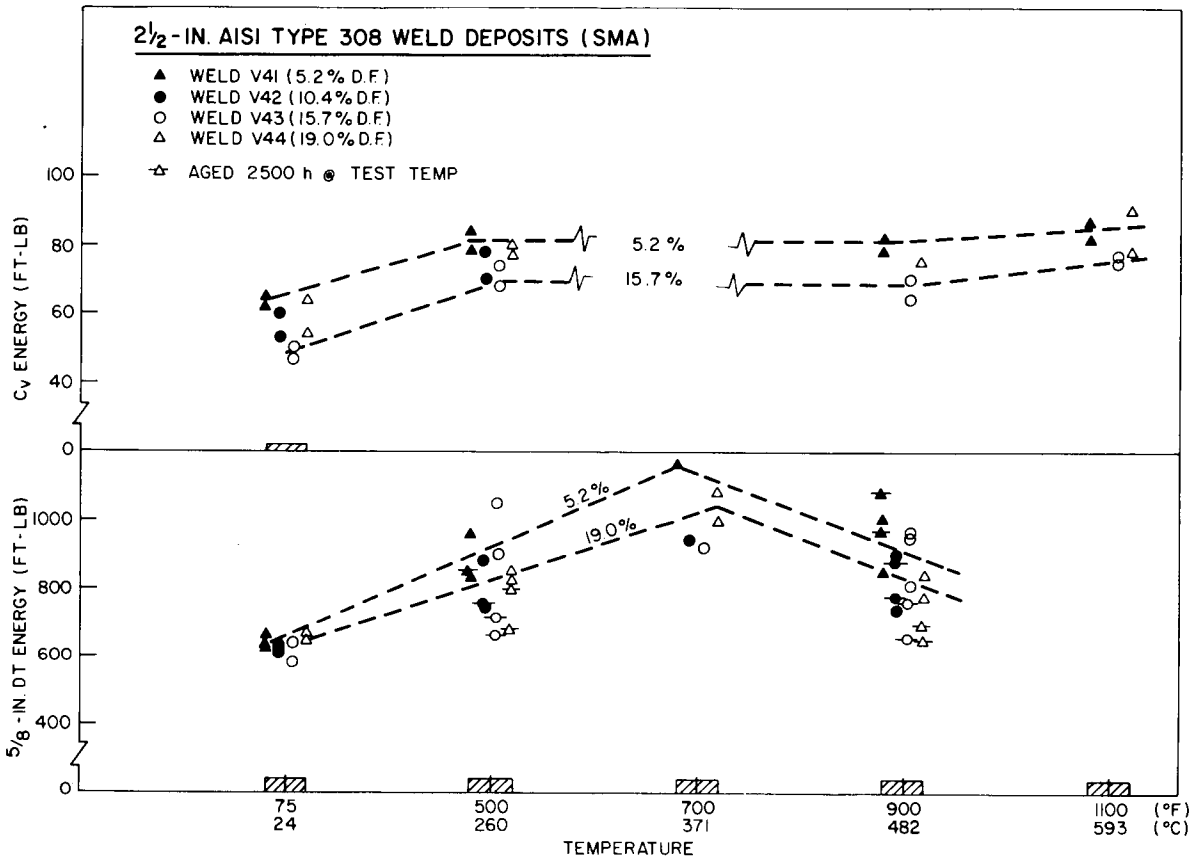

Fig. 41- Notch ductility vs temperature trends for AISI Type 308 stainless steel weld deposits (SMA) with different delta ferrite levels. As-welded and as-welded plus thermally aged conditions.

(24 and 260°C), the DT energy peak in this case cannot be explained by a change in yield strength (see Fig. 4.2). To further test the toughness vs temperature trend, C_v tests at 700°F (371°C) are planned.

Studies of long term (2500 hour) thermal conditioning effects on notch ductility centered on specimens aged and tested at 500°F (260°C) and at 900°F (482°C). A comparison of the DT energy values obtained for as-welded and as-welded plus aged conditions is made in Fig. 4.1 and Table 4.2. The data describe a trend of increasing response to thermal conditioning with increasing delta ferrite content, for both aging temperatures. That is, the welds with delta ferrite contents of FN 5.2 and 10.4 exhibited no change in DT energy absorption while the welds with the higher delta ferrite contents of FN 15.7 and 19.0 experienced significant decreases in DT values. Also, the decreases in DT energy absorption are observed to be somewhat greater for the higher thermal conditioning temperature, 900°F (482°C).

In the coming quarter, tensile specimens representing 500, 700, and 900°F (260, 371, and 482°C) thermally-aged conditions will be evaluated for a further test of relative weld response. Longer thermal conditioning times (2500 hour) are also being considered for the continuing program.

4.2.4 References

1. Hawthorne, J. R., Menke, B. H., "Influence of Delta Ferrite Content on Notch Toughness of Austenitic Stainless Steel Weldments," in Mechanical Properties Test Data for Structural Materials Quarterly Progress Report for Period Ending July 31, 1975, ORNL 5106, Sep 1975, pp. 207-216.

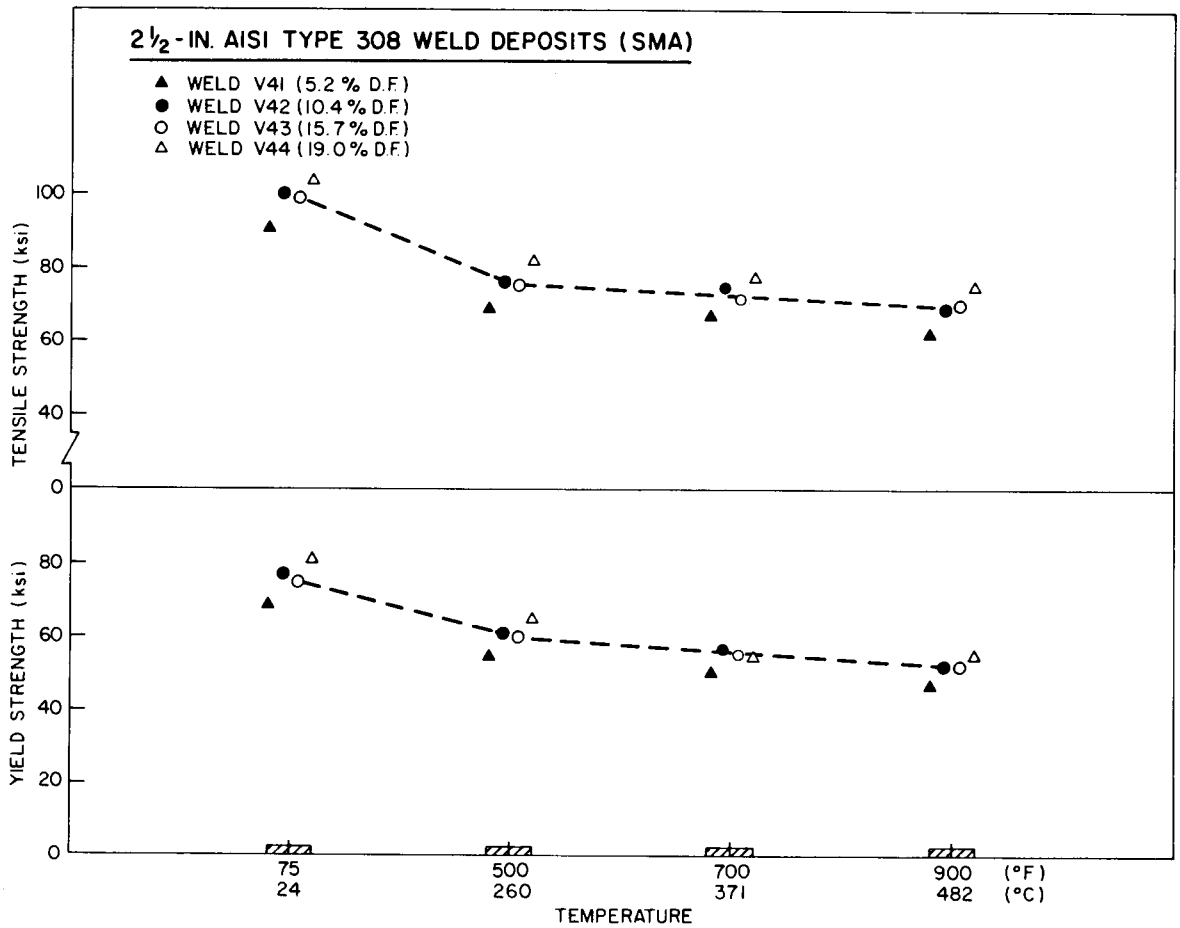

Fig. 4.2- Strength vs temperature trends for AISI Type 308 stainless steel weld deposits (SMA) with different delta ferrite levels. As-welded condition.

Table 4.2

Dynamic Tear (DT) Notch Ductility of AISI Type 308 Shielded Metal Arc Weld Series With Variable Delta Ferrite Content

Weld Code	Delta Ferrite Content[a]	As Welded Condition DT Energy (ft-lb)				As Welded & Thermally Aged DT Energy (ft-lb)	
		75F (24)	500F (260C)	700F (371C)	900F (482C)	500F[b] (260C)	900F[c] (482C)
V41	5.2	637	832	1167	1005	853	969
		662	963	-	846	-	1084
	(avg)	(650)	(897)	(1167)	(925)	(853)	(1026)
V42	10.4	620	740	937	734	754	780
		633	880	-	903	-	890
		(627)	(810)	(937)	(819)	(754)	(835)
V43	15.7	581	904	918	949	670	660
		639	1043	-	963	719	785
		(610)	(974)	(918)	(956)	(694)	(722)
V44	19.0	643	822	1005	840	678	648
		669	851	1085	774	803	694
		(656)	(837)	(1045)	(807)	(740)	(671)

[a] Ferrite number; Magne-Gage determination
[b] Aged 2500 hr at 500F (260C) prior to testing at 500F
[c] Aged 2500 hr at 900F (482C) prior to testing at 900F

5. HANFORD ENGINEERING DEVELOPMENT LABORATORY

H. H. Yoshikawa

5.1 INTRODUCTION

The objectives of the structural materials investigation conducted at the Hanford Engineering Development Laboratory are mainly to provide control data for in-reactor and postirradiation tests and to provide direct and timely assistance to FFTF and Demonstration plant structural design and analysis programs. The HEDL efforts involve evaluation of mechanical properties in the areas of normal and high strain rate tensile testing, creep testing and analysis, and fatigue crack growth and fracture toughness of such materials as weldments, vessel and piping, core support structures and reflectors as well as duct and cladding. Those test results and analyses appropriate to the "Structural Materials Quarterly Report" will be reported here; however those investigations associated with irradiation effects per se will be reported in HEDL publications.

5.2 LMFBR STRUCTURAL MATERIALS - J. J. Holmes and R. L. Knecht

5.2.1 Tensile Properties of A-286

J. M. Steichen, R. L. Knecht

5.2.1.1 Objective

The objective of this program is to determine the effects of irradiation on the mechanical properties of component structural materials (both base metal and weld metal) to support the design, design confirmation and performance prediction of LMFBR systems.

5.2.1.2 Accomplishments and Status

5.2.1.2.1 Scope of Work. A-286 is a precipitation hardenable austenitic stainless steel which is being used extensively as a bolting material in a variety of Fast Flux Test Facility (FFTF) structural components. Anticipated operating conditions for A-286 bolts in these components include temperatures from 200 to 565°C (400 to 1050°F) and total neutron fluences

to slightly less than 1×10^{21} n/cm^2. Safety analyses on these bolts require mechanical properties data representative of anticipated steady-state loadings as well as for postulated accident conditions. Of special significance is the effect of neutron irradiation on mechanical properties.

In the present study the effects of test temperature, strain rate, and thermal aging on the tensile properties of A-286 were determined. Test parameters included strain rates from 3×10^{-5} to 1.0 sec^{-1} and temperatures from R.T. to 649°C (1200°F). Thermal aging was performed in sodium at 538°C (1000°F) for durations to 4000 hours. Results of these tests have been used to ascertain the effects of neutron irradiation on tensile properties[1].

Two heats of A-286 were used in this study. The first (Heat K-58139) was obtained in the form of 1.27 cm (0.5 in.) thick strip and was used for the majority of tensile and strain rate tests and for thermal aging. The second heat (Heat 8790) was obtained in the form of 3.81 cm (1.5 in.) diameter rod and was used to verify that tensile properties of the strip material were consistent with those for prototypic bolting material. Both heats of material were annealed at 982°C (1800°F) for 30 minutes and precipitation heat treated at 718°C (1325°F) for 16 hours prior to testing. Chemical compositions of the two heat of material are given in Table 5.1.

5.2.1.2.2 Results

Unirradiated Behavior Tensile testing of unirradiated A-286 was performed at temperatures from room temperature to 649°C and strain rates from 3×10^{-5} to 1.0 sec^{-1}. Results of these tests provided a complete description of unirradiated tensile properties and also established a basis for ascertaining the effects of neutron irradiation. Tensile property data obtained from each test included the ultimate and 0.2% yield strengths, total and uniform elongations, and reduction of area. Tabular data for these tests have been reported previously[1].

The effect of test temperature on the tensile properties of A-286 is illustrated in Figure 5.1. Data are included in this figure for both heats of test material. As shown in the figure, both the ultimate and 0.2% yield

TABLE 5.1

CHEMICAL COMPOSITIONS OF A-286 TEST MATERIALS

Composition - Wt.%*

Heat No.	C	S	Mn	Si	Cr	Mo	Ti	Al	B	Ni	P	V
K-58139-2	0.044	0.002	1.40	0.53	14.34	1.35	2.28	0.22	0.0047	25.91	0.011	0.21
8790	0.057	0.006	1.51	0.50	14.46	1.37	2.24	0.38	0.005	26.35	0.006	0.33

*Balance - Fe

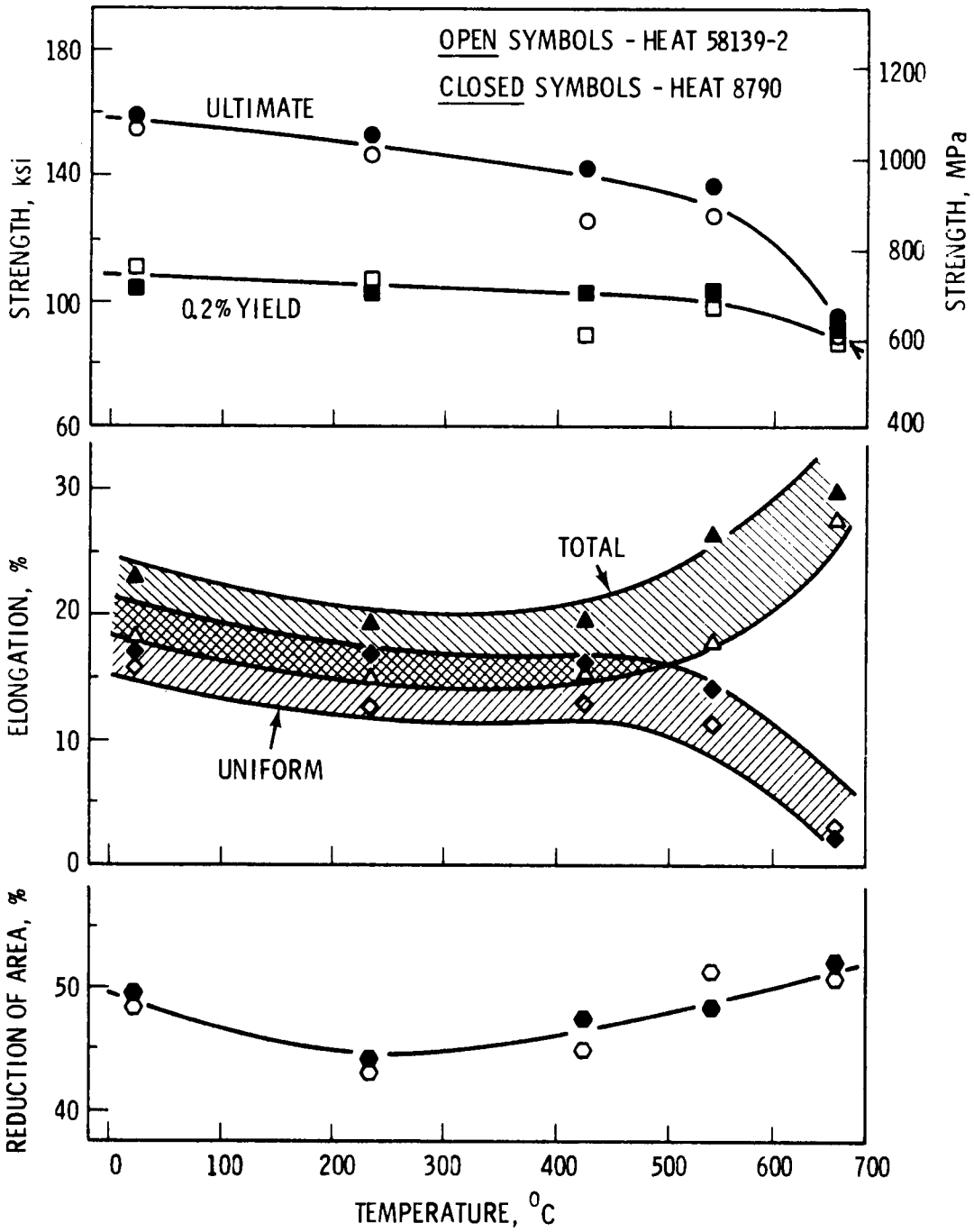

FIGURE 5.1. Temperature Dependence of the Tensile Properties of Unirradiated A-286.

strengths of A-286 decrease with increasing temperature. Also, a convergence in strength properties is observed with increasing temperature resulting in essentially identical ultimate and 0.2% yield strengths at the highest test temperature (649°C). No significant difference in strength properties was observed between the two heats of material.

The temperature dependence of the ductility of A-286 is also shown in Figure 5.1. For temperatures to ∿450°C (850°F) both total and uniform (elongation at maximum load) elongation slightly decrease with increasing temperature. At temperatures above 450°C (850°F) total elongation rapidly increases and uniform elongation decreases with increasing temperature. At the highest temperature (649°C) total elongation approaches 30% while uniform elongation is approximately 3%. Although the trends in total and uniform elongation are consistent between the two heats of material, heat 8790 exhibits slightly greater ductility than heat K-58139. The reduction of area of A-286 is not greatly influenced by test temperature (Figure 5.1). Also, little difference in values is observed for the two heats of material.

The effect of strain rate and temperature on the tensile strength and ductility of A-286 is presented in Figures 5.2-5.6. As shown in Figures 5.2 and 5.3, the ultimate and 0.2% yield strengths are not greatly influenced by strain rate to temperatures of 530°C (1000°F). However, at 649°C (1200°F), both strength properties initially rapidly increase with strain rate to a rate of $\sim 10^{-3}$ sec^{-1} and then slowly increase with strain rate above that rate. The rapid increase in strength at this temperature at the low strain rates is consistent with other results reported for austenitic stainless steels[2] and results because creep controls deformation in this temperature-strain rate region.

As with the strength properties, the ductility of A-286 is not greatly influenced by strain rate for temperatures to 538°C (1000°F) (see Figures 5.4-5.6). At the highest test temperatures (649°C) total elongation (Figure 5.4) and reduction of area (Figure 5.6) slightly decrease and uniform elongation (Figure 5.5) significantly increases with increasing strain rate.

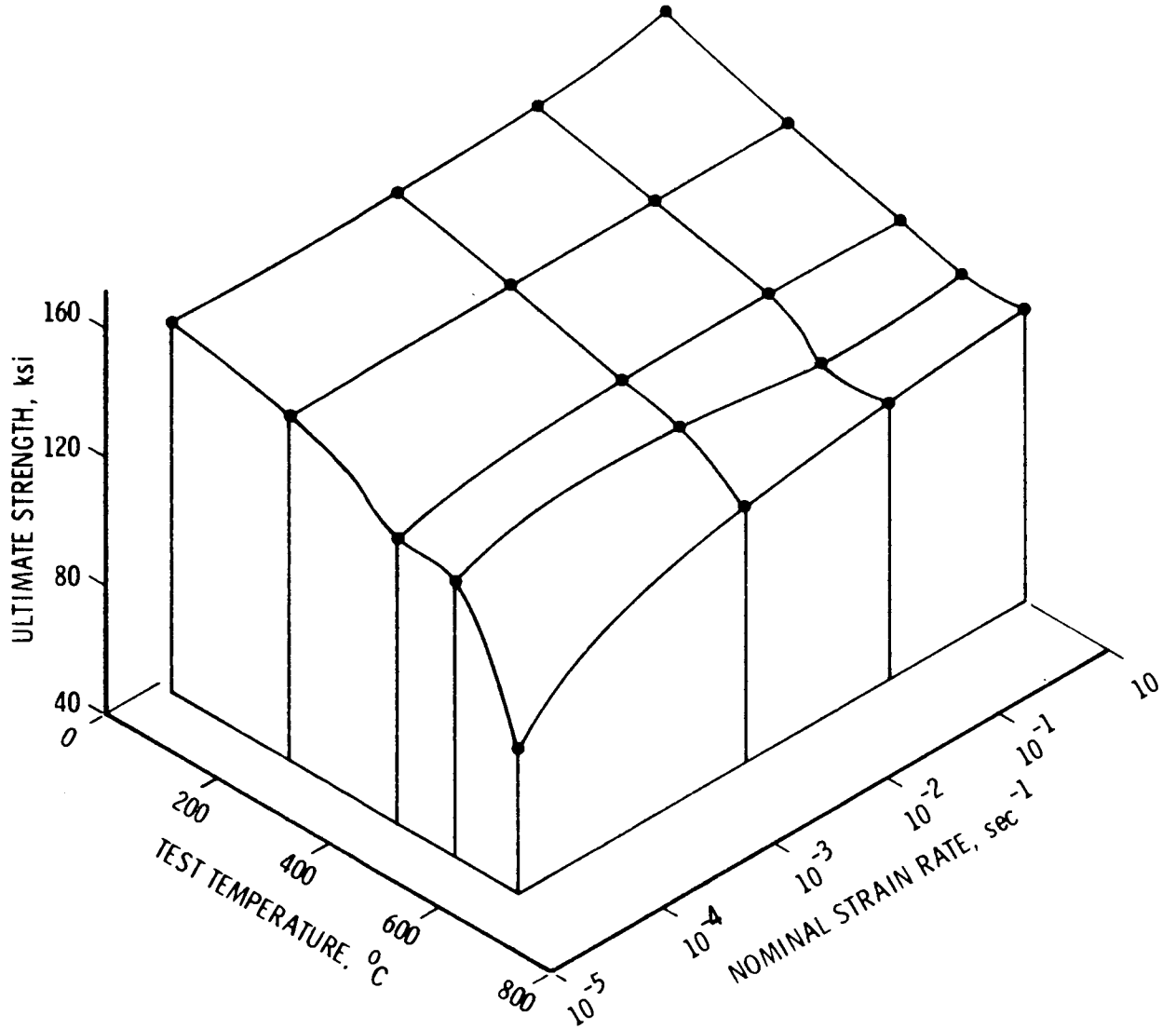

FIGURE 5.2. Strain Rate and Temperature Dependence of the Ultimate Strength of Unirradiated A-286.

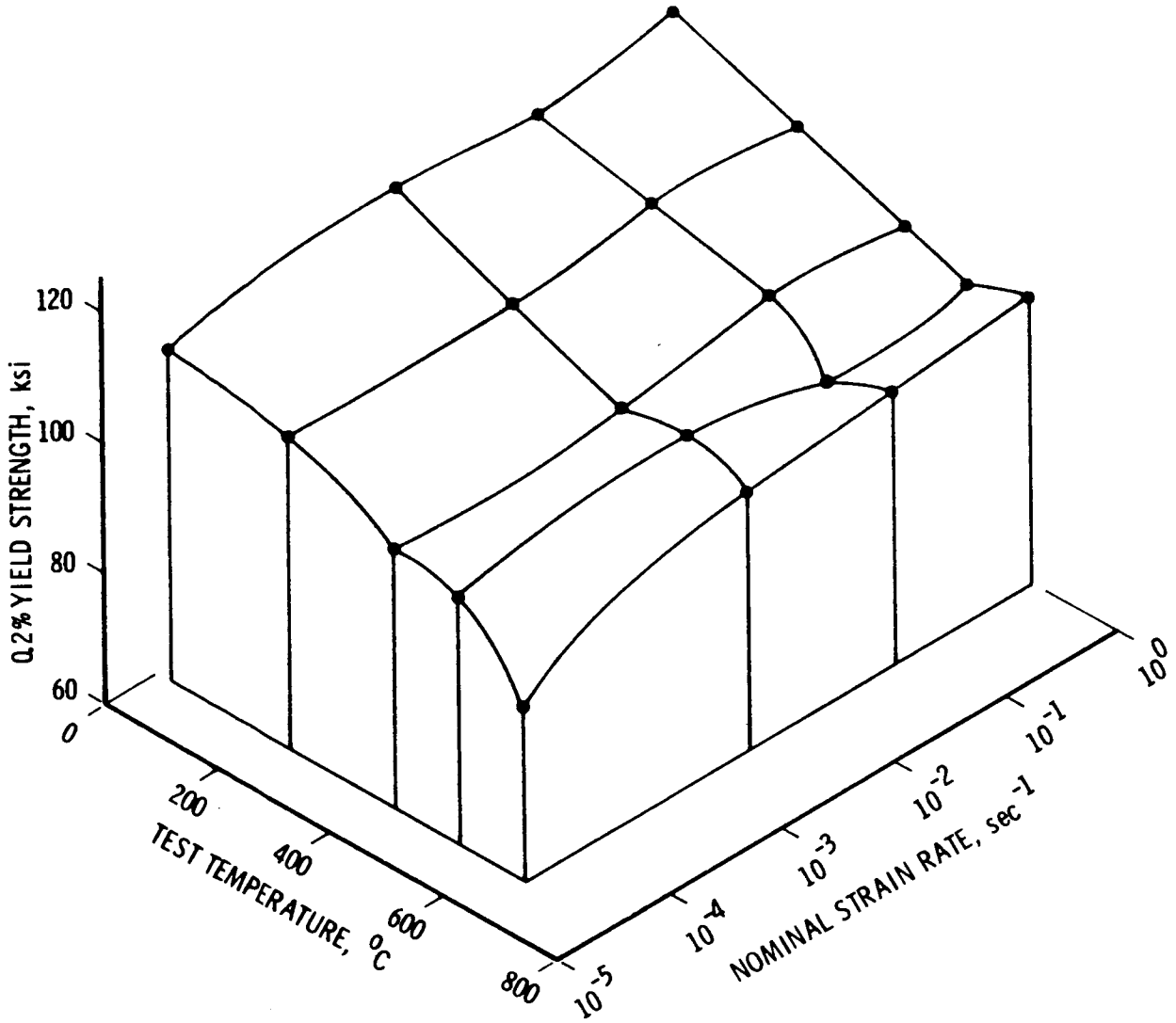

FIGURE 5.3. Strain Rate and Temperature Dependence of the 0.2% Yield Strength of Unirradiated A-286.

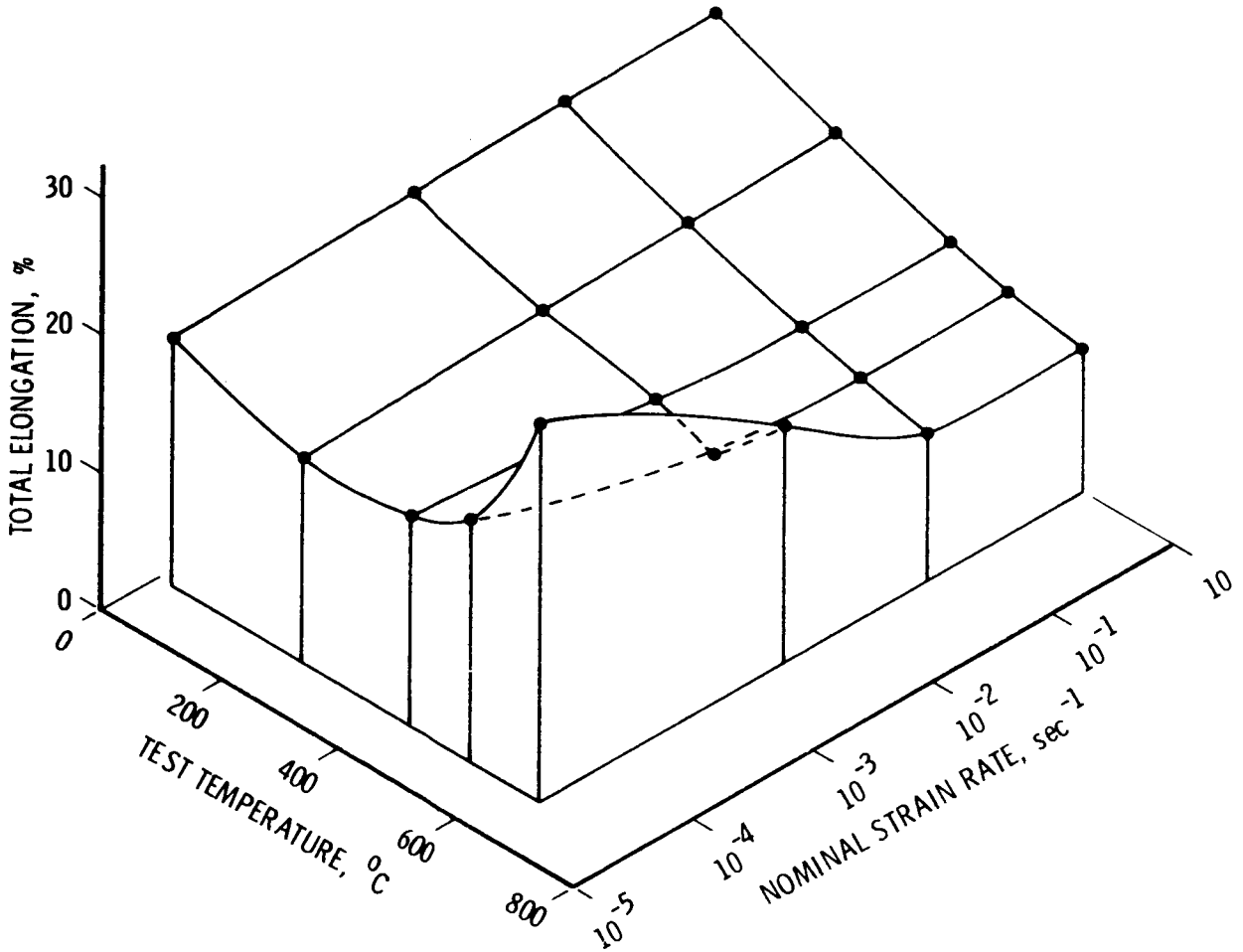

FIGURE 5.4. Strain Rate and Temperature Dependence of the Total Elongation of Unirradiated A-286.

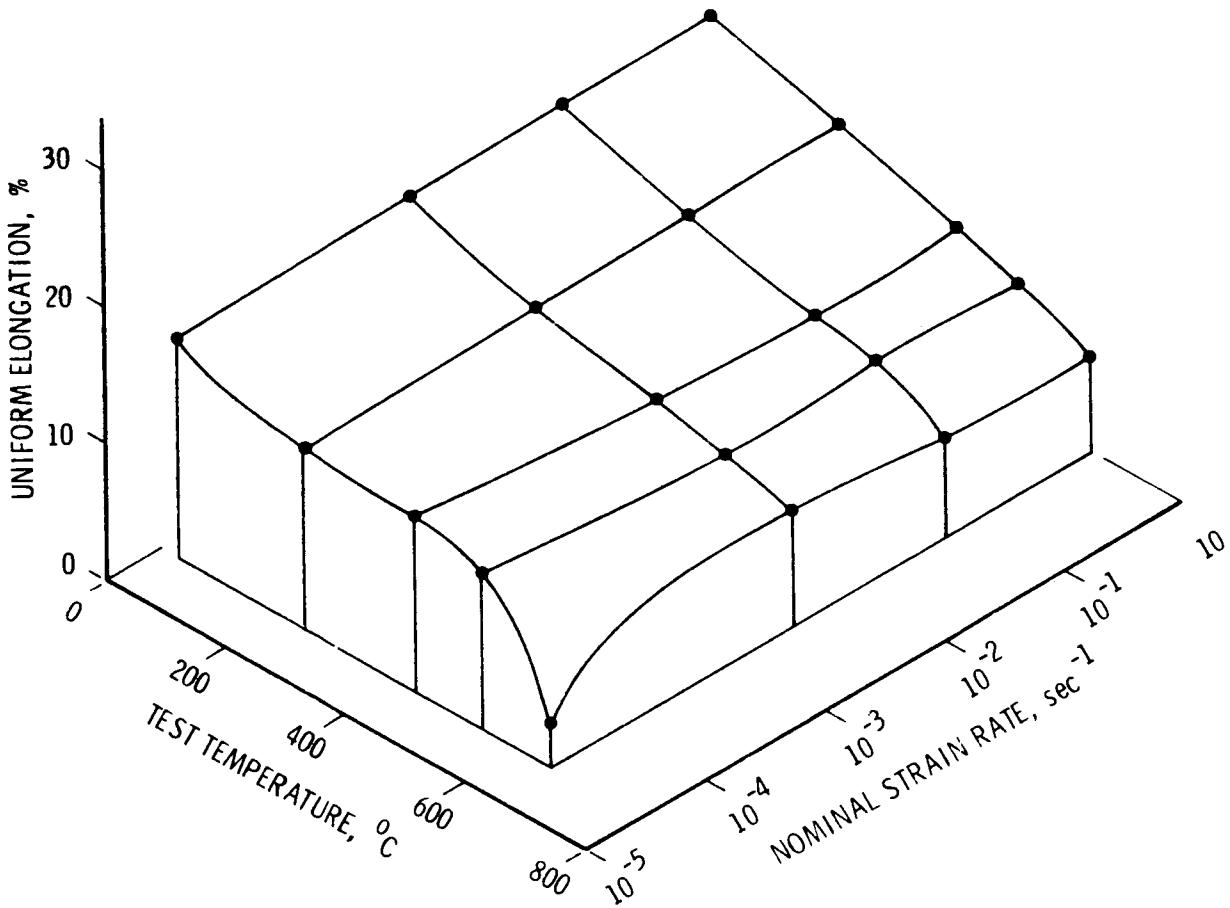

FIGURE 5.5. Strain Rate and Temperature Dependence of the Uniform Elongation of Unirradiated A-286.

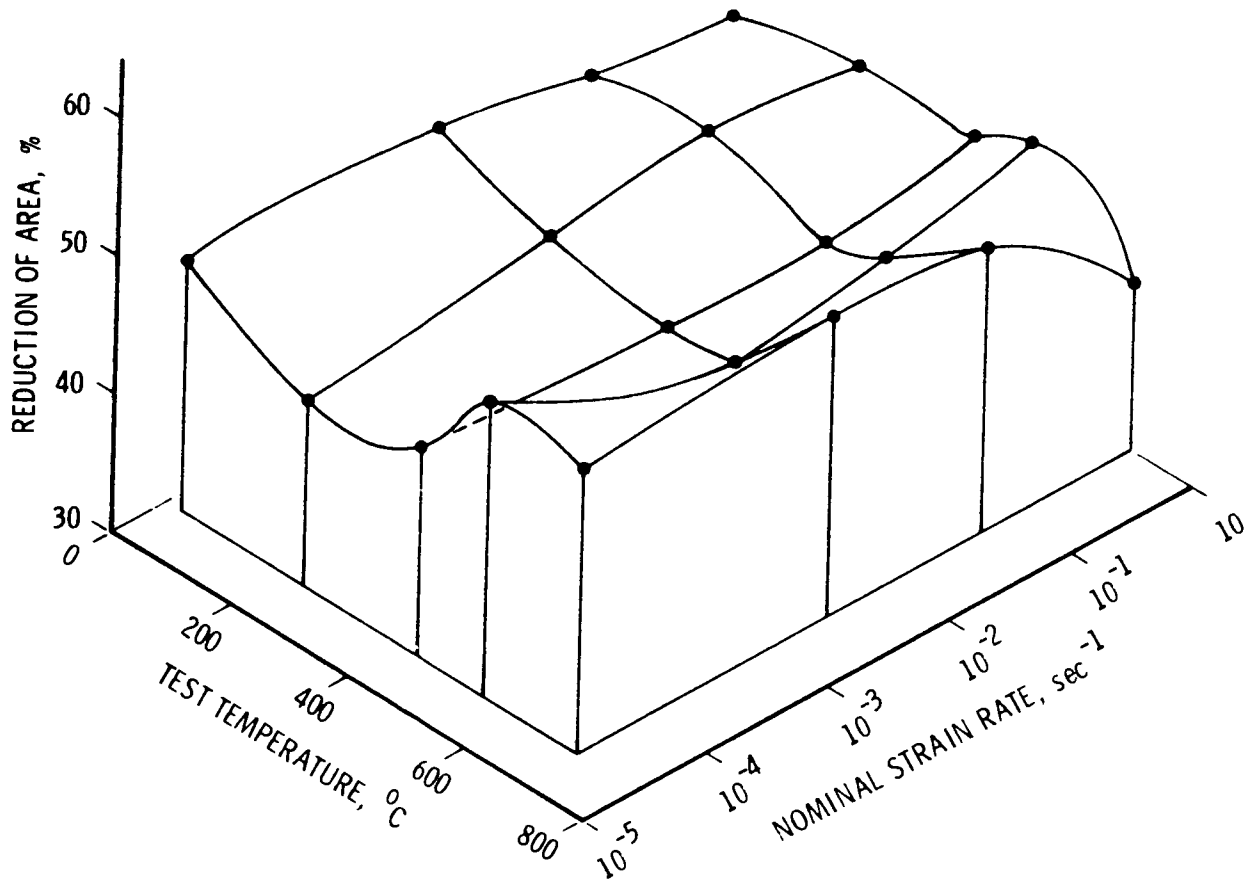

FIGURE 5.6. Strain Rate and Temperature Dependence of the Reduction of Area of Unirradiated A-286.

Thermal Aging Behavior. To allow the separation of thermal effects from irradiation effects, limited thermal aging was performed on the subject A-286. Specimens of Heat K-58139 were exposed in sodium at a temperature of 538°C (1000°F) for durations of 1000 and 4000 hours. Results of tests on aged material are presented in Figures 5.7-5.9.

In Figure 5.7 the room temperature tensile properties of exposed A-286 are presented. Both the ultimate and 0.2% yield strengths slightly increase with exposure time. Also, little effect of exposure time on the ductility of A-286 is observed. Similar behavior is observed for the ultimate and 0.2% yield strengths, total elongation, and reduction of area of exposed material when tested at 538°C (1000°F) (Figure 5.8). The uniform elongation at 538°C (1000°F) appears to decrease with exposures at the same temperature. The effect of strain rate on the tensile properties of exposed material is shown in Figure 5.9. Behavior for unaged material is represented by lines. Two items of significance are observed for the ultimate and 0.2% yield strengths of exposed material. First, exposure at 538°C (1000°F) slightly increases strength properties at each strain rate and second, the strain rate dependence of the strength properties of exposed material is identical to unexposed material.

The total elongation of unexposed and exposed A-286 is slightly reduced by increasing strain rate (Figure 5.9). Also, no distinct difference is total elongation is observed between unexposed and exposed material. Uniform elongation of unaged material remains essentially constant with increasing strain rate. Exposure slightly alters this behavior since the uniform elongation is reduced by exposure at the lowest test rate and is essentially identical at the higher rates. No effect of exposure on the strain rate dependence of reduction of area was observed.

5.2.1.3 Expected Accomplishments

Tensile testing of Inconel 600 at temperatures to 760°C and strain rates to 1.0 sec^{-1} will be completed and results reported in the next reporting period.

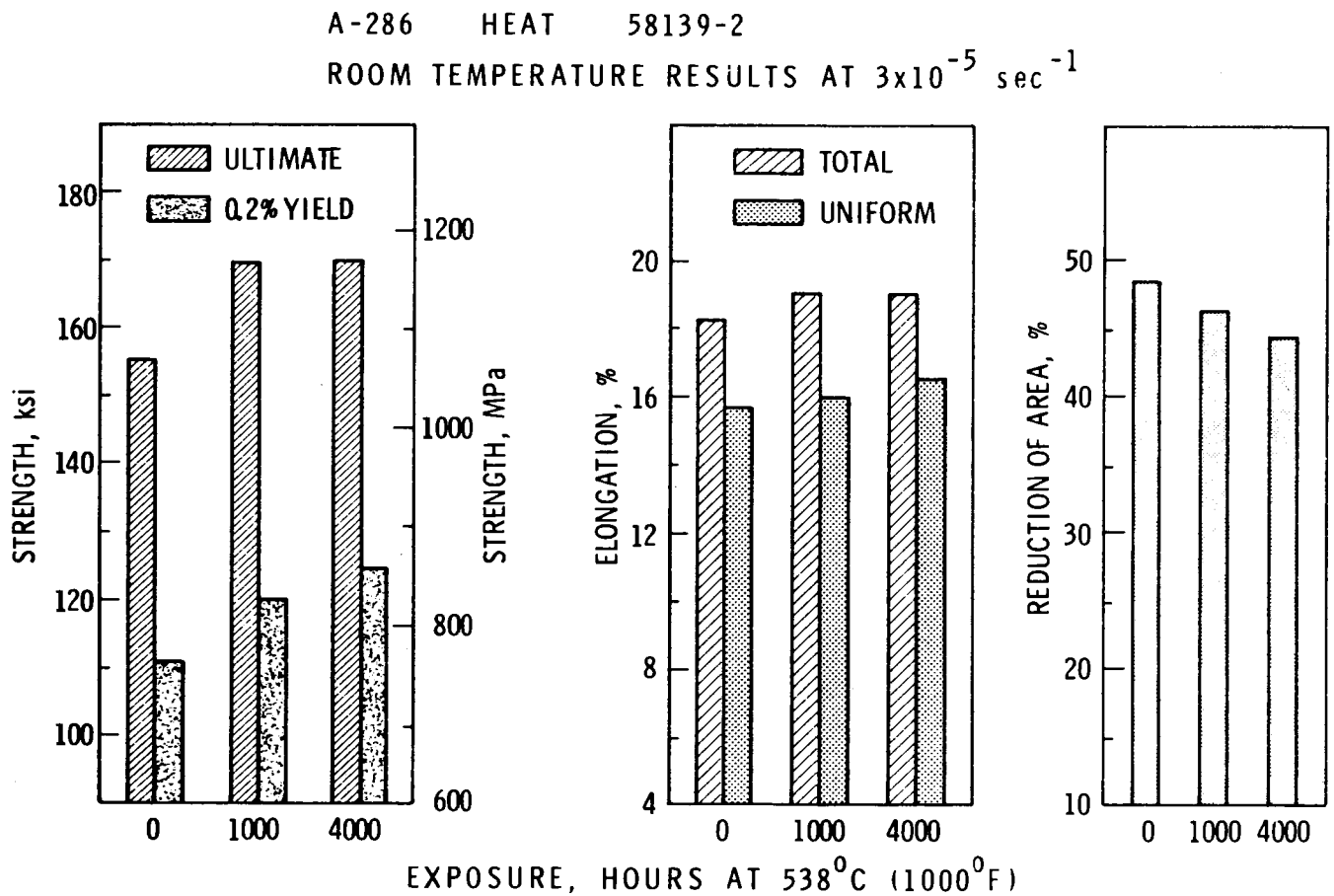

FIGURE 5.7. Room Temperature Tensile Properties of Thermally Exposed A-286.

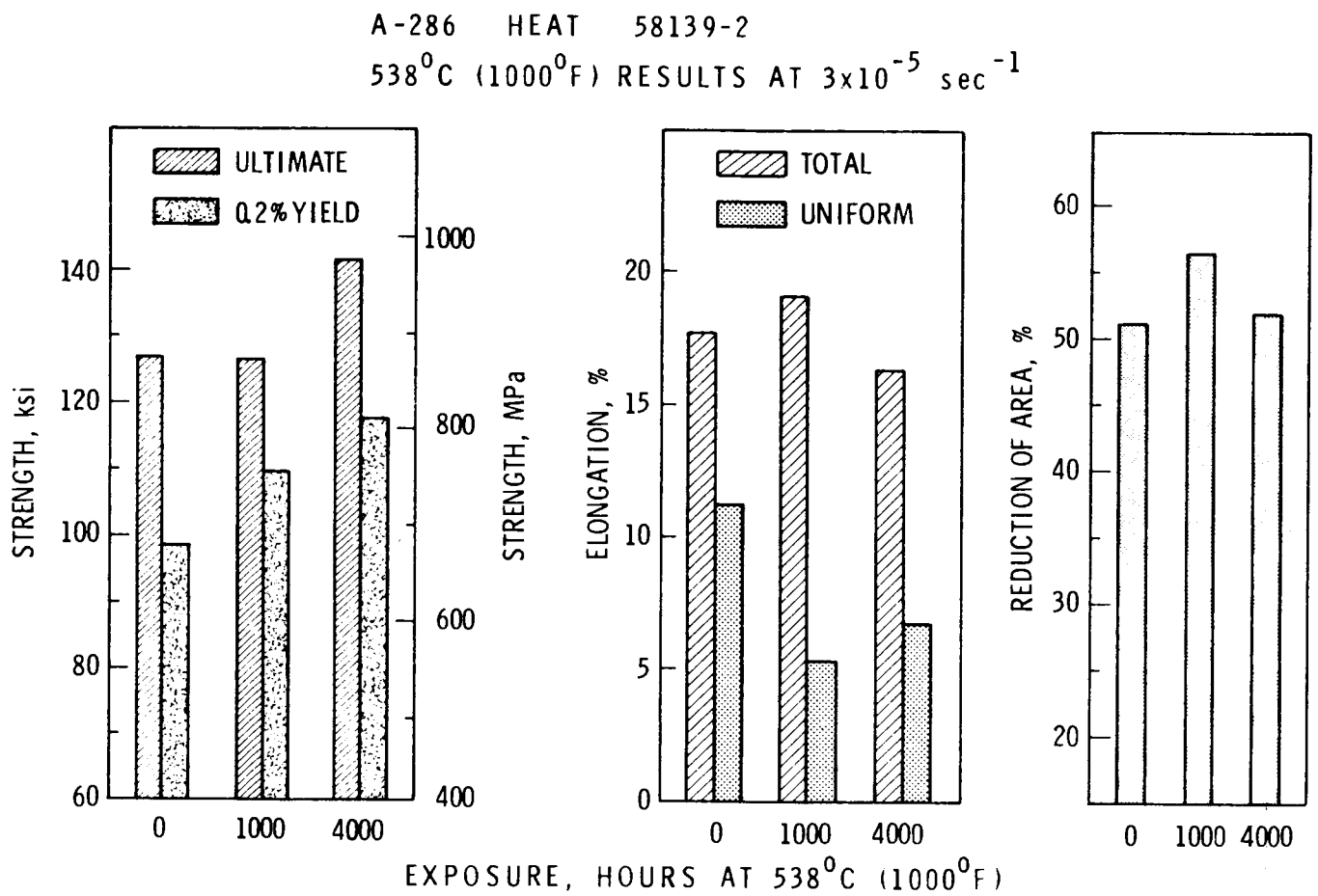

FIGURE 5.8. Tensile Properties of Thermally Exposed A-286 -- Exposed and Tested at 538°C (1000°F).

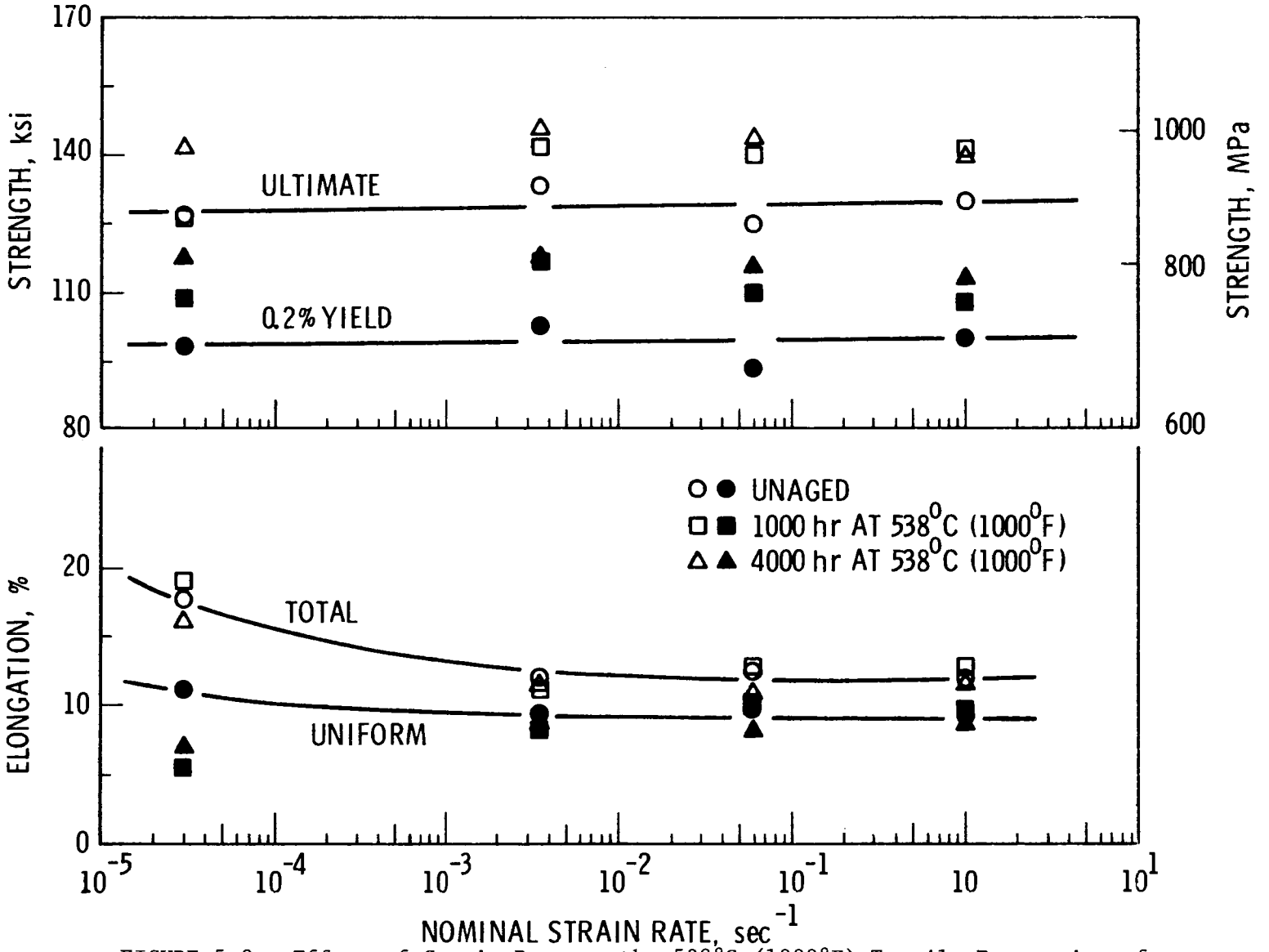

FIGURE 5.9. Effect of Strain Rate on the 538°C (1000°F) Tensile Properties of Thermally Exposed A-286.

5.2.2 Creep and Rupture Behavior of Weld-Deposited Type 16-8-2 Stainless Steel at 593°C

R. L. Knecht, L. D. Blackburn, A. L. Ward

5.2.2.1 Objective

The objective of this report is to determine the effects of irradiation on the creep and fatigue properties of component structural materials (both base and weld metal) to support the design, design confirmation and performance prediction of LMFBR systems.

5.2.2.2 Accomplishments and Status

Introduction

The present investigation was prompted by the selection of Type 16-8-2 stainless steel for the fabrication welding of the hot-leg primary piping (Type 316H) in the heat transport system of the Fast Flux Test Facility (FFTF). Current structural design criteria for nuclear service at temperatures above 426°C[3] employ design rules which are essentially independent of the materials of construction so long as those materials are ductile. Specific design rules are quantified by setting allowable stress values which are derived from material properties[4]. At the present time, allowable stresses are based only on the properties of wrought material. It is nevertheless of some interest to examine weld metal properties in the light of current design practice. This process may be useful in confirming the application of particular welds, and in the long term, may be of value in considering potential extensions of design rules to deal more directly with the behavior of weld regions. In this study, such an examination is illustrated using results obtained from characterization testing of prototypic FFTF piping welds. Emphasis is placed on the time-dependent creep behavior related to rupture, the onset of tertiary creep and deformation as these factors find application in design criteria for establishing design stress levels and evaluating design rules.

The experimental program consisted of stress-rupture testing of all-weld-metal specimens taken from several different welds in large-diameter, thin-wall Type 316H stainless steel piping. Welds were fabricated using a

single process, similar welding parameters and joint design, and different heats of Type 16-8-2 filler metal. Test results should therefore be indicative of property variations which may be encountered in an actual engineering system. Limited results on post-weld heat treatment and thermal exposure effects were also obtained. All tests were conducted at 593°C which is slightly higher than the upper service temperature for FFTF (565°C) but serves to accentuate the time-dependent creep behavior. Only the relatively short-term (i.e. $< 3.6 \times 10^7$ s), high-stress level (i.e. > 200 MPA) properties of the weld materials are considered here, but such properties find direct application in current design criteria for wrought materials. Properties relating to long-term service (e.g. to 7×10^8 s) are clearly of importance to the FFTF application, but were beyond the scope of this investigation. In analyzing test results, statistical evaluations were used extensively to establish real differences and trends and to define minimum property values which are used in the design criteria.

Materials and Procedures

All of the Type 16-8-2 materials were taken from four gas tungsten-arc welds (designated A, B, C and D) produced in 0.71 m diameter Type 316H stainless steel pipe. Three were circumferential butt welds (Welds A, C, and D) and one a longitudinal seam weld (Weld B). In all cases the pipe had a wall thickness of 9.5 mm and the joint configuration was a single V with a 75° included angle. Specimens were taken from a longitudinal orientation relative to the weld axis and thus yielded all-weld-metal specimens. The specimens were a miniature button-head type: 48 mm long, 3.18 mm gage diameter, 28.6 mm gage length and 6.4 mm button-head diameter. Each of the four welds were tested in the as-received condition; Welds A, C and D were as-welded and Weld B had been annealed at 1065°C for one-half hour during fabrication of the pipe. In addition, specimens taken from Weld A were tested after thermal exposure in static sodium at 565°C for periods of 3.6×10^6 s, 1.44×10^7 s, and 3.6×10^7 s; these materials are designated A1, A4 and A10 respectively. For the purpose of analyzing differences among properties of various welds, the aged materials are treated as completely different welds thus leading to seven weld designations: A, A1, A4, A10, B, C, and D.

Three different heats of Type 16-8-2 filler metal are represented in the welds (Welds A, A1, A4, A10 and C used the same heat), all with compositions (in weight percent) in the following ranges: C, 0.05-0.071; Mn, 1.66-1.85; Si, 0.27-0.43; S, 0.019-0.024; P, 0.011-0.019; Cr, 15.76-15.97; Ni, 8.24-8.34; and Mo, 1.46-2.04. Three different heats of Type 316H piping material were used in producing the welds. Mechanical property measurements for two of these heats have been reported[5,6] and all welds except B were produced using these two base materials.

Constant load creep rupture tests were conducted in an inert gas atmosphere at 593°C. Specimen extension during the tests was monitored by measuring total load-train motion outside the hot zone at periodic intervals with precision dial indicators. The testing systems are not calibrated to yield accurate values of the strain which occurs on loading a specimen to the desired creep stress load, therefore specimen extension measurements were only applied to compute creep strain values (i.e. the time-dependent strain which occurs after a specimen is fully loaded). Strain on loading was determined from stress-strain curves obtained from conventional tension tests conducted in air at 593°C using a rigid-beam universal testing machine.

Time to rupture for each test was recorded automatically upon specimen failure. Time to the onset of tertiary creep was determined from creep strain-time curves as the time at which creep rate first began to increase. Creep strain-time curves also provided a data record from which the strain at a given stress and time could be obtained. Some uncertainty in creep strain values at low strain levels (e.g. below $\sim$ 0.01) and short times (e.g. 3-10 x 10^3 s) was introduced in some tests as a result of small temperature changes in the test system during specimen loading; these normal contraction and expansion effects are sensed by the dial indicators as specimen strain. This source of experimental error is generally negligible at creep strain values above about 0.005. All stress and strain values used in this investigation are based on the original cross-sectional area and gage length of the test specimen.

Standard methods of statistical analysis were employed in data evaluations. Methods for linear regression, the computation of confidence intervals, and the comparison of several regression equations by tests of statistical hypotheses followed those described by Wine.[7] Tolerance intervals for the linear regression equations were computed using the equation given by Dixon and Massey.[8]

Weld Property Results

Experimental results for rupture, the onset of tertiary creep and creep deformation for all welds were described by the relations

$$\ln t_r = 81.3456 - 12.176 \ln \sigma \tag{1}$$

$$\ln t_t = 80.0786 - 12.176 \ln \sigma \tag{2}$$

$$\ln t_{\varepsilon_c} = A_{\varepsilon_c} - 13.0 \ln \sigma \tag{3}$$

$$A_{\varepsilon_c} = 87.3633 + 1.32066 \ln \varepsilon_c + 0.446428 [\ln \varepsilon_c]^2 + 1.08131 [\ln \varepsilon_c]^3 + 6.96513 \times 10^{-3} \ln [\varepsilon_c]^4 \tag{4}$$

$$\text{for } 0.20 \geq \varepsilon_c \geq 0.001$$

where t_r is the time to rupture in seconds, t_t is the time to the onset of tertiary creep in seconds, t_{ε_c} is the time to produce a given creep strain, ε_c, in seconds, and σ is the stress in MPa. Statistical hypothesis testing indicated that there was insufficient evidence to conclude that the stress dependence of t_r and t_t was not the same for all welds. Subsequent hypothesis tests indicated that the various welds do not exhibit identical regression equations but the differences in the intercept values in equations (1) and (2) for the individual welds were small enough to warrant the use of a single equation for present purposes. Since plots of $\ln t_{\varepsilon_c}$ against $\ln \sigma$ were quite similar to the analogous plots of $\ln t_r$ and $\ln t_t$, a single description for all welds was adopted without recourse to statistical hypothesis testing. The regression lines, 95% confidence intervals, and 95%/95% tolerance intervals are illustrated in relation to the data for t_r and t_t in Figures 5.10. Experimental creep deformation results are shown in relation to regression lines and tolerance intervals in the isochronous stress-creep strain plots of Figure 5.11.

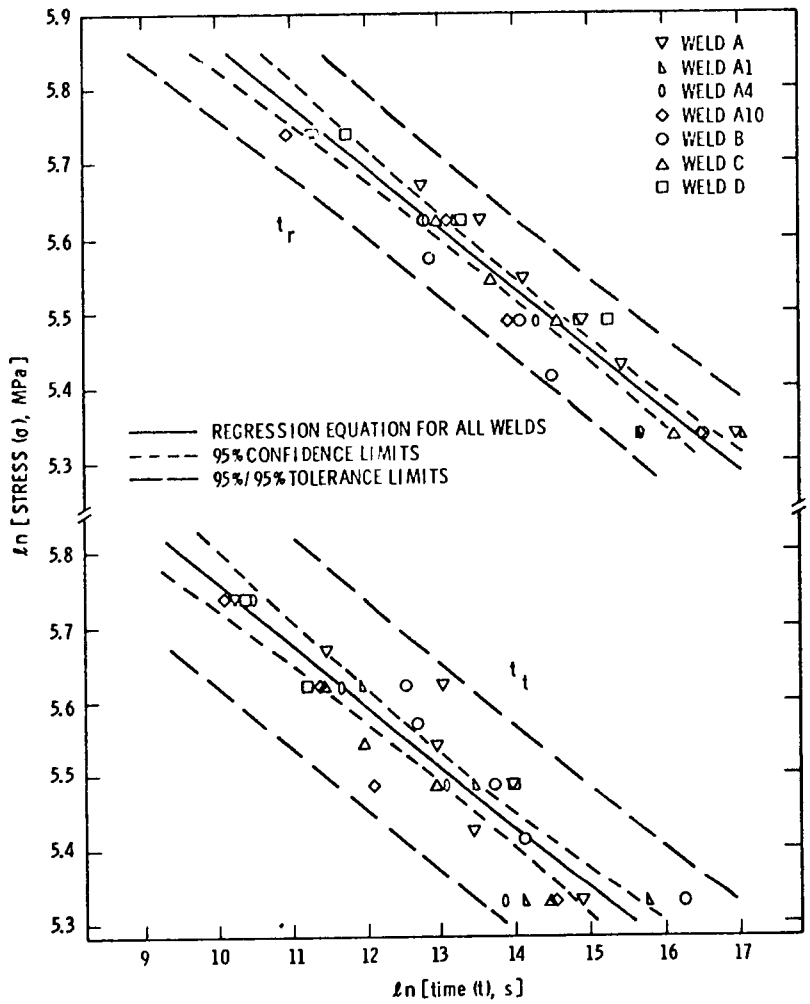

Figure 5.10. Rupture time (t_r) and time to onset of Tertiary Creep (t_t) for Type 16-8-2 Weld Materials at 593°C.

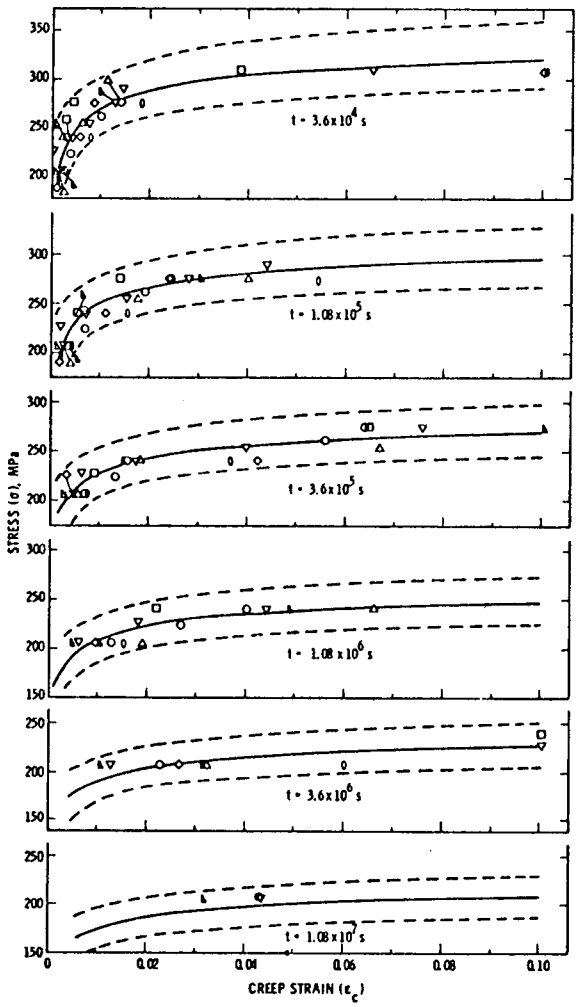

Figure 5.11. Isochronous Stress-Creep Strain Curves for Type 16-8-2 Weld Materials at 593°C.

Elastic-plastic stress-strain curves obtained from tension tests are presented in Figures 5.12. A nominal stress-strain curve representing all A-group welds was constructed by averaging stress values from the four curves at selected strain values. A similar averaging was applied to the curves for Welds C and D to yield a single nominal curve for these materials. The experimental curve for Weld B was used to represent nominal behavior of this material. Isochronous stress-strain curves representing nominal deformation behavior were constructed by adding the creep strain contributions from Figures 5.11 to the elastic-plastic strain values for the nominal tension flow curves at the appropriate stress levels. A set of isochronous stress-strain curves for A-group welds is illustrated in Figure 5.13. Curves for welds C and D or weld B would be somewhat different only because of the different tension flow curves for these materials.

Limited experimental data for additional Type 16-8-2 welds (designated V66 to V74) were reported by King et al.[9] These results could be described by the relations

$$\ln t_r = 79.4901 - 12.176 \ln \sigma \tag{5}$$

$$\ln t_t = 78.6769 - 12.176 \ln \sigma \tag{6}$$

$$\ln t_{\varepsilon_c} = A_{\varepsilon_c} - 17.25 \ln \sigma \tag{7}$$

$$A_{\varepsilon_c} = \begin{cases} 100.5925 \text{ for } \varepsilon_c = 0.005 \\ 103.0255 \text{ for } \varepsilon_c = 0.01 \\ 104.5058 \text{ for } \varepsilon_c = 0.02 \end{cases} \tag{8}$$

Equations (7) and (8) were combined with the tension flow curve description given by King et al to construct isochronous stress-strain curves for these welds.

Base Metal Property Results

Properties of wrought Type 316 stainless steel were obtained from the literature for comparison with the weld metal properties described above. Representative stress-rupture behavior of wrought base metal was obtained from the results of Reference 10, which were derived from an extensive data base on a variety of wrought Type 316 products. Values of the stress to

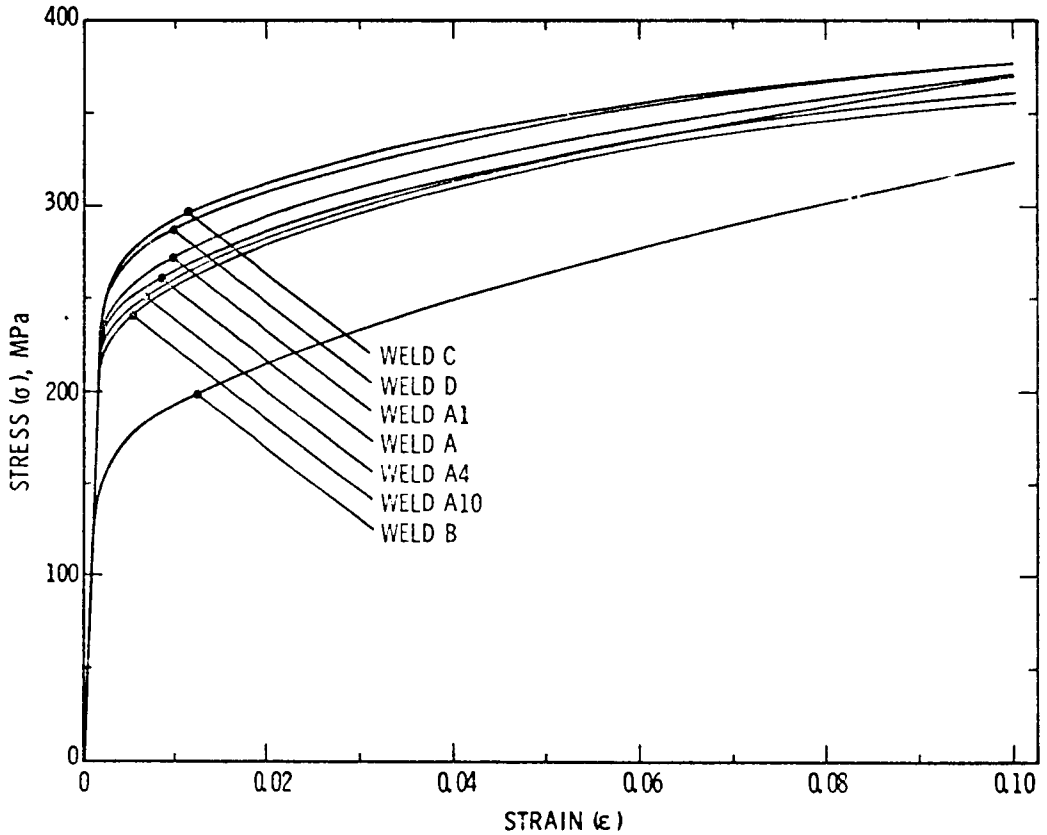

Figure 5.12. Flow Curves for Elastic/Plastic Deformation of Type 16-8-2 Weld Materials at 593°C.

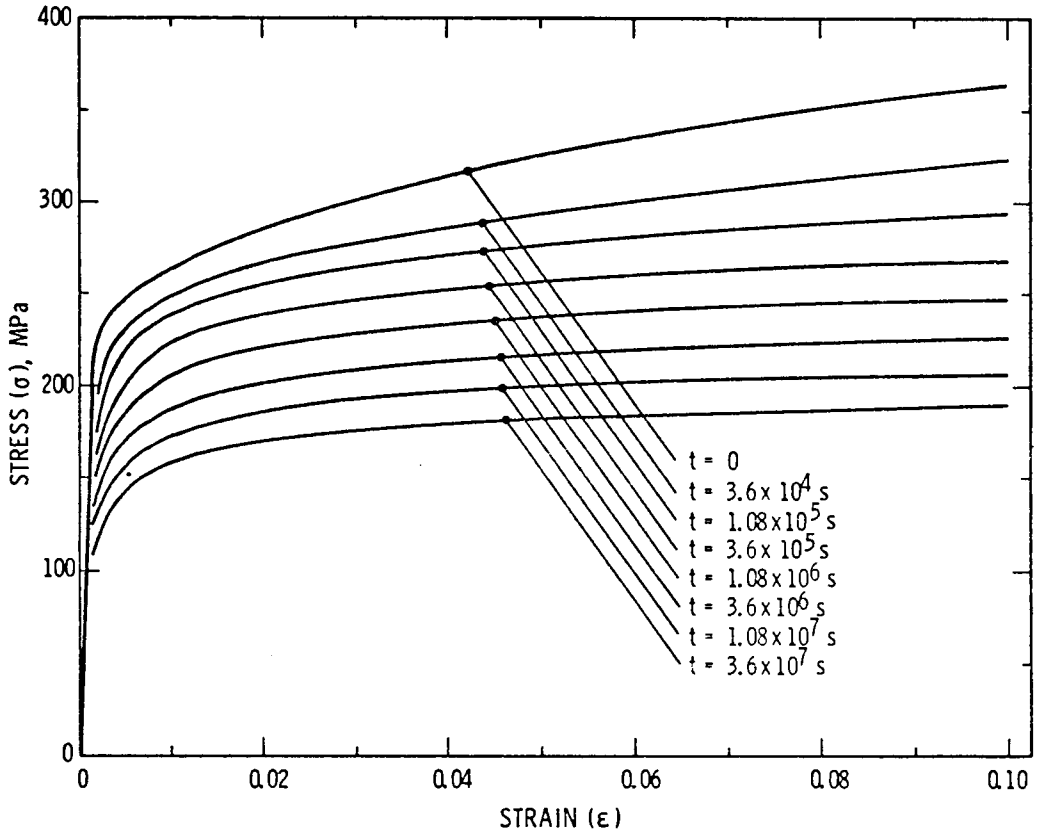

Figure 5.13. Isochronous Stress-Total Strain Curves for Type 16-8-2 Weld Materials at 593°C.

produce rupture in fixed time, σ_r, and the stress to produce the onset of tertiary creep in a fixed time, σ_t, are readily obtained from Reference 10. Isochronous stress-strain curves for wrought Type 316 have been reported by Blackburn.[10]

It was also of interest to consider the properties of the Type 316H piping used in the fabrication of most of the present welds. The stress-rupture results reported by Steichen[6] were described by the relations

$$\ln t_r = 80.3291 - 11.288 \ln \sigma \text{ at } 565°C \tag{9a}$$

$$\ln t_r = 59.6171 - 8.556 \ln \sigma \text{ at } 649°C \tag{9b}$$

$$\ln t_r = 43.6711 - 6.599 \ln \sigma \text{ at } 760°C \tag{9c}$$

$$\ln t_t = 79.4950 - 11.288 \ln \sigma \text{ at } 565°C \tag{10a}$$

$$\ln t_t = 58.3374 - 8.556 \ln \sigma \text{ at } 649°C \tag{10b}$$

$$\ln t_t = 41.9638 - 6.599 \ln \sigma \text{ at } 760°C \tag{10c}$$

Values of σ_r and σ_t at 593°C were obtained by graphical interpolation of the results for these three temperatures. Creep strain results were obtained from the original laboratory records and correlated using the graphical procedure described by Woodford.[11] Creep strain contributions were then added to the tension flow curve to construct isochronous stress-strain curves at each of the three temperatures. Stress values associated with specific strain and time values at 593°C were obtained by graphical interpolation.

Minimum Property Values

Minimum values of the stress to produce rupture, σ_r-min., and the stress to produce the onset of tertiary creep, σ_t-min., for welds are based on the lower tolerance limits in Figures 5.10. It was found that the relations

$$\sigma_r\text{-min.} = 0.9\ \sigma_r \tag{11}$$

$$\sigma_t\text{-min.} = 0.85\ \sigma_t \tag{12}$$

where σ_r and σ_t are the nominal stress values obtained from equations (1) and (2), were a very close approximation to the lower tolerance intervals and were the equations actually used in evaluating minimum values. These

same relations were also used for welds V66 to V74.

Minimum values of the stress to produce a strain of 0.01, σ_ε-min., were derived from consideration of minimum isochronous stress-strain curves. Assuming that a minimum isochronous stress-strain curve can be constructed by combining a minimum tension flow curve with a minimum stress-creep strain curve, it was found that the relation

$$\sigma_\varepsilon\text{-min} = 0.85\ \sigma_\varepsilon, \tag{13}$$

where σ_ε is the stress at a strain of 0.01 from the nominal isochronous stress-strain curve, was a reasonable and convenient approximation to a σ_ε-min based on tolerance limits. Equation (13) was also used to determine σ_ε-min. for welds V66 to V74.

Minimum property values for wrought Type 316 stainless steel were determined by the procedures of Reference 4. In the case of the Type 316H piping, values of σ_r-min. and σ_t-min were again based on lower tolerance limits for the piping data. In the absence of a statistical analysis of deformation results, values of σ_ε-min. for piping were determined from Equation (15).

Discussion

It is generally accepted that variations in weld parameters can lead to differences in the substructural features which influence macroscopic mechanical properties. Thus, in order to produce welds with consistent properties, weld parameters must be controlled by a realistic weld-procedure specification. Welds A, C, and D were prepared using very similar welding parameters, with variations in current, voltage and travel speed typical of those which might be permitted in a specification for an engineering system. That the creep and elastic-plastic properties of the as-deposited materials in the present study are basically very similar, attests to the suitability of the procedure for minimizing property variations among different welds. Welds V66-V74[9] were made using heat inputs (the product of current and voltage divided by the travel speed) which were substantially above the range specified for present welds and because they were produced in thicker plate (12.7 mm) required a greater number of weld passes. The observation of lower strength in these welds suggests

that the softening effect of the higher heat inputs dominated the strengthening tendency of additional passes.

The significantly lower flow stress for plastic deformation exhibited by Weld B is clearly the result of the annealing treatment used in the post-weld fabrication sequence since the as-welded strength would be expected to be somewhat higher (if at all different) than the other welds because of substantially lower heat inputs used. In any case, subsequent structural changes accompanying the plastic deformation that occurs on loading to the creep stress lead to macroscopic creep properties that are very similar to those of the as-welded materials. The flow stress for plastic deformation of welds V66-V74 is also low relative to the present as-welded materials, but creep strain accumulates more rapidly and the onset of tertiary creep and rupture occur earlier in these welds. It would appear that the initial substructure and the subsequent development of deformation substructure in Weld B is different from that in the V66 to V74 welds. By way of contrast with the high temperature annealing treatment, the extended thermal exposures at 565°C have only minor effects on the plastic flow curves or creep behavior of the welds.

Structural design criteria provide a convenient framework for assessing the potential design significance of property differences among welds and base materials. In current design criteria,[3] the allowable stress value for time-dependent behavior, S_t, is defined to be the smaller of 2/3 σ_r-min., 0.8 σ_t-min., or σ_ε-min., where all quantities are evaluated at a specific time, t. These allowable stress values, when used with the specific rules of the design criteria, are intended to preclude failure by ductile rupture or gross distortion. The present evaluation of these three stress quantities for various materials is summarized in Table 5.2. In the general evaluation of wrought Type 316 materials, σ_ε-min. becomes the S_t value for times through 3.6×10^6 s, with 2/3 σ_r-min. becoming the controlling value at 3.6×10^7 s. For a specific base material such as the Type 316H piping, different S_t values are obtained, but σ_ε-min. remains the controlling stress quantity. The σ_ε-min. values for welds are relatively high and as a result either 2/3 σ_r-min. or 0.8 σ_t-min. quickly becomes the smallest stress quantity for these materials. The key point of Table 5.2

TABLE 5.2

COMPARISON OF DESIGN-RELATED STRESS QUANTITIES FOR TYPE 316 STAINLESS STEEL AND TYPE 16-8-2 WELD DEPOSITS

Time, s	Stress Quantity	Stress Values, MPa: Type 316 (Ref. 8)	Type 316H Piping	Type 16-8-2 Welds: A, A1, A4, A10	C, D	B	V66-V74 (Ref. 7)
3.6×10^4	$2/3\ \sigma_r$-min.	207.2	254.8	→ 202.0	→ 202.0	202.0	173.5
	$0.8\ \sigma_t$-min.	231.7	245.3	206.3	206.3	206.3	173.1
	σ_ε-min.	→ 130.3	→ 139.5	211.2	220.6	→ 161.8	→ 161.9
3.6×10^5	$2/3\ \sigma_r$-min.	168.8	202.7	→ 167.2	→ 167.2	167.2	143.6
	$0.8\ \sigma_t$-min.	184.1	195.0	170.8	170.8	170.8	→ 143.2
	σ_ε-min.	→ 122.7	→ 134.8	189.6	200.2	→ 158.3	149.8
3.6×10^6	$2/3\ \sigma_r$-min.	129.4	162.2	→ 138.4	→ 138.4	→ 138.4	118.9
	$0.8\ \sigma_t$-min.	140.7	157.1	141.4	141.4	141.4	→ 118.6
	σ_ε-min.	→ 114.5	→ 124.3	159.0	159.4	148.8	135.6
3.6×10^7	$2/3\ \sigma_r$-min.	→ 95.8	129.5	→ 114.5	→ 114.5	→ 114.5	98.4
	$0.8\ \sigma_t$-min.	102.0	124.9	117.0	117.0	117.0	→ 98.1
	σ_ε-min.	104.0	→ 110.8	134.3	134.3	131.2	119.4

→ denotes the smallest value in each group of three quantities.

is that S_t values for wrought Type 316 are lower than any of the stress quantities for welds. Thus, S_t values derived from these base metal properties provide adequate protection against failure for the weld materials. Essentially the same conclusion is reached if S_t values derived directly from the Type 316H piping data are considered. Only for Welds V66 to V74 at the low longer times are any of the stress quantities for welds lower than the piping S_t values. In these instances, piping values still provide some protection against failure in the sense that S_t is still less than either σ_r-min. or σ_t-min., even though the margin of protection is not as large as intended by the design criteria. Viewed from this standpoint, the detailed differences in properties between weld and base materials are often relatively unimportant. For example, the observation of substantially lower rupture strength in the present Type 16-8-2 welds, compared to that of the Type 316H piping, causes little or no concern since the value of σ_ε-min. for piping determines S_t, which in turn provides adequate protection against stress rupture for the weld materials.

The design criteria also uses material properties in use-fraction summations and the evaluation of creep-fatigue interaction. The use-fraction summation accounts for varying loads at variable times and temperatures and uses the S_t versus t relationship. Since S_t for base materials provides adequate protection for welds in terms of allowable stress values, it also provides adequate protection for welds in the use-fraction summation. Evaluation of creep-fatigue interaction involves the computation of creep damage from the summation $\Sigma(t/t_d)$, where t is duration of stress application, and t_d is the design time to rupture at that stress. The summation applies over all loading conditions. Taking a specific example of Type 316H piping and A-group welds, the use of piping t_d values does not give conservative creep damage values for welds at a given stress level. The welds actually have a smaller t_d value (i.e. lower rupture stress) and hence a greater creep damage value. However, it may not be appropriate to compare creep damage values at the same stress level. In FFTF piping, creep-fatigue interaction arises when thermal transients interrupt steady-state operation. These thermal transients can produce cyclic plastic strains (i.e. fatigue) in portions of the pipe wall, which in turn induce residual stresses that cause creep during subsequent steady-

state operation. Since the cyclic plastic strain is governed primarily by thermal expansion and contraction effects, the cyclic strain range is fixed by the thermal transient conditions rather than material properties. For a fixed strain range, the residual stress magnitude will depend on the cyclic stress-strain curve, and it is possible for a material with a high stress-strain curve (e.g. weld) to develop a lower residual stress than a material with a lower stress-strain curve (e.g. base metal). Thus, the former material, even though it exhibits an inherently lower rupture strength, may be subject to less creep damage since it operates under a lower residual stress which translates to a larger t_d value. Clearly a more complete evaluation of such considerations is required before definitive conclusions can be drawn regarding creep damage calculations for weld materials.

In the earlier discussion, S_t values for base materials were found to provide adequate protection against failure for weld materials. This does not necessarily imply that the mechanical performance of welds will exceed that of base materials in an engineering structure. Although the property differences were not particuarly significant in terms of S_t, they may become important in analyzing the response of a structure to various loadings. Property differences may lead to stress or strain concentrations in weld regions, and hence the allowable stress limit or the strain limit for the weld region may be the controlling feature of the design. Detailed considerations of this type are beyond the scope of the present study. Nevertheless, the descriptions of weld materials presented here should provide useful information for further study of the potential implications of weld metal properties in structural analysis. Such considerations coupled with those of allowable stress values may lead to future design criteria which deal more directly with the properties of weld region. It should be noted at this point that all of the above discussions relate only to the properties of weld metal and the behavior of the base metal/weld metal interface and heat affected zone may also be important in determining the overall performance and failure conditions of the weld region, and additional testing programs are required to investigate this area.

5.2.2.3 Expected Accomplishments

Limited data on the creep and rupture behavior of some of the weld materials will be obtained at 538°C.

5.2.3 Tensile Properties of Wrought and Weld-Deposited Inconel-718

A. L. Ward, R. L. Knecht

5.2.3.1 Objective

The purpose of this work is to provide a description of the preirradiation tensile properties of Inconel-718. Such descriptions form the basis for determining the effects of neutron irradiation which are being studied in support of LMFBR design, design confirmation, operations guidance and safety analysis.

5.2.3.2 Accomplishments and Status

Introduction

The wrought Inconel-718 used in this study was obtained in the form of 12.7 mm thick plate. Miniature buttonhead tension specimens (48 mm long, 3.18 mm gage diameter, 28.6 mm gage length, and 6.4 mm buttonhead diameter) were taken from the plate such that the specimen axis was parallel to the longitudinal forming direction of the plate. Weld metal specimens of identical configuration were obtained from a gas tungsten-arc butt weld in the base plate. The plate was solution annealed prior to welding and specimens were taken both from longitudinal and transverse orientations relative to the weld axis.

All specimens from the wrought material and most of the weld specimens were solution annealed at 954°C for one-half hour and then aged at 717°C for 8 hours, furnace cooled to 621°C and held until the total aging time reached 18 hours (AMS 5596C). A limited number of weld specimens were retained in the as-welded condition for both pre-and postirradiation testing. The chemical compositions of the wrought plate and weld filler metal are as follows (weight percent):

	Plate Ht52C9EK	Filler Metal Ht60C7E
C	0.07	0.04
Mn	0.08	0.09
Fe	18.19	17.97
S	0.007	0.007
Si	0.17	0.18
Cu	0.11	0.10
Ni	53.44	53.84
Cr	18.11	18.04
Al	0.59	0.55
Ti	1.08	1.01
P	0.007	0.01
Co	0.03	0.03
Mo	3.0	3.0
B	0.0032	0.0042
Cb + Ta	5.10	5.12

Results and Discussion

Wrought Base Metal

The tensile properties for the wrought and age-hardened Inconel-718 included in the present study are listed in Table 5.3 and illustrated graphically in Figures 5.14 and 5.15 as functions of test temperature over the range from room temperature to 760°C. The results of multiple tests at each temperature are represented by dashed-line bands to represent the maximum range of the data at any given temperature in the range. For purposes of comparison with postirradiation properties, trend lines representing the locus of mean values based only on the scatter bands have also been constructed.

In general, the overall magnitude of the properties and the behavioral trends, decreasing strength and ductility with increasing temperature, are consistent with those reported by Brinkman and Korth[12] for the same heat of material and with those reported elsewhere for other Inconel-718[13-16]. The properties also conform to the minimum strength and ductility requirements specified by AMS 5596B. The apparent discontinuity in the tensile strength curve, in the range from 200°C to 300°C (Figure 5.14), apparently has not been reported previously and is believed to be associated with the onset of strain aging at these temperatures and this relatively low strain rate[17-18]. The time-dependent nature of the strain aging phenomenon is

TABLE 5.3. TENSILE PROPERTIES OF WROUGHT INCONEL 718
(PLATE, HT. 52C9EK)

Specimen Ident.	Test Temp., °C	Strength, MPa		Ductility, %		
		0.2% Yield	Tensile	Uniform Elong.	Total Elong.	RA
718-1	22	1065	1365	15.5	16.4	30.9
718-2	22	994	1267	18.8	20.0	30.9
718-14	22	1053	1318	18.2	19.0	28.5
718-16	22	1038	1326	18.0	19.5	38.2
718-79	232	995	1218	15.9	19.3	36.9
718-78	232	947	1304	11.9	13.2	27.6
718-3	315	924	1152	16.4	18.9	31.7
718-77	315	970	1188	15.4	17.7	36.1
718-4	427	931	1147	13.5	17.4	30.9
718-5	427	919	1131	14.4	17.9	30.9
718-6	538	897	1120	15.5	17.9	30.1
718-7	538	889	1104	12.2	13.6	25.2
718-8	593	897	1108	14.0	15.0	25.2
718-10	593	891	1101	12.9	14.3	24.4
718-12	649	826	939	6.3	6.8	17.1
718-13	649	855	962	6.8	7.2	15.4
718-9	760	610	621	2.3	4.2	13.8
718-11	760	621	632	2.8	8.4	15.4

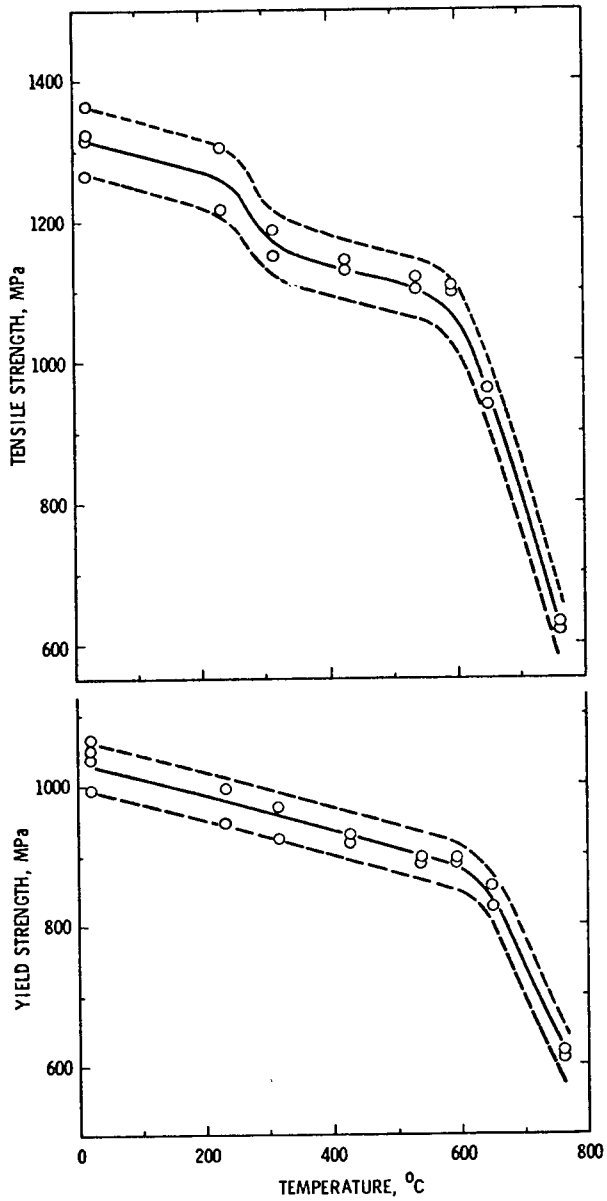

Figure 5.14. Pre-Irradiation Strength of Wrought Inconel-718.

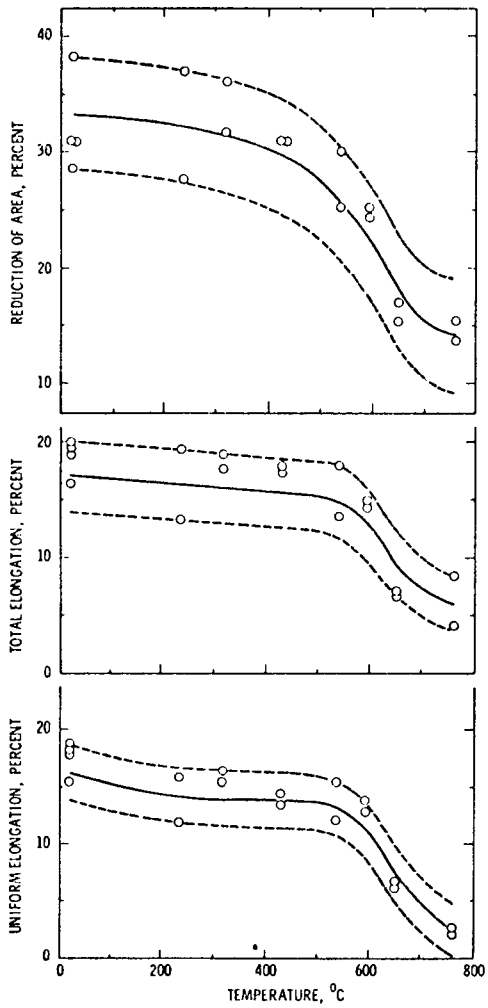

Figure 5.15. Pre-Irradiation Ductility of Wrought Inconel-718.

such that the yield strength, which is obtained from the very early portion of the stress-strain curve, is not affected. All ductility parameters fall sharply as the temperature exceeds ∿600°C (Figure 5.15) coincident with a transition in fracture mode which is transgranular at low temperatures and predominantly intergranular at temperatures of 649 and 760°C. As a point of general interest, tests conducted at 870°C produced results which showed that minima occur in the total elongation and reduction of area curves at about 700-800°C; values approaching 35% and 70% respectively were obtained at 871°C.

Weld Materials

Weld deposited Inconel-718, when subjected to the same age-hardening treatment given the wrought product, exhibits preirradiation yield strengths comparable to those measured for the wrought materials, slightly lower tensile strength and lower ductility (Figure 5.16). Better agreement between weld- and wrought-material yield strength indicates similarity in behavior during the early stages of plastic deformation with the substantive differences arising in those parameters measured at larger deformations associated with instability and fracture. For example, the greatest difference is noted in the reduction of area. As might be expected in weld-metal with relatively coarse grains and a generally less homogeneous microstructure, the data show significantly more scatter than do the data for the wrought material, again primarily in those properties associated with large deformations. No well-defined difference in strength appears to exist between specimens taken from longitudinal and transverse orientations to the weld axis. There does appear, however, a tendency for the transverse specimens to exhibit lower uniform and total elongation values and to fracture in the weld rather than the base metal. In the as-welded condition both transverse and longitudinal specimens showed very low strength and high ductility (Table 5.4). In this case, the transverse specimens produced substantially greater uniform and total elongations than did the longitudinal specimens as a result of the contribution from the annealed base metal contained in the gage section.

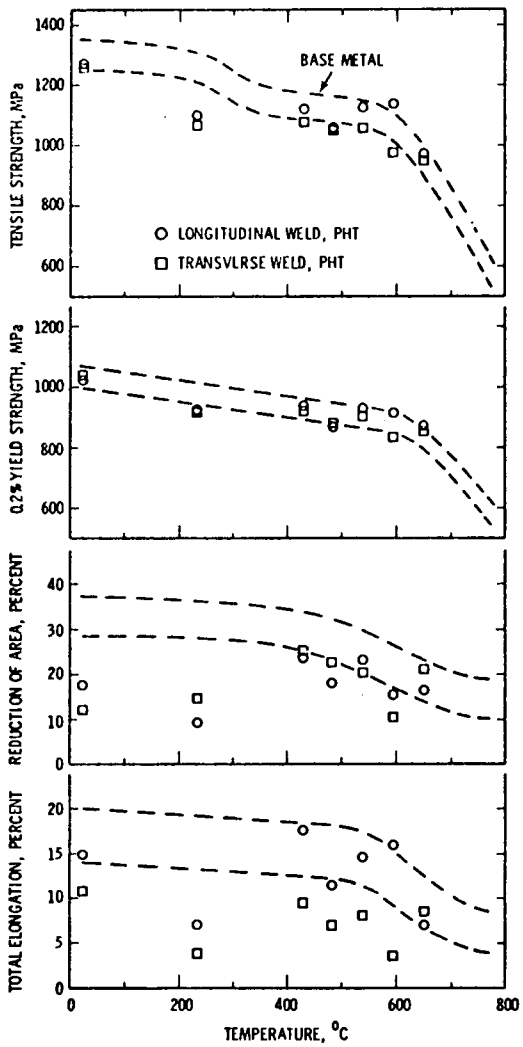

Figure 5.16. Pre-Irradiation Tensile Properties of Weld-Deposited Inconel-718.

TABLE 5.4. TENSILE PROPERTIES OF WELD-DEPOSITED INCONEL 718 (FILLER WIRE HT. 60C7E)

Specimen Ident.[a]	Test Temp., °C	Strength, MPa		Ductility, %			Specimen Material Condition[b]
		0.2% Yield	Tensile	Uniform Elong.	Total Elong.	RA	
7L-2	22	1017	1269	14.5	14.9	17.1	L, PHT
7L-41	232	925	1096	6.9	7.0	8.9	L, PHT
7L-4	427	934	1120	12.7	17.6	23.6	L, PHT
7L-40	482	869	1057	10.1	11.4	17.5	L, PHT
7L-8	538	929	1129	13.3	14.6	22.8	L, PHT
7L-35	593	914	1135	13.8	15.9	15.4	L, PHT
7L-10	649	871	972	6.4	6.9	16.3	L, PHT
7L-1	22	453	806	29.2	29.7	24.6	L, AW
7L-36	538	472	754	27.0	28.9	35.0	L, AW
7L-31	593	486	745	19.7	21.3	22.1	L, AW
7T-4	22	1041	1260	10.7	10.8	12.2	T, PHT
7T-42	232	917	1066	3.8	3.8	14.8	T, PHT
7T-5	427	921	1077	8.8	9.5	25.2	T, PHT
7T-40	482	881	1051	6.6	7.0	22.8	T, PHT
7T-8	538	900	1058	7.6	8.2	20.3	T, PHT
7T-41	593	834	975	3.6	3.6	10.7	T, PHT
7T-13	649	854	949	5.9	8.5	21.1	T, PHT
7T-1	22	430	829	42.0	43.8	35.0	T, AW
7T-3	538	334	727	44.3	46.9	43.9	T, AW

[a] L denotes longitudinally oriented specimens.
T denotes transverse specimens.

[b] PHT denotes specimens given solution anneal and precipitation heat treatment.

AW denotes specimen material in as-welded condition.

5.2.4 Effect of Temperature Upon Fatigue-Crack Growth in Nimonic PE16. J-Integral Toughness of Inconel Alloys 718 and X-750.

L. A. James, W. J. Mills, R. L. Knecht

5.2.4.1 Objective

The objective of this report is to characterize the effects of various parameters upon the fatigue-crack propagation behavior and fracture toughness behavior of reactor structural materials for use in design, safety analysis and operations support.

5.2.4.2 Accomplishments and Status

The specimens employed in the subcritical cracking studies of Nimonic PE16 were of the center-cracked design (W - 2.5 inch). The specimens were fabricated from 0.036 inch sheet, and had received a duplex aging treatment (Annealed 11 min. at 1904°F, A.C. Aged 1 hour at 1652°F, A.C. Aged 8 hours at 1382°F, A.C.). The mechanical properties are listed in Table 5.5.

Crack growth tests were conducted in air at test temperatures of 75°, 600°, 800°, 1000°, and 1200°F and the results are shown in Figures 5.17-5.21, respectively. The results are also summarized in Figures 5.22. It will be noted that, in general, at a given value of ΔK, fatigue-crack growth rates increase with increasing test temperatures. This is in agreement with observations on other nickel-base alloys including Inconel 600[19], Inconel 718[19-20], Inconel 738 LC[21], Inconel X-750[22], and Hastelloy X-280[23]. The crack growth behavior of Nimonic PE16 at each test temperature is also compared to the behavior of conventionally heat-treated Inconel 718 tested under identical conditions, and in general, crack growth rates in Nimonic PE16 are slightly lower than in the Inconel 718. It will also be noted in Figure 5.22 that the curves have a general sigmoidal shape. At high values of ΔK the curves for the various temperatures tend to converge, and at low values of ΔK they tend to curve downward suggesting that they might be approaching a crack growth threshold. Such slope transitions at the lower values of ΔK have also been noted in studies on other nickel-base alloys.[19 23]

Room temperature ductile fracture toughness (J_{Ic}) values of two nickel-base alloys, Inconel 718 (INEL heat treatment) and Inconel X-750

TABLE 5.5. MECHANICAL PROPERTIES OF NIMONIC PE16*

Specimen Number	Test Temp.	0.2% Yield Strength	Ultimate Strength	Uniform Elongation	Total Elongation	Reduction in Area	Site Sequence Number**
T126	75°F (24°C)	89,900 psi (620 MPa)	150,500 psi (1038 MPa)	23.60%	27.67%	48.91%	H10009
T130	600°F (316°C)	81,700 psi (563 MPa)	137,400 psi (947 MPa)	24.05%	25.26%	35.16%	H10010
T135	800°F (427°C)	82,600 psi (570 MPa)	132,100 psi (911 MPa)	21.18%	25.61%	43.48%	H10011
T127	1000°F (538°C)	82,200 psi (567 MPa)	127,400 psi (878 MPa)	18.99%	22.06%	41.76%	H10012
T133	1200°F (649°C)	82,800 psi (571 MPa)	108,200 psi (746 MPa)	8.32%	21.19%	27.17%	H10013

* Strain rate = 1.33×10^{-2} min^{-1}

** HEDL LMFBR Fuel Cladding Information Center

TABLE 5.6

ROOM TEMPERATURE MECHANICAL PROPERTIES

OF INCONEL 718 AND INCONEL X-750

Material	Specimen No.	0.2% Yield Strength	Ultimate Strength	Flow* Strength	Total Elongation	Site Sequence No.**
Inconel 718	T-41	145,350 psi	190,730 psi	168,040 psi	20.04%	H04916
Inconel X-750	T-106	93,090 psi	149,190 psi	121,140 psi	14.33%	H05986

*Flow Strength: $\sigma_f = 1/2\ (\sigma_{ys} + \sigma_{uts})$ where σ_{ys} and σ_{uts} are the yield and tensile strengths, respectively.

**HEDL LMFBR Fuel Cladding Information Center

TABLE 5.7

COMPARISON OF J_{Ic} AND J ACHIEVED AT MAXIMUM LOAD

INCONEL 718

Specimen No.	$J_{Max\ Load}$ (in-lb/(in)^2)	J_{Ic} (in-lb/(in)^2)
472	800	727
474	818	
475	786	

INCONEL X-750

Specimen No.	$J_{Max\ Load}$ (in-lb/(in)^2)	J_{Ic} (in-lb/(in)^2)
523	544	544
524	536	
525	610	

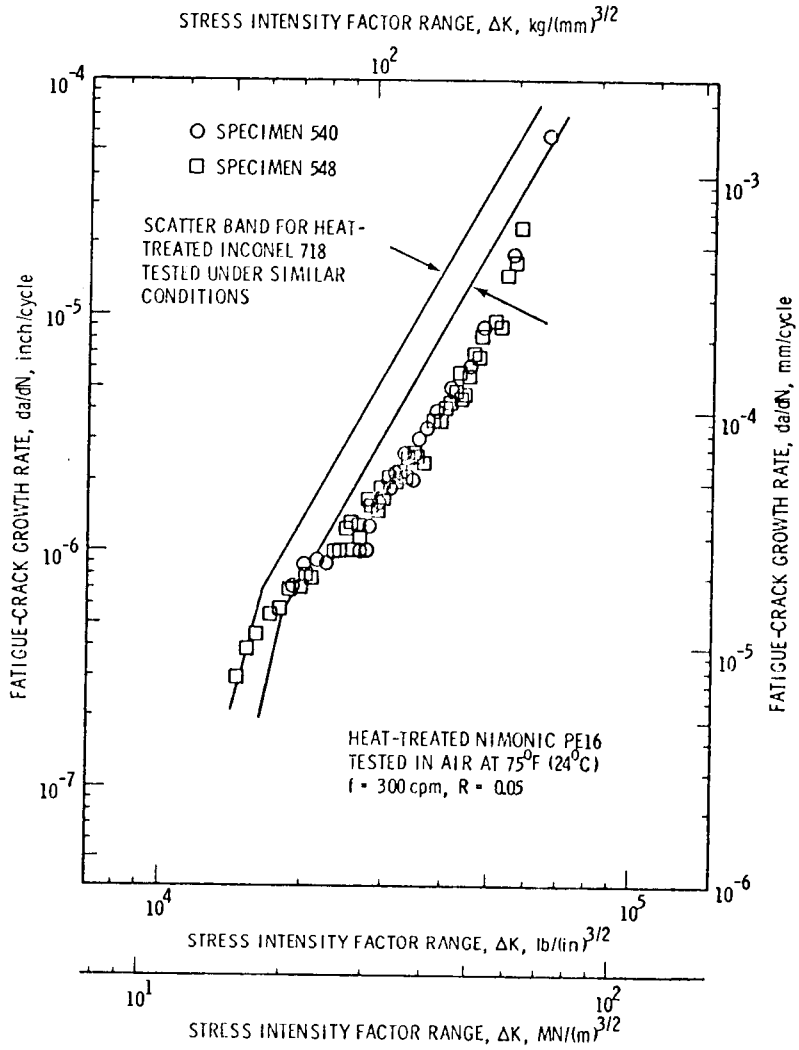

Figure 5.17. Fatigue-crack growth behavior of Nimonic PE16 in air at room temperature.

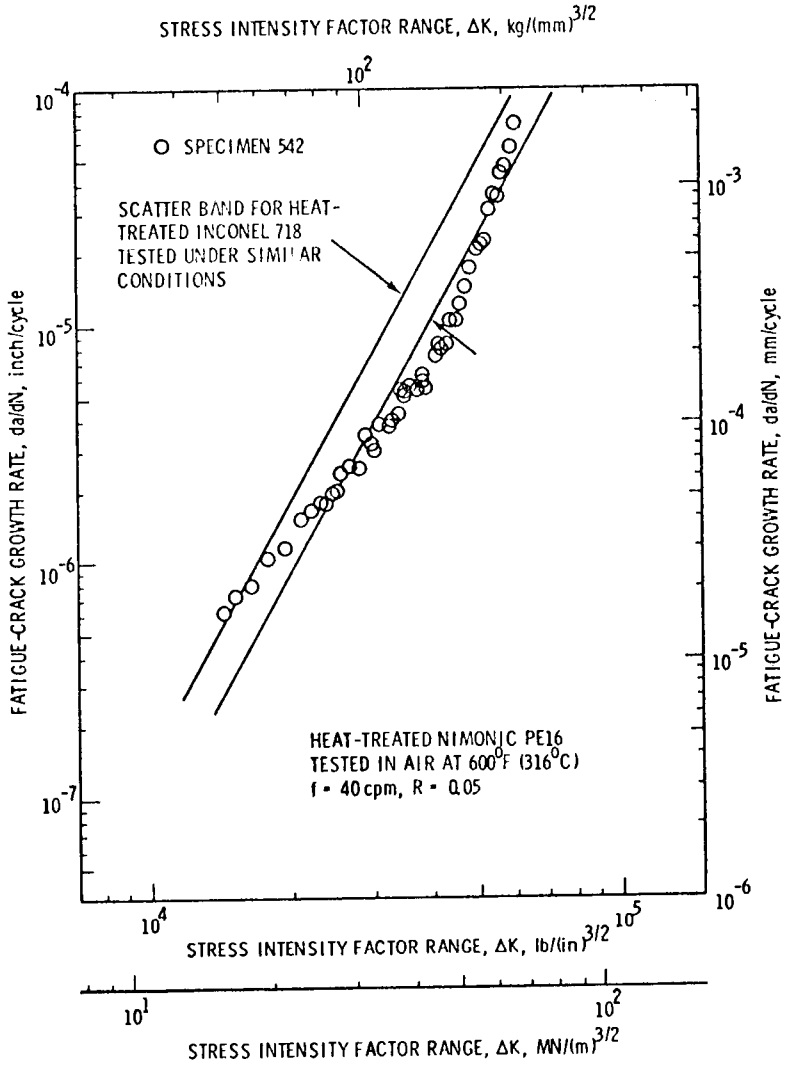

Figure 5.18. Fatigue-crack growth behavior of Nimonic PE16 in air at 600°F.

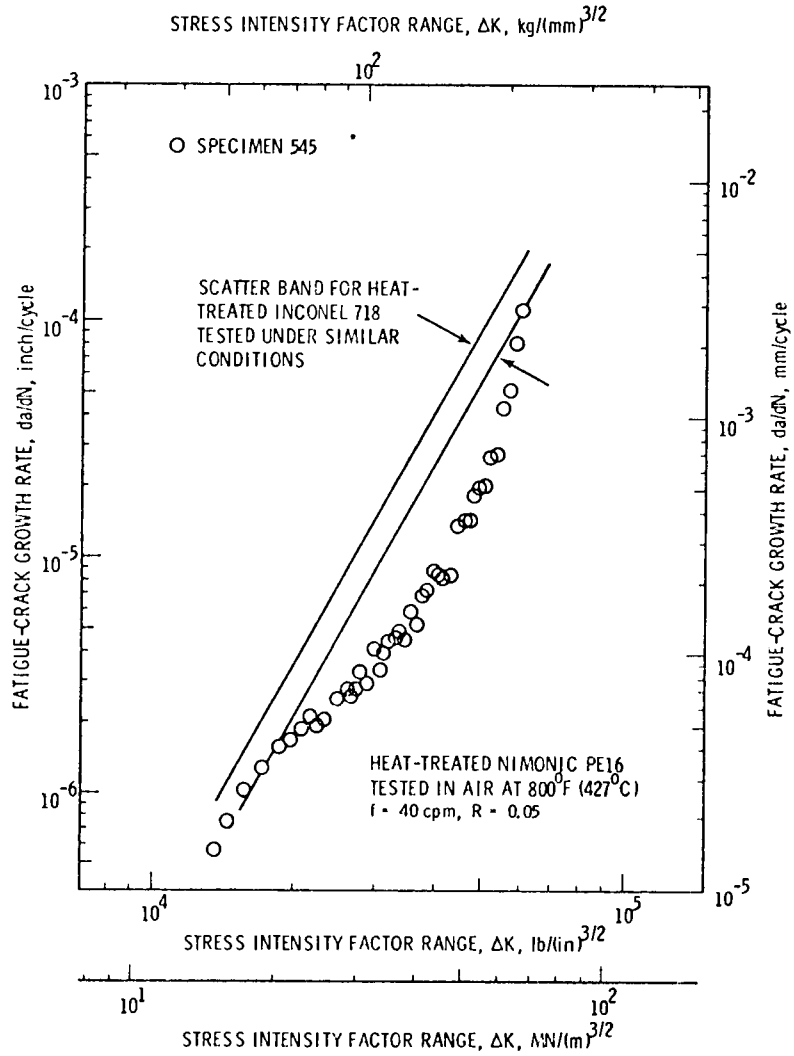

Figure 5.19. Fatigue-crack growth behavior of Nimonic PE16 in air at 800°F.

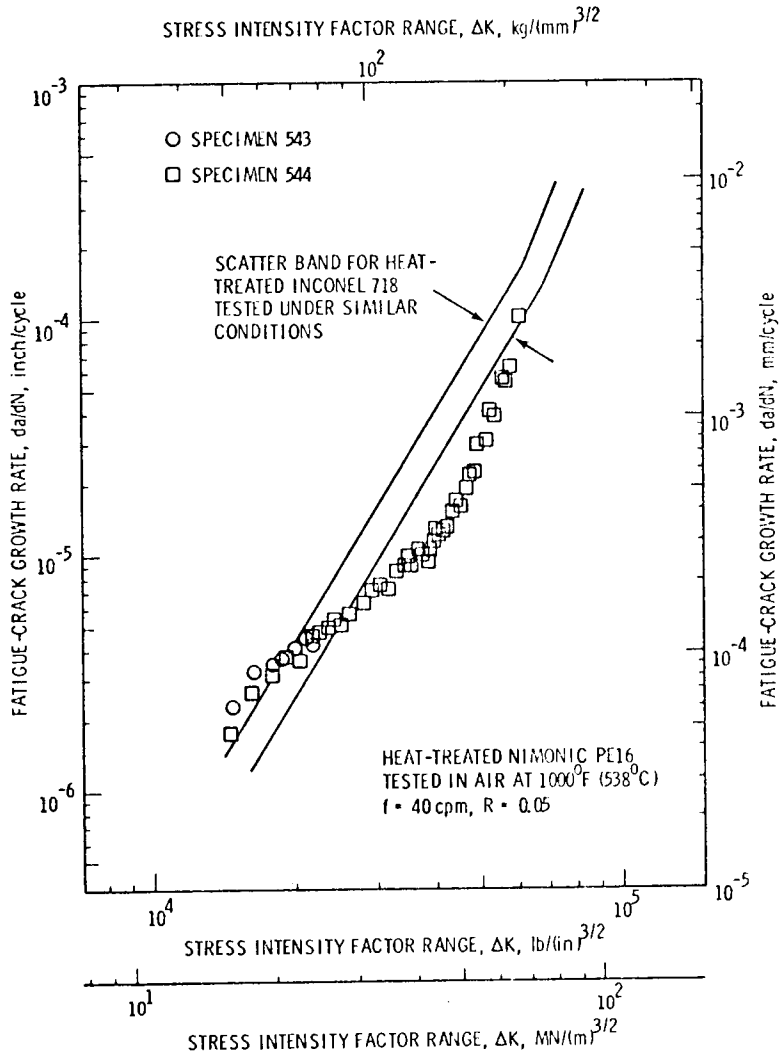

Figure 5.20. Fatigue-crack growth behavior of Nimonic PE16 in air at 1000°F.

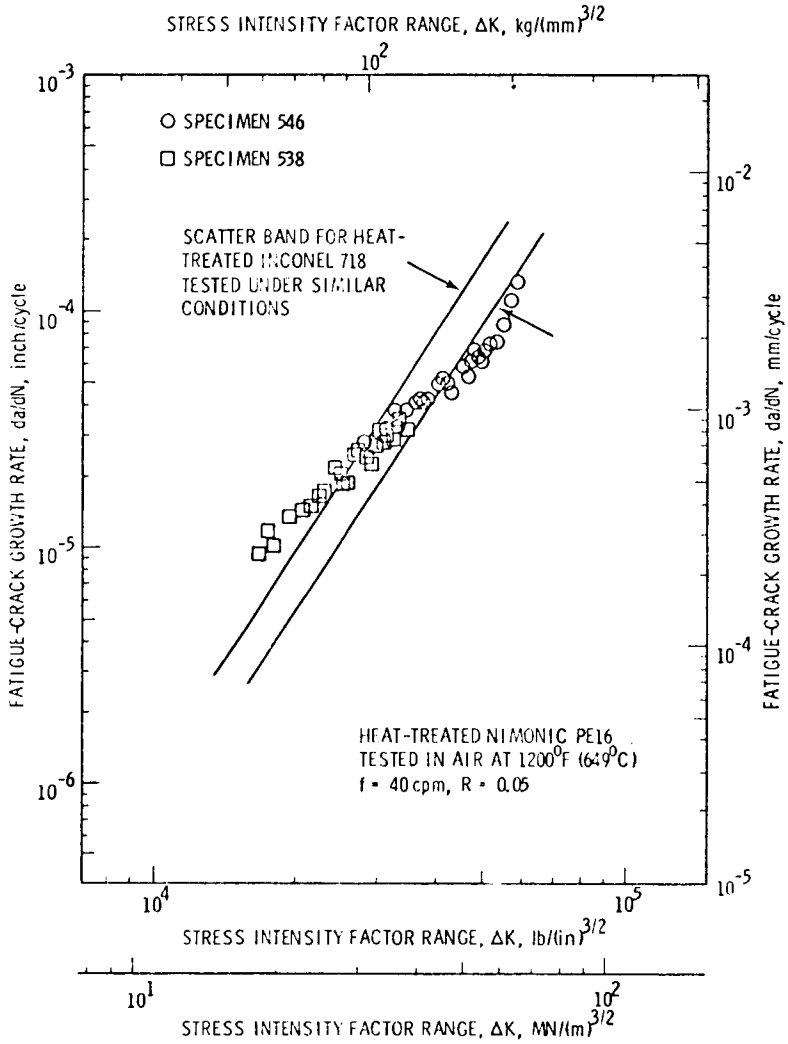

Figure 5.21. Fatigue-crack growth behavior of Nimonic PE16 in air at 1200°F.

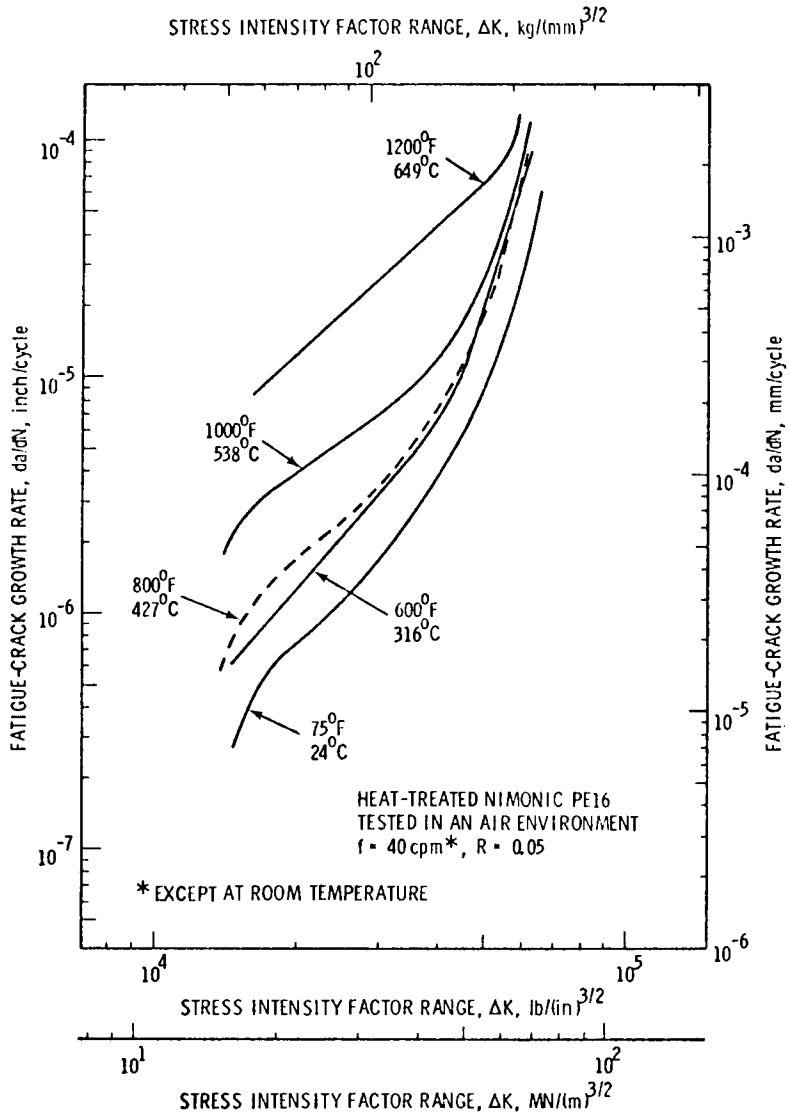

Figure 5.22. The effect of temperature upon the fatigue-crack growth behavior of Nimonic PE16 in an air environment.

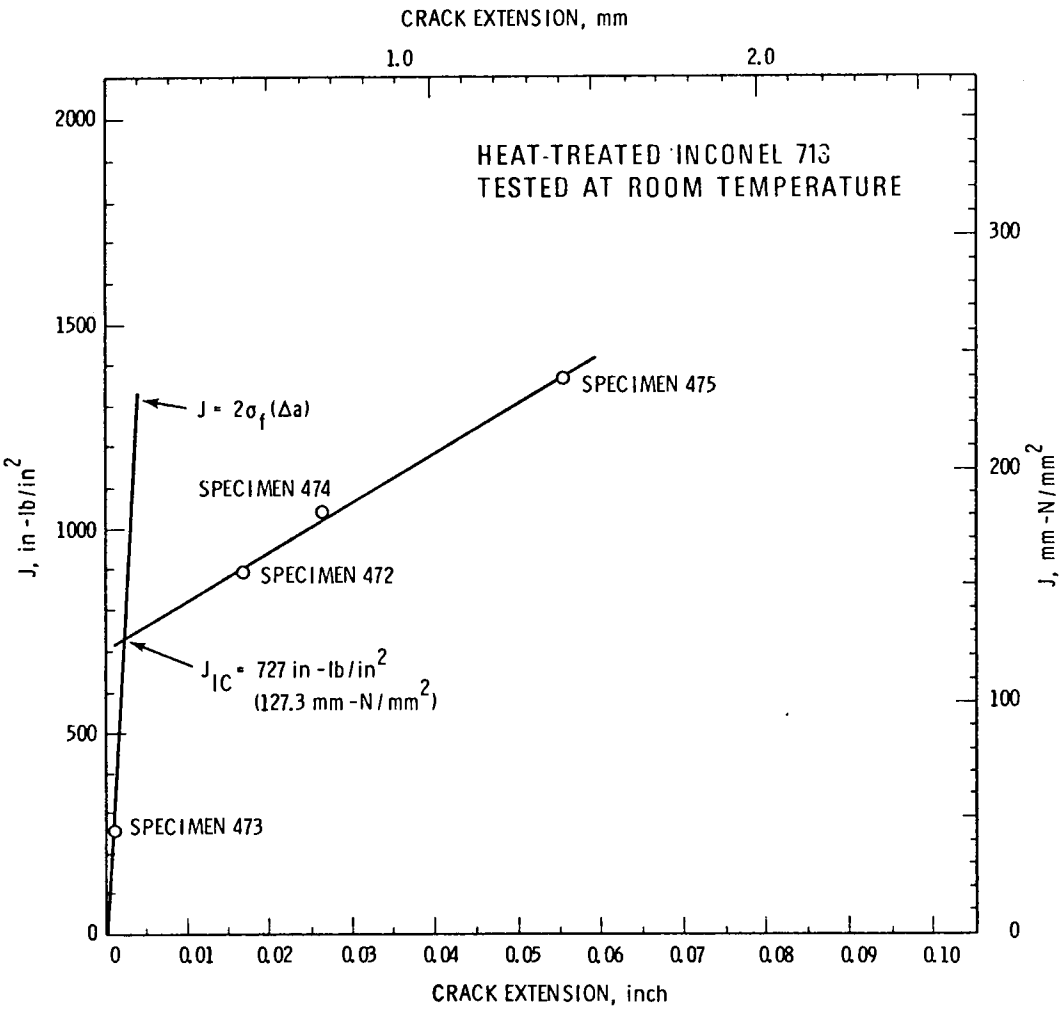

Figure 5.23. J versus crack extension for Inconel 718 tested at room temperature.

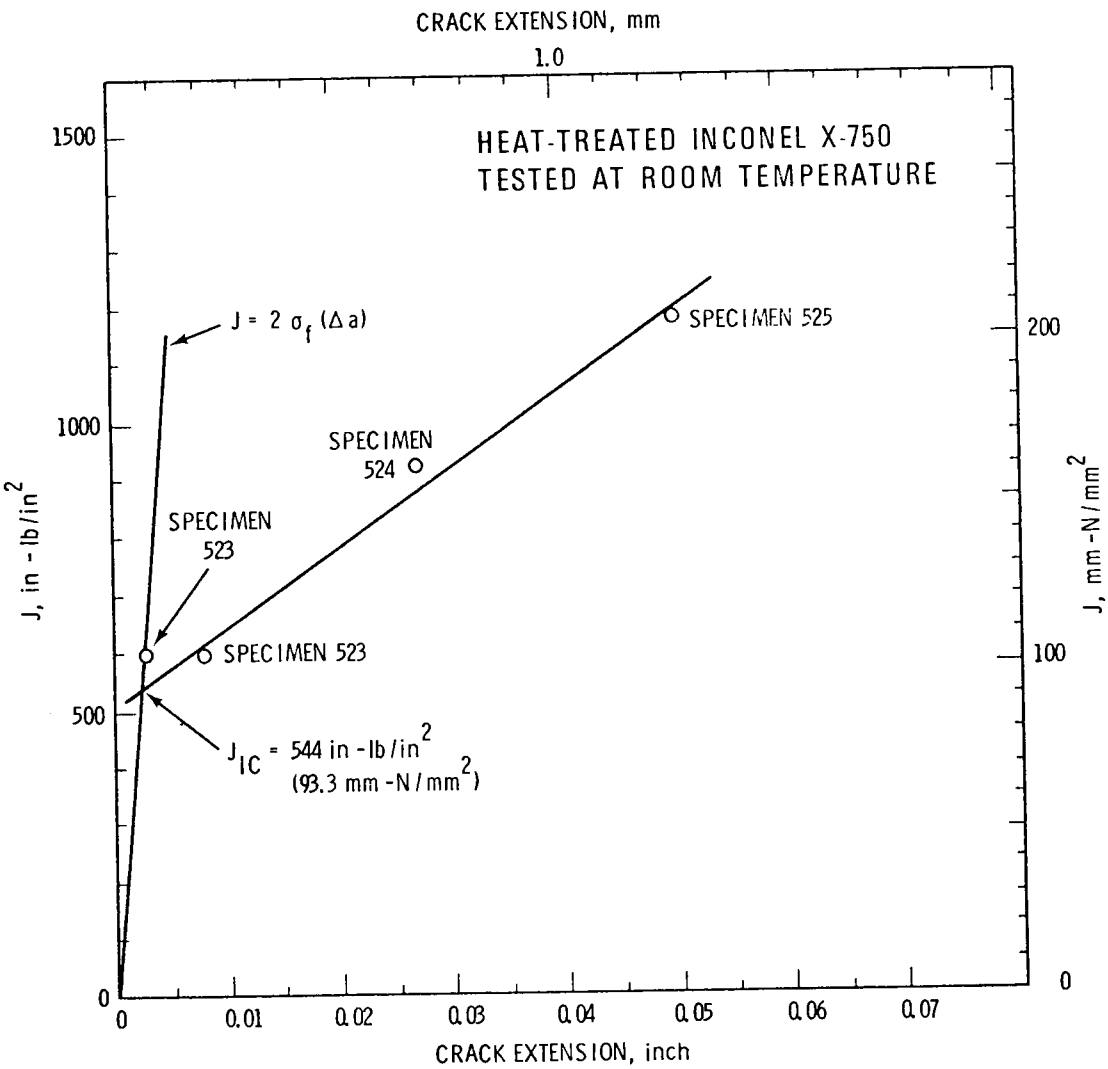

Figure 5.24. J versus crack extension for Inconel X-750 tested at room temperature.

(double aging heat treatment), have been evaluated by the multi-specimen R-curve technique[24]. ASTM Compact Specimens (0.577T) were employed. Room temperature mechanical properties for both alloys are summarized in Table 5.6. The results of the current investigation, illustrated in Figures 5.23 and 5.24, reveal that J_{Ic} for Inconel 718 (727 in-lb/(in)^2) was superior to that of Inconel X-750 (544 in-lb/(in)^2). It is also interesting to note that values of J calculated at maximum load were in good agreement with J_{Ic} values extrapolated from R-curves (see Table 5.7), thereby indicating that crack extension initiated at or near maximum load.

5.2.4.3 Expected Accomplishments

Ambient and elevated temperature ductile fracture toughness (J integral) testing of nickel-base alloys (Inconel 718 and Inconel X-750) and low alloy steels (SA-387, grades C and D) is continuing. The effect of specimen dimension and crack length parameters is being characterized.

Testing to characterize the effect of liquid sodium environment upon the fatigue-crack growth behavior of austenitic stainless steels and nickel-base alloys is expected to resume during this period. J-integral characterization of nickel-base alloys and low-alloy steels will also continue.

5.3 MATERIALS INFORMATION DOCUMENTATION -

J. E. Irvin, R. A. Moen, M. F. Marchbanks

5.3.1 Objective

The objective of this program is to manage, coordinate and distribute the Nuclear Systems Materials Handbook as a standard materials property reference for the nuclear community.

5.3.2 Accomplishments and Status

Nuclear Systems Materials Handbook

More than 220 pages were published and distributed early in January, 1976. Approximately 700 data pages are in various stages of the preparation/review/publication cycle. Two computer programs used to produce

camera-ready masters for the NSMH have been revised and expanded to handle non-linear functions in addition to polynomial expressions. These programs are code named NSMH1 and NSMH2. NSMH1 produces finished tables in the NSMH format, and NSMH2 produces graphs on 35 mm film which are then enlarged and printed to make a camera-ready master.

Update publication package Number 3, containing 120 new and revised pages, was submitted for printing in March, 1976. Distribution of this package to all NSM Handbook holders was in process at the end of April. Table 5.8 is a summary of the publication activity dating from the original issue of the Handbook.

TABLE 5.8. NUCLEAR SYSTEMS MATERIALS HANDBOOK PUBLICATION SUMMARY

Publication Date	Publication Pkg. No.	Number of Pages: Volume 1 New	Volume 1 Revised	Volume 2 New	Volume 2 Revised	Total Pages Per Pkg.	Cumulative Pg. Total*
1-31-75	0	427	-	258	-	685	685
4-17-75	1	0	15	0	3	18	685
12-1-75	2	67	38	64	45	214	845
3-10-76	3	25	70	13	12	120	892

*Note: Revised pages may result in an increase, decrease, or no change in the cumulative number of NSM Handbook pages.

5.4 REFERENCES

1. J. M. Steichen, "Tensile Properties of A-286," *HEDL-TME 75-81*, November 1975.
2. J. M. Steichen, "High Strain Rate Mechanical Properties of Types 304 and 316 Stainless Steel," *HEDL-TME 71-164*, November 1971.
3. Interpretations of ASME Boiler and Pressure Vessel Code, Case 1592, American Society of Mechanical Engineers, New York, 1974.
4. L. D. Blackburn, J. C. Tobin, and R. A. Moen, "Materials Creep Behavior and Elevated Temperature Design," *Nuclear Technology*, 16, October 1972.
5. J. M. Steichen and R. L. Knecht, "Mechanical Properties of Roll-Extruded Nuclear Reactor Piping," ASME Publication No. 75-PVP-41, April 1975.

6. J. M. Steichen, "Mechanical Properties of FFTF Primary Outlet Piping," Hanford Engineering Development Laboratory Report No. HEDL-TME 75-15, January 1975.

7. R. L. Wine, *Statistics for Scientists and Engineers*, Prentice-Hall, Inc., Englewood Cliffs, N. J., 1964, pp. 497-572.

8. J. W. Dixon and F. J. Massey, *Introduction to Statistical Analysis*, McGraw-Hill, Inc., New York, 1956, p. 196.

9. R. T. King, et al., "Properties and Structure of 16-8-2 Stainless Steel Weld Metal," ASME Publication No. 75-PVP-45, June 1975.

10. L. D. Blackburn, "Isochronous Stress-Strain Curves for Austenitic Stainless Steels," *The Generation of Isochronous Stress-Strain Curves*, A. O. Schaefer, Ed., American Society of Mechanical Engineers, New York, 1972, pp. 14-58.

11. D. A. Woodford, "Graphical Solution of a Simple Creep Equation for IN-718," *Materials Science and Engineering*, 16, 1974, pp. 75-78.

12. C. R. Brinkman and G. E. Korth, "Strain Fatigue and Tensile Behavior of Inconel-718 from Room Temperature to 650°C," *Journal of Testing and Evaluation*, Vol. 2, No. 4, 1974.

13. "Thermal and Mechanical Treatments for Nickel and Some Nickel-Base Alloys: Effects on Mechanical Properties," National Aeronautics and Space Administration Report, NASA SP-5106, 1972.

14. H. J. Wagner, R. S. Burns, T. E. Carroll and R. C. Simon, "Nickel Base Alloys - Alloy 718," DMIC Handbook, Battelle Memorial Institute, Columbus, Ohio, 1968.

15. *Inconel Alloy 718*, Huntington Alloys, The International Nickel Company, 1968.

16. H. L. Eiselstein, "Metallurgy of a Columbian-Hardened Nickel-Chromium-Iron Alloy," *Advances in the Technology of Stainless Steels and Related Alloys*, STP No. 369, ASTM, 1965.

17. J. M. Steichen and A. L. Ward, "Effect of Strain Rate on the Tensile Properties of Irradiated Inconel-718," Hanford Engineering Development Laboratory Report, HEDL-TME 76-14, January 1976.

18. J. M. Steichen, "High Strain Rate Tensile Properties of AISI Type 304 Stainless Steel," *Journal of Engineering Materials and Technology*, Vol. 95, July 1973.

19. L. A. James, "The Effect of Temperature Upon the Fatigue-Crack Growth Behavior of Two Nickel-Base Alloys," *Journal of Engineering Materials and Technology*, Vol. 95, No. 4, pp. 254-256, 1973.

20. L. A. James, "Fatigue-Crack Propagation Behavior of Inconel 718," Report HEDL-TME 75-80, Westinghouse Hanford Company, 1975.

21. R. B. Scarlin, "Fatigue Crack Growth in a Cast Ni-Base Alloy," *Materials Science and Engineering*, Vol. 21, No. 2, pp. 139-147, 1975.

22. L. A. James, "The Effect of Temperature Upon the Fatigue-Crack Growth Behavior of Inconel X-750," HEDL-TME 76-39, Westinghouse Hanford Company, 1976.

23. L. A. James, "The Effect of Temperature Upon the Fatigue-Crack Propagation Behavior of Hastelloy X-280," HEDL-TME 76-40, Westinghouse Hanford Company, 1976.

24. J. D. Landes and J. A. Begley, "Test Results from J-Integral Studies: An Attempt to Establish a J_{Ic} Testing Procedure," ASTM STP-560, pp. 170-186, 1974.

6.0 WESTINGHOUSE ADVANCED REACTORS DIVISION

E. C. Bishop, W. E. Ray

6.1 INTRODUCTION

Two programs are being performed at Westinghouse Advanced Reactors Division (ARD). The first program is "Validation of High Temperature Design Methods and Criteria" (189a CW063). Two of the tasks in this program are "Basic Specimen Testing" and "Tubular Specimen Testing". The specimen material for both tasks was supplied from the ORNL reference heat of Type 304 stainless steel and future tests will include specimens from the reference heat of Type 316 stainless steel. The second program is "Component Materials Compatibility" (189a CW065). One of the tasks in this program is "Mechanical Properties".

The basic specimen tests are performed on plates and bars loaded at 1100°F (593°C). Specimen designs have been selected to provide nonuniform stress distributions (uniaxial, plane stress, and plane strain) and to determine the effects of holes, notches, and welds in various orientations. Uniform and stepped loading is applied at levels sufficient to cause significant creep strain in hundreds of hours and rupture in several thousand hours. Test data are used for: verification of constitutive equations for time-dependent material response, validation of analytical techniques for nonuniform stress states, and investigation of strain limits in base metal, welds, and at geometrical discontinuities.

The tubular specimen tests are being run at 1100°F (593°C) with various combinations of internal pressure and axial load to produce a uniform stress state with a range of biaxiality. Load levels have been selected to determine secondary creep rates in 2000 hours with both steady state and step loading. A limited number of tests will be continued to rupture with geometrical discontinuities. The test data are primarily used for verification of constitutive equations and validation of analytical techniques for shells under multiaxial states of stress.

Westinghouse ARD is performing experiments to identify the effects of a flowing sodium environment on the mechanical properties of LMFBR

structural components. The present scope of the program involves three materials: Type 316 Stainless Steel Type 304 Stainless Steel, and Inconel 718. Work on these materials is in support of the CRBRP upper plenum and hot leg piping components design. Inconel 718 is also being evaluated on a limited basis, relative to the thermal transients to be experienced by the thermal baffles in the upper plenum of the FFTF reactor. More extensive evaluations in the material for the CRBRP will follow. Low-cycle fatigue, creep-fatigue, and creep-rupture experiments are being performed in flowing sodium at elevated temperatures on as-fabricated, aged, and sodium pre-exposed samples in order to identify the environmental effects. In addition, in-air experiments are being performed on the same materials to obtain baseline data.

This report covers the work performed during the period from November 1, 1975 to January 31, 1976.

6.2 BASIC SPECIMEN TESTING - M. J. Manjoine (Westinghouse Research Laboratories)

6.2.1 Type 304 Stainless Steel Tests in Progress

6.2.1.1 BTW-2, Transverse Weld in B-Type Plate Model at 19 ksi (131 MPa) and 1100°F(593°C)

At 7337 hours, the accumulated strain is 1.26% and the creep rate is 7×10^{-5}%/h and is still decreasing. The rupture life is estimated to be the same as that of the base metal which is about 9000 hours. No HAZ cracking was evident at the inspection at 6500 hours. The test will be interrupted at 8000 hours for another inspection to determine crack initiation.

6.2.1.2 BAW-2, Axial Weld in B-Type Plate Model at 22 ksi (151.7 MPa)

The first inspection of the weld was made at 1509 hours. The average overall strain was 5% and the average overall creep rate was 2.6×10^{-3}%/h. The estimated minimum creep rate for the base metal at 22 ksi is the same. The inspection revealed that cracks had initiated over the middle 0.6 in. of the gage section. The estimated strain in this region is 6.8%.

The data presented later in this report for the GAW-1 model indicates that the cracking can initiate at a strain of about 4%.

At 2321 hours, the average overall creepation has reached 7% and the average creep rate has continued at 2.5×10^{-3}%/h in spite of the growing cracks.

6.2.1.3 C-4, Plate Model with Central Hole at a Net Section Stress of 18 ksi (124.1 MPa) at 1100°F (593°C)

Due to the low proportional limit of this annealed T304SS and the stress concentration at the holes, yielding initiated at about 8000 psi (55 MPa). The overall plastic deflection was 49.6×10^{-3} in. on loading. At 1030 hours, the test was interrupted for photographic measurement. The overall plastic deflection was 87.4×10^{-3} in. The permanent strain across the hole was 10%.

6.2.2 Type 316 Stainless Steel Specimen Preparation

The type A specimens of the reference heat #8092297, type 316 Stainless Steel, were rough machined to within 0.005 in. and annealed. After finish machining the Vickers hardness (VH) of the gage section was measured[1] for different loads. Table 6.1 gives the hardness (HV), the depth of penetration (h) for the different loads and the history of heat treatments. The data shows that even for finish machining after heat treatment, the surface hardness is increased for a depth of 0.162 mm which is nearly equivalent to the thickness of the metal removed. After reheat treatment, the hardness was uniform with depth of hardness penetration. Other test specimens will be heat treated after final machining.

TABLE 6.1

HARDNESS OF SPECIMEN 6A1

Load	Rough Machined, Heat Treated* and Finished Machined		Re-heat Treated	
Kg	Hardness HV	Penetration Depth h,mm	Hardness HV	Pentration Depth h,mm
5	203	0.043	130	0.054
10	178	0.065	133	0.076
20	158	0.097		
50	145	0.162	130	0.071

6.2.3 Type 316 Stainless Steel Tests in Progress

Tests have been completed on 6D1, a notched bar at 35ksi (241MPa) and 1100°F (593°C). This specimen failed at 335 hours which compares to an estimated 100 hours for notched type 304 Stainless Steel. The next test will be started at 28 ksi (192.8 MPa).

6.2.4 Strain Distributions for GAW-1, Central Axial Weld in Type G Model of Type 304 Stainless Steel at 23 ksi (159 MPa) at 1100°F (593°C)

6.2.4.1 Materials, Test Model and Instrumentation

The test model was formed by welding two plates of annealed type 304 Stainless Steel from heat number 9T2796 with type 309 Stainless Steel weld metal with controlled residual elements.(2) Plates of 1/2 in. (12.7 mm) thickness were separated with a gap which was filled with weld metal. The welded assembly was machined to a thickness of 1/3 in. (8.5 mm). A test model with a uniform straight section, fillets and heads was prepared with a square photo grid of 30 divisions to an inch (about 1.3 mm squares).(3) Extension pieces were welded to each side of the head and at each end to apply the axial load and reinforce the heads. The central axial weld was positioned on the load axis.

*1950°F (1065°C) for 1/2 hr then fast cooled.

A photograph of the gage section, Fig. 6.1,[4] shows the reduced test section. The uniform section length was 0.83 in. (21 mm) long by 3.33 in. (85 mm) wide with a 3/8 in. (9.5 mm) radius at the fillet to the 4 in. (102 mm) wide head. The total reduced section was 1.5 in. (38 mm) long. The type 304 SS extension pieces, 1/3" thick (8.5 mm), on each face were welded at the edges to provide lateral constraint and at two symmetrical pockets to obtain a more uniform axial loading at the gage section but minimizing any thickness restraint.

The dummy blocks located between the fillets, Fig. 6.1, have the same square grid and are used to obtain the scale factor for photographs taken during the creep test. In the recording procedure, the model is unloaded, cooled and the furnace is removed to make the photographs.

6.2.4.2 Test Results

6.2.4.2.1 Comparison of Strain Measurements up to 188 Hours At the initial loading, the strain gages and clip gages indicate that the proportional limit of this composite of weld and base metal in parallel is 12,400 psi (85.7 MPa). The plastic or inelastic strains at 23 ksi (159 m Pa) were 0.048% at the weld centerline (SG 22) and 0.077% for the base metal (SG 25). The inelastic overall deflections were 0.0003 in. (7.6 μm) for clip gage CG1 and 0.0013 in. (32 μm) for clip gage CG2. The latter indicates an initial bending or misalignment of the extensometer parts which corrected itself after the yielding. The inelastic readings of these gages during the first 188 hours of creep testing are compared in Fig. 6.2 with the permanent strains measured from the grid at the end of this period.

The plastic flow and creep resistance of the weld is higher than that of the base metal[2] and this is reflected in the loading and creep strains recorded by the strain gages. Since the weld metal and base metal are in parallel and the heads are reinforced beyond the gage section, the overall deflections of each must be nearly the same across the heads.

A comparison of the other strain gage measurements during the first 188 hours is also presented in Fig. 6.2. The clip gages measure over a longer gage length than that of the weldable strain gages. The

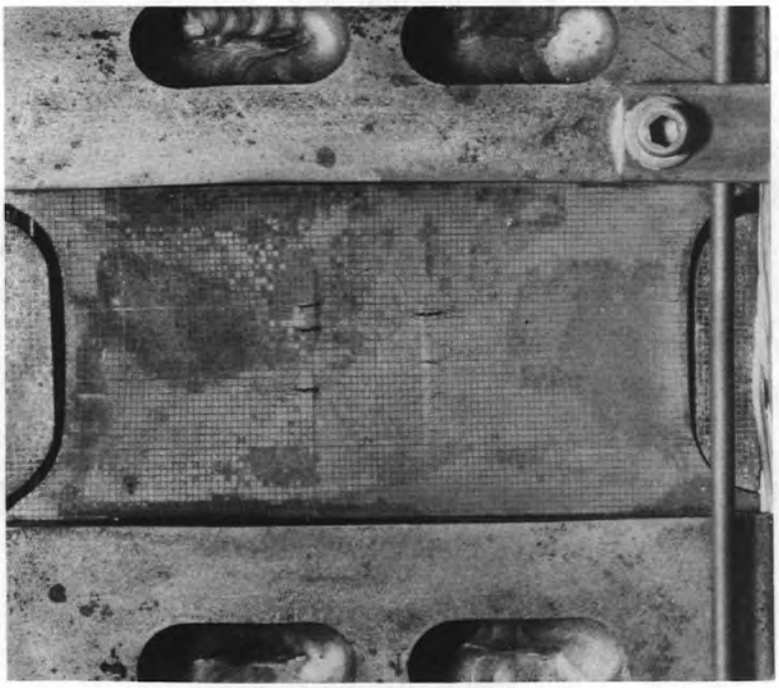

(a) Cracking at Heat Affected Zones

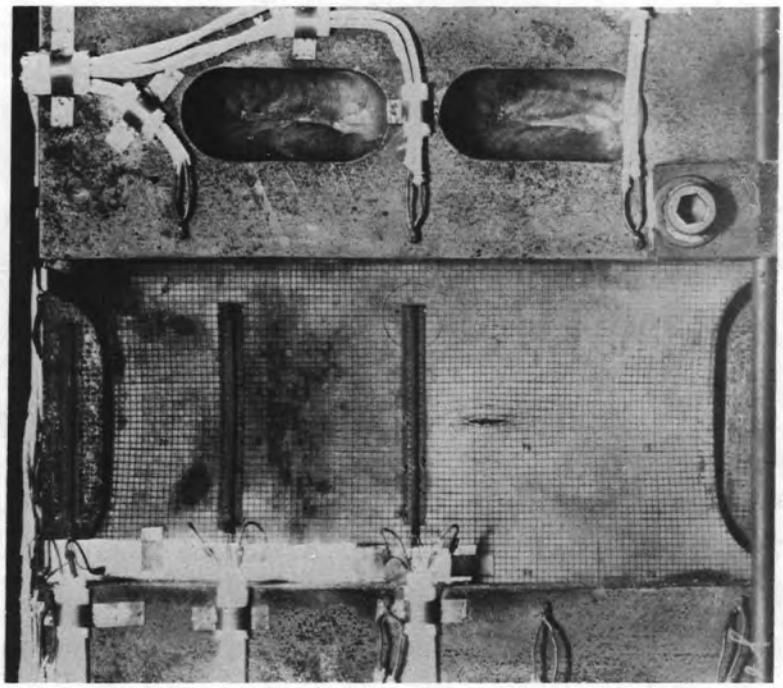

(b) Opposite Side, Instrumentation and Cracking

Figure 6.1. GAW-1 Specimen with Axial Weld After 2886 Hours at 23 KSI (159 MPa) and 1100°F (593°C)

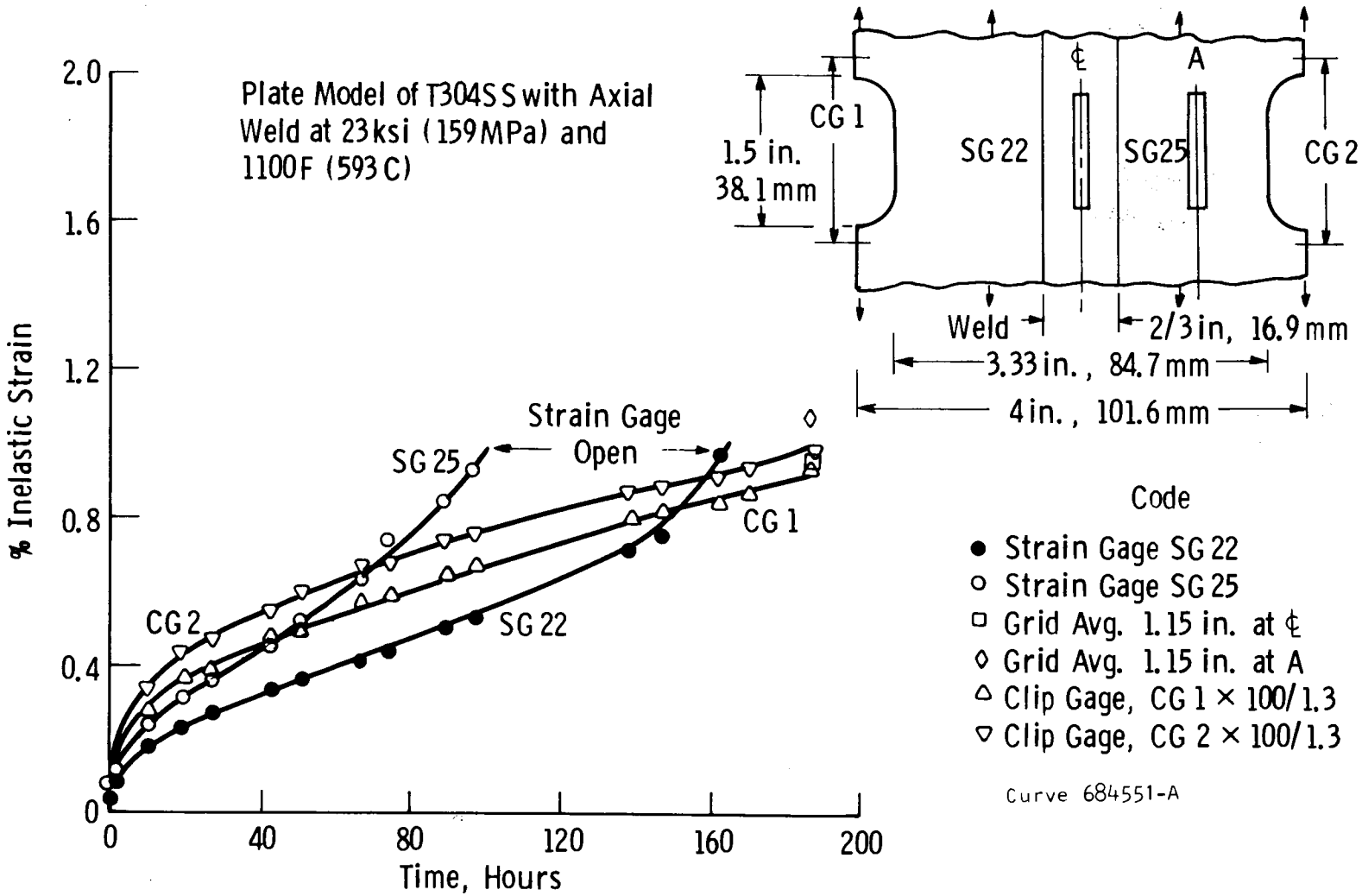

Figure 6.2. Comparison of Strain Measurements up to 188 Hours, Model GAW-1

deflections measured by the clip gages were, therefore, divided by 1.3 in. (33 mm) to obtain a "comparable" strain. The grid measurements and strain calculations were made for the same gage length as that of the weldable strain gages, 1.15 in. (29.2 mm).

Both weldable strain gages started to fail after about 0.7% inelastic strain or about 0.82% total strain. The strain at the centerline of the weld, SG 22, is less than that in the base metal, SG 25, and its creep rate is about the same as that from the clip gages, Fig. 6.2. An extrapolation of SG 22 to 188 hours is nearly the same as that obtained from the grid measurements. The grid measurement at 188 hours for the same location in the base metal as SG 25, A in Fig. 6.2, is about 0.12% strain higher than that at the centerline of the weld. Although the strains from clip gage 2 are slightly higher than those from CG1, the creep curves become parallel after about 40 hours. It is concluded that the initial bending or misalignment of the extensometer rods is corrected by the inelastic strains during this early period.

6.2.3.2.2 Axial Strain Distributions at the Centerline of the Weld. From the photographs of the grid taken at 188 hours and at about 400 hour intervals up to fracture, strain measurements were made along the axial centerline of the welds for every 5 divisions of the grid. The axial strain distributions at the center of the weld are illustrated in Fig. 6.3 for the given creep times. The axial strain is practically zero at the reinforced head where the area is four times that of the uniform section. The strain increases toward mid-length of the uniform section as the constraint of the head diminishes. With increasing creep time, the strain increases for positions along the reduced section. The strain gradient also increases as the effect of the constraint increases with inelastic straining.

The extent of cracking in the heat affected zone is indicated on the curves and this data will be discussed later.

The peak strains from the grid measurements, open circles in Fig. 6.4, are plotted as a function of creep time. The average of the overall creep deflections from the clip gages has been converted to strain assuming a one inch (25.4 mm) gage length which gives a strain comparable to the

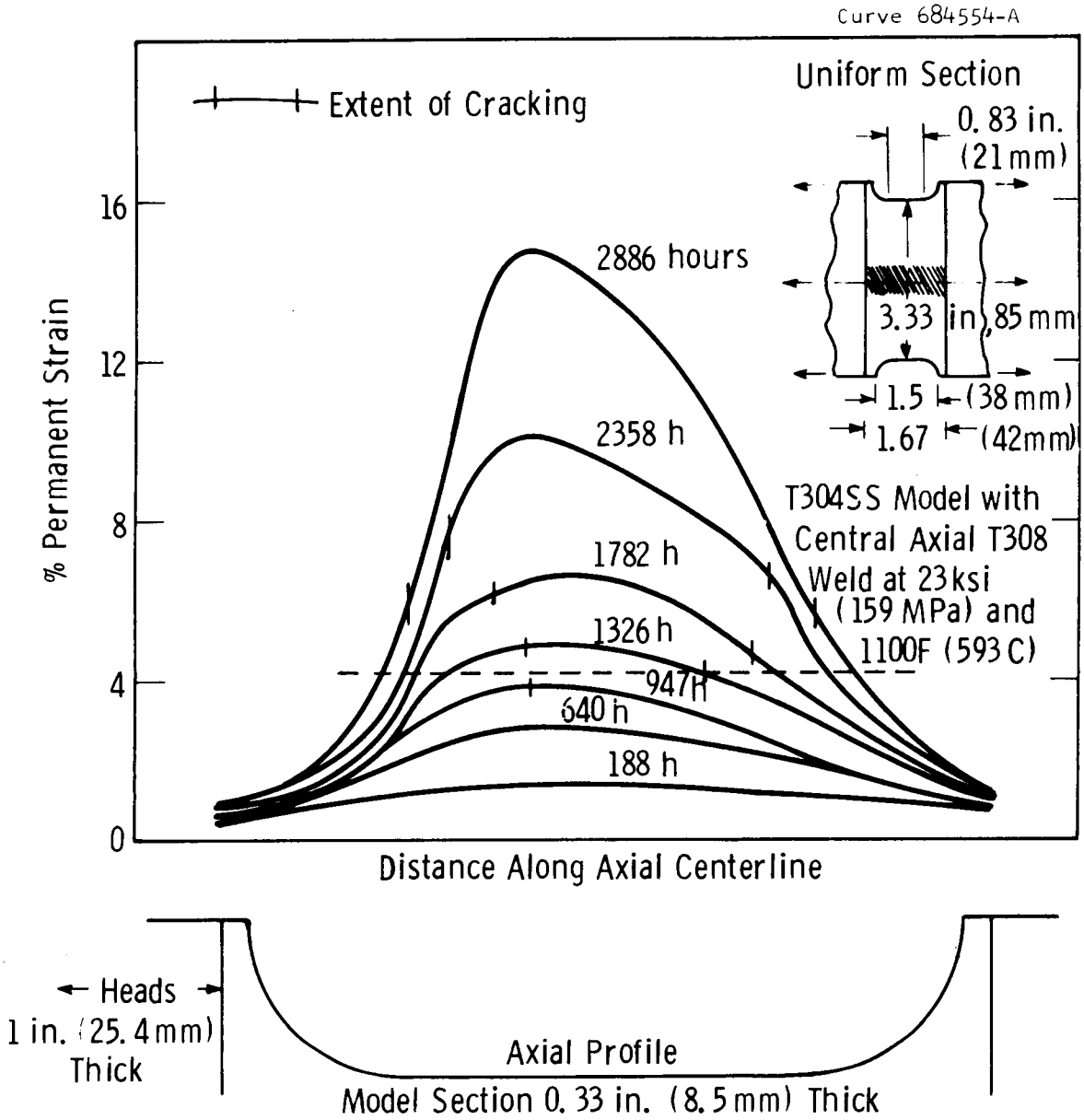

Figure 6.3. Axial Strain Distribution Along Centerline of Weld From Grid Measurements, Model GAW-1

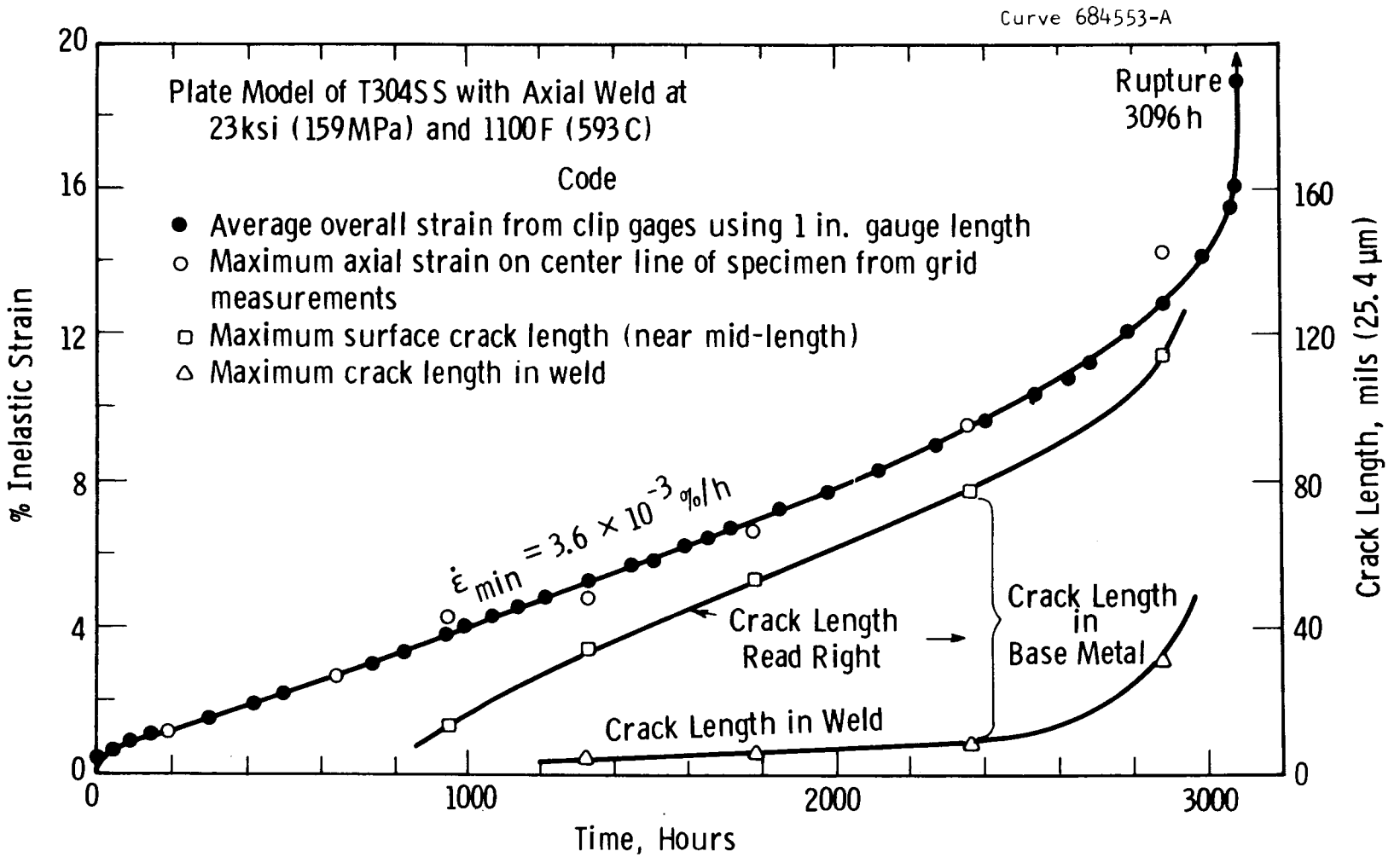

Figure 6.4. Maximum Creep Strains and Crack Lengths Curves, Model GAW-1

maximum at the centerline of the weld. These data give a continuous curve and the trend can be compared with the maximum strains measured from the grid, Fig. 6.4. It can be seen that the agreement is good, the deviation over most of the curve is less than about 1/2% strain.

6.2.3.2.3 Axial Strain Profiles. The axial strain also varies across the width of the reduced section as well as along the length. Since the specimen is symmetrical about the mid-length of the reduced section, the readings from the grid are averaged for similar positions at each end and are plotted in Fig. 6.5 for the time of 1782 hours. At this time, the overall creep rate is still at its minimum for the constant loading but is approaching the instability of the third stage of creep or the increasing creep rate region.

Near the heads, positions 1 and 9 in Fig. 6.5a, the strains are lowest and increase slightly from each side to the centerline. Near the fillets, positions 2 and 8, the strains are highest at the fillets and decrease toward the center. At positions 3 and 7 in the uniform width section, the strain is high at the edges near the fillets and decreases toward the heat affected zone, HAZ, with a local maximum at the center of the weld. Cracking has initiated at the HAZ. For positions 4-6, the strain is nearly uniform across the width. The strain at the left HAZ, Fig. 6.5a, is higher than that at the right because of a large crack at the left, Fig. 6.1a. At mid-length, position 5, the strain increases from the edges to the weld. Since a larger crack is at the right HAZ, Fig. 6.1a, the measured strain is higher than on the left side.

The axial strain as averaged across the width at a given axial length position is given in Fig. 6.5b. The axial permanent strains are essentially zero at the reinforced heads, increase nearly linearly toward mid-length and have two local maximums at the central cracks. The average strain is 5.6 $\pm$ 0.4% for the middle half of the uniform section length.

At 2886 hours (near rupture), Fig. 6.4, long cracks are present near the heat affected zones, Fig. 6.1, so that the strain profiles are becoming distorted near the weld. The lateral strains were measured for each 5 grid divisions across the width at five length positions as

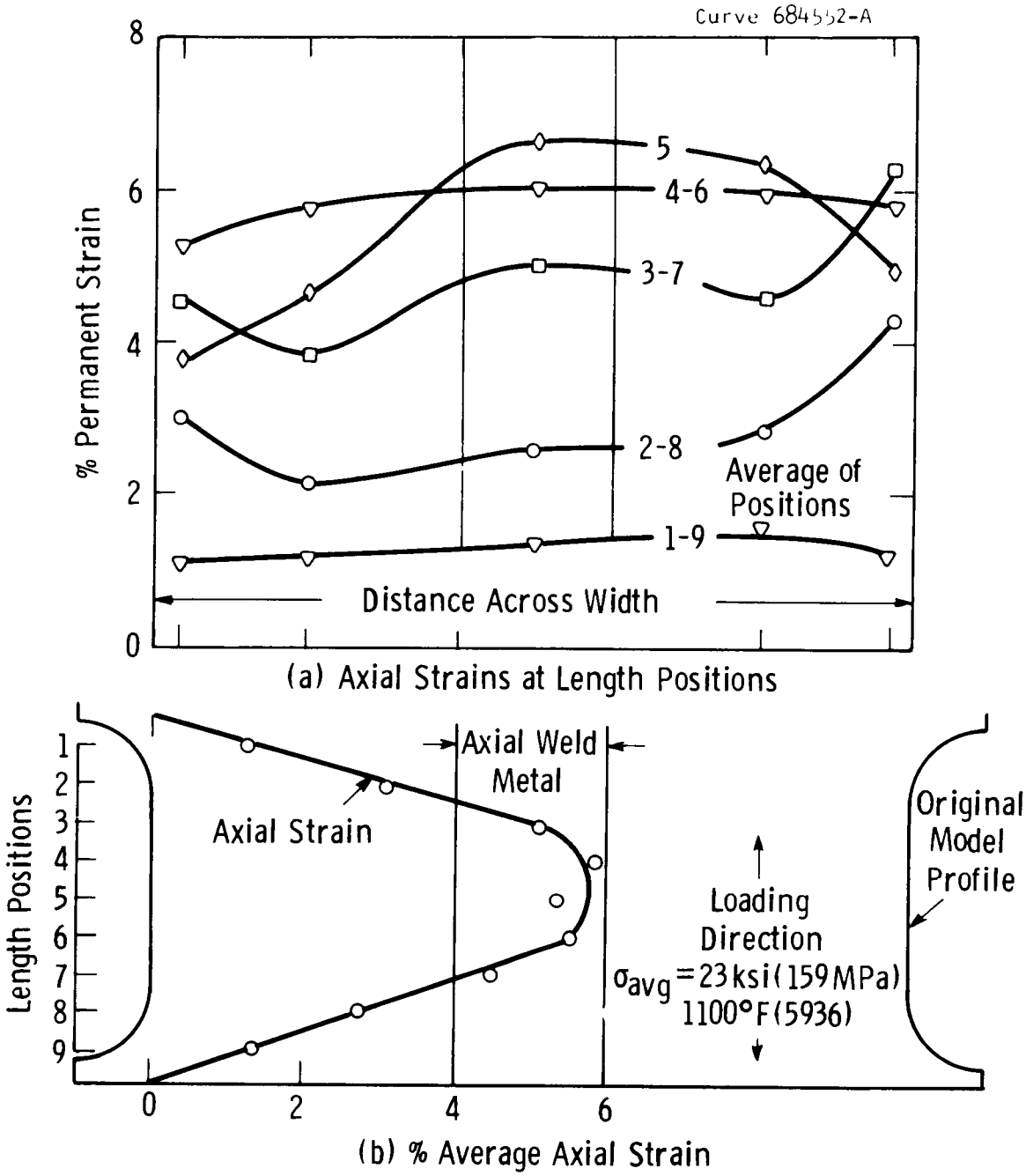

Figure 6.5. Axial Strain Profiles at 1782 Hours From Grid Measurements, Model GAW-1

shown in Fig. 6.6. Near the heads where the lateral constraint is a maximum, the lateral strain (curve a Fig. 6.6-1) is negative and the magnitude decreases from the edges to the centerline and the average strain across the width is only -0.15%, Fig. 6.6-2. Near the middle of the fillet, curve e Fig. 6.6-1, the strains also decrease in magnitude from the edge to the centerline and the average is only -0.65%, Fig. 6.6-2. At the end of the uniform width near the fillet, curve b Fig. 6.6-1, the strains are about -3% at the edges and decrease in magnitude to about -1/% at the centerline.

Near mid-length where the cracks are long, the strain profiles, curves c and d Fig. 6.6-1, show that the lateral strains decrease to a minimum at the heat affected zone, with a local maximum at the center of the weld. The averages of the lateral strain across the width, Fig. 6.6-2, is practically zero at the reinforced heads and increases in magnitude toward mid-length to a peak of about -2.5%.

For comparison, the axial strains were measured for five width positions at the same time of 2886 hours, Fig. 6.7. No discontinuities are shown at the heat affected zones since measurements were not made at these width positions. The axial strain profiles are averaged for similar length positions from each head. Near the fillets, curves 2-8 and 3-7 Fig. 6.7a, the axial strains are highest at the edges because of the strain concentration of the geometry and decrease for positions towards the centerline. Near mid-length, the axial strain increases from the edges to a maximum at the centerline, curves 4-6 and 5 Fig. 6.7a. The average strains across the width, Fig. 6.7b show the steep increase from the heads to mid-length and the similar behavior for each end.

6.2.3.2.4 Crack Initiation and Growth. In Fig. 6.1a, five major cracks are evident. From the grid, the axial location of each crack can be recorded and by checking at these locations in photographs taken earlier in life, the initiation and growth can be followed. The first surface crack to be visible in the photographs is the upper one to the right of the ellipitcal grid marker. This marker was originally a circle with a diameter equal ot the plate thickness which is about half the width of the weld. Normally, this circle is centered in both directions

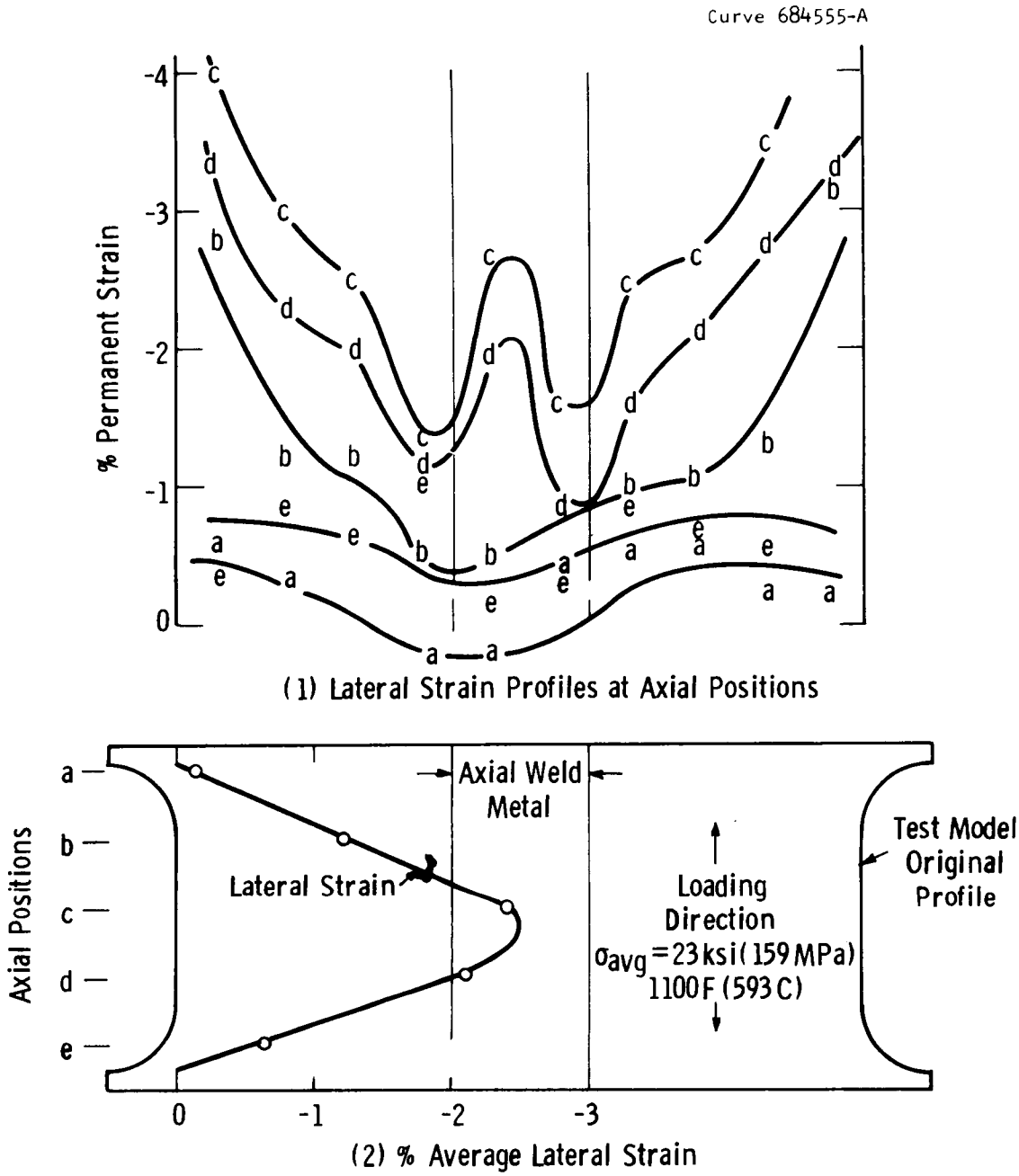

Figure 6.6. Lateral Strain Profiles at 2886 Hours From Grid Measurements, Model GAW-1

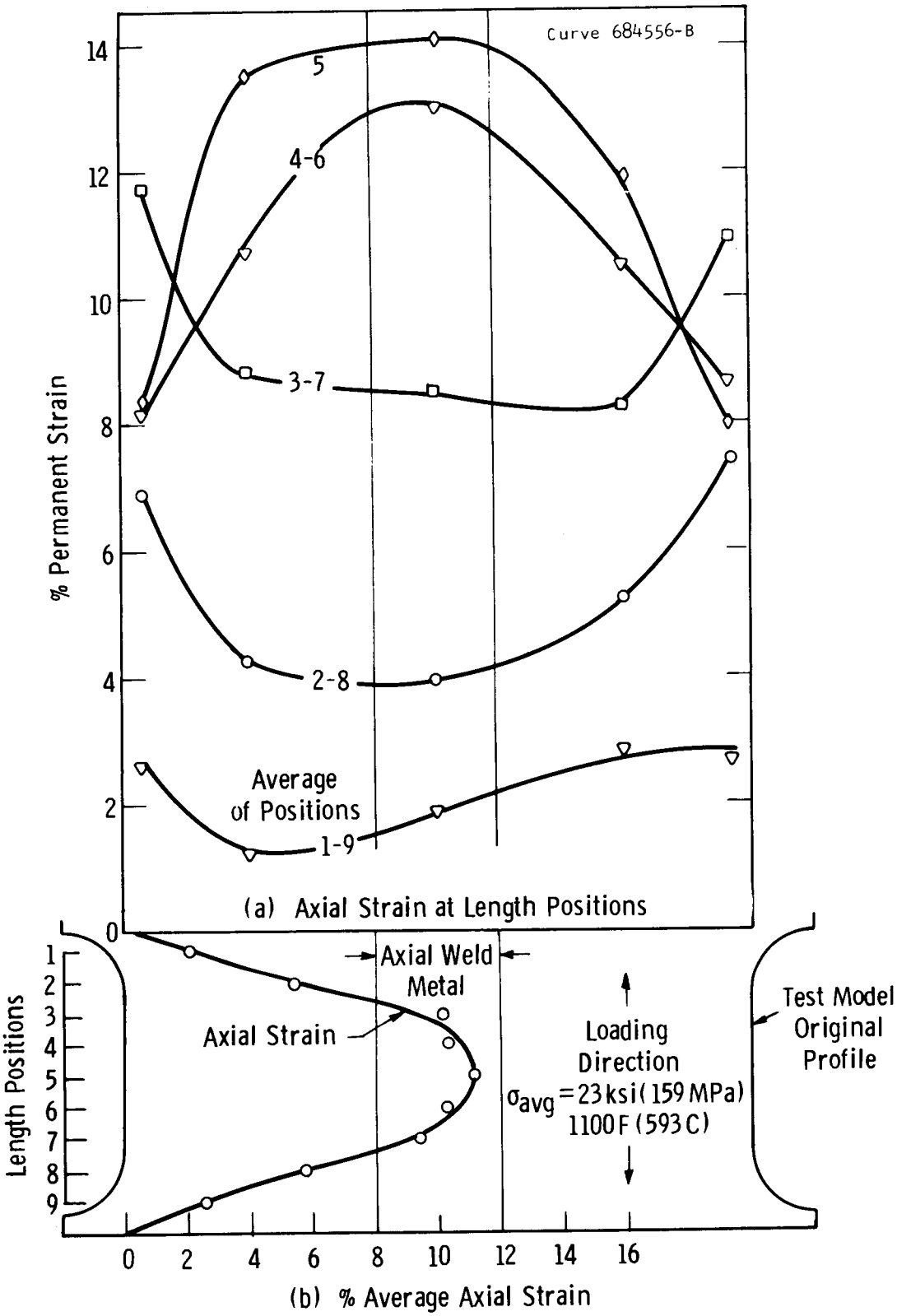

Figure 6.7. Axial Strain Profiles at 2886 Hours From Grid Measurements, Model GAW-1

of the gage section but in this case is only centered on the axial centerline and at a different axial position on opposite faces. The first crack to penetrate the opposite surface, Fig. 6.1b, is the middle crack on the left side of Fig. 6.1a which is about mid-length of the gage section.

An inspection of all photographs indicates that the cracks initiate at the heat affected zone and grow across the width in a direction perpendicular to that of the maximum principal stress and to that of the axial weld. The cracks have a regular spacing in the axial direction since the crack relieves the stress for an axial distance which is a function of the creep strain. The axial extent of the cracking is indicated on the curves in Fig. 6.3; the higher the peak strain the greater is the extent.

The surface length of the first crack, identified above, is plotted in Fig. 6.4 as a function of time, the scale for crack length is on the right ordinate. This crack grew primarily in the base metal at nearly a constant rate similar to the overall creep rate. The creep rate and the crack growth rate increased rapidly when this crack reached a length of about 0.070 in. (1.8 mm).

6.2.4.3 Discussion of Results

Under constant load, the damage mechanism proposed for this composite model is an exhaustion of ductility which will be different for the various zones. This ductility is also a function of the strain rate and the state of stress.[5,6] For the relatively low strain rate of the creep test described here, it is proposed that the creep strain is higher in the grain boundary and damage is accumulated fastest at grain boundaries orientated perpendicular to the direction of the maximum principal stress. The accumulation of voids or separation of grain boundaries relieves the local strain field.

The grain boundary separation and the adjacent grains form a "cell" and additional voids are impeded for a distance of several grains. With continued creep strain, adjacent cells link up in the direction perpendicular to that of the maximum principal stress to form a crack. Fig. 6.1 illustrates that the cracks at the heat affected zones (HAZ) follow a

similar process. The initial crack formed when the local strain at the HAZ near mid-length reached a strain limit of about 4%. With continued creep strain, this magnitude of strain spread along the length and additional cracks formed at regular intervals. The extent of cracking shown in Fig. 6.3 illustrates this strain limit mechanism.

The overall creep rate remained constant during the crack initiation and cracking pattern formation. The crack growth rate into the weld metal was much slower than that in the base metal, Fig. 6.4, and the more ductile weld impeded the linking of cracks on its opposite sides. However, when the cracks grew to a critical length they began to interact as the net section stress increased. This caused an increase in overall creep rate and a more rapid crack growth rate. Fig. 6.3 shows that the cracking pattern continued to grow after the instability, since the creep continued to spread along the gage length.

The constraints at the heads generate triaxial stress. The high reinforcement in the width direction causes a lateral stress which is a maximum at the heads and diminishes toward mid-length of the gage section. The lateral stress increases with increase in axial plastic strain and its effect can be seen in the lateral and axial strain profiles of Figs. 6.6 and 6.7, respectively, at a creep time of 2886 hours. The average lateral strain at the far end of the fillet near the head is only 0.15% or about 13% of the magnitude of the average axial strain. At the end of the uniform section and at the centerline, the average lateral strains are about 1.1 and 2.5% or about 16% or 23% of the magnitude of the average axial strains, respectively.

No direct comparison of the strain profiles from the grid are possible with the other types of strain measurements but the average overall strain measurements were within 1/2% strain of the trend from the clip gages, Fig. 6.4.

6.2.4.4 Conclusions

The strain distribution in a structure or a model containing welds is greatly influenced by the constraint of the geometry and the metallurgical state of the materials in the composite. The photogrid method

of measuring strains is presented as a useful tool for surfaces where the grid can be practically applied and measured. The data for a flat plate of type 304 stainless steel with a central axial type 308 weld illustrate that this method can be used at 1100°F (593°C) with reasonable accuracy when the peak strains are over 1%. Other measurements have been made after testing for over 10,000 hours.

At 2886 hours of creep time for this weldment model with a high degree of plane strain, the axial strain varies from near zero at the constrained ends to over 14% at mid-length, at the center of the section containing the weld.

The comparison of the measurements of the overall strains from the grid with trends of strain gages and overall extensometer within the accuracy of the measurements.

A damage mechanism based on the exhaustion of ductility was correlated with initiation of cracking in the heat affected zones of the weld and regions where the maximum strain exceeded about 4%. The cracks grow in a direction perpendicular to that of the maximum principal stress and initiate at regular axial spacing in the heat affected zones of the weld.

6.3 TUBULAR SPECIMEN TESTING - K. C. Thomas, P. C. S. Wu, C. Daniels

6.3.1 Type 304 Stainless Steel Testing

The current test matrix for testing of Type 304 SS tubular creep specimens is shown in Table 6.2. All of these tests have now been completed. In addition to the nominal test duration of 2000 hours, specimen from tests numbers 14, 16, and 18 are being tested to failure. Most of the Type 304 SS tubular creep specimens have been examined metallographically for final grain size and crack characterization. Microhardness testing was also performed. The results are shown on Table 6.3. The microstructure of the specimens is very similar and displays intergranular cracking only along the outside surface. This microstructure similarity was shown for both post-creep and post-rupture specimens. The specimen was considered to be ruptured in the multiaxial

TABLE 6.2 TEST MATRIX FOR TYPE 304 STAINLESS STEEL TUBULAR SPECIMENS

Test Number	Effective Stress σ_e (psi)	Stress Ratio hoop/axial (σ_θ/σ_z)	Int. Pressure P (psi)	Axial Load L (lb)	Nominal Test Temperature T (°F)	Nominal Test Duration t (hr)	Wall Thickness (mils)
			I - Uniaxial Constant Load Specimens				
1A	25,000	0	0	6872.2	1100	100	50
1B	25,000	0	0	6872.2	1100	100	50
2A	10,000	0	0	5340.1	1100	2000	100
2B	10,000	0	0	5340.1	1100	2000	100 (a)
3A	20,000	0	0	10681.4	1100	2000	100
3B	20,000	0	0	10681.4	1100	2000	100
3C	7,700	0	0	4112.3	1100	2000	100
3D	5,000	0	0	2670.4	1100	2000	100
			II - Multiaxial Specimens				
4	10,000	2.0	1209.5	323.0	1100	2000	100 (b)
5	15,000	2.0	1814.3	484.0	1100	2000	100 (b)
6	20,000	2.0	2716.9	0.0	1100	2000	100 (c)
7	10,000	1.5	1180.0	1211.0	1100	2000	100 (b)
8	15,000	1.5	2000.0	1515.0	1100	2000	100 (c)
9	20,000	1.5	2668.4	2018.6	1100	2000	100 (c)
10	10,000	1.0	1049.4	2670.0	1100	2000	100 (b)
11	15,000	1.0	1574.0	4005.0	1100	2000	100 (b)
12	20,000	1.0	2353.0	5340.7	1100	2000	100 (c)
13	10,000	1.5	612.9	436.8	1100	1100	50
13 (cont.)	15,000	1.5	1030.8	734.7	1100	500	50
13 (cont.)	20,000	1.5	1374.4	979.6	1100	200	50
13 (cont.)	20,000	1.0	1212.1	2591.8	1100	200	50
14	15,000	2.0	930.3	0.0	1100	500	50 (c)
14 (cont.)	15,000	1.5	1030.8	734.7	1100	500	50
14 (cont.)	15,000	1.0	832.5	1780.0	1100	500	50
14 (cont.)	15,000	2.0	930.3	0.0	1100	500	50
15	10,000	2.0	620.2	0.0	1100	1150	50
15 (cont.)	15,000	1.5	1030.8	734.7	1100	500	50

TABLE 6.2 (Continued)

Test Number	Effective Stress σ_e (psi)	Stress Ratio hoop/axial (σ_θ/σ_z)	Int. Pressure P (psi)	Axial Load L (lb)	Nominal Test Temperature T (°F)	Nominal Test Duration t (hr)	Wall Thickness (mils)
15 (cont.)	20,000	1.0	1212.1	2591.8	1100	200	50
15 (cont.)	15,000	2.0	930.3	0.0	1100	200	50
16	12,500	1.0	757.6	1619.9	1100	2000	50
17	12,500	2.0	874.8	0.0	1100	700	50 (c)
17 (cont.)	12,500	1.0	757.6	1619.9	1100	700	50
17 (cont.)	12,500	1.0	832.5	1780.0	1100	500	50
17 (cont.)	20,000	1.0	1212.1	2591.8	1100	100	50
18	12,500	2.0	874.8	0.0	1100	2000	50

(a) Effective stress calculated by:

$$\sigma_e = \sigma_z = \frac{L}{\pi r_{av} t}$$

where: r_{av} = Average radius of the tube wall

t = Thickness of the tube

(b) Effective stress Calculated as per thick cylinder formula by:

$$\sigma_e = \frac{1}{\sqrt{2}} [(\sigma_z - \sigma_\theta)^2 + (\sigma_\theta - \sigma_r)^2 + (\sigma_r - \sigma_z)^2]^{1/2}$$

where: $\sigma_z = \sigma_{axial} = \frac{L}{A} + p \frac{a^2}{b^2 - a^2}$

$$\sigma_\theta = \sigma_{hoop} = p \frac{a^2(b^2 + r^2)}{r^2(b^2 - a^2)}$$

$$\sigma_r = \sigma_{radial} = p \frac{a^2(b^2 - r^2)}{r^2(b^2 - a^2)}$$

(c) Effective stress calculated as per thin cylinder formula by:

$$\sigma_e = [\sigma_\theta^2 + \sigma_z^2 - \sigma_\theta \sigma_z]^{1/2}$$

where: $\sigma_\theta = p \frac{r_{av}}{t}$

$$\sigma_z = \frac{p r_{av}}{2t} + \frac{L}{2\pi r_{av} t}$$

r_{av} = Average radius of the tube

t = Thickness of the tube wall

A = Cross-sectional area of the tube
t = Wall thickness of the tube
a = Inside radius of the tube
b = Outside radius of the tube
r = Radius at the point under consideration
r = a, is used to calculate the maximum σ_e which occurs at the inside fiber of the tube
p = Internal pressure
L = Axial load

TABLE 6.3 A TABLE OF POST TEST GRAIN SIZE AND MICROHARDNESS

TEST NO.	POST TEST GRAIN SIZE (ASTM)	POST TEST HARDNESS $VDPH_{200}$
Uniaxial		
1A	4	125
1B	4	143
2A	2	152
2B	2	153
3A	4	149
3B		
3C	5 with some 2	143
3D		
3F		
Multiaxial		
4	3	125
5	2	141
6		
7	3	140
8	4	150
9	5	148
9A		
10	2	151
11		
12		
13	4	144
14		
14A	1	156
15		
16	2	139
17		
18		

case when the pressure leaked at a rate of 1 psi/min. or greater. This failure criterion resulted in specimens which showed no visible cracks. The only microstructural variation was in multiaxial samples which had cracking to a maximum of one grain depth, whereas uniaxial samples showed cracks up to two grains in depth. The grain size varies from ASTM 1 to 5 and does not seem to correlate with hardness. With few exceptions, the post test Vickers Diamond Pyramid Hardness (load 200 gm) falls between 140 and 150. The exceptions to this are tests 1A and 4. Test 1A was overheated during testing. Test 4 suffered no temperature overshoot during the test, so the low hardness value may be the result of the annealing treatment.

6.3.2 Type 304 Stainless Steel Data Correction

In previously reported data, corrections were not made as to the variation of stress σ, with differences in means of calculating test conditions. The first set of tests were carried out considering the thick wall formula. On examining the behavior the thin wall formula was considered more appropriate. As can be seen from Table 6.2, test numbers 4, 5, 7, 10 and 11 were conducted under conditions calculated from the thick wall formula. In order to compare these five tests to the others in this series, a recalculation of the effective stress was necessary. Table 6.4 lists the effective stress calculated by both equations for tests #4 through 12. The values are based on the equations given in Table 6.2. These equations would not generally give rise to such a large difference; however, the thick wall formula was used to calculate the effective stress at the inside surface of the tube wall, but the thin wall formula assumes a mid wall value.

In addition to corrections of equivalent stress, corrections have been made to compensate for faulty responses of one or more extensometers during creep testing. Three circumferential and two axial readings are taken for each test. Like readings are compared as well as diametral to axial measurements. In all Type 304 SS creep testing the axial readings are reproducible, and show only scatter

TABLE 6.4 COMPARISON OF EFFECTIVE STRESSES

TEST NO.	EFFECTIVE STRESS THICK WALL FORMULA	EFFECTIVE STRESS THIN WALL FORMULA
4	10,000 psi	8,920 psi
5	15,000	13,400
6	22,421	20,000
7	10,000	8,980
8	16,747	15,000
9	22,942	20,000
10	10,000	9,200
11	15,000	13,800
12	19,706	20,000

of the order of .05% strain. The axial readings are very reliable, possibly because the extensometers were further removed from the furnace than the diametral extensometers. Close proximity of diametral extensometers to the furnace causes heat up of the transducers and linear bearing guides. The linear bearing casing is especially affected by heating and probably causes sticking. Besides having better absolute response, the axial strain measurements are based on five times the gage length of diametral gages. The diametral measurements have varying degrees and types of response problems. These are found to be of three basic types related mainly to the effect of heat up on particular types of linear bearings used. When one of these questionable responses is noted, by comparison with the axial readings, the data from that gage is eliminated or corrected.

To compensate for the three types of response problems, three types of data corrections are made. First of all, if the readings of one extensometer clearly indicated sticking throughout the test, these readings are eliminated from averaging of the data. This type of response problem has come about primarily in low stress tests. It generally appears as a constant reading with time while the other two readings increase uniformly relative to each other, and is fairly obvious. The second and most common type of error is evidenced by short term sticking. To correct this, 0.0008 inches is usually added to the readings for the duration of the sticking. The amount added is the estimated frictional drag experienced by the extensometer due to the sliding of the inside rod through the outside tube. This second type of error is most often found when the strain is changing from primary creep to secondary creep. The size of the addition to the data is a characteristic of the extensometer used for measurement and strain independent. Because the error is strain independent, it was most noticeable at low strains. A sketch of the three types of responses can be seen in Figure 6.8. Lastly, an amount is subtracted when the readings jumped above the expected value. This is an unusual type of error which is due to a spring slipping out of position in the extensometer.

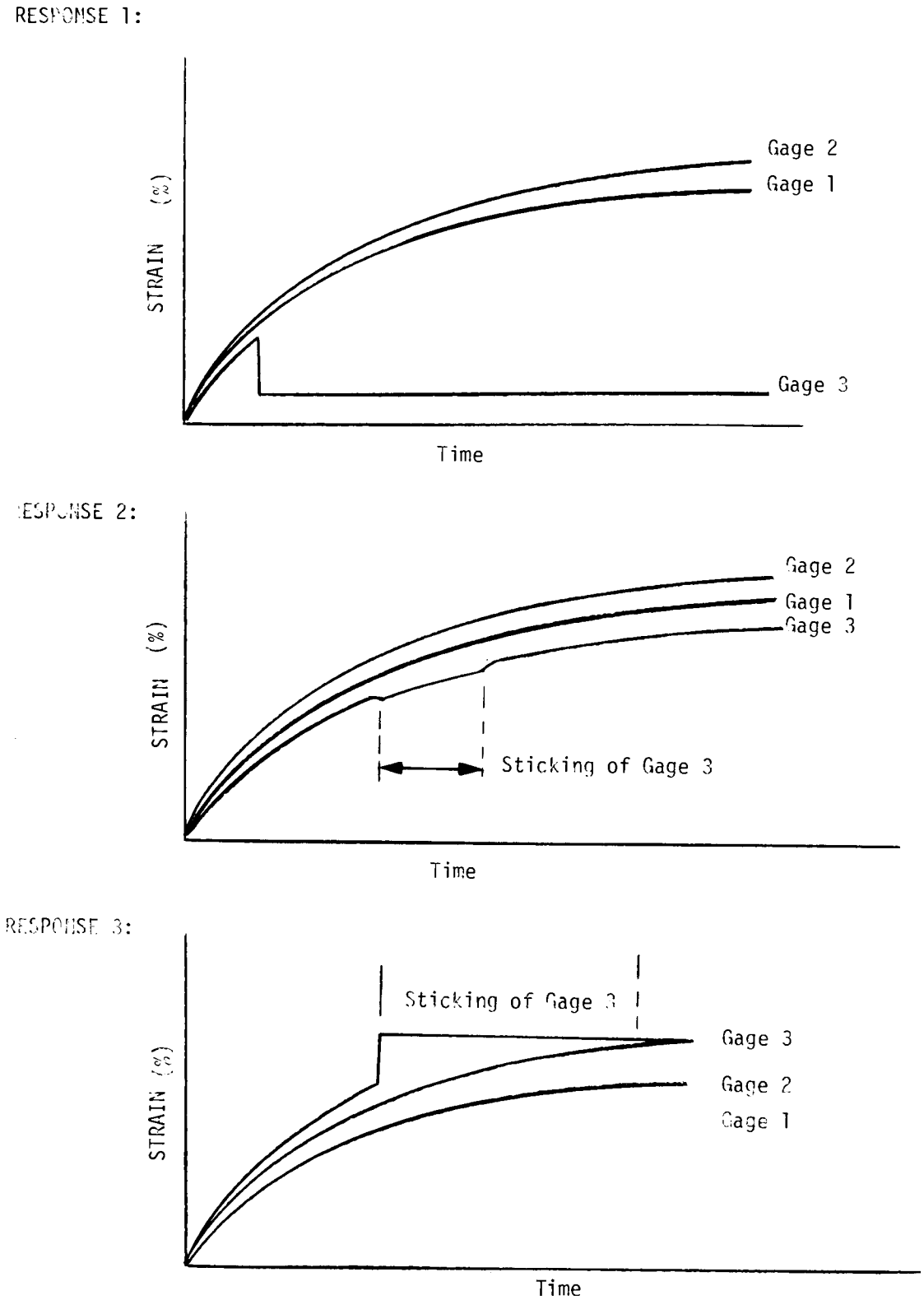

Figure 6.8. Examples of Diametral Extensometer Response

The extensometers are being modified to reduce and/or eliminate these sources of error. In addition, now that the problem has been identified, any necessary corrections can be made during the testing to limit the faulty response to only a few readings. This on-line correction of response has been very effective with recent Type 304 SS tests.

6.3.3 Type 304 SS Data Reduction

Data reduction of the corrected Type 304 SS tubular data continued using the CREEP-FIT data reduction computer program. Corrected data for test numbers 4 through 12 were again fitted to the equation:

$$\varepsilon = \varepsilon_t \left(1 - e^{-rt}\right) + \dot{\varepsilon}_m t \qquad (1)$$

where ε = creep strain (excluding loading strain)

n = integer

$\dot{\varepsilon}_t = f(\sigma, T)$ = constant at fixed σ and fixed T

$r = g(\sigma, T)$ = constant at fixed σ and fixed T

$\dot{\varepsilon}_m$ = secondary creep rate

t = time

Figures 6.9 through 6.25 show tests with corrected effective stresses. Tests 4 through 12 were constant load, 2000 hour tests. Tests 13 through 18 were then being compared to the previously derived equations. Tests 16 and 18 are also 2000 hour tests. The other four tests were conducted for a shorter interval of time prior to changing stress.

Figures 6.14 and 6.15 show test results for number 9 and a test re-run numbered 9A. Test 9 is a thin wall specimen with test thick wall forumlae. This resulted in an effective stress of 38,900 psi. Test 9A was run under the conditions stated in Table 6.2. Individual CREEP-FIT terms are plotted as a function of stress on Figures 6.26 to 6.28. These correlations do not show the stress ratio dependence which was suggested by the previously reported results. Insensitivity

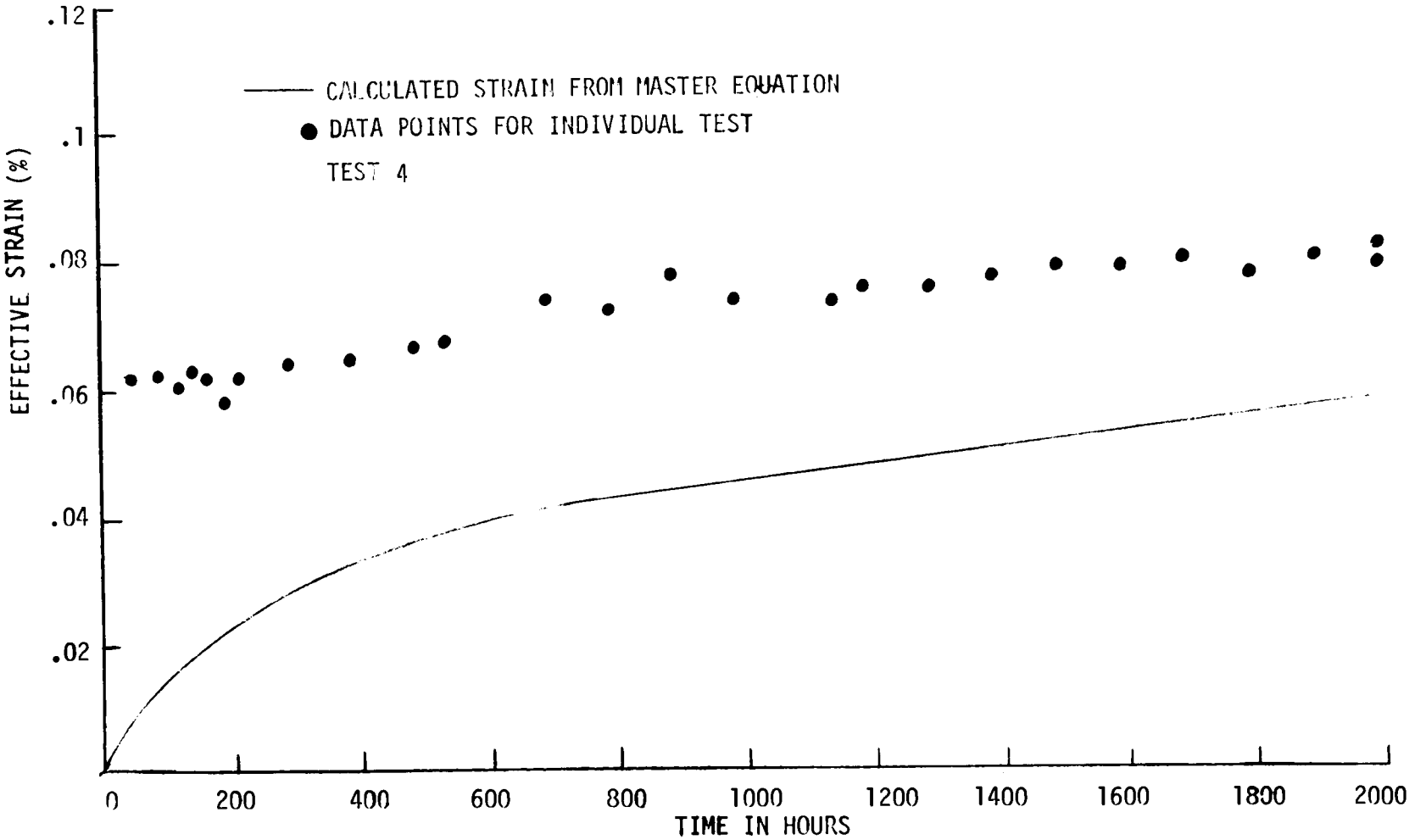

Figure 6.9. Effective Strain vs. Time for Multiaxial Creep
(Effective Stress = 8,900 PSI)

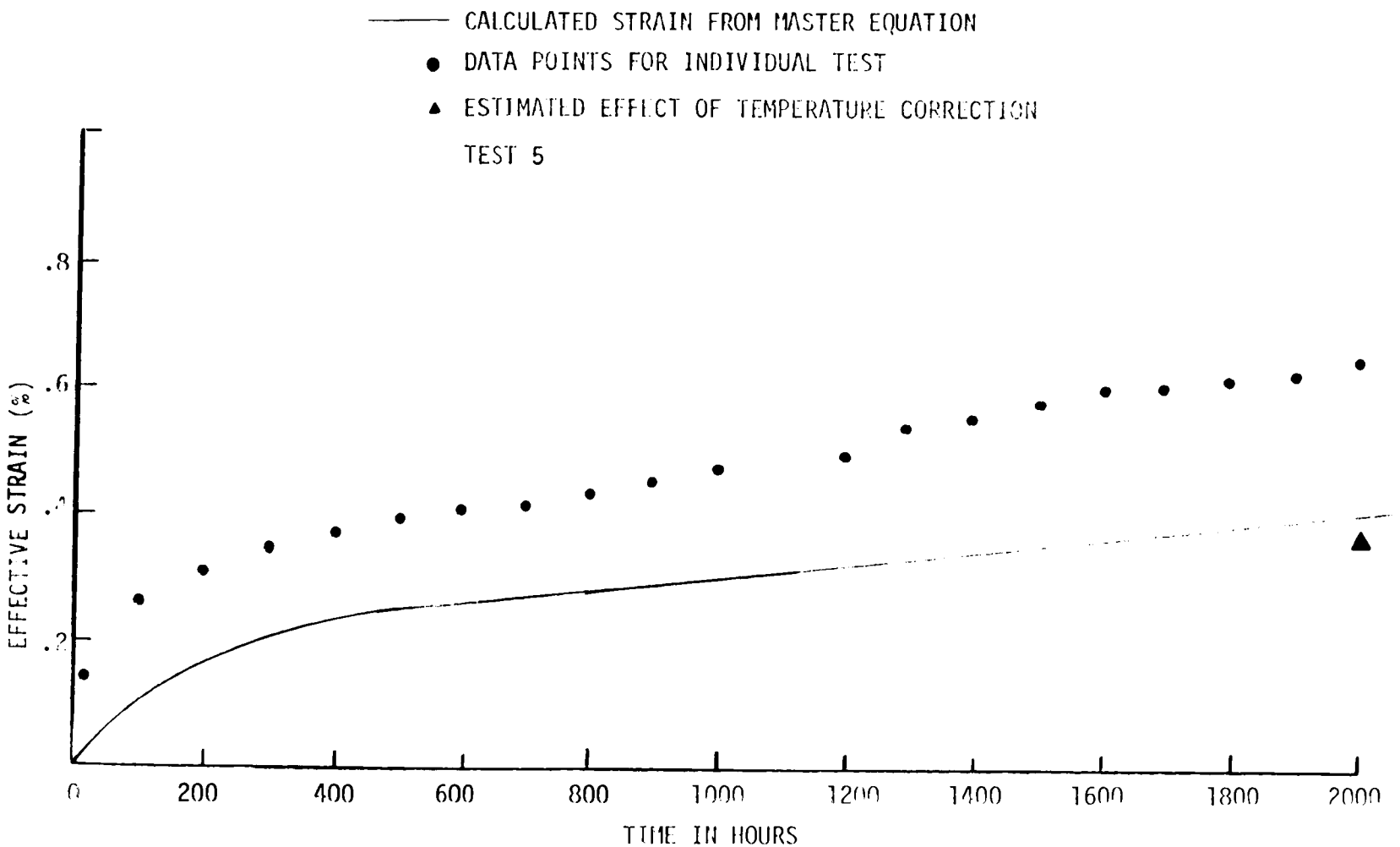

Figure 6.10. Effective Strain vs. Time for Multiaxial Creep
(Effective Stress = 13,400 PSI)

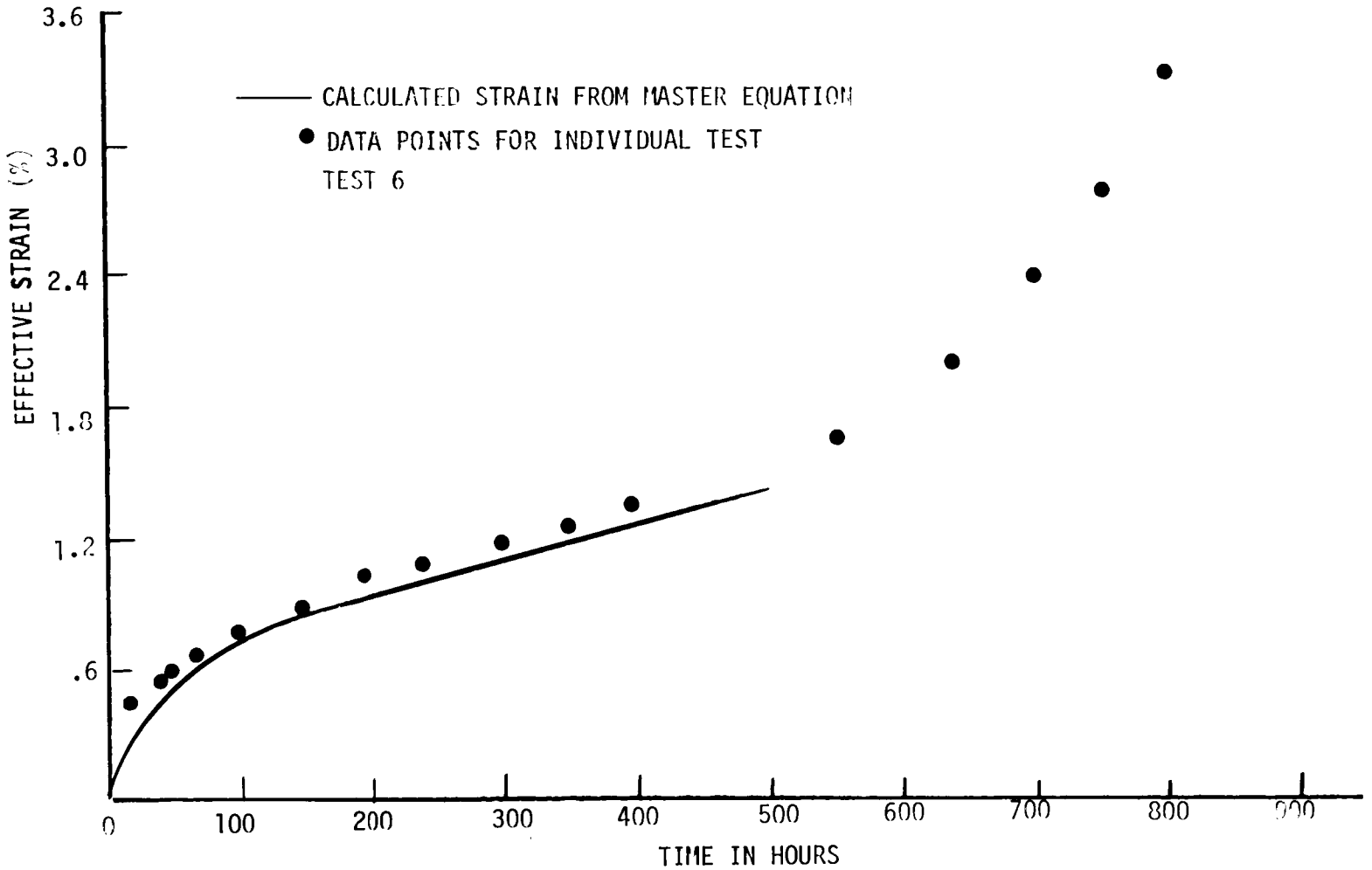

Figure 6.11. Effective Strain vs. Time for Multiaxial Creep
(Effective Stress = 20,000 PSI)

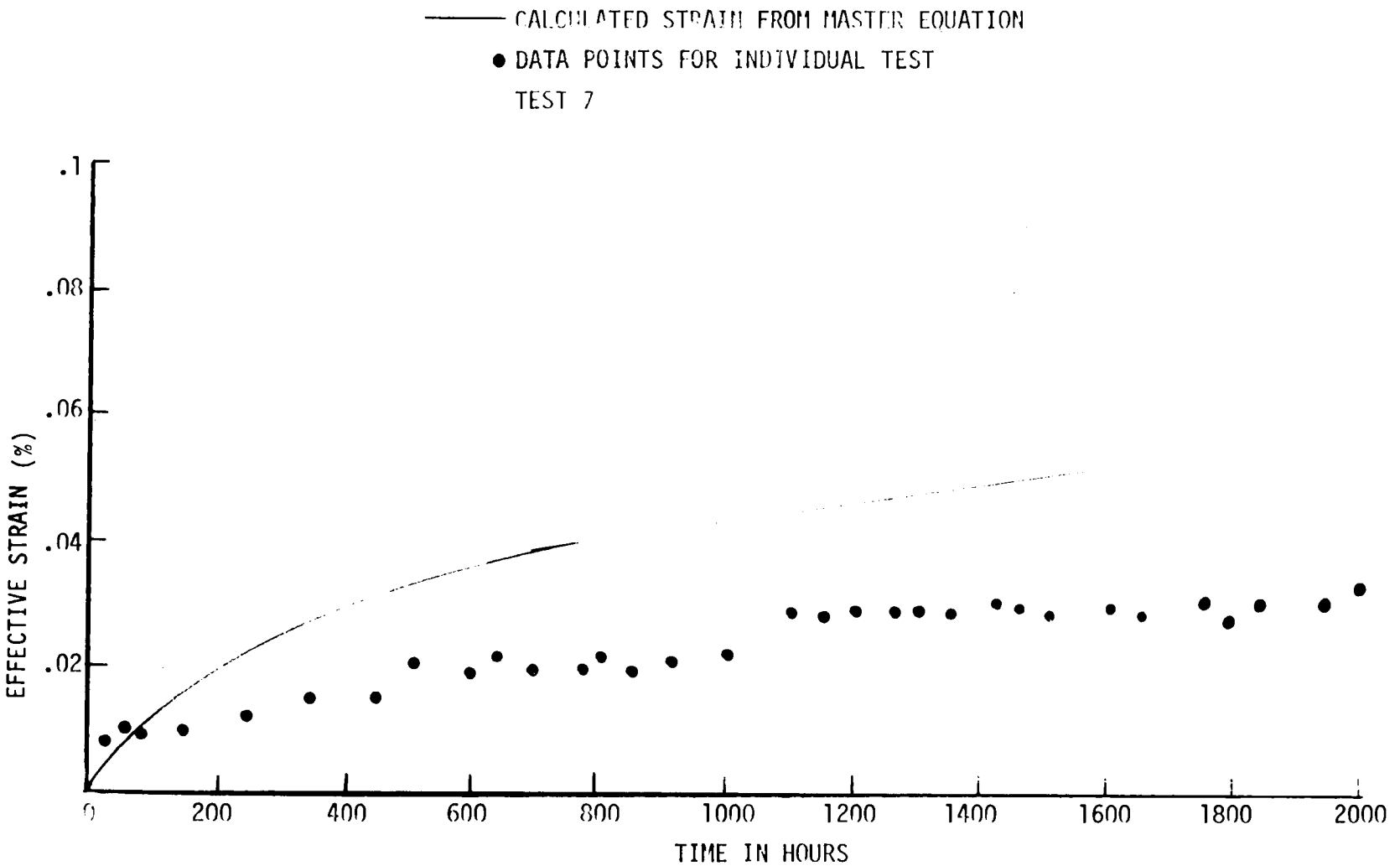

Figure 6.12. Effective Strain vs. Time for Multiaxial Creep
(Effective Stress = 9,000 PSI)

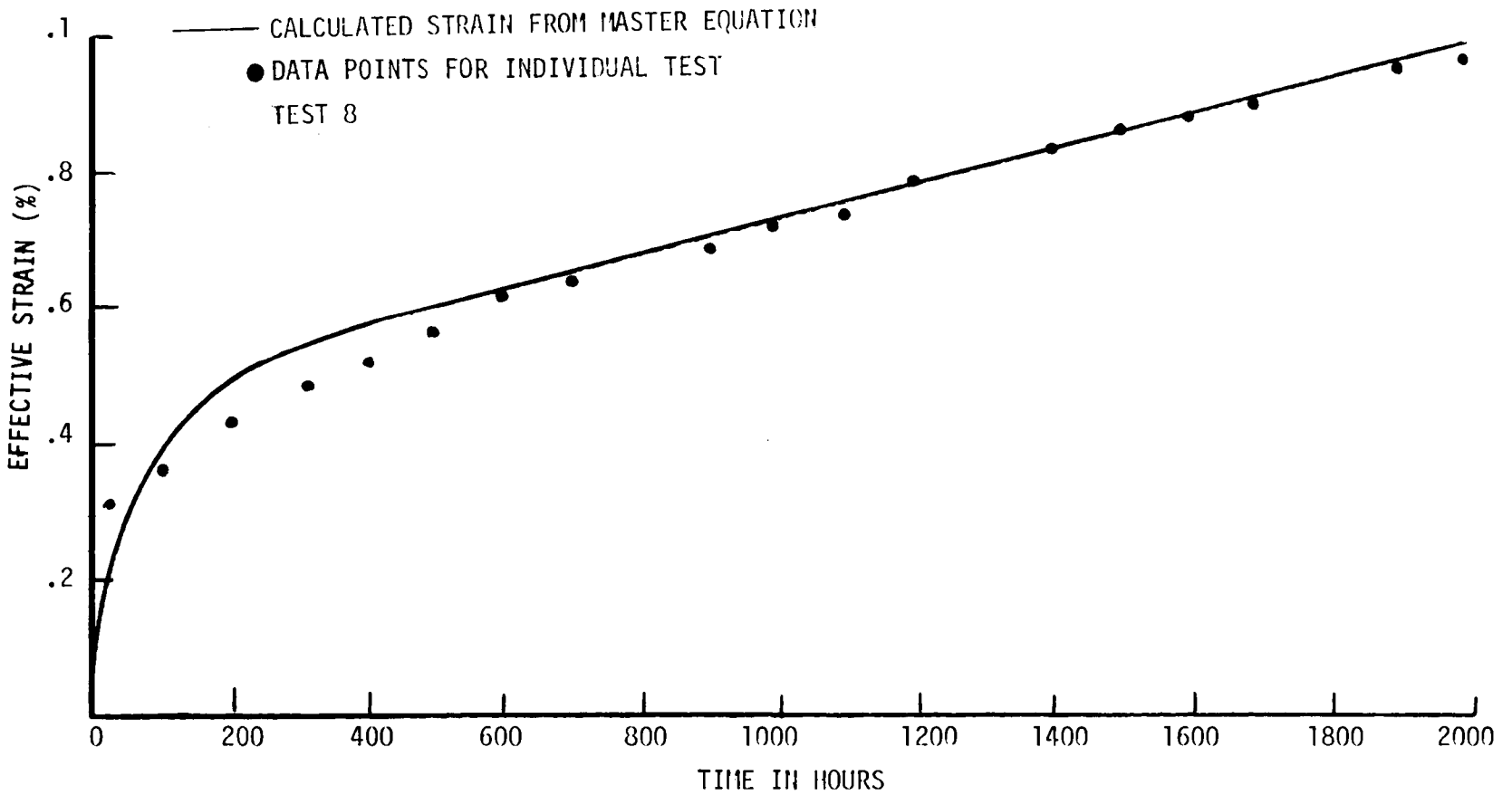

Figure 6.13. Effective Strain vs. Time for Multiaxial Creep
(Effective Stress = 15,000 PSI)

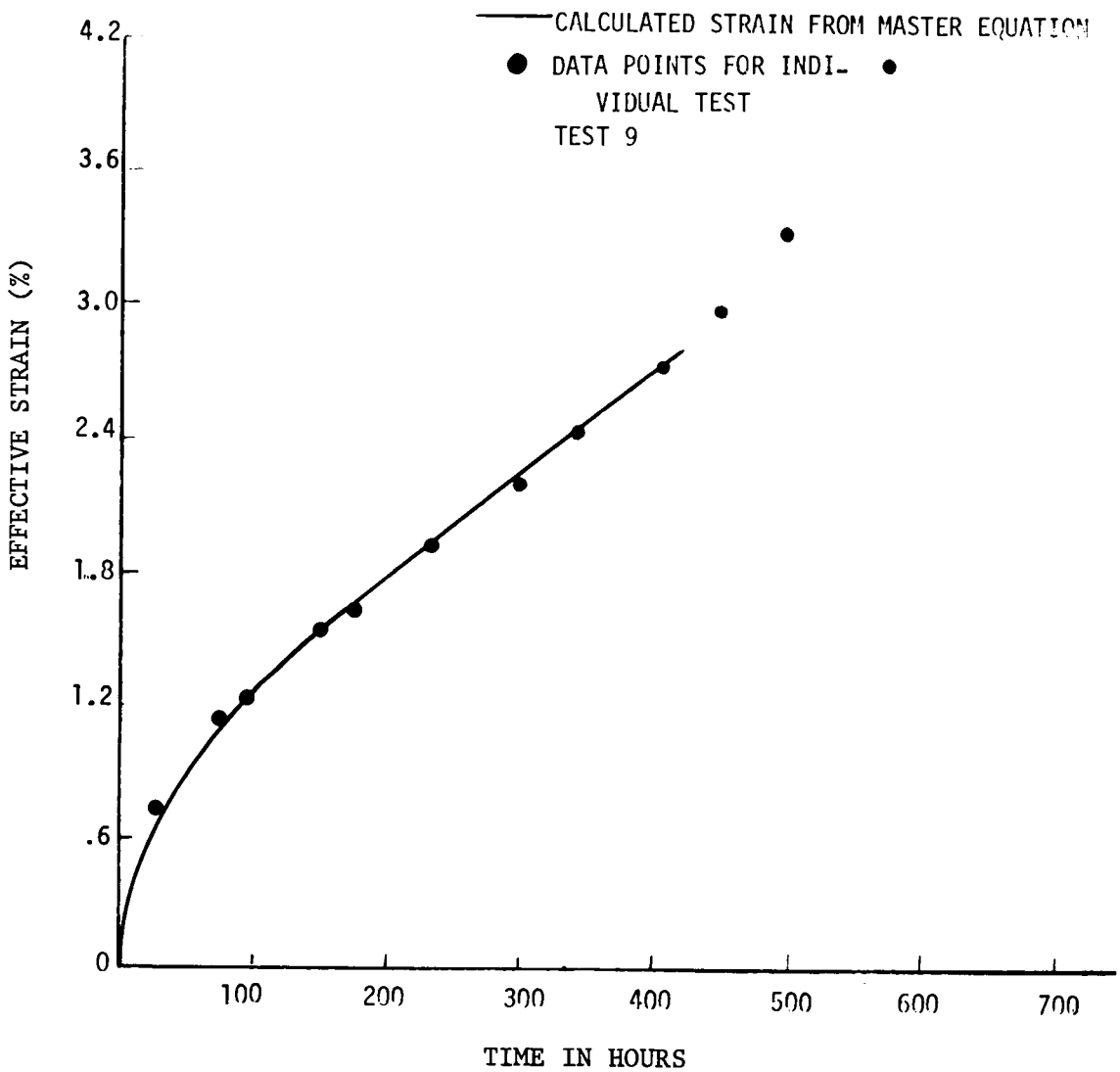

Figure 6.14. Effective Strain vs. Time for Multiaxial Creep (Effective Stress = 38,900 PSI)

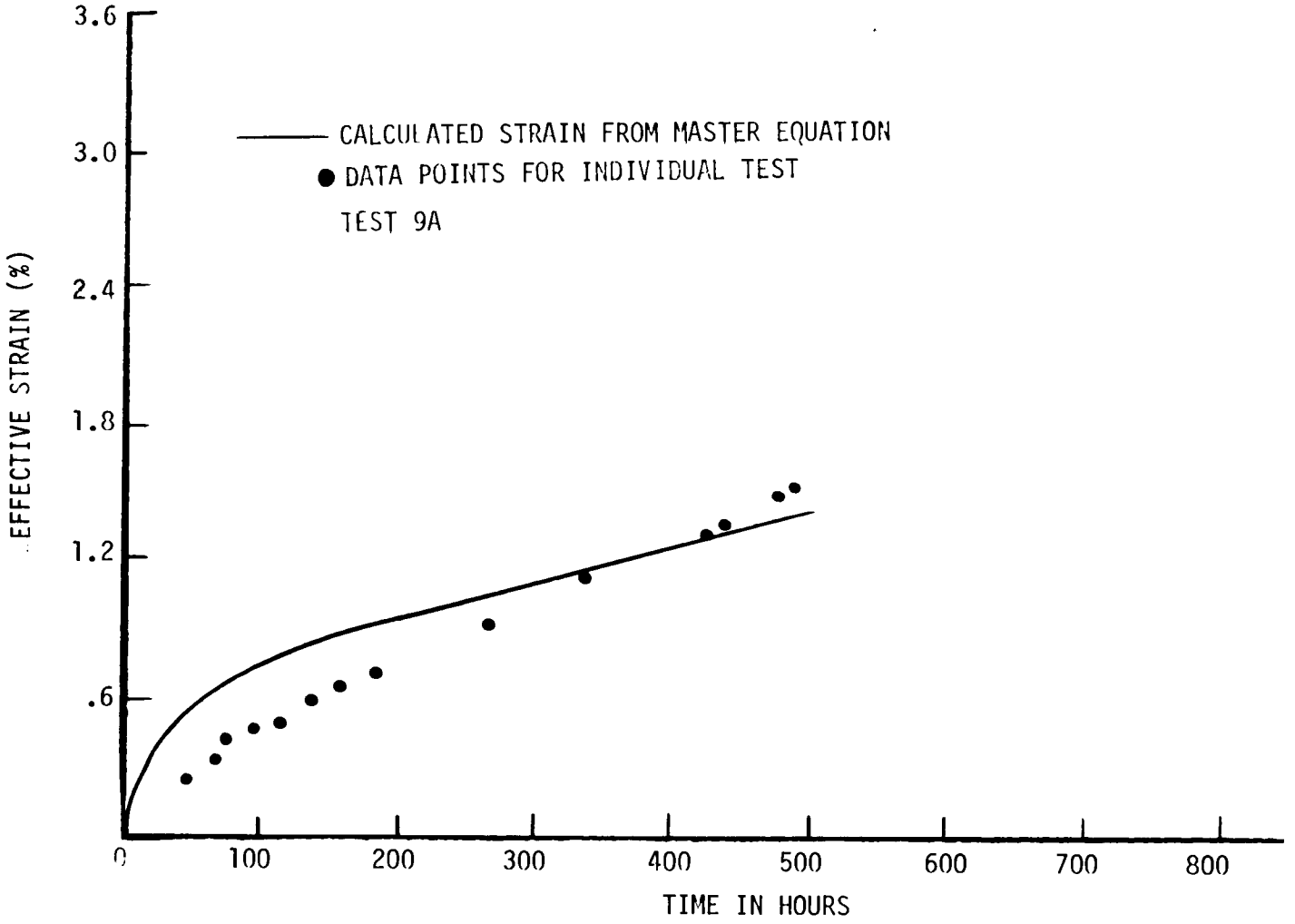

Figure 6.15. Effective Strain vs. Time for Multiaxial Creep
(Effective Stress = 20,000 PSI)

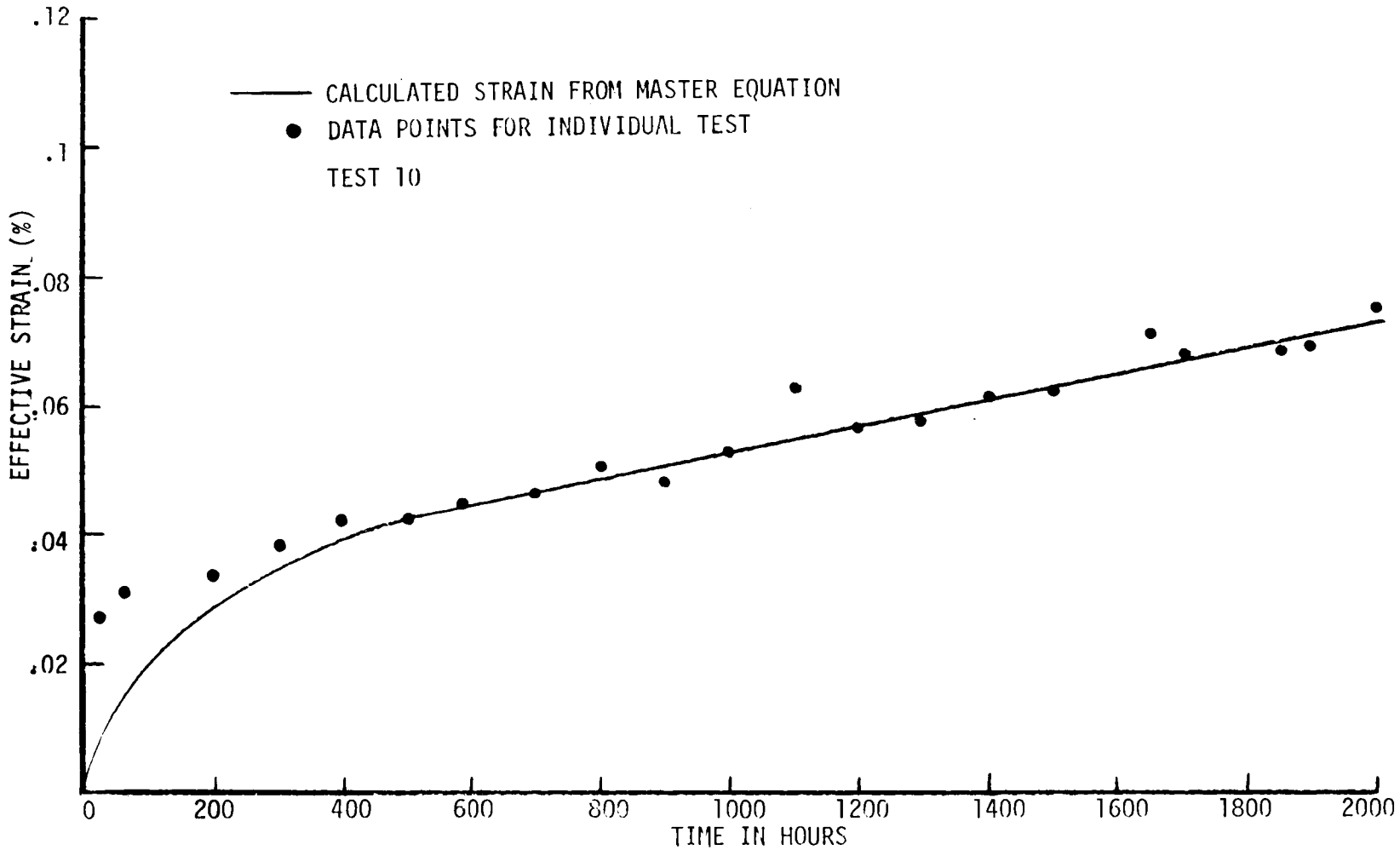

Figure 6.16. Effective Strain vs. Time for Multiaxial Creep
(Effective Stress = 9,218 PSI)

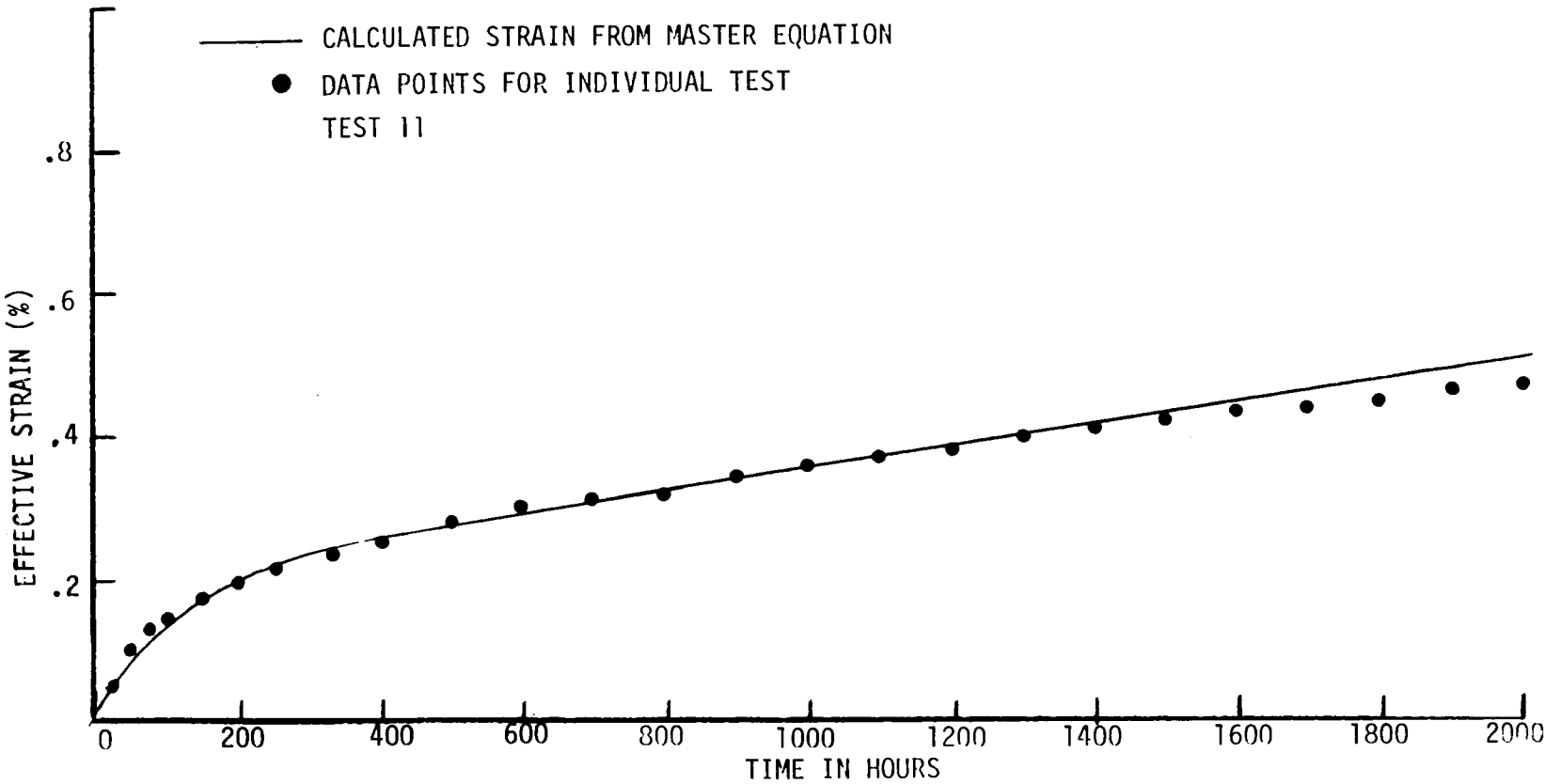

Figure 6.17. Effective Strain vs. Time for Multiaxial Creep
(Effective Stress = 13,800 PSI)

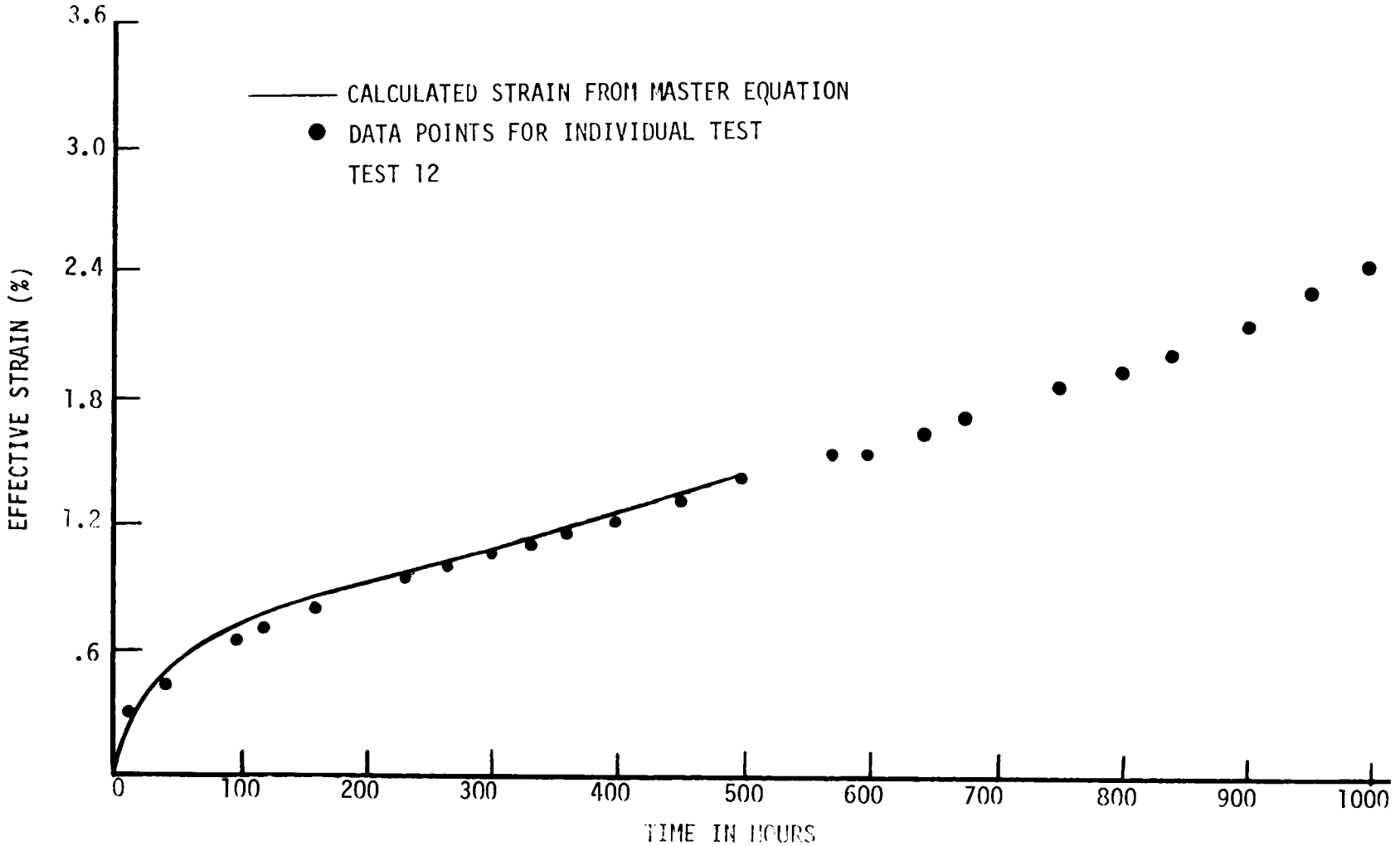

Figure 6.18. Effective Strain vs. Time for Multiaxial Creep
(Effective Stress = 20,000 PSI)

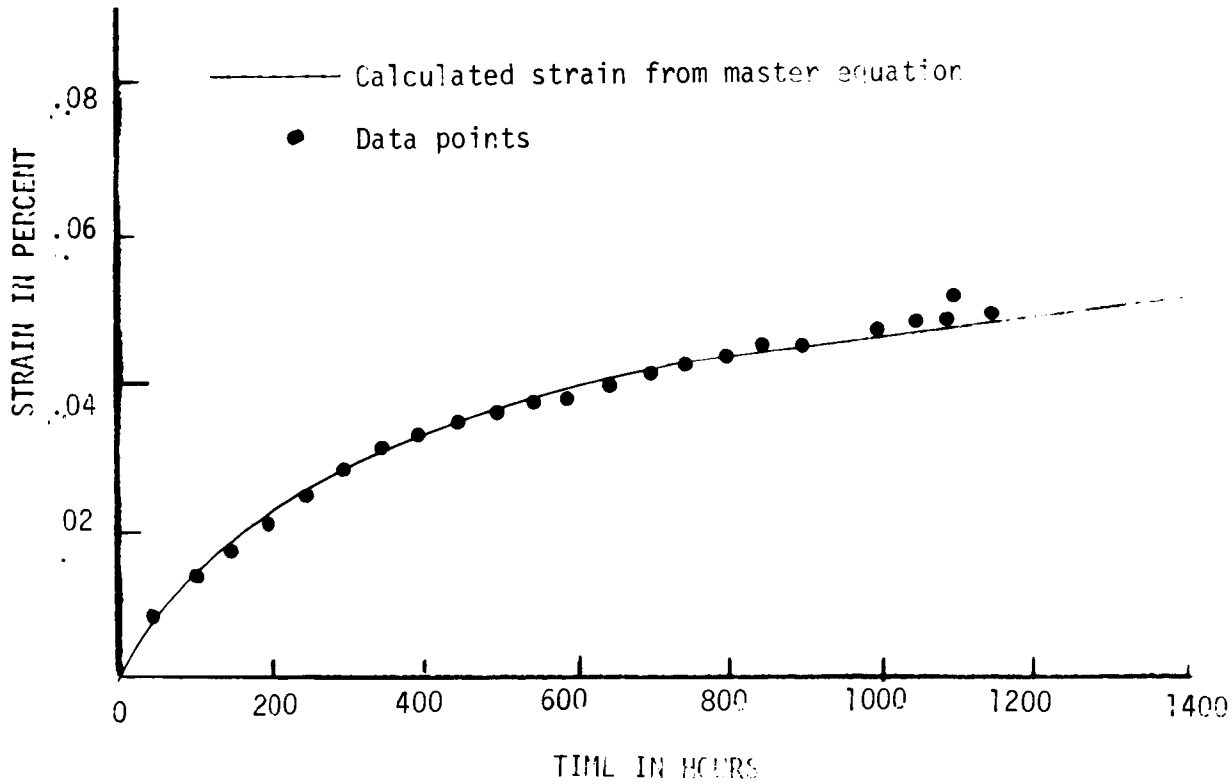

Figure 6.19. Effective Strain vs. Time for Multiaxial Creep Strain - Test 13 (Effective Stress = 8,900 PSI)

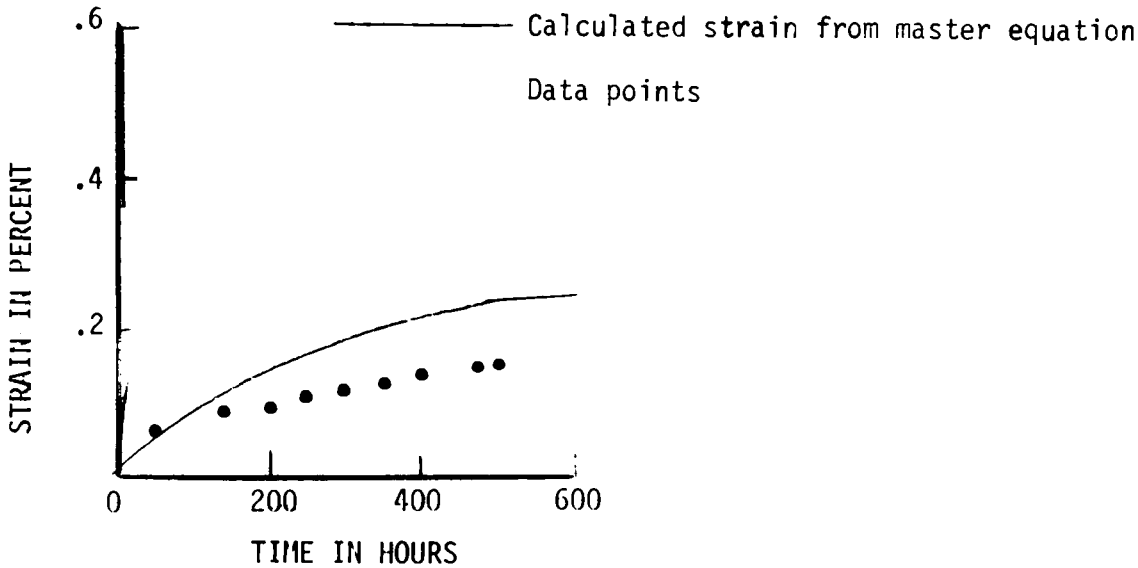

Figure 6.20. Effective Strain vs. Time for Multiaxial Creep - Test 14 (Effective Stress = 13,300 PSI)

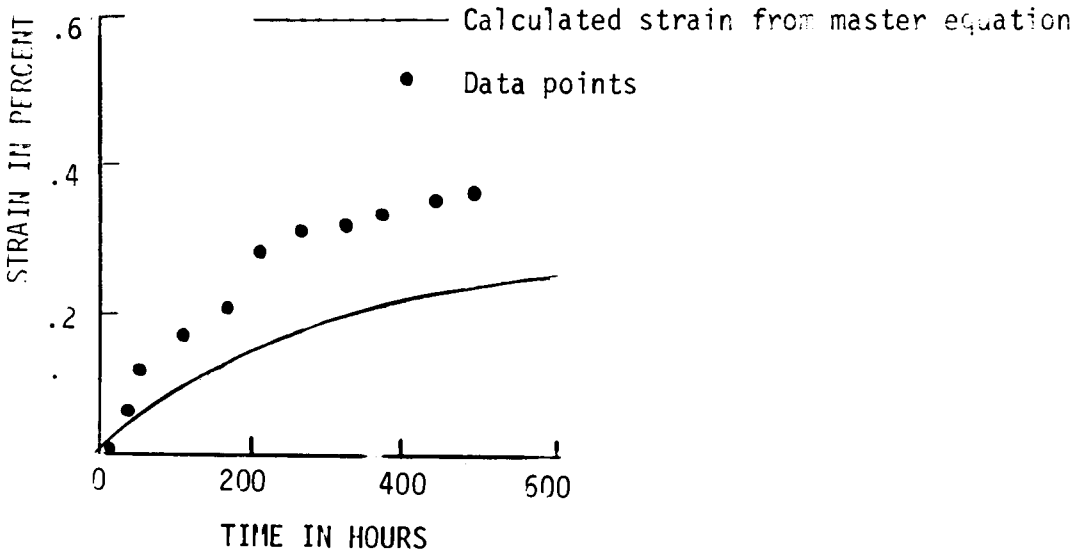

Figure 6.21. Effective Strain vs. Time for Multiaxial Creep - Test 14A (Effective Stress = 13,200 PSI)

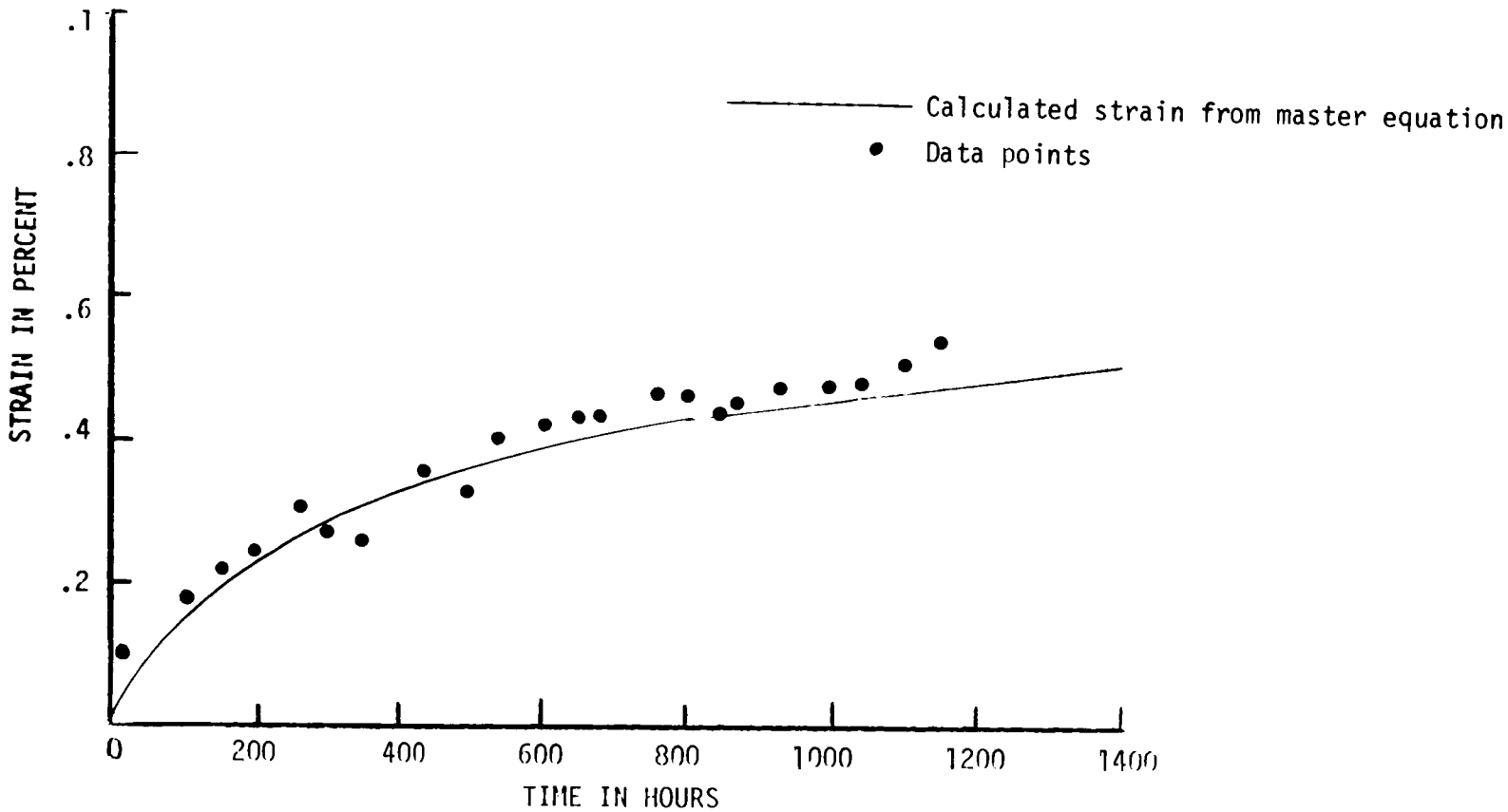

Figure 6.22. Effective Strain vs. Time for Multiaxial Creep - Test 15
(Effective Stress = 8,900 PSI)

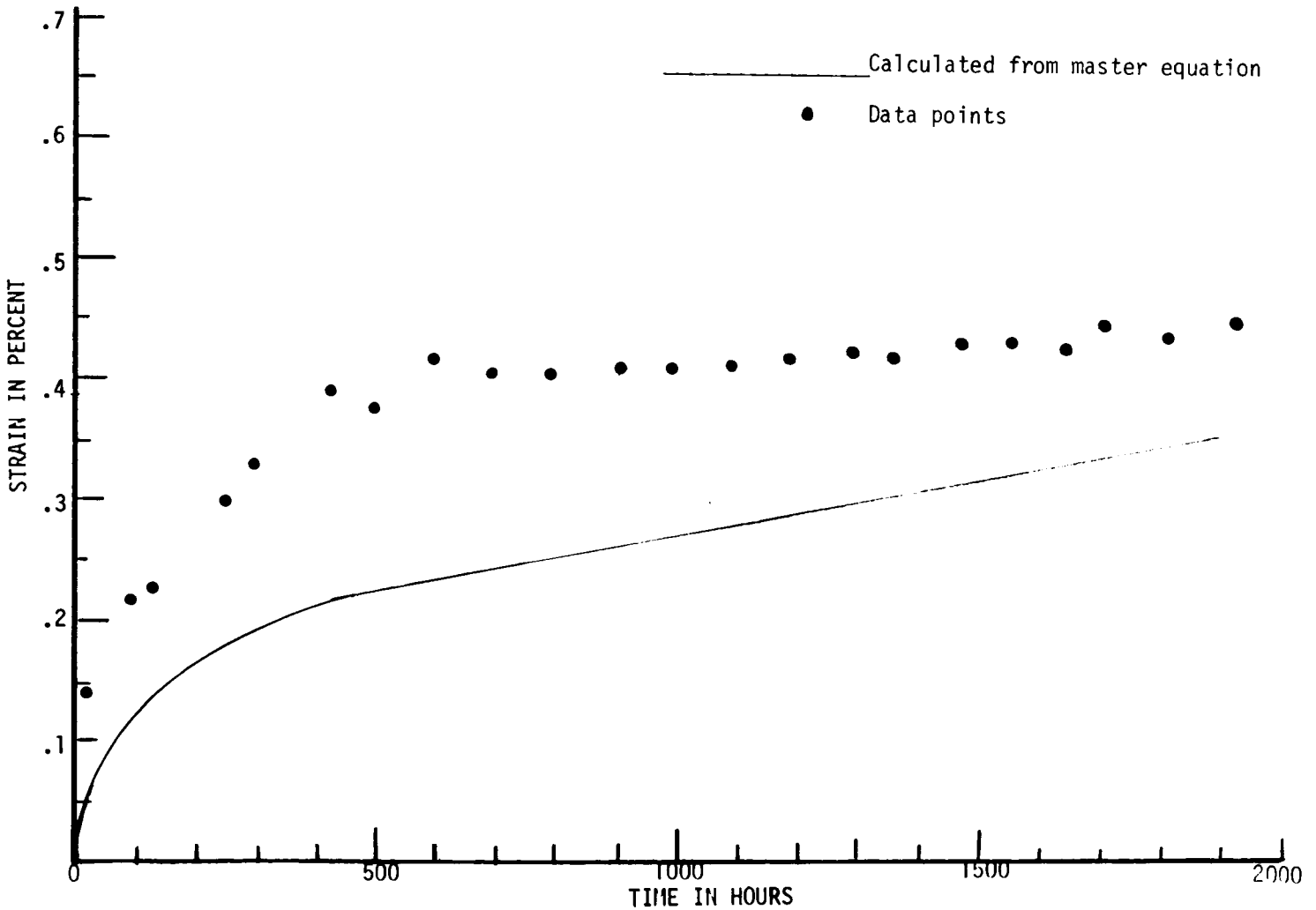

Figure 6.23. Effective Strain vs. Time for Multiaxial Creep - Test 16
(Effective Stress = 12,500 PSI)

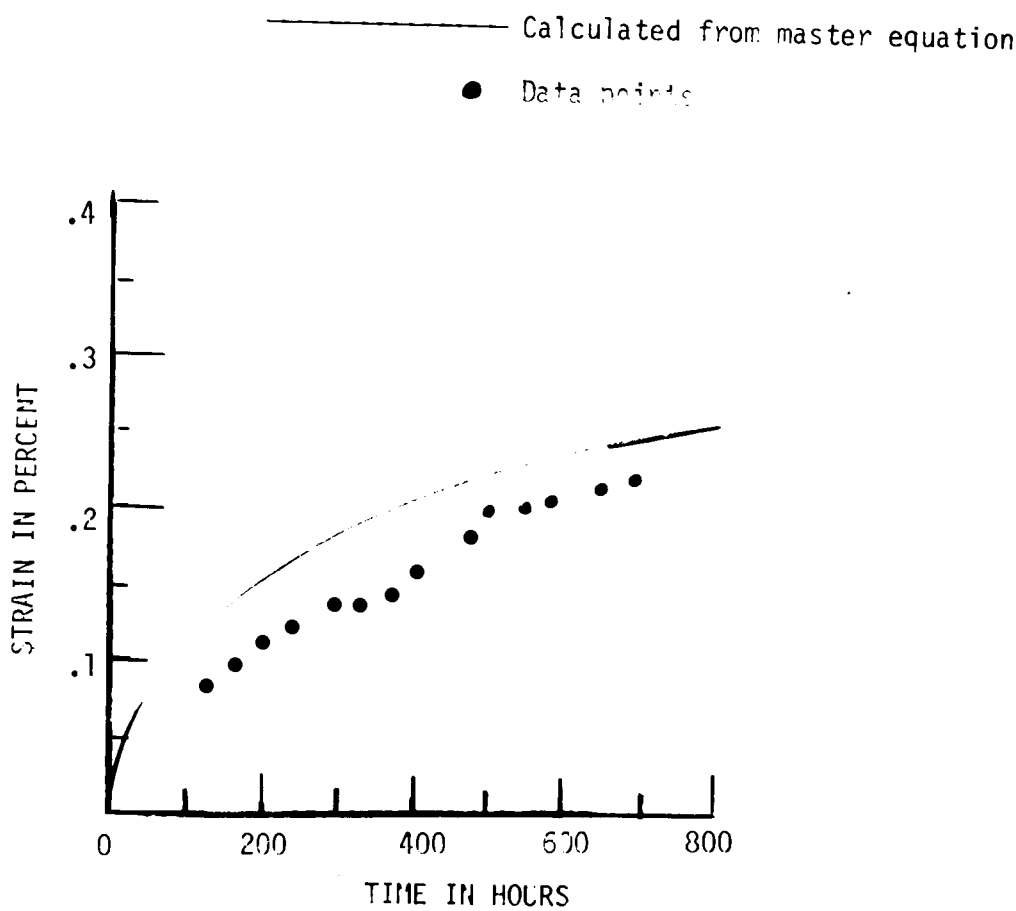

Figure 6.24. Effective Strain vs. Time for Multiaxial Creep - Test 17 (Effective Stress = 12,500 PSI)

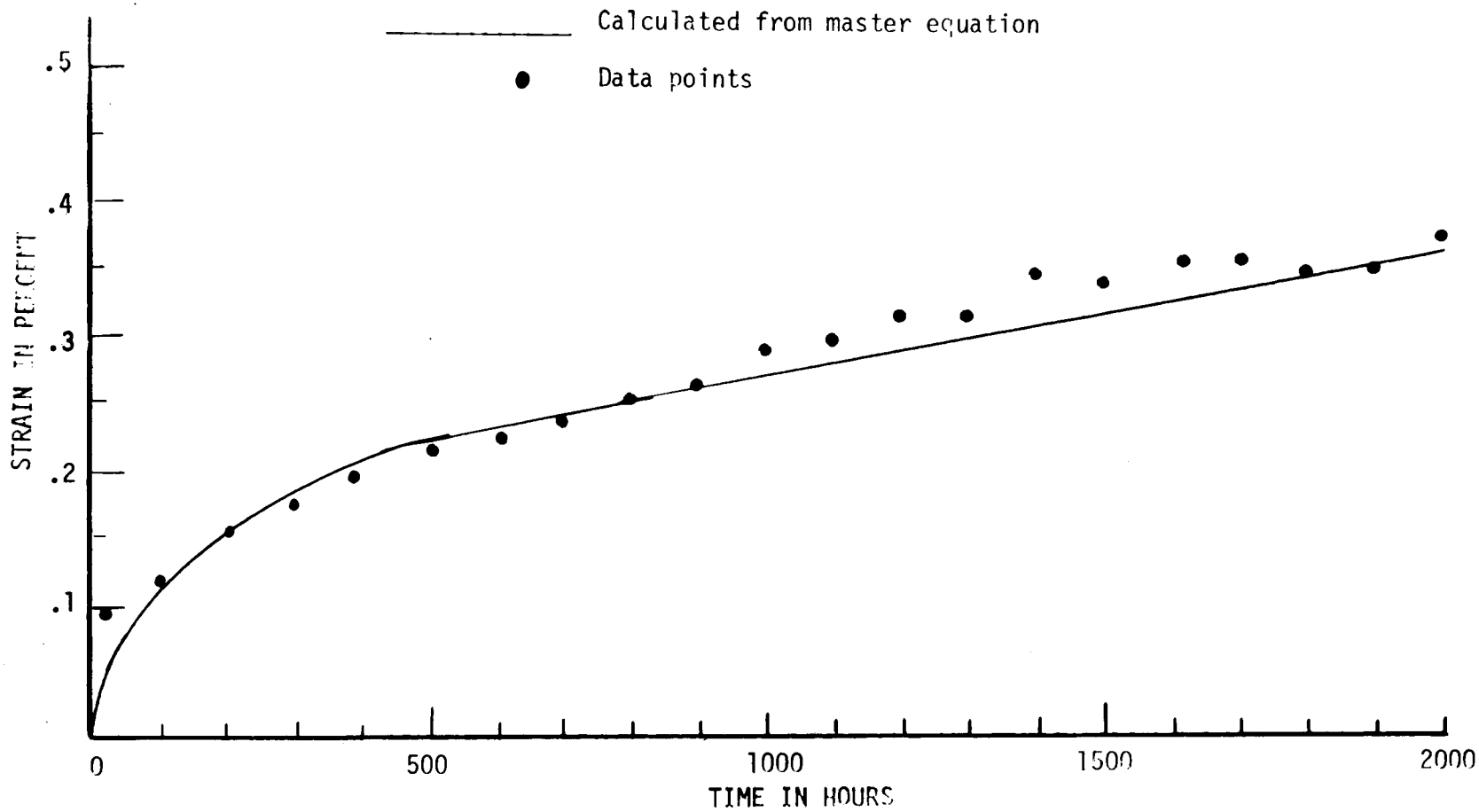

Figure 6.25. Effective Strain vs. Time for Multiaxial Creep - Test 18
(Effective Stress = 12,500 PSI)

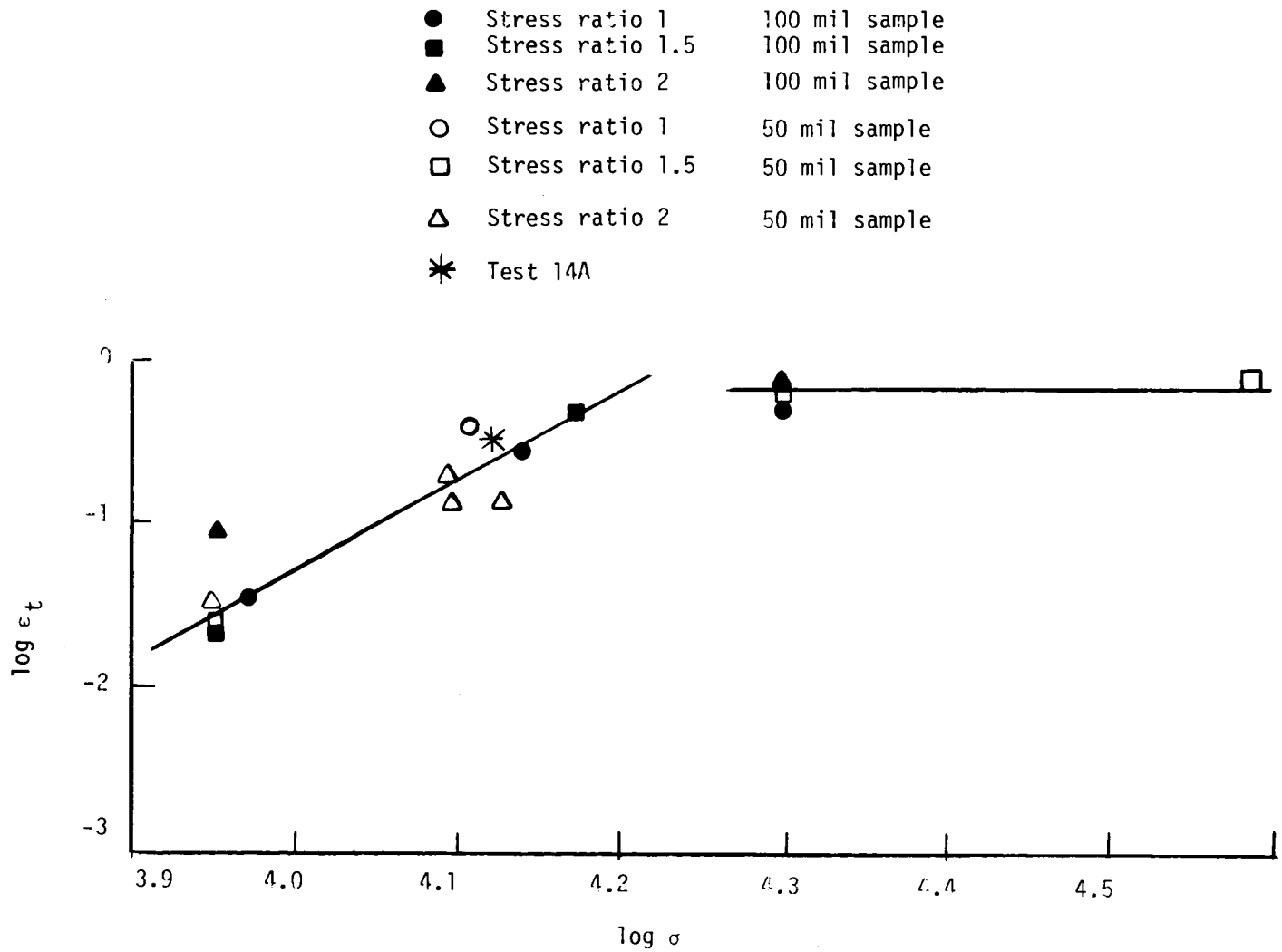

Figure 6.26. Stress vs. ε_t for Multiaxial Creep Equation

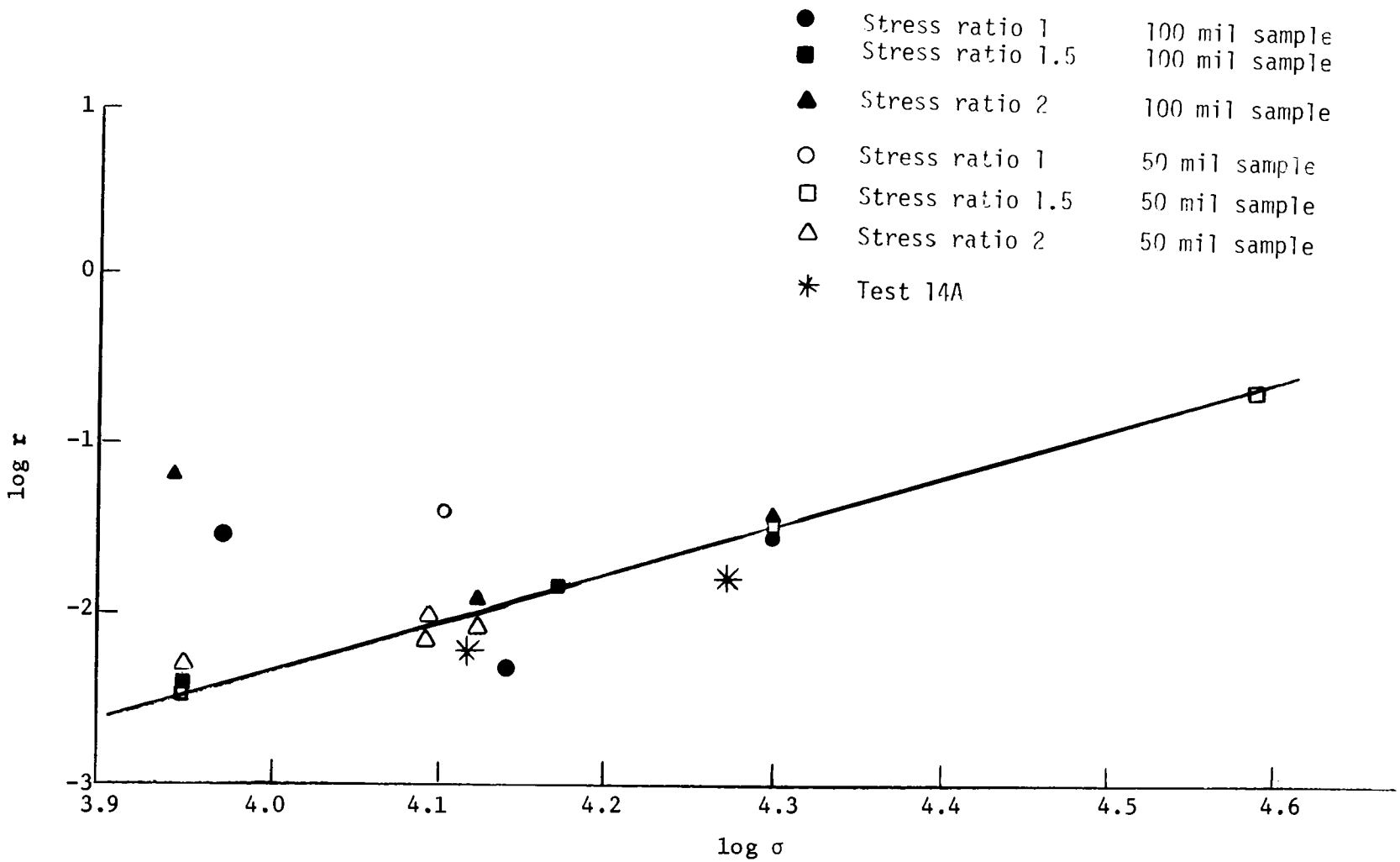

Figure 6.27. Stress vs. r of Multiaxial Creep Equation

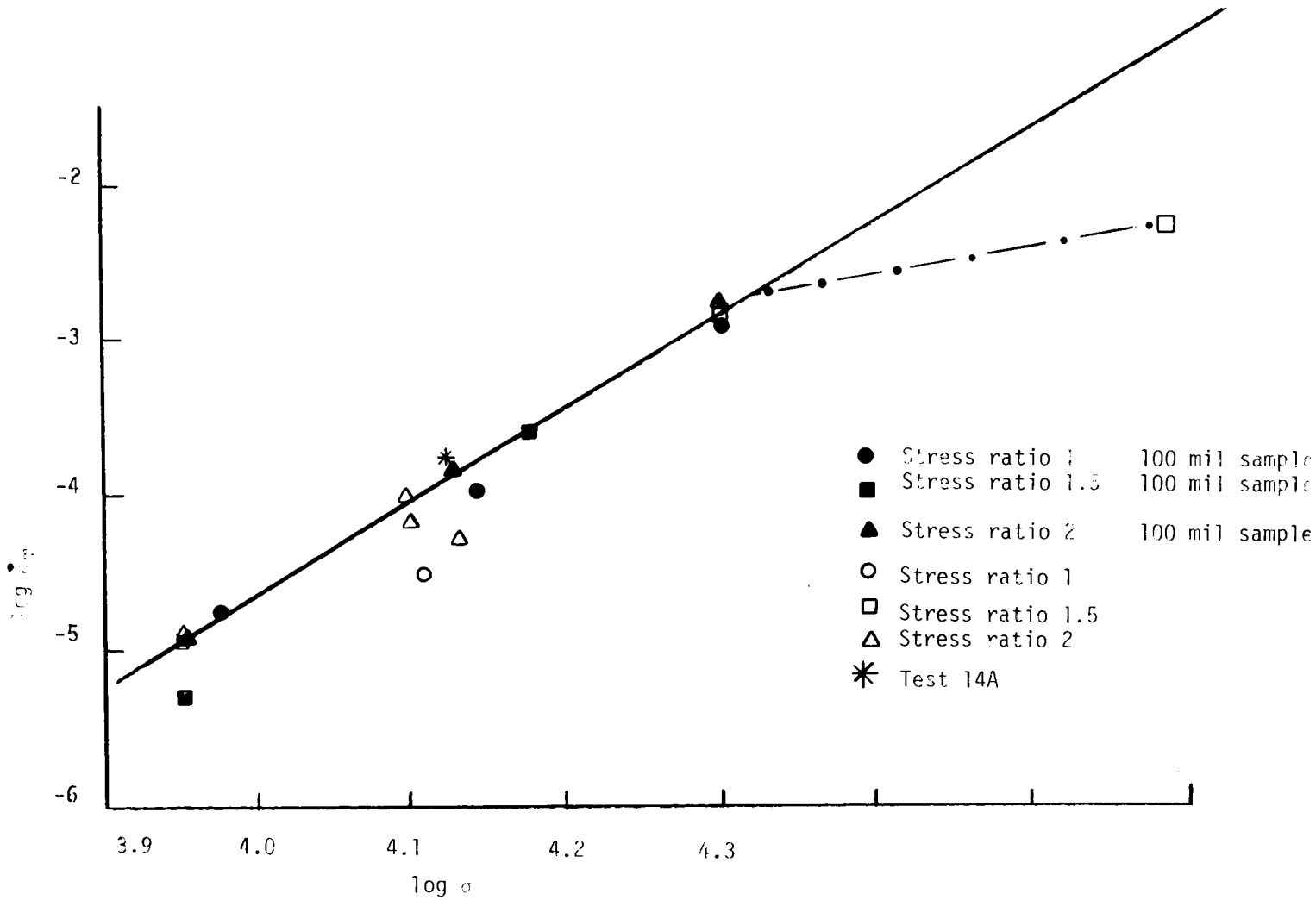

Figure 6.28. Stress vs. ε_m for Multiaxial Creep Equation

to the stress ratio seems to be also displayed to the initial evaluation of results of test numbers 13 through 18.

Tests 4 and 7 show notable variation from the calculated equation. Test 4 displays a very large initial creep with a slightly lower slope than anticipated. It was found that this specimen has a post test hardness of 125 VPW_{250} compared to 145 $\pm$ 6 VPN_{250} for other specimens. This is indicative of a possible heat treatment effect. In addition, test 4 also showed a great deal of instability in the measured circumferential strain. The spread on the measurements at 2000 hours was 0.8% strain with the highest reading being 0.13% strain. Test 7 is a low stress test which suffered a great deal of instability like Test 4. As such, the results of these two tests should not be considered to the same extent as Test 10.

Tests 5 and 9A also show some variation from the calculated equation. Test 5 was conducted at 1115°F. A 15°F higher temperature at 13,400 psi effective stress causes a significant creep variation from expected results of a test at 1100°F. With the available ORNL data on heat effects of reference material, the expected effect at 2000 hours is to cause an approximately 40% increase in effective strain[7]. The estimated corrected value is shown on Figure 6.10 as a triangle. This point corresponds well with the calculated curve for 1100°F. Test 9A is a rerun of 9. At that time, however, due to lack of material, a sample with a weld distortion causing a misalignment was used. This yielded results which are less reliable than tests 6 and 12 but which confirm the trends shown by the higher precision tests.

Secondary creep rates in various tests are very consistent. This holds true for tests with stresses up to 20,000 psi. However, test 9 at 38,900 psi has a substantially lower slope than that which would correspond to the other data. This suggests a change in slope for high stresses.

Test 14 and 14A were conducted under similar conditions. The variation with each other and the master equation seems to be related to set-up problems, rather than materials since the loading strains are almost identical. The axial strain measurements also start at the same point with both tests. After loading, test 14 behaves normally in the axial direction in that it slightly increases during the first few hours of testing and then levels out to a constant small positive value. For test 14A, however, this behavior is not displayed.

In this case the axial strain goes slightly negative in value in the first few hours and retains a constant small negative value. The circumferential strains in both tests follow the same trends. The negative axial strain values of test 14A may be due to experimental set-up. These affect the calculation of the effective strain because they change the sign of a term thus causing an addition to effective strain which would generally be a subtraction. This may account for the values being above the master equation. Test 14 shows a fairly low loading strain for this and subsequent stages of testing. The slope is also smaller than predicted. After rupture testing of test 14, microstructure characterization and hardness will be done.

6.3.4 Type 304 SS Equation Comparison

The above data reduction shows marked variation from anticipated behavior based on previous uniaxial information. Both ORNL and W-ARD uniaxial creep information allow fairly straightforward evaluation of the equation[8]. However, the behavior of high stress level multiaxial tests deviates greatly from this pattern. Because of this behavior, a graphical evaluation of the terms above 20,000 psi stress will be most appropriate. Between 8900 and 20,000 psi stress the values follow equations representing multiaxial behavior:

$$\log \varepsilon_t = 6.88 \log \sigma - 29.0$$

$$\log r = 2.86 \log \sigma - 13.78$$

$$\log \dot{\varepsilon}_m = 6 \log \sigma - 28.64$$

The parameters listed on the previous page have been used to calculate the W-ARD master equation which is shown in Figures 6.9 to 6.18 for tests 4 through 12. This master equation was graphed along with the experimental results for tests 13 through 18.

Very good agreement was found. Tests 13, 15, and 18 all fall on the master equation curve. This variation may be within the sample itself since test 17 is a repeat of test 18 but only to 500 hours.

A compilation of the master equation for each stress level is shown on Figure 6.29. This figure also gives the ORNL uniaxial master equation plot. Comparison between ORNL uniaxial equation and W-ARD multiaxial equation, reveals the following trends. Although the ORNL equation shows a much more pronounced primary creep behavior at low stress levels, the highest stress level shows extremely fast creep. In the W-ARD multiaxial creep equation, secondary creep is in evidence at significantly shorter times. Neither the projection of the W-ARD equation nor the ORNL equation reflect test 9 results. This test stress level is approaching the ultimate tensile strength of the material which is about 40,000 psi[9]. At that high a stress, a different mechanism of creep is probably operating than that around the yield stress at about 10,000 psi[9].

Transient strain, ε_t shows the greatest scatter of the three parameters shown in Figures 6.26 to 6.28. It is very sensitive to loading strain variations which are most significant at low stresses. This may account for the scatter around 10,000 psi ($\log \sigma = 4$). At the high end, the intercept does not seem to be stress dependent. This behavior has not been seen in uniaxial results. R values, as seen in Figure 6.27, also have a more consistent trend than shown in previous fits. Scatter at low stress is related to the ε_t scatter, and r is very sensitive to variations in ε_t.

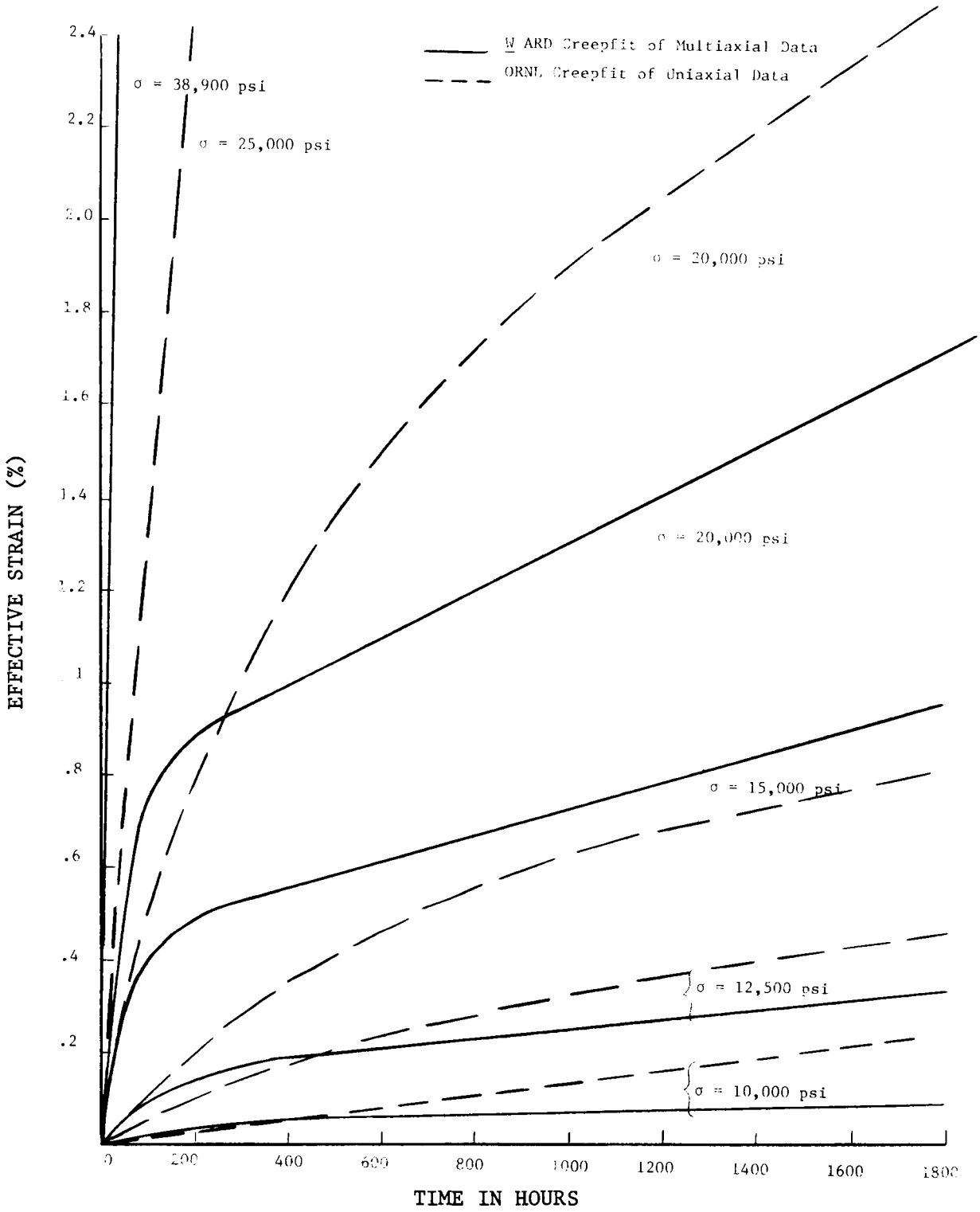

Figure 6.29. Comparison of Creep Laws Used with Type 304 SS (Heat 9T 2796) at 1100°F

6.3.5 Type 304 SS Loading Strain Comparison

The loading strain, as noted in equation (1), is subtracted from all the calculated strains. Consequently, this value only displaces the curve vertically and does not affect its shape. The loading strain value also gives an indication of the character of the material from which the test specimen was made. A fully annealed material will show a very high loading strain coupled with a high initial creep rate and low secondary rate. On the other hand, a cold worked material will show just the opposite behavior.

The loading strains at 1100°F of all the multiaxial tests are shown as a function of initial stress on Figure 6.30. This figure also contains the stress-strain curve for tensile samples (reference heat) tested at 1100°F (863K) by ORNL represented by the solid line. The dashed curves represent the average Type 304 SS tensile properties evaluated at 1100°F and reported in the Nuclear Systems Materials Handbook[10]. The agreement between loading strain of thin walled tubular samples and the tensile properties of a solid bar is within experimental error. It is also noted that there is no appreciable difference between the 50 mil (1.27 cm) and 100 mil (.254 cm) wall thickness specimens with respect to loading strain behavior.

6.3.6 Type 304 Stainless Steel Effect at Stress Ratio on Results

The master equation was derived without respect to stress ratio and relates to only primary and secondary creep rates. The stress ratio effect was not included because the results were not decisive. Despite ignoring stress ratio effects for all of the tests in the first two stages of creep, the master equation showed good agreement with experimental results. However, three tests at 20,000 psi (138 MPa) were measured into the tertiary region. In this region the effects of stress ratio become prominent[11]. The results can be seen in Figure 6.31.

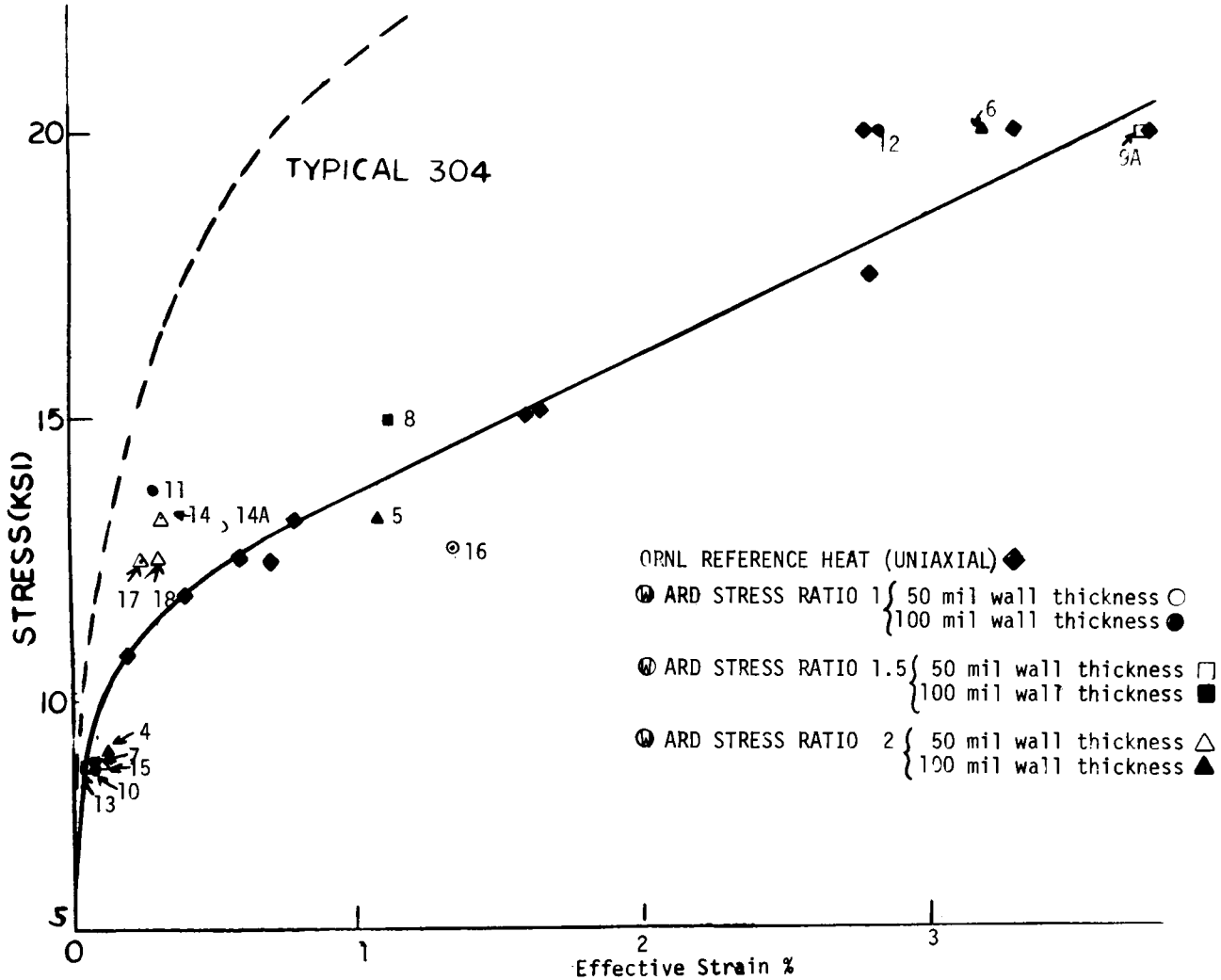

Figure 6.30. Loading Strain of Multiaxial Tests (Stress-Strain Curve for Tensile Tests) vs. Plotted Strain at 1100°F

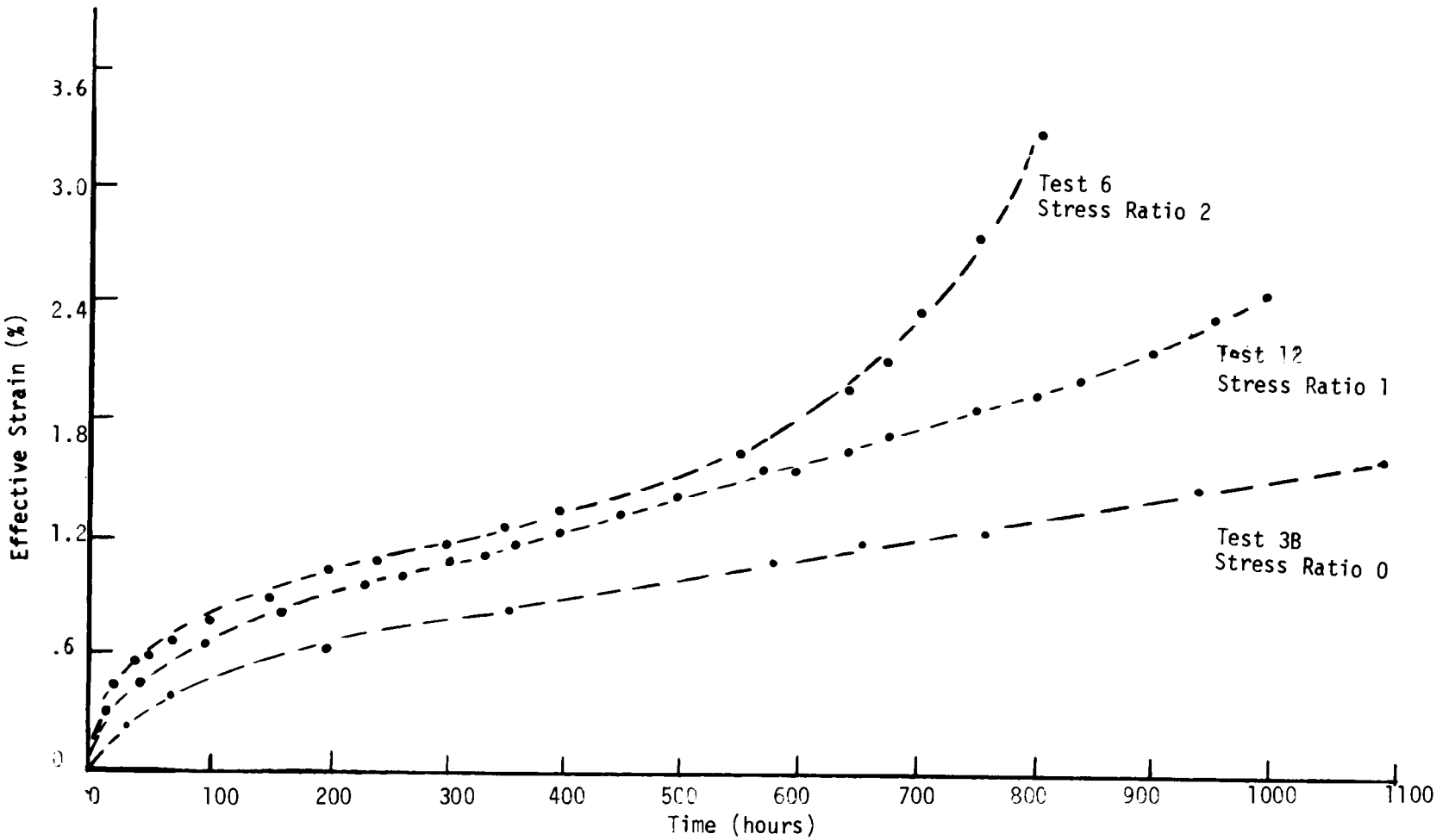

Figure 6.31. A Comparison of 20,000 PSI Stress Tests for Various Stress Ratios

6.3.7 Type 316 Stainless Steel Heat Treatment

6.3.7.1 Heat Treatment

A 9 inch length of 2-1/2 inch O.D. Type 316 SS pipe (ORNL reference heat #8092297) was heat treated to the schedule recommended by ORNL[9]:

Temperature 1950°F (1065°C)

Time - 1.0 hour/inch of thickness with 0.5 hour minimum in inert atmosphere

Cooling - not specified but identified as an important rate variable

The requirements following heat treatment are:

Grain Size - ASTM #3 to #5

0.2% offset yield strength at R.T. - 28 to 32 ksi
.005 in/in at R.T.

A subsequent discussion with ORNL[12] resulted in the following heat treatment sequence for the pipe section:

1. Place in hot furnace at 1950°F (1065°C in flowing argon).
2. When the temperature on specimen surface is within 8°F (5°C) of 1950°F start timing the 0.5 hour residence time.
3. After 0.5 hour at temperature withdraw into a water cooled furnace section and cool by flowing argon.

The pipe section was heat treated with a thermocouple attached to the O.D. in the center of the sample. The temperature trace of this thermocouple is shown in Figure 6.32 along with the cooling rate recommended by ORNL. The agreement of these traces is extremely good.

6.3.7.2 Tensile Properties and Hardness

Following heat treatment, the pipe was sectioned as shown in Figure 6.33 to give three flat tensile specimens in the axial direction and three round specimens in the circumferential direction. The dimensions of the specimens are shown in Figure 6.34.

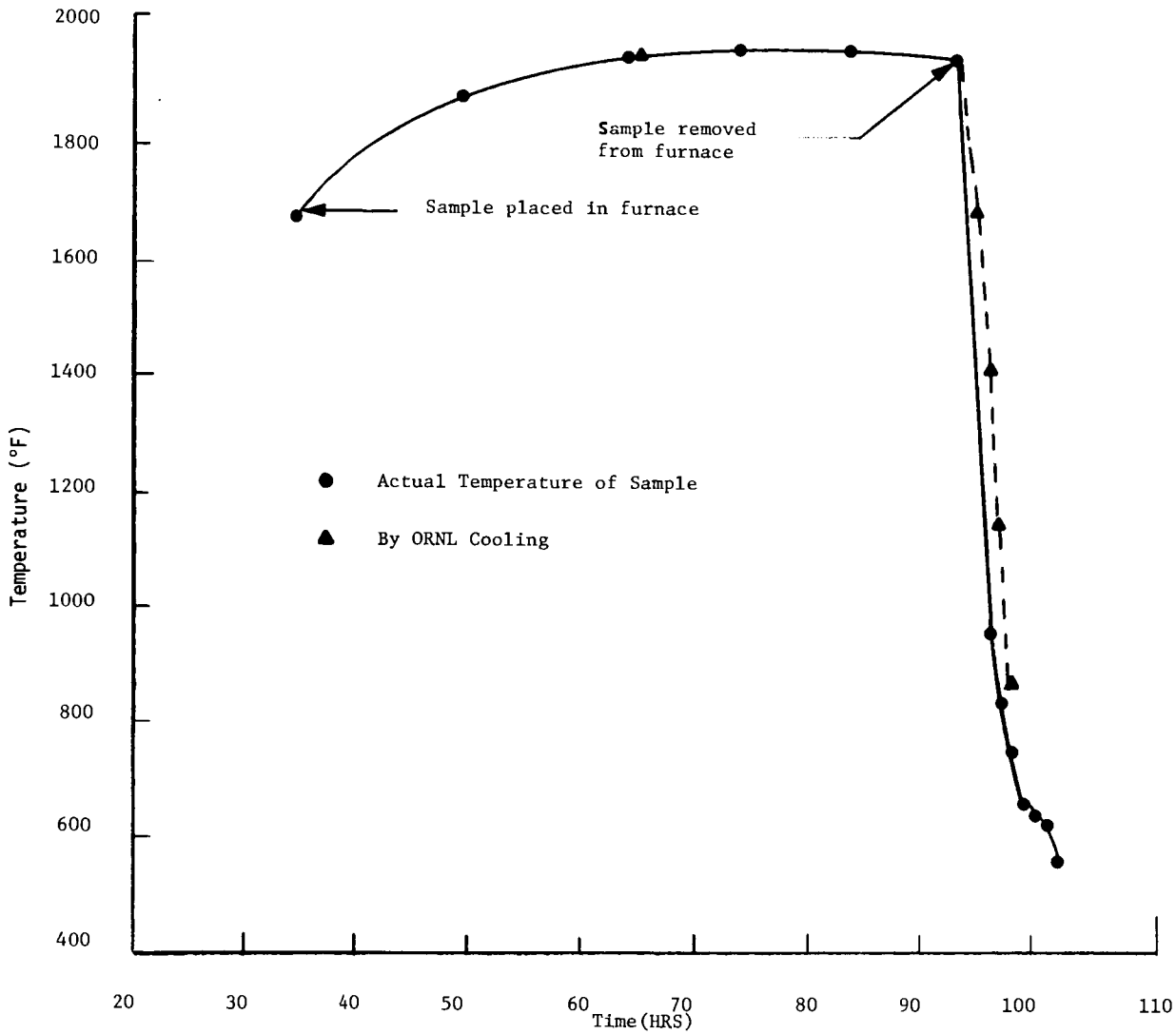

Figure 6.32. Heat Treatment Curve for Type 316 Stainless Steel 2-1/2" O.D., 9" Pipe

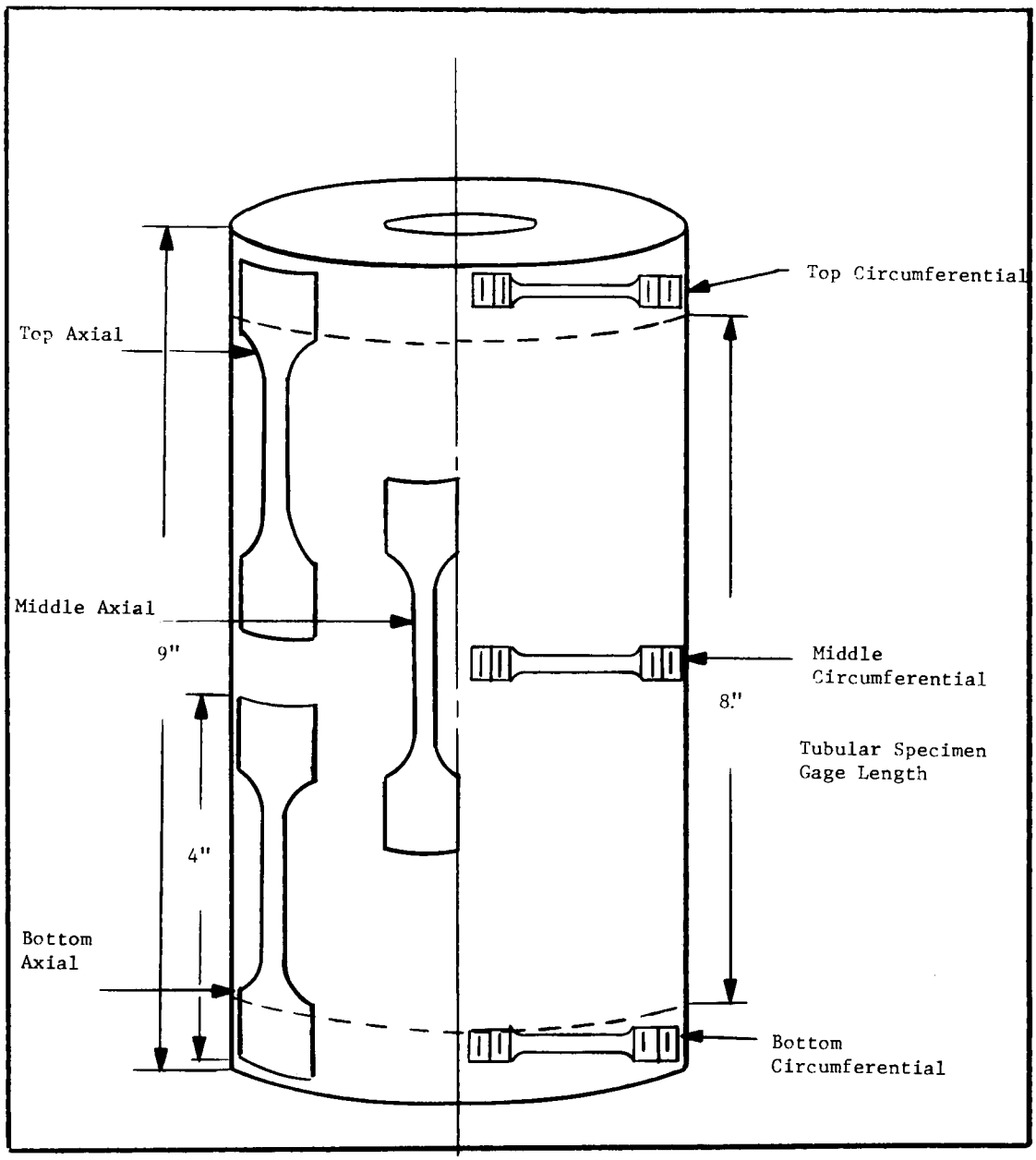

Figure 6.33. Sketch of Tensile Specimen Positions on the Test Pipe

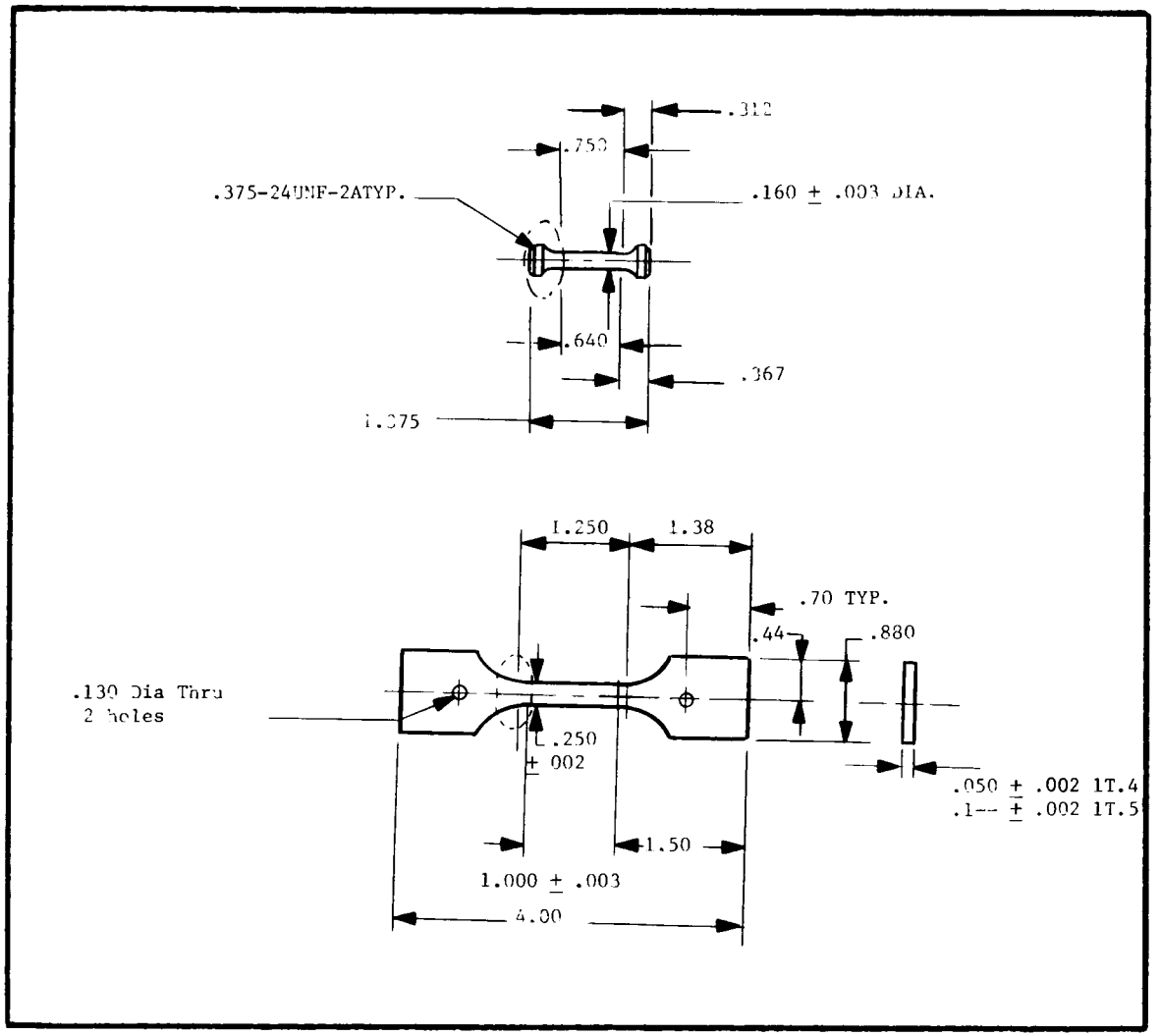

Figure 6.34. Configuration of Tensile Specimens

All axial specimens were tested in strain control at 0.005 in/in/mm with an extensometer attached to the specimen. The load extension curves obtained were serrated in the plastic region as shown in Figure 6.35. It appears that this may be a relaxation effect in the material as on increasing the strain rate the effect disappears. In determining the proof stress the maximum points of the serrations were used.

Circumferential specimens were tested in stroke control. An extensometer was not attached to the gage length due to the non-availability of an extensometer suitable for the short gage length.

Determination of strain in a specimen from stroke measurements is very unreliable, particularly when strains are small. This is illustrated in Figure 6.36 where grip separation, measured by a dial indicator, is shown as a function of stroke reading. It was, therefore, decided to use an assumed elastic modulus of 28×10^6 psi to compute strain and then to determine the 0.02% and 0.2% proof stresses. The maximum points of the serrations was used to compute the load/extension curve.

The properties thus obtained are shown in Table 6.5.

In comparing these data with ORNL data it is noted that while the proportional limit and the 0.2% proof stress values are close there is a large difference in the 0.2% proof stress. This is shown in Figure 6.37. The results would indicate a higher work hardening in the W-ARD treated specimens. The reason for this is probably heat treatment differences between ORNL and W-ARD.

The hardness values obtained on the outside surface of the tube are:

Rockwell B Scale 73 + 1

The hardness values obtained on the inside surface of the tube are:

Rockwell B Scale 68 $\pm$ 3

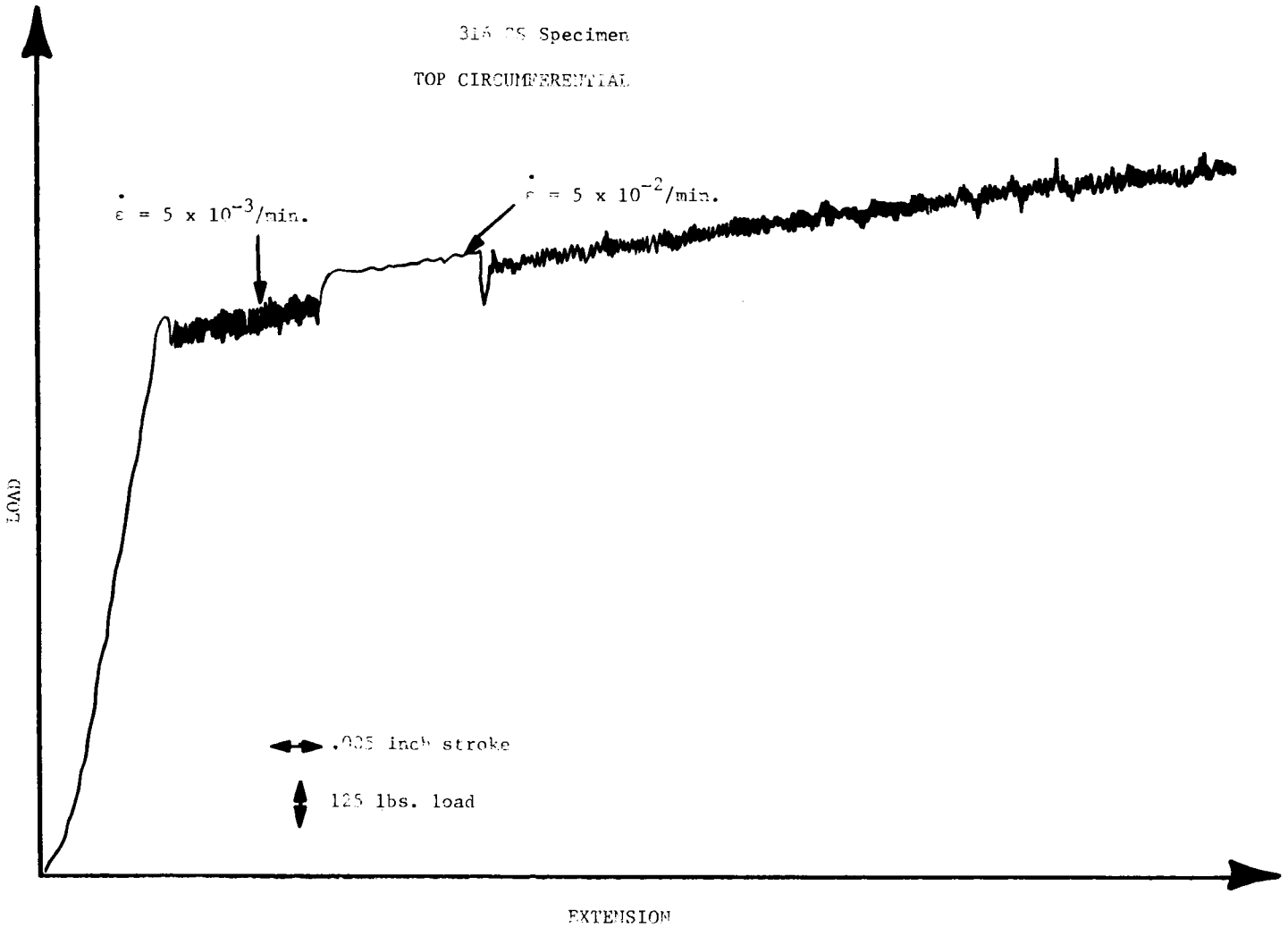

Figure 6.35. A Portion of Stress-Strain Curve Showing Serrations and Strain Rate Effect

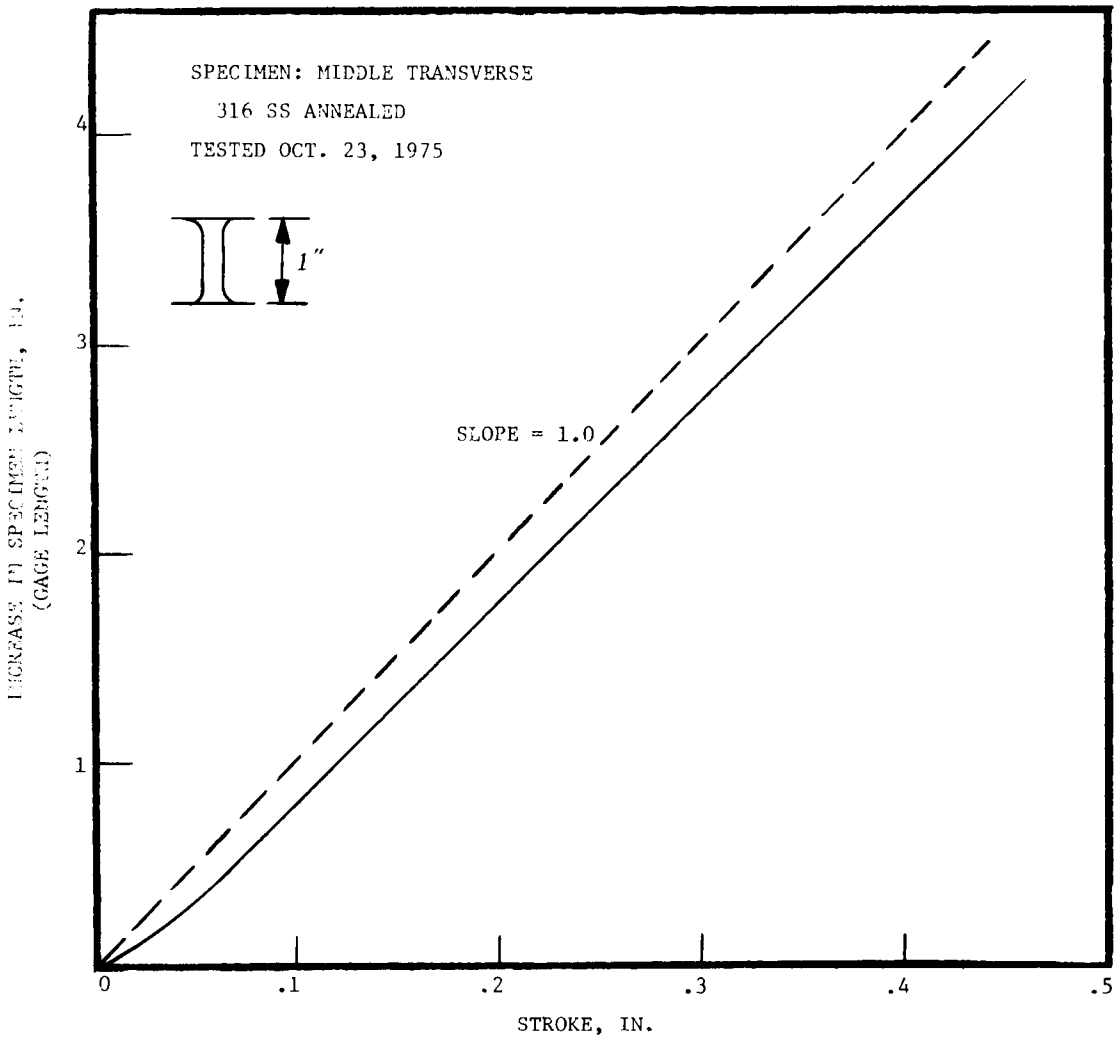

Figure 6.36. A Comparison Between Specimen Extension and Stroke as Measured by the MTS Machine Used for Tensile Testing

TABLE 6.5 MECHANICAL PROPERTIES OF 316 SS (REFERENCE HEAT 8092297)

SPECIMEN DIRECTION AND LOCATION	STRESS, KSI						
	PROPORTIONAL LIMIT	0.02% YIELD	0.2% YIELD	UTS	TOTAL ELONGATION,%	REDUCTION OF AREA, %	REMARKS
AXIAL							
Top	25.2	29.6	29.8	---	----	----	Strain control tests
Middle	20.0	22.8	33.6	---	----	----	
Bottom	24.0	29.6	39.8	---	----	----	
CIRCUMFERENTIAL							
Top	26.0	33.7	44.3	87.5	0.713	.684	Stroke control tests
Middle	25.0	31.8	43.7	88.1	0.69	.711	
Bottom	20.0	27.5	39.5	---	----	----	

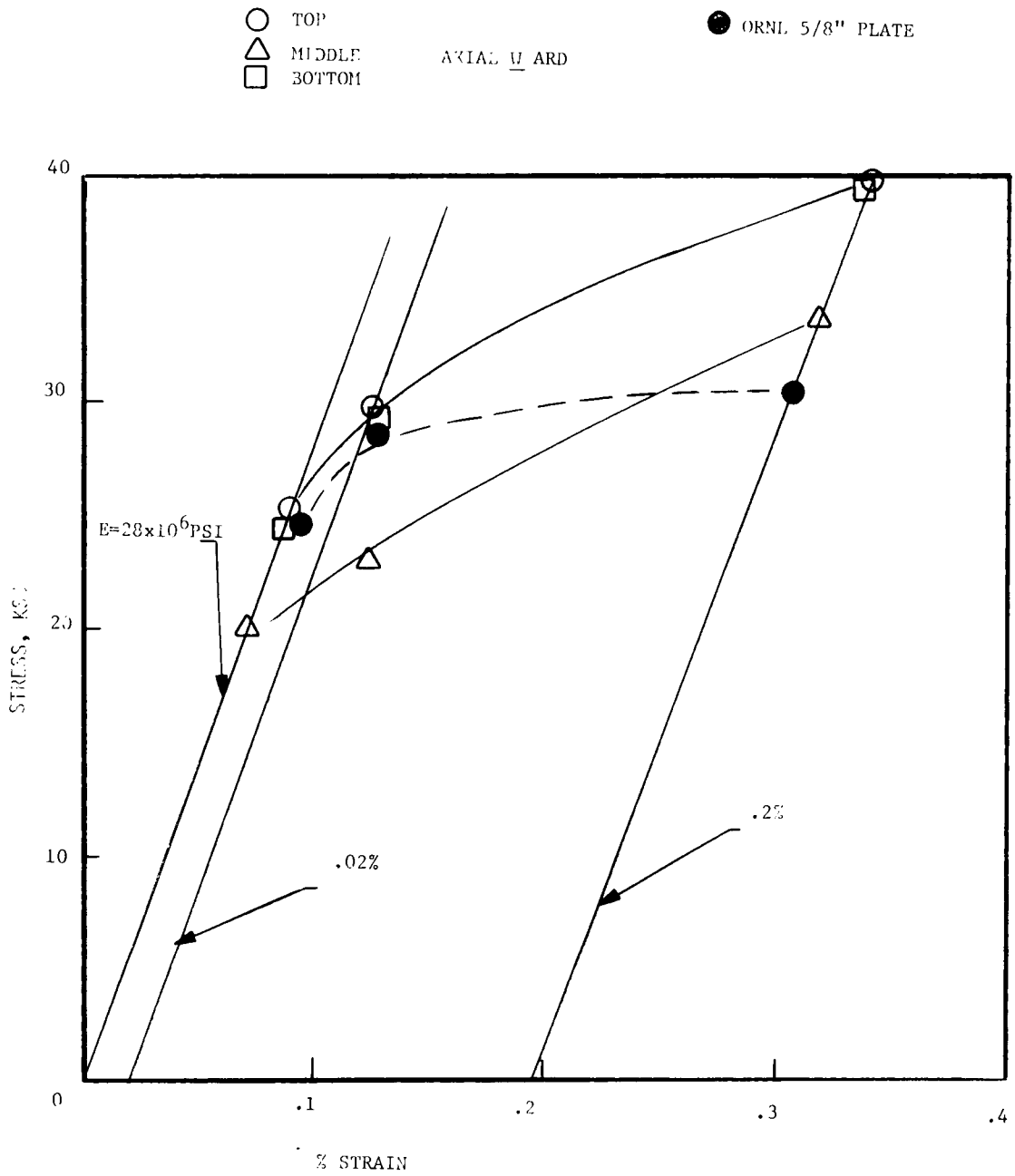

Figure 6.37. Stress-Strain Curves for WARD and ORNL Type 316 SS Specimens

6.3.7.3 Grain Size and Metallographic Examination

Sections of the heat treated pipe specimens were sectioned as shown in Figure 6.33 and examined metallographically. The grain size varied through the pipe wall as follows:

Inner Wall	ASTM #4
Center Region	ASTM #4-4-1/2
Outside Wall	ASTM #2

for the top, middle and bottom sections.

These results are similar to those obtained by ORNL on heat treated Type 306 pipe sections. However, since the O.D. of the pipe is machined by ∿mils to produce a reduced section in the creep specimen the actual grain size of the specimen wall will be ASTM #4 and is within the requirement of ASTM #3 to 5.

6.3.7.4 Fabrication Sequence for Tubular Specimens

The current method of fabricating tubular specimens, which was used for all Type 304 specimens is as follows:

1. Heat treat pipe blank.
2. Rough machine blank to .050° oversize.
3. Weld finish machined end plugs and extensometer lugs.
4. Using the end plugs as reference, final machine gage section.

The above sequence has been successful in producing parts to drawing tolerance. The hardness and 0.2% proof stress values have been within the range obtained by ORNL on specimens heat treated after machining[13]. Since other laboratories are testing similar specimens which have no machining on the gage length after heat treatment, it is believed appropriate at this stage to change the fabrication sequence so that machining of the gage length is not required after heat treatment. To achieve this the following fabrication sequence will be used to investigate whether existing drawing tolerances can be met:

1. Finish machine pipe blank.
2. Weld oversize end plugs.
3. Heat treat in argon.
4. Finish machine end plugs using gage section as reference datum.
5. Weld extensometer lugs.
6. Finish machine extensometer lugs.

Detailed dimensional checks will be made throughout fabrication to control the process.

New heat treatment equipment (furnace, argon purge and cooling system) and specimen temperature monitoring equipment is being built and is in the final stages of completion. Initial furnace calibration will be achieved with about eight thermocouples at strategic locations on the specimen inside and outside surfaces. After completion of this task Type 316 finish machined blanks will be heat treated and used for proof stress, hardness and grain size determinations, and also for pre-production fabrication studies.

6.4 SODIUM EFFECTS ON MECHANICAL PROPERTIES OF STRUCTURAL MATERIALS

P. N. Flagella, J. Kahrs, J. Denne, P. Wu, S. L. Schrock

6.4.1 Type 316 Stainless Steel

Mechanical property evaluations for solution annealed Type 316 SS, as affected by a flowing sodium environment, involves two heats of the material.

The first heat, purchased by Westinghouse ARD, consists of a limited number of test samples fabricated from solution annealed bar material. Sodium exposure and thermal aging of the samples was performed previously. Mechanical property tests in sodium of these samples provides an indication of the effect of the environment, including pre-treatment.

The second heat of solution annealed Type 316 SS to be used for the evaluations was obtained from the HEDL stockpile (Heat 65805) and is in plate form (1.0" thick). The larger number of test samples from this heat will allow a more detailed study on the effects of a sodium environment on the mechanical properties. Sodium exposure and thermal aging of samples at different temperatures for different amounts of time, prior to testing in sodium and in air, is presently in progress.

Creep-rupture testing of samples from the ARD heat of material was continued during this reporting period. Bar samples (0.25" dia. x 1.00" lg gage), each with a different prior history, were creep-rupture tested in flowing sodium at 1100°F (593°C) and stresses of 30.0 and 32.5 ksi. Table 6.6 lists the pre-treatment for each sample as well as the test conditions and results. The data show significant differences in the strain-on-loading, minimum creep rate, rupture life, and ductility between the as-fabricated and the pre-treated samples when tested at the same conditions. Creep-rupture curves for the as-fabricated and sodium pre-exposed samples tested at 30.0 and 32.5 ksi are shown in Figure 6.38. The increase in ductility and decrease in rupture life for the sodium pre-exposed samples is obvious. Somewhat surprising is the lower values of strain-on-loading (ε_o) and the much shorter time to the end of primary creep for the sodium pre-exposed samples when compared to the as-fabricated samples, tested at the same stress. It is considered, these differences are mainly due to the time at temperature during the pre-treatment causing significant changes in the microstructure of the material. Metallographic evaluations have not yet been made but are planned.

Figure 6.39 presents the (total-strain versus time) creep curves, on log-log coordinates, for the as-fabricated samples (Figure 6.39A) and the samples sodium pre-exposed at 1325°F (718°C) for 5,000 hours (Figure 6.39B). The technique expands the short time data, especially the primary creep curve, and condenses the long time data. Although the curve shapes for each figure are quite different; within each figure consistent curve shapes for the two stress levels are shown. When the loading strain, ε_o, for each test is subtracted from the total strain data, the creep-strain versus time curves shown in Figure 6.40 are obtained. The

TABLE 6.6 CREEP-RUPTURE DATA FOR S.A. TYPE 316 SS[a] TESTED IN FLOWING SODIUM AT 1100°F[b]

Sample Number	Stress ksi	Pre-Treatment for 5,000 hr. Envir.	Pre-Treatment for 5,000 hr. Temp. °F	Loading Strain	Hours to Indicated Creep Strain,% 0.5	1.0	2.0	3.0	5.0	7.0	10.0	Min. Creep Rate %/hr.	0.2% Offset Time hr.	0.2% Offset Creep Strain %	Time to Rupture hr.	Total Elong. % Creep Curve	Total Elong. % Post Test
030	32.5	As-Fabricated		8.10	1.7	5.1	16.0	36.0	125	268	446	1.80×10^{-2}	487	11.0	684	29.3	29.7
033	32.5	Sodium	1200	4.32	2.7	9.1	32.7	64.8	135	200	280	2.90×10^{-2}	218	7.7	705	72.3	75.0
037	32.5	Sodium	1325	4.62	3.2	10.3	27.0	46.2	82.0	117	168	5.60×10^{-2}	170	10.2	456	63.9	64.0
031	32.5	Argon	1325	3.40	2.9	7.1	18.4	37.0	77.0	118	185	5.38×10^{-2}	242	13.4	572	80.6	79.7
043	30.0	As-Fabricated		5.70	2.3	12.5	69.0	185	800	1410	1865	3.34×10^{-3}	1510	7.5	2319	27.6	
039	30.0	Sodium	1325	1.34	12.2	32.5	73.5	115	197	280	387	2.42×10^{-2}	348	8.8	1085	63.3	65.6

(a) Westinghouse ARD Heat

(b) Bar samples, 0.25" dia. x 1.00" lg. gage section

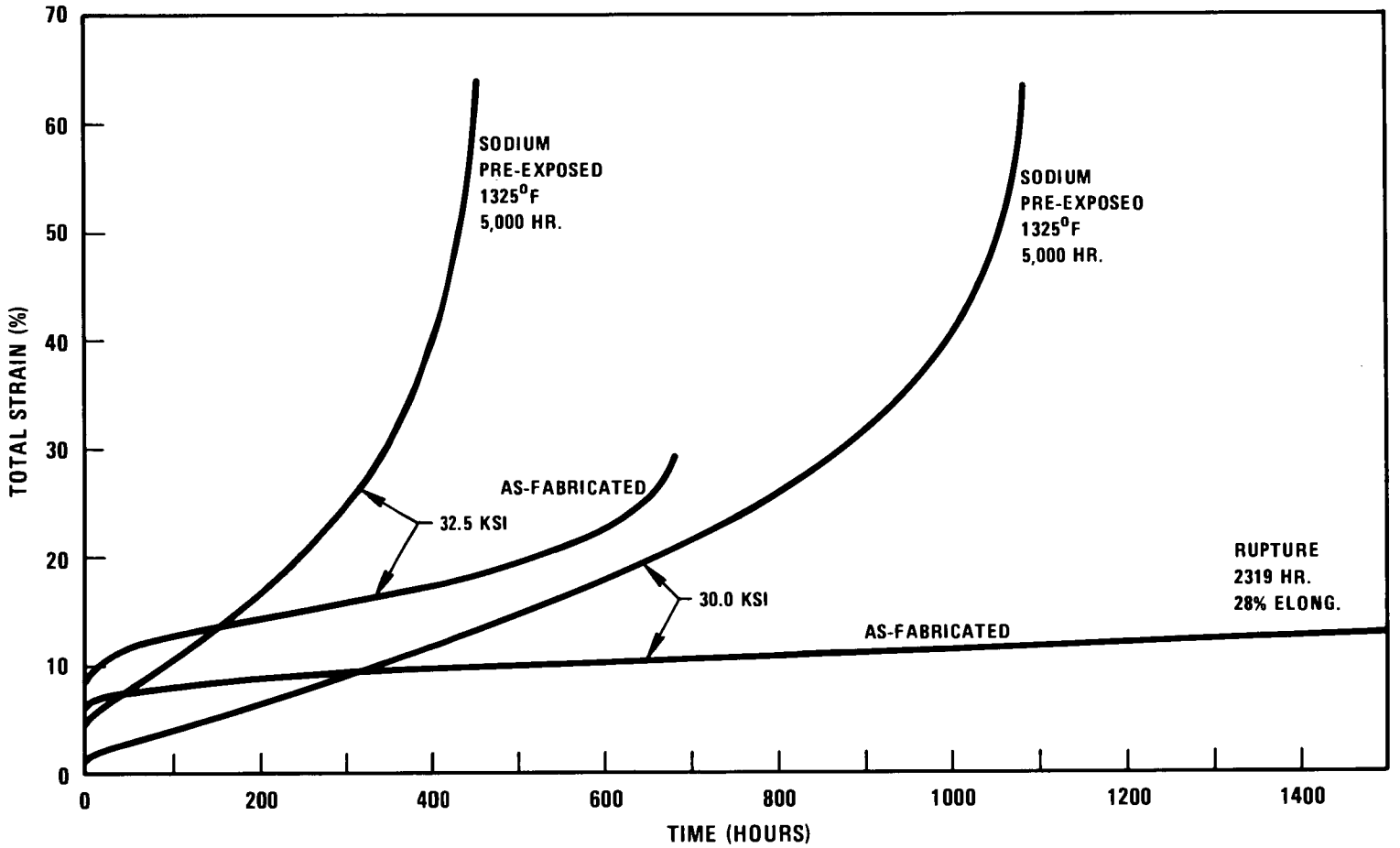

Figure 6.38. Creep-Rupture Curves for S.A. Type 316 SS Tested at 1100°F in Flowing Sodium

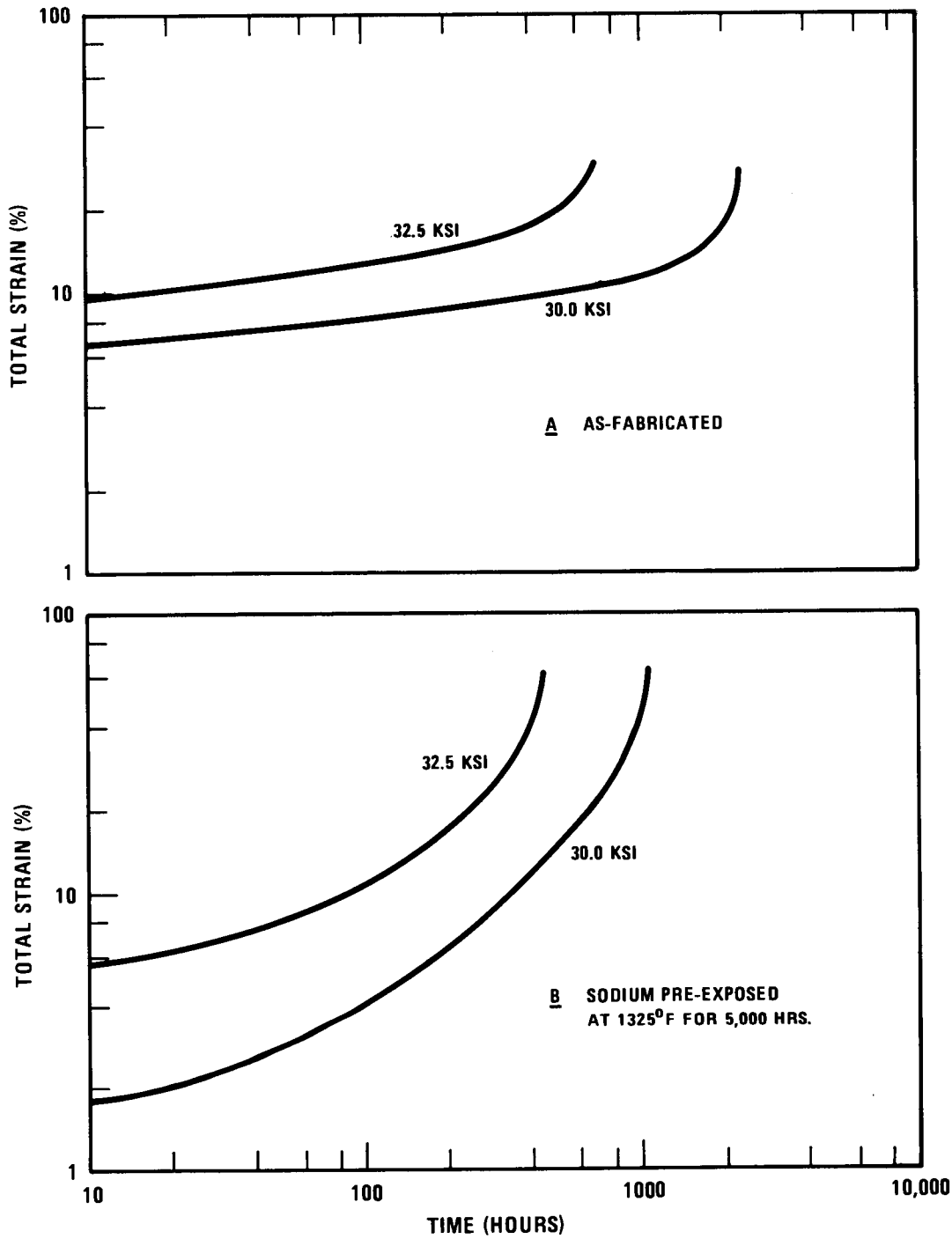

Figure 6.39. Total-Strain Creep Curves (log-log) for S.A. Type 316 SS Tested at 1100°F in Flowing Sodium

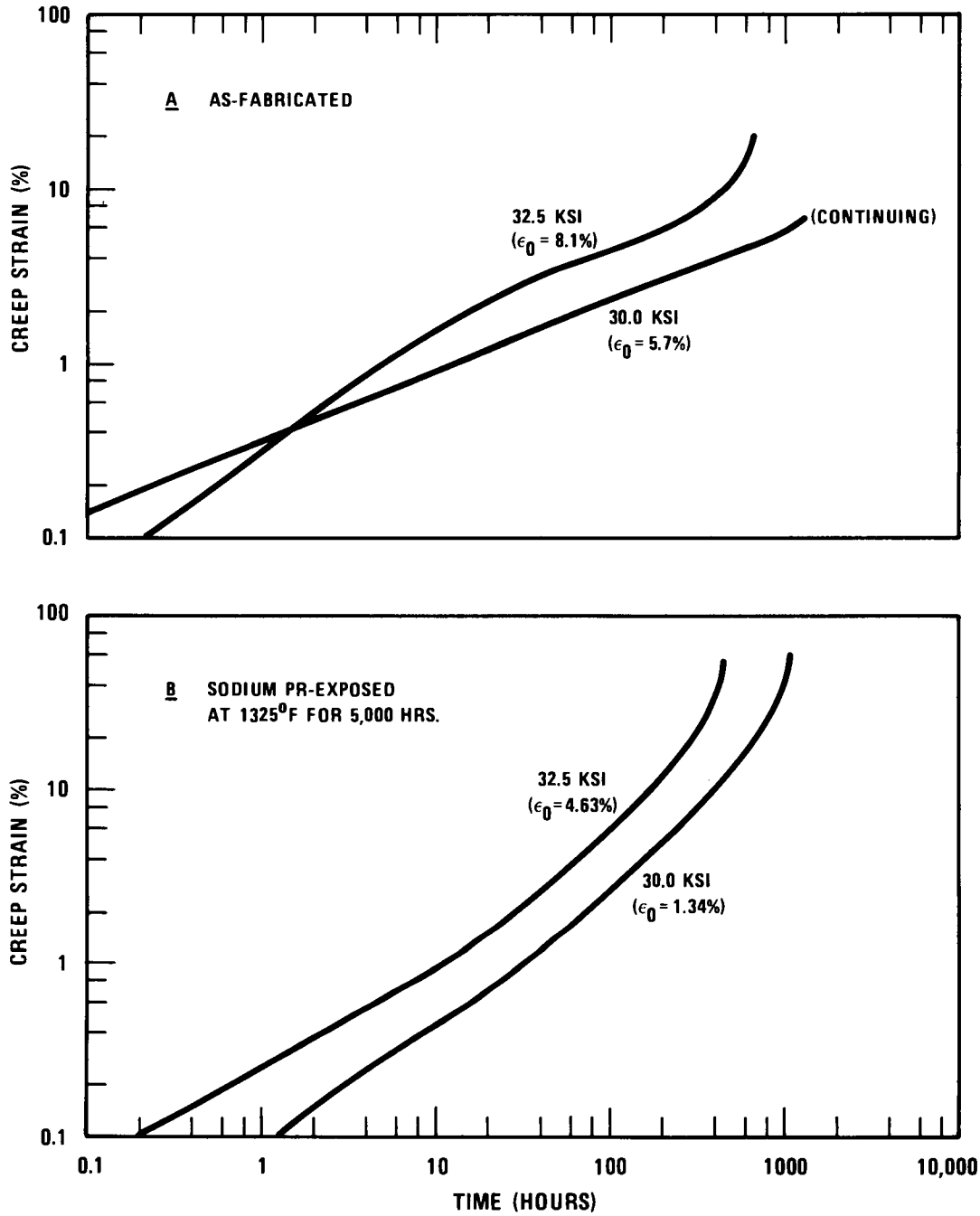

Figure 6.40. Creep-Strain Creep Curves (log-log) for S.A. Type 316 SS Tested at 1100°F in Flowing Sodium

two curves for the sodium pre-exposed samples (Figure 6.40B) show exceptional similarity indicating no difference in the mechanism of creep. On the other hand, the curves for the as-fabricated samples (Figure 6.40A) are quite different from each other, especially to approximately 3.5% creep-strain. This is the region associated with primary creep, indicating possible differences in the creep mechanism at the two stress levels.

This difference in creep mechanism is supported further by the minimum creep rate and rupture life correlations shown in Figures 6.41 and 6.42 respectively. The bulk of the data shown in the figures were published by Blackburn[14] for tests performed in air, and are used for comparison to the results of this report obtained in flowing sodium at 1100°F (593°C). Most creep rate and stress-rupture data, when plotted as a function of stress, are presented on log-log coordinates, as are these data, but in most cases the scale factor for both coordinates are the same. This does allow general curve shapes and data trends to be determined, but does not lend itself to identifying smaller changes in the trend of the data, if they do exist, since the slope of the curves are usually quite shallow. The stress scale for Figures 6.41 and 6.42 have been increased by a factor of 5 (still log-log) over the abscissa, increasing the slope of the curves showing the data trends. This technique also exaggerates data scatter, and interpretation, analysis, and judgment are required to differentiate real trend changes or discontinuities from scatter. Using this approach, Figure 6.41 shows that at 1100°F (593°C) and between approximately 30 and 35 ksi the creep rate data of Blackburn decreases more rapidly than the overall trend. The two in-sodium tests for as-fabricated material show the same trend, with a factor of 2 to 3 increase in creep rate over the in-air results. The two independent sources of data (also involving different test environments) appear to substantiate the deviation from the overall trend. Although the stress-rupture data at 1100°F (593°C) in Figure 6.42 show significant scatter, a similar deviation, from the general trend is strongly indicated between the stresses 30 and 35 ksi using minimum rupture life data in the transition region. Although rupture data beyond 2,500 hours for lower stresses are not available, the Blackburn tests at 30 ksi, (which were discontinued after ∿4,000 hours) appear to

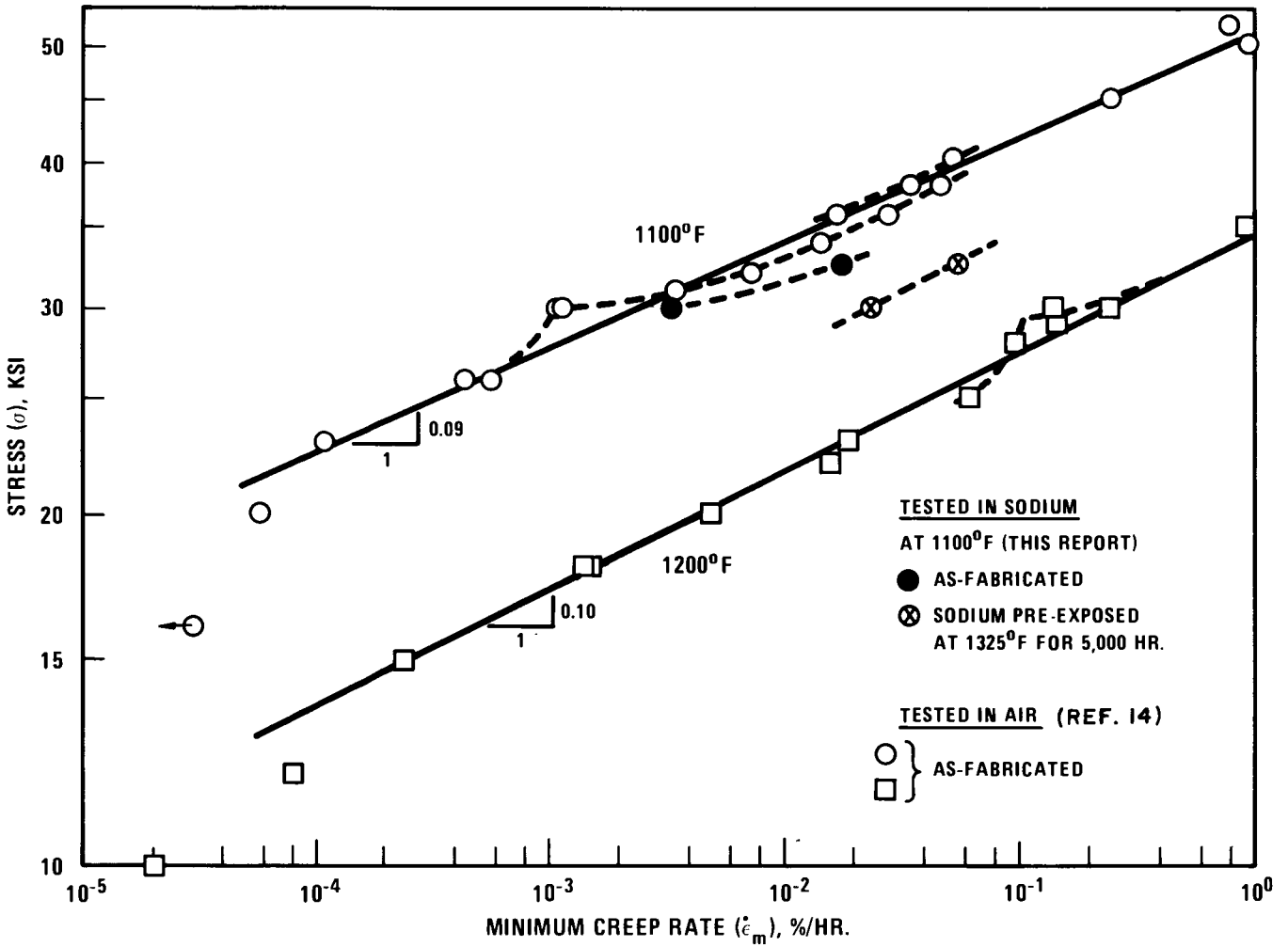

Figure 6.41. Comparison of Creep-Rate Results for S.A. Type 316 SS Tested in Air and Sodium

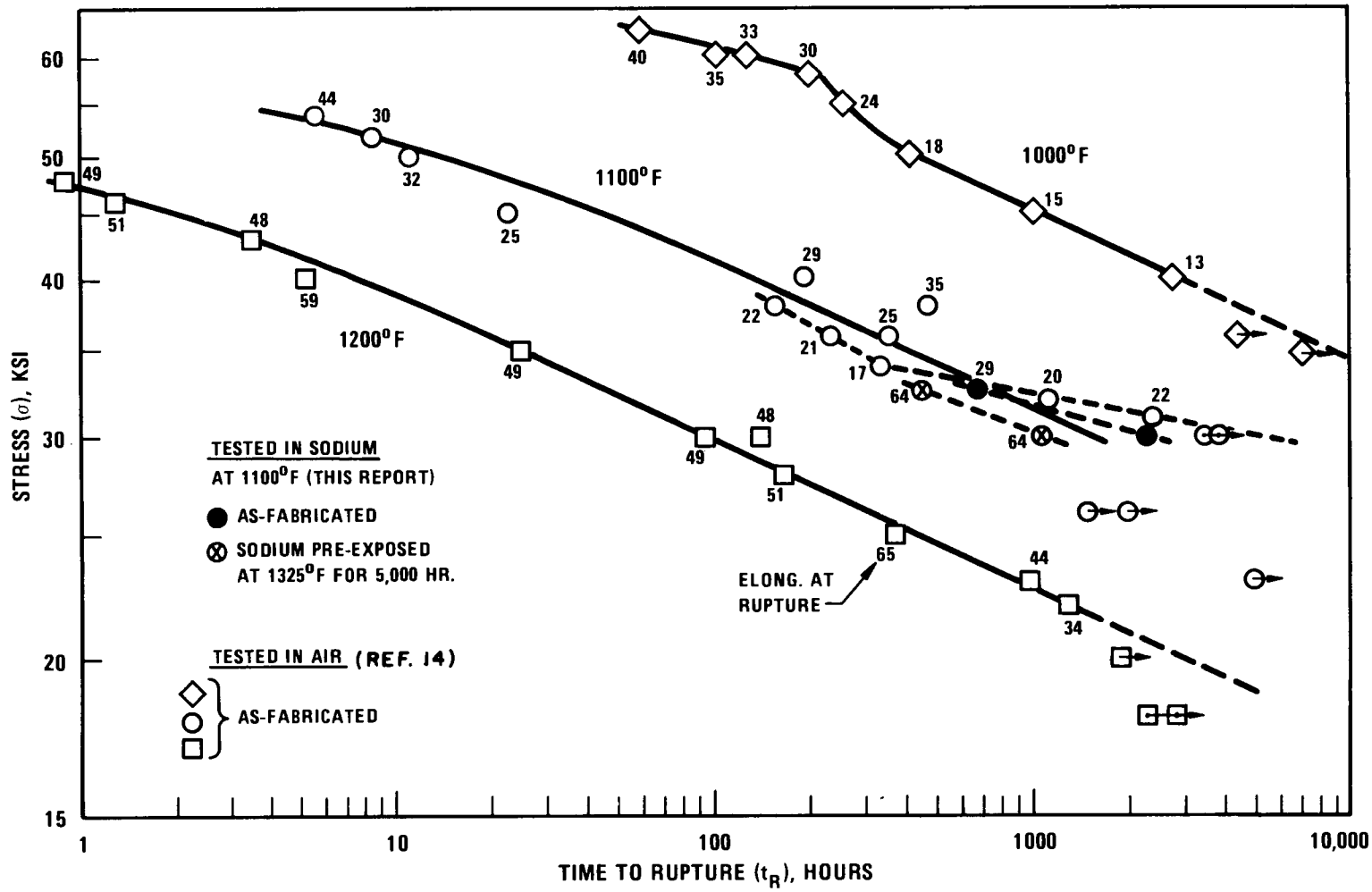

Figure 6.42. Comparison of Stress-Rupture Results for S.A. Type 316 SS Tested in Air and Sodium

support the deviation. Since the minimum creep rate data at 1100°F below 30 ksi appear to again follow the overall trend, the stress-rupture data will also probably follow the overall trend below 30 ksi, but possibly at the sacrifice of rupture ductility. Stress-rupture tests to failure below 30 ksi will be required to evaluate this possibility.

Further analysis was performed on the low cycle fatigue data previously reported[15] for Type 316 SS. The Westinghouse heat of solution annealed material was tested in flowing sodium with 2 ppm oxygen at 1100°F (593°C) after various pre-treatments. The results showed that at a total strain range of 1%, the fatigue life in sodium for as-fabricated material is essentially the same as that obtained in air[16]. On the other hand, at a strain range of 0.5%, the fatigue life in sodium for the as-fabricated material is increased by a factor of two over the in-air data. These results indicate that, as the time of testing in-sodium increases, the more significant the effect of the sodium environment on the fatigue life. Sodium pre-exposure or argon aging of the same material at 1325°F (718°C) for 5,000 hours increased the fatigue life by a factor of four over as-fabricated material when tested at 1100°F (593°C) and a total strain range of 1%, while sodium pre-exposure or argon aging at 1200°F (649°C) increased the fatigue life by a factor of two when tested at 1100°F (593°C) and a total strain range of 1%. These increases in fatigue life are mainly attributed to the metallurgical changes in the material resulting from the thermal pre-treatments, which reduces the strength and increased the ductility. This is supported by the results reported above on the creep-rupture tests at 1100°F in-sodium for the same material, with and without pre-treatment.

Figures 6.43 and 6.44 present the cyclic stress response for the above mentioned low cycles fatigue tests performed in sodium, with Figure 6.45 showing the cycle response for 0.1 hour tension-only hold time tests at a total strain range of 1%. It can be seen that, in all but one case, the stress range for the as-fabricated material is lowest initially, indicating a lower monotonic yield strength. With cycling,

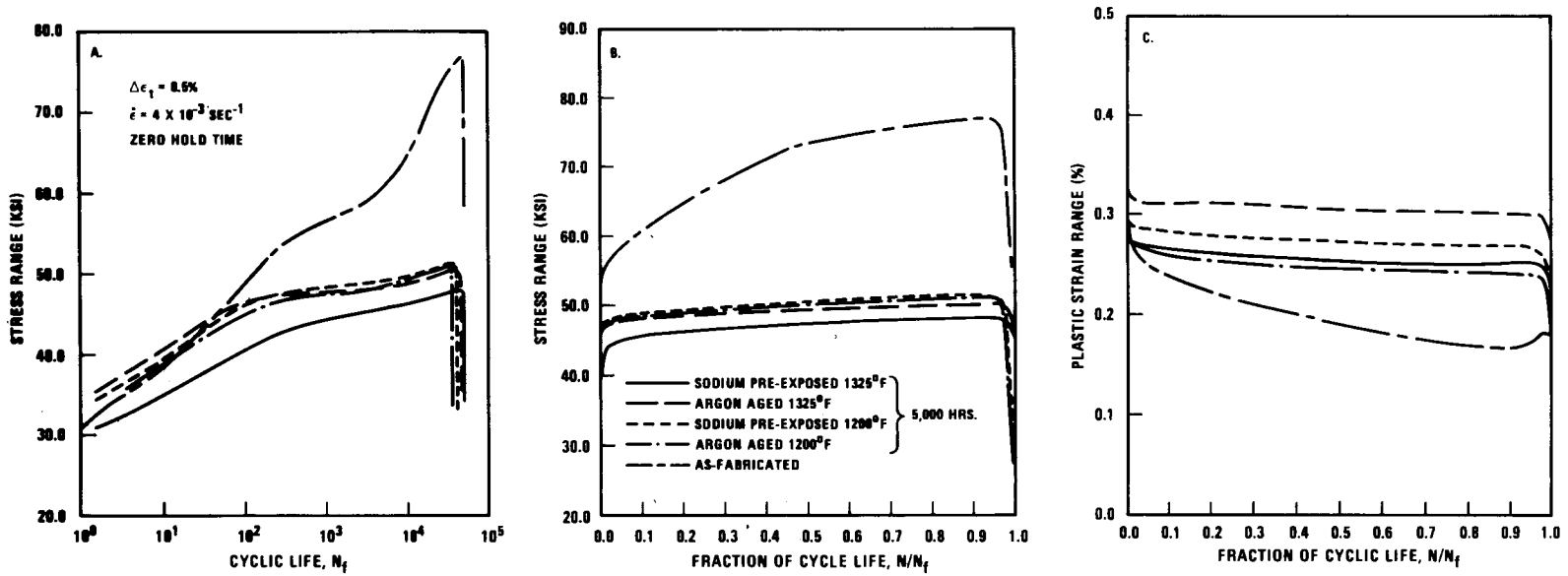

Figure 6.43. Cyclic Stress and Strain Response for S.A. Type 316 SS Tested in Flowing Sodium at 1100°F (593°C) with $\Delta\varepsilon_t$ = 0.5%

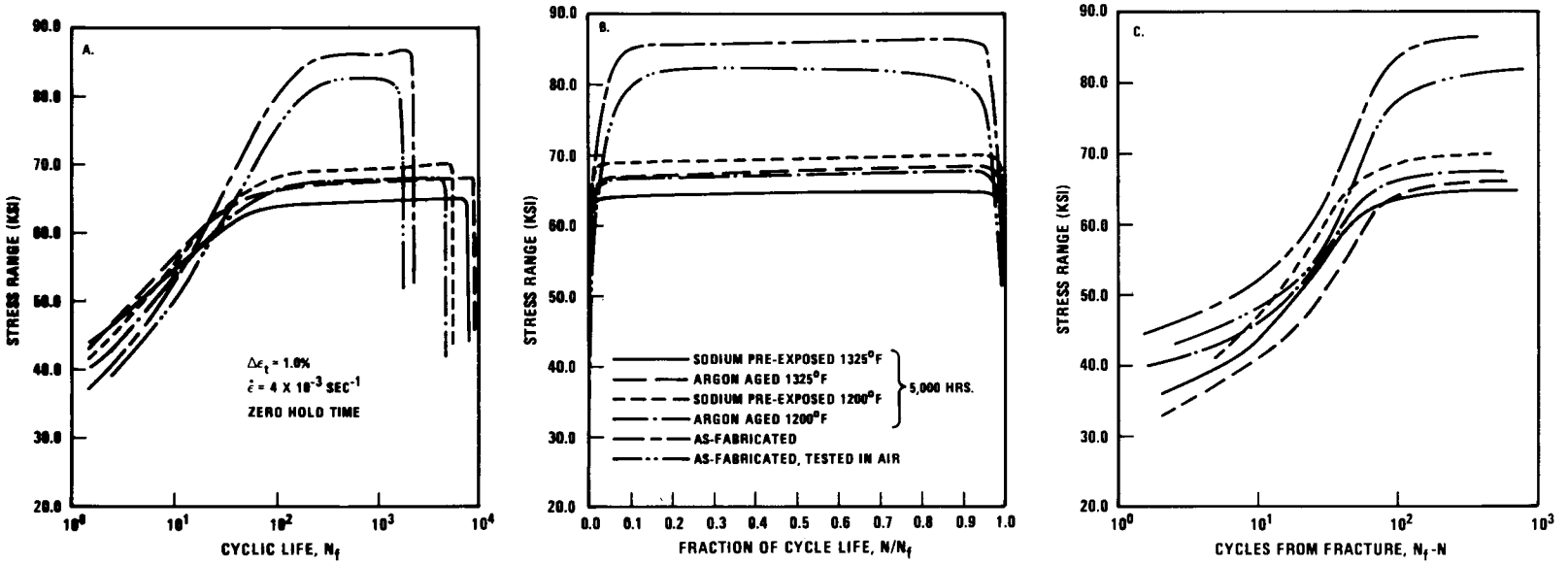

Figure 6.44. Cyclic Stress Response for S.A. Type 316 SS Tested in Flowing Sodium at 1100°F (593°C) with $\Delta\varepsilon_t$ = 1%

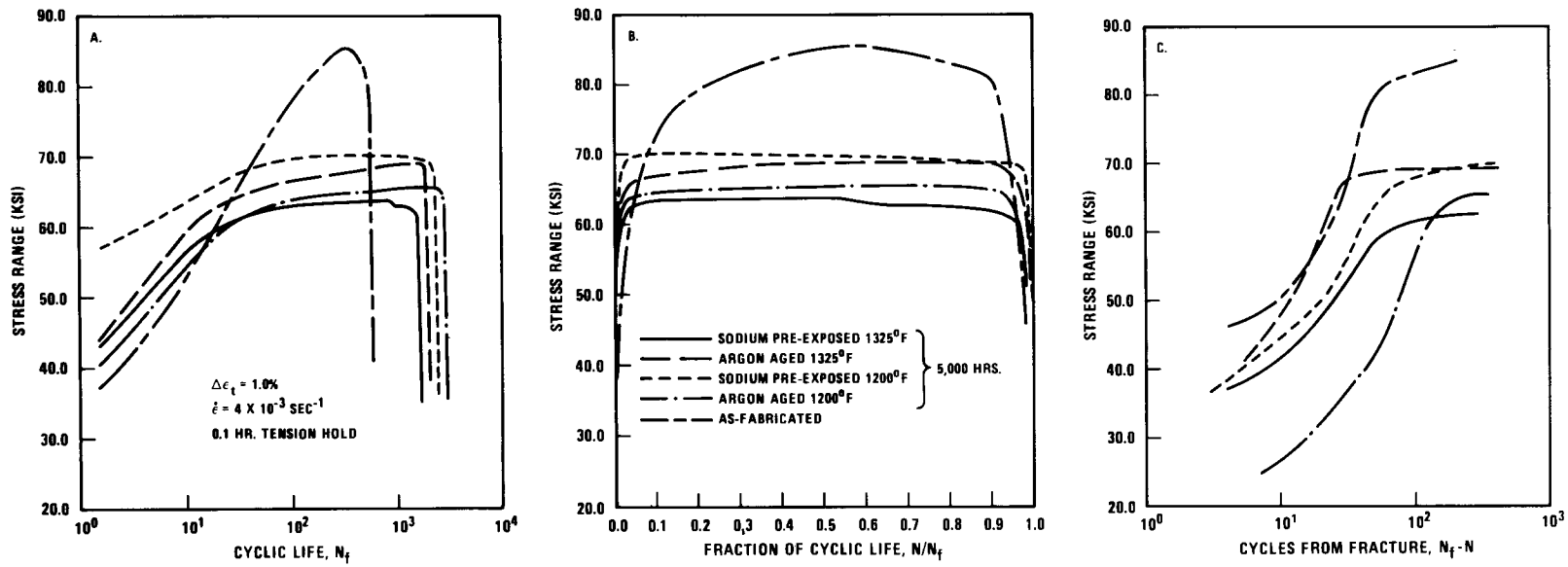

Figure 6.45. Cyclic Stress Response for S.A. Type 316 SS Tested in Flowing Sodium at 1100°F (593°C) with $\Delta\varepsilon_t$ = 1% and 0.1 Hour Tension Hold

the stress range increases to a value significantly higher than any of the tests involving samples with pre-treatment, implying a greater creep strength. This is consistent with the creep-rupture results discussed earlier where, at the same initial stress at 1100°F (593°C), the strain-on-loading was highest for the as-fabricated material, indicating a lower yield strength, but at the same time having the lowest minimum creep rate and ductility. The curves for the 1% strain range tests involving pure fatigue (Figures 6.44A and 6.44B) show that the stress range for all tests are essentially saturated after a relatively few number of cycles. The same can be said for the 0.5% strain range tests, with the exception of the as-fabricated material. In the stress range vs. cyclic life plot (semilog), near saturation is indicated for the as-fabricated material after a few thousand cycles but then secondary hardening takes over. A decreased hardening rate finally occurs near $N_f/2$. In spite of this high stress range, the fatigue life is approximately the same as that obtained for the pre-treated samples at a strain range of 0.5%. This is not the case for the 1% curve. It is interesting to note that the 1325°F sodium pre-exposed samples have the lowest stress range for each of the three test conditions presented in the figures. This may be a sodium effect resulting from the pre-exposure for 5,000 hours.

Figures 6.44C and 6.45C present stress range vs. log cycles-from-fracture for the different tests in an attempt to evaluate crack propagation for pure fatigue and creep/fatigue tests in a sodium environment. No consistent trends or differences are apparent, other than the stress range decrease vs. cycles for the as-fabricated material is more rapid initially. This may be due to the higher stress range associated with these tests. The pure fatigue tests for as-fabricated material (Figure 6.44C) show that the stress range drops off for the in-air test begins much earlier than the in-sodium test. This indicates that crack initiation occurred much earlier for the in-air test.

6.5 REFERENCES

1. T. N. Winter and W. J. McDonald, "Biaxial Residual Surface Stresses from Grinding and Finish Machining 304 Stainless Steel Determined by New Dissection Techniques," Trans. Am. Soc. Mech. Engrs., 91, Series D, pp. 15-22, 1969.

2. R. T. King, G. M. Goodwin, R. S. Crouse, and E. Bolling, "Characterization Tests of Type 308 CRE Stainless Steel Welds in Type 304 Reference Heat Base Metal" in "Mechanical Properties Test Data for Structural Materials Quarterly Progress Report for Period Ending October 31, 1975," ORNL-5107, pp. 112-126, December 1975.

3. M. J. Manjoine, "Determination of Plastic or Creep Strains by Grids" in "Mechanical Testing and Recent Techniques Being Used," STP 608, American Society for Testing and Materials, Phila., Pa. (to be published in 1976).

4. "Validation of High Temperature Design Methods and Criteria. Quarterly Progress Report for Period Ending November 30, 1974, "WARD-HT-3045-8, March, 1975 (Availability: USERDA Technical Information Center).

5. M. J. Manjoine, "Elevated Temperature Mechanics of Metals," in "Mechanical Behavior of Materials," The Society of Materials Science, Japan, pp. 193-214, 1974.

6. M. J. Manjoine, "Ductility Indices at Elevated Temperature," Am. Soc. Mech. Engrs., 97, Series H, pp. 156-161, 1975.

7. "Validation of High Temperature Design Methods and Criteria. Quarterly Progress Report for Period Ending May 31, 1973," WARD-HT-3045-2, August, 1973 (Availability: USERDA Technical Information Center).

8. W. L. Greenstreet, J. M. Corum, and C. E. Pugh, "High-Temperature Structural Design Methods for LMFBR Components. Quarterly Progress Report for Period Ending June 30, 1973," ORNL-TM-4356, December, 1973 (Availability: USERDA Technical Information Center).

9. H. E. McCoy, "Interim Report of Tensile and Creep Data for Type 304 Stainless Steel Plate (Reference Heat 9T2796, 2 in. Thick)," ORNL-TM-4627, October, 1974 (Availability: USERDA Technical Information Center).

10. "Design Data," in Nuclear Systems Materials Handbook, Hanford Engineering Development Lab., Richland, Wash., TID-26666, Vol. 1, Bk. 2.

11. S. Taira and R. Ohtani, "Creep of Tubular Specimens Under Combined Stress," in Advances in Creep Design, Chpt. 15, pp. 289-328, John Wiley & Sons, Inc., New York, 1971.

12. Private communication, K. C. Thomas (WARD) with R. Swindeman (ORNL).

13. "Validation of High Temperature Design Methods and Criteria. Quarterly Progress Report for Period Ending November 30, 1973," WARD-HT-3045 -4, March, 1974 (Availability: USERDA Technical Information Center).

14. The Generation of Isochronous Stress-Strain Curves, ASME/MPC, pp. 15-48, November 1972.

15. ORNL-5112, Mechanical Properties Test Data for Structural Materials Quarterly Progress Report for Period Ending January 31, 1976.

16. C. R. Brinkman and G. E. Korth, "Low Cycle Fatigue and Hold-Time Comparisons of Irradiated and Unirradiated Type 316 Stainless Steel," Met. Trans. 5, pp. 792-794 (1974).

7. UNIVERSITIES

7.1 UNIVERSITY OF CINCINNATI

J. Moteff

7.1.1 INTRODUCTION

The objective of this program is to (a) evaluate the time, temperature and stress-dependent mechanical properties of reactor structural materials, (b) determine the relationship of these properties to the microstructure, (c) show the contribution of the microstructure to the internal stress fields and the subsequent influence on microcracking and the grain boundary sliding behavior during the normal plastic deformation at elevated temperatures and (d) demonstrate the relationship of the hot micro-hardness properties with the hot-tensile properties of a class of commercial and advanced alloys presently under investigation at other laboratories. Special consideration is being given to operating conditions typical of nuclear reactor applications, including the knowledge that radiation environment can influence the substructure of these metals, a circumstance which can lead to significant changes in the conventional mechanical property behavior.

7.1.2 EXPERIMENTAL PROGRAM

Transmission electron microscopy has been used as the primary tool to study the deformation substructure of reactor structural materials resulting from creep, fatigue and tensile testing at elevated temperatures. Complementary work using optical microscopy, scanning electron microscopy and hot-

hardness testing has been performed to characterize the deformation and failure behavior. New work is underway to perform similar studies on the Commercial, the Developmental and the Fundamental alloys being evaluated in the National Alloy Developmental Program with particular attention on the application of hot-hardness measurement as a strength microprobe.

7.1.2.1 Further Analysis of Fatigue Substructure Data for Incoloy 800 (H. Nahm)

The relation between the cell intercept size and the flow stress may be appropriately described by an equation of the following form:

$$\lambda = k_o \left(\frac{\tau}{G} \right)^{-n} \qquad [7.1]$$

where k_o is a constant, τ is the shear stress and $\underline{n}$ takes a value between one and three. The value of one for $\underline{n}$ was theoretically predicted by Holt[1], Kuhlmann-Wilsdorf[2] and Langford and Cohen[3]. Recently Young and Sherby[4] developed a model yielding n = 2. This general relationship has been experimentally confirmed both for the unidirectional deformation[3-14] and for the cyclic deformation[15-21] in a wide range of materials at various testing temperatures.

Recently it was observed in high temperature creep of AISI 304 and 316 stainless steels[9,13] that the dislocation cell or subgrain intercept, λ, has been related to the modulus compensated shear stress by the equations:

$$\lambda \simeq 12b\ (\tau/G)^{-1} \qquad [7.2]$$

for the case of subgrains, and

$$\lambda \simeq 5 \times 10^{-2} b\ (\tau/G)^{-2} \qquad [7.3]$$

for the case of cells, with the transition occurring at a value of τ/G equal to approximately 4.2×10^{-3}. The constant b is the Burgers vector.

The present results for the fatigued Incoloy 800 (Fig. 9 in reference 22) indicate that n is somewhat higher than 2 which is consistent with the results of Challenger and Moteff[10] for fatigued AISI 316 stainless steel at elevated temperature. The difference in the observed value of n is not known at the present time; it appears to be a complex function of the material, alloying and the applied stress as suggested by Young and Sherby[4]. It is also possible that the difference might be from the fatigue deformation.

The subboundary intercept and the dislocation density were found to be a function of the plastic strain range employed as shown in Fig. 9 and Fig. 10, in the reference 22 respectively. The subboundary intercept initially increases and reaches a saturated value with increasing plastic range at constant value of $\Delta\sigma/2G$ (see Fig. 9 of the reference 22). Dislocation density shows the similar dependency on the plastic strain range (see Fig. 10 of the reference 22).

Despite the differences mentioned above, the general inverse relation between the cell size and the flow stress

strongly indicates that a similar deformation mechanism is operating in both monotonic and cyclic deformation. Furthermore, a wide range of parallelisms of deformation mechanisms exist in either single phase or multi-phase materials[15,23-25]. Feltner and Laird[15] interpreted their data for the high amplitude saturation stress observed in Cu and Cu-Al alloys by using Kuhlmann-Wilsdorf's[26] work hardening theory for stage II. Similarly, Calabrese and Laird[25] used Ashby's workhardening theory for plastically non-homogeneous materials[27] to explain the fatigue properties of a two phase alloy (Al - 4% Cu) with particles not penetrated by dislocations. It seems, therefore, quite reasonable to take a similar approach in correlating the present substructure data of Incoloy 800 with the observed fatigue properties.

Since Ashby's theory is going to be slightly modified in interpreting the present fatigue data, it is appropriate to briefly describe Ashby's workhardening theory for plastically non-homogeneous materials, especially for the case of materials with non-deformable plate-like particles. Most materials are "plastically non-homogeneous" because of the existence of the gradients of deformation due to microstructure. For example, the hard particles deform less than the matrix. This difference in deformation should be accommodated by "geometrically necessary" dislocations to allow compatible deformation of the different component in the matrix. Thus, most materials can be defined as "plastically non-homogeneous"

possibly with the exception of single crystals. The other type of dislocations are called "statistically stored" dislocations which result from the mutual trapping of one another, often found in the uniform deformation of single crystal. When the accumulation of "geometrically necessary" dislocation becomes more than that of "statistically stored" dislocation, the former starts to be a controlling factor in the work-hardening behavior of materials.

The density of the "geometrically necessary" dislocations, ρ_G, is given by

$$\rho_G = \frac{1}{\lambda_G} \frac{4\gamma}{b} \qquad [7.4]$$

where γ is the shear strain, b is the Burgers vector, λ_G is "geometric slip distance" which is characteristic of microstructure. For the case of alloys with non-deforming plate-like particles, λ_G becomes the spacing between plates.

A theoretical relationship between the flow stress, τ, and the total dislocation density, ρ_T,

$$\tau = \tau_o + \alpha Gb\sqrt{\rho_T} \qquad [7.5]$$

has been found to be true in a wide range of deformed FCC and BCC metals, where τ_o is the frictional stress, G is the shear modulus, b is the Burgers vector, α is a constant to be $\sim$ 0.3 and ρ_T is the sum of the density of "geometrically necessary" dislocations, ρ_G, and that of "statistically stored" dislocations, ρ_s.

In case ρ_G is dominant, ρ_T becomes equal to ρ_G. Substituting equation [7.4] into [7.5], an equation of the type,

$$\tau = \tau_o + 2CG\sqrt{\left(\frac{b\gamma}{\lambda_G}\right)} \qquad [7.6]$$

is obtained where C is a constant. Equation [7.6] is Ashby's work-hardening theory for the plastically non-homogeneous materials. This relation shows the parabolic stress-strain relationship, often observed in the polycrystalline materials.

Similar to equation [7.4], a relation of the form,

$$\rho = \alpha\left(\frac{\gamma_p}{b\lambda'}\right)^m \qquad [7.7]$$

is assumed to follow in the cyclic deformation behavior of Incoloy 800, where ρ is the dislocation density, γ_p is the plastic shear strain amplitude, b is the Burgers vector, γ' is the cell or subgrain diameter from $\lambda' = 1.68\ \lambda$[1] and α,m are constants. The above assumption appears to be reasonable since the subboundaries, once formed, may play a role as barriers to mobile dislocations similar to the role of phases during deformation; and the dislocation density is expected to increase with increasing plastic strain range. It is not known at the present time, however, what the exact role of subboundaries is on plastic deformation.

Since the observations made by the TEM are essentially made inside a single crystal, the following relations were used to convert the stress and strain in Incoloy 800 into

that of single crystal,

$$\Delta\sigma/2 = \sigma = M_p \tau_s \qquad [7.8]$$

$$\gamma_p = M_p \varepsilon_p = M_p \frac{\Delta\varepsilon_p}{2} \qquad [7.9]$$

where M_p is the numerical factor, $\Delta\sigma/2$ or σ is the saturation stress at half fatigue life, $\Delta\varepsilon_p/2$ or ε_p is the plastic strain amplitude, τ_s is the saturation shear stress for single crystal and γ_p is the saturation shear plastic strain for single crystal. The value of 3.1 for M_p calculated by Taylor[28] for FCC materials was used in the present study. This value may be approximate because M_p appears to be also a function of temperature[28].

In order to check the validity of the assumptions previously made, the dislocation density as a function of the parameters $(\gamma_p/b\lambda')$ for Incoloy 800 is plotted in Fig. 1. Experimental verification of equation [7.7] appears to be satisfactory from Fig. 1, considering the error involved in measuring the dislocation density.

If we substitute equation [7.7] into equation [7.5], the following type of equation is obtained

$$\tau_s/G = A\left(\frac{b\gamma_p}{\lambda'}\right)^n \qquad [7.10]$$

This equation has a form similar to Ashby's workhardening theory, equation [7.6], except for the power relationship instead of the square root of the term $(b\gamma_p/\lambda')$.

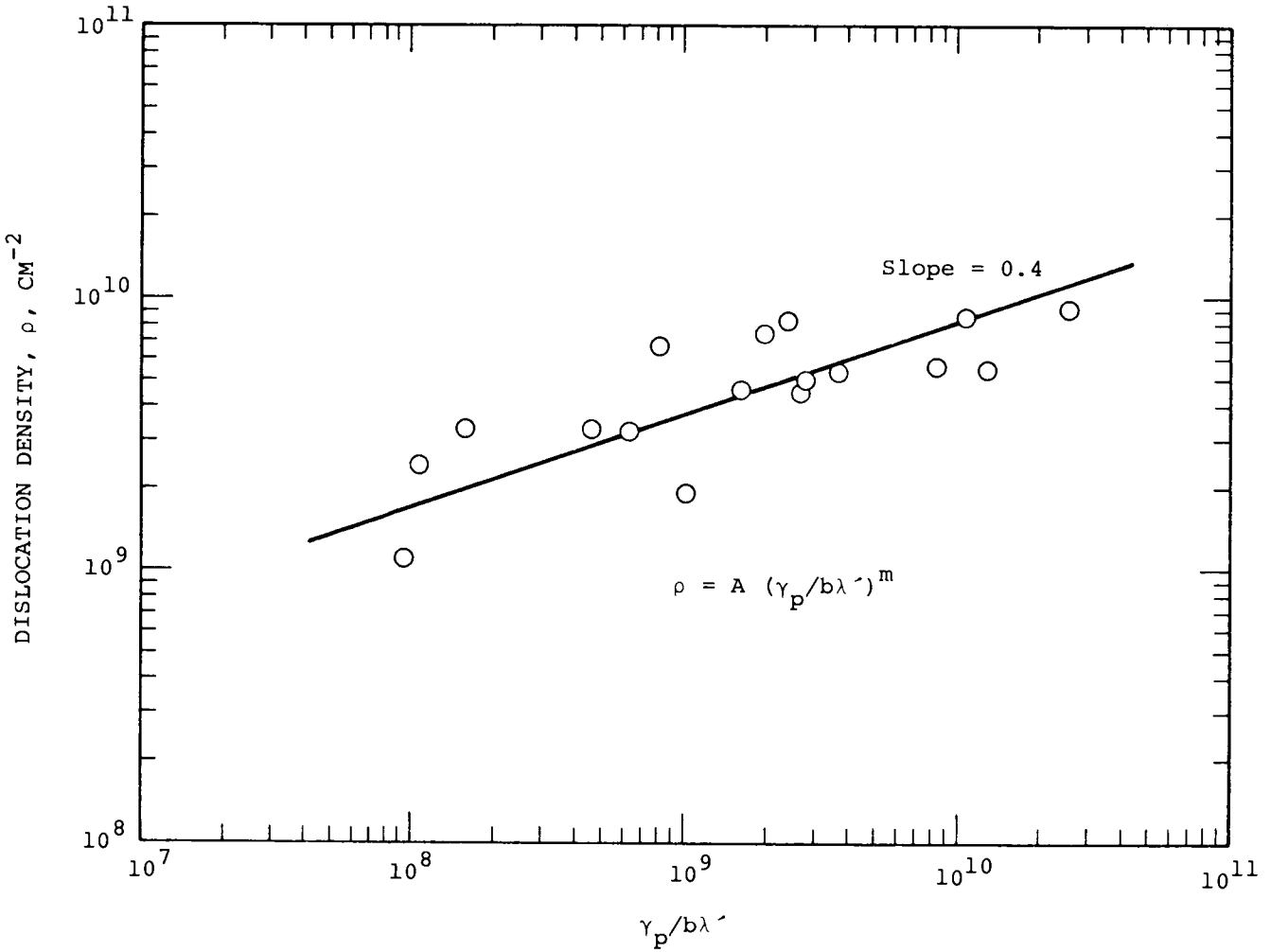

Fig. 1. Correlation of the Dislocation Density, ρ, with the Parameter ($\gamma_p/b\lambda'$) for Incoloy 800.

A plot of the modulus compensated saturation shear stress versus the parameter $(b\gamma_p/\lambda')$ is given in Fig. 2. It is apparent that the data are in excellent agreement with the modified theory. The best fit line through least square analysis[29] was found to be

$$\tau_s = 2.4 \times 10^{-2}\ G\left(\frac{b\gamma_p}{\lambda'}\right)^{0.20\pm0.014} \qquad [7.11]$$

with the multiple correlation coefficient value of ~ 0.95. Fatigue data on AISI 304 and 316 stainless steels by Challenger and Moteff[18,19] and on AISI 304 stainless steel by Nahm and Moteff[30] are included in Fig. 3 with the best fit line for the data on Incoloy 800. It is again evident that the data on the other austenitic stainless steels are well correlated with the modified theory. It is believed that the same type of fatigue mechanism is operating in austenitic stainless steels for a wide range of testing temperatures and test conditions.

At this point of discussion, it seems proper to discuss the influence of second phases in subboundary formation in Incoloy 800. Three types of precipitates (λ', $M_{23}C_6$ and TiN) are identified in fatigued Incoloy 800. Details of identification methods and the effect of precipitates on mechanical properties were discussed previously[31]. Second phase formation during fatigue in Incoloy 800 appears not to affect the subboundary formation. The TEM observations and the evidence of a critical dislocation density for cell

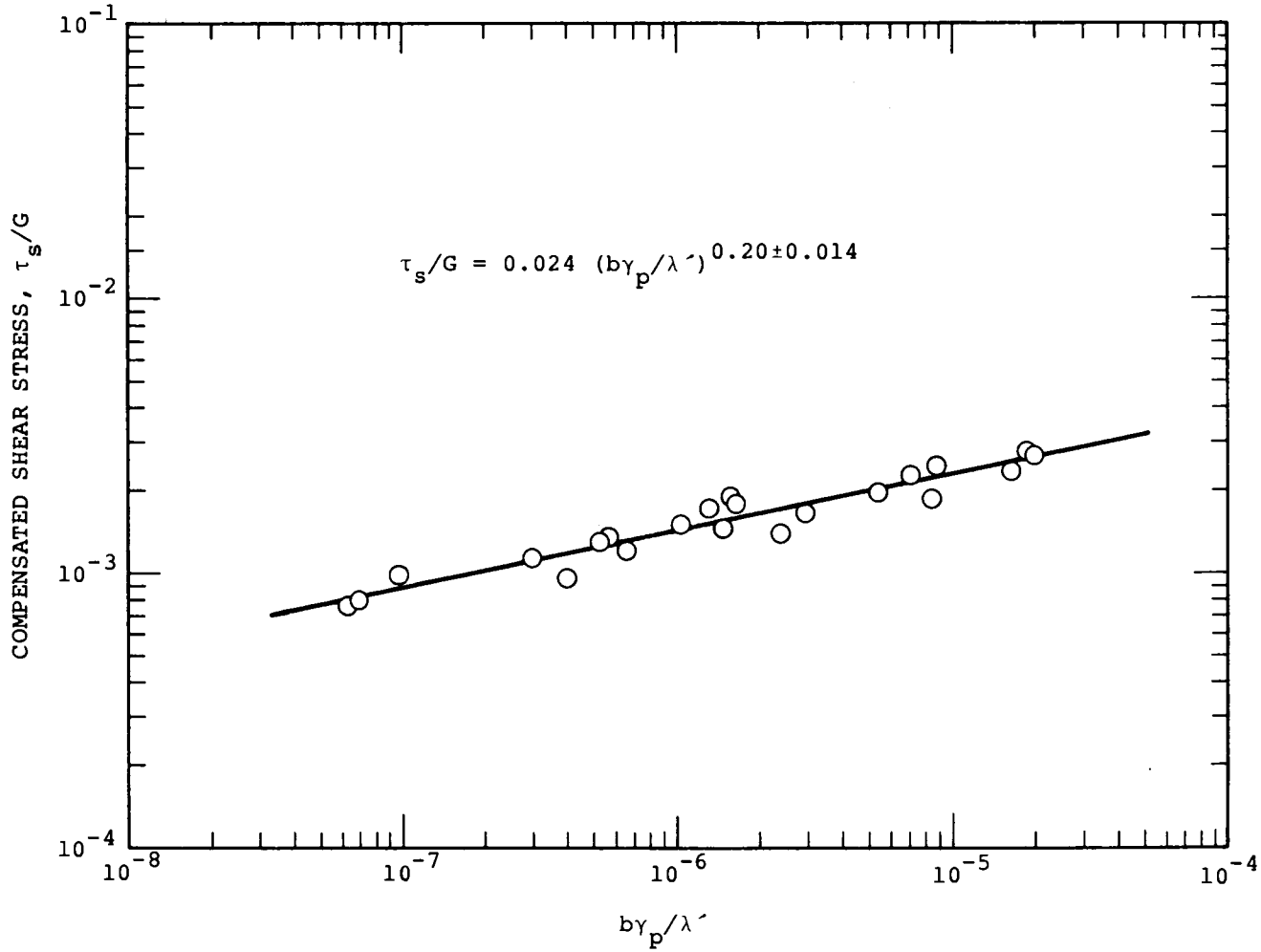

Fig. 2. Correlation of the Shear Modulus Compensated Saturation Shear Stress, τ_s/G, with the Parameter, $(b\gamma_p/\lambda')$ for Incoloy 800.

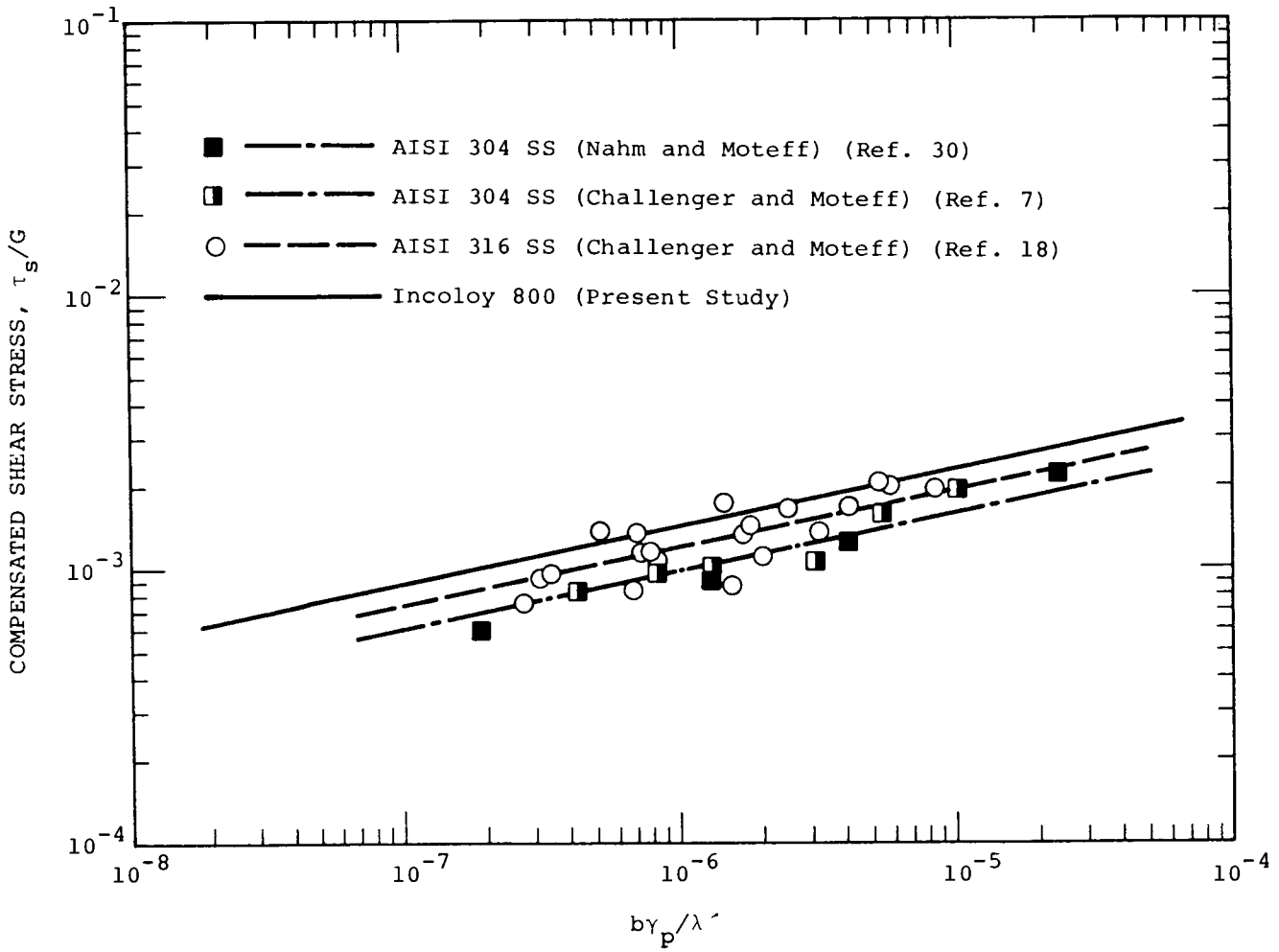

Fig. 3. Correlation of the Shear Modulus Compensated Saturation Shear Stress, τ_s/G, with the Parameter, $(b\gamma_p/\lambda')$, for Several Austenitic Stainless Steels.

formation support this view. The lack of second phase effects on subboundary formation is also consistent with the cells that were observed in the dispersion hardened copper single crystal during fatigue[32-35].

The present result can be interpreted by the concept of "threshold" interparticle geometry as given by Ashby[27]. Second phases control the hardening behavior when particle geometry is similar to that of dislocation cell structure and the interparticle spacing is less than or equal to the self-trapping distance of dislocations. When the spacing between the second phases is larger than the dislocation self-trapping distance (equivalent to the cell size) and the geometry of second phases is quite different from the cell structure, the cyclic behavior becomes that of the single phase materials. The present results on Incoloy 800 belong to the latter case. For example, the substructure observed during creep of Hastelloy X and Udimet 700 did not show any subboundary formation[36]. The reason for this is that the geometry and size of second phases formed in these alloys is quite comparable with the geometry and size of the dislocation cell structure. It is, however, true that the second phase formation contributes to the increase in flow stress. The higher value of saturation shear stress in Incoloy 800 than in AISI 304 or 316 stainless steels, at constant value of the parameter ($b\gamma_p/\lambda'$) (see Fig. 3), could be attributed to the presence of a second

phase such as small TiN particles formed in Incoloy 800.

7.1.2.2 Creep-Microstructure Evaluation of AISI 330 Stainless Steel (H. Jang)

The creep-microstructure evaluation has been initiated on AISI 330 stainless steel which was provided by Hanford Engineering Development Laboratory in the form of 1/4 in. diameter rods. Round creep test specimens were machined from these rods with a gage length 1.00 in. long by 0.125 in. diameter. The complete specimen dimensions are shown in Fig. 4. The specimens, wrapped in Ta foil, were given an annealing treatment at 1100°C for 1/2 hour in a vacuum of $\sim 1 \times 10^{-6}$ torr. No oxidation or discoloration of the specimens occurred during the annealing treatment.

A constant load creep rupture test was performed on a conventional lever type creep testing machine (Arcweld Model C creep-rupture tester) with one of the specimens at 649°C under an applied stress of 30,000 psi. The specimen was heated slowly from the room temperature to the test temperature and soaked overnight at that temeprature before the load was applied. The temperature was monitored by two chromel-alumel thermocouples fastened to the ends of the reduced section. Temperature variation along the gage length of the specimen was held to within ±1°C and temperature control was maintained within ±2°C during the entire test period. The specimen extension was monitored by two dial gages and one LVDT. One dial gage was placed on the load arm, and the

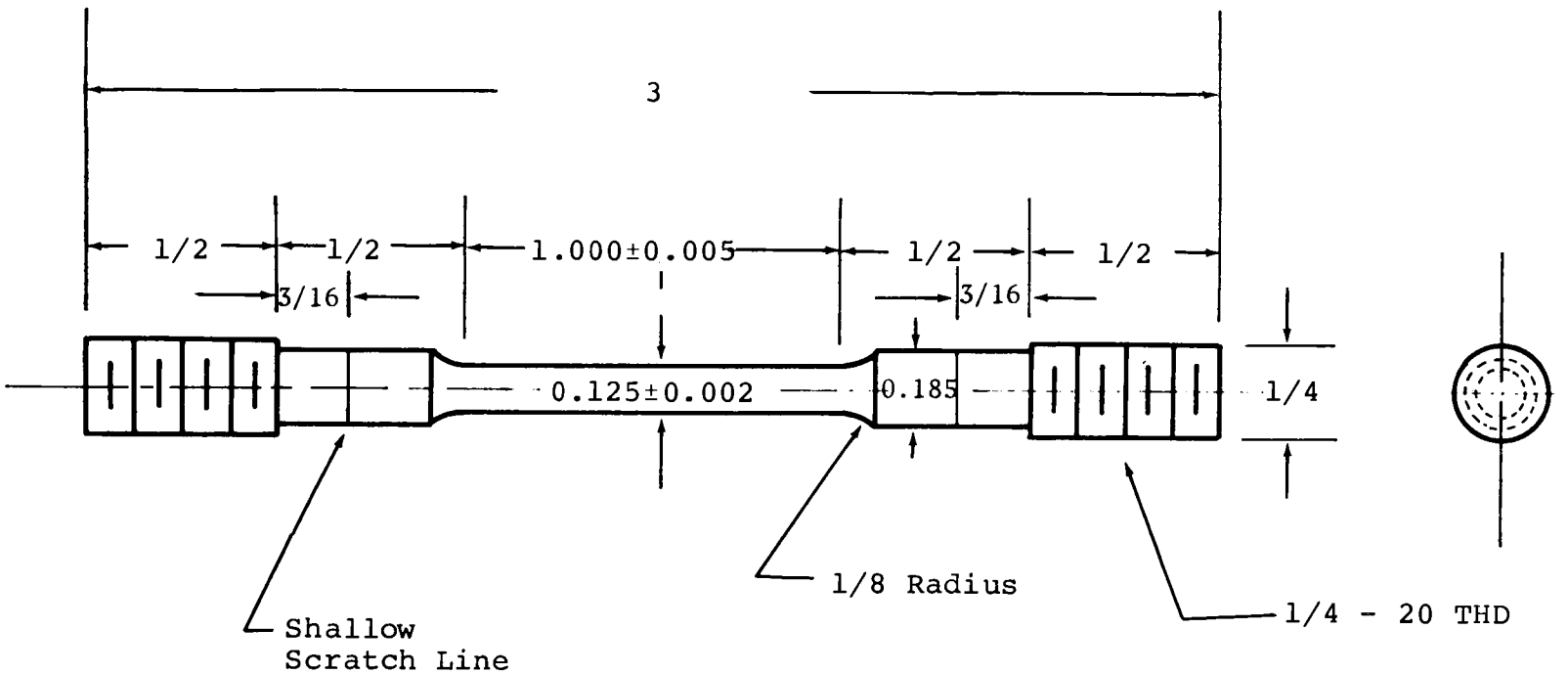

Fig. 4. Drawings of AISI 330 Stainless Steel Creep Test Specimen. (The dimensions are given in inches).

other dial gage and the LVDT were attached to an extensometer which was clamped to the shoulders of the specimen. The dial gages had an accuracy of 2×10^{-4} in. and the LVDT had an accuracy of 6×10^{-5} in. The output of the LVDT was plotted on an X-Y recorder continuously during the test period. When ruptured, the specimen was cooled rapidly in order to preserve microstructures developed in the specimen during the test. An electric fan was used to assist the rapid cooling.

The strain vs. time curve for the specimen tested at 649°C with an applied stress of 30,000 psi is shown in Fig. 5. It shows small primary and secondary creep stages, and a very large tertiary creep stage. The creep rupture data are listed below:

Strain on loading: 1.63%

Strain at the end of primary stage: 2.6%
Time at the end of primary stage: 0.8 hr.

Strain at the end of secondary stage: 5.75%
Time at the end of secondary stage: 6.2 hrs.

Rupture strain: 64.3%
Rupture Life: 29.6 hrs.

Minimum creep rate: 1.04×10^{-4} sec^{-1}

Reduction in Area: 50.2%

A comparison of these data with those obtained from an AISI 304 stainless steel tested under the same test conditions shows that the rupture life of 330 SS is an order of magnitude longer than 304 SS, while the minimum creep rate is smaller

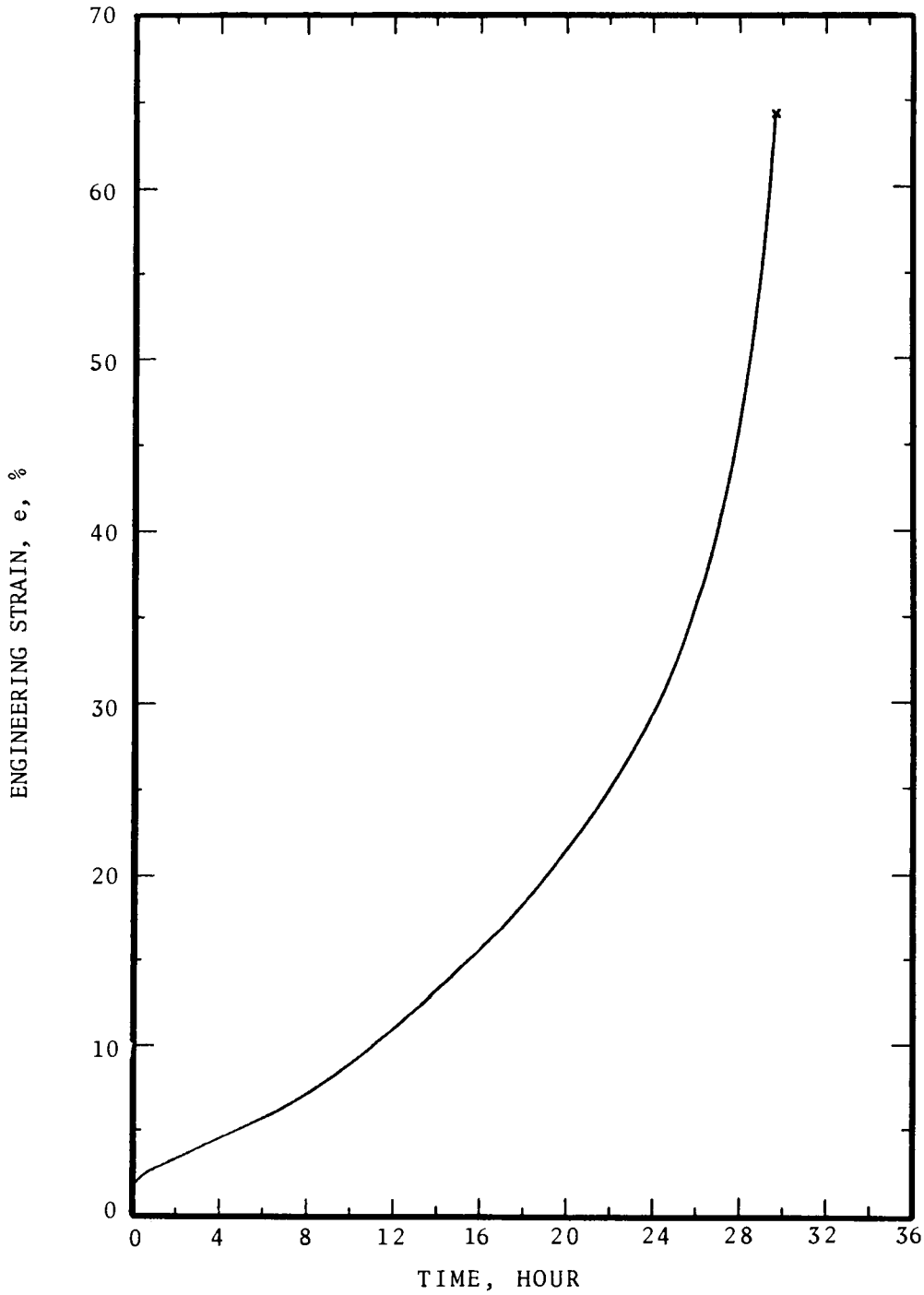

Fig. 5. Creep-Rupture Curve of AISI 330 Stainless Steel Tested at 649°C with an Applied Stress of 30,000 psi.

by a factor of 6-7.

TEM evaluation of this creep-rupture specimen and another creep test at 500°C with an applied stress of 30,000 psi are presently being conducted. Also, other creep tests at a wide range of temperature and stress levles and the subsequent substructural studies are being planned.

7.1.2.3 Creep-Microstructure Evaluation of A286 (A. M. Ermi and H. Nahm)

Material was provided by the National Alloy Development Program Task Group, Hanford Engineering Development Laboratory in the form of ∿ 1mm thick sheets. Most of the time has been spent on the preparation of test specimens and heat treating of this precipitation strengthened stainless steel. The details of the specimens and preliminary creep data with microstructural correlation will be reported in future progress reports.

Before evaluating the creep-microstructure relationship the effect of ageing was studied. A set of specimens was solid-solution annealed at 900°C in air for 2 hours, oil quenched, aged at 720°C for various times, and air cooled. Fig. 6 shows the DPH hardness as a function of ageing time. It is apparent that rapid hardening occurs during the initial ageing period, the hardness increasing slowly thereafter.

Electron and optical microscopy are being performed to study the effects of the heat treatments on the microstructure.

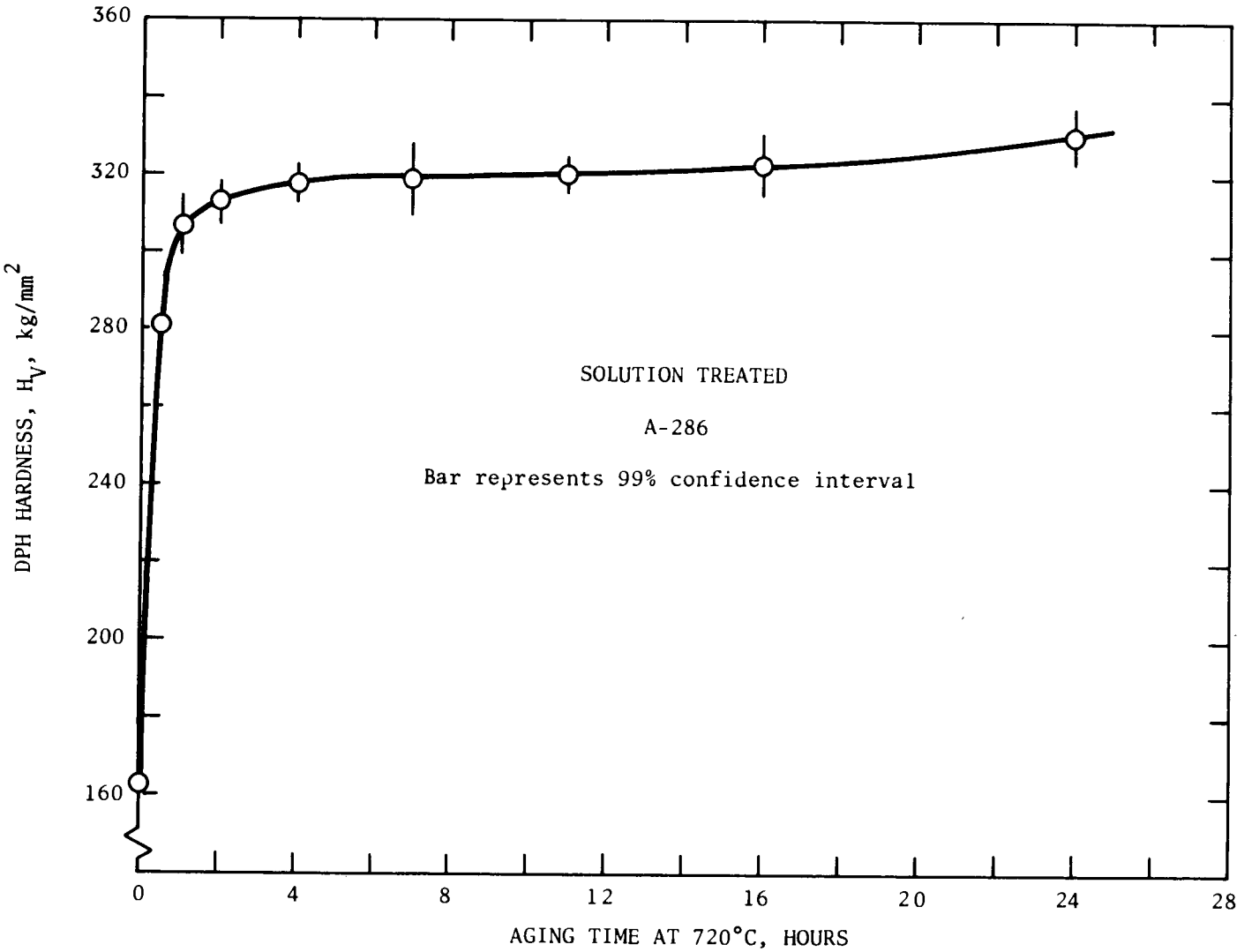

Fig. 6. DPH Hardness versus Aging Time at 720°C for Solution-Treated A-286.

7.1.2.4 Hot-Hardness Measurements on High Temperature Alloy Systems (R. Dorning)

One objective of the hot-hardness test is to determine the relative strength levels at different temperatures so that the initial test conditions for creep and hot tensile experiments can be established. Accordingly, hot-hardness measurements have been made on specimens fabricated from solution treated AISI 330 stainless steel and on aged A-286. The tests were performed in an Argon atmosphere at temperatures up to 1200°C. These results are presented in Fig. 7. The aged A-286 shows hardness levels which are about a factor of three greater than the AISI 330 stainless steel in the temperature range of about 200 to 900°C. The AISI 330 hardness values are very similar to that of annealed AISI 316 stainless steel and much lower than the 20% cold-worked 316 stainless steel as shown in Fig. 7.

7.1.3 REFERENCES

1. D. L. Holt, J. Appl. Phys., 41 (1970) 3197.
2. D. Kuhlmann-Wilsdorf, in "Work Hardening", Gordon & Breach (1968) 97.
3. G. Langford and M. Cohen, Trans. ASM, 62 (1969) 623.
4. C. M. Young and O. D. Sherby, J I S I, September (1973) 640.
5. D. J. Michel, J. Moteff and A. J. Lovell, Acta Met., 21 (1973) 1269.
6. K. D. Challenger and J. Moteff, Scripta Met., 6 (1972) 155.

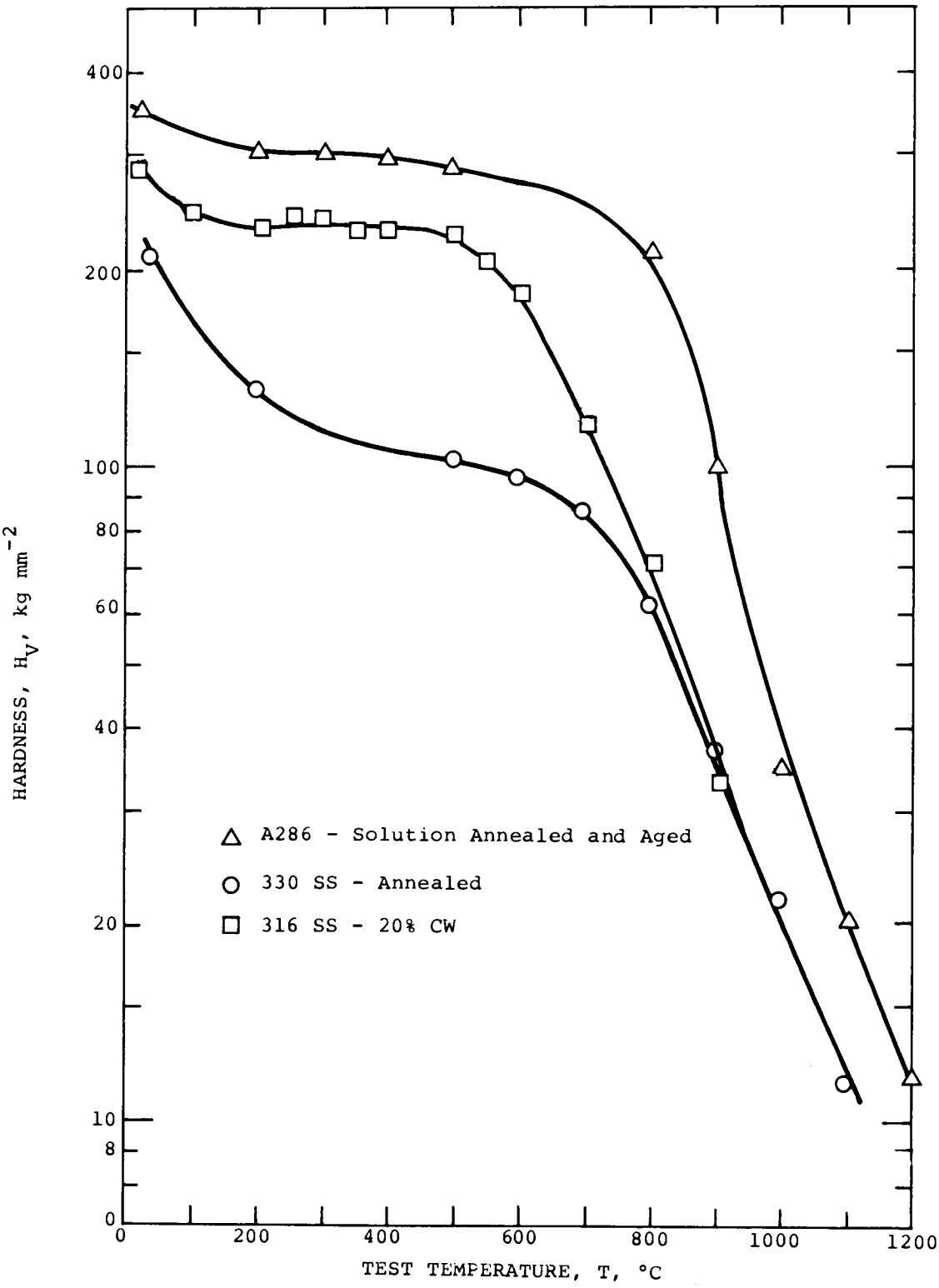

Fig. 7. Plot of Hardness versus Temperature for Several High Temperature Alloys.

7. K. D. Challenger and J. Moteff, ASTM STP 520 (1973) 68.

8. K. D. Challenger and J. Moteff, Met. Trans., 4 (1973) 749.

9. V. K. Sikka, H. Nahm and J. Moteff, Accepted for publication in Mat. Sci. Eng. (1975).

10. F. Garofalo, C. Richmond, W. F. Domis and F. von Gemmingen, Joint Int. Conf. on Creep, Inst. of Mech. Engrs., (1963) I-31.

11. L. J. Cuddy, Met. Trans., 1 (1970) 395.

12. M. R. Staker and D. L. Holt, Acta Met., 20 (1972) 569.

13. R. K. Bhargava, Ph.D. Thesis, University of Cincinnati, Cincinnati, Ohio (1975).

14. C. G. Schmidt, M.S. Thesis, University of Cincinnati, Cincinnati, Ohio (1975).

15. C. E. Feltner and C. Laird, Acta Met., 15 (1967) 1633.

16. P. Lukas and M. Klesnil, Phys. Stat. Sol., 21 (1967) 717.

17. A. Saxena and S. D. Antolovich, Met. Trans., 6A (1975) 1809.

18. K. D. Challenger and J. Moteff, Met. Trans., 3 (1972) 1675.

19. H. Abdel-Raouf, A. Plumtree and T. H. Topper, Met. Trans., 5 (1974) 267.

20. H. Abdel-Raouf and A. Plumtree, Met. Trans., 2 (1971) 1863.

21. H. Abdel-Raouf, T. H. Topper and A. Plumtree, ASTM STP 520 (1973) 300.

22. ORNL-5112, "Mechanical Properties Test Data for Structural Materials," Quarterly Progress Report for Period Endong January 31, 1976.

23. H. D. Nine and D. Kuhlmann-Wilsdorf, Can. J. Phys., 45 (1967) 865.

24. C. Calabrese and C. Laird, Mat. Sci. Eng., 13 (1974) 141.

25. C. Calabrese and C. Laird, Mat. Sci. Eng., 13 (1974) 159.

26. D. Kuhlmann-Wilsdorf, Trans. AIME, 224 (1962) 1047.

27. M. F. Ashby, Phil. Mag., 21 (1970) 399.

28. W. J. M. Tegart, in "Elements of Mechanical Metallurgy", McMillan Co., (1966) New York, 154.

29. Call/360 Version 2 Basic Library Programs, 2nd ed. (1970) G 320-1015-1, I.B.M., New York.

30. H. Nahm and J. Moteff, Unpublished Results, University of Cincinnati, Cincinnati, Ohio.

31. ORNL-5105, "Mechanical Properties Test Data for Structural Materials", Quarterly Progress Report for Period Ending April 30, 1975.

32. O. T. Woo, B. Ramaswami, O. A. Kupics and J. T. McGrath, Acta Met., 22 (1974) 385.

33. W. M. Stobbs and D. F. Watt, in "Proc. 2nd Int. Conf. on the Strength of Metals and Alloys", Vol. II (1970) 560.

34. W. M. Stobbs, D. F. Watt and L. M. Brown, Phil. Mag., 23 (1971) 1169.

35. O. T. Woo, O. A. Kupcis, B. Ramaswami and J. T. McGrath, "Proc. 2nd Int. Conf. on the Strength of Metals and Alloys", Vol. II (1970) 659.

7.2 UNIVERSITY OF CALIFORNIA, LOS ANGELES

(Contribution not received in time for inclusion in this issue.)

8. GENERAL ELECTRIC COMPANY

K. D. Challenger

8.1 INTRODUCTION

The principal objective of mechanical properties testing at the General Electric Company is to characterize the behavior of 2¼Cr-1Mo and austenitic stainless steels in sodium environments relevant to LMFBR steam generators and intermediate heat transport systems. Under conditions predicted for the intermediate sodium system of the CRBRP, 2¼Cr-1Mo will lose carbon to the system and be weakened. The carbon will tend to carburize and embrittle stainless steel components in other portions of the system. The effects of a carburizing environment on creep rupture properties of Type 316 stainless steel will be evaluated along with an assessment of creep-fatigue interactions. In addition, studies of fatigue crack propagation rates in carburizing sodium will be performed in order to assess environmental effects under pertinent intermediate sodium loop loading conditions. The loss of carbon from 2¼Cr-1Mo steel components can result in increased creep rates of the decarburized surface layer with the possibility of ratchetting under cyclic straining. These effects will be evaluated for base metal and weld metal in a decarburizing sodium environment. Elastic-plastic fracture mechanics methods, including J-Integral and Crack Opening Displacement (COD) are being employed to determine the toughness (K_{Ic}) of 2¼Cr-1Mo steel at relevant temperatures and to compute the critical flaw sizes for the onset of rapid fracture. The effects of welding procedure, flaw location and thermal aging are being evaluated. The effect of melting practice and heat treatment on the mechanical behavior of 2¼Cr-1Mo is being evaluated to confirm the properties of consumable remelted 2¼Cr-1Mo meet the appropriate requirements of the ASME B&PV Code for LMFBR steam generators. Metallurgical characterization of 2¼Cr-1Mo steel with special concern for melting practice, heat treatment variations, and other production related variables is being performed. Such characterization augments the transformation from laboratory results to those which are directly relevant to steam generator design and fabrication activities.

8.2 DECARBURIZATION KINETICS AND DESIGN METHODS VERIFICATION TESTING — P. P. Pizzo/L. V. Hampton/J. L. Krankota

8.2.1 Background

The selection of 2¼Cr-1Mo steel as the reference alloy for sodium-heated steam generators was based primarily upon its immunity to stress corrosion cracking in chloride or caustic contaminated environments and its proven fabricability.[1] One of the major concerns with the use of this material for sodium applications is its susceptibility to decarburization during service. Early analyses assumed that relatively thin sections, such as steam generator tubing, would completely decarburize during the LMFBR lifetime, with concomitant severe design stress penalties necessarily imposed.[2] In addition to the assumed carbon losses, the potential for severe carburization of stainless steel components in the loop was also recognized as a potential difficulty.

In the absence of an acceptable theoretical model for decarburization of 2¼Cr-1Mo steel, an approach introduced by Armijo and Krankota[3] was used to analyze the results obtained from many different experiments. This technique treats carbon loss data as if it were corrosion data; that is, the loss of carbon per unit area is described as a function of time. A parabolic time dependence has been observed which suggests that the decarburization process is diffusion controlled. The decarburization rate constants, K*, from all available data were fit to an Arrhenius type expression for design use. Figure 8.1[4-22] shows the results of this analysis. The "data class" and the weighting applied to each class are defined in the NSM Handbook entry for decarburization of 2¼Cr-1Mo steel.[23] Based upon the upper limit curve given in Figure 8.1, estimates of carbon

*Where K is defined by:

$$K = \frac{gm^c}{cm^2 - sec^{\frac{1}{2}}}$$

$$M = \frac{gm^c}{cm^2} = Kt^{\frac{1}{2}}$$

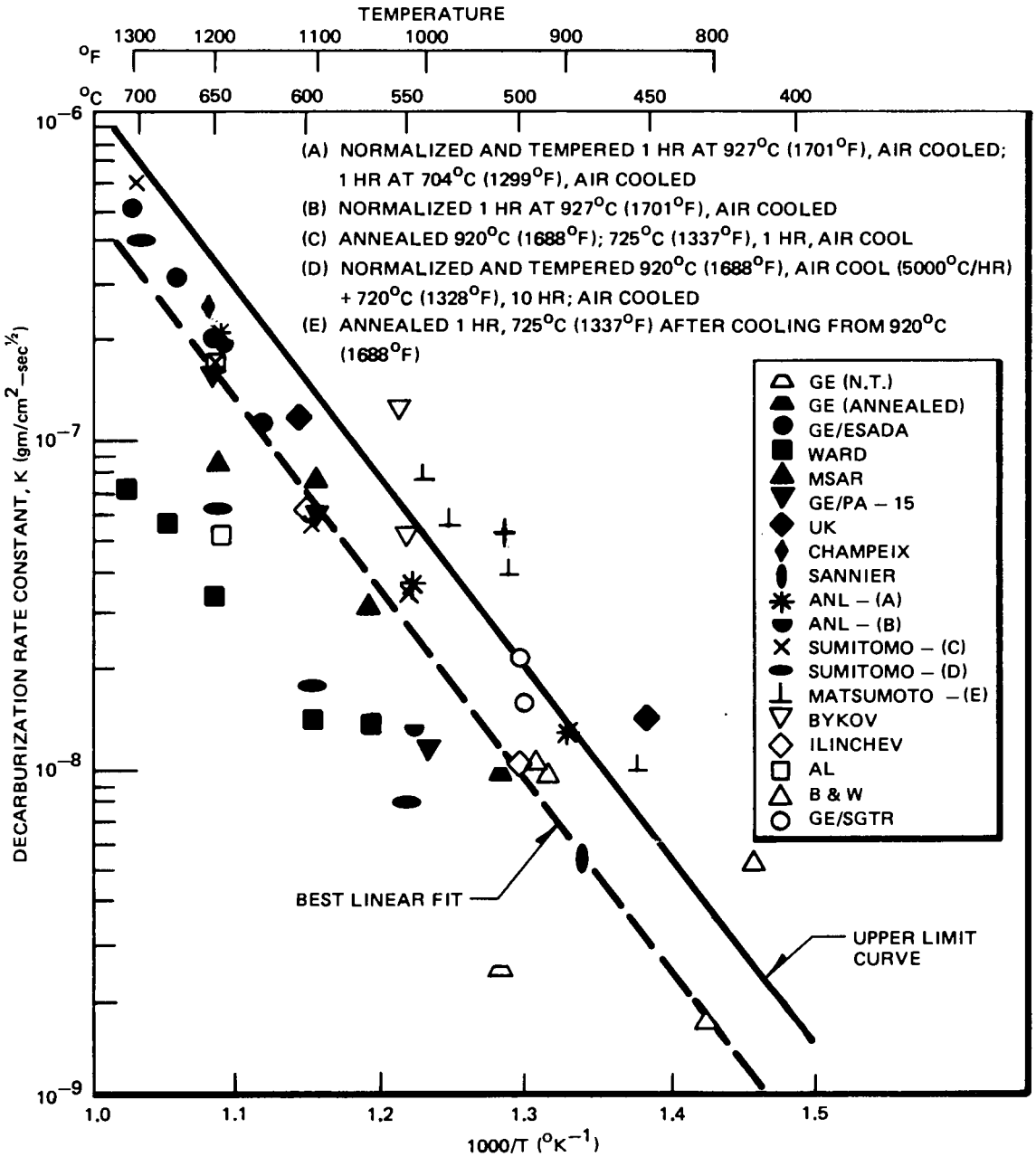

Figure 8.1. Decarburization Rate Constants for All Investigations + GE (Weld Metal-Interim)

loss and associated design stress penalties can be made for steam generator components. These predictions of decarburization kinetics indicate that steam generator tubes would not be expected to lose more than 300 ppm carbon in the design life of the CRBRP. Only a small design stress penalty (<10%) is associated with this loss. While the handbook approach suggests that decarburization kinetics are too slow to yield a carbon loss at end-of-life of greater than 300 ppm for CRBRP steam generator tubing,* WARD experiments, utilizing thin foils, imply that the "equilibrium" carbon content of 2¼Cr-1Mo in 510C (950F) sodium will be approximately 700-900 ppm.[7] The design stress penalty associated with these predictions of carbon loss can be accommodated.

Design analysis for high temperature components requires a consideration of creep/fatigue interaction to accommodate the effects of transient loading. A recent study has provided creep/fatigue interaction information for 2¼Cr-1Mo[24] under conditions of uniform microstructure (i.e. no decarburized surface layer) with no ratcheting strains permitted. Steam generator tubes will experience cyclic loading with the potential to accumulate ratcheting strains, due to a weaker surface layer, as compared to the bulk metal. Interrupted creep tests on 2¼Cr-1Mo pipe, tubing and weld metal are being undertaken to assess the effects of such loading on partially decarburized material. Uniaxial tests will be performed on sodium-filled and inert gas-filled pipe samples in order to characterize the effect of stress cycling on creep strains. Tubing and all-weld-metal tubes will be internally pressurized in sodium and argon environments to assess the effects of creep/fatigue on rupture life in a decarburizing environment. Description of the samples, test facilities, and test matrix is included in earlier reports,[25,26]

8.2.2 Decarburization Studies

Further decarburization studies have been initiated to determine the effects of processing and heat treatment on the carbon transport kinetics of 2¼Cr-1Mo steel. Pot conditions remain the same as with previous runs,

*Tubing specification sets initial carbon levels of 700-1100 ppm.

i.e., 510C (950F) static, titanium-gettered sodium. Electroslag Remelted (ESR), Vacuum Arc Remelted (VAR) and extra- low carbon (ELC-Sumitomo) 2¼Cr-1Mo foils (approx. 0.3 x 10 x 80 mm [0.0118 x 0.394 x 3.15 in.]) were given a variety of annealing and normalizing and tempering treatments (Table 8.1). Such treatments lead to a variety of different microstructures, and therefore, possibly different decarburization rates in sodium. The effect of heat treatment on the carbon transport properties of 2¼Cr-1Mo has recently become a well-documented phenomenon.[27,28,29] The current study will limit the heat treatments to those that will produce the range of microstructures that may be present in the Clinch River Plant steam generators. In addition, the more subtle effect of melting practice will be studied.

The test matrix for this phase of the decarburization study calls for exposure times of 1500, 6000 and 10,000 hours for each of the heat treatments listed in Table 8.1.

Also included in subsequent decarburization runs will be 152.4 mm. (6 in.) lengths of ESR and VAR annealed* plant-prototypic tubing. These tubes will also be exposed for 1500, 6000, and 10,000 hours, whereupon surface layers will be removed for carbon analysis, and a carbon gradient defined.

Aside from the metallography and carbon analysis planned for the upcoming decarburization experiments, carbide extraction and identification will be performed on selected specimens before and after sodium exposure.

8.2.3 Mechanical Properties of 2¼Cr-1Mo Steel in Decarburizing Sodium

The study of the mechanical properties of decarburized 2¼Cr-1Mo steel has been redefined on the basis of the first phase test results reported in the January 1976 GE Quarterly.[30] The Phase II testing will consist of three major efforts. The test matrices for the current scope of testing will be described in this report. Appropriate test specimens are being fabricated, and testing will commence in April 1976.

---

*927C (1700F) for ½ hr., cooled to 707C (1305F), held for 2 hrs., air cooled to room temperature.

Table 8.1. Test Matrix Heat Treatment Effects on Decarburization

VAR, ESR and ELC* (Sumitomo)

A. Isothermal Anneal

927 ± 14C (1700 ± 25F) ½ hr.
cool to 716 ± 8C (1320 ± 15F)
in less than 10 minutes, hold
for ½, 1*, ½ and 2 hrs.*

B. Same as A with PWHT 727C (1340F) - 4 hrs.

C. Normalize (Simulate Weld Heat Affected Zones)

927 ± 14C (1700 ± 25F) 1 hr.
Air cool to R.T.
PWHT 727 ± 19C (1340 ± 35F)
for 0, 1, 2 and 4 hrs.

D. Tube samples, VAR and ESR, for Carbon Profile Determination

1. Isothermally annealed (as received) 927C (1700F) cool to 707C (1305F), hold for 2 hours, air cool.
2. Isothermally annealed as in (1) plus PWHT of 4 hours at 727 ± 19C (1340 ± 35F).

Table 8.2 describes the test matrix for 510C (950F) tensile testing of pre-exposed 2¼Cr-1Mo steel. The purpose of this program is to measure the degradation in elevated temperature yield strength and tensile strength as a function of pre-exposure time in the specific titanium gettered environment selected for this investigation. The data of Charnock, Cordwell, Cwyther and Hobdell[31] suggest the importance of correlating mechanical properties changes with reproducible and consistent carbon activity excursions. Tensile sheet specimens will be tested for this study. Coupons 1.52 mm. (0.06 in.) thick will be exposed in titanium gettered sodium for times ranging from 100 to 1000 hours. After exposure, the coupons will be ground to 0.76 mm. (0.030 in.) from one side, then tested. A carbon gradient similar to that obtained in the 0.76 mm. (0.030 in.) thick tubular creep specimens is predicted. The data from this program will be correlated with creep property measurements to isolate yield strength reduction in the analysis of creep strength degradation.

Test matrices have been established for the creep testing of both uniaxial and biaxial stress states. The uniaxial creep test program, will determine the creep property variations as a function of pre-exposure conditions (time at 510C [950F]). The test specimens used are tubular creep specimens with a 0.76 mm. (0.030 in.) wall. The properties to be evaluated are (1) time to rupture (2) minimum creep rate and (3) strain-to-failure. Effort will be made to isolate pre-exposure influence on properties from effects associated with sustained decarburizing potential. The test matrix for uniaxial creep is given in Table 8.3.

The biaxial creep test program, likewise, is designed to determine property variations as a function of pre-exposure to decarburizing sodium. However, pressure pin specimens will be tested over a broad range of stress. Data from this program may indicate the necessity for a complete creep evaluation with the uniaxial specimens (analogous to that of Table 8.3) at a second stress level. Rupture data over stresses ranging from 175 to 255 MPa (25.4 to 37.0 ksi.) will be obtained from biaxial creep tests performed as depicted in Table 8.4.

Table 8.2. Elevated Temperature Tensile Test Matrix

Material: 2¼Cr-1Mo Steel
Melting Practice-ESR
Isothermal Anneal
Post-Weld Treatment (727C (1340F) for 4 hours)

Specimen Configuration: Tensile Coupons (0.76 mm. (.030 in.) sheet)

Test Parameter: $T = 510C\ (950F)$
$\varepsilon_o = 10^{-3}\ sec^{-1}$ (strain rate)

Quantity	Pre-Exposure	
	time	Environment (one surface)
2	0	--
2	100	Na (Ti Gettered)
2	200	Na (Ti Gettered)
2	300	Na (Ti Gettered)
2	400	Na (Ti Gettered)
2	500	Na (Ti Gettered)
2	750	Na (Ti Gettered)
2	1000	Na (Ti Gettered)

Table 8.3. Uniaxial Creep Test Matrix

Material: 2¼Cr-1Mo Steel
Melting Practice-ESR
Isothermal Anneal
Post-Weld Treatment (727C (1340F) for 4 hours)

Specimen Configuration: Tubular Creep Specimen

Test Parameters: T = 510C (950F)
σ = 240 MPa (35 ksi)

Quantity	Pre-Exposure time	Pre-Exposure Environment (ID/OD	Test Environment (ID/OD)
3	0	-	Ar/Air
1	0	-	Na/Air
1	250 hrs.	Ar/Ar	Ar/Air
1	250 hrs.	Na/Ar	Ar/Air
1	250 hrs.	Na/Ar	Na/Air
1	500 hrs.	Ar/Ar	Ar/Air
3	500 hrs.	Na/Ar	Na/Air
1	1000 hrs.	Ar/Ar	Ar/Air
1	1000 hrs.	Na/Ar	Ar/Air

NOTE: All Na exposures titanium gettered

Table 8.4. Biaxial Creep Test Matrix

Material: 2¼Cr-1Mo Steel
Melting Practice-ESR
Isothermal Anneal

Specimen Configuration: Pressure Pin Specimens

Test Parameter: T = 510C (950F)

Quantity	Pre-Exposure		Test Environment (ID/OD)	Stress	
	time	Environment (ID/OD)		MPa	(ksi)
2	0	-	Ar/Ar	255	(37.0)
4	0	-	Ar/Ar	235	(34.1)
2	0	-	Ar/Ar	215	(31.2)
4	0	-	Ar/Ar	195	(28.3)
2	0	-	Ar/Ar	175	(25.5)
2	1000	Ar/Ar	Ar/Ar	235	(34.1)
2	1000	Ar/Ar	Ar/Ar	195	(28.3)
2	250	Ar/Na	Ar/Na	235	(34.1)
2	500	Ar/Na	Ar/Na	235	(34.1)
2	1000	Ar/Na	Ar/Na	235	(34.1)
2	250	Ar/Na	Ar/Na	195	(28.3)
2	500	Ar/Na	Ar/Na	195	(28.3)
2	1000	Ar/Na	Ar/Na	195	(28.3)
2	1000	Ar/Na	Ar/Na	255	(37.0)
2	1000	Ar/Na	Ar/Na	215	(31.2)
2	1000	Ar/Na	Ar/Na	175	(25.5)

NOTE: All Na exposures titanium gettered.

Anomalies in biaxial creep data reported in the January 1976 GE Quarterly[30] have been resolved. The pinhole porosity associated with weld metal specimens pre-exposed to decarburizing sodium, resulted when a high temperature, 704C (1300F), excursion occurred. It has been discovered that this excursion was an inherent characteristic of the sodium purification cycle that preceeded all biaxial tests in sodium. As a result, the previously reported data[30] for 2¼Cr-1Mo biaxial stress rupture strength, closed and partially closed data points, Figure 8.2 (Figure 3.6 of the previous GE quarterly report, GEAP 14029-6), should be disregarded. The error in the sodium purification cycle has been corrected and the next series of tests on prototypical ESR 2¼Cr-1Mo isothermally annealed tubing is ready to start.

8.3 MECHANICAL PROPERTIES OF STAINLESS STEEL IN CARBURIZING SODIUM — J. F. Copeland/P. P. Pizzo

8.3.1 Fatigue Crack Growth Studies

8.3.1.1 Background

The objective of this program is to determine the environmental influence of liquid sodium on the fatigue crack propagation rates for annealed Type 316 stainless steel. To be prototypic of expected LMFBR Intermediate Heat Transport System (IHTS) piping conditions, this testing is being done at low frequency (0.5 cycles per minute [cpm]) and 510C (950F). Additionally, the existence of a high carburizing potential in the liquid sodium environment is a distinct possibility.[32] Since the exact carburizing potential of the IHTS sodium has not been determined, this experiment is being run under the most severe conditions, of carbon-saturated sodium. The use of carbon-saturated sodium also allows the acceleration of carburization in order to represent design life conditions with a relatively short-term test. Control tests in air are also being performed under the same loading conditions, in order to truly discern environmental effects. These results will show whether or not penalties or allowances for crack growth in secondary system sodium are required or warranted.

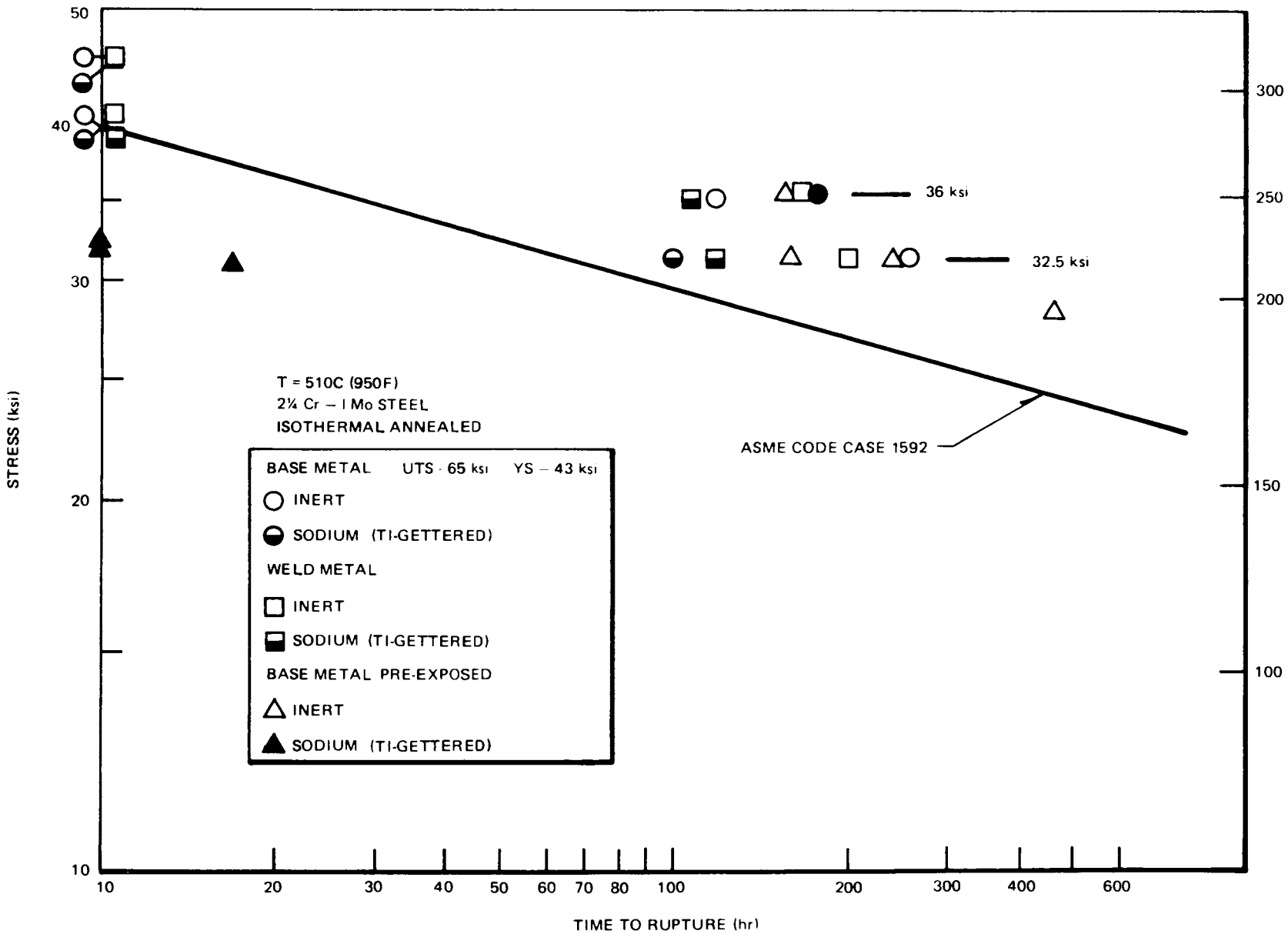

Figure 8.2. Biaxial Creep Tests, 2¼Cr-1Mo Steel: Rupture Data

ASTM E399, 12.7 mm. (0.5 in.) thick, 3-point bend specimens were machined from annealed 15.9 mm. (5/8 in.) Type 316 plate[32] and fatigue precracked. Specimens to be tested in air were aged at 510C (950F) for 1000 hrs. in air. Those to be fatigued in high carbon sodium were pre-exposed in Loop A sodium with a Grade 1050 carbon steel source at 510C (950F) for 1000 hrs. The carburization incurred by these specimens during sodium pre-exposure was previously reported[33] and is typical of that anticipated[32] for a 30-year LMFBR design life with a 2¼ Cr-1Mo steel carbon source.

Fatigue crack growth tests were performed in air and flowing, high carbon sodium in two specially designed fatigue test facilities.[32] Three tests could be run concurrently in each facility. After loading for an estimated number of cycles, the specimens were withdrawn and examined for crack growth. When the crack growth approximated 0.76 mm. (30 mils) the specimen was fractured to accurately measure crack growth. A crack growth rate was then computed from the ratio of crack extension to cycles. The stress intensity factor range (ΔK) was calculated at half the crack extension. Preliminary results for tests in air and sodium are shown in Figure 8.3, and compared to other data.[34,35,36,37] The control data (air) is in excellent agreement with previous results.[34,35]

8.3.1.2 Current Progress

During the last quarter, three more crack growth rate tests were completed in air at 510C (950F), and the results are shown in Figure 8.3. These tests complete the fatigue crack growth control (air environment) curve for the loading frequency of 0.5 cpm. An analysis[30] of fatigue crack growth rates and the concurrent carburization rate has indicated that tests in carburizing sodium at even lower frequencies than 0.5 cpm may be required in order to permit an environmental influence on crack growth rate. In pursuit of this objective, control tests at 0.033 cpm were initiated after completing the 0.5 cpm tests. Three tests have been completed (1000 hr. run), but have not yet been analysed. Foils to monitor carburization during the first six tests in sodium (shown in Figure 8.3) were analyzed, and indicated a low carburizing potential.

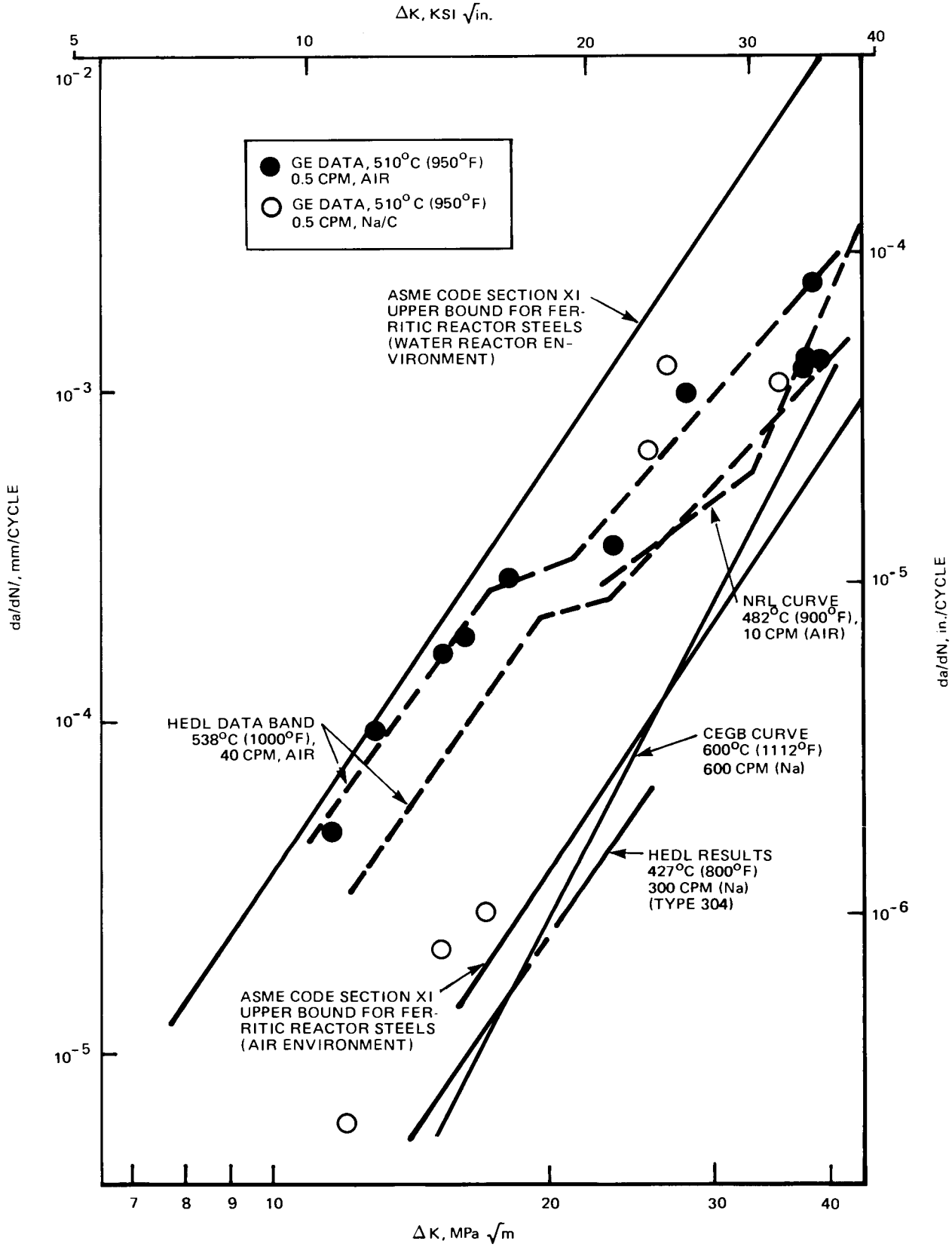

Figure 8.3. Comparison of Fatigue Crack Propagation Rates at Elevated Temperatures Including Results from GE (Type 316), HEDL (Type 304 & 316), CEGB (Type 316), NRL (Type 316), and the ASME Code (Ferritic Steels) (Ref. 34, 35, 36, 37)

Therefore, the crack growth rates for sodium environment shown in Figure 8.3 do not represent the most potentially severe environment, that of carbon saturated sodium. The depleted carbon source was replaced, and a run to fully carburize new piping and the test vessel was completed during the last quarter. A run in the high carbon sodium at 0.5 cpm, to repeat the low ΔK results shown in Figure 8.3, has been initiated.

During this relative lull in testing activity, electronic digital timers were installed for the loading systems, and are functioning perfectly. The load systems were also recalibrated after approximately six months of use. One load station had an error of 4%. Adjustments were made to correct this error, and a load cell system is being established to recalibrate the facility, in situ, prior to each run.

Twenty additional precracked specimens completed their pre-exposure for 1000 hr. at 510C (950F). Ten specimens were aged in Loop A sodium, and ten were aged in air. Carburization of the sodium-aged specimens was adequate. GTA weldment preparation and inspection was completed. Crack growth and tensile test characterization specimens are currently being machined from the weld. Additionally, twenty new base metal specimens were received from the fabricator and sent for fatigue precracking. Efforts during the next quarter will center on performing 0.033 cpm tests in air, 0.5 cpm tests in high carbon sodium, and the initiation of 0.033 cpm tests in high carbon sodium. Weld specimens will be precracked in preparation for pre-exposure and testing.

In order to more accurately assess the relevance of this program to LMFBR piping design and inspection, a cursory analysis to predict cyclic lives of components was performed. This analysis is presented in Appendix 8.1. It is imperative to recognize the assumptions regarding initial defect size, applied stress range, and crack growth equation which were employed in these computations. Nevertheless, the calculations do indicate that, under a very severe combination of conditions, the cyclic life of a 12.7 mm. (0.5 in.) thick pipe may be on the order of 1000 cycles, which is approximately equal to the number of transient events predicted for a 30 year LMFBR life. The determination of the material (including environmental influences) crack growth equation is critical, since

increasing da/dN by a factor of ten (shift up one decade on Figure 8.3) will decrease the cyclic life by a factor of ten. The accurate assessment of this equation, including any potential environmental degradation, is the objective of this program.

8.3.2 Creep/Fatigue Study

Effort toward characterizing the elevated temperature mechanical behavior of Type 316H stainless steel in a carburizing sodium environment continues. Twelve tubular creep specimens have been fabricated, and they are presently being pre-exposed to carbon saturated sodium for 1000 hrs. Pre-exposure will be completed in March 1976, and testing will resume in April 1976.

Two test programs are planned for the current phase of testing. Creep tests will be performed on (1) annealed and on (2) annealed and pre-strained 316H specimens.

The annealed 316H test matrix is analogous to that previously reported.[38] Monotonic creep test data will be obtained at 510C (950F) for carburized and control data over a broad stress range. Initial stress levels will range from 380 MPa (55.5 ksi) to 535 MPa (77.8 ksi).

A second effort will involve uniaxial creep testing of annealed *and pre-strained* 316H stainless steel. The test matrix for this study is detailed in Table 8.5. This study is necessitated by the large variation in instantaneous plastic strain (strain upon loading) exhibited by creep specimens tested in the temperature/stress regime of interest. Creep data as a function of pre-strain will be used to isolate the influence of carburization on elevated temperature behavior.

Specimens for the test matrix of Table 8.5 will be strained (under constant crosshead displacement rate) at 510C (950F) to a predetermined strain. Upon reaching that strain, specimens will be cooled in situ (under load control conditions). Subsequent creep testing will be performed at 510C (950F) and 400 MPa (58 ksi).

Table 8.5. Uniaxial Creep Test Matrix (Pre-Strained Specimens)

Material: Tp. 316 H Stainless Steel Annealed (Tube)

Specimen Configuration: Tubular Creep Specimen

Creep Test Parameters: $T = 510C$ (950F)

$\sigma = 400$ MPa (58 ksi)

Quantity	Pre-Exposure Conditions		Specimen	Creep Test Environment (ID/OD)
	Temp. (C)/Time	Environment (ID/OD)	Pre-Strain[a]	
1	510/1000 hrs.	Ar/Air	0.25 ε_u	Ar/Air
1	510/1000 hrs.	Na/Air	0.25 ε_u	Na/Air
1	510/1000 hrs.	Ar/Air	0.50 ε_u	Ar/Air
1	510/1000 hrs.	Na/Air	0.50 ε_u	Na/Air
1	510/1000 hrs.	Ar/Air	0.75 ε_u	Ar/Air
1	510/1000 hrs.	Na/Air	0.75 ε_u	Na/Air

NOTE: (a) $\varepsilon_u \equiv$ the strain corresponding to σ_{UTS} (at 510C, $10^{-3}S^{-1}$) determined from hot tensile testing of a 1000 hour sodium exposed specimen.

(b) Specimens pre-strained after pre-exposure to sodium or argon.

(c) All specimens cooled under load control conditions from pre-straining operation.

(d) All creep tests initiated under 400 MPa test stress conditions.

(e) All Na exposures performed with high carbon steel source.

8.4 FRACTURE TOUGHNESS OF LMFBR STEAM GENERATOR MATERIALS — J. F. Copeland

8.4.1 Background

The objective of this program is to determine fracture toughness values (K_{Ic}) at 24C (75F) and higher temperatures, for potential LMFBR Steam Generator shell and tubesheet materials. These results will be combined with Charpy V-notch and drop-weight test values (RT_{NDT} determinations) and tensile test results to evaluate resistence to fracture. The essence of this approach to prevent fracture is set forth in the K_{IR} curve of Appendix G to Section III of the ASME Boiler and Pressure Vessel Code. No toughness data on 2¼Cr-1Mo steel was included in the derivation of the Code K_{IR} curve. Therefore, testing is required at hydrostatic test and at service temperatures to assure that the present K_{IR} curve approach is adequate for this material. In order to evaluate the fracture toughness of 2¼Cr-1Mo above the Nil Ductility Transition Temperature (NDTT), it is necessary to employ elastic-plastic fracture toughness testing methods, such as the J-Integral approach.

Thick section 2¼Cr-1Mo steel plates were procured for this program and heat treated to represent potential LMFBR material conditions. The emphasis is on air-melted material, although some testing has been done on Vacuum Arc Remelted (VAR) steel. Information on test material chemical composition and nonmetallic inclusion characterization is found in Reference 30. Initial tensile, Charpy V-notch, drop-weight NDT, and fracture toughness (J_{Ic}, K_{Ic}) test results are also given.[30] The effects of heat treatment on the preceding mechanical properties and on microstructure were previously discussed.[30]

8.4.2 Current Progress

Construction of the furnace for elevated temperature fracture toughness testing has been completed. Equipment is also on hand for the determination of slow crack growth initiation, by the measurement of crack tip displacements. Two 122 cm. (48 in.) long, 8.9 cm. (3.5 in.) thick SMAW weldments of 2¼Cr-1Mo steel were received from the fabricator. They passed the nondestructive examination and, especially from the standpoint of a

straight edge joint geometry, appear to be excellent test welds. One of the two welds is shown in Figure 8.4. Machining of the SMAW specimens has been initiated and eighteen base metal Compact Tension Specimens, with corresponding Charpy and tensile specimens, were received from the fabricator. Precracking will be initiated and these specimens will be used to determine the toughness as a function of test temperature at temperatures up to 510C (950F). A recheck of Charpy toughness results on material given an embrittling treatment (1000 hr. at 510C [950F]) was completed. These specimens, taken from a fractured CTS, verified previous Charpy results. They indicate that, although temper embrittlement is shown by Charpy tests, it is not necessarily manifested by CTS results, which employ a crack growth initiation criterion. The results also verify a reduction in Charpy upper shelf energy as a result of the embrittling treatment. The final current group of specimens being aged at 510C (950F) for 1000 hr. will be completed by the end of this Quarter. New base plate material has been ordered for future weld studies and is also scheduled to arrive at the end of the Quarter. These future efforts will include the influence of the recently specified 40 hour post weld heat treatment.

A recurring problem in elastic-plastic fracture toughness testing is the determination of slow crack growth initiation.[40] A variety of methods, including ultrasonics, acoustic emission, electrical potential systems, multiple displacement gages, a load-unload compliance method, a sensitive load cell method, and multiple specimen testing have been attempted with inconsistent success. Even the multiple specimen test method,[40] which seems the most commonly accepted, and which has been used to date in this study, has shortcomings. An obvious disadvantage is the requirement for a relatively large number of test specimens to establish a single fracture toughness data point. Even then, the accuracy of determining that single data point may depend on the scatter of the test results, the assumed shape of the J-Integral versus crack extension curve, and the proximity of the crack extension data to the crack opening stretch line. In consideration of the aforementioned problems, an objective of the current program is to establish a single specimen method to determine the onset of slow crack extension, for the

Figure 8.4. Shielded Metal Arc Test Weldment of 2¼Cr-1Mo Steel, 122cm (48 in.) x 66cm (26 in.) x 8.9cm (3.5 in.) thick

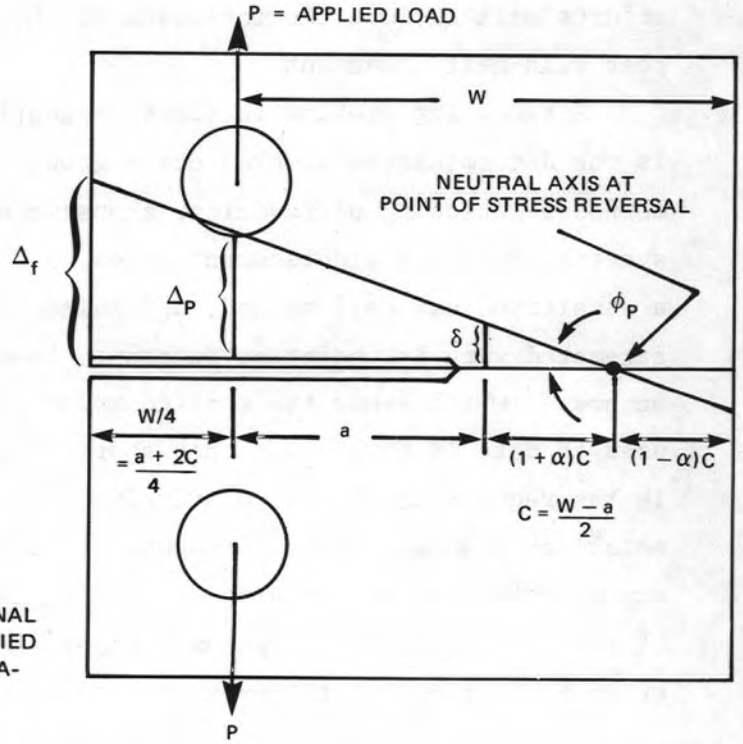

Δ_f, Δ_P, AND δ REPRESENT DISPLACEMENTS

α = DIMENSIONLESS PARAMETER EQUAL TO THE RATIO OF THE WIDTH OF THE INTERNAL STRESS BLOCK EQUILIBRATING THE APPLIED LOAD AT PLASTIC COLLAPSE, TO THE LIGAMENT WIDTH (2C)

Figure 8.5. Representation of Specimen Crack Opening Displacements for a Compact Tension Fracture Toughness Specimen

calculation of J_{Ic}. A theoretical evaluation of displacement measurement methods is presented in Appendix 8.2 (terms are defined in Figure 8.5). It can be seen that a significant change in displacement rate at the crack tip (for constant stroke rate control at the specimen load points) should occur during crack extension. Attempts will be made to apply this fact, toward determining crack extension initiation, during the next Quarter. The multiple specimen method will constitute a fall-back position.

8.5 METALLURGICAL CHARACTERIZATION OF VAR AND ESR 2¼Cr-1Mo ALLOY STEEL — H. P. Offer

As reported previously,[44] an isothermal transformation study was completed on five heats of VAR, four heats of ESR, and three heats of air melted 2¼Cr-1Mo steel. The study was conducted to determine the pearlite phase time-temperature transformation boundary of this steel; in that a ferrite-pearlite microstructure appears desirable[1] from the standpoint of long term property stability. The specimens were austenitized for ½ hour at 916C (1680F), salt pot quenched and held for times from 30 to 300 minutes at 690, 704, and 718C (1275, 1300, and 1325F), and then water quenched. The resulting microstructures and hardness values (Table 8.6) indicate that time for transformation decreased with increasing temperature.

This study was expanded to include isothermal transformation at 732C (1350F) for times from 30 to 300 minutes. The hardness values resulting from this treatment are generally less than the hardness values resulting from the 718C (1325F) treatment for corresponding hold times. The microstructures of the 732C (1350F) heat treatment specimens contain more proeutectoid ferrite and less martensite/bainite than the corresponding specimens held at 718C (1325F). This result is not in complete agreement with the isothermal transformation diagram for 2¼Cr-1Mo steel in the Nuclear Systems Materials Handbook, which shows a ferrite phase boundary and a pearlite phase boundary minimum formation time at 704C (1300F).

The microstructures of a typical heat (Vacuum Arc Remelted heat 91506 with 0.10% carbon) are shown at 400 X and 1000 X magnification in

Table 8.6. Brinell Hardness Values* of 2¼Cr-1Mo Specimens From Isothermal Transformation Study

Heat #	Carbon (wt.%)	Temp (°C)	Isothermal Hold Time (minutes) 30	45	60	90	120	180	300
VAR 56067	0.11	704	195	195;185	150	165;150	150;147	144	---
		732	163	183	137	149;162	149	142	138
ESR R0110	0.10	704	185	159;159	144	141;139	141;144	141	---
		732	203	176	154	141;157	142	143	139
VAR 55262	0.09	704	190	151;190	162	162;139	150;150	150	---
		732	208	196	170	153;172	172	158	136
VAR B9783	0.165	690	237	305	276;276	222;255	197	180	170
		704	294	250	225;222	165;167	156	162	156
		718	210	163	159;159	148;142	140	141	147
		732	216	180	163;161	155;153	152	144	141
VAR B9784	0.153	690	263	248	235;234	210;228	190	172	170
		704	245	213	182;178	162;165	159	159	153
		718	213	182	154;159	144;148	151	147	147
		732	183	182	180;160	154;157	156	142	140
VAR 91506	0.10	690	305	273	245;250	247;238	222	205	185
		704	293	260	225;222	198;210	195	167	154
		718	222	197	178;178	170;174	155	148	142
		732	174	169	154;150	144;146	140	139	132
ESR 9796	0.153	690	362	352	352;322	342;342	301	219	192
		704	347	305	268;283	235;240	205	165	163
		718	309	265	234;235	185;185	159	153	151
		732	372	269	239;228	169;174	177	154	146
ESR 9797	0.155	690	265	235	228;228	250;245	234	195	176
		704	313	290	262;257	228;228	182	169	160
		718	276	235	213;216	172;163	157	150	153
		732	311	266	205;245	188;175	159	145	145
ESR 91505	0.088	690	228	234	222;216	203;200	187	185	163
		704	205	195	185;190	185;185	160	157	151
		718	200	165	176;157	137;157	147	153	139
		732	196	185	159;176	158;176	155	144	135
Air Melt 113632	0.147	690	322	313	287;283	260;255	237	195	174
		704	273	237	210;219	180;180	165	159	154
		718	228	200	169;172	156;151	150	147	147
		732	275	220	173;212	161;212	152	153	144
Air Melt 279251	0.09	690	205	197	185;190	178;172	165	160	156
		704	182	169	159;156	160;162	157	151	144
		718	163	153	147;151	147;147	147	144	137
		732	161	157	145;149	150;149	146	143	143
Air Melt 5P4430	0.09	690	187	174	162;167	151;157	154	148	140
		704	163	156	153;150	153;150	150	142	141
		718	144	140	138;141	144;141	137	139	135
		732	140	151	149;139	138;139	135	134	139

*Value reported is the average of at least three measurements.

M3-33 Specification: Maximum Brinell 165 (R_B 85)

690°C = 1275°F; 704°C = 1300°F; 718°C = 1325°F; 732°C = 1350°F

Figures 8.6 to 8.14 for hold times of 60, 90, and 120 minutes at 704, 718, and 732C (1300, 1325, and 1350F). The brinell hardness versus isothermal hold time is shown in Figure 8.15 for 690, 704, 718 and 732C (1275, 1300, 1325, and 1250F) hold temperatures. Table 8.7 gives the product chemical composition for the twelve heats studied. These results will be used to determine the isothermal anneal treatment which will produce the best achievable microstructure for CRBR steam generator tubing in conjunction with continuous type furnace time limitations.

8.6 REFERENCES

1. G. J. Licina and J. F. Copeland, "A Review of 2¼Cr-1Mo Steel for Steam Generator Applications in the Clinch River Breeder Reactor," GEAP-20589 (August 1974).
2. "Task VI Final Report, Vol. 4, Steam Generator Development," NEDC-13655 (Oct. 1970).
3. J. L. Krankota and J. S. Armijo, "Decarburization Kinetics of Low Alloy Ferritic Steels in Sodium," *Met Trans.*, *3*, pp. 2515-2523, (Sept., 1972).
4. M. C. Rowland and D. E. Plumlee, "Sodium Mass Transfer: XXII - Metallurgical Examination of the Test Loops," GEAP-4838 (Oct. 1965).
5. J. M. Scott, *et. al.*, "Sodium Heated Steam Generator Model Tests at SGTR: Volume 1," GEAP-10580-1, (June 1972).
6. J. L. Krankota and J. S. Armijo, "The Kinetics of Decarburization of 2¼%Cr-1%Mo Steel in Sodium," *Nuc Tech.*, *24* (November 1974).
7. "Sodium Technology Program - Component Materials Compatibility," WARD-NA-3045-11 (August 1974).
8. D. E. Plumlee, R. W. Lockhart, and L. E. Pohl, "Sodium Mass Transfer: XVIII - Studies of Carbon Movement in Pumped Sodium Test Loops," GEAP-4834 (June 1965).
9. M. C. Rowland, *et. al.*, "Sodium Mass Transfer: XIX - Long-Term Exposure Effects in a Bimetallic Type 316 Stainless Steel - 2¼Cr Test Loop," GEAP 4835 (April 1965).
10. L. H. Kirschler, R. H. Hiltz, and S. J. Rodgers, MSAR 64-81 (July 1964).
11. L. H. Kirschler, R. H. Hiltz, and S. J. Rodgers, MSAR 69-42 (April 1969).

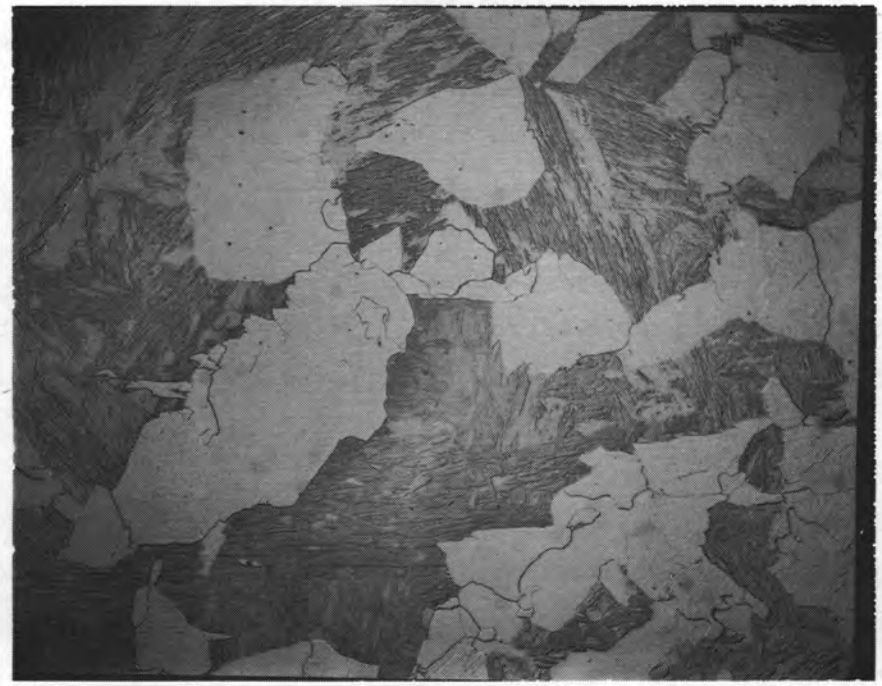

HEAT VAR 91506 – 60 min. AT 704°C (1300°F) 400X

HEAT VAR 91506 – 60 min. AT 704°C (1300°F) 1000X

Figure 8.6. Microstructure of Isothermally Annealed 2¼Cr-1Mo Steel at 704°C (1300°F) for 60 Minutes

HEAT VAR 91506 – 90 min.AT 704°C (1300°F) 400X

HEAT VAR 91506 – 90 min AT 704°C (1300°F) 1000X

Figure 8.7. Microstructure of Isothermally Annealed 2¼Cr-1Mo Steel at 704°C (1300°F) for 90 Minutes

HEAT VAR 91506 – 120 min AT 704°C (1300°F) 400X

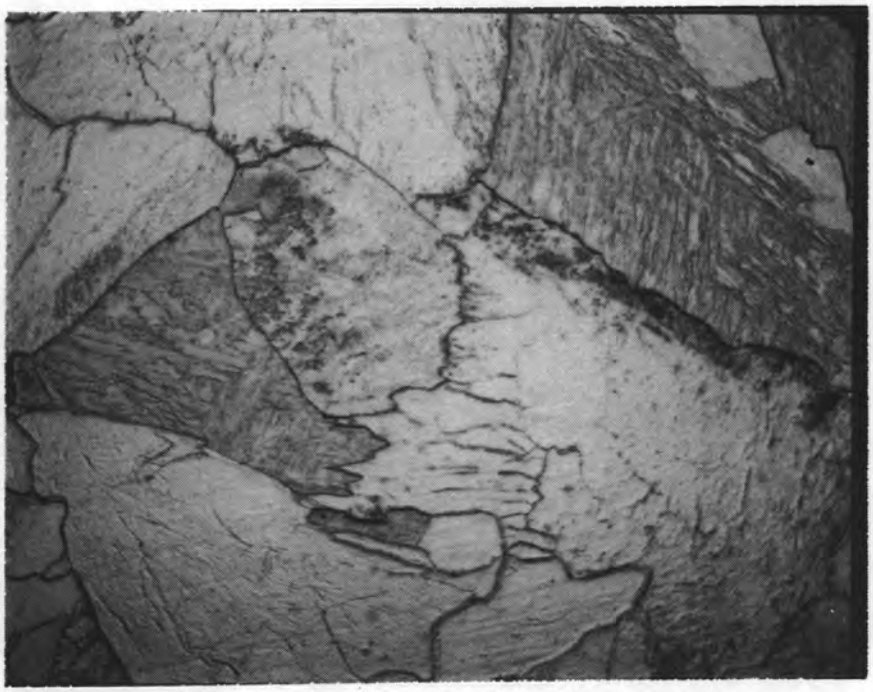

HEAT VAR 91506 – 120 min AT 704°C (1300°F) 1000X

Figure 8.8. Microstructure of Isothermally Annealed 2¼Cr-1Mo Steel at 704°C (1300°F) for 120 Minutes

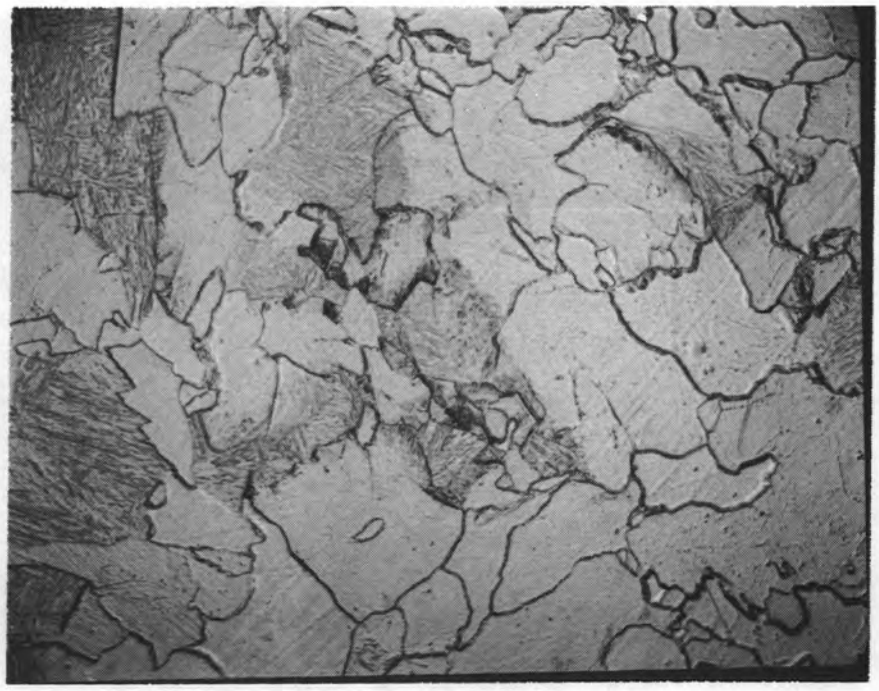

HEAT VAR 91506 – 60 min AT 718°C (1325°F) 400X

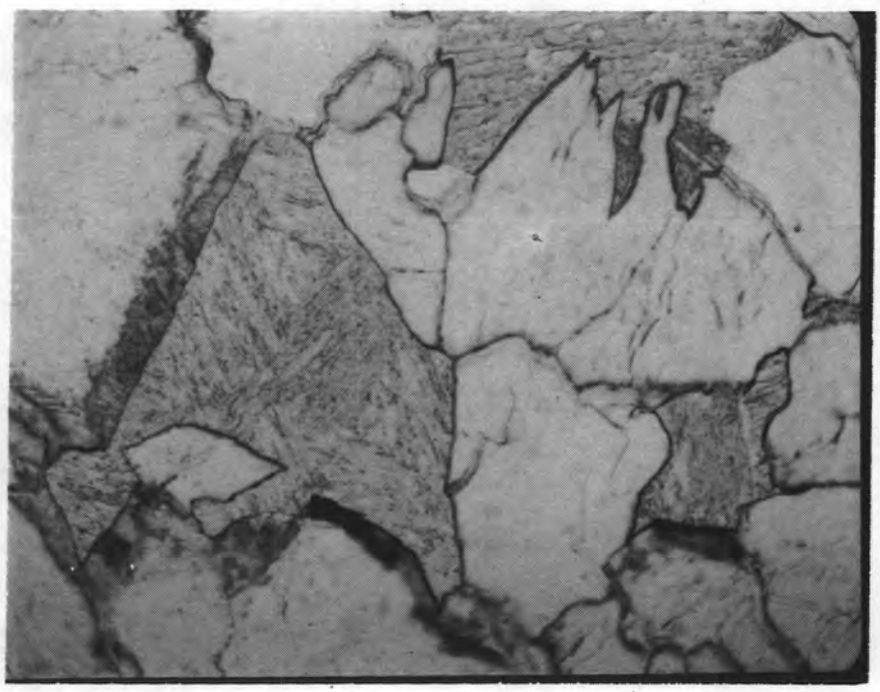

HEAT VAR 91506 – 60 min AT 718°C (1325°F) 1000X

Figure 8.9. Microstructure of Isothermally Annealed 2¼Cr-1Mo Steel at 718°C (1325°F) for 60 Minutes

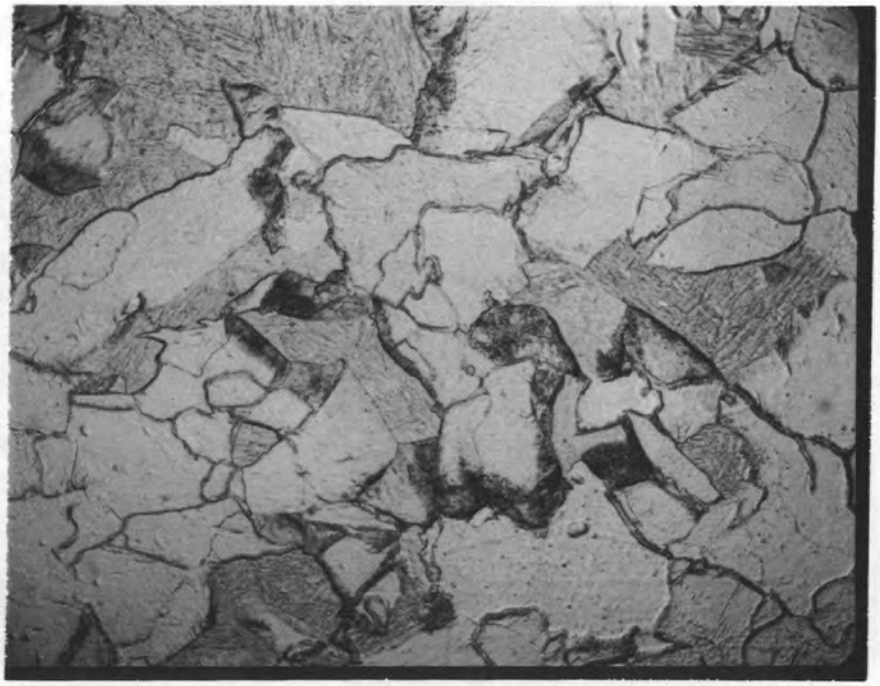

HEAT VAR 91506 – 90 min AT 718°C (1325°F) 400X

HEAT VAR 91506 – 90 min AT 718°C (1325°F) 1000X

Figure 8.10. Microstructure of Isothermally Annealed 2¼Cr-1Mo Steel at 718°C (1325°F) for 90 Minutes

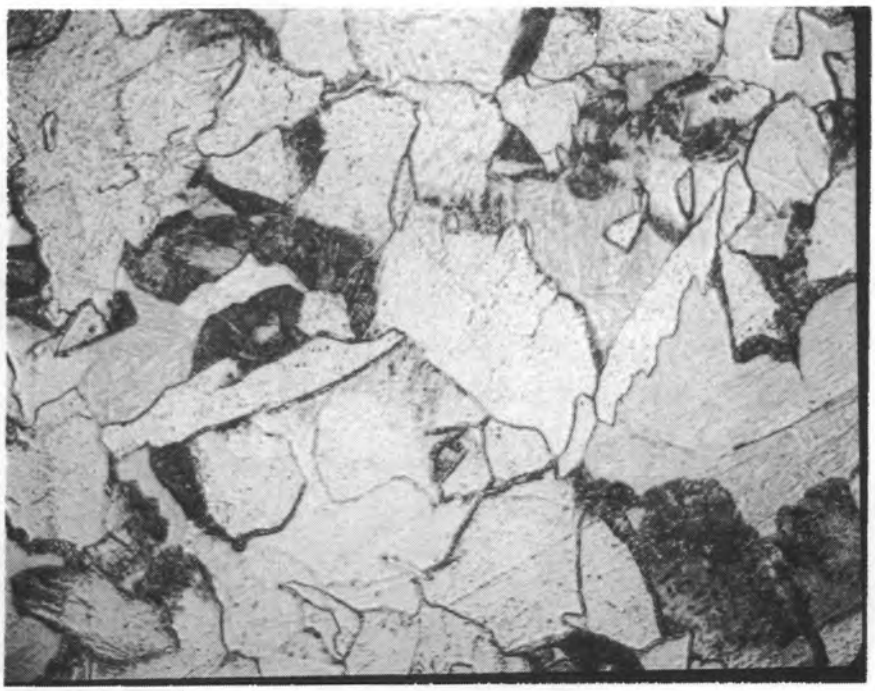

HEAT VAR 91506 – 120 min AT 718°C (1325°F) 400X

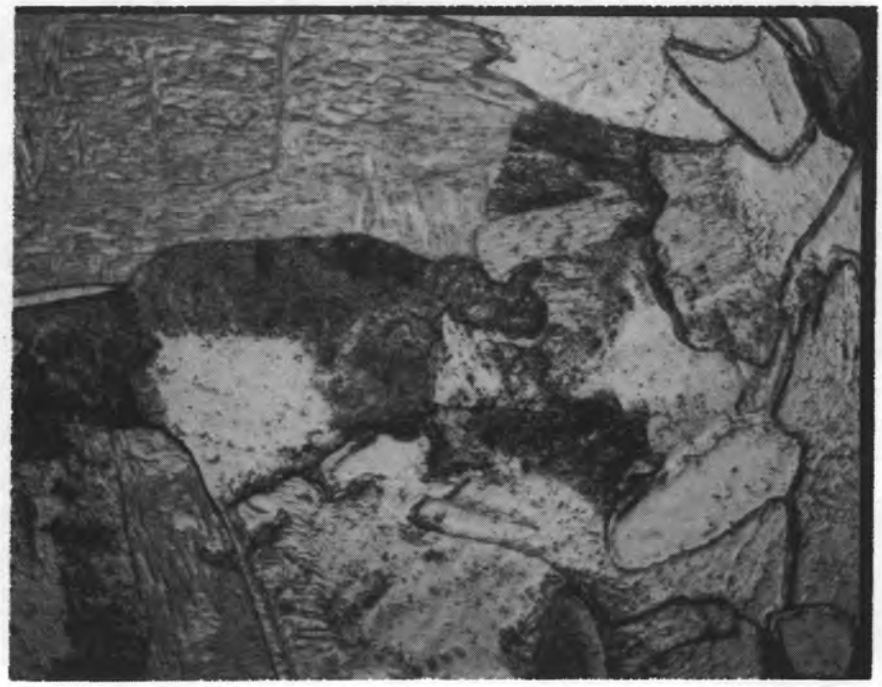

HEAT VAR 91506 – 120 min AT 718°C (1325°F) 1000X

Figure 8.11. Microstructure of Isothermally Annealed 2¼Cr-1Mo Steel at 718°C (1325°F) for 120 Minutes

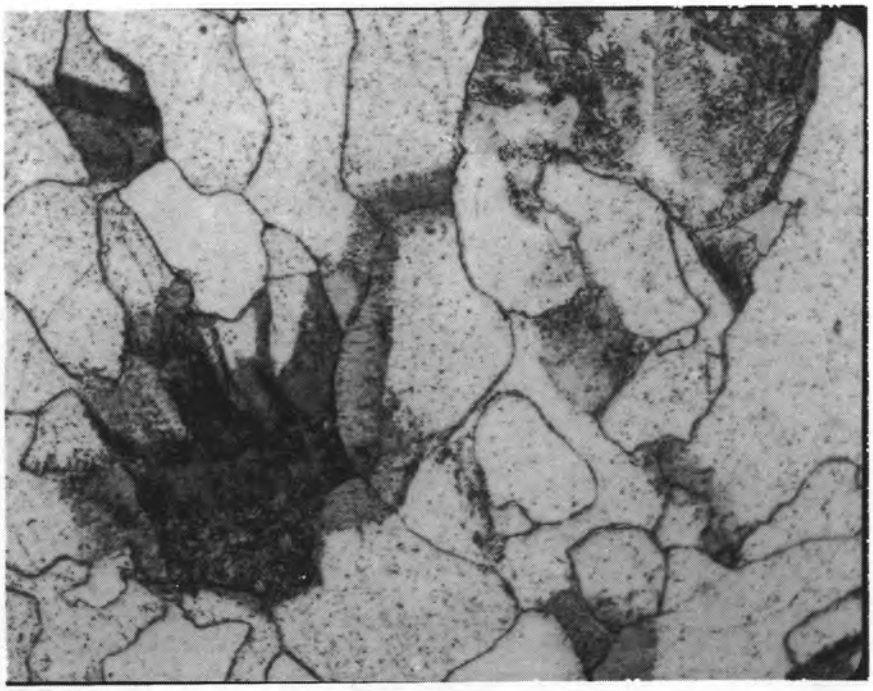

HEAT VAR 91506 – 60 min AT 732°C (1350°F) 400X

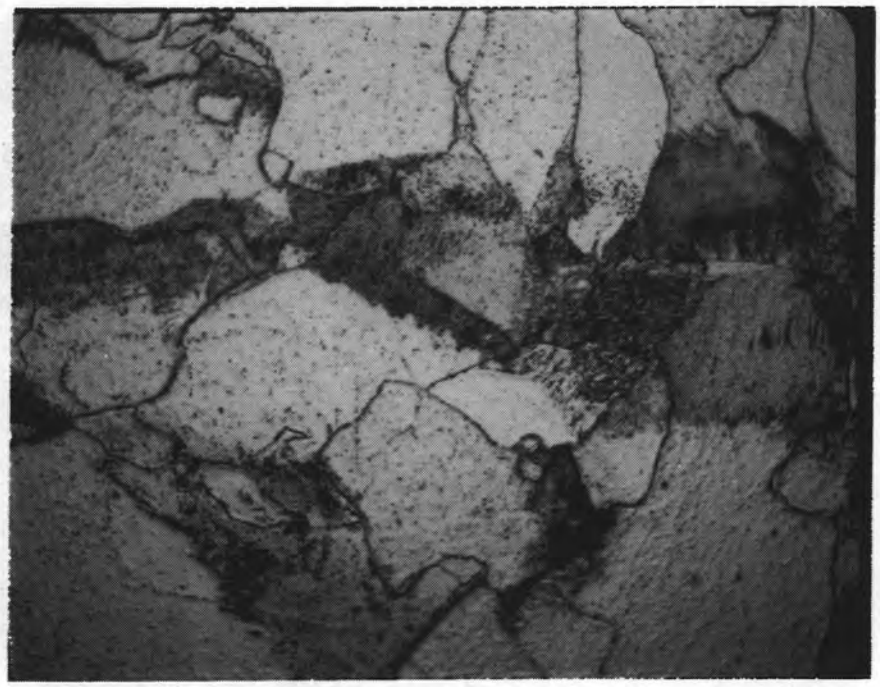

HEAT VAR 91506 – 60 min AT 732°C (1350°F) 1000X

Figure 8.12. Microstructure of Isothermally Annealed 2¼Cr-1Mo Steel at 732°C (1350°F) for 60 minutes

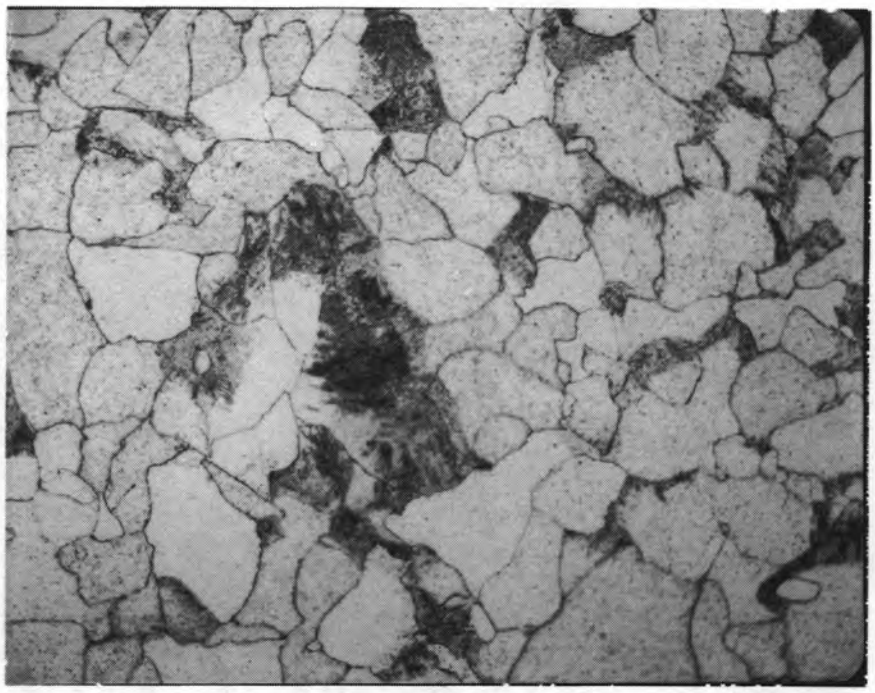

HEAT VAR 91506 – 90 min AT 732°C (1350°F) 400X

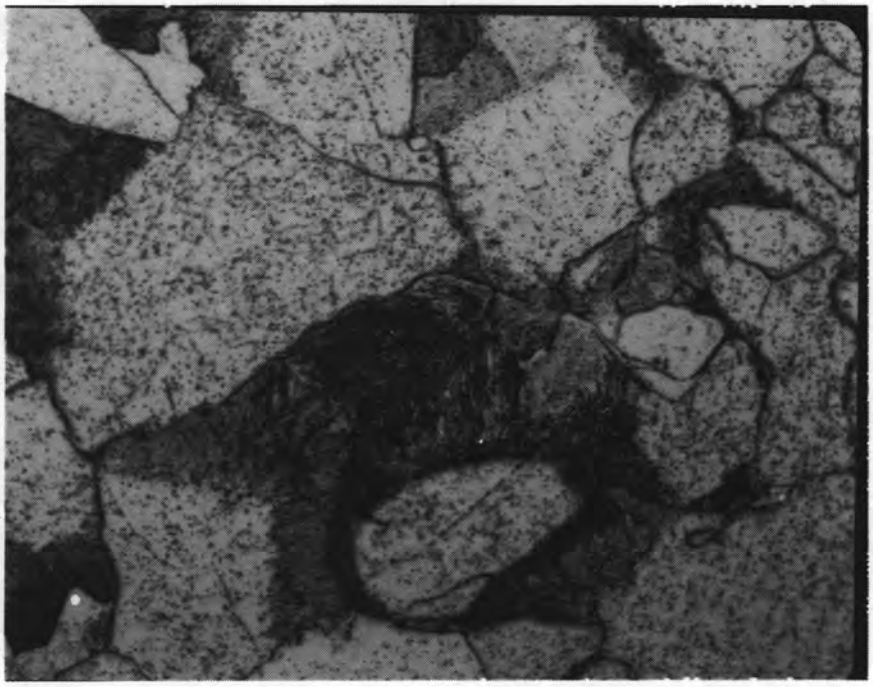

HEAT VAR 91506 – 90 min AT 732°C (1350°F) 1000X

Figure 8.13. Microstructure of Isothermally Annealed 2¼Cr-1Mo Steel at 732°C (1350°F) for 90 Minutes

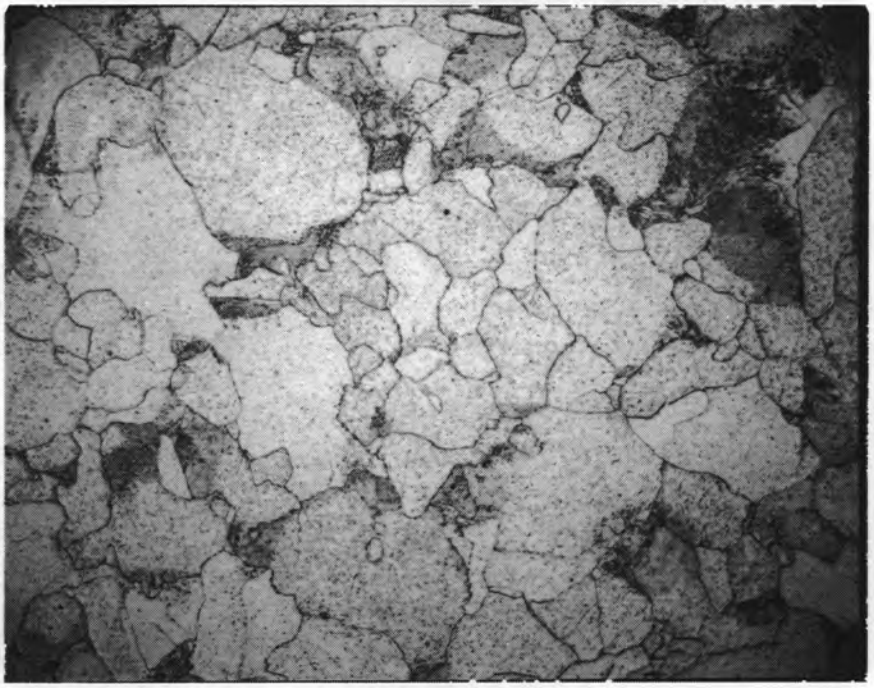

HEAT VAR 91506 – 120 min AT 732°C (1350°F) 400 X

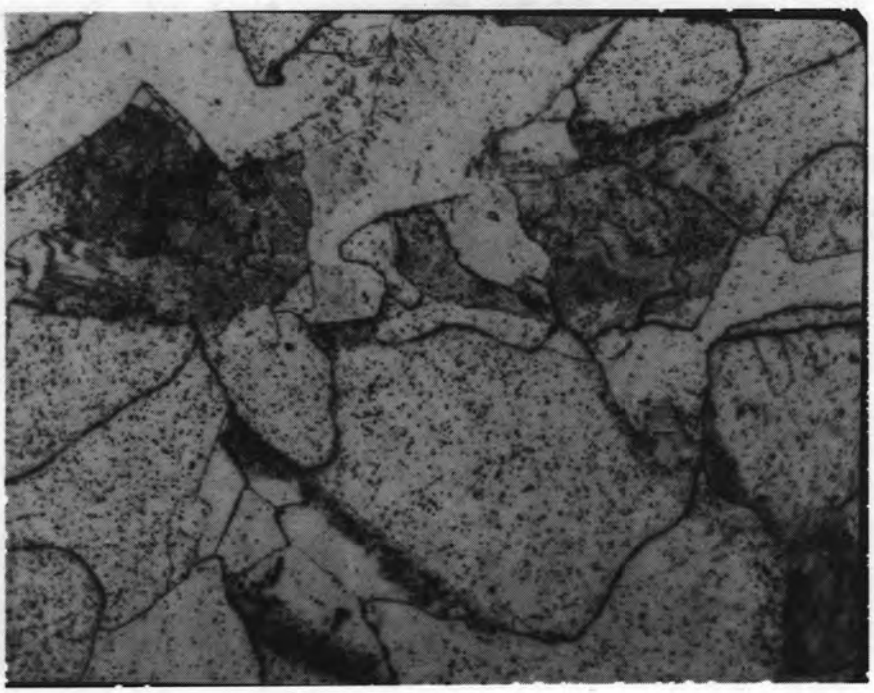

HEAT VAR 91506 – 120 min AT 732°C (1350°F) 1000X

Figure 8.14. Microstructure of Isothermally Annealed 2¼Cr-1Mo Steel at 732°C (1350°F) for 120 Minutes

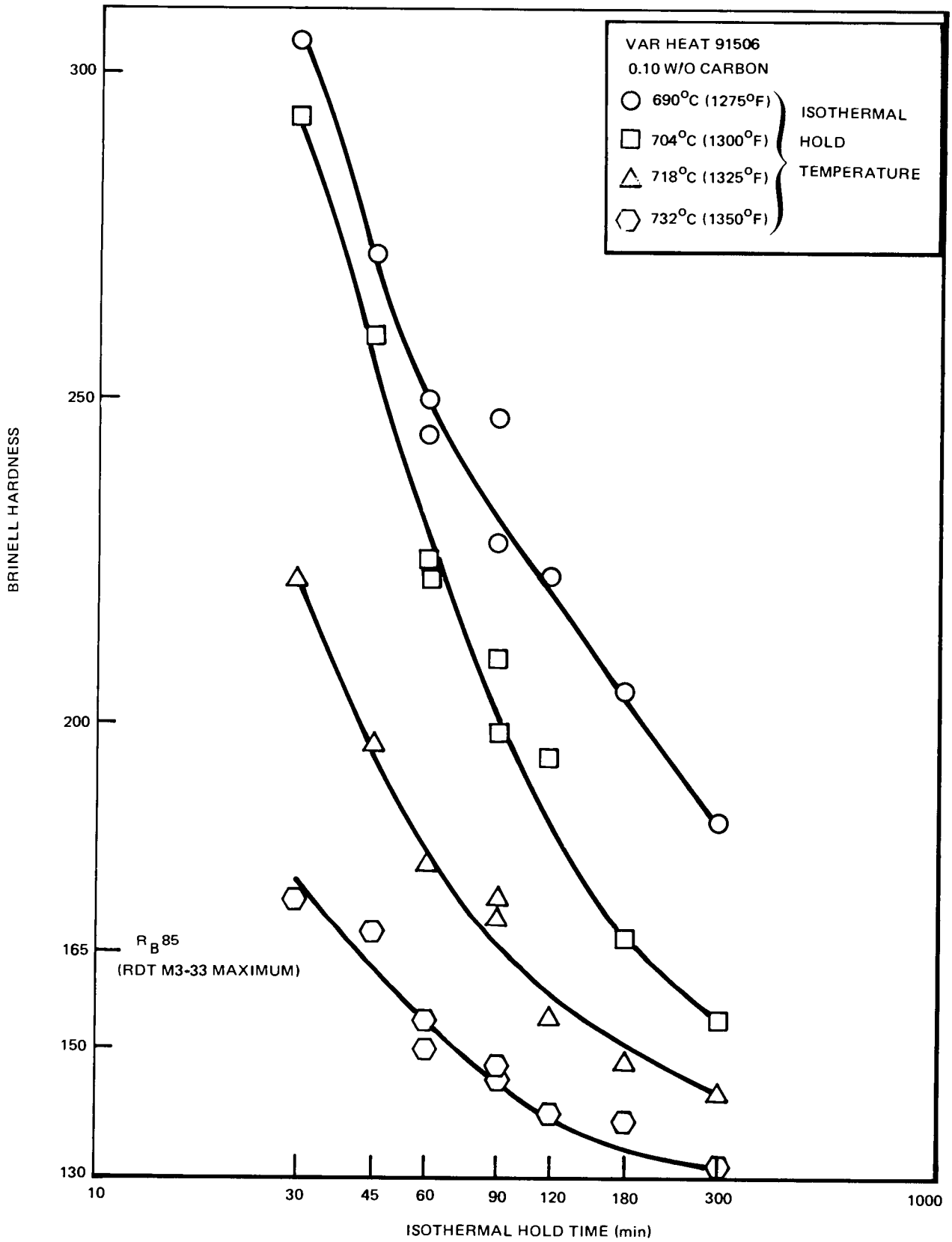

Figure 8.15. Isothermal Transformation for 2¼Cr-1Mo Steel, Vacuum-Arc Remelted Heat 91506

Table 8.7. Chemical Analysis of 2¼Cr-1Mo Steel for Isothermal Transformation Study

Heat Number	Al%	Sb%	As%	C%	Cr%	Co%	Cu%	H%	Mn%	Mo%	Ni%	N%	O%	P%	Si%	S%	Sn%	Ti%	V%
VAR 56067	0.005	<0.002	0.006	0.098	2.31	<0.002	0.08	0.0007	0.42	0.99	0.17	0.006	<0.001	0.010	0.28	0.015	<0.002	0.002	0.006
ESR R0110	0.027	<0.002	0.010	0.100	2.26	<0.002	0.10	0.0005	0.50	0.99	0.15	0.008	<0.001	0.013	0.09	0.007	<0.002	<0.002	0.013
VAR 55262	<0.005	<0.002	0.008	0.099	2.26	<0.002	0.09	0.0006	0.50	1.00	0.15	0.008	<0.001	0.013	0.07	0.016	0.004	<0.002	0.013
VAR B9783				0.165*	2.40				0.39	1.10			0.014	0.009	0.20	0.034*			
VAR B9784				0.153*	2.39				0.34	1.08			<0.005	0.013	0.21	0.025*			
VAR 91506				0.10	2.32		0.05		0.39	1.02	0.06			0.011	0.39	0.005			
ESR 9796				0.153*	2.44				0.47	1.09			0.008	0.009	0.14	0.016			
ESR 9797				0.155*	2.42				0.46	1.08			0.008	0.007	0.19	0.017			
ESR 91505				0.088	2.25		0.06		0.46	1.02	0.05			0.011	0.30	0.004			
Air Melt 279251				0.09	2.32				0.52	0.93				0.12	0.36	0.009			
Air Melt 5P4430				0.09	2.35				0.40	1.00				0.006	0.23	0.012			
RDT M2-19	Minimum			0.070	1.90				0.30	0.87					0.20				
RDT M3-33	Maximum			0.110	2.60		0.35		0.60	1.13	0.25			0.015	0.40	0.015		0.03	0.03

*Average Values

12. L. H. Kirschler, R. H. Hiltz, and S. J. Rodgers, MSAR 69-207 (October 1969).

13. L. Champeix and O. Konovaltschikoff, *Proceedings of the International Conference on Sodium Technology*, pp. 93-103, ANL-USAEC Report ANL-7520-Part 1, (Nov. 1968).

14. J. Sannier, *et al.*, *Report on BNES Conference on Corrosion and Effects of Environment on Materials Properties in Nuclear Systems*, pp. 137-147, London (July 1971).

15. G. Ilinchev, *CEMA Symposium of Atmoic Power Stations with Fast Reactors - Volume I (Obninsk)*, pp. 462-477, Joint Publications Research Service, Washington, D. C. (July 1969).

16. W. J. Anderson, G. J. Sheffield, and J. Birkle, NAA-SR-7544 (Nov. 1963).

17. L. H. Kirschler, R. H. Hiltz, and S. J. Rodgers, MSAR 72-286, (December 1972).

18. V. N. Bykov, *et al.*, "The Problems of Corrosion Resistance of Structural Materials in Sodium," *CEMA Symposium of Atmoic Power Stations with Fast Reactors (Obninsk) Volume I*, pp. 426-461 (July 1969) .

19. A. Thorley, B. Longson, and J. Prescott, "Effect of Exposure to Sodium on the Mechanical Properties and Structure of Some Ferritic, Austenitic and High Nickel Alloys," TRG Report 1909 C (1969).

20. D. W. Koch, P. J. Kovach, BAW-1280-37 (June, 1966).

21. S. Ohta, "2¼Cr-1Mo-Nb Steel: A New Steel for Steam Generator Tubes of Sodium Cooled Fast Breeder Reactors," Central Research Lab Kobe Steel. Ltd. (in Reactor Steels Studies in Japan UCLA-34 pp. 177-179).

22. J. Motz, *Zeit, Fur Metallkunde*, Vol. 55, pp. 489-494, (1964).

23. Nuclear Systems Materials Handbook, Decarburization of 2¼Cr-1Mo Steel (January 1975).

24. R. M. Curran and B. M. Wundt, "A Study of Low-Cycle Fatigue and Creep Interactions in Steels at Elevated Temperatures," to be published.

25. Steam Generator Materials Engineering - First Quarterly Report, GEAP 14029-1 (Oct. 1974).

26. Steam Generator Materials Engineering - Second Quarterly Report, GEAP 14029-2.

27. K. Natesan, *et. al.*, (ANL), Compatibility of Fe-2¼Cr-1Mo steel in Sodium Environment. To be published in Nuclear Technology.

28. T. Yukitoshi, *et. al.*, (Sumitomo, Ltd.), Comparison of Various Chromium-Molybdenum Low Alloy Steels for LMFBR Steam Generators. To be published in Nuclear Technology.

29. K. Matsumoto, *et. al.*, Carbon Transfer Behavior of Materials for LMFBR Steam Generators. To be published in Nuclear Technology.

30. Sixth Quarterly Report, Steam Generator Materials Engineering, October - December 1975, GEAP-14029-6, U.S. ERDA Contract AT(04-3)-893, Task 18, January 1976.

31 W. Charnock, J. E. Cordwell, J. R. Gwyther and Mr. R. Hobdell, CEGB Report #RD/B/N2980, October 1974.

32. "Program for the Development of Design Data - LMFBR Steam Generator Materials", prepared for the ERDA under contract AT(04-3)-893, Task 10-G and Task 18, July 16 & 17, 1975.

33. Fifth Quarterly Report, Steam Generator Materials Engineering, July - September 1975, GEAP-14029-5, U.S. ERDA Contract AT(04-3)-893, Task 18, October 1975.

34. L. A. James, "Effect of Thermal Aging Upon the Fatigue-Crack Propagation of Austenitic Stainless Steels", *Met. Trans.*, Vol. 5, Apr. 1974. pp. 831-838.

35. P. Shahinian, et al, "Fatigue Crack Growth in Type 316 Stainless Steel at High Temperature", *Trans. ASME*, Nov. 1971, pp. 976-980.

36. P. Marshall, "The Fatigue Behavior of Annealed AISI 316 Stainless Steel in Air and High Temperature Sodium: Review and Preliminary Results", Central Electricity Generating Board, Report RD/B/N 3236, November 1974.

37. L. A. James and R. L. Knecht, "Fatigue-Crack Propagation Behavior of Type 304 Stainless Steel in a Liquid Sodium Environment", *Met. Trans.*, Vol. 6A, January 1975, pp. 109-116.

38. A. S. Kobayoshi and W. L. Moss, "Stress Intensity Magnification Factors for Surface-Flawed Tension Plate and Notched Round Tension Bar", Fracture 1969, edited by P. C. Pratt, Chapman and Hall Ltd., London, 1969.

39. W. J. Clark, Jr., "Fracture Mechanics and Nondestructive Testing of Brittle Materials", *J. Engr. for Industry,* February 1972, pp. 291-298.

40. J. D. Landes and J. A. Begley, "Test Results from J-Integral Studies: An Attempt to Establish a J_{Ic} Testing Procedure", *Fracture Analysis, ASTM STP 560,* ASTM, 1974, pp. 170-186.

41. J. R. Rice, P. C. Paris, and J. G. Merkle, "Some Further Results of J-Integral Analysis and Estimates", *Progress in Flaw Growth and Fracture Toughness Testing, ASTM STP 536,* ASTM, 1973, pp. 231-245.

42. J. G. Merkle and H. T. Corten, "A J-Integral Analysis for the Compact Specimen, Considering Axial Force as Well as Bending Effects", Presented at the ASME Pressure Vessels and Piping Conference, Miami Beach, Fla., June 24-28, 1974 ASME Paper No. 74-PVP-33.

43. J. F. Copeland, "Influence of Sulfur Content on the Fracture Toughness Properties of 2¼ Percent Cr-1 Percent Mo Steel", Presented at the ASME Pressure Vessels and Piping Conference, San Francisco, June 1975, to be published in ASME J. of Pressure Vessel Technology.

44. Mechanical Properties Test Data for Structural Materials-Quarterly Progress Report Ending October 31, 1975. ORNL-5107.

APPENDIX 8.1

The relationship between cyclic life, assumed material fatigue crack propagation behavior, assumed applied stresses, and assumed initial crack size and geometry follows.

The fatigue crack growth law given by straight-line behavior in Figure 8.3 is of the form

$$\frac{da}{dN} = C_o \, \Delta K^n \qquad \text{Eq. 8.1}$$

where da/dN is the crack extension per cycle, ΔK is the applied stress intensity factor range, and C_o and n are constants.

The ASME Code curves for ferritic materials are shown on Figure 8.3 for the purpose of comparison with the austenitic stainless steels of the current study. It can be seen that crack growth rates for the austenitic steels are generally greater than for ferritic steels. Also, the equation representing the upper ASME Code line in Figure 8.3 may be used to approximate the current upper bound for austenitic stainless steel crack growth data. That equation is

$$\frac{da}{dN} = (0.3795 \times 10^{-9}) \, \Delta K^{3.726} \qquad \text{Eq. 8.2}$$

where da/dN is in in./cycle, and the ΔK units are ksi$\sqrt{\text{in}}$. This crack growth equation will, therefore, be employed to compute the cyclic life of a 12.7 mm. (0.5 in.) thick austenitic stainless steel pipe. Of course there are many necessary assumptions for such a calculation at this time, and this exercise is only meant to demonstrate the influence of certain assumptions on cyclic life. More specific data on initial flaw sizes (inspection limits), applied stresses, and environmental effects on the crack growth equation are required in order to make a more accurate prediction.

For a semi-elliptical surface flaw

$$\Delta K^2 = \frac{1.21\ a\ \pi\ \Delta\sigma^2}{Q} \qquad \text{Eq. 8.3}$$

where $\Delta\sigma$ is the applied stress range and

$$Q = \phi^2 - 0.212\ \left(\frac{\sigma}{\sigma_{ys}}\right)^2 \qquad \text{Eq. 8.4}$$

where ϕ is a complex flaw shape parameter (elliptic integral) and σ_{ys} is the material yield strength. According to Kobayashi[38] an additional factor to account for the finite thickness of the pipe should be applied to Eq. 8.3. This factor, combining the elastic (free front surface) and plastic (back surface plasticity) magnification factors, is about 1.8 in this case. Curvature effects are negligible for a large diameter pipe. Therefore, Eq. 8.3 becomes

$$\Delta K^2 = \frac{2.18\ a\ \pi\ \Delta\sigma^2}{Q} \qquad \text{Eq. 8.5}$$

This equation may be expressed, for convenience, as

$$\Delta K = \Delta\sigma\sqrt{Ma} \qquad \text{Eq. 8.6}$$

where, in this case

$$M = \frac{2.18\ \pi}{Q} \qquad \text{Eq. 8.7}$$

Substituting Eq. 8.6 into Eq. 8.1, integrating, and solving for N, the cyclic life, gives (for $n \neq 2$)

$$N = \frac{2}{(n-2)\ C_o M^{n/2}\ \Delta\sigma^n} \left[\frac{1}{a_i^{(n-2)/2}} - \frac{1}{a_f^{(n-2)/2}} \right] \qquad \text{Eq. 8.8}$$

where a_i and a_f are the initial and final crack depths, respectively.[39]

Eq. 8.8 will be solved for several illustrative cases using the assumed crack growth law of Eq. 8.2 and an assumed crack aspect ratio (length/depth) of 20/1. In all cases the final crack depth will be taken as, a_f = 12.7 mm. (0.5 in.), that to penetrate the pipe wall.

Case I.

a_i = 0.508 mm. (0.020 in.)

$\Delta\sigma$ = 275.8 MPa. (40 ksi.)

Solving:

N = 1,700 cycles

Case II.

a_i = 0.508 mm. (0.020 in.)

$\Delta\sigma$ = 137.9 MPa. (20 ksi.)

Solving:

N = 25,500 cycles

Case III.

a_i = 2.54 mm (0.10 in.)

$\Delta\sigma$ = 275.8 MPa. (40 ksi.)

Solving:

N = 340 cycles

Case IV.

a_i = 2.54 mm (0.10 in.)

$\Delta\sigma$ = 137.9 MPa. (20 ksi.)

Solving:

N = 5,080 cycles

Increasing da/dN by a factor of ten (shift up one decade on Figure 8.3) will decrease these cyclic lives by a factor of ten. Therefore, the importance of accurately assessing the crack growth equation, including any possible environmental degradation, is apparent.

APPENDIX 8.2

The relationship of crack opening displacement measurements to the determination of stable crack growth initiation for a Compact Tension fracture toughness specimen follows.

Case I:

Constant strain energy input rate to the test specimen: This is approximated when tests are performed on tension test machines where hydraulic fluid is compressed at a constant rate to apply an increasing strain energy, as with opening a manual valve a constant amount.

The equation for J-integral, J, from the area, A, under a load - load point displacement curve, P vs. Δp, and specimen thickness B is[40]

$$J = \frac{2\ A}{B\ (W-a)} \qquad \text{Eq. 8.9}$$

where W and a are defined in Figure 8.5. For the above case dA/dt, where t is time, is constant. Therefore, dividing by dt

$$\frac{dJ}{dt} = \frac{2dA/dt}{B\ (w-a)} \qquad \text{Eq. 8.10}$$

when B (W-a) is a constant. However, when crack growth occurs "W-a" will start to decrease. Therefore, if dA/dt remains constant, and B(W-a) is decreasing, dJ/dt must increase when slow crack growth occurs. The equations for J, as functions of the P vs. Δp curve are the following[41]

$$J = \frac{P\ \Delta\ p}{B(W-a)} \left[1 + 16\beta D_2^{\ 2} \left(\frac{P}{P_{lim}}\right)^2 \right] \qquad \text{Eq. 8.11}$$

for P < limit load, P_{lim}

and

$$J = \frac{P\ \Delta\ p}{B(W-a)} \left[2 - \frac{\Delta p,\ lim}{\Delta p} (1 - 16\beta D_2^{\ 2}) \right] \qquad \text{Eq. 8.12}$$

for P > limit load, P_{lim}

where β and D_2 are approximately constant and indicate the stress state.

It can be seen that Eq. 8.11 and 8.12 also include the term B(W-a) in the denominator. Thus, the influence of d[B(W-a)]/dt is also shown, in Eq. 8.11 and 8.12, on dJ/dt. However, an increase in crack length will also influence the specimen limit load properties. This effect will force a more rapid rate of Δp ($d\Delta p/dt$), since the limit load is being lowered as the crack grows. A more simplistic interpretation could be based on the equation relating the stress intensity factor, K, to the crack opening displacement, δ,

$$K^2 = \delta\ \sigma_{ys}\ E \qquad \text{Eq. 8.13}$$

where σ_{ys} is the yield strength and E is the elastic modulus. Since K^2 is directly proportional to J, any change in dJ/dt would also be shown in $\frac{dK^2}{dt}$, and thus in $d\delta/dt$. The term $d\delta/dt$ is related to $d\Delta p/dt$ by trigonometry,[42] and can thus be used as a test criterion for crack extension.

The above considerations have been successfully applied[43] to determine the onset of crack growth by monitoring $d\Delta p/dt$ or $d\Delta f/dt$. However, the method appears to be dependent upon the type test machine used (for constancy of dA/dt) and the sensitivity of the test specimen limit load properties to an increase in a/W ratio.

Case II:

Constant stroke control rate, $d\Delta p/dt$: This can be accurately controlled with a closed loop electro-hydraulic test system, and thus, is a favored method.

From Figure 8.5, which follows the teachings of Reference 44, the following equation relating Δp to δ can be derived.

$$\delta = \left[\frac{1 + \alpha}{W/C + \alpha - 1}\right] \Delta p \qquad \text{Eq. 8.14}$$

Dividing through by dt,

$$\frac{d\delta}{dt} = \left[\frac{1 + \alpha}{W/C + \alpha - 1}\right] \frac{d\Delta p}{dt} \qquad \text{Eq. 8.15}$$

With this test, $\frac{d\Delta p}{dt}$ is a constant (stroke rate control). Therefore, any change in $d\delta/dt$ will be effected by a change in the term in brackets, in Eq. 8.15, as the crack grows. The effect of crack extension on this term, and thus, on $d\delta/dt$, will be calculated as follows.

For a 50.8 mm (2 in.) thick Compact Tension Specimen with an initial crack length of a = 33 mm. (1.3 in.)

$$\frac{d\delta}{dt} = 0.228 \frac{d\Delta p}{dt} \qquad \text{Eq. 8.16}$$

When the crack is extended to a = 35.54 mm. (1.4 in.) by stable crack growth during the test

$$\frac{d\delta}{dt} = 0.190 \frac{d\Delta p}{dt} \qquad \text{Eq. 8.17}$$

Therefore, a decrease in the coefficient of 16.7% is achieved by extending the crack 2.54 mm. (0.1 in.). This should be reflected by a similar increase in $d\delta/dt$. Thus, by measuring the rate of opening at the crack tip, the initiation of slow crack extension should be detectable.

INDEX

Test	Material	Page
Creep Test Data		
Base-Line Data		
	type 304 SS welded plate	286, 288–302
	type 304 SS tube	302–336
	type 316 SS bar	288
	type 316 SS tube	337–347, 395–400
	16-8-2 weld metal	144–146
	Inconel 82 weld metal	182–186
	2 1/4 Cr-1 Mo weld metal	386–395
	2 1/4 Cr-1 Mo steel	386–395
Correlations		
	type 304 SS	40–48, 63–108
	type 316 SS	63–127
	2 1/4 Cr-1 Mo steel	148–158
Effect of Cycling		
	type 316 SS tube	395–400
	2 1/4 Cr-1 Mo tube	386–396
	2 1/4 Cr-1 Mo weld metal	386–395
Effect of Environment		
	2 1/4 Cr-1 Mo	189–191
	Hastelloy X	189–191
Effect of Hold Time		
	type 316 SS	395–400
Effect of Irradiation		
	type 16-8-2	245–259
Effect of Sodium Exposure		
	type 304 SS	40–48
	type 316 SS tube (carburizing)	395–400
	2 1/4 Cr-1 Mo weld metal	386–395
Microstructure Evaluation		
	AISI 330 SS	375–379
	A286 SS	379–380

Test	Material	Page
Elastic Constants		
Dynamic Measurements		
	type 316 SS	129–135
	Incoloy 800H	129–135
Fatigue-Creep Interaction		
	type 304 SS	3–34, 34–40
Fatigue Test Data		
Correlations		
	Incoloy 800	364–374
Crack Growth Rate		
Base-Line Data		
	Nimonic PE16	268–281
	type 316 SS plate, weld	395–400
	2 1/4 Cr-1 Mo	205–209
	Hastelloy X	209–211
Effect of Frequency		
	type 316 SS plate, weld	395–400
Effect of Hold Time		
	type 316 SS plate, weld	395–400
Effect of Stress Intensity Factor		
	type 316 SS plate, weld	395–400
Effect of Sodium Exposure		
	type 316 SS plate, weld	395–400
Cyclic Fatigue Test Data		
	type 304 SS	3–34, 48–50
Effect of Sodium Environment		
	type 304 SS	48–50
Life Prediction under Creep-Fatigue Conditions		34–40
Regression Analysis		
	type 304 SS	3–34
Cyclic Stress-Strain Behavior		
	2 1/4 Cr-1 Mo	164–175

Test	Material	Page
Fatigue Test Data (Continued)		
Data Analysis		
	2 1/4 Cr-1 Mo	158–164
	HTGR alloys	198–202
Effect of Hold Time		
	Hastelloy X	202–205
Effect of Sodium Environment		
	type 316 SS plate	347–360
Strain-Controlled Tests		
	Hastelloy X	192–197
Hardness Data		
	16-8-2 weld metal	138–140
Correlations		
	AISI 330 SS	381–382
	A286 SS	381–382
	type 316 SS, 20% cold worked	381–382
Isothermal Transformation		
	2 1/4 Cr-1 Mo	405–418
Microstructure		
	16-8-2 weld metal	135–139
Tensile Test Data		
Base-Line Data		
	type A286	232–235
	Inconel 718	260–267
	Inconel 82 weld metal	177–180
	Inconel 617	187–189
	16-8-2 weld metal	140–144
	2 1/4 Cr-1 Mo	402–405
Correlations		
	type 316 SS	55–91
	type 304 SS	63–91
Effect of Aging		
	type A286	241–244

Test	Material	Page
Tensile Test Data (Continued)		
Effect of Strain Rate		
	type A286	235–240
	2 1/4 Cr-1 Mo	147
Toughness		
Charpy V-Notch		
	2 1/4 Cr-1 Mo steel, weld	402–405
Drop Weight NDT		
	2 1/4 Cr-1 Mo steel	402–405
Dynamic Tear		
	type 308 SS weld deposits	223–229
J-Integral		
	Inconel 718	268–281
	Inconel X-750	268–281
	2 1/4 Cr-1 Mo steel, weld	402–405

ORNL-5150
UC-79b, -h, -k
(Liquid Metal Fast
Breeder Reactors)

INTERNAL DISTRIBUTION

1–2. Central Research Library
3. Document Reference Section
4–8. Laboratory Records Department
9. Laboratory Records, ORNL RC
10. ORNL Patent Office
11. R. J. Beaver
12. R. G. Berggren
13. J. J. Blass
14. M. K. Booker
15. C. R. Brinkman
16. D. A. Canonico
17. J. Corum
18. W. R. Corwin
19. F. L. Culler
20. J. E. Cunningham
21. J. H. DeVan
22. R. G. Donnelly
23. D. P. Edmonds
24. G. Fee
25. M. H. Fontana
26. W. R. Gall
27. B. L. Greenstreet
28. J. C. Griess, Jr.
29. J. P. Hammond
30. W. O. Harms
31. R. L. Heestand
32. R. F. Hibbs
33–35. M. R. Hill
36. D. O. Hobson
37. H. Inouye
38. P. R. Kasten
39. J. F. King
40. R. T. King
41. R. L. Klueh
42. K. C. Liu
43. C. T. Liu
44. A. L. Lotts
45–65. W. R. Martin
66. W. J. McAfee
67. H. E. McCoy
68. H. C. McCurdy
69. C. J. McHargue
70. J. Merkle
71. P. Patriarca
72. S. Peterson
73. H. Postma
74. C. E. Pugh
75. P. L. Rittenhouse
76. D. N. Robinson
77. T. Roche
78. J. L. Scott
79. Myrtleen Sheldon
80. V. K. Sikka
81. G. M. Slaughter
82. W. J. Stelzman
83. J. P. Strizak
84. R. W. Swindeman
85. D. B. Trauger
86. J. R. Weir, Jr.
87. G. D. Whitman
88. T. Yahr
89. Paul M. Brister (consultant)
90. John Moteff (consultant)
91. Hayne Palmour III (consultant)
92. J. W. Prados (consultant)
93. N. E. Promisel (consultant)
94. D. F. Stein (consultant)

EXTERNAL DISTRIBUTION

95–96. ERDA DIVISION OF NUCLEAR FUEL CYCLE AND PRODUCTION, Washington, DC 20545

Director

97–98. ERDA DIVISION OF REACTOR RESEARCH AND DEVELOPMENT, Washington, DC 20545

Director

99–100. ERDA OAK RIDGE OPERATIONS OFFICE, P.O. Box E, Oak Ridge, TN 37830

Research and Technical Support Division
Director, Reactor Division

101–354. ERDA TECHNICAL INFORMATION CENTER, Office of Information Services, P.O. Box 62, Oak Ridge, TN 37830

For distribution as shown in TID-4500 Distribution Category, UC-79b (Fuels and Materials Engineering Development); UC-79h (Structural Materials Design Engineering); UC-79k (Components)

☆ U.S. GOVERNMENT PRINTING OFFICE: 1976-748-189/362